UNIVERSITÄT BONN
Physikalisches Institut

Sensitivity of the ATLAS experiment in pp-collisions at a centre of mass energy of 14TeV at the LHC to a Higgs boson with large decay-width to invisible final states

von
Andreas Ludwig

Abstract: So far experimentally not ruled out, the stealthy Higgs scenario proposes a hidden scalar sector, to which only the Higgs has non-vanishing and possibly large couplings. Due to decays into the scalars the Higgs acquires a possibly large extra invisible width and thus can be hidden at colliders. We present a sensitivity study of the ATLAS experiment at the LHC for invisible decays of a Higgs boson produced in weak boson fusion, with the non-standard coupling being a free parameter. Signal hypotheses are generated for Higgs masses between 130 GeV and 800 GeV and for coupling strengths to the hidden scalars from 0.1 to the very large value of 25. The study using a detailed detector simulation assumes 30 fb^{-1} of data collected at $\sqrt{s} = 14$ TeV. An artificial neural network is designed, aiming to exploit adaptively shape differences in the input variables distributions and their correlations in order to allow for discrimination between the signal hypotheses and background. The uncertainty in the energy scale of reconstructed jets is found to be the major systematic uncertainty, limiting the sensitivity. For a Higgs mass larger than 200 GeV the exclusion of the stealthy Higgs model is found not to be feasible with 30 fb^{-1} of data. We estimate the value of the coupling, for which the canonical discovery channels for a heavier Higgs boson will need more than 30 fb^{-1} of ATLAS data.

Post address:
Nussallee 12
D-53115 Bonn
Germany

BONN-IR-2011-16
Bonn University
December 2011
ISSN-0172-8741

Angefertigt mit Genehmigung der Mathematisch-Naturwissenschaftlichen Fakultät der Rheinischen Friedrich-Wilhelms-Universität zu Bonn

Referent:	Prof. Dr. Michael Kobel
Korreferent:	Prof. Dr. Ian C. Brock
Tag der Promotion:	18.11.2011
Erscheinungsjahr:	2011

Diese Dissertation ist 2012 auf dem Hochschulschriftenserver der ULB Bonn unter
`http://hss.ulb.uni-bonn.de/diss_online` elektronisch publiziert.

Contents

1. Introduction

In the twentieth century the ancient speculative question what the nature of matter is, was first time tackled systematically by experiments, that used higher and higher energies to resolve the building blocks of matter on smaller and smaller scales. Since the late sixties of the last century subatomic particles copiously discovered in these experiments could be ordered in an elegant group theoretical approach which later due to its predictive successes and excellent resilience to experimental challenges was believed to be the standard model (SM) of particle physics. The SM not only devised a place for all observed subatomic particles in an analogue to the periodic table, but also successfully described the forces between these constituents of matter on these small scales.

In particular the SM model can explain the masses of particles by the so-called Higgs mechanism. The Higgs field vacuum expectation value provides a symmetry breaking in the electroweak sector of the model and gives mass to the observed particles. Also this mechanism predicts a remaining scalar field, the Higgs boson. Its mass however is not predicted and bounds on its mass can be theoretically be derived only indirectly. The Higgs boson, as the last predicted particle in the SM, is not discovered so far, though it is searched for almost 40 years in experiments.

This fact is usually explained by assuming that the Higgs boson mass is higher than the energy range of the experiments conducted. Therefore, the current and new particle collider experiments like the ones at the Large Hadron Collider (LHC) at CERN (Conseil Européenne pour la Recherche Nucléaire) in Geneva, aim to complete and verify the successful history of the SM with the exploration of the Higgs sector in an unprecedented high energy range. The LHC is designed to cover the complete energy range in which the mechanism of symmetry breaking has to take place. From the strong theoretical argument of finite probabilities in scattering amplitudes the scale of particles connected to symmetry breaking must be in the order of a TeV.

Experimentally the SM was successfully tested to a high degree without finding significant deviations that indicate physics beyond the SM. There is however the theoretical possibility to introduce alternative models of dynamical symmetry breaking that do not need Higgs bosons. These alternatives, which comprises physics beyond the SM, would be discovered likewise in this energy range of the new collider experiments, if realised in nature. This is often referred to as a no lose theorem [48], since either the Higgs mechanism or its alternatives can be verified.

However, there is a third possibility which spoils this win-win situation, namely that the Higgs boson escapes the experimental detection. With the Higgs sector still experimentally not explored, theoretically many extensions of the SM are thinkable, which lead to consequences for the Higgs detectability and search strategies. Some of them as the stealthy Higgs scenario pursue the very destructive ansatz to present mechanisms of hiding the Higgs. In this thesis we focus on the stealthy Higgs scenario, asking how would be the prospects to detect the Higgs at the LHC, if it was not only decaying to an invisible final state, but the invisible decay width becomes essentially a free parameter, too. Such a scenario could turn out to be quite a nightmare for the searchers.

In Chapter 2 we set the theoretical framework of the Higgs mechanism, list some existing constraints and give a review of extensions with focus on invisible decays that could influence the Higgs search strategies. The experimental setup and details on event reconstruction are described in Chapter 3 before we discuss in Chapter 4 the general picture of high energy collision events among which the invisible Higgs decays may be found. The developed strategy for the event selection is characterised in Chapter

5. Supplementary information is shifted to the appendices. Appendix A gives information about the study of various central jet vetoes in detailed detector description and Appendix B summarises the steps in optimisation of the multivariate classifier used in event selection. In Chapter 6 the most important sources of experimental systematic uncertainties and the impact on the result are estimated before the results of the sensitivity study are presented in Chapter 7. This work is concluded in Chapter 8 with the interpretation of the result in context of a stealthy Higgs model and previous or similar studies and a summary and outlook in Chapter 9. For reference, the publication of the OPAL search for a broad invisible Higgs at LEP, mostly done during this work, is included in Appendix C together with an attempt to interpret this results in an extra-dimensional model is given in Appendix D.

2. Fundamental theoretical concepts for invisible Higgs searches

In this chapter we want to portrait the motivation for complementing the exploration of the Higgs sector with searches for invisible Higgs boson decays. While – as we will see – in the SM the invisible Higgs decays play no role, they can be first hints on the existence of physics beyond the SM.

We start directly with briefly reminding the reader on the canonical description of the Higgs mechanism which does not favour invisible Higgs decays, before we start to discuss extensions of the basic mechanism. In this overview we thereby focus only on theoretical models that include the possibility of a sizable branching of the Higgs boson into undetectable final states. While we will only quote some key words and references for some of these models, we want to give more details on two models that additionally predict a large decay width even for a light Higgs boson, below the W boson pair threshold. The first is a model with Higgs graviscalar mixing in the context of presence of large extra dimensions and the second is the so-called stealthy Higgs model, where the existence of a hidden scalar sector interacting with the Higgs makes its decay width an effective free parameter. We argue that both models can lead to an unfavourable situation where the visible search channels will lose much of their discovery potential. Also these models have to be tested in order to answer whether the Higgs boson has escaped the earlier searches at the LEP and TeVatron collider experiments. We will finish this chapter with a short overview of the experimental status of searches for invisible Higgs decays.

2.1 The Higgs mechanism in the standard model

The standard model (SM) of particle physics is an experimentally so far unchallenged prediction [130] of the dynamics and particle content observed in the subatomic world. It uses the language of group theory which gives a beautiful representation of all particles found so far by the experiments, classifying them as vectorial bosonic states accounting for the force carriers or as chiral fermions as fundamental building blocks of matter.

With the exception of gravity, this model describes all particle interactions by local gauge groups, which symmetries mirror the symmetry of the Lagrangian under these gauge transformations. In this formalism the SM is contained in a direct product of groups $SU(3)_c \otimes SU(2)_{I_w} \otimes U(1)_Y$.

A non Abelian Lie group $\mathrm{SU(3)_c}$ generated by the colour charges c represents exchange particles of the strong force, formulated in the theory of quantum chromodynamics (QCD). The electroweak force is represented in the unbroken phase by the the weak isospin I_w group $SU(2)_{I_w}$ together with the Abelian group of $U(1)_Y$ given rise by the hypercharge Y.

The electroweak sector has to be completed by a complex Higgs doublet, from which a physical state, the Higgs boson, should be observable in the broken phase of the SM. While at the energy scale tested so far all particles predicted in the SM have been observed over the last 40 years, the Higgs boson is still the missing piece in the particle puzzle.

Today, a detailed description on the SM can be found copiously in the textbooks of particle physics, e.g. [87], at this place we want to restrict ourselves to the description of the symmetry breaking via the Higgs mechanism in the electroweak sector. A detailed survey of this topic can also be found in recent articles [62, 146].

2.1.1 Electroweak symmetry breaking

The electroweak interaction can be described by a so-called Yang Mills theory or quantum flavour dynamics (QFD). in an unified way by a $SU(2)_I \otimes U(1)_Y$ gauge group above a certain energy scale. But as we will see, the symmetry of this theory is spontaneously broken. In the broken phase the carriers of the weak force are the three physical weak vector bosons, W^+, W^- and Z^0 and the photon mediates the electromagnetic interaction.

The fermionic matter is divided into three families which are assigned a flavour quantum number. For example the Lagrangian of the first family, which comprises of the left handed electron neutrino doublet $\mathrm{L} := \binom{\nu_\mathrm{e}}{\mathrm{e}}_\mathrm{l}$ and the right handed electron $\mathrm{e_r}$ is given by

$$\begin{aligned} \mathscr{L}_{\mathrm{QFD}} &= \bar{\mathrm{e}} i\gamma^\mu \partial_\mu \mathrm{e} + \bar{\nu}_\mathrm{l} i\gamma^\mu \partial_\mu \nu_\mathrm{l} - \frac{1}{4}\mathrm{B}^{\mu\nu}\mathrm{B}_{\mu\nu} - \frac{1}{4}\vec{\mathrm{W}}^{\mu\nu}\vec{\mathrm{W}}_{\mu\nu} \\ &+ \bar{\mathrm{L}}\gamma^\mu g' \frac{Y}{2}\mathrm{B}_\mu \mathrm{L} + \bar{\mathrm{e}}_\mathrm{r}\gamma^\mu g' \frac{Y}{2}\mathrm{B}_\mu \mathrm{e}_\mathrm{r} + \bar{\mathrm{L}}\gamma^\mu g \frac{1}{2}\vec{\sigma}\vec{\mathrm{W}}_\mu L\,. \end{aligned} \tag{2.1}$$

One identifies the first four terms[1)] in Eq. 2.1 with the kinetic terms of propagating electron, neutrino and the gauge fields connected to the hypercharge, B_μ and the gauge field of the weak isospin group, W^j_μ (j = 1 to 3). To break down further the dynamics of the gauge fields one uses the following definition of the tensor fields, $\mathrm{B}_{\mu\nu} = \partial_\mu \mathrm{B}_\nu - \partial_\nu \mathrm{B}_\mu$ and $\vec{\mathrm{W}}_{\mu\nu} = \partial_\mu \vec{\mathrm{W}}_\nu - \partial_\nu \vec{\mathrm{W}}_\mu + ig\vec{\mathrm{W}}_\mu \times \vec{\mathrm{W}}_\nu$. Here, the last sum term expresses the self interaction of the gauge bosons. The remaining terms in Eq. 2.1 define the interaction of the fermions with the gauge fields. The fermions couple with a strength g' to the weak hypercharge fields B_μ and with a different coupling strength g to fields W^j_μ of the weak isospin group.

As a local gauge theory the Lagrangian has to be invariant under the local transformation of its states $\Psi \to \Psi' = S \circ \Psi$. Hence, the gauge fields in Eq. 2.1 have to be introduced into the theory to counter the additional terms from the covariant derivative, that occur in the Lagrangian if the local gauge is of the form $S \equiv SU(2)_I \otimes U(1)_Y$. The explicit form of this abstract rotation in $\chi(x_\mu)$ or $\alpha(x_\mu)$ as function of the covariant coordinates x_μ is

$$S = \exp(i\frac{1}{2}\hat{Y}g' \cdot \chi(x_\mu)) \times \exp(i\frac{1}{2}g\sum_{j=1}^{3}\alpha_j(x_\mu)\sigma_j)\,. \tag{2.2}$$

As one sees, the Pauli matrices σ_j are the generators of the $SU(2)_I$ part while the hypercharge oparator $\hat{Y}$ generates the Abelian part of the transformation.

It should be emphasised at this point that the demand of local gauge invariance forbids the introduction of explicit mass terms for the gauge bosons or the fermions, since those terms would spoil the invariance directly.

The electroweak gauge bosons combine to eigenstates under the electrical charge in the following way,

$$\mathrm{W}^\pm_\mu = \frac{1}{\sqrt{2}}(\mathrm{W}^1_\mu \mp \mathrm{iW}^2_\mu)\,. \tag{2.3}$$

And the mixing of the remaining B_μ with W^3_μ provides the uncharged mediators. Their mixing matrix is determined by the value of the Weinberg angle $\cos\theta_W$:

$$\begin{pmatrix}\mathrm{W}^3_\mu \\ \mathrm{B}_\mu\end{pmatrix} = \begin{pmatrix}\cos\theta_\mathrm{W} & \sin\theta_\mathrm{W} \\ -\sin\theta_\mathrm{W} & \cos\theta_\mathrm{W}\end{pmatrix}\begin{pmatrix}\mathrm{Z}_\mu \\ \mathrm{A}_\mu\end{pmatrix} \tag{2.4}$$

[1)] Many recent observations, e.g. of solar neutrino oscillations seen by the SNO experiment [15] confirm, that neutrino have a small mass and hence an off-diagonal mixing matrix for neutrinos and right-handed neutrinos ν_r have to be introduced. For that reason in a SM with neutrino masses Eq. 2.1 has to be expanded in principle by terms of the form $\bar{\nu_r} i\gamma^\mu \partial_\mu \nu_r$, which we decide to neglect here.

In relation to the gauge couplings the Weinberg angle is given by

$$\sin\theta_W = \frac{g'}{\sqrt{g^2+g'^2}} \text{ or } \cos\theta_W = \frac{g}{\sqrt{g^2+g'^2}}. \tag{2.5}$$

The theory with the mixing matrix given in 2.4 is consistent with the observed electromagnetic charge, if the following so-called Gell-Mann-Nishijima-relation holds true.

$$Q_{\text{el}} = \frac{Y}{2} + I_w^3 \tag{2.6}$$

In this relation, the electric charge is Q_{el} depending on hypercharge Y and the projected weak isospin, I_W^3. The elementary charge can be expressed as $e = g\sin\theta_W = g'\cos\theta_W$. The charged eigenstates W and the neutral Z boson have been discovered more than 20 years ago at CERN. Their mass has been experimentally determined quite accurately with $M_{\text{W}} = 80.4$ GeV and $M_{\text{Z}} = 91.2$ GeV [120]. The SM therefore has to explain these masses without introducing explicit mass terms of the form $\frac{1}{2}M_{\text{W}}^2\text{W}_\mu^+\text{W}^{-\mu}$ or $\frac{1}{2}M_{\text{Z}}^2\text{Z}_\mu\text{Z}^\mu$, which would spoil the symmetry.

A further complication for a theory describing massive gauge bosons is the fact that these will have a longitudinal degree of freedom additionally to the transverse polarisations. In high energetic W boson scattering (Fig. 2.1) these longitudinal component will lead even at Born level to a divergent s-wave amplitude. The divergence will inevitably violate unitarity at energies of approximately 1 TeV which of course is not physical.

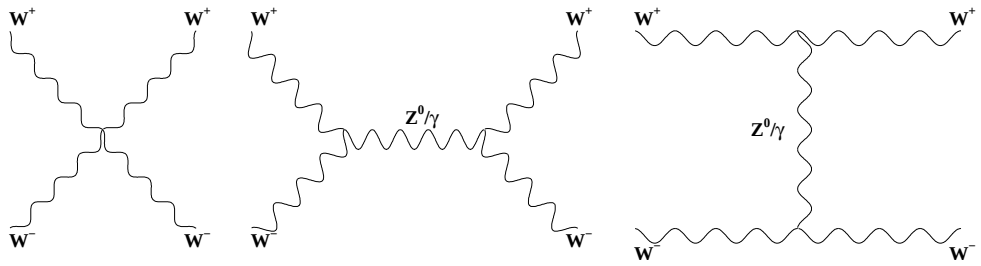

Fig. 2.1: *Leading order Feynman graphs for the longitudinal scattering of W-pairs. Such diagrams with a s-channel exchange of a Z boson or photon will lead to a divergent s-wave scattering amplitudes for energies of about 1 TeV.*

It is the great merit of Weinberg [151] and Salam [139] to have devised a consistent solution in 1967 for both problems within the SM, continuing ideas of Higgs and others [71, 90, 97, 98, 109] and also Glashow [83]. The problem of unitarity violation can be avoided, if one postulated the additional exchange of a scalar particle in the scattering. Such additional diagrams (Fig. 2.2) will exactly cancels the divergent ones.

At the same time the interaction of gauge bosons with a corresponding scalar field, called the Higgs field, provides an elegant mechanism to generate the gauge boson masses. The excitations of this scalar field provide the necessary scalar particles, dubbed Higgs bosons.

2.1.2 Generation of particle masses

The introduced Higgs field is ubiquitous with a non vanishing vacuum expectation value (vev). Therefore, if the terms for the Higgs field are added to complete the SM Lagrangian, the full $SU(2)_{I_w} \otimes U(1)_Y$ symmetry is preserved only for only one of the excited states, $\binom{0}{0}$. Since the vacuum expectation value of the Higgs is finite, the ground state is now distinguished, and exhibits a lower symmetry corresponding to a $U(1)_{\text{Q}_{\text{el}}}$ symmetry group. This reduction of symmetry by the Higgs vacuum expectation value is

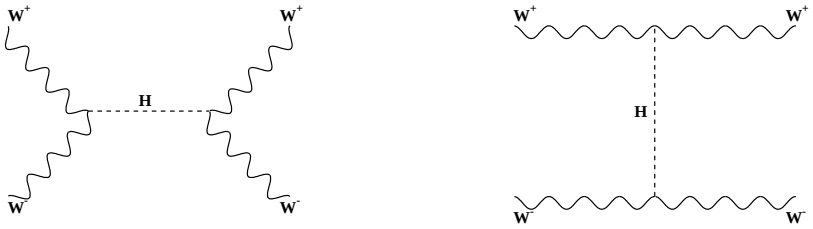

Fig. 2.2: *Tree level Feynman graphs with the Higgs boson exchange that compensate for the divergent longitudinal scattering modes and therefore, keep this scattering unitary.*

called spontaneous symmetry breaking. Formally it can be described by adding a complex doublet of elementary scalars together with an appropriate potential for these doublet fields to the Lagrangian. For the choice of the potential one has to comply with the following conditions.

1) In order to break $\mathrm{SU(2)_{I_W}} \otimes \mathrm{U(1)_Y}$, the scalar field has to carry non vanishing hypercharge and weak isospin. Then the scalar field automatically couples to the gauge fields. On the other hand $\mathrm{U(1)_{Q_{el}}}$ should remain an intact symmetry, since it can be identified with the group of quantum electrodynamics. Therefore, at least the component with non vanishing vacuum expectation value must carry $\mathrm{Q_{el}} = 0$, and thus has no couplings terms, in order to avoid breaking of that group.

2) All interaction terms especially the electromagnetic self interaction are confined to mass dimension 4 in order to keep the Lagrangian renormalisable.

3) The aim of the spontaneous symmetry breaking is to provide 3 longitudinal degrees of freedom for the vector boson. Therefore, the scalar field must have at least 3 degrees of freedom.

Thus, the minimal realisation of the scalar field Φ that fulfils all 3 conditions, is a complex doublet with 4 degrees of freedom. Each component possesses hypercharge and isospin:

$$\Phi = \begin{pmatrix} \Phi_3 + i\Phi_4 \\ \Phi_1 + i\Phi_2 \end{pmatrix} \quad \Phi_i \text{ real} \quad Y = 1,\ I_W = \frac{1}{2},\ I_W^3 = \pm\frac{1}{2} \tag{2.7}$$

The Lagrangian is extended by the following terms describing the Higgs boson dynamics:

$$\mathscr{L}_{\mathrm{Higgs}} = (D_\mu \Phi)^\dagger (D^\mu \Phi) - V(\Phi) \text{ with} \tag{2.8}$$

$$V(\Phi) = -\mu^2 \Phi^\dagger \Phi + \lambda (\Phi^\dagger \Phi)^2 \text{ with } \mu^2,\ \lambda > 0 \text{ and} \tag{2.9}$$

$$\mathrm{D}_\mu \Phi = (\partial_\mu - \frac{1}{2} i g \vec{\sigma} \vec{\mathrm{W}}_\mu - \frac{1}{2} i g' Y \mathrm{B}_\mu)\Phi \tag{2.10}$$

The specific choice of the Higgs mass parameter $\mu^2 > 0$, and the self coupling $\lambda > 0$ which guarantees a stable vacuum, results in the widely known Mexican hat potential shape. For two of the four components the potential is depicted in Fig. 2.3. Obviously, the whole potential is rotational invariant, but picking an arbitrary point on the minimum circle (e.g. position of the ball in Fig. 2.3), one recognises, that seen from this position the rotational invariance is lost. This represents a simple analogue to the spontaneously breaking of $\mathrm{SU(2)_{I_W}} \times \mathrm{U(1)_Y} \rightarrow \mathrm{U(1)_{Q_{el}}}$ if the system contains a ground state with

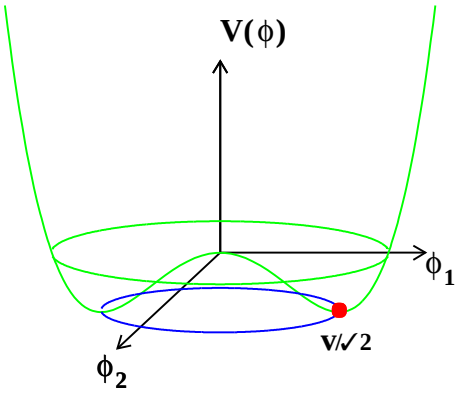

Fig. 2.3: *Visualisation of the Higgs potential projected in two degrees of freedom. Though overall rotational symmetric, the potential is not symmetric viewed from the position of the ball. The minimum is shifted away from the origin to a circle with the vacuum expectation value of* $\frac{246}{\sqrt{2}}$ GeV $= 174$ GeV*, which is remarkably nearly the top quark mass. The mass of the Goldstone bosons is proportional to the curvature i.e. the second derivative. Therefore, the Goldstone bosons oscillating along one of the (three) flat directions (in the picture along the circle) remain massless. Only the oscillation against the slope of the potential leads to a massive state, and the mass depends on the curvature of the Higgs potential.*

non vanishing vev. The minimum of the total Lagrangian where the potential is minimised, is reached under the condition

$$\Phi^\dagger\Phi = \frac{\mu^2}{2\lambda} \equiv \frac{v^2}{2}\,. \tag{2.11}$$

In this formula $v = \frac{\mu}{\sqrt{\lambda}}$ is the non zero vev. Its value follows from Fermi's constant $G_F = 1.167 \times 10^{-5}$ GeV^{-2} to be $v = (\sqrt{2}G_F)^{-1/2} = 246$ GeV.

Using the freedom to reparametrise the Lagrangian by a coordinate transformation into the minimum of the form $\Phi \to \frac{1}{\sqrt{2}}\binom{0}{v+H}$ then the oscillations of a physical state around the minimum are given by:

$$\Phi(x) = e^{i\vec{\pi}(x)\vec{\sigma}}\begin{pmatrix} 0 \\ \frac{v+\mathrm{H}(x)}{\sqrt{2}}. \end{pmatrix} \tag{2.12}$$

It is interesting to follow up what happened to the degrees of freedom during the reparametrisation. One identifies three of them, namely $\vec{\pi}(x)$, as the three Goldstone bosons [85][2)] , that have to occur since the global symmetry of the Lagrangian is broken. They are unphysical because they can be incorporated via an unitary gauge $U(\pi(x)) = e^{-i\vec{\pi}(x)\vec{\sigma}}$ as the longitudinal degrees of freedom for the gauge bosons. By this the gauge boson are no longer massless, in accordance with the experimental observation.

The remaining fourth degree of freedom $\mathrm{H}(x)$ becomes after the reparametrisation mass depending on the curvature of the potential and represents the physical Higgs boson. It has spin and charge parity numbers $\mathrm{J}^{\mathrm{CP}} = 0^{++}$ and carries also hypercharge $Y = 1$, and weak isospin $\mathrm{I}^3_{\mathrm{w}} = -\frac{1}{2}$ but no electrical charge, $\mathrm{Q}_{\mathrm{el}} = 0$.

Lastly, there are no explicit mass terms for the fermions. Instead so-called Yukawa couplings, λ_{f}, which couple both the left handed and right handed component of a fermion f to the Higgs field Φ are introduced by hand in such a way that they yield the physical masses observed for the fermions. For

[2)] *Goldstone's theorem* applies to broken continuous global symmetries. It states that whenever a global symmetry of the Lagrangian is not simultaneously the symmetry of the vacuum state, then for each generator of this symmetry which is not annihilating the vacuum state, a massless scalar or pseudoscalar, so called Goldstone bosons, with the same quantum numbers is present.

example for the first family the terms of Eq. 2.13 are completing the Lagrangian [3)]

$$\mathscr{L}_{\text{Yukawa}} = \lambda_e \bar{L} \Phi e_r + \lambda_u \bar{q} \tilde{\Phi} u_r + \lambda_d q \Phi d_r + h.c. \tag{2.13}$$

with $q = \binom{u}{d}_l$ and the charge conjugated Higgs field $\tilde{\Phi} = i\sigma_2 \Phi^*$, that is necessary to give mass to the quarks that carry the isospin $I_w^3 = +\frac{1}{2}$. This procedure can be regarded as arbitrary since the SM has no predictive power for particle masses.

In a common analogue the attractive interaction between particles and the ubiquitous Higgs field is compared to friction by which the slowed down particles acquire an effective mass proportional to v.

In the following, we summarise the effective mass terms that arise from the Higgs mechanism.

$$\begin{aligned} M_W &= v\,\frac{g}{2} \\ M_Z &= v\,\frac{\sqrt{g^2+g'^2}}{2} \\ m_f &= v\,\frac{\lambda_f}{\sqrt{2}} \\ M_H &= v\,\sqrt{2\lambda} = \sqrt{2}\mu \end{aligned} \tag{2.14}$$

The Higgs boson's couplings to the other particles are proportional to their masses, so the Higgs boson couples strongest to the weak bosons and the top and bottom quark. Using the vertices and the vertex factors present in the Weinberg-Salam theory, there are the following couplings to fermions and weak bosons ($V = W^{\pm}, Z^0$) and Higgs self couplings:

$$g_{Hf\bar{f}} = \frac{m_f}{v} \quad g_{HVV} = \frac{2M_V^2}{v} \quad g_{HHVV} = \frac{2M_V^2}{v^2} \quad g_{HHH} = \frac{3M_H^2}{v} \quad g_{HHHH} = \frac{3M_H^2}{v^2}.$$

Additional to the trilinear coupling one can derive from the Lagrangian , as we see, quartic couplings of type HHZZ, HHWW and HHHH. But there are no couplings at tree level to the massless photon as $HA_\mu A^\mu$ or $HHA_\mu A^\mu$. Thus the $H \to \gamma\gamma$ decay has to be mediated over quark loop diagrams and is therefore strongly suppressed.

Invisible Higgs and the SM

The possibilities for invisible decays of the Higgs boson within the SM are extremely disfavoured. The only possibility is over the decays into two Z bosons which subsequently decay both into neutrino pairs. But the branching ratio for a decay chain like $H \to ZZ \to \nu\bar{\nu}\nu\bar{\nu}$ is depending on the Higgs mass and anyway strongly reduced by the square of the branching of the Z boson into neutrinos. In most of the interesting cases it will be well below a percent.

As one sees, the properties of the Higgs boson are completely determined as soon as its mass, which is a free parameter of the SM, is known. As long as the Higgs mass remains unknown one has to describe its production and decay properties as function of its mass.

[3)] Finite neutrino masses were not expected in the original SM, but these can be easily introduced into Eq.2.13 via the Higgs mechanism and using the appropriate Yukawa couplings $\lambda_{/nu}$ for neutrinos. The most simple way is to introduce Dirac mass terms of form $m_D \bar{\nu_l} \nu_r + h.c$, between a right-handed neutrino ν_r and the adjoint spinor of the left-handed neutrino $\bar{\nu_l}$. If there exist a left-handed (ν_l) and a right-handed $(\nu_l)^C$ Majorana neutrino the relation $(\nu_l)^C = (\nu^C)_r$ holds true. In general explicit Majorana mass terms of form $\frac{1}{2} m_M (\bar{\nu}^C \nu + \bar{\nu} \nu^C$ can be present in models with lepton number violation. In such models the so-called see-saw mechanism [61] offers the theoretical explanation for the smallness of the neutrino masses.

Important Higgs production and decay modes at the LHC

For the intended sensitivity study at the LHC we compare the various production modes of the Higgs boson, which can be exploited in an invisible Higgs search. The cross section of the production mechanisms, namely weak boson fusion, weak boson associated production, gluon fusion and top associated production, as function of the Higgs mass are displayed in the left part of Fig. 2.5. The k-factors, which are defined as proportionality factor between NLO and LO cross section for gluon-fusion at the LHC at centre of mass energy of 14 TeV are as high as up to 200%. For weak boson fusion the k-factors are of the order of 5%. For W boson associated production, Z boson associated production and top quark pair asscociated the k-factors are of the order of 20% to 25% respectively. The Higgs is predicted to be produced at the LHC at the design centre of mass energy of 14 TeV abundantly by gluon gluon fusion processes mediated over a top quark loop. This is the production process with by far the highest cross section. This gluon fusion contributes, e.g. for $M_{\mathrm{H}} = 130$ GeV with $\sigma_{gg\to \mathrm{H}}$ =47.44 pb [58] about one order of magnitude more than the weak boson fusion. Though missing transverse energy from the invisible Higgs decay is present, this signature alone will not be sufficient considering the hadronic environment and other background sources of of missing energy in the detector to uniquely identify the event in such production mode. Unfortunately, only production channels with much lower cross sections are usable for identifying subsequent invisible Higgs decays in the hadronic environment of the LHC. These are (see leading-order diagrams in Fig. 2.4) the weak boson fusion and the weak boson associated Higgs production and the production of Higgs bosons accompanied by a pair of top quarks, since all these channels provide a topology that can be triggered in the detector.

Among these three production modes the weak boson fusion promises over a large mass range the highest cross section and experimental sensitivity. But one can see in Fig. 2.5, that for light Higgs boson masses the weak boson associated production mode still has a relatively high cross section. Therefore, by measuring the missing energy and identifying a leptonic decays of a weak boson in the event, searches in the weak boson associated production mode can contribute to the sensitivity for invisible decays of low mass Higgs bosons. Searches for invisible Higgs decays in the top quark associated production, try to identify the events by finding the two b-quark jets and one or two leptonic W boson decays from the $t \to b\mathrm{W}$ decays in the event. Also the searches require large missing energy. Experimentally in this channel it will be challenging to tag b-quark jets efficiently. Searches in the top quark associated Higgs production mode are expected to contribute to the sensitivity for invisible Higgs decays if the Higgs mass is lower than 200 GeV.

The decay modes as function of the Higgs mass in the SM are shown in the right part of Fig. 2.5. The hypothetical invisible Higgs decays (not shown in the graph since not relevant in the SM) would compete with the visible decay modes of the SM model. How much the rates of the visible SM decays are reduced depends on the beyond SM physics assumptions. The branching ratio of Higgs to invisible has of course large influence on the detectability of the signal.

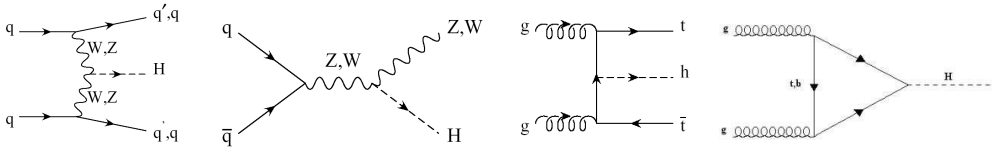

Fig. 2.4: *Leading order Feynman graphs expected for the production of the Higgs boson at the LHC. From left to right displayed are weak boson fusion, weak boson associated production, top associated production and finally gluon fusion production processes.*

To establish that the invisible decays stem from the Higgs and not another invisibly decaying particle one needs to confirm the observation in as much as possible production channnels in order to identify the

Higgs by its SM predicted ratios of abundance in the various production processes.

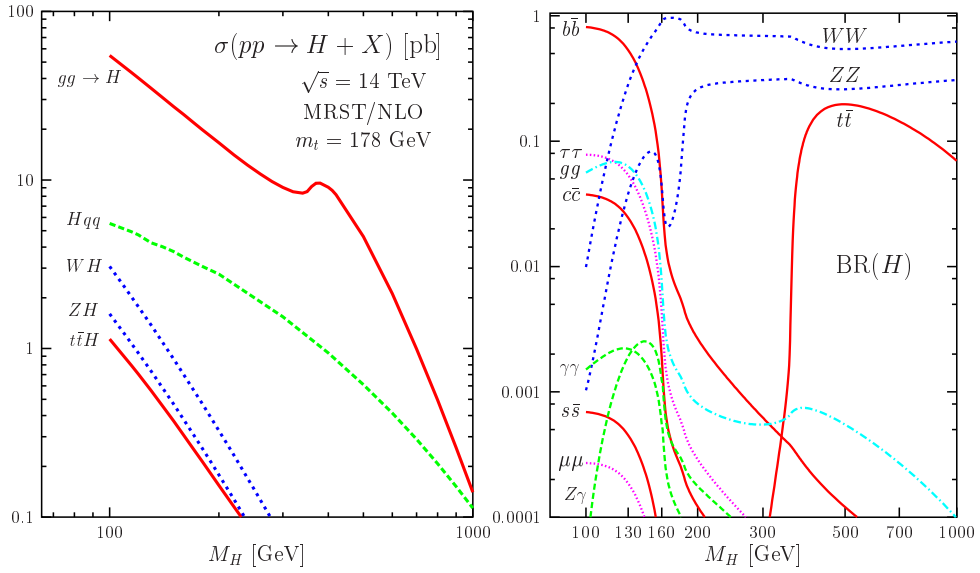

Fig. 2.5: *The mass dependence of the SM production cross section of the Higgs boson at a LHC centre of mass energy of 14 TeV (left) and the SM decays of the Higgs boson (right). Graph taken from [62].*

2.1.3 Theoretical constraints on the Higgs mass

Though the Higgs boson mass is not predicted by the SM, its value is not totally arbitrary, if the SM is believed to be a physical theory at least to some cut off scale Λ. In the following we give theoretical constraints.

1) **Unitarity**
Scattering probabilities of any process must not exceed unity. Therefore, the requirement of unitarity is equivalent to $\mathscr{R}e(\mathscr{A}_S) \leq 1/2$ in the s-wave amplitude. For example in the weak boson scattering (Fig. 2.1) this yields $\mathscr{A}_S = -\frac{G_F m_H^2}{4\sqrt{2}\pi}$. One estimates as upper value for the Higgs mass

$$m_H^2 \leq \frac{2\sqrt{2}\pi}{G_F} \approx (850\ \ \mathrm{GeV}/c)^2\,. \tag{2.15}$$

If the Higgs is heavier than that value, its regularisation of the amplitude will become effective only after unitarity violation since the heavy Higgs is decoupled in the scattering. The mechanism of regularisation of the amplitudes works always, if there are any counterbalancing scalar loops present. The cancellation of divergent graphs is not depending on the specific mass of the scalar in the loop. Therefore, we cannot derive a prediction on a lower value of the Higgs mass, from the requirement of unitarity.

2) **Triviality bound**
The value of the Higgs self coupling λ (corresponding to the left graph of quartic Higgs interaction in Fig.2.6) is subject to perturbative corrections. Neglecting for a moment loop contributions from the top quarks, the evolution of the Higgs self coupling with the energy scale Q is described by its renormalisation group equation (RGE) [62].

$$\frac{\mathrm{d}}{\mathrm{d}\log(Q^2/v^2)}\,\lambda(Q^2) = \frac{3}{4\pi^2}\,\lambda^2(Q^2) + \text{higher orders}\,. \tag{2.16}$$

With the reference scale set to v, what appears to be the natural scale of electroweak physics, the solution at one–loop is given by

$$\lambda(Q^2) = \lambda(v^2)\left[1 - \frac{3}{4\pi^2}\lambda(v^2)\log\frac{Q^2}{v^2}\right]^{-1}. \tag{2.17}$$

The Higgs self coupling varies logarithmically with the squared energy Q^2. One can analyse first the case where this equation is evaluated far below the electroweak scale. In the limit $Q^2 \to 0$, the self coupling of the Higgs approaches from above zero, staying positive definite

$$\lambda(Q^2) \sim \frac{\lambda(v^2)}{\log(\infty)} \to 0_+ .$$

But for the vanishing coupling, there is no interaction, which is called a trivial theory and the Higgs would be massless. Obviously a trivial theory will not be suitable to describe the Higgs mechanism in nature.

3) **Landau pole**
For rising centre of mass energies the graph in the middle of Fig.2.6 is responsible for driving λ and by that the mass of the Higgs to the highest physical scales, which is the Planck mass ($\mathcal{O}(10^{19}$ GeV)). This divergent behaviour in the evolution equations for λ is called a Landau pole. From a practical point of view one often demands from an effective physical theory to be free of Landau poles only up to a cut-off energy scale Λ_C.

Hence, varying to values far above the electroweak scale ($Q^2 \to \infty$) yields a situation where the coupling becomes, in logarithmic increase though, infinite. By the requirement that up to a given Λ_C the coupling keeps finite, i.e. $\frac{1}{\lambda(\Lambda_C)} > 0$ we find an upper bound on the Higgs mass to be $\mathrm{M_H}^2 < \frac{8\pi^2 v^2}{3\log\Lambda_C^2/v^2}$.

4) **Stability of the vacuum state**
There has to be a stable vacuum for the electroweak sector. Hence, for any evolution scale Q^2 the positiveness of the coupling $\lambda > 0$ has to be preserved in Eq. 2.8 of the Higgs potential. So far we argued considering only Higgs loop contributions but at least the Yukawa couplings of the top quark, which are of the order of 1, play an important role in the one loop corrections to λ (right graph of Fig.2.6).

In [62] we find the corresponding expression

$$\frac{\mathrm{d}\lambda}{\mathrm{d}\log(Q^2/v^2)} \simeq \frac{1}{16\pi^2}\left[12\lambda^2 + 6\lambda\lambda_t^2 - 3\lambda_t^4 - \frac{3}{2}\lambda(3g'^2 + g^2) + \frac{3}{16}\left(2g'^4 + (g'^2 + g^2)^2\right)\right], \tag{2.18}$$

where the top quark Yukawa coupling is given by $\lambda_t = \sqrt{2}m_t/v$ and calculation results depend much on the experimental uncertainty of m_t. If we are interested to make a statement on vacuum stability we have to evaluate the Eq. 2.18 in case of a small self-coupling λ, i.e. a light Higgs boson. For λ much smaller than λ_t, g, g', the RGE simplifies to

$$\frac{\mathrm{d}\lambda}{\mathrm{d}\log(Q^2/v^2)} \simeq \frac{1}{16\pi^2}\left[12\lambda^2 - 12\frac{m_t^4}{v^4} + \frac{3}{16}\left(2g'^4 + (g'^2 + g^2)^2\right)\right] \tag{2.19}$$

and the solution [62], taking again the weak scale, $Q^2 = v^2$, as the reference point, where the Higgs potential $V(v)$ is minimal, is

$$\lambda(Q^2) = \lambda(v^2) + \frac{1}{16\pi^2}\left[-12\frac{m_t^4}{v^4} + \frac{3}{16}\left(2g'^4 + (g'^2 + g^2)^2\right)\right]\log\frac{Q^2}{v^2}. \tag{2.20}$$

If the coupling λ is too small, the top quark contribution can be dominant and could drive it to a negative value $\lambda(Q^2) < 0$. But if scalar potential becomes $V(Q^2) < V(v)$ by radiation corrections, the vacuum is not stable anymore, since it has no minimum. Therefore, one gets a lower bound on the Higgs boson mass. It should be larger than the value

$$M_H^2 > \frac{v^2}{8\pi^2}\left[-12\frac{m_t^4}{v^4} + \frac{3}{16}\left(2g'^4 + (g'^2+g^2)^2\right)\right]\log\frac{Q^2}{v^2}\,. \tag{2.21}$$

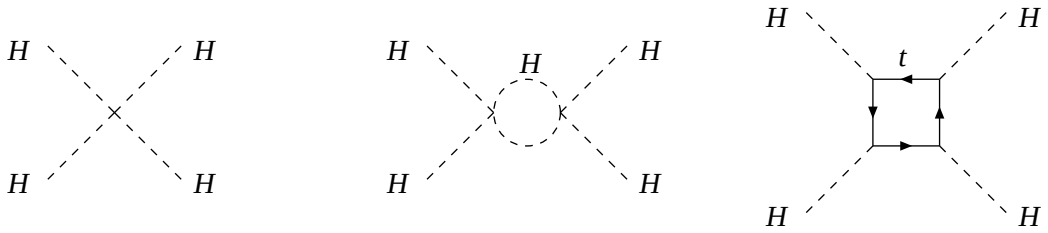

Fig. 2.6: *Tree level Feynman graph of the Higgs quartic coupling λ (left graph) and its most important radiative corrections (middle and right graph).*

If one combines the demand of vacuum stability and a non trivial theory free of a Landau pole, the strongest restriction on the Higgs mass will occur, if one postulates the validity of the SM up to the Planck scale. In this case one would expect to find the Higgs in the mass range between 130 GeV and 190 GeV. In Fig. 2.7 are shown the theoretical bounds as they follow from the evolution of λ. the calculations were performed with $m_{\text{top}} = 175$ GeV. If the SM is valid only up to 1 TeV, the Higgs mass should be somewhat between 50 GeV and 800 GeV. With other words the observation of a Higgs boson with 400 GeV would be consistent with a scale of new physics within the theoretical errors at about 10 TeV to 100 TeV.

2.1.4 Hints on the Higgs mass from electroweak precision measurements

Apart from these strictly theoretical arguments for the restriction of the Higgs boson mass, indirect observations have been made. First of all these are the electroweak precision measurements. Though several experiments contributed to a variety of precise known observables, the huge amount of data collected by the LEP experiments has the largest impact on the precision of most of the electroweak observables at the Z-pole e.g. the vector boson's mass and width or partial width ratios or forward backward asymmetries, A_{FB}[4] , or contributions of (hadronic) vacuum polarisation to the electroweak coupling, or hadronic cross sections and many more. At the SLD experiment the left right asymmetries, A_{LR}[5] , could be measured at the Z-pole directly and very precise [131], since a highly polarised electron beam of the SLC accelerator collided with unpolarised positrons. LEP data together with other SLD measurement and TeVatron experiments contribute to the data with high momentum transfer Q^2 [6] , which can be at LEP of order of several hundreds to thousands GeV^2. Details on the fitted data is found in the review article about electroweak precision data in [120].Assuming only SM physics the SM parameters can be fitted for the best agreement with the observables. As an example how sensitive such observables are, we take the very well measured masses and widths of the weak bosons. These values can be predicted from corrections of the weak bosons propagator. Both, the Higgs and the top quark contribute to radiative corrections to the weak bosons propagators on loop level. If the calculations to

[4] One defines the leptonic asymmetry in the final state as $A_{FB} = \frac{\sigma_F - \sigma_B}{\sigma_F + \sigma_B}$, with $\sigma_F(\sigma_B)$ being the cross section of the l^- travelling forward (backward) with respect to the e^-.

[5] With $\sigma_R(\sigma_L)$ being the cross section of the incident right(left)-handed electron one defines $A_{LR} = \frac{\sigma_R - \sigma_L}{\sigma_R + \sigma_L}$

[6] In terms of the azimuthal scattering angle θ and the Mandelstamm variables one can approximate $Q^2 = t \approx -\frac{s(1-\cos\theta)}{2}$.

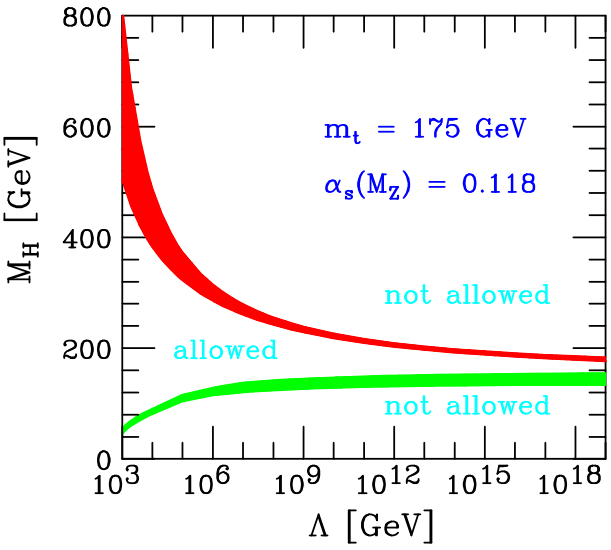

Fig. 2.7: *Constraints on the Higgs mass following from the energy scale Λ at which the perturbative description of electroweak interaction in the SM is assumed to break down. Higgs masses in the range between the lower and upper band are allowed. The width of the bands accounts for their theoretical uncertainty. The evolution in energy of the Higgs self-coupling under the constraint of positive definiteness including top quark loop contributions yields the lower contour. It therefore depends also on the knowledge of the top quark mass. The upper contour follows from the condition that no Landau pole occurs in the evolution below the scale Λ. (taken from [132])*

loop level are known, the precision of the top quark mass measurement is good enough to search the best compatible Higgs mass value and its uncertainties in a fit to data. Though the sensitivity is limited by the fact that the radiative corrections by the top quark loops are a function of m^2_{top} and thus much larger than the only weak logarithmic dependence from the Higgs mass in the loop, $\log(M_{\text{H}})$. The limits on the Higgs mass derived from such fits may differ considerably by some factor from the real value, once it is known, due to the only logarithmic dependence.

There exists also a number of observables from experiments like E158 and NuTeV(E815) at SLAC and others in the low Q^2 realm. Such data consist e.g. of precision measurements of Møller scattering by E158 [23], where in average the momentum transfer was $Q^2 = 0.026\ \text{GeV}^2$. At the NuteV experiment [152] where muon neutrinos of energy were deep inelastically scattered at nucleons, low values down to $Q^2 \lesssim 1\ \text{GeV}^2$ could be probed. Other low Q^2 data from atomic parity violation or polarised deep inelastic scattering experiments is also used in the fits [120]. The fit to the low Q^2 data is shown separately since it prefers to be consistent with slightly higher Higgs masses as one sees in the distinct area in Fig.2.8. The central (red) ellipse in Fig.2.8 gives the 90% CL contour that is compatible with low and high Q^2 data. A larger part of this contour had been already directly excluded by LEP 2. Obviously the best fit prefers a rather light Higgs boson in the SM. But it should be kept in mind that extensions of the SM may avoid the constraints to a light Higgs between roughly 80 GeV to 200 GeV imposed by the electroweak precision data.

2.1.5 Open problems of the Standard Model

As we have seen, the SM gives an elegant way to generate the observed masses for the vector bosons and incorporates fermion masses, but in some respects masses remain a problem of the SM. First of all the mass of the Higgs boson is a free parameter of the theory. A good model is expected to predict masses for its content. Though this might be regarded a minor flaw in contrast to the success of the SM, we will

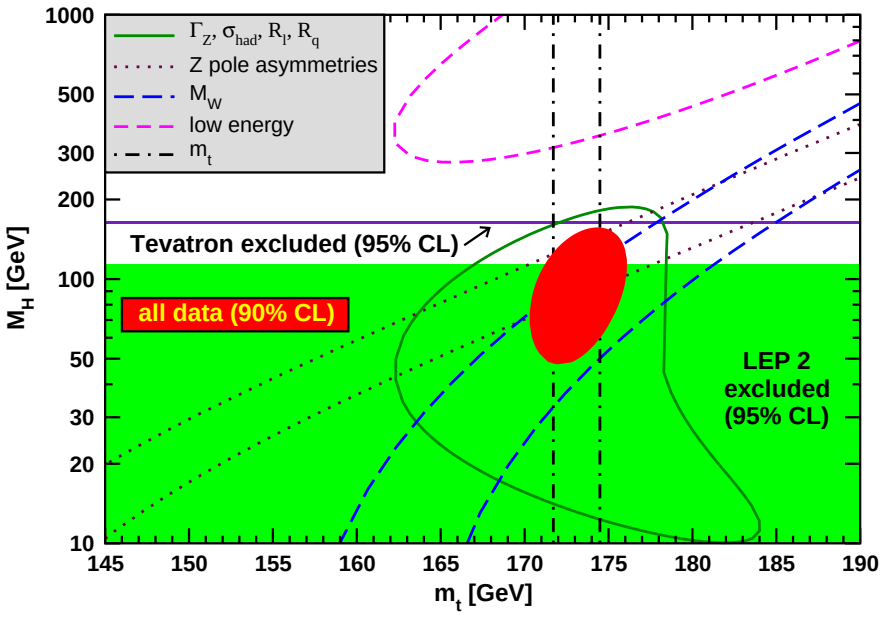

Fig. 2.8: *One standard deviation contours (39.95%) uncertainties in M_H as a functions of m_t. The coloured dashed lines correspond tho the various inputs of the fit. One sees that the low energy data prefers a more heavy Higgs boson while the Higgs is expected to be light according to the high energy data. The central red ellipse is the combined fit at 90% CL ($\Delta\chi^2 = 4.605$) that is allowed by all electroweak data combined. The green area and the violet band are the direct exclusion at 95% CL of the LEP 2 and the TeVatron data respectively (taken from [120]).*

list in this section some arguments that nourished the belief that the SM is only an effective low energy description which has to be replaced by a physical more complex theory at higher scales.

Hierarchy problem and fine-tuning

As argued before the Higgs mass is subject to loop corrections on the value of its self coupling λ. In the summation of the loop contribution two different types of loops are summed up, namely virtual boson loops and virtual fermion loops. While the virtual boson loops (Fig.2.6, middle) are counted positive and raise the value of the correction to λ, the fermion loops count negative hence limiting the radiative corrections. On each order of perturbation theory the freedom in the choice of the Yukawa couplings (here especially the top quark Yukawa coupling becomes important) can be utilised to tune the Yukawa couplings to exactly the value where their negative loop contribution cancels exactly the positive bosonic loop contributions. In that way one can control the radiative corrections to the self coupling λ to an arbitrary level, which otherwise would result in a divergent contribution to the Higgs mass. Without this so-called fine-tuning of the Yukawa coupling the Higgs boson mass would not be confined to the electroweak symmetry breaking scale but would be driven by the loop corrections to the highest physical scale which would then be the new scale of symmetry breaking namely the Planck scale. In other words, the Higgs mass is not naturally protected by any remaining symmetry or some other mechanism derived by first principles, but has to be stabilised by a delicate technical procedure by hand. The unexplained feature of the SM that there is a such a huge difference in the scale of electroweak symmetry breaking to the Planck scale of about 10^{16} GeV is often referred to as the hierarchy problem in the SM.

Additional to the parameters that have to be adjusted and are not naturally in the theory, the SM encountered further problems.

Gauge coupling unification

If one uses the renormalisation group equations for the evolution of the gauge group couplings to the highest energies, one finds that they will not unify in one point. This is contradicting the naïve expectation that at a certain scale all physics can be derived from one symmetry group, which obviously cannot be the SM symmetry group.

Missing dark matter candidate

Since the results of the WMAP Collaboration in 2008 [99] indicated that 23% of mass and energy density in the universe is nonbaryonic cold dark matter (CDM), it turned out to be problematic for the SM not to provide a candidate for such a stable and weakly interacting exotic particle. The attempt to explain the gravitational effects of the CDM with tiny masses of the relativistic neutrinos failed.

Baryogenesis and strong CP problem

Another cosmological argument stems from baryogenesis in the early universe. In order to explain that matter had been more abundant than antimatter, hence the universe after the annihilation today consists of baryons and radiation but no more antimatter, Sakharov [138] devised already 1967 three conditions under which such an outcome can occur. These conditions are

1) the possibility of baryon number violation

2) CP and C parity violation

3) a phase transition in which the interactions departed from thermal equilibrium.

It may well be that the phase transition from the electroweak symmetry breaking was strong enough to provide the non thermal equilibrium. The problem in connection to the SM is that baryon number experimentally is conserved on the classical level. The possibility of baryon number violation via triangle anomaly is suppressed at least below electroweak scale. Further the SM contains C and CP violation (complex phase of CKM matrix) in the weak sector. Though it is problematic that the observed CP violation in the weak sector is far too small to explain the observed ratio of baryons to photons in the universe [102], measured by WMAP as

$$\frac{n_{\mathrm{B}}}{n_{\gamma}} = (5.1^{+0.3}_{-0.2}) \times 10^{-10}. \tag{2.22}$$

In addition the Lagrangian of the QCD allows CP violation but very precise measurements on the anomalous neutron magnetic moment indicate that QCD preserves CP to a very high degree of accuracy. This exhibits a twofold flaw of the SM, firstly it can not explain baryogenesis and secondly it needs again a high degree of fine tuning to render the sources of CP violation in the QCD Lagrangian ineffectively in accordance with the experiments. This is called the strong CP problem in the SM.

The listed arguments among others are a strong motivation to consider theoretical extensions and alternatives to the SM though it has been very successful to describe the particle world in collider experiments at the weak symmetry breaking scale.

2.2 Extensions of the Standard Model and possibility of invisible Higgs

Some of the flaws described in Sec.2.1.5, lead to extensions of the SM or alternative models that introduced new physics. In the following we sketch those concepts that via the new physics also motivate enhanced invisible Higgs decays.

2.2.1 Supersymmetric extension and decay into neutralinos

The Haag-Lopuszanski-Sohnius theorem [91] states that the most general symmetry of the Lagrangian in a four dimensional quantum field theory besides its internal symmetries and Poincaré invariance allows for a new kind of symmetry, the so-called supersymmetry [121]. Supersymmetric extensions have been widely explored, indeed it became a popular method to solve the hierarchy problem without fine-tuning to protect the Higgs mass by introducing this new symmetry.

Supersymmetry connects fermions with equally massive bosonic counterparts and vice versa, thus doubles the particle spectrum of the SM. The consequence is that for each divergent bosonic Feynman graph in the correction to the Higgs self-coupling an adequate fermionic Feynman graph with opposite sign exists, therefore the divergence is automatically cancel in the summation.

All supersymmetric particles carry the so-called R parity number -1, while the ordinary particles have R-parity 1. In many, not all, supersymmetric models the R-parity is strictly conserved. Obviously there is no indication of a supersymmetric partner of the electron or muon, hence the supersymmetry has to be broken and supersymmetric theories include a new scale of supersymmetry breaking usually in the TeV range. Also the sypersymmetric group renormalisation equation lead to the unification of gauge coupling at the grand unification (GUT) scale, $\mathcal{O}(10^{16}\ \text{GeV})$, which is widely regarded a strong argument that nature may be supersymmetric. The simplest supersymmetric extension is known as minimal supersymmetric SM (MSSM) [67, 116].

Invisible Higgs decays in supersymmetric extensions

The Higgs sector of the MSSM consists of two complex doublets and a vev for each doublet. Two doublets are necessary to give mass to the up and down type fermions in this model. Since the two doublets provide more degrees of freedom as needed for weak boson masses, the spectrum of physical Higgs state after symmetry breaking consists of a light SM like Higgs (h) and a heavy Higgs (H) along with a pseudoscalar A and two charged Higgs bosons $H^{\pm}$. In a collider, supersymmetric particles with R-parity conservation can be produced only in pairs. Decay chains of supersymmetric particles have to end at a lightest supersymmetric particle (LSP), which is stable and interacts only weakly. Therefore, supersymmetric theories conveniently supply a candidate for the CDM in the universe. Which of the supersymmetric particles occupies the place of the LSP in the sypersymmetric mass spectrum and with what mass depends from the parameters of the model. In some cases this LSP is the superpartner of the graviton (gravitino) or the superpartner of a neutrino (sneutrino) or a neutralino. For many parameter choices the LSP is the lightest of the four neutralino states $\tilde{\chi_1}^0, ..., \tilde{\chi_4}^0$. These neutralinos are Majorana fermions originating from the mixing of the superpartners of the photon (photino), of the Z-boson (zino) and of the two neutral Higgs bosons (higgsinos).

Decays of one of the neutral Higgs bosons into the LSP can occur depending on the masses, e.g. $h \rightarrow \tilde{\chi_1}^0 \tilde{\chi_1}^0$. This would lead to a sizable invisible branching ration of the Higgs, though the invisible decay width in this two body decay would remain narrow.

A recent more complex supersymmetric model on basis of the exceptional group E_6, the so-called E_6SSM [94], provides in its low energy limit an extended Higgs sector and additional $U(1)_N$ group factors to the SM gauge group, that give rise to novel invisible Higgs decays. In this case there are 3 families of Higgs doublets and singlets, from which only one family acquires a non-vanishing vacuum expectation value. The other masses of the fermionic component of the singlet superfield of the remaining two families are related to the vevs of the first family and these so-called inert neutralinos $\tilde{\chi}^0_{1,2}$ are naturally candidates for cold dark matter in the allowed mass range below 60-65 GeV [94], since they are the (N)LSPs for most scenarios. The model succeeds also to predict the correct spin independent elastic cross section ($\mathcal{O}10^{-44} cm^2$ via a Z-pole resonance, which would be very well in accordance with dark matter contributions to Ω_M found by WMAP, and additionally the suggested limits on the cold dark matter mass of 40-80 GeV, from the CMDS-II experiment observation ([16, 94]). As there are light

massive singlets states present the SM like Higgs can decay dominantly invisible $h \to \tilde{\chi_1}^0 \tilde{\chi_1}^0$ and nearly invisible $h \to \tilde{\chi_2}^0 \tilde{\chi_2}^0 \to \tilde{\chi_1}^0 \tilde{\chi_1}^0 \ell^+ \ell^-$ with two soft leptons (invariant dilepton mass $m_{\ell^+\ell^-} < 10$ GeV), as well as mixed Higgs decay cascades into $h \to \tilde{\chi_2}^0 \tilde{\chi_1}^0$. For some benchmarks scenarios with $m_h = 115$ GeV and $m_h = 130$ GeV, branching fraction of more than 95% into the invisible and into nearly invisible channels are predicted, which experimentally are difficult to measure at the LHC. In particular the invisible decays gain a branching in the range from 49 % to 58 % for $m_h = 130$ GeV and from 49 % to 83 % for $m_h = 115$ GeV depending on the benchmark point. The additional channels add a small additional width to the total Higgs width, which, however, stays below 200 MeV.

2.2.2 Hiding the Higgs

After the LEP experiments did not find a Higgs boson the LHC should clarify the nature of the Higgs sector. As we have seen it is a peculiarity of this sector that the Higgs mass enters the electroweak precision data only logarithmically. This leaves space for introducing more scalar matter in form of singlets. Singlets would interact with the Higgs sector. Such models were studied with some concern, since it was realised that for example if such a singlet acquires a vev it can mix with the Higgs, which would alter the Higgs observables. E.g. in [28, 117] some models where referenced that introduce such phantom sectors [47]. The universal mechanism how the Higgs singlet mixing via a non diagonal mass matrix dilutes the Higgs mass peak was studied. A simple scaling $\frac{1}{\sqrt{N}}$ of the significance of a given SM discovery channel with the number N of introduced singlets that have masses in the mass range where the channel becomes most promising is derived in [28]. The conclusion is that already three scalars, each with the same mixing amplitude to the Higgs, and masses of 118 GeV, 124 GeV, 130GeV will hide the Higgs even in 100 fb^{-1} LHC data. In some other parts though the Higgs will still be discoverable.

In the following, we will name models that are physically motivated beginning with one additional singlet and generalising later to arbitrary many singlets. Thereby we focus on models that force invisible Higgs decays with gauge singlets and on models that contain an effective mechanism to provide invisible Higgs decays due to the extra scalars.

Invisible Higgs decays into scalar dark matter candidate added to the SM

There have been attempts [40, 57] to minimally extent the SM with stable scalar singlets with respect to the SM gauge group, S, suitable to explain the CDM content of the universe. The couplings of the Higgs to these scalars should be $\mathcal{O}(0.1-1)$ in order to provide enough CDM in thermal equilibrium. This coupling may provide a large contribution to an invisible Higgs decay over a large part of the interesting parameter space. Typically the interesting mass range in this model is given by 100 GeV$< M_{\mathrm{H}} <$200 GeV and 10 GeV$< M_{\mathrm{S}} <$ 100 GeV. In Fig. 2.9, the ratio $R = \frac{\Gamma_{\mathrm{H}}(SM)}{\Gamma_{\mathrm{H}}(SM)+\Gamma_{\mathrm{H}\to\mathrm{SS}}}$ of the total SM Higgs width to the width of the Higgs in the SM plus the additional scalars S, for Higgs of mass 120 GeV and 200 GeV is shown (taken from [40]). The effect of the scalars becomes quickly less important as soon the Higgs mass is larger as $2M_{\mathrm{W}}$. For the light Higgs the phase space effects due to the threshold for decays into S pairs at $M_{\mathrm{H}} \sim 2M_{\mathrm{S}}$ is visible in the left panel of Fig. 2.9. Also the coupling has to be lower since the cross section of the primordial annihilation would have become larger close to the Higgs resonance.

Invisible decays of Higgs bosons to Majorons

The lepton number L is conserved in the SM, so it can be thought of as protected by a global $U(1)_L$ symmetry. In models that explain neutrino masses via the see saw mechanism (sketched e.g in [61]) this symmetry has to be violated by the vev of a $SU(2)_{I_w} \times U(1)$ gauge singlet field σ. Accordingly, a physical pseudoscalar Goldstone boson appears after the breaking which is called Majoron J [50]. It was early discussed [34, 60, 105–107] that this may lead to invisible Higgs decays $h \to JJ$ (in MSSM also

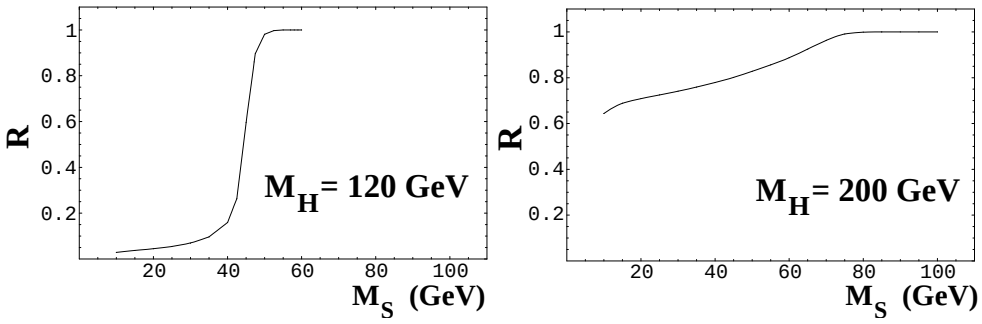

Fig. 2.9: *Invisible decays in a model with a CMD scalar. The ratio R of the total Higgs width in the Standard model over the same width in the Standard Model supplemented by the singlet scalar, plotted as a function of* M_S. *Left:* $M_H = 120$ GeV. *Right:* $M_H = 200$ GeV. *Taken from [40].*

$A \to JJ$) since they interact weakly. Therefore, this would introduce a new source of invisible decay, possibly enhancing the invisible decays of the Higgs in the MSSM. This additional invisible decay width would be comparable to the SM width for a light Higg boson.

Theory with 4th generation neutrinos

Besides from the benefit of explaining some astrophysical measurements [32], the introduction of a fourth neutrino may provide enough CP violation to to fulfil the Sakharov conditions [102]. A fourth generation neutrino N with a mass m about 50 to 80 GeV would be compatible with the measurements of the invisible Z boson width at LEP, as argued by [32]. As before we are only interested in the implications for invisible Higgs decays. These are indeed possible because the lifetime of the 4th neutrino is assumed to be large. The contributions to the width depends then of the phase space available which result in the following relation:

$$\Gamma(H \to N\bar{N}) = \frac{\sqrt{2}}{8\pi} G_F m^2 M_H \left(1 - \frac{4m^2}{M_H^2}\right)^{3/2}, \tag{2.23}$$

where m and M_H are the masses of the neutrino and Higgs boson respectively. In Fig. 2.10, which is taken from [32], the impact on the branching ratios of the Higgs in the interesting light Higgs mass range is displayed for two masses of the 4th neutrino at the lower and upper allowed value. An interesting

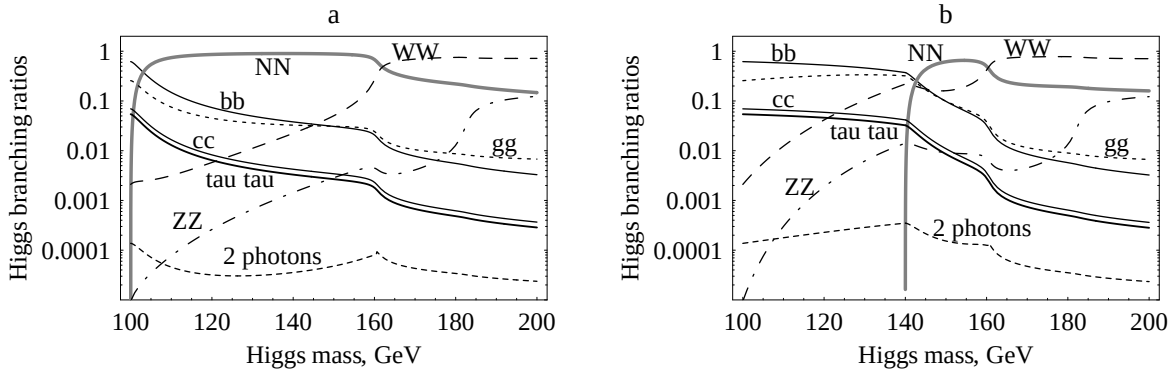

Fig. 2.10: *Branching ratios of the Higgs decay modes into a hypothetical 4th heavy neutrino:* $H \to N\bar{N}, b\bar{b}, WW, ZZ, c\bar{c}, \tau^+\tau^-, gg, \gamma\gamma$. *a)* $m = 50$ *GeV, b)* $m = 70$ *GeV. Taken from [32].*

comment is also made in [32] regarding the failure of LEP to find the Higgs. The LEP invisible result interpreted in this scenario, assuming $m = 50$ GeV, corresponds to a lower limit on $M_H > 113.5$ GeV.

The LEP result in this scenario implies either, that the Higgs is heavier than this lower bound or that the mass difference $|2m - M_{\mathrm{H}}|$ is very small. In that case there would be a huge phase space suppression for such a Higgs decay. In fact if the lifetime of N is larger than the age of the universe astrophysical constraints demand the mass difference to be less than 3 to 4 GeV in this scenario.

A very similar approach is published in [59] where in the need to have a WIMP candidate of mass between 10 GeV to some TeV, a new fermion doublet and a corresponding singlet is introduced into the SM. This results after mixing into the physical states in a stable and massive Majorana fermion. Since only the mass of the new fermion enters as new parameter, it occurs a very similar possibility of strongly enhanced branching for invisible Higgs decays occurs below $M_{\mathrm{H}} = 160$ GeV.

Generalised two Higgs doublet model with nearly massless invisible Higgs

In [76], the invisible decays in the class of two Higgs doublet models are further studied. In these models, the SM contains two Higgs doublets, where one vev v_ϕ of the doublet ϕ is used to provide masses for gauge bosons, quarks, and charged leptons at the usual scale of electroweak symmetry breaking of $SU(2)_{I_w} \times U(1)$. But in this model the true symmetry of the electroweak sector is extended by the discrete Z_2 symmetry to $SU(2)_{I_w} \times U(1) \times Z_2$. Also 3 additional $SU(2)_{I_w} \times U(1)$-singlet right handed neutrinos, N_R, are present. This is done to present an alternative for neutrino mass generation compared to the canonical see saw mechanism. Namely the vev v_χ of the second Higgs doublet χ, which couples only to neutrinos, is used to spontaneously break the Z_2 at the very low scale of 10^{-2} eV and give masses of that order to the Dirac neutrinos. The Yukawa couplings between left handed SM neutrinos and the extra right handed neutrinos are proportional to that v_χ and combine them to massive Dirac neutrinos. In addition to providing a new mechanism for generating tiny masses for the neutrinos, the model has interesting implications for neutrinoless double beta decay, which is prohibited since there are only Dirac neutrinos, and the Higgs signals at high energy colliders, due to invisible decays, as well as in astrophysics and cosmology. The invisible Higgs decays especially for low Higgs masses (Fig. 2.11, taken from [76]) occur in the following way. As in the MSSM there is a heavy scalar which in this model is taking the role of the SM like Higgs and therefore called h. And we find a pseudoscalar (A) together with the charged Higgses in the spectrum. But the lightest scalar, denoted here by σ, is nearly massless (because of the tiny v_χ). The lightest scalar σ is quasi stable or decays into neutrinos $\sigma \to \nu\bar{\nu}$, which in any case leads to a missing energy signature. As mentioned, h is very SM like with respect to the decays into SM particles but the new channel which opens is the invisible decay $h \to \sigma\sigma$.

Starting from the most general potential for the two doublets which preserves Z_2 symmetry,

$$V = -\mu_1^2\,\phi^\dagger\phi - \mu_2^2\,\chi^\dagger\chi + \lambda_1(\phi^\dagger\phi)^2 + \lambda_2(\chi^\dagger\chi)^2 + \lambda_3(\phi^\dagger\phi)(\chi^\dagger\chi) - \lambda_4|\phi^\dagger\phi|^2 - \frac{1}{2}\lambda_5[(\phi^\dagger\chi)^2 + (\chi^\dagger\phi)^2], \tag{2.24}$$

one can calculate the physical Higgs mass states. It is handy to define a general Higgs coupling λ^* out of the quartic couplings in the potential above. λ^* is defined to be equal to $\frac{(\lambda_3+\lambda_4+\lambda_5)^2}{\lambda_1}$. Then the new invisible decay width of the more heavy neutral scalar h can be written as

$$\Gamma(h \to \sigma\sigma) = \frac{\lambda^* m_h}{64\pi}. \tag{2.25}$$

As Fig. 2.11 indicates, for some choices of λ^* there is a substantial branching of invisible Higgs decays for masses below 200 GeV expected.

2.2.3 Extension with extra dimensions and Higgs graviscalar mixing

A natural way to avoid the hierarchy problem was proposed when inspired from higher dimensional string theory, it was realised that the observed values of Newton's constant G_{N}, corresponding to a tiny gravity

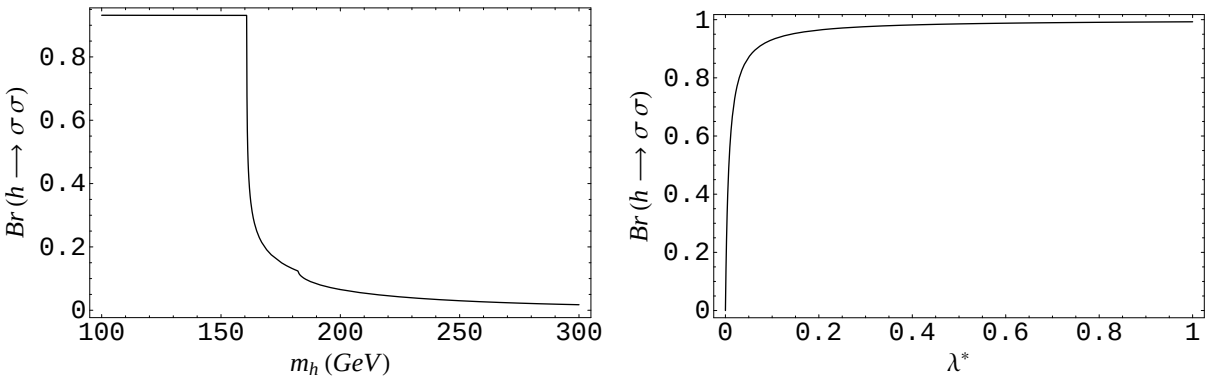

Fig. 2.11: *Invisible branching in the 2HDM with very light Higgs σ. Left panel: Branching ratio for $h \to \sigma\sigma$ as a function of m_h for the value of the parameter, $\lambda^* = 0.1$. Right panel: Branching ratio for $h \to \sigma\sigma$ as a function of λ^* for $m_h = 135$ GeV. Taken from [76].*

in our world, may be explained by the existence of additional spatial dimensions. Current precision measurements of the inverse gravitational law by Cavendish-like experiments would allow for such extra dimensions to be as large as in the sub-millimetre range [12]. Since this is very large compared to the Planck length, these class of models comes under the name large extra dimensions, and the first model introducing this ideas was called according its authors, Arkani-Hamed, Dimopoulos and Dvali [24, 25], the ADD model.

In such models the real scale of quantum gravity is lowered to the TeV range very close to the scale of electroweak symmetry breaking, which would not pose a hierarchy problem any more. In other words no symmetries would be needed to protect the hierarchy between the Higgs mass at Fermi scale and the Planck scale which would be the natural scale of symmetry breaking, if radiative corrections to the Higgs mass were allowed. In the following we will summarise shortly some important aspects of extra dimensional theories before describing their influence on the properties of the Higgs boson.

Geometrical reformulation of the hierarchy problem

String theory offers an alternative picture of the geometrical structure of the universe, introducing generically many extra dimensions. In such spaces exist embedded submanifolds called D-branes according to their dimensionality, D, on which particles described as string excitations interact. The unobservability of more than three spatial dimension so far is build into such theories by compactifying these extra dimensions on a scale below detectability.

In models that claim large extra dimensions the D-dimensional world is geometrically $\mathscr{M}^4 \otimes X^\delta$ the direct product of the Minkowsky space $\mathscr{M}^4$ we inhabit and of an extra δ-dimensional space X^δ, which is called the bulk. Hence, the dimensionality D of the complete product space is D$= 4+\delta$.

The metric of the space hence factorises as the line element is given by

$$ds^2 = g_{IJ}\mathrm{d}X^I\mathrm{d}X^J = \eta_{\mu\nu}\mathrm{d}x^\mu\mathrm{d}x^\nu + h_{ij}(y)\mathrm{d}y^i\mathrm{d}y^j \tag{2.26}$$

with $I,J = (0,..,3+\delta)$ with independent subspace coordinates x on the brane $\mu,\nu = (0,...,3)$ and y in the bulk $i,j = (1,...,\delta)$.

In general, each extra dimension can have individual extensions as long as these are undetectable and also the size of the compactification volume V_δ is of choice. But the easiest approach is to describe all extra dimensions on the same footage that is compactified to the same volume. A genuine choice would be the torus, $V_\delta = (2\pi R)^\delta$, and common extension R. In that way the radius of compactification, R, as well as the number of regarded extra dimensions δ are the parameters.

In the basic formulation of large extra dimensions the SM fields are confined to the 3-brane of the Minkowski space. Gravity waves are allowed to expand into the bulk since they arise from the global metric g_{IJ}. This has consequences for the observed Planck mass.

Gravity observed in our 4 dimensional world is very weak. The Planck mass in 4 dimensions, $M_{\rm Pl}$, corresponds to the to the observed Newton's constant $G_{\rm N}$ via the relation $M_{\rm Pl} = \frac{1}{\sqrt{G_{\rm N}}} = 1.2 \times 10^{19}$ GeV. In the following, the reduced 4 dimensionally observed Planck mass $\overline{M}_{\rm Pl} = \frac{1}{\sqrt{8\pi G_{\rm N}}} = 2.4 \times 10^{18}$ GeV is used. According to the Gauss flux theorem one can deduce from the surface integral of the flux the magnitude of the charge $G_{\rm N}$. In this case the incomplete integration of the 4 dimensional surface collects only a fraction of the flux, hence concludes that the enclosed charge $G_{\rm N}$ is weak, hence $\overline{M}_{\rm Pl}$ huge. But the real fundamental D-dimensional reduced Planck mass $\overline{M}_{\rm D}$ can be considerably lower since its value would be known after complete surface integration. In other words the size of the compactified extra dimensions volume blows up the value of $\overline{M}_{\rm D}$ to the observed $\overline{M}_{\rm Pl}$.

$$\overline{M}_{\rm Pl}^2 = V_\delta \times \overline{M}_{\rm D}^{2+\delta} \tag{2.27}$$

In order to have not a big hierarchy one may wants to set e.g. $\overline{M}_{\rm D} = 1$ TeV. In that way R has to be from sub-millimetre to a few fermi in case of $\delta = 2$ to 6 ($\delta = 1$ is excluded since it would alter the gravitation at solar system scales). So $\overline{M}_{\rm D}$ replaces R as model parameter, which is chosen that the hierarchy between weak and gravity scale is absent.

Coupling between SM particles and gravity

We sketch now (following [11]) how gravity in extra dimensions can be felt by the SM particles on the brane. The key is to note that graviton components present on the brane can couple to the energy momentum tensor. Thus, the action is the Einstein-Hilbert term in the bulk and a brane term containing the SM gauge interactions

$$S_{int} = \frac{\overline{M}_{\rm D}^{2+\delta}}{2} \int {\rm d}^D x \sqrt{|g|} R + \int {\rm d}^4 x \sqrt{-g_{ind}} \mathscr{L}_{\rm SM}\,, \tag{2.28}$$

where for the bulk term the Ricci scalar curvature R is found by contraction of the Ricci tensor $R = g^{IJ} R_{IJ}$ in the D dimensions. In the brane term on the submanifold only the brane induced metric $(g_{ind})_{\mu\nu}$ is active in the coupling of gravity to the brane SM fields.

Since the gravitational field follows from the metric, one can expand the metric g_{IJ} in case of weak gravity around a flat metric $g_{IJ} = \eta_{IJ} + \frac{2}{\overline{M}_{\rm D}^{1+\delta/2}} h_{IJ}$. From this expansion an endless number of Kaluza-Klein excitations, the so-called Kaluzu-Klein towers (KK), describe the gravity in the bulk (details on the Fourier expansion and gauge see e.g in [11] p.349).

$$h_{IJ} = \sum_{n_1=-\infty}^{+\infty} ... \sum_{n_\delta=-\infty}^{+\infty} \frac{1}{\sqrt{V_\delta}} h_{IJ}^{(n)}(x) e^{-i\sum_{j=1}^{\delta} n_j y_j}\,. \tag{2.29}$$

In Eq. 2.29 the gravity in the bulk h_{IJ} with $I,J = (0,..,3+\delta)$ is a superposition of an infinite number of KK states excitations $h_{IJ}^{(n)}$, indexed with the excitation level (n). The Fourier expansion of the bulk excitations has components in each regarded extra dimensions indicated by the sums running over n_1 up to n_δ. As one sees the compactification volume enters in the expansion of states. The consequence is that the density of Kaluza Klein states is very high, almost continuous in mass, since the mass of the n-th excitation is given by $m_n = n/R$, if compaction on the torus is assumed. E.g. for $\delta = 2$ and $\overline{M}_{\rm D} = 1$ TeV, the masses range is of order $\Delta m_n = 1/R \sim 10^2 mm^{-1}$ or 10^{-1} eV for $\delta = 6$ is $\Delta m_n = 1/R \sim 10$ MeV. Also the graviton states tend to be very light and are very long lived ($\sim 10^{10} yr$). The zeroth mode of the

scalars should have mass of $\geq 1mm^{-1}$ or 10^{-3} eV in order to avoid deviation of Newtons's law on that scale.

After unitary gauge these modes appear also in the Lagrangian, but now towers are present for various spin configurations of the gravity fields. In the ADD model only the graviton (J=2) and the graviscalar (J=0) interact with the gauge fields, the graviphoton (J=1) is not interacting with SM fields at tree level. This can be seen when finally the interaction Lagrangian is written down. In the expansions of the gravity restricted onto the brane the interaction reads

$$\mathscr{L}_{\text{int}} = -\frac{1}{\overline{M}_{\text{Pl}}} \sum_{\vec{n}} \left[G^{(\vec{n})\mu\nu} - \frac{\kappa}{3}\eta^{\mu\nu} H^{(\vec{n})} \right] T_{\mu\nu}\,. \tag{2.30}$$

Here $G^{(\vec{n})\mu\nu}$ sums up the tower of gravitons by the indices of the states as entry of the vector $\vec{n}$. Likewise $H^{(\vec{n})}$ stems from the trace of the tower of graviscalars, and $T^{\mu\nu}$ is the energy momentum tensor constructed from $\mathscr{L}_{\text{SM}}$. For convenience we also defined $\kappa = \sqrt{\frac{3(\delta-1)}{\delta+2}}$. Important for the following is to note that for $\delta \geq 2$ there is a tower of massive graviscalars with very dense mass spacing.

The massive KK modes of the graviton (J=2) were extensively studied since they could be directly produced in colliders like LEP and TeVatron and would indicate the existence of extra dimensions. Searches for graviton production yielded constraints on M_{D} between 0.6 and 1.6 TeV. These constraints are detailed listed in [11] depending on the assumed δ together with astrophysical constraints (which are much less stringent for $\delta < 4$).

Invisible and broad Higgs in ADD

We will discuss only the graviscalar modes $H^{(\vec{n})}$ since the ADD model provides a mechanism for a large width of the Higgs by mixing with graviscalars explained in the following. To this end it is sufficient to look at the part of the Lagrangian where the Higgs field mixes with the Ricci scalar. Effectively the action is thus evaluated at the brane meaning that $R(g_{ind})$ is now the Ricci tensor of the 3-brane and g_{ind} the induced metric on this sub manifold

$$S = -\xi \int d^4x \sqrt{-g_{ind}} R(g_{ind}) \Phi^\dagger \Phi\,. \tag{2.31}$$

Here, the strength of the mixing is the free parameter ξ. One also a last time reexpresses the gravity scalars by taking only the real part $s_{\vec{n}}$ in proper normalisation of $H^{(\vec{n})} = \frac{1}{\sqrt{2}}(s_{\vec{n}} + i a_{\vec{n}})$ and after the usual shift into the Higgs field minimum $\Phi = ((v+\text{H})/\sqrt{2}, 0)$, the mixing term in the Lagrangian becomes

$$\mathscr{L}_{mix} = -\frac{2\sqrt{2}}{\overline{M}_{\text{Pl}}} \xi v M_{\text{H}}^2 \kappa H \sum_{\vec{n}>0} s_{\vec{n}}\,. \tag{2.32}$$

In [66] the evaluation of the Higgs propagator is presented, allowing additionally for graviscalar mixing. It is found that the Higgs can acquire a considerable invisible width, $\Gamma_{\text{inv}} \equiv \Gamma(h \to graviscalar)$, mainly because of the high density of graviscalars that give the Higgs a high probability for mixing.

$$\begin{aligned} \Gamma_{\text{inv}} &\equiv \Gamma(h \to graviscalar) = 2\pi \xi^2 v^2 \kappa^2 \frac{m_h^{1+\delta}}{M_D^{2+\delta}} S_{\delta-1} \\ &\sim (16\,MeV) 20^{2-\delta} \xi^2 S_{\delta-1} \kappa^2 \left(\frac{m_h}{150\,GeV}\right)^{1+\delta} \left(\frac{3\,TeV}{M_D}\right)^{2+\delta}, \end{aligned} \tag{2.33}$$

where $S_{\delta-1} = 2\pi^{\delta/2}/\Gamma(\delta/2)$ denotes the surface of an unit radius sphere in δ dimensions while M_{D} is related to the D dimensional reduced Planck constant $\overline{M}_{\text{D}}$ by $M_{\text{D}} = (2\pi)^{\delta/(2+\delta)} \overline{M}_{\text{D}}$.

Additionally to mixing, the Higgs can of course also decay directly into a pair of graviscalars. According to [66] the width is given by

$$\Gamma(h \to \textit{graviscalar pairs}) = \frac{2}{\pi}\frac{m_h^{3+2\delta}v^2}{M_{\mathrm{D}}^{4+2\delta}}\xi^4\kappa^4\left[\frac{\pi^{\delta/2}}{\Gamma(\delta/2)}\right]^2 I\,. \tag{2.34}$$

Here, I is an integral that has to be computed numerically. It has a very small value. Even for a large $\xi \sim 10$, it remains small like, e.g. $I \sim 0.011$ for $\delta = 2$. The value of I is much lower for $\delta \geq 2$. The contributions of the direct decay into graviscalars can be safely neglected against the width from mixing as long as m_{h} is not larger than M_{D}. Even then it will be a small effect.

As one can see in the left-hand panel of Fig. 2.12, if $M_{\mathrm{D}} = 2$ TeV$, \xi = 1$, a hypothetical $\delta = 2$ offers the largest the branching into invisible graviscalars over the whole range from very light to Higgs masses $M_{\mathrm{H}} < 2M_{\mathrm{W}}$. With higher extra-dimenionality, the very light invisible Higgs becomes suppressed. We give also impressions of the invisible width. In the left-hand panel of Fig. 2.13, a very light Higgs $M_{\mathrm{H}} = 120$ GeV$, \delta = 2$ and $M_{\mathrm{D}} = 1$ TeV acquires for rising ξ a quite sizable invisible width, compared to the MeV SM width, in $\mathcal{O}(50\,\mathrm{GeV})$. On the right=hand panel for the extreme heavy Higgs mass $M_{\mathrm{H}} = 1$ TeV$, \delta = 2$, the total decay width into invisible states is plotted in dependence of M_{D} and for various mixing parameter values ξ. Clearly, the mixing width scales with the mixing strength but also the closer the gravity scale comes to the electroweak scale the larger the invisible Higgs width becomes.

While in electron positron colliders the recoil mass spectrum can be reconstructed and hence exhibits the total width of the Higgs, the width of the Higgs can be visible at a hadron collider in an invariant mass scan over processes where a Higgs boson propagates in the s-channel as in WW-scattering. Further it should be noted that the invisible width can be quite competitive even for a Higgs boson that can decay into W-bosons. This width would reduce the LHC Higgs yield in the standard observable channels (such as WW) by a factor of $\frac{1}{1+r}$ where $r \equiv \frac{\Gamma_{\mathrm{inv}}}{\Gamma_h^{SM}}$. Therefore, it could be necessary to conduct invisible Higgs searches [18, 31] e.g. in the weak boson fusion topology when the canonical channels fail to deliver a signal. For illustration purposes in the right-hand panel of Fig.2.12 contours of r in the m_{h}, ξ plane are shown for a scenario with $M_{\mathrm{D}} = 2$ TeV and $\delta = 2$. In parameter spaces where the invisible width becomes considerably larger than the detector resolution it may also give experimental complications to find such a smeared out signal over background.

Dirichlet Higgs in an universal extra dimension

Even when the final state is not consisting of weakly interacting particles, a very large width can make the Higgs unobservable in the detector. The following scenario may be an example. Recently, a model [92,93] belonging to the class of universal extra dimensions (UED [133]) was proposed leading to a large invisible decay width.

The model has only one extra dimension compactified on a line segment (scale length L) with a flat metric. As typical for universal extra dimensions, the SM particles wave functions may extent into the 5^{th} dimension bulk. In this scenario fermions and the Higgs doublet can be in the bulk, and contrary to the SM, this scenario needs no Higgs potential, since a vev for the Higgs doublet is induced by imposing Dirichlet boundary conditions [7)] on the ends of the segment. The wave function of the Higgs in the bulk becomes a linear superposition of its Kaluza-Klein excitations, so a physical Goldstone boson is still present in the bulk, though the zeroth mode in the bulk is eliminated by fulfilling the boundary condition.

Interestingly this model predicts a deviation of the top Yukawa λ_t to be smaller by 10%. With respect to this deviation a reevaluation of the production cross sections yields that they are reduced by 19% compared to the SM. Since all production modes are affected in the same way, the branching ratios

[7)] The boundary conditions can be most general expressed for the Higgs doublet Φ as: $\partial\Phi(x, \pm\frac{L}{2}) = 0$ and $\Phi(x, \pm\frac{L}{2}) = \binom{v_1}{v_2}$.

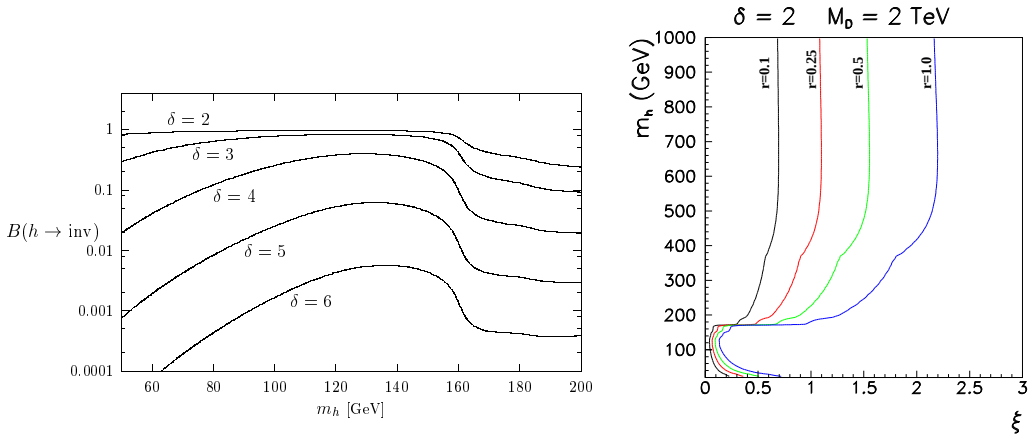

Fig. 2.12: *Invisible branching in the graviscalar mixing model. Left: Invisible Higgs branching depending on* m_h *in a typical ADD scenario with large mixing (*$M_\mathrm{D} = 2$ TeV$, \xi = 1$*) with various extra dimensions* δ*. (taken from [81]). Right: Contours of* $r \equiv \frac{\Gamma_\mathrm{inv}}{\Gamma_h^{SM}}$ *in the* m_h, ξ *plane. From left to right* $r = 0.1, 0.25, 0.5$ *and* 1.0*. Fixed model parameters are* $M_\mathrm{D} = 2$ TeV *and* $\delta = 2$*. Processes wit SM particles in initial and final state will experience a suppression of the cross section in s-channel by* $\frac{1}{1+r}$*(taken from [66]).*

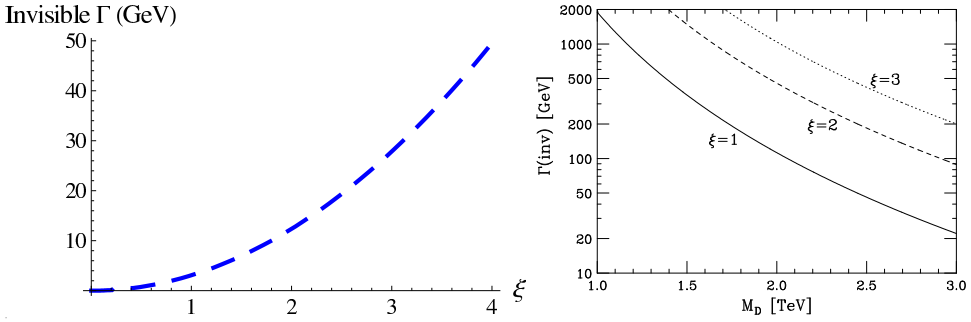

Fig. 2.13: *Examples for the size of invisible width in the graviscalar mixing model. Left: Total invisible width as function of* ξ *for a light Higgs boson* $m_\mathrm{h} = 120$ GeV *in* $\delta = 2$ *and* $M_\mathrm{D} = 1$ TeV *(taken from [66]). Right: Total invisible width of Higgs boson into one and two graviscalars for the extreme assumption of* $m_\mathrm{h} = 1$ TeV*. as a function of* M_D *for various values of* ξ *(*$\xi = 1$ *solid,* $\xi = 2$ *dashed,* $\xi = 3$ *dotted) with fixed* $\delta = 2$*(taken from [31]).*

stay unchanged. The higher KK excitations of the Higgs in the bulk can be directly produced by gluon gluon or weak boson fusion.

While the SM electroweak fits prefer a light Higgs, this model needs a very heavy SM like Higgs boson on the brane. Since this value is not depending of the Higgs self coupling (there is no potential) but only on the compactification length L, there are no theory constraints by triviality or vacuum stability for the Higgs mass. The mass of the n-th KK excitation becomes a function of the compactification length $m_{KK} = ((n+1)\pi/L)^2$, hence the zeroth mode on the brane is the lightest SM like Higgs which has $m_0 = \pi/L$. From the unobservable scale length follows that the Higgs zero mode has to be heavier that 600 GeV. If one evaluates in this model the vacuum polarisations under the influence of the higher KK excitations for the Peskin-Takeuchi parameters [124], one finds that such a high Higgs mass is not contradicting the present electroweak precision data, but as in the SM, clearly the lower value of 600 GeV is preferred.

Concerning the decay of the heavy SM like Higgs, the decay into gauge bosons is of special importance. Since there is no Higgs potential this decay occurs only through gauge interaction. When defining the ratio of the coupling WWH in this model to the SM by $r_{\mathrm{WWH}} = 0.9$, the estimate for the decay width yields

$$\Gamma_{\mathrm{H}\to\mathrm{W}^+\mathrm{W}^-} \approx \frac{g^2}{64\pi}\frac{M_{\mathrm{H}}^3}{M_{\mathrm{W}}^2} r_{\mathrm{WWH}}^2 \,. \tag{2.35}$$

Because of the large (> 600 GeV) Higgs mass, one expects $\frac{M_{\mathrm{H}}^2}{M_{\mathrm{W}}^2} \gtrsim 40-50$. Therefore, one recognises the width in Eq. 2.35 comparable to the Higgs mass, but certainly larger than the SM expectation. In this case the rapid Higgs decay or the smearing out of the Higgs will result in its unobservability.

2.2.4 The stealthy Higgs scenario

As seen above, the introduction of scalar gauge singlets into the SM leads naturally to invisible Higgs decays. The decay width is depending on the number and density of such extra states. In the following we now describe a model that generically generates invisible Higgs decays with arbitrary width since the additional states are abundantly present. Though it is very similar in this respect to the Kaluza-Klein towers, it extents the SM only minimal without assumptions on new symmetries or extra dimensions.

Since 1995, J.J van der Bij und T. Binoth together with collaborators developed this very simple extension of the SM, known as stealthy Higgs scenario [36], that allowed quantitative statements on the influence of a hidden scalar sector with strong couplings to the Higgs sector on the Higgs observables at colliders. As the name indicates, the very pessimistic consequence for many model parameters will be that the Higgs can escape detection at collider experiments since the experimentally important signal to background ratio decreases.

Extension with a O(N)-symmetric scalar multiplet

Technically, an arbitrary large number N of scalars, that for simplicity are called Phions, φ, extends the SM. Since those phions are gauge singlets, they do not participate in strong or weak interactions. On detector level they therefore remain invisible and therefore could also provide a CDM candidate. The introduction of Phions inflates the number of parameters only in a minimal way. New parameters to the model are the mass shared by all Phions m_φ, and the Phions self coupling κ as well as the coupling to the Higgs sector ω. Thus, the SM Higgs boson is the only particle which interacts with the scalars.

Even if the Phions are strongly coupled to the Higgs and modify the Higgs propagator in the resulting width, it is shown in [17, 148] with a non perturbative calculation that the Phion bubbles affect the Higgs propagator earliest on two-loop level. The analysis in [17] indicates that the first large effect of the phions

to the electroweak correction will be thus at the three loop level. On the other hand it is known that in the SM precision variables, like the the ρ parameter or the Peskin-Takeuchi parameters [124], are only little sensitive to Higgs mass effects on two loop-level. Consequently, the proposed extension with the new scalars entering only at the two-loop level is not contradicting current observations, because those small two-loop effects are currently well below experimental precision and do not influence the precision fits. The scalar part of the Lagrangian (Eq. 2.1) can be replaced by

$$\mathscr{L}_{\text{Scalar}} = \mathscr{L}_{\text{Higgs}} + \mathscr{L}_{\text{Phion}} + \mathscr{L}_{\text{int}}.$$

The explicit terms read then

$$\begin{aligned}
\mathscr{L}_{\text{Higgs}} &= -\partial_\mu \Phi^\dagger \partial^\mu \Phi - \lambda\,(\Phi^\dagger\Phi - \frac{v^2}{2})^2 \\
\mathscr{L}_{\text{Phion}} &= -\frac{1}{2}\,\partial_\mu \vec{\varphi}\,\partial^\mu \vec{\varphi} - \frac{1}{2} m_\varphi^2\,\vec{\varphi}^2 - \frac{\kappa}{8N}\,(\vec{\varphi}^2)^2 \\
\mathscr{L}_{\text{int}} &= -\frac{\omega}{2\sqrt{N}}\,\vec{\varphi}^2\,\Phi^\dagger\Phi.
\end{aligned} \tag{2.36}$$

As before, $\mathscr{L}_{\text{Higgs}}$ contains the Higgs sector of the SM with the vev of the Higgs causing the spontaneous symmetry breaking $SU(2)_{I_w} \times U(1)_Y \to U(1)_{Q_{\text{el}}}$. New contributions arise from the Phions described by the term $\mathscr{L}_{\text{Phion}}$. Most conveniently they can be collected in the N real components of $\vec{\varphi} = (\varphi_1, \ldots, \varphi_N)$, which is the representation of a O(N)-symmetric multiplet. Further, the introduction of the $O(N)$ symmetric multiplet allows for the use of $\frac{1}{N}$ expansion techniques. It is a desirable simplification to forbid hereby a vev for one of the multiplet components $< 0|\vec{\varphi}|0 > \neq \vec{0}$. Since a vev for the Phions would result in a non diagonal mass matrix, the phions would mix with the Higgs boson. After the unitary gauge has removed the would-be Goldstone bosons from the theory, this mixing of the Higgs boson with the Phions would modify the couplings of the lightest scalar to the gauge bosons. The couplings of the lightest scalar would contain as factor the cosine of the mixing angle stemming from the non diagonal mass matrix reducing effectively the SM Higgs production cross section given in Fig. 2.5. We will not consider this case and assume $< 0|\vec{\varphi}|0 > = \vec{0}$.In order to avoid a vev for the multiplet we choose $\omega > 0$, which leads to a new phenomenology, detailed in the following.

In $\mathscr{L}_{\text{Phion}}$, one identifies a kinematic term for the Phions and a direct mass term as well as the self coupling of the Phions, which is suppressed by a factor $\frac{1}{\text{N}}$.

More interesting is the interaction part of the Lagrangian $\mathscr{L}_{\text{int}}$, which couples the Phions to the Higgs. After symmetry breaking, the non vanishing vev induces additionally an effective mass for the Phions. The effective mass depends on ω and has the suppression factor $\frac{1}{\sqrt{N}}$. Thus, the total mass of the Phions is $m = \sqrt{m_\varphi^2 + \frac{\omega v^2}{4\sqrt{N}}}$. Additionally, since $\omega > 0$, the physical Higgs boson can decay invisibly into a pair of Phions.

For the theoretical bounds of the model the renormalisation group equations of the model must be inspected. These read ([36]) with the definition $q = \log(Q/Q_{ref}), \partial_q = \partial/\partial q$ in leading order in $\frac{1}{N}$

$$\begin{aligned}
(4\pi)^2 \partial_q \lambda &= 24\lambda^2 + \lambda(12\lambda_t^2 - 9g'^2 - 3g^2) \\
&\quad -6\lambda_t^4 + (3g^4 + 6g^2 g'^2 + 9g'^4)/8 + \omega^2 \\
(4\pi)^2 \partial_q \omega &= \omega\,(24\lambda + \kappa + 6\lambda_t^2) \\
(4\pi)^2 \partial_q \kappa &= 8\omega^2 + \kappa^2/3 \\
(4\pi)^2 \partial_t \lambda_t &= 9/2\lambda_t^3 - (8g_3^2 + 9/4g'^2 + 17/12g^2)\lambda_t
\end{aligned} \tag{2.37}$$

And with the shorthand notation $g_i = (g, g', g_3)_i$, the evolution of gauge couplings above can be summarised as:

$$g_i^{-2}(q) = g_i^{-2}(0) + c_i/(8\pi^2)q, \quad c_i = (-41/6, 19/6, 7)_i (i = 1,2,3).$$

The running of the couplings is determined, if we fix initial conditions at $q = 0$ by $Q_{ref.} = 2M_Z$ as initial point. In the scale evolution of the RGE for the Higgs self coupling λ now contributions dependent on the Higgs Phion coupling ω occur at the one-loop level. If ω represents a strong coupling, the negative contribution of the top quark Yukawa coupling to λ can be partly cancelled. Therefore, the lower bounds on the Higgs mass are reduced as ω increases, until the Landau pole is reached. While the RGE for the most important top quark Yukawa coupling stays unchanged with respect to the SM, two new equations govern the evolution of κ and ω. As reference scale in the evolution of the latter two one fixes $\kappa(2M_Z) = 0$, since this allows for the largest parameter space in the (ω, M_H) plane. However, as in the case of the pure SM, the investigation with respect to vacuum stability and Landau pole behaviour in the RGE for λ at a certain cut off scale Λ_C yields boundaries for the Higgs mass which this time become also a function of the coupling ω. The upper bounds on ω are inferred because only the coupling to the hidden sector in this model can be strong but the Higgs self couplings should remain perturbative. These boundaries are shown in Fig. 2.14. As before, the assumption of validity of the model up to the Planck scale sets the most stringent constraints on the Higgs mass. This would allow for a Higgs mass between 145 GeV to 175 GeV and $\omega < 0.75$. This small range is very similar to the range in Fig. 2.7 if the highest cut-off is considered. The largest allowed range for Higgs mass and coupling coincides with a scale that limits the validity of the model to 1 TeV. In this case, ω below 13.2 and Higgs masses between 77 GeV and 483 GeV are allowed. In the case of non vanishing κ, the bounds are more restrictive, because the Landau pole moves to lower energies as the coupling increases [37].

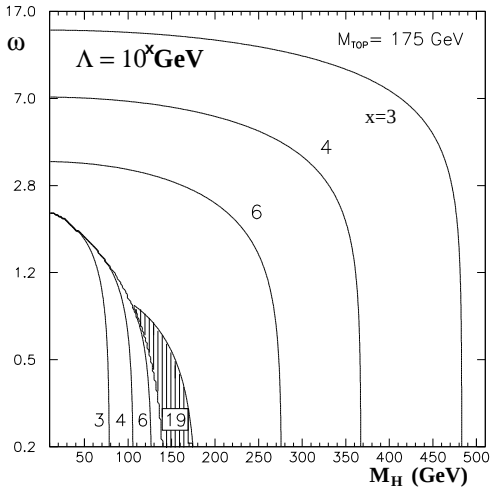

Fig. 2.14: *Allowed and theoretically forbidden regions in the parameter plane, inferred from the validity of the group renormalisation equations of the stealthy Higgs model (taken from [36]). The evolution of λ and ω was fixed at $2M_Z$ by $\kappa(2M_Z) = 0$ and then ω was varied. This choice guarantees the largest possible allowed parameter range. $\Lambda = 10^x$ GeV denotes the cut off scale up to which the self coupling λ remains perturbative. The upper right contours follow for various values of exponents* x *follow from the requirement that there shall be no Landau pole below Λ. The lower left contours are consistent with the demand that corrections to λ in dependence of m_t result in a positive definite λ which yields a stable vacuum state. Again assuming the validity of the model up to the Planck scale $\Lambda = 10^{19}$ GeV, the parameter of the model and the Higgs mass are most restricted (hatched region). Compare the analogue Fig. 2.7*

Modification of the Higgs propagator by scalar singlets

To be able to study strong couplings and therefore rapid decays with large decay widths into the invisible final state, the radiative correction occurring in the Higgs propagator due to Phion loops have to be calculated in the limit $N \to \infty$. Since ω can be non perturbative, the $\frac{1}{N}$ expansion technique is used. Details of the derivation and the evaluation are given in [17, 35, 77–79, 148].

If one is only interested in the effect of the broadening of the Higgs, further simplifications can be made. One neglects κ as a small effect and sets $m_\varphi = 0$. The latter is not really important because results for the decay width can be easily rescaled for massive Phions with the appropriate phase space factor [37].

It should be noted, since the Phions occur in the loop correction to the Higgs propagator, that it does not matter for the result that in the limit $N \to \infty$ the induced Phion mass is vanishing. At this point we give only the result of the modified Higgs width[8)] in case of the presence of Phions [36, 37]:

$$\Gamma_H = \Gamma_H^{SM} + \frac{\omega^2 v^2}{32\pi M_H}. \tag{2.38}$$

If one has a distinctive Phions mass $m_\varphi > 0$, the formula is rescaled [149] according to

$$\Gamma_H = \Gamma_H^{SM} + \frac{\omega^2 v^2}{32\pi M_H} \times \sqrt{1 - \frac{4{m_\varphi}^2}{{M_H}^2}}. \tag{2.39}$$

As soon as the Higgs is heavier as two vector bosons, the predicted SM decay width of the Higgs rises strongly. In Fig.2.15 one sees the large deviation predicted by the stealthy Higgs scenario with respect to the decay width of the SM even for very light Higgs bosons. For the intended sensitivity study we restrict the parameter space by the minor assumptions of $\kappa = 0,\ m_\varphi = 0$. This leaves only two parameters that characterise the scenario. Because of Eq. 2.38, one can specify a parameter point or a signal hypothesis in the model by (M_H, Γ_H) or (M_H, ω). Also it was analysed [77, 79] using the $\frac{1}{N}$-expansion, which effect the occurrence of a possibly large ω in the evolution equations Eq. 2.37 can have for the position on the Higgs pole. An saturation of the Higgs boson mass at roughly 800 GeV was found, while the width became an essentially free parameter in dependence of ω. As a consequence sizable invisible width of the Higgs is expected even if it is heavier than $2M_W$, which has to taken into account when searching the Higgs at the LHC.

Shaping the cross section of the process $H \to \varphi\varphi$

When searching for Higgs bosons in the stealthy Higgs scenario, two strategies can be applied depending on the value of ω. Because a very weak coupling to the hidden scalar sector would result only in a small invisible width, which would mean a small invisible branching, the direct search for invisible decays can be very difficult. In this case, indications for the existence of these scalars may be gathered by precisely measuring the visible branching and compare them to the SM prediction. Though this indication is not unique for the stealthy Higgs scenario (and still depends on assumptions on the Phion mass), it may turn out that the size of suppression is more compatible to this scenario than for example the graviscalar mixing.

As soon as ω is strong enough to produce competitive rates or dominance of invisible decays, direct searches can be applied. For light Higgs bosons, as in the kinematic range of LEP, this situation will be realised for relatively small couplings. For the extended mass range the SM Higgs width can be considerable and the reach for smaller ω is limited.

[8)] In this context the pole mass M_H and corresponding width Γ_H is defined by the position of the pole in the propagator evaluated on the real axis and not by its position in the complex plane.

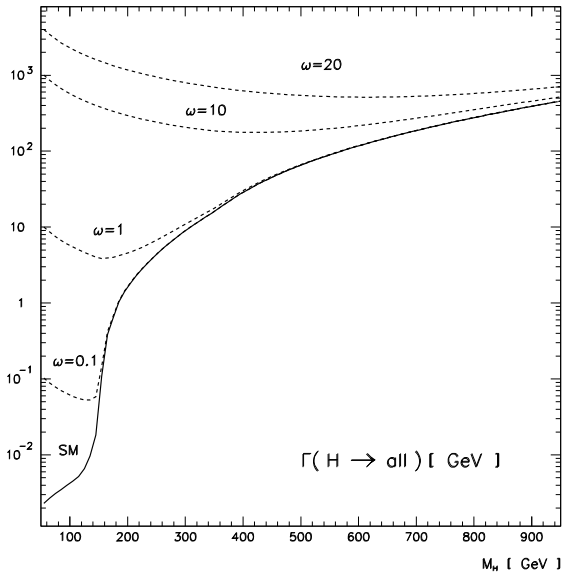

Fig. 2.15: *Total width of the Higgs boson decays (dashed) for various values of the coupling ω in the stealthy Higgs scenario compared to the SM width prediction (solid) [36]. The branching BR into invisible final states is defined by* $BR = \frac{\Gamma_{\mathrm{TOT}} - \Gamma_{\mathrm{SM}}}{\Gamma_{\mathrm{TOT}}}$.

The cross section $\sigma_{invisible}$ of such a process can be approximated generically by rescaling the SM production cross section (that are unchanged in case of no mixing with Phions) with the Breit-Wigner function that accounts for the invisible width contributions of the Phions by the parametrisation of Eq. 2.38. In this formula s_I is the invariant mass square of the decayed Higgs. The invisible part of the width is denoted by $\Gamma(H \to \not{E})$ and $\Gamma(H \to \mathrm{All})$ is the total width according to Eq. 2.40. So the relativistic Breit-Wigner term scales with the invisible branching. The distribution of the invariant Higgs masses in the broad Higgs goes along with their production cross section

$$\sigma_{(\mathrm{H}\to\not{E})} = \int ds_I \, \sigma_{SM}(s_I) \, \frac{\sqrt{s_I} \quad \Gamma(H \to \not{E})}{\pi((M_H^2 - s_I)^2 + s_I \, \Gamma(H \to \mathrm{All})^2)} \, . \tag{2.40}$$

2.2.5 Summary of theoretical motivation of invisible Higgs decays

In summary of this little overview we note the following:

1) Invisible Higgs decays are theoretically well motivated in many models.

2) In competition with the SM decay modes, invisible modes can be dominant for Higgs masses below $2M_{\mathrm{W}}$. For some models even for higher Higgs masses the branching into invisible final states can be considerable.

3) Invisible decays of narrow Higgs bosons occur for decays in only one particle with a given mass. The experimental sensitivity of dedicated invisible Higgs searches, e.g. at the LHC should be sufficient in that case.

4) Extremely broad (visible or invisible) Higgs decay widths occur for decays into dense spectra of final states or due to the modification of the Higgs propagator by the presence of such states. The experimental sensitivity can be expected to be deteriorated severely at the LHC.

5) Since in models which allow for broad invisible Higgs decay the allowed Higgs mass and width of the decay can vary considerably, mass and width dependent searches complement the dedicated Higgs searches with narrow invisible width.

6) All experimentally disadvantageous effects are present for example in the very simple stealthy Higgs scenario, whose parameters allow for a scan in mass and width. Therefore, the sensitivity study presented here will focus on the stealthy Higgs model. Results in this scenario can be seen as exemplary for the other and may be interpreted in similar models like the ADD with Higgs graviscalar mixing.

2.3 Experimental status of searches for invisible Higgs decays

After having extensively motivated the possibility of various kinds of invisible Higgs decay signatures, we give now the status of the experimental searches that consider such models.

LEP searches for invisible Higgs decays

At the LEP electron positron collider searches for the invisible Higgs boson decays had been performed. Most searches made the assumption of invisible decays within the MSSM or exotic models like the Majoron models. The final result (see Fig. 2.16) excluded an invisibly decaying Higgs boson up to $M_{\mathrm{H}} = 114.4$ GeV at 95% CL [89]. That is the same lower limit as it was set by the SM searches at LEP. At LEP, the production of the Higgs in association with the Z boson was used to look for invisible Higgs decays. The techniques of the recoil invariant mass [9)] spectrum of the Z decay products could be applied since the beam energy of the electrons was exactly known. Indeed, since only narrow Higgs decays were modelled, the sensitivity of the invisible searches became competitive to the visible searches and bounded only by the kinematic limit of the LEP collider.

Additionally, the OPAL Collaboration performed a dedicated search allowing for a broad decay width in invisible Higgs decays [10]. Here, upper limits in the order of 0.1 pb could be set on many mass and decay width combinations, and also a part of the stealthy Higgs parameter space was excluded for masses below 106 GeV and $\omega \lesssim 6$. Since the intended sensitivity study is trying to extend this search in the same model, a detailed comparison will be undertaken in the interpretation of the results in Section 8.4.

Difficulties to find invisible Higgs decays in the TeVatron

At the TeVatron, the associated Higgs production is a promising production mode for discoveries. however, the signal to background ratio is much lower compared to LEP and the impact of systematic uncertainties is harder to control. So far after collecting roughly 5.4 fb^{-1} of data [9], the TeVatron experiments have not published any search for the invisible Higgs decays (see review in [120]). Searches using the associated Higgs production, weak boson fusion, and $t\bar{t}$ associated production are challenging since they have to deal with a lower cross section than at the LHC and the collection of a large integrated luminosity is needed. E.g. using $q\bar{q} \rightarrow \mathrm{ZH} \rightarrow l^+l^- + E_{\mathrm{T}}^{\mathrm{miss}}$ for a Higgs with $M_{\mathrm{H}} = 120$ GeV at TeVatron, a 5σ observation of the invisible Higgs boson is expected to be possible only with an integrated luminosity of $30\mathrm{fb}^{-1}$ of data [117, 153]. This is roughly three times the integrated luminosity that TeVatron will have collected by the end of its data taking in October 2011 and that is needed to discover such a Higgs at the LHC. Therefore, with the start of data taking at the LHC, good experimental prospects, and a wide range of scenarios motivating invisible Higgs decays at hand, the invisible Higgs searches will play a role in its early physics program [7, 29].

[9)] The *recoil mass* is defined as $\mathrm{M}^2_{\mathrm{Recoil}} = (1 - \frac{2\mathrm{E}_{\mathrm{VIS}}}{\sqrt{\mathrm{s}}})\mathrm{s} + \mathrm{M}^2_{\mathrm{VIS}}$, were the visible decay products of the Z boson are measured in the detector as E_{VIS} and M_{VIS}.

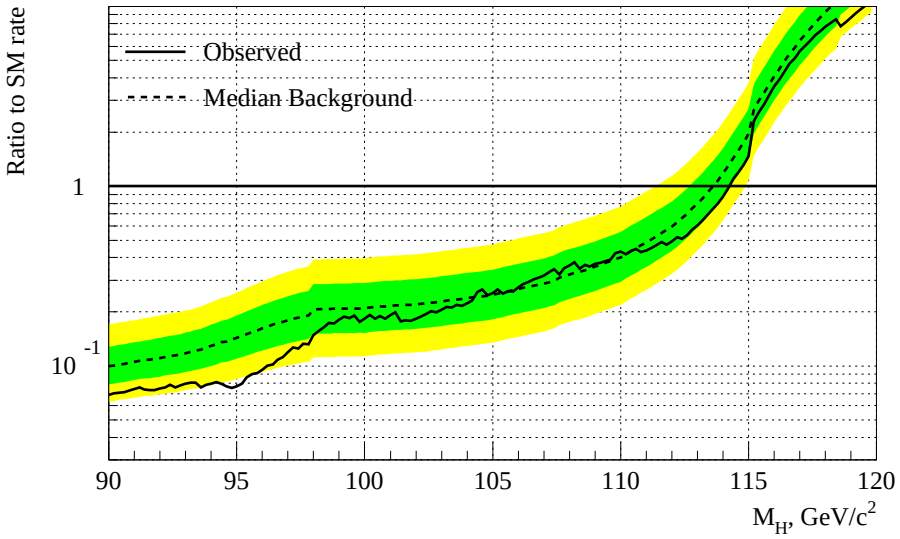

Fig. 2.16: *Combined result of the LEP experiments on exclusion of invisible Higgs decays. Using data up to* $\sqrt{s} = 209$ GeV*, the lower mass limit was found to be 114.4 GeV(taken from [89]).*

3. The experimental environment

This chapter is dedicated to a short description of the experimental setup in which the sensitivity study is intended to take place. This overview can by now means cover the details of the huge experimental efforts at the the LHC comprehensively, for which we will refer to the literature. Instead we will only focus on facts that have some connection or give supporting information to the intended sensitivity study, e.g. change of acceptance and efficiency by design differences in various parts of the detector. We start with shortly introducing the collider ring of the LHC before describing the most important detector elements and the main steps of data acquisition and reconstruction of events.

3.1 The Large Hadron Collider (LHC)

Located 100 meters underground near Geneva the large hadron collider is a proton proton collider with a circumference of 27 km. Since protons collide the emitted synchrotron radiation which is inverse proportional to the fourth power of the accelerated particle mass is not limiting the accessible centre of mass energy and the machine is designed to be operated at an unprecedented centre of mass energy of $\sqrt{s} = 14$ TeV. As one conveys from Fig. 3.1 the LHC ring is the last expansion state of a refined accelerator system of the ample CERN laboratory, consisting of proton or heavy ion sources, and pre-accelerators, and storage rings that accumulate the injected current. The preparation of the proton beams to reach the injection energy of 450 GeV is described in [72], we just mention at this place some machine characteristics of the LHC ring itself. For the acceleration the LHC posses 8 superconducting RF cavities operated at 400 MHz.In order to be able to bend protons accelerated at design centre of mass energy on the ring trajectory a maximal magnetic field of 8,73 T can be delivered by each of the 1232 superconducting dipole magnets. A slice plane through one of such a dipole is shown in 3.2. The special design of the dipole makes it possible to house the two beam lines, needed for equally charged particles to revolve in opposite directions, in one cryostat that is cooled down to 1.9 K. For focusing the beams additional 392 quadrupole magnets with a high gradient of $233\frac{T}{m}$ are used. In total the magneto-optics that keeps the beams precisely focused and on the nominal track consists of 7000 magnets.

Depending on the number of particles in the bunches filled in the ring, an experimentally very important quantity can be derived, namely the so-called instantaneous luminosity. The higher the luminosity the higher the yield of inelastic interactions that can be recorded. The rate of proton-proton interactions per second depends on the number of particles N_b per colliding bunch as well as on the number of bunches in the ring are n_b, and the size of the bunches given by their dispersion σ_x and σ_y and lastly the frequency f of the collisions. By design 2808 counter-revolving bunches of $\sim 10^{11}$ protons each collide every 25 ns ($f = 40$ MHz) in the LHC interaction points. Assuming equally filled bunches of protons, hence the square, one expresses the instantaneous luminosity L_{instant} as

$$L_{\text{instant}} = \frac{N_b^2 \cdot n_b \cdot f}{4\pi \cdot \sigma_x \cdot \sigma_y} = \frac{N_b^2 \cdot n_b \cdot f \cdot \gamma \cdot F}{4\pi \cdot \varepsilon \cdot \beta^*}. \tag{3.1}$$

In the right part the beam dispersions σ_x and σ_y have been expressed by the machine parameters ε, the emittance, and β^*, the beta function at the interaction point, as well as a geometrical factor F. The gamma factor of the particles is denoted γ. The design goal for the LHC is to deliver an instantaneous luminosity of $10^{34} cm^{-2} s^{-1}$.

At four interactions points the beams collide and each cavern around these interaction points hosts an large experiment designed to make optimal use of the delivered luminosity. These are two omnipurpose high energy detectors, namely ATLAS (A Toroidal LHC Apparatus) [6] and CMS (Compact Muon Solenoid) [49] that can record proton and ion run data and are capable to cover experimentally a very ample physics research program. The other two experiments have specialised research programs. The experiment LHCb (Large Hadron Collider beauty) [21] will be able to investigate B meson physics and study CP violation in that sector with high statistics and precision. The ALICE (A Large Ion Collider Experiment) [8] experiment will focus on measurements with heavy Pb ions. In such nucleus-nucleus collisions occur high values of energy density, which can initiate the formation of a primordial quark-gluon plasma. These heavy ion runs will open a new window for the study of the strong interactions. Some additional displaced experiments extend the possibility of measurements of physics in the extreme forward directions close to the beam line, like diffractive events. One of these is TOTEM (TOTal Elastic and diffractive cross section Measurement) [22] which consists of roman pot detectors $\pm$147 m and $\pm$220 m away from the CMS interaction point. TOTEM measures elastic and diffractive scattering and aims to determine the total p-p cross sections with a luminosity independent method. The other one is the LHCf (LHC forward) [13] experiment located $\pm$140 m away from the ATLAS interaction point. LHCf will measure neutral particles, e.g. to calibrate hadron interaction models of extreme high energy cosmic rays. Finally to be installed during a shut down 2011 a small experiments called MoEDAL (Monopol and Exotics Detector At the LHC) [125] will search for long-lived and stable exotic ionising particles as magnetic monopols stemming from the collisions, using plastic nuclear tracker devises.

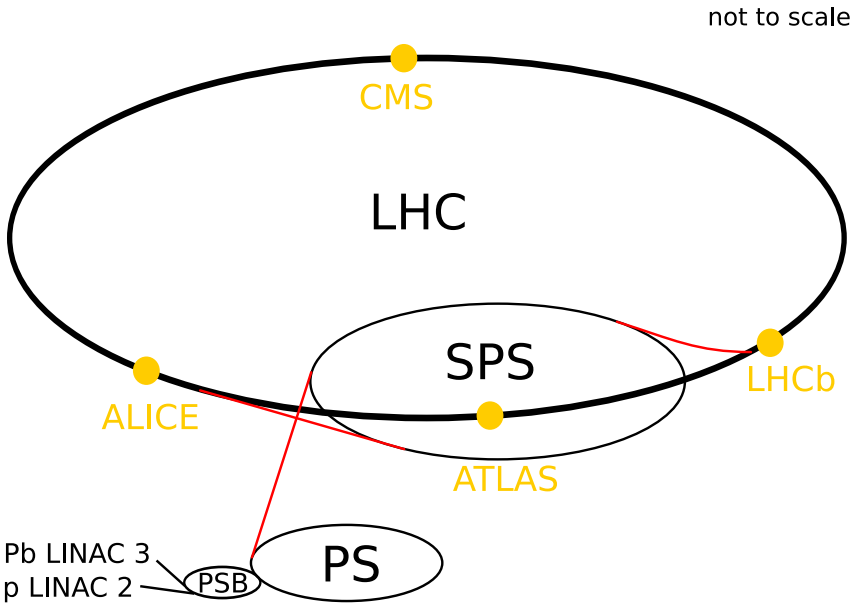

Fig. 3.1: *The CERN accelerator complex shares infrastructures for the various experimental sites. The not to scale schematic only displays the part of the accelerator complex used to fill the LHC ring. For proton-proton collisions the LHC ring is fed with protons accelerated transferred from the source by Linac2 (Pb ions from Linac 3) at a maximum energy of 50 MeV into the proton booster synchrotron PSB where they are boosted up to 1.4 GeV followed by the proton synchrotron (PS) which gives the protons energies of 25 GeV. The injection energy to the LHC of 450 GeV is reached in the super proton synchrotron SPS. The LHC can accelerate the proton bunches up to 7 TeV. By design the bunches collide every 25 ns (40 MHz) in the LHC interaction points.*

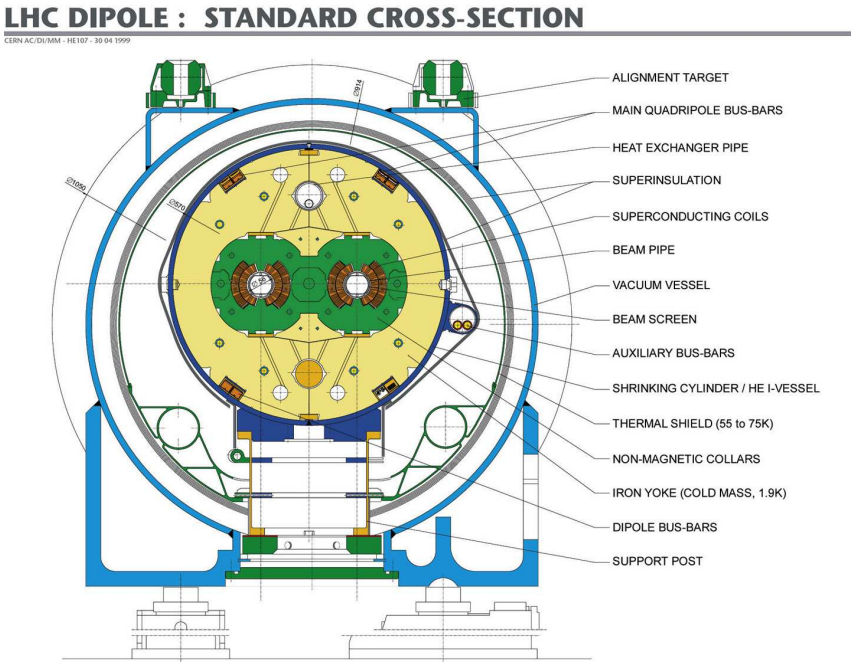

Fig. 3.2: *Section through one of the 1232 standard dipole bending magnets used in the LHC. The special design house in one cryostat kept at 1.9 K two beam lines in which the counter revolving proton beams are bended to the trajectory by the special field configuration.*

The LHC running

The operation of the LHC started on the 10^{th} of September 2008 but the test phase was interrupted only nine day later by an incident, in which the suddenly evaporating of the cold mass of a dipole caused large mechanical damage. The subsequent intense failure study and repair efforts were completed in November 2009. Since March 2010 the regular data taking at a reduced centre of mass energy of $\sqrt{s} = 7$ TeV, with having exceeded an instantaneous luminosity of about $2 \times 10^{32} cm^{-2} s^{-1}$ so far. There are also heavy ion runs at up to $\sqrt{s} = 5.5$ TeV per nucleon, interlaced to the proton proton data taking. It is intended to record an integrated luminosity of about 1 fb^{-1} of proton proton data per experiment until end of 2011. After that a shut down of 15 to 18 month will prepare the LHC to run $\sqrt{s} = 7$ TeV, at design luminosity of $10^{34} cm^{-2} s^{-1}$ from 2013 on. This so called high luminosity phase will pose new challenges on data acquisition since on average the remnants of 23 inelastic interactions are present in a detector. Implications of such a level of so-called pile up will be explained in the next chapter. The intended running for three years expects to collect 100 fb^{-1} per year and experiment. Further ahead are plans to use the years after 2015 for a major upgrade of ring to the Super LHC (SLHC) and of the detectors [80] to reach at least luminosities of $10^{35} cm^{-2} s^{-1}$ maybe from 2019 on.

3.2 The ATLAS detector

Before describing the general layout of the ATLAS detector and give details to some important sub-detectors, we start with the definition of coordinates used in ATLAS.

The ATLAS coordinate system

Positions in the ATLAS detector are given in a right-handed coordinate system with its origin in the nominal interaction point. The x-axis points from the origin towards the centre of the LHC ring and the

y-axis is pointing to the surface. The z-axis is pointing along the beam line.. More often the Cartesian coordinates are replaced by the azimuthal angle ϕ in the $x-y$-plane, beginning on the positive x-axis and the polar angle θ, beginning at the positive z-axis and the radius r. The rapidity y is commonly used, since it is Lorentz invariant under boosts in z-directions and becomes conveniently to describes properties of particles produced in strong interactions. Its definition for a particle with the energy E and a momentum p_z in the z-direction is

$$y = \frac{1}{2}\left(\frac{E-p_z}{E+p_z}\right). \tag{3.2}$$

Especially if the momenta are so high that the mass can be safely neglected, as it is commonly the case for the LHC, the equation simplifies to the definition of the so-called pseudorapidity η with

$$\eta = -\ln\left(\tan\left(\frac{\theta}{2}\right)\right). \tag{3.3}$$

The polar angle of 90° is equivalent to $\eta = 0$ and is often referred to as '*central*' w.r.t. to the detector. The exact beam axis corresponds to $\eta = \pm\infty$ and is referred to as '*forward*' or '*backward*' direction in the detector. Therefore, positions in ATLAS will be given in η, ϕ and r or z. For the physics the latter are of minor importance because the p_z of the colliding partons in the protons is unknown and the centre of mass system of the collision is undetermined. The only defined and conserved initial condition in the colliding proton system is that the transverse momenta vanish. Therefore, in ATLAS transverse observables (defined in the $x-y$-plane) are extensively used. e.g the transverse momentum p_T or missing transverse energy $E_\mathrm{T}^\mathrm{miss}$. Spatial distances are often given in the η, ϕ space as $\Delta R = \sqrt{\Delta\eta + \Delta\phi}$.

ATLAS uses an uniform magnetic field in the tracking system to measure the particle momenta. The helical charged particles trajectories are described by the following parameters: momentum p_T w.r.t. the beam, and the point of the closest approach of the track to the beam axis d_0, which is the impact parameter of the track, and $\phi_0 = \tan^{-1}\frac{p_y}{p_x}$ at the transverse impact parameter, and $\cot\theta = \frac{p_z}{p_\mathrm{T}}$, and lastly z_0 the location of the transverse impact parameter in z.

3.2.1 General building scheme of ATLAS detector

An overview of the ATLAS detector is shown in Fig. 3.3. Its overall dimensions are 44 m long and 25 m in diameter with a total weight of approximately 7000 t. For the precise measurement of collision events the ATLAS detector provides coverage of a large fraction of the solid angle, which is almost full azimuthal angle symmetry and coverage without cracks and large acceptance in pseudorapidity about 4.9. In detector components closer to the beam line the particle flux can be very large so that in particular radiation hardness of the components is required. The occupancy of the detector is also large because if one assumes collisions every 25 ns, producing relativistic particles that would move approximately 7.5 m in the detector in average particles of 2 or 3 bunch crossing can be expected to be present in the detector volume.

Beginning from the beam line the three main sub-components are

1) the inner detector, which is used for tracking and particle identification,

2) next the calorimeter to determine electromagnetic and hadronic energies allowing for reconstruction of jets, which are coherent and locally confined sprays of particles stemming from decays of a hadronic particle, and the determination of $E_\mathrm{T}^\mathrm{miss}$ in the event and identifying electrons and photons

3) and lastly the muon spectrometer system which triggers on muons and measures momenta of the high energetic muons that transverse the inner detector and calorimeter.

Another characteristic design principle of the detector is that each subsystem is divided into a cylindrical barrel part and two adjacent end-caps or wheel structures next to the barrel. The sub-detector designs in end-cap and barrel can differ and also the transition regions contain inactive material and support structures and place a discontinuity, which results in lower efficiencies of measurements near this transition regions.

3.2.2 Magnetic fields for momentum measurements in ATLAS

Momenta of charged particles can be measured by the sagitta of their trajectory that is bended by the Lorentz force in a magnetic field. ATLAS uses two magnetic fields for this purpose. First the inner detector is placed completely in a superconducting solenoid which is cooled down to 4.9 K, producing an almost uniform 2 T field along the beam axis. Particles with less than 500 MeV will curl in such a strong field that they cannot be measured by the inner detector. To save material place in front of the calorimeter that deteriorates the energy measurement in the calorimeter, the solenoid uses the cryostat of the surrounding calorimeter and the iron absorber structures as flux return yoke. The second field is produced by 8 large air core toroid superconducting magnets which entered the acronym of ATLAS. The coil in the barrel are 25 m long and in the end cap 5 m long, where they are also housed in the same cryostat placed behind the calorimeter end-caps. The whole toroidal magnetic field is inserted into the muon system where it provides the bending of high energetic muon up to $\sim$ 3 TeV in the $r-z$-plane. The field lines are a torus around the beam line and ϕ-symmetric. Since there are strong radial forces the support structures of the coils must be strong. The field is not perfectly uniform. It varies in the barrel ($|\eta| < 1.4$) between 0.2 T and 2.5 T the smaller coils in the caps ($1.6 < |\eta| < 1.7$) produce 0.2 T and 3.5 T field. but due to interference of the overlapping fields in the transition region ($1.4 < |\eta| < 1.6$) the field strength is reduced there. Nevertheless the field configuration is almost orthogonal to the muon trajectories and the use of air coil toroids minimises the distortion of the resolution by multiple scattering of the muons.

3.2.3 Inner detector

The cylindrical inner detector (ID) with the measures from radius $r = 50.5mm$ to $r = 1.15m$ and a length of $7m$, is completely placed inside the 2 T solenoid. The ID provides the tracking with the requirement of good charged particles momentum resolution (for $p_{\mathrm{T}} > 0.5$ GeV). The tracking of charged particles is possible with the ID in the range $|\eta| < 2.5$. The detection efficiency has to be high and the innermost vertex detector has to be able to resolve secondary vertices, which are typical for decays of particles with longer lifetime as the tau lepton or B mesons. The identification of a secondary vertex aids offline reconstruction of tau lepton or flavour tagging of jets. Also good vertex resolution is needed to discriminate the inevitable present tracks of pile up events from the tracks of the physical interesting events. Therefore, the vertex detector is placed directly at the beam line. Multiple scattering of charged particles is reduced to the minimum in this way, since it can only happen in the beam pipe wall and the ID support structures. Also the vertex detector is designed as very high resolving pixel detector. If the LHC is in 25 ns bunch spacing mode one expects in the order of 1000 charged particles per bunch crossing in the $|\eta| < 2.5$ acceptance range of the ID. Therefore, in order to have a low occupancy in the vertex detector and a high precision position of the 3 points of the emerging tracks, the pixel detector has to have high granularity. The more the detector elements are located at larger radii the more coarse the sensor segmentation can be, since the density of tracks is lower. Hence the next vertex detector called semiconductor tracker (SCT) using stereo pairs of silicon micro-strip sensors measuring up to four additional track points with radii between $r = 30cm$ to $r = 53cm$. Both precision trackers contribute to the secondary vertex recognition. Lastly the ID is completed by a transition radiation tracker (TRT). The straw-tubes in this detector add many additional points, typically 36 per track, of the trajectories but provides only $r-\phi$ information. But

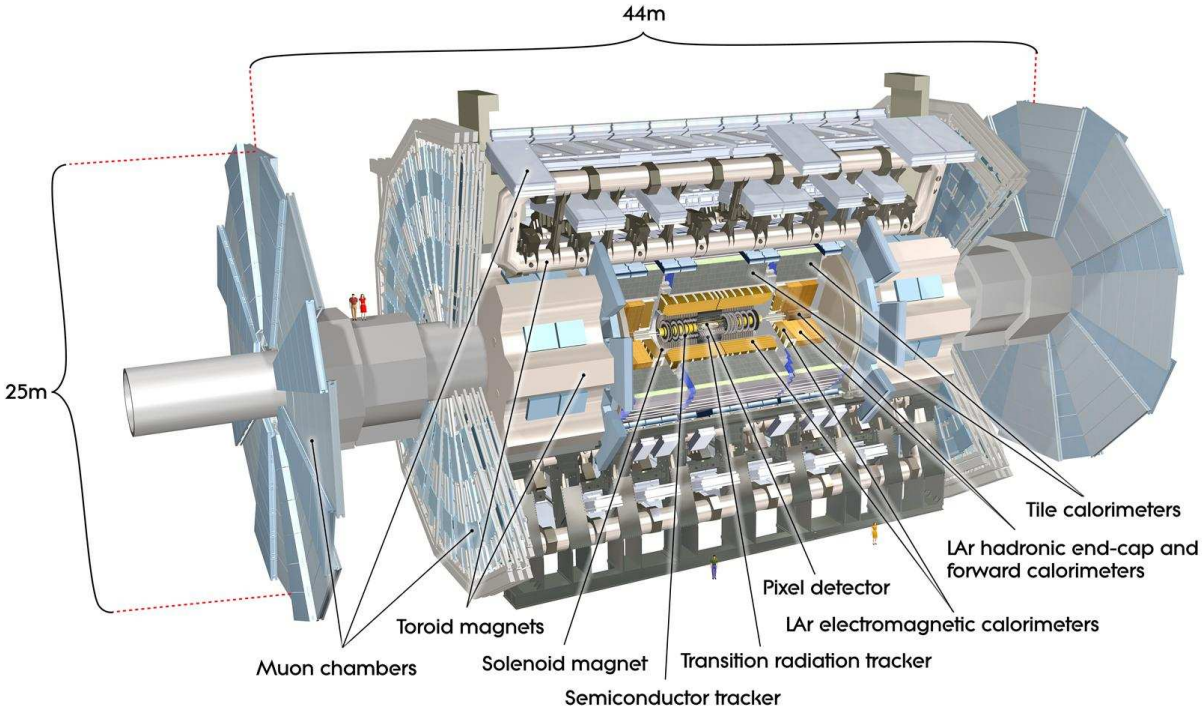

Fig. 3.3: *Cut away picture of the complete ATLAS detector.*

the combination of many TRT hits at outer radii representing a large lever arm with the precision tracker hits give a very robust pattern recognition and precision in $r-\phi$ and z coordinates. Also the Cherenkov light yield in the tubes can be used for discrimination between particles like pions and electrons. A segment of the barrel part of the ID is shown in Fig. 3.4. The radii occupied by the three components pixel, semiconductor tracker and the TRT are indicated. The whole material budget of the inner detector, concerning on-board electronics sensors material and the support structures, was minimised in order to reduce multiple scattering and showering of particles before the calorimeters. Besides the displayed barrel the pixel detector and the SCT have additional discs in the end-caps to provide the acceptance in forward and backward directions. The detailed design is described in [1, 6].

The overall expected resolution for tracks by the ID is estimated [2] as

$$\sigma(d_0) = 11 \oplus \frac{73}{\frac{p_T}{\mathrm{GeV}}\sqrt{\sin\theta}}(\mu m) \tag{3.4}$$

$$\sigma(z_0) = 87 \oplus \frac{115}{\frac{p_T}{\mathrm{GeV}}\sqrt{\sin^3\theta}}(\mu m)\,. \tag{3.5}$$

and the single particle momentum resolution achieved is

$$\frac{\Delta p_T}{p_T} = 5\cdot 10^{-5}\frac{p_T}{\mathrm{GeV}} \oplus 0.01\,. \tag{3.6}$$

The combined inner detector system also guarantees a high tracking efficiency of $\varepsilon_{\mathrm{track}} > 90\%$ for pions and $\varepsilon_{\mathrm{track}} > 99\%$ for muons within the acceptance of $|\eta| < 2.5$.

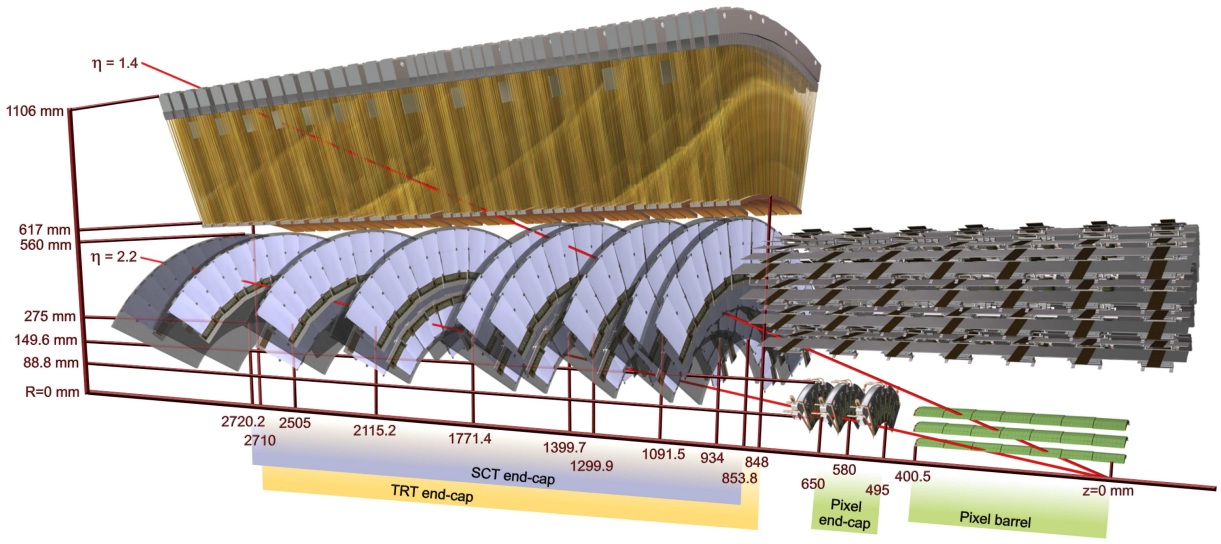

Fig. 3.4: *ID segment consisting of the pixel and semiconductor precision trackers and the transition radiation tracker. Displayed are the end-cap disc of the pixel and SCT detector at the left and a part of the barrel can be seen in the right part. The TRT end cap is limited to* $|\eta| < 2$*. For illustration to example tracks of* $p_T = 10$ GeV *undistorted by the magnetic field are shown at* $\eta = 1.4$ *and* $\eta = 2.2$*. The former track is measured in* $50 \times 400 \mu m^2$ *sized pixels in three layers before traversing the 4 stereo double layers of silicon micro-strips with a pitch of* $80 \mu m$ *in barrel and discs. Finally in the TRT typically 30-40 of the 4mm drift tubes respond to the traversing track. The later track with* $\eta > 2$ *will only be measured in the precision trackers.*

Pixel vertex detector

The innermost pixel detector [4] covers a pseudorapidity of $|\eta| < 2.5$ and consists of three layers of sensor modules in the barrel and three discs equipped with modules in the end-cap structures. The layers in the barrel are located at $r = 5.05cm$, and $r = 8.85cm$, and $r = 12.25cm$ and comprise of 1456 modules. On each of the discs 48 modules are assembled and the discs are at $z = \pm 49.5cm$, and $z = \pm 58.0cm$, and $z = \pm 65.0cm$. In total there are 1744 modules installed in the pixel detector. On each of these modules the sensor array is read out by 16 customised design front end chips, from which each is connected to the 18×168 pixels. Therefore, the 1744 modules contain each 47232 pixels. Since some pixel at the edges are chained to one read out channel of the front end chips, one module has in total 46080 read out channels. This results in more than 80 million channels for the pixel detector. The pixel detector has more channels than all other sub-detectors together. The power consumptions of the electronics is so large that a special cooling system has to be installed in the pixel detector.

The pixel themselves are small enough to provide low occupancy, few double hits and high precision position measurement. A sensor pixel has the measure of $50 \times 400 \mu m^2$. It acts as a pn junction or diode which is depleted by high voltage. If an ionising particle enters the sensor electron hole pairs are created in the silicon. The electrons drift to the cathode side of the junction and are collected at special small bump bonds that build the connection to the readout chips. The intrinsic spatial resolution reached is $10 \mu m$ in $r - \phi$ and $115 \mu m$ in z direction for the barrel. On the discs the resolution is likewise $10 \mu m$ in $r - \phi$ and $105 \mu m$ in the r coordinate.

Silicon micro-strip tracker

The second precision tracker, which can give spatial coordinates is the SCT. It occupies the space between $r = 30cm$ and $r = 52cm$. Since it is more far away from the interaction point in radius the track density is lower and hence, the segmentation is chosen to be more coarse and the resulting precision reaches not quite the pixel detector precision. The SCT is designed as a silicon micro-strip detector. Likewise the pixel detector it has a barrel part with for 4 layers, detecting tracks within $|\eta| < 1.4$, and 9 disks with modules covering the region $|\eta| < 2.5$. in each end-cap.A module is consisting of 4 silicon sensors. A silicon sensor is $6.4 \times 6.4cm^2$ (in the barrel) and this area is segmented in 768 strips with a pitch of $80\mu m$. Effectively double silicon detectors are formed by wire bonding to sensors which result in a strip-length of $12.8cm$ in such a double detector. The double sensors are glued back to back. It is important to notice that in order to resolve ambiguities and get access to the z coordinate, the double layer sensor modules are joined under a stereo angle of $40mrad$ between front and backside. The intrinsic spatial resolution of the stereo strips is $17\mu m$ in $r-\phi$ and in z direction $518\mu m$. Though it is not as complex as the pixel detector, in total 6.34 million channels in the SCT have to be read out by the electronics.

Transition radiation tracker

The TRT [5] is not a precision tracker and can give only $r-\phi$ position information, with a precision of $130\mu m$. But he gives a large number of hits, in average 36 hits, in the outer radial region of the ID between $r = 50.54cm$ and $r = 108.2cm$, which help in combination with the other trackers to have a robust pattern recognition and track finding. The TRT covers only tracks in $|\eta| < 2$. It is build up of drift tubes the so called straw-tubes. As all sub-detectors, it has a barrel part with 73 straw planes that are parallel to the beam axis. The barrel part is covering $|\eta| < 0.7$ and consists of about 50 k straws. The tubes in the barrel part are $144cm$ long. In the adjacent end-caps 160 straw planes each are assembled. The straw-tubes are $37cm$ long and arranged radially in 14 wheels each. The TRT has approximately 351000 read out channels.

A straw-tube has a diameter of $4mm$ and is filled with a gas mixture of 70 % Xenon, and 27% carbondioxide, and 3% oxygen at a pressure of 5 bar to 10 bar, which was chosen under the consideration of the radiation environment expected. In the center of the tube a $50\mu m$ diameter gold-plated rhenium-tungsten wire is kept under high voltage. The ionising particles traversing the tube sets free electrons and the produced electrons drift with constant velocity to the wire, eventually starting an avalanche in the high field close to the wire which amplifies the signal. Since the drift velocity is constant the drift circles can be calculated and give the $r-\phi$ position information. Also the straw-tubes are surrounded by a radiator material, namely polystyrene fibres. Since the TRT in this way is transparent and presents a traversing particle many alternating layers with changing refraction indices, the Cherenkov light of relativistic particles can be exploited. If an ultra-relativistic particle ($\gamma > 1000$) crosses the radiators it emits transition radiation under small angle at the boundaries. These additional photon have a high probability to make subsequently a photoelectric effect in the gas that contain a major fraction of Xenon with high Z number. The electrons from the photoelectric effect yield a higher signal in the straw-tube. The additional signal amplitude due to transition radiation is especially high for electron while for heavier particles like pions it is much lower. Therefore the detection of transition radiation helps to identify electrons.

3.2.4 Calorimeter system

The complete sampling calorimeter system of ATLAS, shown in Fig. 3.5, consists of roughly 196 k calorimeter cells (and read out channels) and covers in full ϕ symmetry the range up to $|\eta| < 4.9$. The calorimetry should be able to precisely measure energy deposited by different particles like electrons or photons or hadronically decayed taus and jets. Hence, the calorimeters have to provide enough stopping

power that the showers from these particles are fully contained in the calorimeter volume so that 'punch through' of .e.g hadrons into the outer detector are rare events. But muons and neutrinos can escape from the calorimeters, as well as hypothetical new weakly interacting particles. This gives rise to a genuine missing transverse energy signature. In addition to the requirement from physical process measurement, over this large range the radiation levels and particle fluxes vary largely. Hence, the calorimeter combines various technical designs to adapt to those requirements. The ATLAS calorimeter system consist of three main subsystems. An electromagnetic calorimeter (named liquid argon (LAr) electromagnetic barrel and electromagnetic endcap calorimeter (EMEC) in Fig. 3.5) covering $|\eta| < 3.2$. This system is specialised for detection of the energy deposited by electromagnetic processes, and placed in the inner radii in front of a hadronic calorimeter. The layout of the electromagnetic calorimeter in the range $|\eta| < 2.5$ is optimised for precision measurements. The barrel part and the end-caps are each placed in physical or mechanical separated cryostat tanks with a small spacing between them. The hadronic calorimeter (named Tile barrel and Tile extended barrel in Fig. 3.5) is covering $|\eta| < 1$ in the barrel, and $0.8 < |\eta| < 1.7$ in the extended barrel and $1.5 < |\eta| < 3.2$ in its hadronic calorimeter end-caps (named HEC in Fig. 3.5). The hadronic calorimeter optimised to contain and sample the energy deposited in nuclear interactions by hadronic particles that usually transverse the electromagnetic calorimeter. A forward calorimeter (named FCal in Fig. 3.5) finally covers the extreme forward range $3.1 < |\eta| < 4.9$ and combines electromagnetic and hadronic measurements. The cryostat vessel for the electromagnetic end-caps houses also the HEC and the FCal, since these calorimeters are based on LAr technology.

Electromagnetic calorimeter

The electromagnetic sampling calorimeter is based on lead as passive absorber and liquid argon as active medium. In order to minimise material in front of the electromagnetic calorimeter the cryostat vessel for the liquid argon houses also the ID solenoid. Kapton electrodes are covering the absorbers, packed with an interlaced honeycomb structure as spacer for the absorbers and the electrodes. For the geometry of absorbers and kapton electrodes an accordion shape has been chosen. This design guarantees full ϕ symmetry without any cracks and the possibility of fast read out in the front or the rear of the electrodes. Hence the uniformity in ϕ and the linearity of the calorimeter response is very good. Fig. 3.6 shows a segment of the accordion shaped LAr calorimeter at $\eta = 0$. In the barrel, $|\eta| < 1.5$, the accordion waves are axial and run with ϕ, while in the the end-caps, $1.4 < |\eta| < 3.2$, the waves are parallel to the radial direction and run axially. In the barrel the geometry allows to adjust the folding angle of the accordion shape such that for outer radii the liquid argon drift gap is constantly at $2.1mm$. In the end-caps though the gap increases with the radius from $0.8mm$ to $3.1mm$.

Absorbed incident photons and electrons start an electromagnetic shower comprising of secondary electron positron pairs or bremsstrahlung and Compton effect photons. This showering can start in the first sampling layer, which corresponds to radiation length of $4.3 \cdot X_0$[1)]. As can be seen in Fig. 3.6, the position of the shower as well as its shape in η can be very precisely determined in the first layer since the granularity is $\Delta\eta \times \Delta\phi = \frac{0.025}{8} \times 0.1$ in $|\eta| < 1.4$ and $1.4 < |\eta| < 1.475$ with $\Delta\eta \times \Delta\phi = 0.025 \times 0.025$. In the end-caps only a small part of the first layer can match to that precision. Granularities in the first precision layer of the end-caps $\Delta\eta \times \Delta\phi = \frac{0.025}{8} \times 0.1$ to $\Delta\eta \times \Delta\phi = 0.025 \times 0.1$ are typically for the region of $1.5 < |\eta| < 2.5$. The remaining parts are much coarser. Especially in $1.5 < |\eta| < 2.5$ the first layer has no finer granularity like the second layer, namely $\Delta\eta \times \Delta\phi = 0.1 \times 0.1$. Since it represents $16 \cdot X_0$, the maximum of the electromagnetic showering occurs in the second layer, which in most cases contains the complete shower. Only a small fraction of the shower is expected to reach the third layer. The third sampling layer, which is only installed in $|\eta| < 2.5$, represents therefore only $2 \cdot X_0$, with a reduced

[1)] The *radiation length* is a material constant, e.g in liquid Argon ($Z = 18$) a with density of $19.55 \frac{g}{cm^3}$ is about 14 cm. For high energy electrons the radiation length is mean distance for the loss of all but $\frac{1}{e}$ of their energy due to bremsstrahlung. In case of high energy photons the radiation length is $\frac{7}{9}$ of the mean free path for pair-production.

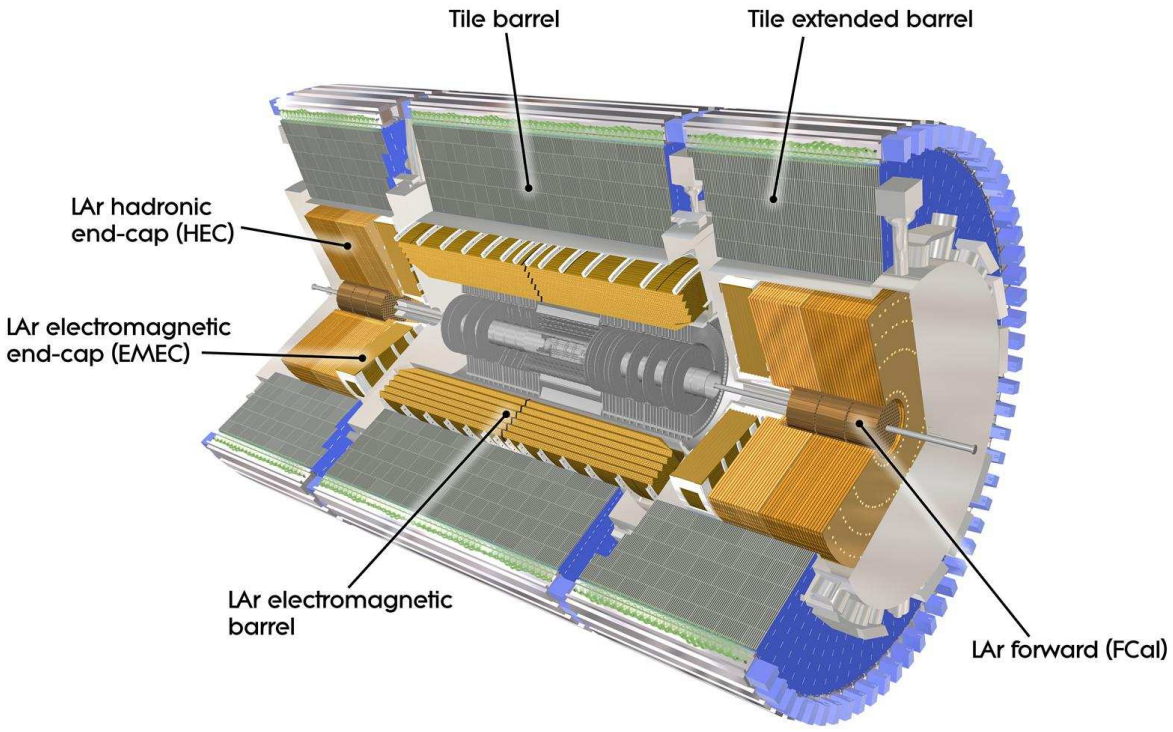

Fig. 3.5: *Artistic cut-away view of the ATLAS calorimeter system. Atlas uses different kinds of sampling calorimeters. The liquid argon calorimeter in the centre is depicted in gold colours and the outer lying hadronic tile calorimeter in grey. Clearly visible is the trifold structure of the whole calorimetry in barrel and end-cap or extended barrel components. The corresponding parts of the liquid argon calorimeter house separate cryostats. Due to the high particle flux the forward calorimetry uses special designed liquid argon calorimeters with different geometry shown in darker gold.*

granularity of $\Delta\eta \times \Delta\phi = 0.05 \times 0.025$ in barrel and end-caps likewise. For the range $2.5 < |\eta| < 3.2$ the electromagnetic calorimeter provides in the end-caps only two sampling layers with granularity of $\Delta\eta \times \Delta\phi = 0.1 \times 0.1$. The total thickness of the electromagnetic calorimeter adds up to $24{\cdot}X_0$ in the barrel and $26{\cdot}X_0$ in the end-caps.

In the $|\eta| < 2.5$ range the granularity of the calorimeter is very fine to assist the ID in the precision measurement of electrons and photons, in the rest of the calorimeter the granularity is more coarse, but meets the requirements for good jet reconstruction and $E_{\mathrm{T}}^{\mathrm{miss}}$measurement. Since the granularity and precision of the electromagnetic calorimeter in $|\eta| < 2.5$ matches to those of the ID, it is used for triggering on photons and electrons likewise. To that purpose electronically the read out is combined to so-called trigger towers (indicated also in Fig. 3.6) with a granularity of $\Delta\eta \times \Delta\phi = 0.1 \times 0.1$. Also in the other compartments of the calorimeter such trigger towers are combined to be able to trigger on jets.

Hadronic calorimeter

The largest part of the hadronic calorimeter, located in the barrel in pseudorapidity $|\eta| < 1$ and continued in $0.8 < |\eta| < 1.7$ as extended barrel and occupying the space between $r = 2.28m$ to $r = 4.25m$, is designed as a scintillator tile calorimeter (TileCal). As absorbers serve iron plates and the $3mm$ thick plastic scintillator plates, called tiles, are arranged alternately in between. Secondary particles coming out of the absorber produce light flashes in the scintillator. Wavelength shifting fibres transport the light yield to photo multiplier tubes that transform it to a signal proportional to the energy sampled. Also in order to correct for the energy loss in the transition region between the mechanical disconnected barrel and extended barrel inter TileCal scintillators (ITC) are used in the gap. The tile calorimeter consists of three sampling layers and has a granularity of $\Delta\eta \times \Delta\phi = 0.1 \times 0.1$ in the first two layers and of $\Delta\eta \times \Delta\phi = 0.2 \times 0.1$in the last layer. All three layers represent 9.7 λ_{int} [2)] at $|\eta| = 0$. This is sufficient to shield the muon system from hadronic punch-through and allows an energy resolution for the measurement of high energetic jets.

Since the level of radiation and the expected particle flux becomes critical for scintillators in the region of $1.5 < |\eta| < 3.2$, the hadron calorimeter design has to be changed to a radiation hard liquid argon calorimeter. The so-called hadronic end-cap calorimeter (HEC) uses copper absorbers and liquid argon as active medium. The copper absorbers are flat plates leaving a $8.5mm$ parallel liquid argon gap. In these gap 3 readout electrodes are inserted so that the maximal drift distance is $1.8mm$. The HEC consists of two wheels on each side which have 32 of such modules mounted. The outer radius of the wheel is $r = 2.03m$. The two wheels of one HEC side provide 4 sampling layers and since hadronic showers are usually more smeared compared to electromagnetic showers, a granularity of $\Delta\eta \times \Delta\phi = 0.1 \times 0.1$, in $1.5 < |\eta| < 2.5$, and $\Delta\eta \times \Delta\phi = 0.2 \times 0.2$ in $2.5 < |\eta| < 3.5$, is sufficiently accurate.

Forward calorimeter

In the extreme forward region $3.1 < |\eta| < 4.9$, the forward calorimeter(FCal) [26] is placed $4.7m$ away form the IP. The particle flux is highest there, and therefore, the design of the calorimeter had to be changed again to cope with the radiation densities. Since it is very radiation hard, liquid argon is used again as active material, but a design was searched in which the gaps can be smaller, because the high density of traversing particles should not cause long latency by positive ion build up and saturation. Hence the FCal has three segments each $45cm$ long surrounding the beam pipe. The first compartment uses copper as absorber, which can remove the heat very fast. The adjacent two use tungsten as absorber, which provide a very high absorption length. While the first segment FCal1 is optimised for electromagnetic energy measurements, the tungsten segments FCal2 and FCal3 are used for hadronical calorimetry.

[2)] The interaction length λ_{int} is the mean free path of a particle before undergoing an interaction that is neither elastic nor quasi-elastic (diffractive), in a given medium.

All three segments of the very dense FCal add up to $\sim 210X_0$ and $\sim 10\lambda_{\text{int}}$. The thin liquid argon gaps that allow for drift times of $61ns$, are achieved by taking the absorber as rod. The rod is kept at high voltage and is surrounded by a grounded tube as electrode. This configuration is mechanically stabilised by a radiation hard plastic spacer precision wire winding around the rod. The tubes are inserted into a honeycomb structures, such way that they lay in concentrically bundles around the beam axis. The drift space is $250\mu m$ around the copper rods and $375\mu m$ and $500\mu m$ respectively, around the tungsten rods in the two last segments, that are a little bit less exposed to the particle flux. The granularity of the FCal cannot be so high as in the other calorimeters, but in the electromagnetic layer FCal1 a granularity of $\Delta xy = 3.0cm \times 2.6cm$ is used in a ring around the beamline defined by $3.15 < |\eta| < 4.30$. In two other rings defined by $3.10 < |\eta| < 3.15$ and very close to the beamline $4.30 < |\eta| < 4.83$ the granularity is four times finer than the latter. The hadronic FCal2 reaches granularities of $\Delta xy = 3.3cm \times 4.2cm$ in a ring around the beamline defined by $3.24 < |\eta| < 4.50$ and four times finer granularity in the regions $3.20 < |\eta| < 3.24$ and $4.50 < |\eta| < 4.81$. The FCal3 has a granularity of $\Delta xy = 5.4cm \times 4.7cm$ in a ring around the beamline defined by $3.32 < |\eta| < 4.60$ and reaches a four times higher granularity in the regions $3.29 < |\eta| < 3.32$ and $4.6 < |\eta| < 4.75$. Fig. 3.7 shows the location of the FCal in the shared cryostat vessel with the HEC in the left panel, the mounting of the rods-tubes near the beam-pipe is illustrated in the right panel. In the design of the FCal it was intended to meet especially the requirements of reliable $E_{\text{T}}^{\text{miss}}$measurement and forward jet tagging as used in studies of weak boson fusion final states.

Material budget in front of the calorimeters and presampler layers

In principle for all presented particle detector components, large amounts of passive (not equipped with active sampling devises and no read out or dead cells) in front of the detector component is disadvantageous for the precision of the measurement. Such inactive material is often unavoidable since is comprises of cryostat walls, support structures, cables, electronic, and cooling pipes and alignment control systems. Of course, naturally there is a trade of in the designs between function and the so-called material budget. The effects that deteriorate the measurement of particles are that the particles may be absorbed before leaving a signal in the active regions or that their trajectory from the IP to the active sampling region is distorted by many multiple scatterings (which affect especially track reconstruction). Another effect that complicates the correct measurement of particle energies in the calorimeter, is the in the material in front of the calorimeter the particles begin an early shower. In order to give a precise measurement calorimeters are designed to contain the complete shower of particles, the energy of the early shower is lost and may be accounted wrongly for missing energy in the event. In ATLAS a presampler system tries to measure this early showering and correct the calorimeter energies for this effect. In a pres-ampler module segmented printed circuit cathodes and three conductive anode layers are interleaved and glued between glass-fibre composite plates. The anode layers are supplied with $+2kV$ voltage and the signal is read out capacitively in reference to the grounded central anode layer. The granularity of the pres-ampler is $\Delta\eta \times \Delta\phi = 0.025 \times 0.1$. The presampler is placed in $|\eta| < 1.52$ to correct for showering in the cryostat and between $1.5 < |\eta| < 1.8$ to compensate for inefficiencies in the transition region between barrel and end-cap. The left panel of Fig. 3.8 shows the variation in η of inactive material in front of the electromagnetic liquid argon calorimeter as well as the thickness of the presampler in unit of the radiation length . The right panel gives a detailed view of the material distribution in the transition region between barrel and end-cap, where likewise the presampler is installed. In this so called gap region the measurement is extremely difficult, which reflects as a dip in the reconstruction efficiencies for objects like electrons or jets in the region. Furthermore, in Fig. 3.9 the stopping power of the hadronic calorimeter system is characterised in term of the interaction length λ_{int} over the complete pseudorapidity range of the calorimeters. Also inactive material in front of the calorimeters and the interaction length equivalent of the electromagnetic calorimeter are displayed. As the figures show, though ATLAS has full ϕ symmetric calorimeter, in the η direction the design and material budget can vary. Naturally also a geometrical

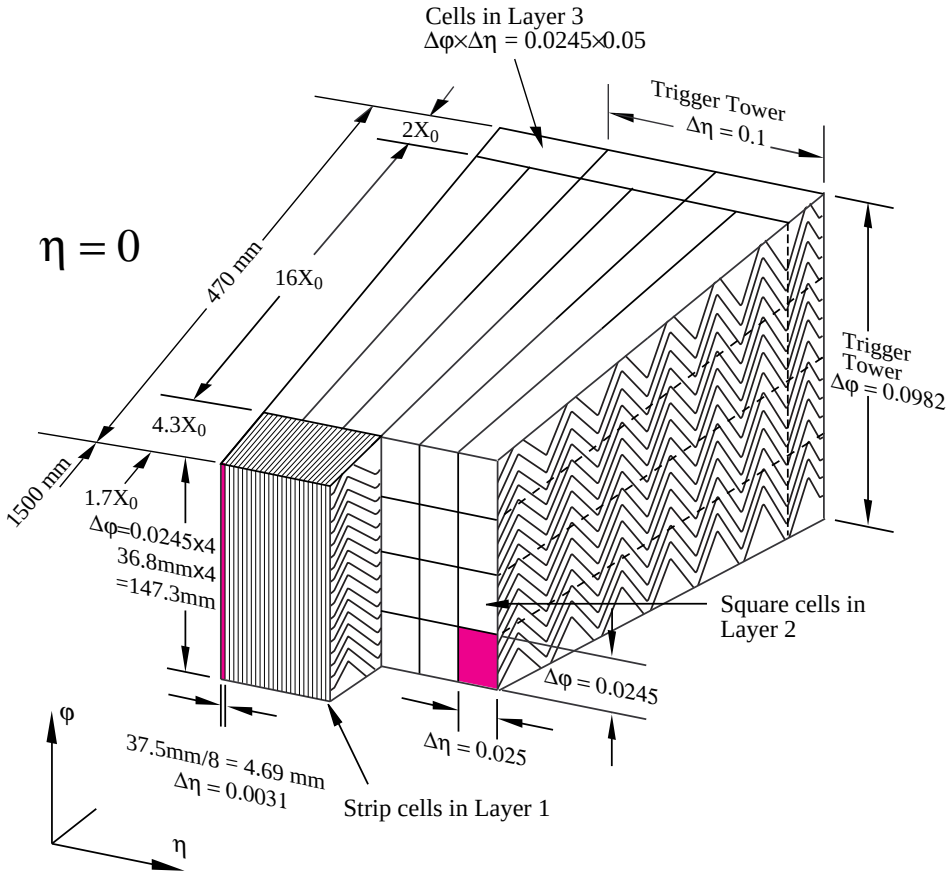

Fig. 3.6: *A segment of the liquid argon accordion structure in the central barrel. One identifies three readout layers of varying interaction length. While the first layer has a very fine η segmentation allowing for precision measurement of the shower shape, the second layer within its $16 \cdot X_0$ is absorbing the largest part of the electromagnetic shower. the granularity of cells in each layer is characterised in $\Delta\eta \times \Delta\phi$. Clearly visible is the ganging of the electrodes in ϕ. The welding angle of the accordion is changing with the radius to guarantee a constant LAr gap and drift times. Not shown is the pres-ampler in front of the accordion structures that measures early showering of particles staring in the cryostat wall. The sketch also illustrate how the less granular so-called trigger towers are formed from the cells in the layers.*

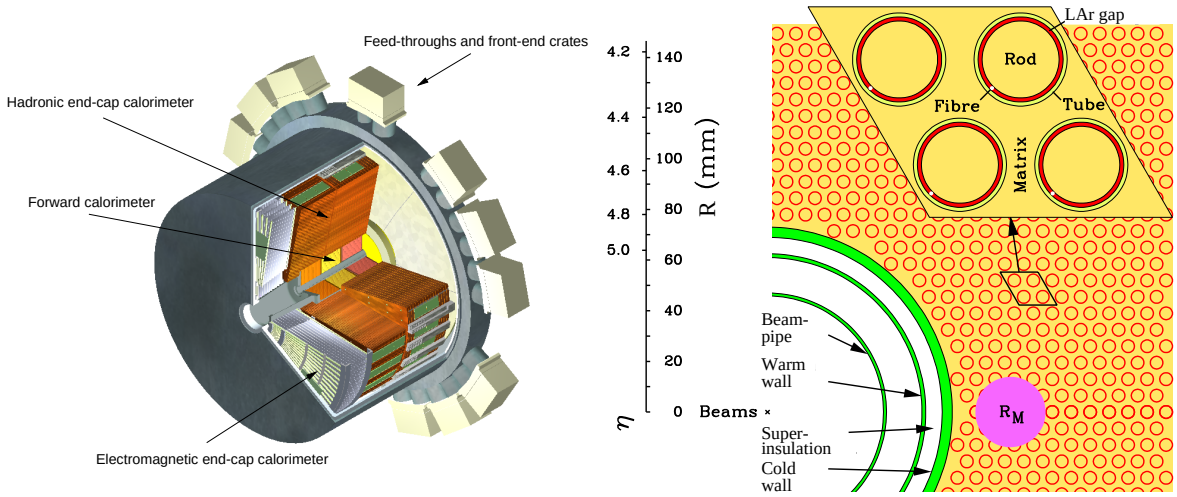

Fig. 3.7: *Left panel: The LAr end-cap cryostat with HEC and the electromagnetic and two hadronic FCal segments. Right panel: Layout of the rod-tubes and the supporting honeycomb structure in the FCal modules surrounding the beam pipe.*

effect is present because with higher pseudorapidity particles transverse more material, visible e.g. that the constant thickness of the beam pipe wall poses more radiation length with high pseudorapidity. Additionally large variation over the range in inactive material especially in the transition region between barrel and end-cap $1.35 < |\eta| < 1.6$ as well as the region about $|\eta = 3|$ show discontinuities in material as well as different material in the active detector elements design in the latter case. These differences in properties are reflected for example in performance differences between forward and barrel calorimetry.

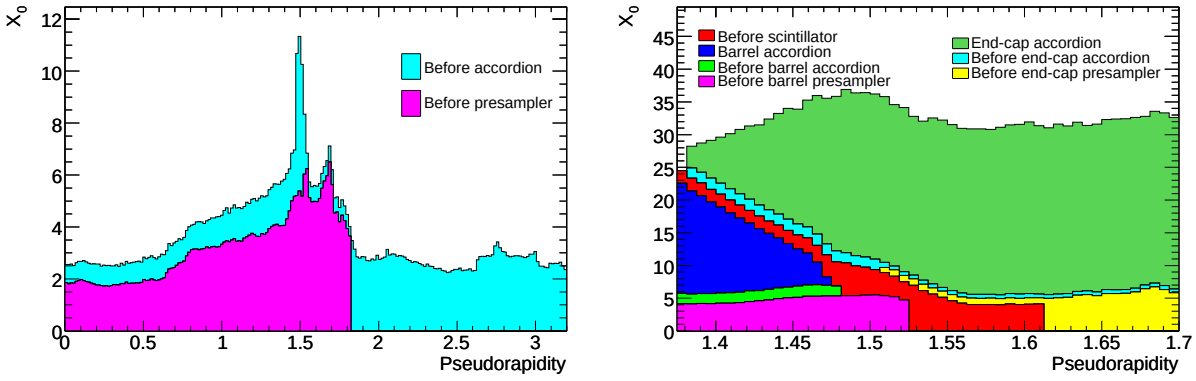

Fig. 3.8: *Cumulative amounts of material in front of the presampler of the accordion structures of the electromagnetic calorimeter, expressed in radiations length X_0 as function of $|\eta|$. The right panel shows the full range while the left panel zooms into to crack region between the barrel and end-cap cryostats. Inactive and active material of the pres-ampler and crack scintillators and the thickness of the accordion structures are shown.*

Energy resolution

Finally we want to characterised the energy resolution of the calorimeter system. As a consequence of the well motivated design differences in the calorimeter system and the presence of transition regions and varying amounts of material in front the calorimeter or different granularity achieved, the energy

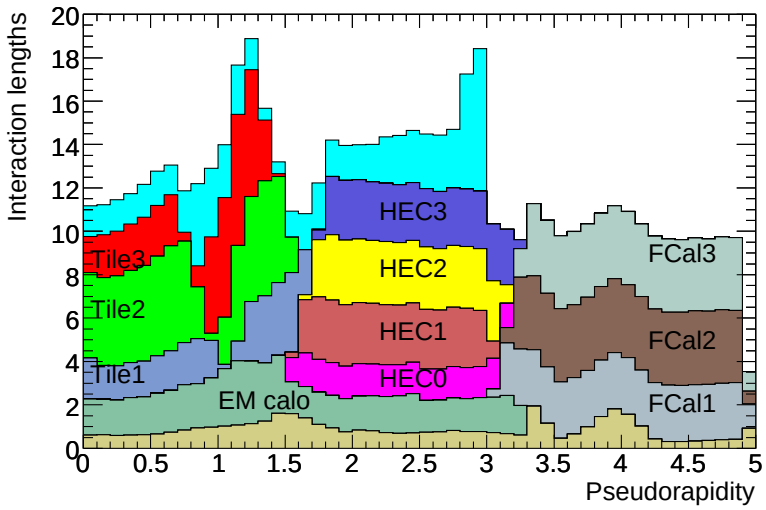

Fig. 3.9: *Cumulative amounts of material in the calorimeter system as function of $|\eta|$ expressed in the hadronic interaction length λ_0. The inactive material in front of the electromagnetic calorimeter as well as the material by the active electromagnetic calorimeter, as EM calo, are shown. Tile, HEC, and FCAl refer to the material in the active hadronic layers of barrel end cap and forward hadronic calorimetry, respectively.*

resolution is not uniform. For the electromagnetic calorimeter it is expected [2] to reach an energy resolution of

$$\frac{\sigma(E)}{E} = \frac{0.1}{\frac{E}{\text{GeV}}} \oplus 0.007\,. \tag{3.7}$$

Hadronic calorimetry has to deal always with a worse resolution compared to the electromagnetic calorimeter. The energy resolution of the hadronic calorimeter is expected to differ also between barrel and end-caps, and is given by

$$\frac{\sigma(E)}{E} = \frac{0.5}{\frac{E}{\text{GeV}}} \oplus 0.03(|\eta| < 3.2) \tag{3.8}$$

$$\frac{\sigma(E)}{E} = \frac{1.0}{\frac{E}{\text{GeV}}} \oplus 0.10(|\eta| > 3.2))\,. \tag{3.9}$$

It is also reasonable to assume that the varying properties at least between the barrel and forward calorimetry will result in different systematic uncertainties e.g. for derived measurements like the energy of the jets reconstructed in the different η ranges. This will be considered when discussing the systematic uncertainties of the presented sensitivity study.

3.2.5 Muon spectrometer

A conceptual layout of the ATLAS muon system is presented in Fig, 3.10. The position of muons can be measured within $|\eta| < 2.7$ by the muon system. In the barrel region tracks are measured in detectors that are arranged in three cylindrical layers along the beam axis at $r = 5m, r = 7.5m$, and $r = 10m$. In the end caps the position detectors are assembled orthogonal to the beam axis in four wheels located at $|z| = 7m, |z| = 10m, |z| = 14m$, and a $|z| = 21 - 23m$. Usually a muon can be measured in three stations to determine the sagitta. The large dimensions of the muon system result from the fact that the air coil

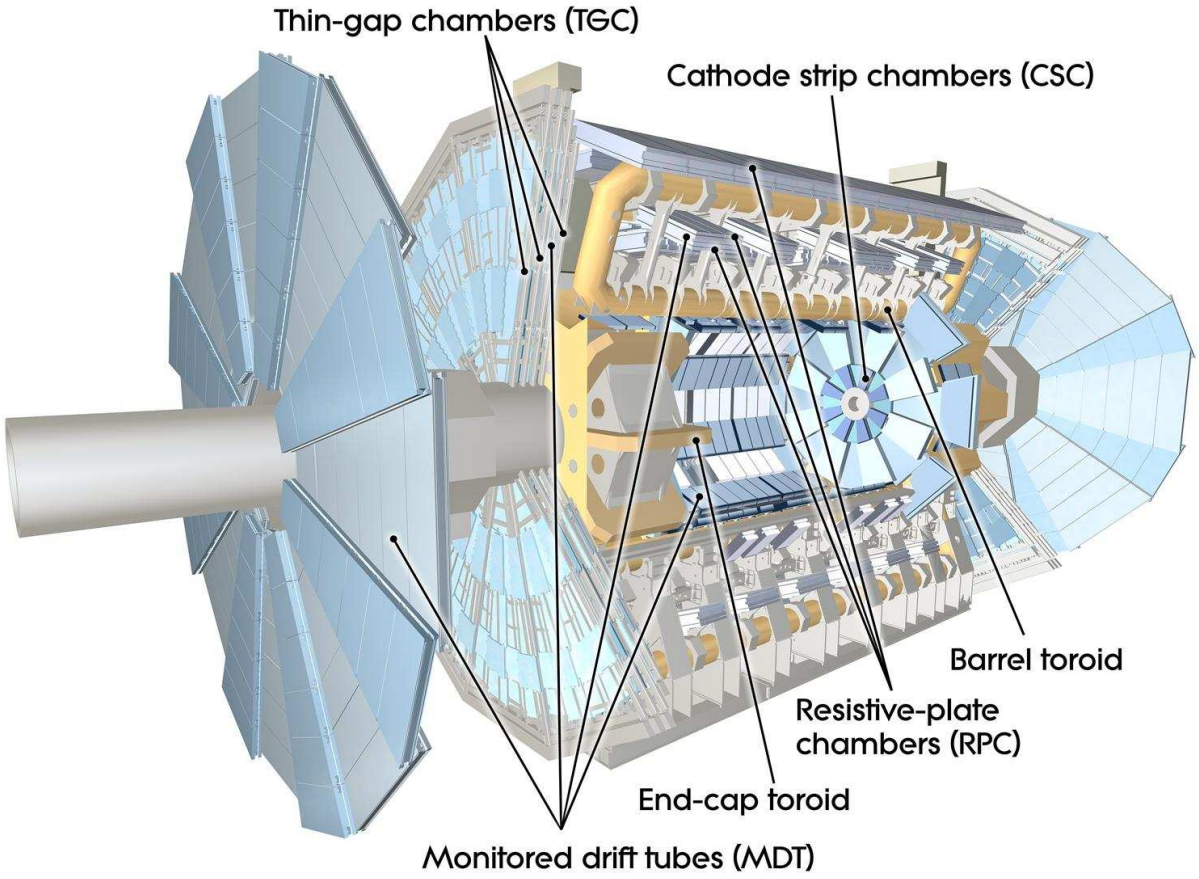

Fig. 3.10: *Artistic view of the ATLAS muon system with inner detector and calorimeters cut out. The muon system comprises of precision chambers (MDT and CSC) and also fast trigger chambers (TGC and RPC). The precision chambers measure the momentum of the high pt muons up to 3 TeV in the toroidal magnetic field coils. Muons are bended in the* $r-z$*-plane. The position of muons is measured within* $|\eta| < 2.7$ *, and for triggering* $|\eta| < 2.4$ *is used.*

toroids have been chosen to generate the B-field, which bends the muons in the $r-z$-plane. The air coil design minimises multiple scattering of the muons in the material and allows to perform a relative precise stand alone measurement of the muon properties even after they passed the inner detector and calorimeters. Since the very high energetic muons can only marginal be bended in the inner detector, the momentum measurement is performed for these muon only be the muon system. For lower energetic muons of the order of about 100 GeV with a meaningful measured sagitta in the ID, this information is statistically combined in the track pattern recognition with the muon chamber hits, to improve the track measurement significantly [2]. The aim is to reach, at highest luminosity, for high p_{T} muons a precision of less than 10 %, namely

$$\frac{\Delta p_{\mathrm{T}}}{p_{\mathrm{T}}} = 0.1 \text{ at a } p_{\mathrm{T}} = 1 \text{ TeV}. \tag{3.10}$$

Below 1 TeV the precision is better, typically a few percent.

The design of the muon system detectors depends on the expected radiation level and the relative high level of expected particle flux even so far away of the interaction point. E.g so-called cavern background of neutrons stemming from activated material will pose one possible background at highest luminosities. Also chambers for triggering demand fast response but less precise position information. Therefore four different types of detectors are used, namely two types of precision chambers for precise tracking called monitored drift tubes (MDT) and cathode strip chambers (CSC). For triggering muons, two types of fast trigger chambers called resistive plate chambers (RPC) in the barrel and thin gap chambers (TGC) in the wheels are available. In the following a short overview over the design principles of the various chambers is given.

Precision chambers

The first type of precision chambers are the monitored drift tubes. In one MDT, from 3 to 8 cylindrical aluminium drift tubes of a diameter of $3cm$ are filled with a drift gas mixture (93% argon and 7% carbon dioxide) at 3 bar are combined. In the centre of each tube a $50\mu m$ diameter tungsten-rhenium sense wire under high voltage is collecting the electrons from ionisation and avalanche effect. The spatial resolution is $80\mu m$ perpendicular to the wire direction, which corresponds to the $r-z$ plane. The time resolution of the MDT is $750ns$. The muons system has 1150 MDTs placed in the range of $|\eta| < 2.7$ (innermost layer $|\eta| < 2$).

The second type of precision chambers are cathode strip chambers (CSC). These are flat multi-wire proportional chambers with $30\mu m$ anode wires out of rhenium-tungsten filled with a drift gas mixture of 80% argon and 20% carbon dioxide. The read out cathodes are segmented into strips. When applying charge interpolation with neighbouring strip a spatial resolution of $60\mu m$ in the $r-z$ plane can be reached. The time resolution of the CSC is only $4ns$. Due to their higher granularity and relative insensitivity to the neutron background the CSC are designed to withstand a demanding rate and background condition. Hence, 32 CSCs are installed in the innermost layer in the range of $2.0 < |\eta| < 2.7$.

Trigger chambers

In the range of the muon system, $|\eta| < 2.7$, also special fast trigger chambers are installed to trigger on muons. The time resolution of the trigger chambers $20ns$. For triggering, the full ϕ range but only the range in $|\eta| < 2.4$ is used. The trigger system identifies bunch crossings with muons of interest and further provides well defined p_{T} thresholds. More important it also adds the orthogonal coordinate (in the wire direction) to precision chamber measurements. The first type of trigger chambers are the resistive plate chambers. In the RPC two resistive plates are kept in a parallel distance of $2mm$ by insulating spacers distance. The gap is filled with a gas mixture (94.7 % $C_2H_2F_4$, 5 % iso-butane and 0.3 % SF_6). In the gap a gradient field of $4.9kV/mm$ amplifies the ionisation electrons stemming from

the traversing ionising particle by an avalanche effect, leading to a fast signal. In the barrel region of $|\eta| < 1.05$, 606 RPC are mounted on both sides of each MDT layer. The spatial resolution of a RPC can be quantified as $\Delta\eta = 30mm$ and $\Delta\phi = 3cm$. The second trigger chambers are the thin gap chambers. A TGC is a customised multi-wire proportional chamber, operated in saturation mode to guarantee the quick response. The gas mixture to tune the fast response is 55% carbondioxide and 45% n-pentane. In particular the TGC has radial strips that give the azimuthal information in addition to the wire read out that gives the radial coordinate in bending direction. In the remaining region of $1.05 < |\eta| < 2.7$, i.e. from the barrel to the end-cap, located near the middle MDT wheel, 3588 TGCs are installed. Depending on their position the TGCs give a resolution of $\Delta\eta = 7-36mm$ and $\Delta\phi = 2-3cm$. The precision chambers are read out in 385 k channels and the trigger chambers add 691 k of read out channels.

Alignment control

The MDT and CSC muon chambers have been mounted with a position precision better than $5mm$ and $2mrad$. Since the overall dimensions of the muon system are large and the support structures are under the influence of considerable radial forces of the B-field, the monitoring of the relative position and alignment of the MDT chambers is important. The relative precision of the chambers has to been known within $30\mu m$ for reliable operation. A dedicated system with approximately 12000 precision mounted alignment optical sensors guarantee the knowledge of positioning of the chambers within $20\mu m$ and between non adjacent towers withing a few millimetres, which is in the end important for a good mass resolution in multi muon finals states.

3.2.6 Far forward and luminosity detector stations

Far away from the interaction point (IP) smaller forward detectors measure physics processes in extreme forward direction, from which the relative and absolute instantaneous luminosity can be calibrated. The following detectors are used.

LUCID

The LUCID(LUminosity measurement Using Cerenkov Integrating Detector) detector is located ± 17 m. At this point the detector measures the particles emerging from inelastic p$-$p interaction or secondary processes. The measured rate is proportional to the luminosity with nan error of 1% for $10^{33} cm^{-2} s^{-1}$ and an order of magnitude more accurate as the value derived from beam parameters. Since the particle flux is very high radiation hard design is obligatory. Lucids exploits the emitted Cerenkov light in 20 perfluorobutane filled aluminium tubes bundled at 10 cm around the beam pipe, for a fast response times within the bunch spacing and radiation hardness.

ALFA

The ALFA (Absolute Luminosity For ATLAS) detector is used to intercalibrate the relative measurements of LUCID. This scintillating fibre detector is inserted into the beamline at ± 240 m and can measure as close as ~ 1.5 mm to the beam. This way ALFA is able to measure elastic proton proton collisions under a scattering angle of only $3\mu rad$. This scattering in the Coulomb nuclear interference region is well understood and can be related via the optical theorem to the total cross section. The aim is to achieve an absolute measurement of the instantaneous luminosity with 3% precision.

ZDC

The ZDC (Zero Degree calorimeter) is at ± 140 *m* from the IP and measures photons and neutrons in the region $\eta > 8.3$. Such spectator neutrons, can be used to determine the centrality in heavy ion collisions. The ZDC is a compact calorimeter of tungsten steel absorbers and quartz strip scintillators. Though ZDC could serve in initial data taking as additional minimum bias trigger to suppress beamgas events in coincidence, it will be removed in normal proton runs to avoid radiation damage.

BPTX

Two electrostatic beam pickup detector stations, called BPTX (Beam Pick up for Timing bunch Crossings) [123], are placed at ± 175 *m* away along the beam pipe. As part of the LHC beam instrumentation, they are used by ATLAS for the timing purposes. The BPTX monitoring system measures the phase between collisions and LHC clock with a precision better than 100 ps in order to guarantee a stable phase relationship for optimal signal sampling in the sub-detector front-end electronics. The BPTX can also supply a level-1 trigger for bunches that cross the ATLAS detector, which is used e.g. for minimal bias events triggering in connection with the ID (see 3.2.7).

3.2.7 Trigger and data acquisition

Each sub-detector is associated to timing and trigger control logic and the trigger and data acquisition system (collectively TDAQ). We will make some remarks how the trigger system, that decides on the storage of interesting data for offline reconstruction, is organised and what physical objects are triggered.

Trigger

The ATLAS trigger system is consisting of three levels with each level refining the selection of events that will written down by the DAQ system on disc for the offline analysis. This economical mandatory, because even if it was technical solvable, the storage and reconstruction of all events delivered by the LHC any 25 ns would not be sensible since only a small fraction contains physical interesting events.

A schematic of the three ATLAS stages of triggering is shown in Fig.3.11. Clearly the very first decision at the so-called level-1 (L-1) is the most important and has to be very fast. The level-1 uses only a very limited amount of the detector information and makes a decision within $2.5\mu s$. It is realised as hardware trigger system to guarantee the speed. While technically an upgrade to 100 kHz at level-1 is possible, the level-1 trigger is able to reduce the rate to about $\sim 75kHz$, leaving some bandwidth reserve. While waiting for the trigger decision, this is the so-called latency time, the read out system has to buffer the complete event information. At the level-1, for electrons and photons in the events the trigger towers of the electromagnetic calorimeter are used. For the hadronic decay products that form sprays of secondary particles or jets or the hadronic tau decays the trigger towers in the hadronic calorimeter are included. Determining the multiplicity of jets in the events and to be able to trigger on their transverse momentum is very crucial for ATLAS analyses. Also the level-1 trigger can divide jets in central jets or forward jets (per default $4.9 > |\eta| > 3.2$), above some predefined trigger thresholds of uncalibrated transverse energy. The level-1 trigger can also give a crude estimate of the uncalibrated $E_{\mathrm{T}}^{\mathrm{miss}}$ above predefined trigger thresholds in the event. For all these physical different objects optimised cluster sizes of the required trigger towers responding have been devised. Typically the identified regions of interest require clusters of 1×2 or 2×2 to 4×4 trigger towers in the specified calorimeter. For electron , τ and γ triggering isolation criteria can be applied at level-1. The $E_{\mathrm{T}}^{\mathrm{miss}}$ is using a calorimeter map with the granularity $\Delta\eta\Delta\phi = 0.2 \times 0.2$ the same as in the jet p_{T} determination in the barrel. The muons are solely triggered by the trigger chambers of the muon spectrometer. One basic requirement of the level-1 trigger is to uniquely identify the bunch crossing of interest. In the large muon system the time-of-flight for

muons is comparable to the bunch crossing period. Really challenging is the identification of the bunch crossing in the calorimeter triggers though, since the pulse shape in the calorimeters extends over several bunch crossings. As indicated in the Fig. 3.11 the level-2 trigger (L-2) uses the information of the regions of interest (ROI) of the level-1, which contains $\eta - \phi$ or p_{T} and energy sums of triggered objects. The level-2 trigger can apply more selection criteria on the identified region of interest and access if necessary more detailed event information. The level-2 decision has to be made in $40ms$. At that stage the rate is reduced to $\sim 3.5kHz$ already. The final step of the eventfilter uses offline algorithms and accesses all detector information for the event building on a large array of computer farms near the cavern. Level-2 and eventfilter are often called high level trigger (HLT) since they use much more refined algorithms and access more detector information. The final event size, written to storage elements is $\lesssim 1.5Mb$ at a rate of 200 MHz

Minbias trigger

In the beginning of data taking with moderate instantaneous luminosity the measurement of general properties of p−p collisions are of interest. Thus the ATLAS detector has to be able to trigger for minimal bias collision events, without selecting any particular final state configuration or at least minimise influence of the actual final state on the trigger decision in such events. Therefore, ATLAS has to systems two trigger these minimal bias events, described and studied in [147].

A hardware based first level trigger is called minimal bias trigger scintillator (MBTS), which consist of 2 ϕ-symmetrical rings of 2cm thick polystyrene scintillators with wavelength-shifter fibre, located $3.6m$ away from the nominal centre of the detector. The MBTS is sensitive to proton proton collisions in the forward regions of $2.1 \lesssim |\eta| \lesssim 3.8$. Additionally, the second method is used as control samples. In this case events with hits in the trackers of the ID well be selected of randomly triggered beam crossings (identified by the BPTX).

3.3 Event reconstruction

The DAQ system reads out the detector in terms of digitised electrical signals coming from the subdetectors. It is the task of event reconstruction software to build up a view of the events in terms of physical final state objects like jets and leptons or missing energy in the detector, which then can be related in the physics analysis with properties of the studied (hard) process. The event reconstruction is performed offline. The complete ATLAS detector software, detector simulation packages and all reconstruction algorithms are provided by the Athena software package. In data taking always the most actual release containing the permanent evolving algorithms, is used. Data recorded earlier is from time to time reprocessed with the newest reconstruction algorithm. E.g. in the data taking in end of 2010 the release Athena 15 and 16 are used. Also it is intended to supply roughly one third of data in simulated events reconstructed with the same offline algorithms for the studies and comparison with data. Details on the ATLAS event data model can be found in [56, 68, 104].

In the following we shortly give some remarks on the reconstruction of physical objects important for the studied final state. The description refers to the used validated Athena release 12.6.5 in use in the years 2007 and 2008 for the studies published in [7].

3.3.1 Jet reconstruction

If hadrons with short lifetime are produced in a proton collision, they decay in more hadrons and also emit gluonic bremsstrahlung. These sprays of particles, stemming from the hadronisation of a high energetic parton, are usually spatially confined to a small solid angle and referred to a jet. The energy of the jet can be detected as deposition in neighbouring clusters of calorimeter cells. Coordinates of

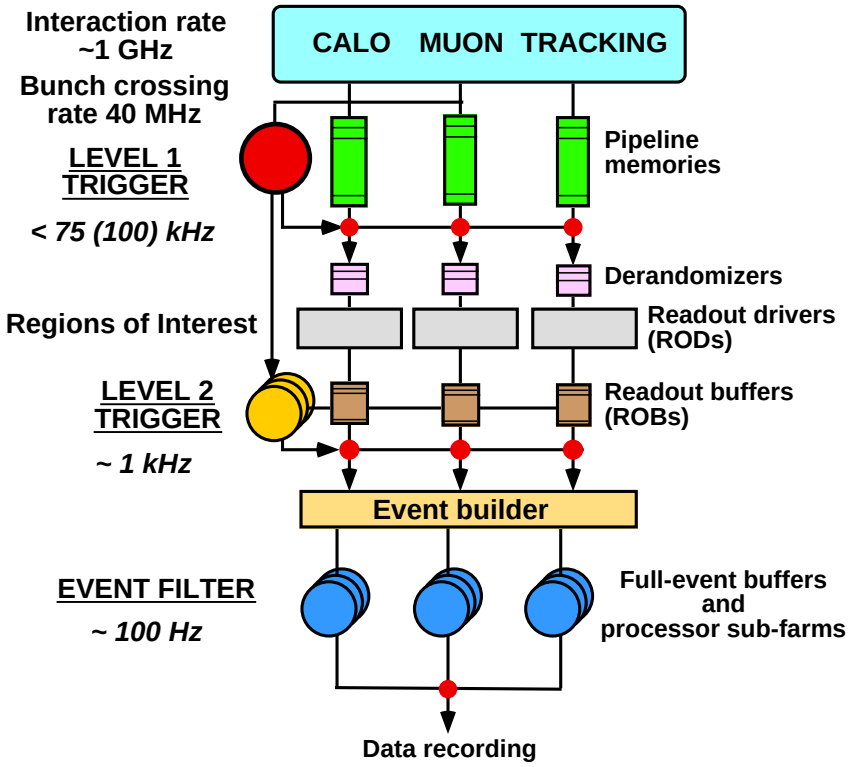

Fig. 3.11: *The three levels of triggering in the ATLAS data acquisition. The intended trigger rates at each level are displayed along at the right hand side. The very coarse L-1 trigger reduces most of the bunch crossing rate of 40 MHz and gives the identified regions of interest (ROI) by the triggers tracking hits or calorimeter trigger towers or muon trigger chambers to the L-2 trigger. This trigger sees the full event information and uses algorithms similar to the offline reconstruction.*

the barycentre of cells in $\eta - \phi$ determine the jet axis with respect to the nominal IP. Since the ATLAS calorimeter is non compensating, i. e. that the response to the hadronic part of shower is less effcient as to the electromagnetic shower component, the calorimeter cells have to be calibrated for their response to hadrons. Reconstructed calorimeter jets are solely formed by collecting the cells over a certain noise threshold with a jet clustering algorithm. In this study a seeded cone jet clustering algorithm with an opening angle of ΔR is used. This algorithm proceeds as follows.

1) E_{T} **ordered seed list**
   All calorimeter cell with transverse energy over a specified transverse energy larger E_{T}^{seed} are stored in a descending E_{T} ordered list.

2) **Combination of proto-jets from seeds**
   To the highest E_{T} seed all seeds with a $\eta - \phi$ distance smaller as ΔR are combined[3)]. The combined object has a jet axis defined by the bary-center of the seeds. Seeds from the list, that are in the vicinity smaller ΔR of the jet axis are combined, until the jet axis is not changing its direction any more.

3) **Storing distinct proto-jets**
   If the combined object has not been found before, it is inserted in a list of so-called proto-jets.

4) **Iteration on seed list**
   Then the next highest seed is taken from the list and the combination of step 2) is performed and so on until all seed have been used as starting point for proto-jet finding.

5) **Merging proto-jets**
   After all seeds have been processed and a complete list of proto-jets is available, overlapping proto-jets are merged into one if the shared fraction of transverse energy in the two objects exceed a value f. If the shared fraction is less than f, the cells in the overlap are assigned to the nearest jet.

5) **Cone-Jets**
   The split and merge algorithm of 4) iterates over the complete list of proto-jets. The surviving proto-jets are retained as cone jets.

Calorimeter jets in ATLAS are assumed to be massless jets. In the presented sensitivity study the choice for the three parameters is $\Delta R = 0.4$, $E_{\mathrm{T}}^{seed} > 2\,\mathrm{GeV}$, $f = 0.5$. To speed up the reconstruction, the seeds used are not single cells but groups of cells, the so-called calorimeter towers. These are found by dividing the calorimeter into a $\Delta\eta \times \Delta\phi = 0.1 \times 0.1$ grid, and summing over the energies of the cells in that box. Sometimes, due to the geometry the border of the grid divides a physical cell, then the energy of this cell is divided between the adjacent calorimeter towers. Another detail that has to be observed, is that due to energy fluctuation and the baseline subtraction of the expected cell noise (perfomed online) some cells or even whole towers can have negative energy. Calorimeter towers with negative energy are summed to neighbouring positive energy towers, before the jet clustering starts. Jets are calibrated to hadronic scale of the calorimeter by the so-called H1-style weighting, which along with more details on jet reconstruction is described in [7]. Furthermore, only jets with $p_{\mathrm{T}} > 7\,\mathrm{GeV}$ are kept in the jet collection.

The presented algorithm has the disadvantage to be not infra-red safe, which can result in spurious jets. There are more refined and infra-red safe algorithm, e.g. the seedles cone algorithm, SIScone [140], the k_T algorithm [70] or its variant the anti-k_T algorithm [145], which proved to be superior [145] to the

[3)] Seeds are combined by using the E scheme, i.e. adding the four vectors of the seeds using the rapidity *y* coordinate, since the combined object is massive.

simple cone algorithm. In Athena release 12 only the k_T algorithm had been implemented as alternative. Nevertheless, we choose to use the cone algorithm in the study since it has a pendant in the fast detector simulation described below. We assume that for the kinematic of the highest and next-to-highest p_{T} jets in the event, the detailed simulated cone jets would match best with the fast simulated cone jets.

The jets found within the range of $|\eta| < 3.2$ are often called central jets in distinction to the so-called forward jets reconstructed in $|\eta| > 3.2$. This distinction may be motivated by different calorimeter properties and the fact that the reconstruction in the extreme forward region has a lower efficiency and potentially higher uncertainty.

Due to the high precision vertexing with the ID the access to secondary vertexes is possible. This information is used for flavour tagging, i.d. labelling jets with secondary vertices stemming from B and D mesons. The jet collection is assigned a b-tag weight, which is a measure for the probability that the jets originates from a B meson. Jets that are not flavour tagged are called light jets, assuming them to originate from gluons or u,d,s flavopured quarks.

3.3.2 Photons, electrons, muons and hadronic tau decays

Photons and electrons are found in the electromagnetic calorimeter. The algorithms are seeded with a sliding window algorithm, which constructs a fixed size cluster. Specifically to the kind of lepton optimised sliding windows and quality cuts help to discriminate the particles. For electron and photons the shower shape and energy isolation in the calorimeter are evaluated. If an electron in the range of $|\eta| < 2.5$ is found, it has to have a matched track in the ID. For a lepton with $p_{\mathrm{T}} > 20$ GeV the energy resolution of the calorimeter starts to exceeds the ID momentum resolution. Muons are triggered and found in the muon system by track fitting between the muon chamber hits. For low p_{T} muon candidates the pattern recognition algorithm try to match hits from the ID to the muon hits. Jets are discriminated from more pencil like isolated energy depositions of hadronical tau lepton decays in the calorimeter by further cuts and evaluation of shower shape and other variables in a tuned tau identification likelihood. Especially the precision information of the first electromagnetic layer assist in constructing discriminating variables. In the range of $|\eta| < 2.5$ the number of tracks can also contribute as criterion.

3.3.3 Overlap removal

All particle identification, except the muons, or jet reconstruction algorithm access simultaneously the calorimeter cells above the noise threshold. From these cells the algorithms select seeds and independently build up the reconstructed object. This can lead to ambiguities that the same physical object, namely clustered calorimeter energy is reconstructed in various objects. E.g. one can think of a situation were the same cluster passes all criteria for jet reconstruction as well a for electron reconstruction. Therefore, between reconstructed objects that spatially overlap in a small ΔR cone, a decision has to be made in which order the objects should be uniquely labelled, i.e. disregarding the alternative labels from the object collections. The overlap cone for electrons, photons and hadronic tau candidates is chosen to be $\Delta R = 0.1$. Since jets are broader objects the overlap cone size for jets is chosen to be $\Delta R = 0.3$. Since the probability of reconstructed muons, stemming from the muon sub-system, fake a calorimeter jet is vanishing, reconstructed muons can always been kept. Overlapping objects are kept in the following priority order: reconstructed electrons, photons, hadronic taus and lastly jets. By this choice one of the possible 'views' on the energy deposition in the calorimeter is uniquely defined in term of particles. The Atlas data model provides a package called HighPTView customised by physics and performance groups for e.g. overlap removal and ntuple skimming. The overlap removal in the used samples, has been made with the HighPTview package from Athena release 12.6.5.

3.3.4 Transverse missing energy

The $E_{\mathrm{T}}^{\mathrm{miss}}$ is the transverse missing energy. The transverse missing energy is mainly determined in the calorimeters. In order for the cell based $E_{\mathrm{T}}^{\mathrm{miss}}$ reconstruction to work, a good hermicity of the calorimeter system is necessary. Since the energy in the $x-y$ plane before the collision is vanishing, the missing energy in the event after the collision can be deferred by vectorially summing over the energy depositions of all visible particles. The opposite direction of the resulting vector is the $E_{\mathrm{T}}^{\mathrm{miss}}$ vector. Its absolute is non vanishing in case of weakly interacting particles (and muons) escaping the calorimeter. Main reconstruction steps are listed in the following.

1) The $E_{\mathrm{T}}^{\mathrm{miss}}$ reconstruction operates on hadronically calibrated calorimeter cells, vectorially summing up the components of the $E_{\mathrm{T}}^{\mathrm{miss}}$ vector.

2) The $E_{\mathrm{T}}^{\mathrm{miss}}$ components are corrected for the muons, which are only minimal ionising particles and can carry away out of the calorimeter a large transverse energy. The information of independently from the calorimeter reconstructed muons is used for the correction. To avoid fakes the muons must have matched tracks in ID and muon system.

2) The $E_{\mathrm{T}}^{\mathrm{miss}}$ is corrected for the expected energy loss in dead material, like the cryostat in front of the calorimeter or in poorly instrumented gap regions (considered are $1.1 < |\eta| < 1.7$ and $2.9 < |\eta| < 3.5$). The correction may be of about 5%.

3) A refined calibration of $E_{\mathrm{T}}^{\mathrm{miss}}$ is performed. All formerly reconstructed objects are associated to the calorimeter clusters they are made of. Clusters are assigned in the order electrons, photons, hadronic taus, jets, and muons. The energy of the cluster is replaced by the reconstructed object's energy. This has the important effect that clusters from electrons and photons are set back to the appropriate electromagnetic scale. From this configuration $E_{\mathrm{T}}^{\mathrm{miss}}$ can be calculated again.

4) Unclustered hadronically calibrated cells are included in this calculation if they are above a noise cut optimised for $E_{\mathrm{T}}^{\mathrm{miss}}$ measurement.

More details on $E_{\mathrm{T}}^{\mathrm{miss}}$ reconstruction and expected performance with Athena release 12 can be found in [7].

3.3.5 Geant4 based detailed detector simulation

For many studies it is desirable to use simulated Monte Carlo generator events. The detector software Athena has to be able to realistically describe the detector response for these simulated events in term of digitised signal, which then can be passed to the same reconstruction algorithms that usually are intended to reconstruct data events. The simulated events additionally contain most of the generator truth information.

The Athena package, hence posses a detailed geomodel detector description and can use the standard GEANT-4 [14, 19] package, which provides a detailed transport model for all particles in matter, to simulate the response of the detector. Typically the full simulation of an event in the detector using GEANT-4 takes about 900 CPU seconds. While the simulation in the small and rather simple sensor elements of the complete ID takes about 150 CPU seconds, the simulation of the response of the calorimeter, especially in the EMEC and FCal, can be identified as bottle neck. The detailed simulation of the charge transport in the many calorimeter cells with GEANT-4 takes about 760 CPU seconds, five times longer than the ID with its many channels. For the used simulated events also realistic misalignment of detector components within the expected tolerances is considered. Simulated events that are processed in such a way are sometimes called FullSim events. The samples used in the sensitivity study were simulated with Athena release 12.6.5.

3.3.6 Fast detector simulation

For many feasibility and acceptance studies an alternative to the detailed detector simulation was introduced. This packages called ATLFAST-1 [46] provides a rough estimate of the detector response in much less than a second per event. The main advantage of the package is the speed, which allows very well to study e.g. the kinematics and acceptance of even vary large backgrounds, by generating some magnitudes more events as in detailed detector simulation. But for all detailed studies as detector effects, calibrations, fake rates and so on, this package is not sufficient.

The speed of ATLFAST-1 is possible by largely using parametrisation of quantities, devised from fully simulated events, and by extremely simplifying the calorimeter system. Since the presented sensitivity study used larger samples of ATLFAST-1, we shortly describe to which extends ATLFAST-1 simplifies the detector.

Main simplifications in ATLFAST-1

1) There is only one calorimeter cell layer, hence no difference in granularity and the response of the electromagnetic and hadronic calorimeter, assuming full compensation.

2) The efficiencies over the whole calorimeter range, which has for all stable generated particles an acceptance down to $|\eta| < 5$, are equal. This neglects poorly instrumented regions or inefficient regions like the extreme forward calorimetry.

3) The granularity of the calorimeter is largely reduced. The calorimeter consist of cells with $\Delta\eta \times \Delta\phi = 0.1 \times 0.1$ in $|\eta| < 3.2$.For $3.2 < |\eta| < 5$ the granularity is $\Delta\eta \times \Delta\phi = 0.2 \times 0.2$. Since all simulation and reconstruction is by-passed in ATLFAST-1 this calorimeter representation is corresponding more to a (η, ϕ) coordinate in the calorimeter volume, not more.

4) Calorimeter cell entries are made by propagation of the generated four-vectors of stable particles through the ID magnetic field. In this the solenoid magnetic field inside ID is assumed to be perfectly homogeneous and the starting of all stable particles is the nominal origin. The calorimeter cell closest to the (η, ϕ) coordinate of the particle leaving the ID volume is filled with the generated particle energy.

5) No effects of distortions like multiple scattering, conversions, energy loss in dead material and misalignment in the ID or the calorimeter are present. Instead appropriate energy resolutions, devised from detailed detector studies are used to smear the final state particles and jets to account for an overall effect.

Jets in ATLFAST-1

Though the calorimeter jets in ATLFAST-1 are also cone jets with an opening angle $\Delta R < 0.4$, the algorithm with respect to the detailed simulation is even more simplified since it is an non iterative cone jet algorithm, i.e. the algorithm is not searching for the stable jets axis as described in point 2) section 3.3.1. The axis is fixed by the choice of the seed. Jet building proceeds as follows. After the unsmeared energies are deposited into the cells were the stable particle incident to calorimeter, a list of seeds corresponding to the calorimeter towers, but with ATLFAST-1 granularity, is generated with descending E_{T} order. For the seeds in the list $E_{\mathrm{T}}^{seed} > 1,5$ GeV is required. Then clusters are formed by running the cone algorithm with $\Delta R < 0.4$, non iteratively on each seed. Another simplification is that each ATLFAST calorimeter tower can belong only to one cluster, meaning the split and merge procedure of point 4) section 3.3.1 is skipped. The clustering algorithm keeps only clusters with energy above 5 GeV in the list of proto-jets. In the next step ATLFAST-1 uses the truth position information about

isolated electrons and photons and non-isolated muons in the calorimeter. While clusters associated to the isolated electrons and photons are removed from the proto-clusters the energy of non isolated muons is added to the associated proto-cluster. If the energy of these corrected clusters is larger than 10 GeV, they are counted as reconstructed cone jet. Finally the energy of the corrected cluster is smeared with the jet energy resolution function to yield the cone jet energy.

Photons, electrons, muons, taus and b-flavour jets in ATLFAST-1

As indicated above, the reconstruction of stable particles like electrons, photons, muons, and hadronically decayed taus is based on the generated four vectors of these particles. Hence, there is no fake reconstruction in ATLFAST-1 possible. Since the calorimeter response of the particles is found by the smearing of their truth information according to the specific resolution, there is no ambiguity and need of overlap removal in ATLFAST-1 samples. Further ATLFAST-1 is not correcting for reconstruction efficiencies for muons and electrons itself. Corrections have to be applied by hand. Into the identification of jets from B mesons or the jets of hadronic taus, randomised identification and missidentification are included, according to a parametrisation from detailed detector simulation.

Missing transverse energy in ATLFAST-1

After all stable truth particles have been assigned to reconstructed objects, smeared within the resolution, ATLFAST-1 loops again over the truth container. All reconstructed objects,photons, isolated electrons, muons, taus, jets, and also non-isolated muons and all remaining calorimeter clusters that did not end up in jets, since they failed the reconstruction jet p_{T} cut, are used in the $E_{\mathrm{T}}^{\mathrm{miss}}$ calculation. If unclustered towers are present, their energy is smeared according to the jet resolution parametrisation and these energy is included to the calculation.

Comment on refined event reconstruction used in data taking

Simulated events are of course reconstructed with the same algorithms used for the data event reconstruction. The study presented used the Athena release 12, as the updated sensitivity studies of [7] did. In the year 2010 the actual data taking uses Athena release 15 and 16. A comment on possible differences from the choice of releases on the sensitivity may be in order. The overall detector design was fixed in release 12 already, which was one motivation to study the ATLAS physics as an update to the performance expectations in the ATLAS technical design report of 1999. But the details of the detector geometry are updated in the data bases of the new release. Also the complete missing object trigger simulation is in the new releases. The simulated events with the new releases are available with real events overlayed for the pile up of the corresponding instantaneous luminosity and its influence, e.g. on $E_{\mathrm{T}}^{\mathrm{miss}}$ resolution can be studied with releases 15 and 16. A major difference, which may have impact on the results, are the changes from seeded cone jets to a more refined and theoretical well motivated jet algorithm, the anti-k_t algorithm [41] on base of topological adjoined clustered cells, became the standard in the new releases. Also the calibration of the energy in calorimeter clusters became more refined and can now start to use in-situ calibration methods with data. Even object base calibration and energy flow algorithms and also track based jets are under development and under study in the more recent releases. Together with knowledge of the detector from the commissioning, these new features in the releases give rise to the assumption that the optimistic performance aims of the TDR, e.g. an overall uncertainty of the jets energy of about only 1% can be reached in future. As we will demontrate in chapter 6 especially the jet energy scale has crucial impct on the sensisivity. In that sense we regard our sensitivity study as conservative since we used less refined algorithms than those availabel today and assumed more pessimistic uncertainties e.g. the jet energy scale.

4. Modelling of signal and background processes

In this section we want to describe event simulation of the signal events and of the most important SM backgrounds by various MC event generators. We start with a short overview over the expected physical interactions that can be recorded by the ATLAS detector, and explain which components of collision events the MC events generators have to model.

4.1 Characteristics of proton proton collision at the LHC

Since spring 2010 the LHC accelerator is operated at a centre of mass energy of 7 TeV, having thereby superseded the TeVatron collider with its 2 TeV centre of mass energy, and gives first interesting glimpse into a so far unexplored energy realm. The picture one has to draw of the proton proton collision recorded in a detector at these high energies depends largely on the instantaneous luminosity and the achieved centre of mass energy, $\sqrt{s}$.

The total cross section for the proton proton interaction, $\sigma_{tot}(s)$ at 14TeV was recently estimated to be $\sigma_{tot}(14\text{ TeV}) = (106.3 \pm 5.1\text{ (syst.)} \pm 2.4\text{ (stat.)})mb$ [103]. The total rate can be expressed as the sum of elastic (σ_{elas}) interactions, contributing roughly a quarter to a third to the total rate, smaller single diffractive (σ_{sd}), double diffractive (σ_{dd}) contributions and last but not least non diffractive (σ_{nd}) contributions, representing roughly a half to two thirds of the rate.

$$\sigma_{tot}(s) = \sigma_{elas}(s) + \sigma_{sd}(s) + \sigma_{dd}(s) + \sigma_{nd}(s) \tag{4.1}$$

Proton proton interactions are dominated by soft partonic collisions but may also have (semi) hard components, leading to scattered jets in the detector. As one can see from the right-hand column of schematic drawings in Fig. 4.1 the individual sub-processes tend to populate specific regions of the detector. The acceptance of the detector and its triggers differs therefore for the individual contributions. In particular if one or more protons keep intact they will most likely vanish in the beam pipe without leaving traces in the detector. Moreover the diffractive processes leave large regions of the detector depleted from hadronic energy. The recorded fraction of each process is experimentally determined by the trigger system. Applying trigger conditions for specific processes implies inevitably to bias the choice of the collected sub-samples. Therefore experimentalists introduced the the notion of minimum bias events. These events can be triggered by dedicated minimum bias trigger menus but the selected samples should be as inclusive and unbiased as possible. Though the definition of minimal bias explicitly depends on the trigger conditions it is often referred to as non single diffractive events defined by Eq. 4.2. It should be stated though that this terminology is not unique, e.g. in theory context, minimal bias is often identified with the non diffractive inelastic interactions σ_{nd}.

$$\sigma_{nsd}(s) = \sigma_{tot}(s) - \sigma_{sd}(s) - \sigma_{elas}(s) \tag{4.2}$$

The ATLAS detector will be able to measure a large fraction of minimum bias events, which mostly are the result of semi-hard scattering.. As the left plot of Fig. 4.1 indicates, the overwhelming fraction of the non single diffractive events will consist of QCD multijet production, and despite the fact that it will be a very interesting achievement to measure these cross sections, the interesting hard interaction which give information about possible new physics have a cross section typically nine orders of magnitude

lower. Even the next dominant SM processes like W and Z boson production in association with jets and top pair and single top production are more than 6 orders of magnitude below the QCD background rate. Fortunately such processes, as well as the hypothetical new physics, reveal themselves typically by characteristic energetic leptons or b-tagged jets or large missing energy but will only be visible if there is an efficient level-1 trigger system.

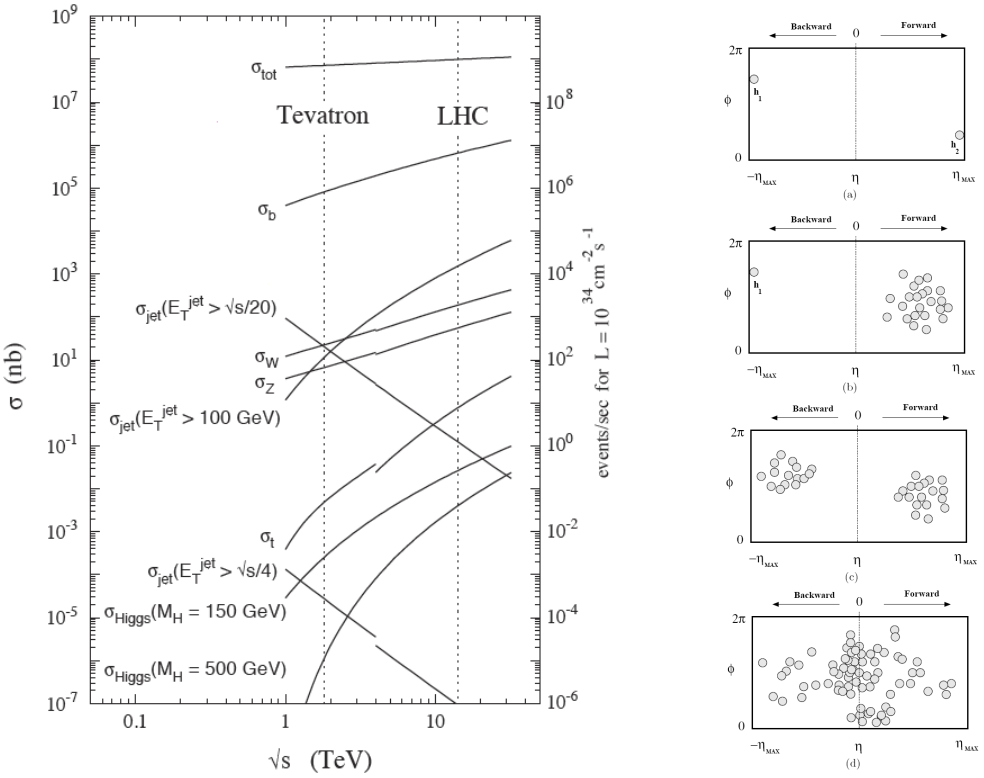

Fig. 4.1: *left: The cross sections of the SM processes at very high centre of mass energies as in the Tevatron collider or expected the LHC. The right-hand scale give the rate of expected events for the LHC running at design luminosity of* $10^{34} cm^{-2} s^{-1}$*. Found in [43]. right: schematic view of (a) elastic (b) single-diffractive (c) double-diffractive and (d) non-diffractive hadron hadron interactions in* $\eta - \phi$ *space*

4.1.1 Modelling from the hard process to jets

Hard process

Interesting physics interactions exhibit a large transverse momentum when two partons in the proton beams hit "head on". In this scales the governing QCD is still perturbative. These so-called hard scattering will be modelled by MC event generators by evaluating the corresponding matrix element to a certain order at the physical scale of transverse momentum transfer of between the scatterers, neglecting the exchange of soft gluons. This sets the highest scale compared to the subsequent scales. Since the cross section of the partonic interaction σ_{ij} is perturbative, a factorisation ansatz is valid to describe the influence of the rest hadronic initial state in the colliding colour neutral protons. The probability that a parton of a certain flavor carrying a fraction x of total proton momentum takes part in partonic scattering at these scales is governed by the parton distribution functions $f(x_i, \mu_f^2)$. These have to be evaluated at the factorisation scale μ_f^2, for which it was chosen to factorise the partonic scattering from the rest of

the proton. The parton distribution functions have to be multiplied with the partonic cross section in determination of the total cross section. As one sees in Eq. 4.3 the probabilities of parton 1 to take part at the scattering is given by its pdf $f_i(x_1,\mu_f^2)$, likewise for parton 2 by $f_j(x_2,\mu_f^2)$ and the probability of the scattering process between the two partons is σ_{ij}. Also the phase space integration for the outgoing scattered partons is performed in this step to find the cross section.

$$\sigma = \sum_{i,j} \int\int \mathrm{d}x_1 \mathrm{d}x_2 \, f_i(x_1,\mu_f^2) f_j(x_2,\mu_f^2) \sigma_{ij}(\hat{s},\mu_\mathrm{R}) \tag{4.3}$$

In the partonic scattering cross section σ_{ij} denotes $\hat{s} = x_1 x_2 s$ the effective centre of mass energy of the parton scattering, and the couplings are evaluated at the renormalisation scale μ_R, according to the underlying theory. In a detector though, sprays of colour neutral particles, reconstructed as jets, are measured and not single hard scattered colour charged partons. To correctly describe the connection between the hard scatterers and the measured particles two more scales are involved.

Parton shower approach

Directly after the scattering gluons are radiated off by accelerated colour charges, which start a cascade of radiation themselves, often referred to as parton shower. This includes also the modelling of initial state (ISR) and final state (FSR) radiation, which can be understood as QCD bremsstrahlung of accelerated ingoing and outgoing scatterers. While in principle processes like $q \to qg$ can be included in matrix elements, the finite order of evaluation can lead to uncancelled collinear or soft divergent contributions. Amplitudes of matrix elements are only safe from such divergences for very energetic scatterers well separated in phase space. Therefore, the approach of parton showering is used by the generators, where the potentially divergent soft contributions are treated in a shower model. The complexity and the choice of ordering schemes and scales of the shower model differ specifically for the individual MC event generators. As an ordering parameter Q, which distinguishes the different regions of hard to soft dynamics, can be used for example the virtuality of the involved partons, their relative transverse momentum or the relative angle between them. The collinear and soft emissions are evolved according to different ordering parameters starting at a scale related to the hard scattering (Q^2_max) down to an energy scale where the partons combine to colour neutral hadrons, the so called hadronisation scale. The lower scale also corresponds to a smaller value of the ordering parameter.

Even in the shower model the divergences coming from $q \to qg$ will occur at some softer scales. These divergent parts would lead to radiation emission probabilities larger than unity. Introducing the ordered shower model leads to a meaningful correction of this probability interpretation. If the splittings occur in intervals of ΔQ then the splitting probability into a very soft or collinear parton in one interval may be itself larger unity, but this completely neglects the probability of no splitting in an interval. For example, nuclear decays, can only occur (i.e. split) in a considered time interval if there was no decay in the interval before. As one waits longer the probability to have undecayed nucleons becomes smaller, hence also the rate of decays in a radioactive source will slowly fall, motivating the well known exponential nuclear decay law.

In the following, we summarise shortly the description of Sudakov weights given in [142]. First, we consider the the general splitting of nearly massless partons of type $a \to bc$. The energy fraction of the initial parton a that is carried by b is denoted as z. Splitting probabilities, $\mathscr{P}_{a\to bc}$, relate the cross section of the matrix element with emission $\sigma_{ME_{a\to bc}}$ with the leading cross section σ_0 for $2 \to 2$, and follow from approximating the matrix element in the soft and collinear regime. The DGLAP [20, 64, 86] equation summarises the rules and governs the evolution in z and Q scales.

$$\mathrm{d}\mathscr{P}_{a\to bc} = \frac{\sigma_{ME_{a\to bc}}}{\sigma_0} = \frac{\alpha_s}{2\pi}\frac{\mathrm{d}Q^2}{Q^2} P_{a\to bc}(z)\mathrm{d}z \tag{4.4}$$

In the formula above functions $P_{a\to bc}(z)$ are called splitting kernels. These are theoretically well determined for all kinds of partons taking part in the splitting. The divergences appear separated in the DGLAP equation. The so-called collinear or mass divergences appear at $Q^2 \to 0$ and for $z \to 1$ the splitting kernels can exhibit a soft divergence.

It is natural that these probabilities are universal, if one recalls that in the collinear regime one dominant Feynman graph contributes. By knowing these universal probability differential equations, it is possible to iterate subsequent emission and hence build up the whole shower.

One can get the total branching probability $P_{branching}$ over an infinitesimal small evolution scale change $\mathrm{d}Q^2$, when summing over all possible types of splittings and integrating over all allowed daughter parton's energies z in this evolution step.

$$P_{branching} = \sum_{b,c} \int_z \frac{\mathrm{d}\mathscr{P}_{a\to bc}(z')}{\mathrm{d}z'} \mathrm{d}z' \tag{4.5}$$

It is important not to neglect the probability $P_{nobranching} = 1 - P_{branching}$ that nothing happens in the evolution step $\mathrm{d}Q^2$ and include this to the DGLAP equations, as so-called Sudakov weight. The Sudakov weight $\Delta(Q^2_{\max}, Q^2)$ is defined as the probability that when starting at $Q^2_{\max}$ then evolving down to an arbitrary lower scale Q^2 in this interval no additional emission occurred. The integration of Eq. 4.5 over all $\mathrm{d}Q^2$ and together with probability conservation (see [142]) lead to the analytical form of the Sudakov weights.

$$\Delta(Q^2_{\max}, Q^2) = \exp\left(-\sum_{b,c} \int_{Q^2}^{Q^2_{\max}} \frac{\mathrm{d}Q'^2}{Q'^2} \int \frac{\alpha_s}{2\pi} P_{a\to bc}(z')\,\mathrm{d}z' \right) \tag{4.6}$$

Thus the DGLAP equation acquires the form of

$$\mathrm{d}\mathscr{P}_{a\to bc} = \frac{\alpha_s}{2\pi} \frac{\mathrm{d}Q^2}{Q^2} P_{a\to bc}(z)\,\mathrm{d}z \, \exp\left(-\sum_{b,c} \int_{Q^2}^{Q^2_{\max}} \frac{\mathrm{d}Q'^2}{Q'^2} \int \frac{\alpha_s}{2\pi} P_{a\to bc}(z')\,\mathrm{d}z' \right) . \tag{4.7}$$

In this probabilistic interpretation the weighting of DGLAP probabilities with the exponentially falling probabilities of the Sudakov form factors renders the splitting amplitudes finite in the soft regime.

In the scetched way the splitting of the complete final state shower can be constructed. The calculation has to fulfill energy-momentum conservation. After the construction of the final state shower all information of particle splittings and momenta and energy are given to start with the reconstruction of the ISR splittings that would lead to such a shower history. Similar DGLAP equations are used to treat ISR in a backward evolution to construct an initial state constellation that would have ended up in accordance with the constructed final state radiation pattern.

Hadronisation and decay

The parton shower still does not describe the process on the basis of colourless bound states; this is done in the hadronisation step. The single partons are combined to hadrons and their phase space is determined in accordance with overall-energy momentum conservation. As soon as the partons become confined the strong interaction becomes non perturbative. There is no way to calculate this transitions from partons to hadrons by first principles and the generators use highly phenomenological models in this step. The hadrons found in the final state are decayed according to their measured branching ratios. These decay products can then subsequently enter the detailed detector simulation to model the detector response.

4.1.2 Matching matrix element results and parton shower

As described so far this modelling works directly for generators that treat the $2 \to 2$ process in the matrix element on Born level and leave the rest of the event modelling to the shower. But the first or even the first few real emissions from a matrix element, i.e. $2 \to n$ process with $n > 2$ giving the (jet) multiplicity of the process, can be of special interest, since they occur at energy scales lower but typically relatively close to the scale of the $2 \to 2$ process. Experimentalists for example could be interested to have the first real emission correctly treated in the matrix element, i.e. calculate the p_{T} spectra and $\eta - \phi$ directions for the emitted partons exactly. This would allow to compare experimentally reconstructed third or fourth hardest jets in p_{T} event shape variables with the real parton emission pattern predicted by the matrix elements.There are event generators that treat real emissions in the matrix element calculation. For example Sherpa [84] allows the treatment of an arbitrary number of real emissions from an otherwise strictly leading-order matrix element. Such generators afterwards apply a shower model to account for all possible emission in the event. This poses the problem that the emissions stemming from the matrix element could potentially been double counted if the independent shower model starts its work at the hard scale. Therefore, if emissions from the matrix element occur, they have to be matched to the shower avoiding double counting of emitted energy. Also it is clear that the phase space description of emission close to the hard scattering by the matrix element is superior to those from the shower, but from a certain lower scale, the shower model fills the soft emission phase space more efficient and in good approximation. The choice of the right matching scale y_{cut}, below which the shower takes over the emission of partons alone, is crucial to fill the complete phase space of the events smoothly without larger discontinuities at the matching scale.

It is desirable that the matching is generic and works automatically for arbitrary partons (in praxi still only a few) in the final state. Several alternative matching algorithms have been developed to solve this problem, detailed reference and a comparison of the various method applied to W boson production at the TeVatron and predictions for the LHC can be found in [100].

In the following we try to shortly summarise the concept of CKKW [110] matching used in the Sherpa event generator. Matching of hard matrix element emission with showers includes the very intuitive use of a jet algorithm. Since any jet algorithm collects and merges particles in pseudo-particles up to a certain cut-off condition that is related to the relative spacing of particles in phase space and allows to measure changes of "jet" multiplicities as function of the resolution parameter. The CKKW matching proceeds as follows.

1) The first step deals with finding the probabilities for a specific final state multiplicity and its cross section. Since the cross sections of the higher multiplicity processes $2 \to n$ may eventually diverge one usually treats the partons like jets and defines first of all a suitable cut off scale y_{cut} for the smallest relative distance in phase space between the partons that yields no divergent cross section. As measure of distance in phase space between (pseudo) particles i and j often the resolution parameter y_{ij} of a Durham or $\mathrm{k}_\perp$-jet algorithm [44] is chosen. Evaluating the matrix element and its emission only above the scale y_{cut} one is able to calculate meaningful cross sections σ_i for the individual $2 \to i$ "jet" multiplicities. The multiplicity depends of course also on the running of α_s which is evaluated at the scale y_{cut}. The knowledge of the cross sections σ_i automatically defines the probability of the $2 \to i$ process as $P(2 \to i) = \sigma_i / \sum_j \sigma_j$.

2) Randomly events are generated in $2 \to i$ configurations according to their probability $P(2 \to i)$ of the matrix element emission.

3) Step 2 has determined the final state configuration of the event by the matrix element. In Step 3 begins the reconstruction of a shower history for this configuration by finding splittings or mergings with a jet algorithm. The final state configuration with the highest multiplicity is hereby considered. It is asked how such a configuration could have been reached equivalently via a hypothetical

showering starting at the legs of the leading order matrix element (usually $2 \to 2$ process for jet production). The problem is similar to backwards evolution of the ISR in showering.

All partons emitted in the matrix elements are fed as seeds into a $k_\perp$ algorithm, starting at the lowest resolution parameter the so-called matching scale y_{cut}. Next the value of the y_{ij} merging condition is raised in iterations with the effect that eventually at some scale corresponding to a y_{ij} partons are merged to a pseudo particle. Only mergings that are physical are allowed since the merged configuration should be interpretable as a hypothetical shower splitting at this individual scale y_{ij}. The iteration with rising values of y_{ij} is continued until the leading order matrix element parton configuration i.e. the $2 \to 2$ process is reached.

4) Step 4 continues building the hypothetical shower history by construction of the Sudakov weights. From Step 3 all the scales of the hypothetical splitting are known, namely y_{begin}, the scale where the jet algorithm merged, hence the hypothetical parton emerged down until y_{end} where the next splitting is reached or y_{cut} if the emerged parton belongs already to the final state. Thus the Sudakov weights can be calculated from all branchings or non-branchings of the parton's "propagators" in the event. They acquire the form of

$$\frac{\Delta(y_{\text{begin}}, y_{\text{cut}})}{\Delta(y_{\text{end}}, y_{\text{cut}})} \tag{4.8}$$

As before the Sudakov weights account for the non emission probability between the scales y_{begin} and y_{end}.

5) The hypothetical shower history should be evaluated with appropriate running of the strong coupling $alpha_s$. This is assured in Step 5. In order to use the correct running of α_s at each merging (splitting) scale y_{begin} the Sudakov weights are multiplied by the following weight

$$\frac{\alpha(y_{\text{begin}})}{\alpha(y_{\text{cut}})}. \tag{4.9}$$

In such way the complete hypothetical shower history from the leading order scale down to y_{cut} is constructed in the language of showering and can be stored.

6) Like in a hit and miss approach the event is randomly kept according to its combined weight from Sudakov weight and running coupling correction. If the event is rejected then the algorithm returns to Step 2.

7) In Step 7 the parton shower is applied for emission below the matching scale y_{cut}. As explained above, the matrix element/parton shower matching divides the phase space of the event into two disjunctive regimes where partons come from the matrix element and some that is populated by the shower i.e a matching algorithm must contain the possibility to veto a partons from the shower that are produced above the matching scale y_{cut}.

On the legs of the hard process of the leading-order $2 \to 2$ process the parton shower is evoked starting at the scale related to the hard scattering. But all splittings that would also occur in the hypothetical shower history since they would happen above the matching scale are now vetoed in the shower. Only the splittings below this scale are kept since they provide the matched continuation of the matrix element generated configuration below the matching scale.

4.1.3 Underlying events

Multiple parton-parton scattering accompanying the hard process in a proton-proton collision is usually referred to as underlying event activity. An intuitive sketch is displayed in Fig. 4.2. The outgoing

two hard scattered jets are accompanied by coherent initial and final state radiation. Additionally softer multiple parton interactions can occur in the proton remnants that are present. This is called the underlying event. The modelling of the underlying event activity uses phenomenological models, that are extrapolated from lower centre of mass energies measurements and so far untested at higher energies.

Monte Carlo event generators find the probability of multiple interactions in a proton proton collision with model of the matter distribution within the hadrons. Most generators supply various matter distributions together with some free parameters and form factors to tune these to data. The underlying event is often tuned to experimental data of hadron collider experiments like UA5 or the TeVatron experiments. It is obvious that an underlying event tune at higher energies can not change matter distribution parameters without losing the valid low energy description of the underlying event. After the matter distribution parameters are fixed at the low energies data a model specific extrapolation to LHC energies is performed. Since the extrapolation to LHC energies depends on the specific model it can lead to significantly differing predictions.

Also since the hard process leaves a lot of energy for accompanying partons, the underlying event comprises $2 \rightarrow 2$ processes that can in principle start close below the scale of the hard process, Q_{hard}. In order to be compliant with the overall energy momentum conservation each of the subsequent other parton scatterings is modelled at an appropriate lower scale of transferred transverse momentum. The most important parameter is the scale Q_{cut}, the lowest momentum transfer, down to which these processes are allowed. The value of Q_{cut} can be as well fixed by e.g the TeVatron data. In the simplest ansatz the value of Q_{cut} at the LHC can be exponentiated from this reference scale according to

$$\mathrm{Q}_{cut}^{LHC} = \mathrm{Q}_{cut}^{TeV} \times (\frac{E_{cm}^{LHC}}{E_{cm}^{TeV}})^{\alpha_r}. \tag{4.10}$$

Since the ratio of centre of mass energies and the cut value of the reference scale are given, the exponentiation parameter α_r becomes the only free parameter to adjust the underlying event activity at the LHC centre of mass energy. The evolution with α_r connects the reference scale given by the TeVatron centre of mass energy and LHC energies.

A second important influence on the underlying event models in MC generators becomes clear if one recalls that the QCD $(2 \rightarrow 2)$ processes account for the underlying event. The probability for partons in the hadron to take part in a scattering processes of a transferred momentum scale t is therefore strongly depending on the parton distribution function (PDF) probed at the corresponding scale. Since the PDF sets are the result of complicated fitting procedures to a variety of experimental data sets, the predictions of the PDF sets at the probed scale can largely differ. Therefore the cross section of the underlying event scattering is a function not only of the energy scale t but also of the probability for finding the partons $f(t, PDF)$ in a certain flavour and momentum state, hence this probability depends of the PDF set used. The interplay of these factors is summarised symbolically in the following Eq.4.11.

$$\mathrm{d}\sigma^{UE}(2 \rightarrow 2) \approx f(t, PDF) \frac{\alpha_s^2(t)}{t^2} \mathrm{d}t. \tag{4.11}$$

4.1.4 Pile Up

Pile up, which we describe in the following, has two components, one physical related to the bunch crossings and one instrumental component related to integration times.

In the LHC densely packed bunches of protons are collided at bunch crossing rates up to 40 MHz. This is resulting in experimental challenges. If in one bunch crossing an interesting hard physics interaction is triggered, it is predicted that for design luminosity on average 24 additional primary interaction vertices of minimal bias events will be present in the detector. The occurrence of multiple primary vertices from minimum bias events is called in-time pile up referring to the actual triggered bunch crossing.

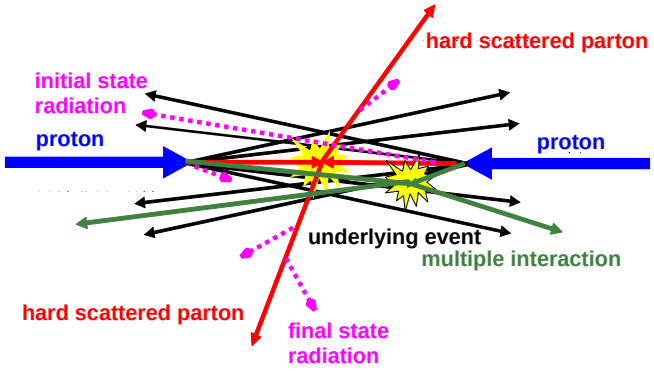

Fig. 4.2: *Sketch of a proton proton collision in the LHC. Any further scattering of partons additionally to the hard process is usually accounted for as underlying event or sometimes referred to as multiple interactions.*

To identify the hard interaction among the vertices correctly is crucial and will be possible with the good spatial resolution of the inner detector.

While the electronics of the inner detector is read out promptly the larger and more complex calorimeter system has a longer integration time before read out. Since the calorimeter integrates over a couple of bunch crossings before and after the triggered event, energy deposition of pile up from several bunches add up. Accumulated electronic signals over this time are called out-of-time pile up.

During integration time cavern background also contributes as additional source of hits not correlated to the interesting event to pile-up effects. Cavern background can be understood as a 'gas' of neutral and charged particles, which is present in the detector hall stemming from material activation and other secondary processes. The largest component are neutrons from the activated material. They can fly around in the hall for seconds before they are thermalised. Together with an also present and abundant hard photon component from activation this 'gas' can produce subsequently Compton electrons and spallation protons. The cavern background has no correlation with the individual bunch crossings and it is expected to add very many extra hits to the muon position chambers and trigger chambers in addition to prompt particles that escape the calorimeter system.

The experimental impact of pile up can be large. Even if the the p_{T} of jets reconstructed from pile up is most of the time very low, pile up affects any simple isolation criteria. E.g. for lepton identification in the calorimeter one checks that there is an energy deposition focused to some predefined small region surrounded by a much larger region where only very few energy is deposited. If this isolation belt is hit by pile up jets the identification criteria will not work and fewer isolated leptons are found. Isolation criteria of this kind are also used by analyses designed in non pile up scenarios for ambiguous object identification. Pile up is a very important issue currently under study and future analyses in pile up scenarios need refined algorithms that identify jets contributed by pile up and exclude them from the criteria to find isolated particles originating from the primary vertex.

From the simulation point of view it is possible to add in the detailed detector simulation randomly specially simulated minimal bias events and modelled cavern background to the digitised detector response. Since data is available, the overlay of real minimum bias events is done. Unfortunately there were no simulated pile up samples with Athena release 12 available. The study presented had to neglect the influence of pile up on the results.

4.2 Modelling of the signal process

As argued in Chapter 2, among the exploitable production modes of the Higgs boson for observation of succeeding invisible decays, the weak boson fusion [42, 128] promises over a large mass range the highest cross section and hence experimental sensitivity. Therefore, the simulation of signal Monte Carlo events focused on this production mode.

4.2.1 Weak boson fusion topology

Kinematics of the process

In lowest order two diagrams mediate the process $qq \rightarrow qqVV \rightarrow qqH$, (see Fig. 2.4 a) where the V indicates a W or Z boson that is emitted from the incoming quarks. The virtual weak W or Z bosons couple to the Higgs. The Higgs is produced at central rapidities in the detector and tends to yield central decay products (in this specific case the undetectable decay products appear only as missing transverse momentum, $E_{\mathrm{T}}^{\mathrm{miss}}$). Since the masses of the weak gauge boson provide the scale of the process a medium mass Higgs boson may be emitted typically with $p_{\mathrm{T}} \approx 60 - 120$ GeV.

The outgoing quarks give rise to two jets which enter the detector at large rapidity compared to the Higgs decay. Since the transverse momentum p_{T} of the outgoing quarks is governed also by the mass scale of the emitted weak boson, against which the quark is recoiling, the p_{T} is typically sufficient that both jets reach the hadronic calorimeter and will be reconstructed. These jets are often the leading and subleading jet reconstructed in the event, with a moderate to sizable transverse momentum[1)]. In a large fraction of events the jets from the outgoing quarks lie in opposite hemispheres of the detector and their difference in pseudorapidity is several units. Signal events that stem from the weak boson fusion process in the LHC are identified by these so-called tagging jets in the ATLAS detector.

Possibility to veto central hadronic activity

The prospects of Higgs searches within weak boson fusion raised when it was discovered that for the signal there should be a strong suppression of soft hadronic radiation in the pseudorapidity range between the tagging jets, the so called rapidity gap [30].

It is characterising for the signal process that between the two electroweak scattered quarks there is no net colour exchange in the t-channel. Hence the colour singlet exchange in the t-channel, leaves only the possibility of additional soft gluon radiation along with the leading jets in forward and backward direction under small angles. In contrary in background processes taking part in strong interaction a colour octet is exchanged in the t-channel, which gives rise to a soft gluon radiation pattern emitted mainly in the central region between the tagging jets.

While the depletion of soft hadrons in the central region maybe not visible considering also pile up, it was shown in [30] that a discrimination between electroweak and strong processes may be feasible even at high luminosity if one looks for jets in a low p_{T} range of 15-40 GeV instead, since the jet algorithms try to collect the hadronic particles that stem mostly from one interaction point. Rejecting events with one or more of such small p_{T} jets in between the tagging jets is called minijet veto or central jet veto.

The different population with additional jets in the region between the tagging jets for processes with colour singlet and colour octet exchange can be visualised in the so-called Zeppenfeld plot (Fig. 4.3). For events containing additional jets the distance of the third jet in pseudorapidity to the averaged tagging jet pseudorapidity is called $\eta_3^\star = \eta_3 - \frac{1}{2}(\eta_1 + \eta_2)$. We compare in Fig. 4.3 the shape of the Zeppenfeld distribution for events containing a third jet. The signal which is expected to radiate most

[1)] We characterise jets by their p_{T} and η, ϕ values. Though the jets in this study are calorimeter based jets and the calorimeters measure energy deposits, hence transverse energy E_{T}, for high energetic jets E_{T} can be replaced by p_{T} as well as the rapidity, y, of a jet becomes equal to the pseudorapidity η.

of the additional jets close to the two leading jets is plotted as magenta histogram. The two important backgrounds of W and Z bosons are shown in two components each. The background from graphs containing strong interaction is shown as light blue for the W boson and light green for the Z bosons. The events stemming from electroweak graphs are the dark blue histogram for W bosons and the dark green for the Z bosons. Additionally the shape of the third jet distribution in a QCD dijets sample is displayed as black histogram. One sees in Fig. 4.3 that the hadronic radiation, thus the third jet, is mostly close to the tagging jets emitted, corresponding to larger values of $|\eta_3^\star|$. But processes with QCD graphs tend to populate the region of $\eta_3^\star \approx 0$ which is the direction between the tagging jets. This effect is most prominent for the dijet background. But even the weak samples populate this area with jets. It can be interpreted as the effect of showering and especially the underlying event contributions.

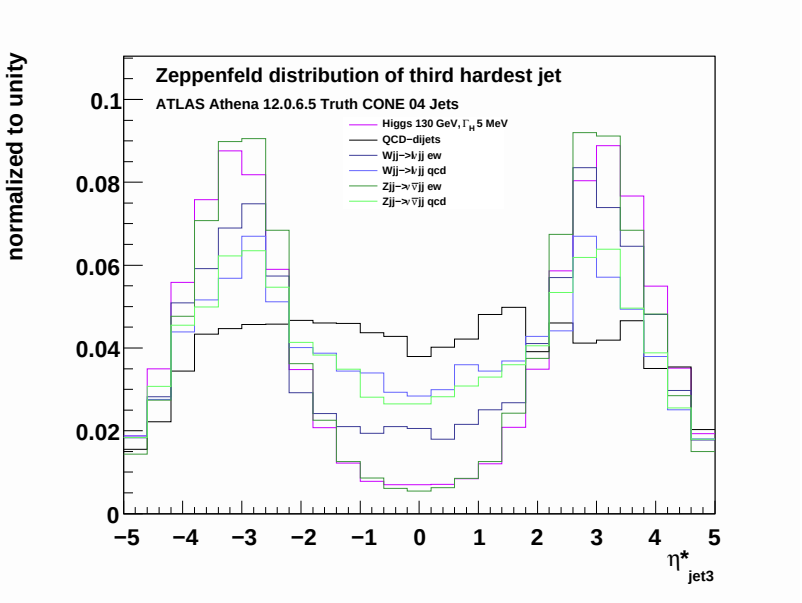

Fig. 4.3: *Distribution of $\eta_3^\star = \eta_3 - \frac{1}{2}(\eta_1 + \eta_2)$ the distance of the averaged rapidity of the two tagging jet to the third leading jet for various physics processes. The jets were combined from final state particles (except muon and neutrinos) on generator level. All jets were required to have a $p_T >$ GeV. Compared is $\eta_3^\star$ distribution of the an invisibly decaying Higgs signal with mass of 130 GeV generated with Sherpa (magenta histogram) to some of the background processes. The QCD dijet background (black histogram) is generated with Pythia 6.4. Sherpa samples of the W/Z plus jets background are shown split in events stemming from electroweak graphs (ew) and strong interacting graphs (qcd). The light blue histogram is the strong and the dark blue histogram is the electroweak contributions in the W plus jets background. Likewise the light green histogram is the contribution from strong graphs in the Z plus jets background, the dark green histogram of the electroweak graphs.*

In simulated events the minijet veto depends, aside from details of jet reconstruction, mainly on the modelling of the strong processes, the radiation pattern of additional jets and especially on the underlying event. Because the underlying event is present even for the weak boson fusion processes as well it fills the region between the tagging jets with minijets. The modelling of these effects is done differently in the specific generators. In Appendix A an attempt was made to find a way of vetoing mini jets that is as robust as possible against different generator models.

This study used only simulated events which could not be tuned to ATLAS data so far. To become independent from generator differences it will be important to use the early LHC data to tune the generators to data and later measure those veto probabilities in data. Currently promising efforts [136] in

ATLAS started to refine the minijet veto by track vertex association and gain more robustness against the influence of pile up jets. Therefore it is expected that ATLAS analyses will be able to make good use of the minijet veto even under pile-up conditions.

As we will see later demanding two leading jets in opposite hemispheres of the detector exhibiting a large pseudorapidity gap of roughly four units to each other and vetoing events with mini jets in the central region will form the core technique to identify the signal in weak boson fusion topology.

4.2.2 The Sherpa event generator

Sherpa [84,113] is a multipurpose MC event generator that evaluates the matrix elements of the generated processes at leading order (LO). Unlike in many other event generators the user is not selecting via a code a special set of diagrams that enter the matrix element calculation, but defines the particles present in the initial state (IS) and in the final state (FS). To select a set of Feynman diagrams for the process the user also defines the orders of electroweak and strong couplings (defining in this way additional emissions from the matrix element). Then for a defined initial state, in case of the LHC proton-proton collisions, and specified final state, the Sherpa module AMEGIC++ [111] automatically constructs the exact matrix elements for given number of electroweak and strong couplings and performs the phase space integration. The APACIC++ 2.0 module [112] matches the outgoing partons to a virtuality and angular ordered parton shower. This matching uses the CKKW matching algorithm [45] (previously outlined in 4.1.2) in order to avoid double counting of additional gluon radiation emerging from the hard matrix element.

A matching scale with the parton shower of $y_{\text{cut}} = (5\,\text{GeV}/14\,\text{TeV})^2$ for $2 \to 4$ processes and of $y_{\text{cut}} = (20\,\text{GeV}/14\,\text{TeV})^2$ for the $2 \to 5$ and $2 \to 6$ processes, respectively is chosen.

For processes that contained only weak vertices, the strong couplings in the Sherpa samples were adjusted to account up to 3 jets from the matrix element. When processes with only strong vertices on Born level were generated with Sherpa, it was possible to allow for up to 4 jets from the matrix element. If Sherpa samples had been produced inclusively with strong and weak graphs, again the number of jets from the matrix element was restricted to 3.

Underlying event settings in Sherpa

Sherpa also allows to apply an underlying event model in proton-proton collisions. The corresponding Sherpa module for generating the underlying event is called AMISIC. While the additional jets originating from matched parton shower radiation of the leading jets tend to be radiated off under small angles to these jets, the gluon radiation from the underlying event populates also the central η region between the tagging jets. In Sherpa the reference scale, appearing in Eq. 4.10, Q_{cut}^{TeV} is set to 2.25 GeV and the exponentiation parameter for centre of mass energy dependence α_r is chosen to be 0.25. This specific Sherpa underlying events tune is fixed at Run II TeVatron data as the starting point for the Sherpa exponentiation of the cut scale. In that way one can be sure that the tune has some connection to existing measurements. The CTEQ6L [126] parton distribution function were used in event generation and as well for the underlying event.

Matrix element for the signal process

Sherpa also provides a very flexible framework for including new physics models, since it allows to define additional parameters, couplings and Feynman rules that are compiled in corresponding libraries and calculates the matrix elements for the hard processes.

Alternative MC event generators like Pythia [143] and Herwig [55] use the process $H \to ZZ^{(\star)} \to \nu\bar{\nu}\nu\bar{\nu}$ to simulate invisible Higgs decays in accordance with the SM. This approach will certainly run

into troubles to generate larger invisible decay width due to threshold effects for invariant mass far off shell and the default use of the narrow width approximation[2)].

In the modified Sherpa version on basis of release 1.0.11, direct two body decays of type H$\rightarrow \nu\bar{\nu}$ are incorporated via Feynman rules. The finite width of the Higgs boson is treated correctly in the propagator.

In order to generate the signal, Sherpa uses diagrams that include electroweak couplings to the order 4 and strong couplings up to the order 1 that originate from a proton proton initial state and end in final state defined by a neutrino antineutrino pair from the Higgs boson decay accompanied by two or three jets.

Diagrams that fulfil these criteria can belong to different classes of processes. Counting also the couplings at decay vertices (as it was convention up to Sherpa release 1.0.11) one sees that not only the intended weak boson fusion but also the weak boson associated production can contribute. To demonstrate this Fig. 4.4 shows the invariant mass of the leading and subleading jets at truth level in the event for a Higgs boson mass of 130 GeVgenerated by Sherpa and alternative generators. The signal generated with the described settings for Sherpa in comparison to the pure weak boson fusion process settings for Herwig and Pythia. In the very high invariant dijet mass range theoretically all three generators should give the same distribution of dijet masses since the weak boson fusion dominates completely. The observed difference comes from the different generator shower model, tunes and scales settings. In the Sherpa signal sample a Higgs boson with a mass of 130 GeV is produced in both, vector boson fusion and weak boson associated Higgs production ($\approx$ 20 %) as is clearly confirmed by the peak below 100 GeV in Fig. 4.4 where the associated production graphs contribute.

As stated above for the signal samples up to three jets were generated by the exact matrix element and matched.One can deduce from the ratio of cross sections for $2 \rightarrow 4$ and $2 \rightarrow 5$ sub-processes that typically one forth of the Sherpa events have a third jet originating directly from the matrix element and not from a parton shower. Such jets from the matrix element are hard enough to lie well above the matching scale, softer contributions will be populated with the shower approach.

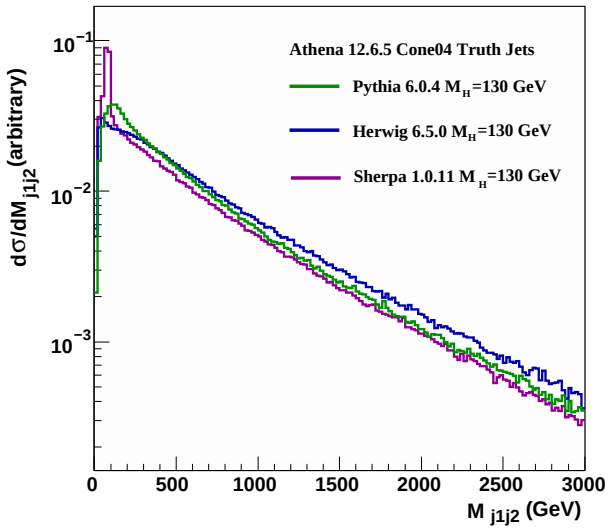

Fig. 4.4: *Comparison of an invisible Higgs signal with mass of 130 GeV generated with Sherpa and in weak boson fusion with Pythia and Herwig. The invariant dijet mass of the leading and subleading jets in the truth collection of events exhibits different behaviour in the range about 100 GeV due to additional diagrams in Sherpa, including WH and ZH production.*

[2)] At least a Pythia option allows the dynamical calculation of decay width in a relativistic Breit-Wigner propagator

4.2.3 Choice of model points in the $M_H - \omega -$ plane

The theoretically detectable rate of invisible decays depends among other things on the branching ratio for the invisible decays. On the one hand the SM width rises steeply for higher Higgs masses. On the other hand, the invisible width as quoted in Chapter 2 depends inversely on the Higgs mass and quadratically on the coupling strength of the Higgs to the hidden scalars. Though rather small and perturbative couplings to the hidden scalar sector may be of particular theoretical interest, their direct observation would be difficult even for relatively light Higgs masses.

There is however always the possibility of an indirect observation. If such invisible decays are present and are competing with the SM decays one would observe in the SM searches a reduction of the visible cross section of Higgs production.

Though the electroweak precision data prefers the existence of a light Higgs boson, these data is not sensitive to the influence of an hypothetical hidden sector (Chapter 2). With no hint for allowed or preferred values of the Higgs mass, we have to extend the study of the stealthy Higgs scenario to higher masses. But in this case, invisible branching becomes competitive to SM branchings only at non perturbative values of the coupling to the hidden scalars.In Fig. 4.5 we show the theory values we expect for the invisible cross section of a stealthy Higgs produced at the LHC at $\sqrt{s} = 14$ TeV in weak boson fusion and Higgs strahlung as function of the coupling ω to the hidden sector. We display examples of four Higgs boson masses, showing that the maximal value for higher Higgs masses is reached only for larger values of the coupling ω. Generally, one also notes that the value of invisible cross section is bounded from above by the corresponding production cross section of the SM Higgs boson (horizontal dashed lines in Fig. 4.5) . Additionally the production cross section falls steeply with higher Higgs masses.

For the choice of the lower mass starting point of the study, it would have been desirable to have sensitivity for Higgs masses about 110 GeV for a continuation in the context of the LEP 2 searches. But without knowing selection efficiencies for such masses beforehand, a suppression of the the large backgrounds displayed in Fig. 4.1will demand a rather hard cut on missing transverse energy. Automatically this reduces the sensitivity for such low Higgs boson masses. The lowest Higgs mass in this study is therefore 130 GeV. The highest pole mass is 800 GeV for which the production cross section is even at centre of mass energy of 14 TeV small.

It is expected that the sensitivity mostly depends on the invisible Higgs cross section. But also there is the possibility that the detection efficiency of the invisible signal is reduced by a widely smeared out invariant mass spectrum.

Thus the covering of a large fraction of the allowed $M_H - \omega -$ parameter space is challenging. Signal events were produced in a mass range between 130 GeV and 800 GeV and the coupling to the hidden scalar sector was varied between $25 \geq \omega \geq 0.1$. For each parameter point marked with a star in Fig. 4.7 25×10^3 events were produced with detailed detector simulation and 2×10^6 with fast detector simulation ATLFAST-1. Instead of presenting a table with all cross sections Fig. 4.6 depicts the cross section over the mass range in dependence of the chosen coupling ω.As before we observe that for each Higgs mass, there is a ω value for that the maximal invisible rate is expected.

The notion of a confined particle resonance is usually limited when its width becomes equal to its mass. Since this may be an interesting scale for the sensitivity some samples where generated with the condition that width is equal to the particle pole mass.

4.2.4 Reweighting with SM production cross section

During we validated the modified Sherpa 1.0.11 version, we confirmed that Sherpa generates the assigned Higgs width for decays of the Higgs boson into neutrinos (which in any experimental aspect are equal to the hidden scalars in the detector). One example of an invariant mass spectrum of the two neutrinos

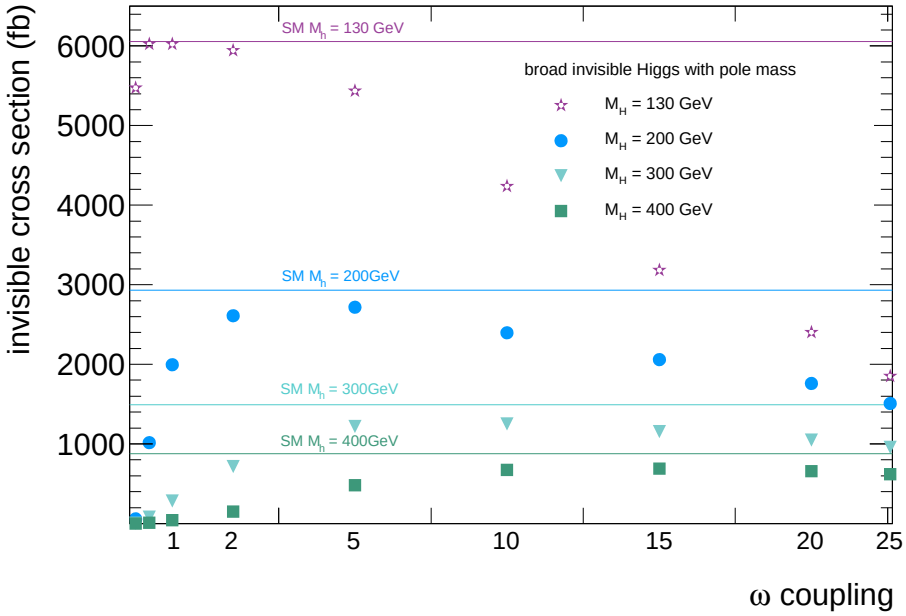

Fig. 4.5: *Dependence of the invisible cross section in the stealthy Higgs scenario from the coupling parameter ω for some Higgs masses. We assume that the Higgs is produced at the LHC at centre of mass energy of $\sqrt{s} = 14$ TeV in weak boson fusion and Higgsstrahlung. For small couplings only a small fraction of the Higgs bosons decays into the invisible channel. For comparison we introduced a horizontal, dashed line of the corresponding visible SM Higgs production cross section for each example mass. The maximum of invisible rate is bounded by the SM cross section and falls again for very high couplings.*

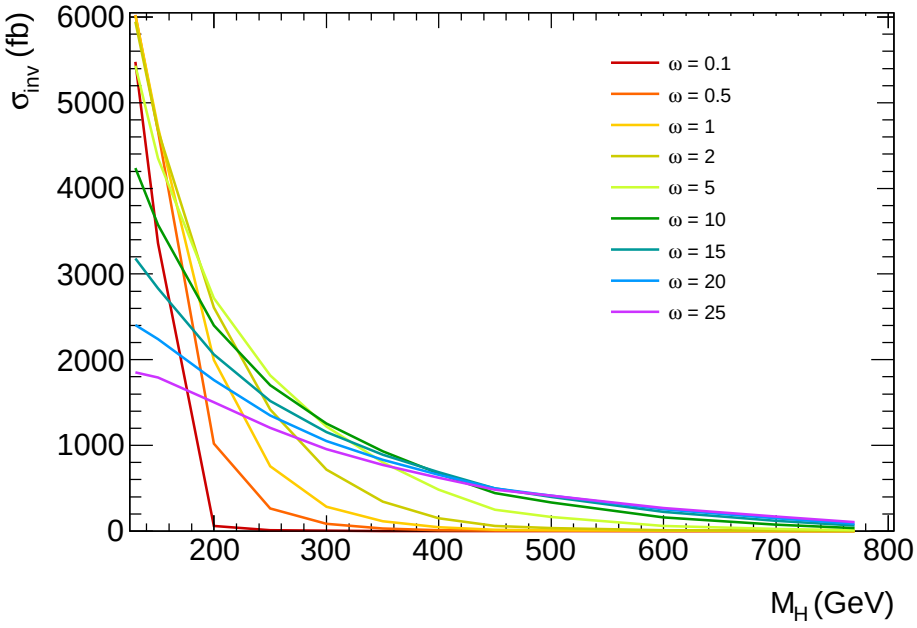

Fig. 4.6: *Dependence of the cross section from the coupling parameter ω and the Higgs mass M_{H}.*

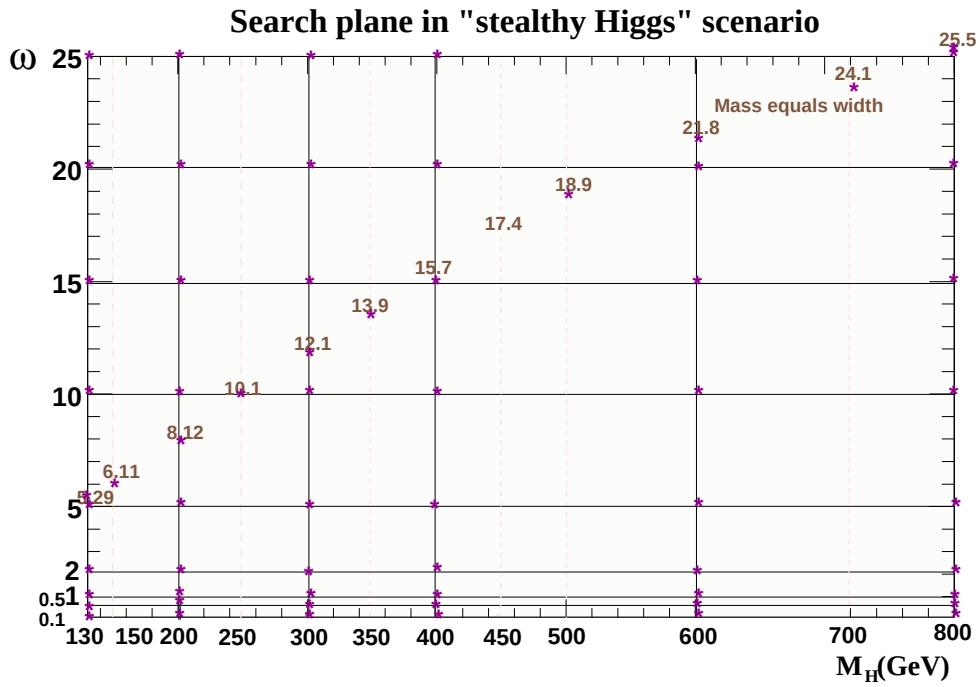

Fig. 4.7: *Schematic overview over the studied parameter plane in stealthy Higgs scenario. The two parameters are the pole Higgs boson mass M_H and the coupling to the hidden scalar sector ω. At crossings of the solid lines signal MC samples were generated. Additionally model points where the nominal Higgs mass equals its width were generated.*

from the hard process as found in the truth collection is displayed as red histogram in Fig. 4.8. One sees an asymmetry in the tails since phase space in a two body decay rises with the invariant mass. But obviously Sherpa does not fold in the SM production cross section of an invisible test mass contributing to the mass spectrum of the broad Higgs, which is included in the blue histogram in Fig. 4.8.

Since the SM cross section enters the total cross section in the stealthy Higgs scenario, as explained in Chapter 2, the SM cross section was multiplied as function of the the invariant Higgs masses, assigning an event weight.

To find the numerical values of the SM cross section for each contributing Higgs mass, fits to SM Higgs production cross sections compiled for the LHC [114] were used. These fits where made to values calculated by the the program FeynHiggs-2.4.1 [96].

It is stated in [114] that for vector boson fusion the Higgs production cross section is known at NLO in QCD. Results have been obtained with MCFM [69]. The PDF used is CTEQ6M and the renormalisation and factorisation scales are set equal to the Higgs-boson mass. The theoretical uncertainty is estimated to be less than 10 %. Detailed information to NLO calculations for this process can be found in [33, 73, 95]. Higgs boson production in association with a weak boson is known at NNLO in QCD and NLO in electroweak calculations. The fit results for associated production have been obtained by the LH2003 Higgs working group [27], by combining NNLO QCD corrections calculated in [39] with the NLO electroweak corrections from [51]. The PDF used is MRST2001 and the renormalisation and factorisation scales are set equal to the Higgs-vector-boson invariant mass. The residual theoretical uncertainty is estimated to be less than 5 %.

In Fig. 4.9 the fitted functions used for calculation of a normalised shape weight as function of the invariant test mass are displayed for weak boson fusion and the two kinds of associated production with weak bosons. The chosen fit functions for the WH(ZH) associated production cross section produce an artifact, i.e. they exhibit an exponential rise if the invariant Higgs mass is larger than 1565 GeV (1870

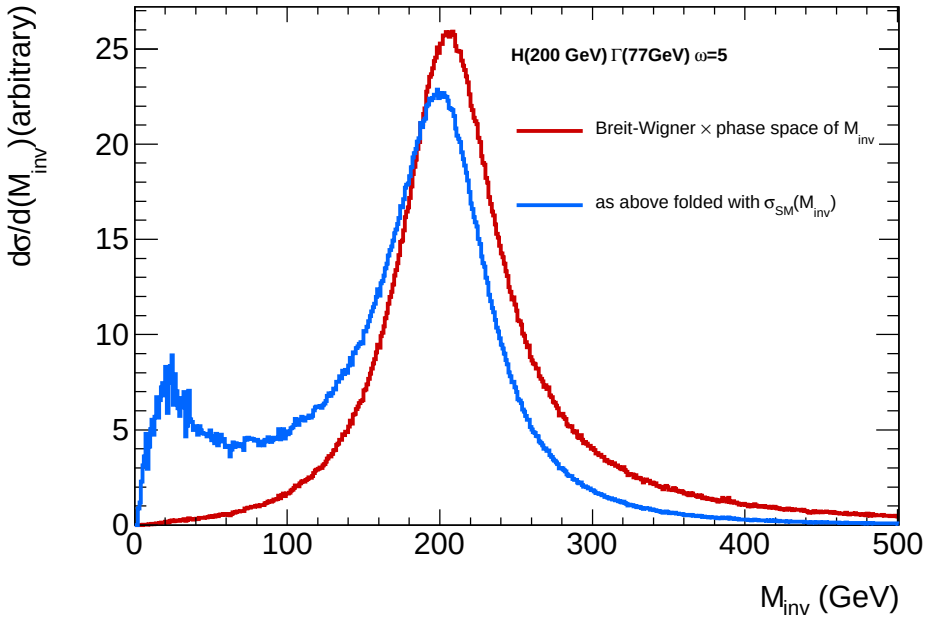

Fig. 4.8: *An example, for a Higgs with mass of 200 GeV and a coupling $\omega = 5$, of the shape reweighting of the Sherpa signal MC samples. The red histogram shows the invariant Higgs mass distribution generated with Sherpa. The asymmetry in the tails stems from the rise of the two body decay phase space. The folding of this generated distribution with the SM production cross section at each invisible mass, shown as blue histogram, shifts the whole spectrum to lower invariant masses, because higher masses are suppressed and the production of lower masses gets a higher weight.*

GeV) and are therefore set to zero for such invariant masses.

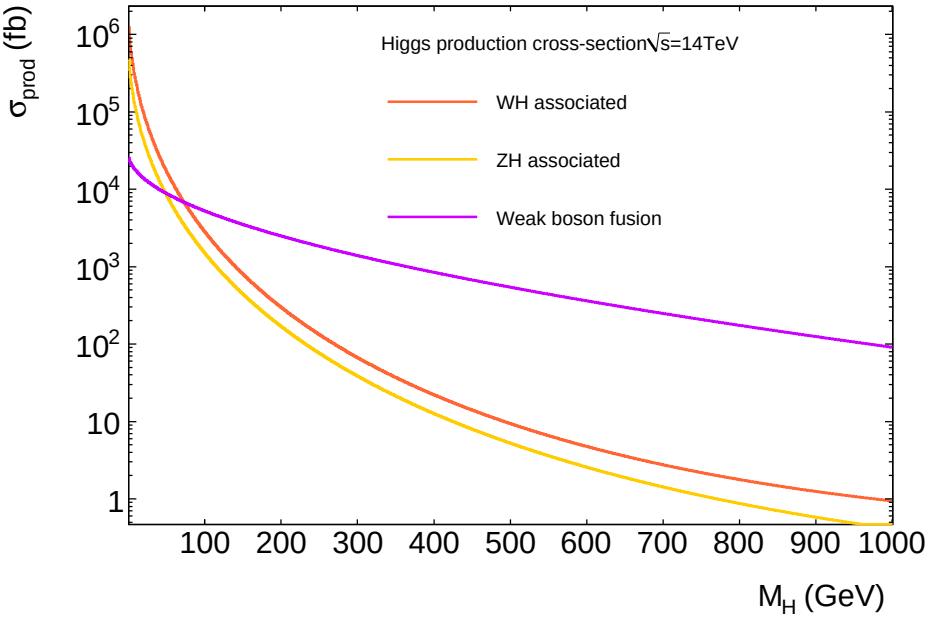

Fig. 4.9: *Fits to the mass dependence of the SM production cross section of the Higgs boson at a LHC centre of mass energy of 14 TeV. The production in association with a top quark pair or by gluon fusion is not depicted and not considered.*

In order to not change the total cross section the weights were normalised such that the sum of all weights corresponds to the number of signal MC events, i.e. only the shape of the invariant mass distribution was changed.

In Fig. 4.8 an example of the original and reweighted invariant neutrino mass spectrum is presented.

After the shape reweighting, the actual shape of the stealthy Higgs invariant mass spectrum is the combination of a Breit-Wigner resonance with a linear rising phase space contribution and the multiplied production cross section for a given invariant mass in the spectrum. Only a few masses are generated with low invariant masses below, the become enhanced with a relatively high production cross section weight contribution, and form the rising structure at the lower end of the mass spectrum in the blue histogram in Fig. 4.8. Since the events there are very sparse statistical fluctuations are more visible than in the rest of the spectrum. Since the reweighting clearly shifts the spectrum to the lower masses, one expects the selection efficiency, e. g. with respect to a cut on the missing transverse energy, of the shape-reweighted samples to be slightly lower.

4.3 Background processes

Any SM process that can produce events with two moderate p_{T} jets and sizable missing transverse $E_{\mathrm{T}}^{\mathrm{miss}}$ can contribute as background process for a weak boson fusion search. In particular due to mismeasurement in the detector and misidentification in the reconstruction, this is also true for events that are not produced in weak processes. In the following the considered backgrounds are described.

4.3.1 W boson plus jets production and W$\rightarrow l\nu$ decay

A dominant background which can fake the signal consists of W boson production in association with jets, where the W boson decays into a lepton. The NLO cross section of this process is of the order 61.5 nb [129] at a centre of mass energy of 14TeV taking into account a branching fraction B(W$\rightarrow l\nu$) $\approx$ 10 %.

The leading-order graphs of the W boson production are displayed in the right column of Fig. 4.10. At event generation it was decided to produce the strong diagram samples separately from the weak graphs samples, even if the electroweak diagrams of the W boson production contribute only on the promille level. This was done firstly for validation purposes and further to have the opportunity to study the behaviour of the much more signal like electroweak component in the various selection steps, since the electroweak part of the W boson cross sections is of the same order as the signal cross section.

Sherpa was used for event generation of both classes of events.

Due to the neutrino in the event coming from the heavy W boson there is a considerable amount of real $E_{\mathrm{T}}^{\mathrm{miss}}$ in the event. Usually the lepton from the W boson is well separated from the surrounding jets and would be reconstructed as an isolated lepton. This distinguishes the W boson plus jets event from the signal where no leptons outside jets are expected. But in case that such a lepton is not separated from the jets in the event or escapes detection in the detector raising the value of $E_{\mathrm{T}}^{\mathrm{miss}}$, this handle for discrimination against signal is lost.

The accompanying jets recoiling against the W boson tend to reach central parts of the detector, eventually in a larger spacing in pseudorapidity between the leading jets. Though their invariant dijet mass tends to be often lower than that of the signal. Additionally from the gluon emission in the t-channel in strong graph, also additional soft jets may populate the central region between the recoiling jets.

4.3.2 Z boson plus jets production and Z$\rightarrow \nu\bar{\nu}$ decay

The irreducible background comprises of Z plus jets events, where the Z boson decays into a neutrino antineutrino pair. The leading order Feynman graphs of Z boson production with additional jets (“ Z plus jets”) is depicted in the left column of Fig. 4.10. The electroweak graph is is indistinguishable to the signal if the decaying Z boson is replaced by a decaying Higgs boson. For Z boson plus jets production at $\sqrt{s} = 14$ TeV the NLO cross section is of the order of 12 nb [129] taking into account a branching B(Z$\rightarrow \nu\nu$) $\approx$ 20 %.

In such events the neutrinos immediately provide a large missing transverse energy, which, due to the boost of the Z boson, is directed centrally into the detector most likely distant to neighbouring jets. The recoiling jet system allocates moderate p_{T} tagging jet candidates. A selection of events sensitive to the signal is expected to select a large fraction of events of the component with electroweak vertices (upper row of Fig.4.10), which has a cross section of the order of the signal cross sections. The strong component with colour exchange (lower row of Fig.4.10) is more likely to be vetoed by the minijet veto. Since the Z boson is close in mass to the W boson the description of the topology and kinematics of the recoiling jet system is very similar to the description in 4.3.1.

As above Sherpa was used for event generation of both classes of events.

4.3.3 Z boson plus jets production and Z$\rightarrow l^{-}l^{+}$ decay

This separable constituent of the SM background is expected to have a NLO cross section of roughly 6 nb [129]. Such events can be confused with the signal in case that at least one of the lepton is not within detector acceptance therefor giving rise to a fake missing transverse energy signature, while e.g. the other light lepton may be mistaken for a jet. Events with decays into tau leptons though can contain real

neutrinos from leptonic tau decays. In addition a hadronical tau decay may end up a wrongly assigned tagging jet candidate. Sherpa produced the events not separating between strong and electroweak graphs.

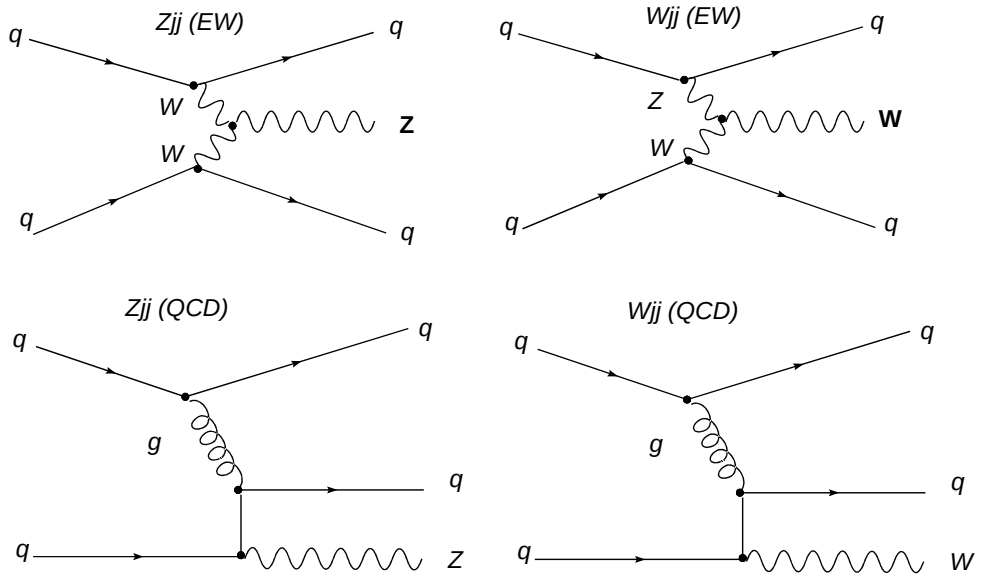

Fig. 4.10: *Leading order graph for the production of Z or W bosons at the LHC. The dominant mode in both cases is the production via strong interaction (lower row).*

Filtering on generator level for weak boson fusion compliant topologies

The W and Z boson plus jets production processes are examples of backgrounds dominantly produced due to strong interaction, that have a large rate at the LHC but only rarely contain a topology that fakes the signal. It would be rather inefficient and a waste of resources to produce the complete samples in detailed detector simulation only to witness that most of the events will not pass the trigger requirements. ATLAS provided therefore a filtering to enrich the samples with events that may pass the weak boson fusion criteria on jets after full reconstruction.

If this filtering is applied, the events have to pass a special selection process that is operated already on generator level of the particles. The final state particles are combined by a simple cone jet algorithm. It is then tested by the filter whether the events contain at least two of such generator level jets within the maximal η acceptance $|\eta| < 5$. One jet with a $p_{\mathrm{T}} > 20$ GeV the other at least a $p_{\mathrm{T}} > 15$ GeV and spacing in $\Delta\eta > 2$ is required. Also it is checked that the event contains a jet pair with an invariant dijet mass above 300 GeV. The efficiency of this generator level jet filtering is given in the fourth column of Tab. 4.1 for the individual W and Z boson plus jet samples samples.

Background normalisation to higher order rates

Higher order corrections are usually positive for the LHC. Hence it is desirable to use at least NLO corrected background rates for consistency if the signal is normalised to NLO. The proportionality factor between NLO and LO cross section is usually called k factor in the literature. For many processes the calculation of k factors are difficult but in case of W boson and Z boson plus jets production at a hadron collider a new cross section integrator FEWZ [119] was used in [129] to get the cross section at NNLO level. For better agreement with the experimental conditions the acceptance range can be specified in FEWZ. With given dependencies on the parton distribution function uncertainties and the remaining QCD scale dependencies the error on the NNLO cross section by FEWZ is estimated to be of the order of

process		generator	LO cross sec.	efficiency	events	
W+jets	$W \to e\nu_e(st)$	Sherpa1.1.1	17900pb	0.055	412k	(2.1×10^6)
	$W \to \mu\nu_\mu(st)$	Sherpa1.1.1	18087pb	0.053	308k	(2.3×10^6)
	$W \to \tau\nu_\tau(st)$	Sherpa1.1.2	18114pb	0.053	318k	(2.2×10^6)
	$W \to e\nu_e(ew)$	Sherpa1.1.1	41.2pb	0.33	55k	(9.4×10^5)
	$W \to \mu\nu_\mu(ew)$	Sherpa1.1.1	41.4pb	0.33	109k	(9.4×10^5)
	$W \to \tau\nu_\tau(ew)$	Sherpa1.1.1	40.6pb	0.31	162k	(9.6×10^5)
Z+jets	$Z\nu\nu(st)$	Sherpa1.0.11	8504pb	0.04	330k	(2.1×10^6)
	$Z \to \nu\nu(ew)$	Sherpa1.0.11	9.6pb	0.3	421k	(7.8×10^5)
	$Z \to ee$	Sherpa1.1.1	1692pb	0.07	53k	(2.9×10^5)
	$Z \to \mu\mu$	Sherpa1.1.1	1691pb	0.04	46k	(3×10^5)
	$Z \to \tau\tau$	Sherpa1.1.1	1689pb	0.055	48k	(3×10^5)
top pairs	$t\bar{t}(l \geq 1)$	MC@NLO3.3	833pb	0.54	419k	(48×10^6)
dijets	p_T/GeV$\in [10,17)$	Pythia6.4	17.6mb	1	560k	(4.8×10^6)
	p_T/GeV$\in [17,35)$	Pythia6.4	1.38mb	1	352k	(4.7×10^6)
	p_T/GeV$\in [35,70)$	Pythia6.4	93.3μb	1	132k	(4.8×10^6)
	p_T/GeV$\in [70,140)$	Pythia6.4	5.88μb	1	320k	(4.8×10^6)
	p_T/GeV$\in [140,280)$	Pythia6.4	0.308μb	1	306k	(4.9×10^6)
	p_T/GeV$\in [280,560)$	Pythia6.4	12.5nb	1	271k	(4.9×10^6)
	p_T/GeV$\in [560,1120)$	Pythia6.4	0.360nb	1	321k	(4.8×10^6)
	p_T/GeV$\in [1120,2240)$	Pythia6.4	5.71pb	1	293k	(4.7×10^6)
	p_T/GeV≥ 2240	Pythia6.4	24fb	1	-	(4.8×10^6)

Tab. 4.1: Summary of used MC samples to model the SM background. The process and the used generator along with the generator LO cross section and filter efficiency of generator or ATLAS weak boson fusion prefiltering and available number of MC events are listed. In case of the dijet production the p_T range of the transferred momentum is denoted in column 2. Numbers in the last column in brackets are the corresponding samples in fast detector simulation used in parts of the later analysis.

10%. According to the recommendation by ATLAS Collaboration [129] the leading order cross section for the W boson plus jets sample is corrected with a k-factor of 1.32 and the Z boson plus jets sample with a k-factor of 1.37 to NNLO.

4.3.4 Top pair production $t\bar{t}$

Top pair events characteristics

The top quark pairs contribute at a centre of mass energy of 14TeV with ($\sigma_{t\bar{t}}$=833 $\pm$ 100) pb [129] to the SM background. A top pair can be produced at the LHC dominantly via gluon fusion Fig. 4.11 a)-c) or about 13% in quark antiquark annihilation Fig 4.11 d). A peculiarity of the top quark system is

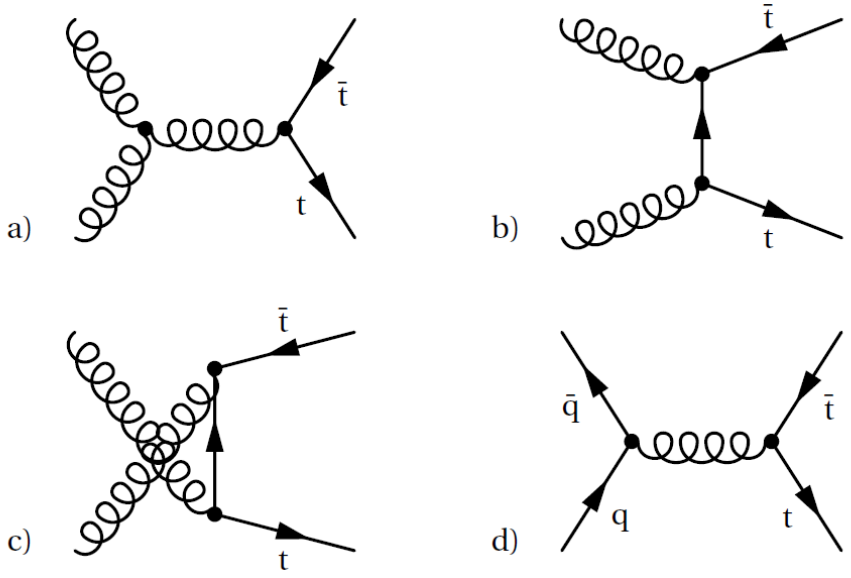

Fig. 4.11: *Leading order diagrams for top quark pair production. At the LHC mostly gluon initiated production a)-c) dominates over quark antiquark annihalition.*

its lifetime of only $10^{-24}s$ which is one order of magnitude too short for the hadronisation into a bound state. Within the SM 99% of the top quark decays are predicted to go into a bottom quark and a W boson. According to the subsequent decay of the W boson one finds three classes namely fully hadronically or semi-leptonically or dileptonically (Fig.4.12).

The used sample is filtered on generator level for the non fully hadronic decays demanding at least a leptonic W boson decay, which are about 54% of all top pair decays, since the lepton can be triggered. The ATLAS filter for weak boson fusion topology was not applied

Events from this background class can fake the signal since they contain real missing transverse energy $E_{\mathrm{T}}^{\mathrm{miss}}$ from neutrinos if one or both W bosons decay leptonically. Then in order to fake the signal the same as described in 4.3.1 applies for the isolated lepton from the W bosons. For dileptonic events this misidentification or escape must occur twice which is not so likely.

The top quark pairs present an event class with rather many jets (up to 6 jets in leading order for the fully hadronic events) in the final state. These events look more spherical in the detector, without exhibiting a specific rapidity gap. At least two of the jets stem from bottom quarks and may have enough p_{T} to be recognised as tagging jets. Experimentally these jets can be identified by b-tagging algorithms. If a B meson decays inside the jets leptonically, the lepton is likely to stay close or in the jets and will not be found as isolated lepton in the reconstruction. Moreover the neutrino can contribute to the $E_{\mathrm{T}}^{\mathrm{miss}}$

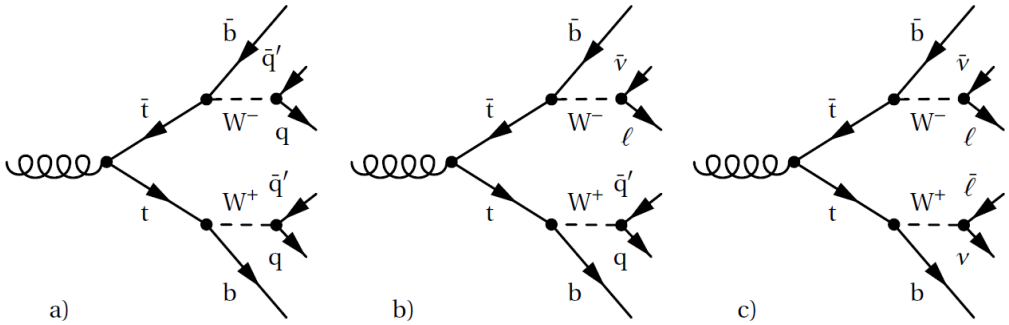

Fig. 4.12: *Top pair decays classified according to the W boson decay. a) fully hadronic b) semi-leptonic c) dileptonic decay topology*

in the event. Also the balance of $E_{\mathrm{T}}^{\mathrm{miss}}$ can be instrumentally enhanced if one the many jets hits a poorly instrumented region.

Generation of top pairs with MC@NLO generator

MC@NLO [74, 75] is a standalone matrix element generator which matches NLO calculations of rates for QCD processes with a parton shower Monte Carlo event generator (HERWIG/JIMMY [55]) for simulating hadronisation and the underlying event. Compared to the Sherpa generator, MC@NLO follows a more ambitious approach. If a $2 \rightarrow n$ process should be modelled, MC@NLO additionally treats the process with one real emission (i.e. $2 \rightarrow n+1$) and all virtual contributions to the $2 \rightarrow n$ process, so it evaluates the matrix element on NLO.

The matching in this case is done in the following way. In the $2 \rightarrow n$ process an analytical calculation can be performed since it is evaluated at an infrared safe scale. Next it is studied how one additional splitting in a shower starting at the n outgoing legs would populate the $2 \rightarrow n+1$ phase space. The trick is that this analytical result contains the same singularities as the $2 \rightarrow n+1$ matrix element. The subtraction of the analytical branching expression from the $2 \rightarrow n+1$ matrix element expression assumes a cancellation of the divergent terms. Hence the physical $2 \rightarrow n+1$ matrix element is found and a finite cross section for $2 \rightarrow n+1$ can be calculated. Since the cross section at leading order for $2 \rightarrow n$ is not suffering any divergences, MC@NLO can start generating events of the $2 \rightarrow n$ and $2 \rightarrow n+1$ topology according to their cross sections and apply the parton shower for each event type to the outgoing legs.

At a given higher scale the parton shower has to be matched with the matrix element. It can occur that the cross section prediction of the shower activity differs from the prediction of the NLO cross sections from the matrix element for this scale. Hence a correction has to be applied so that the overall cross section of the sample is the correct NLO one. This is done in this case ($t\bar{t}$production) by assigning approximately 10 %-15 % of the generated events the negative weight -1 instead of the default weight 1. This weight has to be taken into account when normalising or filling histograms.

The fraction of events with negative weights that have to be introduced to give the right NLO cross section for the sample depends on the generated process. The fraction of negative weights cannot be automatically determined and has to be introduced separately in MC@NLO whenever a new process is generated with MC@NLO or changes in the shower model are made.

In a last step to build a completely generated event, the multiple parton-parton interactions that contribute to the underlying event are produced by the interfaced JIMMY v4.1 generator, which uses angular ordered showering.

4.3.5 QCD dijet background

QCD dijet characteristics

The QCD dijet production at the LHC is a $2 \rightarrow 2$ process, symbolically depicted in Fig. 4.13. This production has a very large cross section in the order of almost 20 mb at the LHC, accounting for almost the complete non diffractive rate. Kinematically most events are easy to separate from the signal process. But rare events can fake the signal topology.

Compared to the signal process the average p_{T} of the two emerging leading jets is lower and the spectrum of jet p_{T} falls steeper. The two jets often enter the detector at central rapidities but the two jets are very often back to back so that the $\Delta\Phi_{\mathrm{jj}}$ distribution peaks sharply at π. In the $\Delta\eta_{\mathrm{jj}}$ only a small fraction of dijet events exceeds a spacing of more than 4 units of pseudorapidity. The angular distribution of the jets is the cause that the invariant dijet mass spectrum $\mathrm{M_{jj}}$ falls faster as for the signal. But the main difference between signal and dijets is the amount of missing energy in the event, which is theoretical very small in a dijet event. The only source of real $E_{\mathrm{T}}^{\mathrm{miss}}$ in this process are leptonic meson decays leading to neutrinos flying in or close to a jet. Events where such a neutrino creates a lot of real missing energy are sparse though. Nevertheless dijet events can show a considerable amount of purely instrumental $E_{\mathrm{T}}^{\mathrm{miss}}$. Sources for this so-called "fake" $E_{\mathrm{T}}^{\mathrm{miss}}$ are first of all incomplete jet measurements for jets that are partly in the beam pipe or hit one of the poorly instrumented regions like the the gap between barrel and endcap and the crack region $1.35 < \eta < 1.57$. Such jets will not be fully contribute to the global p_{T} balance in the event. Also all other kind of mismeasurements, e.g. of jet energy or misidentification may contribute to incorrect evaluation of the missing transverse energy in the event.

Finally since coloured particles scatter in the hard process the dijet system can be surrounded by softer jets emitted likewise in the central region.

Generation with the Pythia event generator

The leading order event generator Pythia 6.4 [143] is used to calculate the hard interaction of a $2 \rightarrow 2$ partonic scattering process. To enhance the yield of interesting events with higher transverse momentum transfer in this scattering the scale of the transverse momentum transfer evaluated in the matrix element is binned for the individual samples. As on can see in the end of Tab. 4.1 that the cross section for the momentum transfer in the hard scattering larger than 1 TeV is still in the order of magnitude of a typical medium mass Higgs signal.No NLO correction factors for the Pythia samples were available and also no filter for weak boson fusion was applied to the samples, that are used in various physics analyses.

Since Pythia 6.3 the old mass ordered parton shower [144] based on simple string fragmentation was replaced by a new shower model [141]. This uses the evolution of interleaved transverse-momentum-ordered showers and sums over all ISR occurring in previous multiple interactions in the showering. The new so-called power shower model leads to a considerably harder p_{T} spectrum in the jets and is believed by the author to give a much more accurate modelling of the underlying physics.

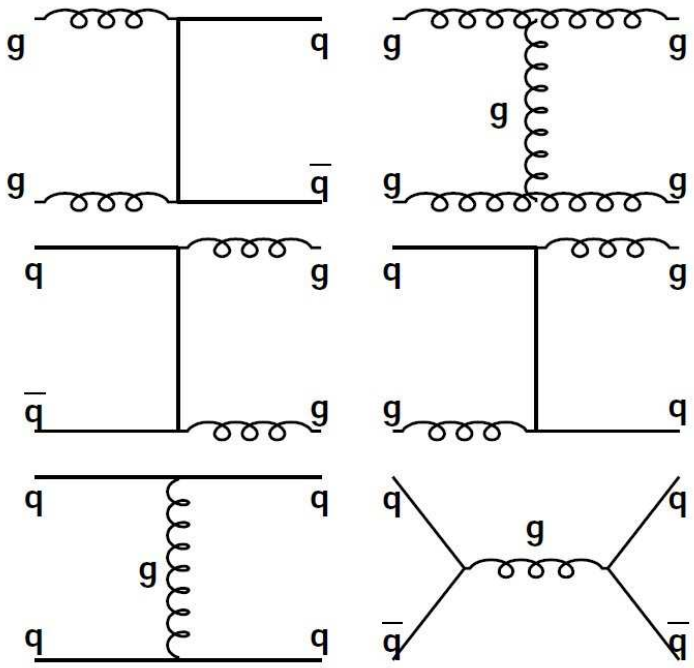

Fig. 4.13: *Examples for the simplest diagrams for the QCD dijet production at the LHC. The gluon induced graphs and gluon- quark scattering are important in leading-order at the LHC. Graphs containing antiquarks $\bar{q}$ become important at scales of low Bjorken-x. For large scales of Bjorken-x the $\bar{q}$ quarks occur in higher order graphs.*

5. Search strategy for invisible Higgs decays with large invisible decay width

In this chapter two alternative event selections are presented. The first one comprises rather loose preselection cuts and a final selection using a multivariate classifier. The second one is a simple cut-based event selection based on formerly published ATLAS sensitivity studies [7] to an invisible Higgs signal. While the first selection is aimed to reach optimal discrimination power between signal and background specifically in the studied model points, the second selection serves mainly as cross check for the results of the multivariate method.

As argued in chapter 2 the weak boson fusion channel promises the highest sensitivity towards invisible Higgs decays over a large mass range. Therefore the preselection of the multivariate analysis and the cut-based selection prepare final states in the weak boson fusion topology. Before describing the cut-based and in particular the multivariate analysis in greater detail, we start though with a brief citation of a dedicated ATLAS study [122] on the important question whether triggering such topologies will be feasible in the ATLAS detector.

5.1 Triggering invisible Higgs decays in weak boson fusion event topology

The trigger is very important as first step in the data acquisition. It determines the kind of physics processes of interest and the rate of such events that are recorded for further data analyses. The choice of a certain trigger menu is guided by the requirements to have a preferably unscaled trigger rate and a high signal acceptance[1)].

In ATLAS the bandwidth of recordable events at level-1 is $\mathcal{O}(100\,Hz)$. The wish to use this bandwidth optimal under varying data taking conditions, e.g. instantaneous luminosity upgrades, drives the studies of trigger menus. Therefore, available trigger menus and corresponding rates are subject to changes with the time. Also it is desirable to have dedicated triggers for a physics process, since building complex triggers from combinations of simple trigger menus will lead to problems in the determination of trigger rate and acceptance if the individual trigger need to run at different prescales. However, since each trigger uses a part of the total bandwidth, the number of dedicated triggers is limited.

Since triggered level-1 objects are defined coarse regions of interest in contrast to higher level triggers objects or offline reconstructed objects which are using the complete event information, one expects that the number of triggered events not necessarily coincides with the number of reconstructed objects. In particular a level-1 region of interest may fail the harder quality criteria of object reconstruction and final object identification algorithms applied by offline analysis. Therefore, it is desirable to have information about the complete trigger history of a physics object in order to apply trigger cuts in event simulation.

Without these dedicated trigger objects an offline estimation of events will be difficult. This is because an offline analysis selects a number of physic objects, reconstructed by offline algorithms using

[1)] We define (see [122]) acceptance as $A = n_{Level-1+Offline}/n_{Offline}$ where $n_{Level-1+Offline}$ is the number of events that have passed both the level-1 trigger threshold and the offline selection cuts. While $n_{Offline}$ is the total number of events that passed the offline selection cuts without applying the level-1 trigger thresholds. Here the offline selection are the analysis cuts usually performed on the data recorded by the data acquisition. It is assumed that these cuts are not modifying the acceptance, since they select a sub-sample of the triggered events.

not the triggered objects as seeds to their algorithms. One can ask which fraction of these reconstructed events would additionally have passed the demanded trigger. These numbers must not necessarily coincide since the individual trigger efficiency is described by a turn on curve and the resolution of measured quantities, e.g. jet energies or $E_{\mathrm{T}}^{\mathrm{miss}}$, may be different. By evaluating the trigger information of a selected event one can correct the yield of selected events with the trigger efficiencies. Only the introduction of object trigger information, i. e. each reconstructed object contains information of the related trigger objects, from Athena release 14 onwards provided a convenient way to introduce the trigger to the selection. Unfortunately the used detailed detector simulation of Athena release 12 does not devise means for dedicated trigger studies. Trigger simulation based on trigger event information was first introduced in Athena release 13.

ATLAS detailed trigger study for an invisible Higgs in weak boson fusion topology with Athena release 12

Detailed studies for the rate of an invisible Higgs level-1 trigger by ATLAS [122] using a special level-1 trigger simulation together with Athena release 12 had been undertaken previously. In the following the recommendations from this study [122] are summarised.

First of all the study [122] described some fundamental properties of the events in weak boson fusion, that are important for the trigger strategy:

1) Objects for triggering
   The main features that can be exploited to trigger on invisible Higgs decays in weak boson fusion topology is to search for two tagging jet candidates in opposite hemispheres of the detector and a sizable amount of missing transverse energy. But such events will also occur in a strongly interacting collider environment for some fraction of very abundant dijets events.

2) Pseudorapidity distribution of tagging jet candidates
   In spite of the common notion the tagging jet candidates do not need to be both in extreme forward direction in case the transverse momentum transfer is asymmetric. Indeed when defining the forward region as $4.9 > |\eta| > 3.2$ and a central region as $|\eta| < 3.2$ the study [122] found that after applying the cut to define the weak boson topology, almost three quarters of the two tagging jets represented a mix, i.e. one forward jet (FJ) combined with one central jet (CJ).

3) Underestimation of the level-1 $E_{\mathrm{T}}^{\mathrm{miss}}$ with respect to offline $E_{\mathrm{T}}^{\mathrm{miss}}$
   Since the level-1 trigger operates at the electromagnetic scale for energy depositions in the calorimeter and not with any hadronic energy calibration of the calorimeter cells and in addition applies a 1 GeV cut to cells of the trigger towers, the jet transverse energy as well as the missing transverse energy tend to be underestimated with respect to corresponding offline quantities.

4) Already implemented trigger items usable for invisible Higgs
   At the time of the study [122] ATLAS utilised at level-1 only one trigger menu usable in invisible Higgs context. This menu, introduced for SUSY searches, demanded one jet with transverse energy above 50 GeV in the central region and a $E_{\mathrm{T}}^{\mathrm{miss}} > 60$ GeV, which yields at a dijet rate of 18 kHz providing a 68% signal acceptance.

Starting from the observed tagging jet topology the study investigated combined triggers more suitable for this topology. Also it was studied whether combined or a topological trigger conditions, i.e. two jets in opposite hemispheres or redefinition of the boundary between forward and central jets can lead to an improved acceptance and background rate reduction.

In particular the study [122] evaluated amongst some others the following interesting level-1 trigger conditions summarised in Tab. 5.1 for an invisible decay of the Higgs produced in weak boson fusion,

using 95%, 80% and 60% signal acceptance as working points. The assumed peak luminosity has been $2 \times 10^{33} cm^{-2} s^{-1}$ and no pile up added.

	level-1 condition	E_T(GeV)	E_T^{miss}(GeV)	A(%)	R_{dijets} (Hz)
1)	any 2 jets within $\|\eta\| < 4.9$	20	60	95	18
1a)	any 2 jets within $\|\eta\| < 4.9$	20	80	95	2
2)	1 forward jet within $3.2 < \|\eta\| < 4.9$	20	60	80	19
3)	1 forward $\oplus$ 1 central jet	20	50	60	0.3
4)	1) $\oplus$ opp. hemisph. $\eta_{jet1} \times \eta_{jet2} < 0$	20	60	95	10.8
5)	2 opp. hemisph. jets in $1.6 < \|\eta_{Ji}\| < 4.9$	20	60	95	3

Tab. 5.1: Results of cited Atlas study [122]. Signal acceptance A and the most important dijet rate R_{dijets} for exemplary suggested level-1 trigger conditions.

The results and conclusions of the study important in our context were:

1) Control over impact of pile up on the trigger
   Though high luminosity pile up was not added and theoretical uncertainties on the dijet rate may be large, the result presented in [122] is quite promising because it shows that all discussed menus could be operated at a suitable rate below 20 Hz. If pile up leads to higher rates, there is much bandwidth left to cope with the increase.

2) Preferred low trigger thresholds of the jet triggers
   Generally it was found that the background rate does not depend much on the trigger thresholds of the jet triggers. Therefore the jet trigger threshold should kept as low as possible to avoid acceptance losses, since it falls steeply with higher jet thresholds. The reduction of the dijet rate is any time possible by only slightly hardening the level-1 trigger cut on the uncalibrated missing energy.

3) Favoured trigger strategy for low luminosity
   For the early low luminosity scenario at ATLAS a trigger solution like 2) in Tab. 5.1 may be sufficient. Trigger conditions as 3) in Tab. 5.1 generally are limited in their acceptance to roughly 75 %, and may be therefore disfavoured. But they also pick up the lowest background rate without additional conditions. This reduction may be even sufficient to run this trigger at higher luminosities.

4) Favoured trigger strategy for high luminosity
   It was concluded in [122] that the more complicated topological triggers using a new defined boundary are a promising alternative to reduce the dijet rate to the desired level without compromising the signal acceptance. Especially the choice 5) in Tab. 5.1 provides excellent high acceptance and the lowest background rate. But due to their relatively high complexity these options may be used only under high luminosity conditions, to provide still manageable trigger rates.

5.2 Preselection of events for the multivariate analysis

After this summary about trigger prospects for the studied channel, we start now to describe the event preselection, which has to consider the possibility of triggering the events, too.

Offline trigger estimation

The shortcomings in Athena release 12 in online trigger simulation leads to a poor mans estimation of trigger efficiencies by making cuts on offline reconstructed objects, intending to select a very similar phase space to the one prepared by analogous trigger conditions.

Aware about the complications introduced by combinations of triggers it was decided to model the offline cuts for a combined trigger of the type L1_XE80 $\oplus$ L1_J23 $\oplus$ L1_FJ23. In this shorthand notation for level-1 trigger items XE stands for a $E_{\mathrm{T}}^{\mathrm{miss}}$ trigger, J for a central jet trigger, FJ for a forward jet trig ger. The numbers behind that letters denote the threshold value in GeV where the turn-on curve reaches 90 % efficiency.

Though this trigger topology is expected not to provide the highest acceptance it corresponds to trigger items that were under discussion in Athena release 12 and 13 at that time. Also it is expected to have a very low rate for dijet events without making use of special topological conditions. If the analysis is feasible with such a menu, there will be much bandwidth spared as "safety factor" in case it should turn out that pile up effects and theoretical uncertainties on dijets production lead to an underestimated dijet event rate.

The uncalibrated level-1 trigger thresholds of the chosen combined trigger would lie well below the following offline selection cuts, that would not be influenced by the turn on behaviour of the trigger. For these reasons the trigger cuts are simulated offline by the condition

(P1) one reconstructed jet (p_{T}>23GeV) within $|\eta| < 3.2$ and one reconstructed jet (p_{T}>23GeV) within $4.9 > |\eta| > 3.2$ and $E_{\mathrm{T}}^{\mathrm{miss}} > 80$ GeV in the event.

Preselection cuts

The following cuts will enrich the samples with signal-like weak boson fusion topology and events with a high fraction of missing transverse energy. Since eventually a multivariate analysis is made on these samples, cuts on variables that maybe used also in the multivariate analysis are kept rather loose. The sequence of preselection cuts is as follows.

Finding the tagging jet candidates is the first step to prepare the weak boson fusion topology. The leading jet with $p_{\mathrm{jet}1}^{\mathrm{T}}$ and the subleading jet with $p_{\mathrm{jet}2}^{\mathrm{T}}$ in the event are considered as tagging jet candidates. The average signal $p_{\mathrm{jet}}^{\mathrm{T}}$ is larger as for typical dijets. Thus, we require

(P2) $p_{\mathrm{jet}1}^{\mathrm{T}} > 40$ GeV.

(P3) $p_{\mathrm{jet}2}^{\mathrm{T}} > 35$ GeV.

Both jet p^{T} cuts are hard enough to assure that the plateau of the reconstruction efficiency for the jets is reached. These cuts are followed by three more topological cuts (P4-P6) that accumulate the weak boson fusion topology.

(P4) $\eta_{\mathrm{j}1} \times \eta_{\mathrm{j}2} < 0$, with $\eta_{\mathrm{j}1}$ and $\eta_{\mathrm{j}2}$ are the pseudorapidity of the leading and subleading jet respectively, demands the two tagging jet candidates to be in opposite hemispheres of the ATLAS detector.

(P5) $\Delta\eta_{\mathrm{j}1\mathrm{j}2} > 4.2$ is the requirement of a large rapidity gap between the leading and subleading jet, as it is typically found for weak boson fusion processes

(P6) $M_{\mathrm{j}1\mathrm{j}2} > 600$ GeV, with $M_{\mathrm{j}1\mathrm{j}2}$ being the invariant mass of the leading and subleading jet, which especially is expected to be larger in weak boson fusion as for QCD dijet production.

(P7) vetoing of central mini jets. Events are rejected if an additional jet with $p_{\mathrm{jet}}^{\mathrm{T}} > 20$ GeV if found in a range of $|\eta| < 3.2$. The abundance of mini jets is expected to be higher in the background

processes, hence events with mini jets are vetoed. The veto used is found to be a simple and robust criterion for the veto of mini jets, if different underlying event models and event generators are compared as done in App. A.

(P8) $E_{\mathrm{T}}^{\mathrm{miss}} > 110$ GeV. This very hard cut selects events that appear to have a large $E_{\mathrm{T}}^{\mathrm{miss}}$, as expected from the signal. This cut is passed only by a small fraction of dijet events with large fake transverse missing energy.

(P9) vetoing identified isolated leptons. Events are rejected if an electron or muon with $p_{\mathrm{T}} > 20$ GeV or a tau lepton with $p_{\mathrm{T}} > 30$ GeV is identified by the standard reconstruction algorithms in the event. The veto is only applied if the identified lepton is isolated to the next jet. The lepton is checked for having at least a $\Delta R_{\mathrm{nextjet}} > 0.2$ to the nearest jet, to be called isolated. Especially semileptonic decays of the W boson plus jets background is expected to be reduced by this veto.

Shape of the distributions of the variables in the preselection for an example hypothesis and backgrounds

In order to motivate the sequence of preselection cuts we show in Fig. 5.1 the shape of the preselection's kinematic cuts variables for an example hypothesis, which corresponds to a signal with $M_{\mathrm{H}} = 200$ GeV and a coupling $\omega = 5$, and backgrounds. The distribution of a variable is displayed with the previous cuts of the sequence applied. We display the signal and the W and Z boson backgrounds in detailed detector simulation. For backgrounds, for which only sparse events are available and cut factorisation is applied (see Sec. 5.2.1) like QCD dijets, we show the distributions of the larger fast detector simulation samples. Since we want to display the background shape differences, the distributions are normalised to unit area. One observes that the dijet samples exhibits an extremely hard p_{T} spectrum for the leading jet, peaking around 180 GeV. The hard spectrum is the result of the preceding hard $E_{\mathrm{T}}^{\mathrm{miss}}$ cut in the offline trigger simulation. The QCD dijet sample contains no real $E_{\mathrm{T}}^{\mathrm{miss}}$, but in the fast detector simulation the resolution of $E_{\mathrm{T}}^{\mathrm{miss}}$ is smeared. In QCD dijet events that are in tail of a large $E_{\mathrm{T}}^{\mathrm{miss}}$ the momentum of the jet counterbalancing the $E_{\mathrm{T}}^{\mathrm{miss}}$ has to be in average very hard too. Thus the $E_{\mathrm{T}}^{\mathrm{miss}}$ condition in the trigger simulation selects preferably the tiny fraction of dijets events with much p_{T} for one jet and much $E_{\mathrm{T}}^{\mathrm{miss}}$. In the unit normed plotting the distributions one zooms therefore into the hard p_{T} tail of the QCD dijets. As Tab. 4.1 shows that dijets are generated in Pythia 6.4 with cuts on the hard scattered parton momentum p_{T}^{parton}. We especially produced for these plots ten times more dijets with a cut on the hard parton emission in the interval of $p_{\mathrm{T}}^{parton} = 140$ GeV to $p_{\mathrm{T}}^{parton} = 280$ GeV as in the other p_{T}-bins. Therefore, we retain relatively many entries in the plots after offline trigger, exhibiting the properties of a hard jet p_{T}-spectrum. The signal and other backgrounds contain real $E_{\mathrm{T}}^{\mathrm{miss}}$ and can pass the $E_{\mathrm{T}}^{\mathrm{miss}}$ precut in the offline trigger easily. In such events the p_{T} of the jets can be as low as p_{T}-threshold the offline trigger required.

5.2.1 Factorisation approach for the dijet background in the preselection

The kinematics of the dijet background is sufficiently different from the signal that it can be well separated by the preselection cuts. But this background has a far too large cross section to have a sufficient amount of MC events available to describe the rare events in the tails of the distributions that possibly can pass the preselection cuts. So the situation can occur that all MC events are rejected by the preselection or only a handful survives. Since the weights of such events can be very large, the error on the few expected events or the expected "zero" events are very large, too.

If one intends to estimate the expected number of events after preselection, a factorisation of the selection cuts can be tried. If all cuts are completely independent from each other or uncorrelated the efficiency $\varepsilon_{\text{after n}^{\text{th}}\text{ cut}} = \prod_{i=1\ldots n} \varepsilon_i$ factorises into the efficiencies $\varepsilon_i = N_i^{\mathrm{sel}}/N^{\mathrm{all}}$ that has the i-th cut on

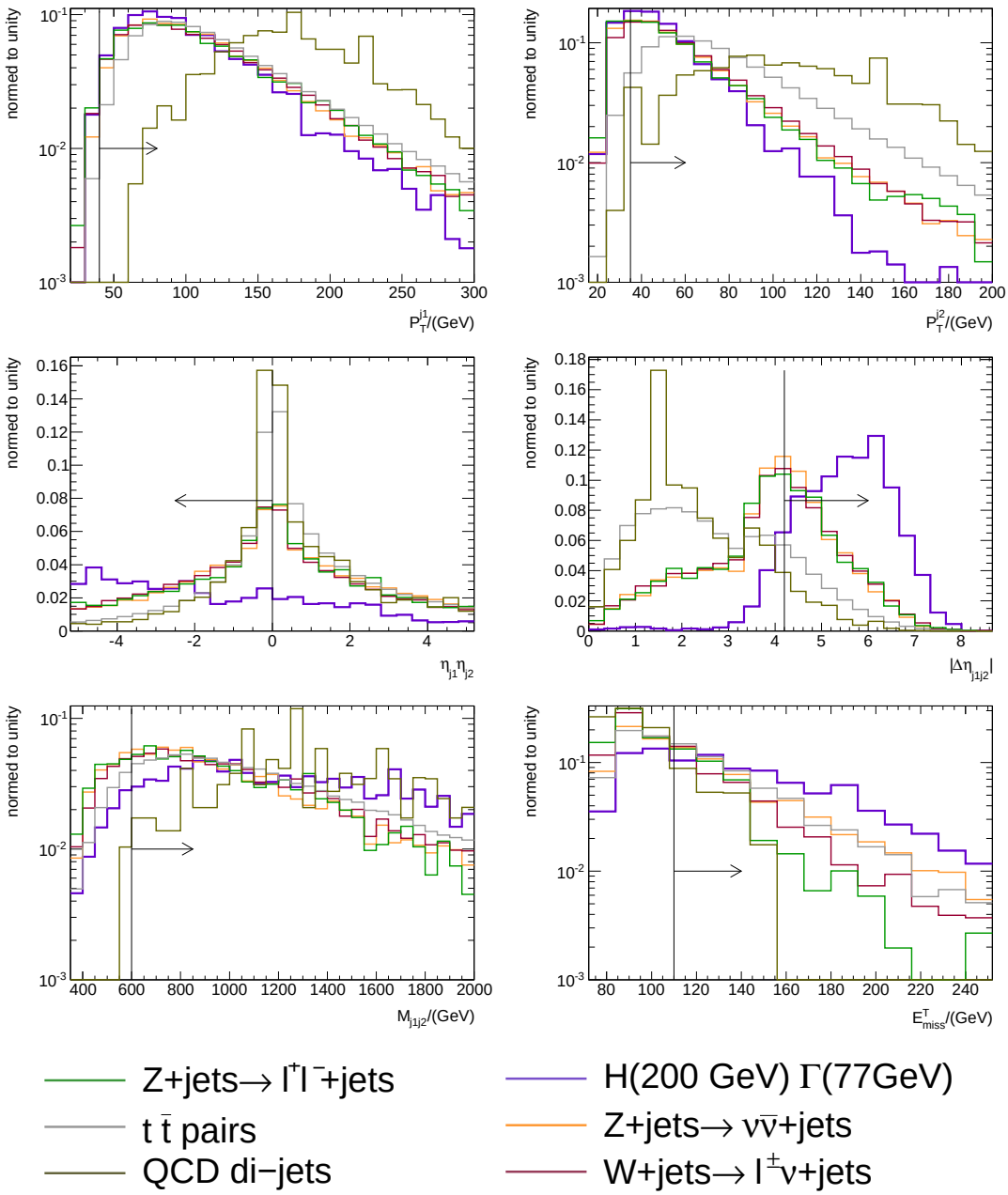

Fig. 5.1: *Distribution of the preselection's kinematic variables for signal and backgrounds. Plotted is a signal, $M_H = 200$ GeV and a coupling $\omega = 5$, and W and Z boson backgrounds (using detailed simulated samples) along with QCD dijets, $t\bar{t}$ and $Z \to \ell^+\ell^-$ plus jets backgrounds (using fast detector simulation because of the MC statistics). The distributions are scaled to unity for easier shape comparison.*

the whole sample N^{all}. This situation will rather rarely occur in reality since most of the times cuts are correlated to some degree, which means $\varepsilon_{\text{after n}^{\text{th}}\text{ cut}} \neq \prod_{i=1\ldots n} \varepsilon_i$. Therefore, if correlated cuts are factorised, the background rejection will be wrongly estimated. In such case one has to investigate the correlations between the variables and group highly correlated cuts in blocks of cuts. These single blocks are than assumed to be independent from each other and the total cut efficiency can be calculated as $\varepsilon_{\text{after n.}^{\text{th}}\text{ cut}} = \prod_{j=1\ldots n'_{\text{block}}} \varepsilon_j$ from the selection efficiencies of the single block j given by $\varepsilon_j = N_j^{\text{block sel}}/N^{\text{all}}$.

In the following we describe the blocks used to estimate the dijets background via factorisation. The grouping of cuts is summarised in Tab. 5.2. The factorisation of the mini jet veto and the isolated lepton veto are possible, because the additional jet activity and the occurrence of isolated leptons can be assumed at lowest order to be independent from the tagging jets kinematics. Thus they are grouped in individual blocks, namely block 3 and block 5. Also the cuts on the tagging jets were grouped as in the preselection factorisation, forming block 2. These describe the topology of the jets hence should be performed on the sub-sample that contains at least a central and a forward jet, which we require like in the offline trigger but without cut on $E_{\text{T}}^{\text{miss}}$ (see block 2 in Tab. 5.2). Loosening the $E_{\text{T}}^{\text{miss}}$ cut provided more dijets for the evaluation of the efficiencies of the dijets after these grouped cuts. The jet p_{T} of the dijets is found to be well enough uncorrelated to factorise the $E_{\text{T}}^{\text{miss}}$ cut in the preselection (see block 4 in Tab. 5.2). If some conditions in a group of cuts like the requirement of a central and forward jet in block 2 and 3 overlap with a preceding conditions like the offline trigger in block 1, this is of course taken into account and corrected for in the factorised numbers in the succeeding cut. We also define via block 6 a sub-sample which enhances the weak boson fusion topology and applies two very soft cuts on $E_{\text{T}}^{\text{miss}} > 20$ GeV and $E_{\text{T}}^{\text{miss}} > 50$ GeV. This sub-sample is not used in the factorisation of the dijets in the preselection but on this sample later in Section 5.3.5, the efficiency of dijets in the multivariate analysis is estimated.

	combined cuts
Block 1	CJ$\oplus$FJ$\oplus E_{\text{T}}^{\text{miss}} > 80$ GeV (P1)
Block 2	CJ$\oplus$FJ$\oplus E_{\text{T}}^{\text{miss}} > 0$ GeV weak boson fusion topology (P2-5) $M_{\text{j1j2}} > 600$ GeV (P6)
Block 3	CJ$\oplus$FJ$\oplus E_{\text{T}}^{\text{miss}} > 0$ GeV mini jet veto
Block 4	$E_{\text{T}}^{\text{miss}} > 80$ GeV $\rightarrow E_{\text{T}}^{\text{miss}} > 110$ GeV
Block 5	isolated lepton veto
Block 6	block 2 $\oplus E_{\text{T}}^{\text{miss}} > 20$ GeV $\oplus E_{\text{T}}^{\text{miss}} > 50$ GeV

Tab. 5.2: Combination of cuts used in the factorisation for the QCD dijet samples in the preselection (Block 1 -5) and later (Sec. 5.3.5) in the multivariate selection (Block 6).

Cutflow table for example signal hypothesis $M_{\mathrm{H}} = 200$ GeV and $\omega = 5$,

In Tab. 5.3, we summarise the effect of the preselection cuts (P1) to (P9) on a typically signal with $M_{\mathrm{H}} = 200$ GeV and $\omega = 5$ (second column) and the various background: $W \to l\nu$ plus jets (third column), $Z \to \nu\nu$ plus jets (forth column), $Z \to \ell^+\ell^-$ plus jets (fifth column), $t\bar{t}$(sixth column) and QCD dijets (last column). For the latter two backgrounds we quote the factorised cutflow estimate. The factorisation estimates that the QCD dijets background is dominantyy after preselection cuts, this is the consequence of the relative loose preselection cuts, e.g in M_{j1j2}.

cut	Signal	W$l\nu$+jets	Z$\nu\nu$+jets	Z$\ell^+\ell^-$+jets	top pairs	QCD dijets
(P0) before preselection	81505	116729216	12699703	11465219	13844500	5.385×10^{14}
(P1) trigger	11508	3280105	720660	75800	656559	10574800
(P2) jet 1 $p_{\mathrm{T}} > 40$ GeV	11302	3216367	711500	74544		
(P3) jet 2 $p_{\mathrm{T}} > 35$ GeV	8774	2666320	572507	60646		
(P4) $\eta_{\mathrm{j1}} \times \eta_{\mathrm{j2}} < 0$	6872	1340955	274124	30011		
(P5) $\Delta\eta_{\mathrm{j1j2}} > 4.2$	6090	597966	122115	15264		
(P6) $M_{\mathrm{j1j2}} > 600$ GeV	5728	511821	102254	12836	41396	911712
(P7) vetoing of central jets	4267	184644	47201	5346	2989	380419
(P8) $E_{\mathrm{T}}^{\mathrm{miss}} > 110$ GeV	3003	73389	24337	1625	1425	128990
(P9) isolated leptons veto	2982	55350	23863	856	578	126014

Tab. 5.3: Cutflow of the preselection in number of expected events in 30 fb^{-1}. The signal sample shown is a Higgs boson with $M_{\mathrm{H}} = 200$ GeV and $\omega = 5$.

5.2.2 Signal efficiencies in the preselection

As mentioned in Sec. 4.2.4 we introduced shape weights for the events of each signal hypothesis. The signal efficiencies are the fraction of selected shape weights to the total sum of shape weights. Unfortunately the efficiencies are overall quite low, indicating the presence of a difficult jetty environment in which isolating the signal due to tagging jets is challenging. Generally these signal efficiencies for the preselection were found to be in the range between 2.5 % to about 6.6 %. Especially the higher efficiencies are observed for signal hypotheses with heavier or broad Higgs bosons. This may be due to the tails to higher $E_{\mathrm{T}}^{\mathrm{miss}}$ in such events. The presented signal $M_{\mathrm{H}} = 200$ GeV and $\omega = 5$ has a preselection efficiency of about 3.7 %.

5.2.3 Influence of various MC event generator models on the signal's preselection efficiency

If a selection uses as discrimination criteria the properties of additional jets other than the tagging jets, these are very likely to depend on to the specifically used modelling of MC generator and and the tuning parameter that govern the additional jet activity. Since we had detailed simulated samples of signal events available produced with different MC generators and various tunes, we can compare these various signals in the preselection for the multivariate analysis, to get a feeling for the possible impact of such model differences in the analysis. Though especially a comparison of underlying event properties and generator tune for the background would be of interest, the huge background samples were unfortunately not available produced by various generators. In the following Tab. 5.4 we compared a signal of a Higgs boson with a mass of 130 GeV. These samples are generated with the corresponding SM width of some MeV and the decay is completely into invisibly particles. The assumed LO cross section is about 3.9 pb

according to the SM weak boson fusion process at a centre of mass energy of 14 TeV. All signal events are normalised to the same cross section and sample size and the quoted errors stem from the MC statistical uncertainty. In brackets the relative efficiency in percent is given. The second column displays the result for a Sherpa sample without underlying event switched on. In the third column the expected events for the Sherpa 1.0.11 generator in the underlying event event tune used by this analysis are given. The fourth column is the result with Herwig 6.5 and the two last columns show the selection for Pythia 6.4 MC events with old and new parton shower respectively. Especially the theoretical modelling between Pythia old and new parton shower is very different. Details about the generators and the used models and parameters can be found in Chapter 4 for Sherpa and Pythia and in Appendix A for all Sherpa tunes and also all used generators. At this point we want show only the relevant difference in the preselection.

cut	**MC-generator comparison**				
	Sherpa		**Herwig**	**Pythia**	
	no UE	UE tune		old PS	new PS
(P0) before cuts	47k $\pm$ 217(100%)	47k $\pm$ 217(100%)	47k $\pm$ 217(100%)	47k $\pm$ 217(100%)	47k $\pm$ 217(100%)
(P1) trigger	6143 $\pm$ 78(13%)	6190 $\pm$ 79(13%)	6941 $\pm$ 83(15%)	7376 $\pm$ 86(16%)	6206 $\pm$ 79(13%)
(P2) jet 1 $p_{\mathrm{T}} > 40$ GeV	6046 $\pm$ 78(98%)	6092 $\pm$ 78(98%)	6907 $\pm$ 83(99%)	7325 $\pm$ 86(99%)	6142 $\pm$ 78(99%)
(P3) jet 2 $p_{\mathrm{T}} > 35$ GeV	4637 $\pm$ 68(77%)	4764 $\pm$ 69(78%)	5405 $\pm$ 74(78%)	6045 $\pm$ 78(83%)	4691 $\pm$ 68(76%)
(P4) $\eta_{\mathrm{j1}} \times \eta_{\mathrm{j2}} < 0$	3368 $\pm$ 58(73%)	3441 $\pm$ 59(72%)	4383 $\pm$ 66(81%)	4605 $\pm$ 68(76%)	3688 $\pm$ 61(79%)
(P5) $\Delta\eta_{\mathrm{j1j2}} > 4.2$	2895 $\pm$ 54(86%)	2930 $\pm$ 54(85%)	3827 $\pm$ 62(87%)	3798 $\pm$ 62(82%)	3229 $\pm$ 57(88%)
(P6) $M_{\mathrm{j1j2}} > 600$ GeV	2674 $\pm$ 52(92%)	2748 $\pm$ 52(94%)	3609 $\pm$ 60(94%)	3594 $\pm$ 60(95%)	2999 $\pm$ 55(93%)
(P7) vetoing of central jets	2081 $\pm$ 46(78%)	2056 $\pm$ 45(75%)	3111 $\pm$ 56(86%)	2257 $\pm$ 48(63%)	2538 $\pm$ 50(85%)
(P8) $E_{\mathrm{T}}^{\mathrm{miss}} > 110$ GeV	1438 $\pm$ 38(69%)	1379 $\pm$ 37(67%)	2100 $\pm$ 46(68%)	1512 $\pm$ 39(67%)	1774 $\pm$ 42(70%)
(P9) isolated leptons veto	1428 $\pm$ 38(99%)	1371 $\pm$ 37(99%)	2077 $\pm$ 46(99%)	1498 $\pm$ 39(99%)	1764 $\pm$ 42(99%)

Tab. 5.4: Comparison of signal generated with different underlying event tunes and MC generators in the cut flow for the preselection in number of expected events in 30 fb^{-1}. The expected statistical error of the events is given by the numbers in small print following the $\pm$ and the number in brackets is the relative cut efficiency in %. The signal samples simulate a Higgs boson with $M_{\mathrm{H}} = 130$ GeV and invisible width of 5 MeV produced in weak boson fusion at $\sqrt{s} = 14$ TeV, corresponding to a cross section of 3.9 pb. In the second column the expected events for the Sherpa 1.0.11 generator with the underlying event switched off are given. The third column displays the result for the Sherpa UE event tune used by this analysis. The fourth column is the result with Herwig 6.5 and the two last columns show the selection for Pythia 6.4 MC events with old and new parton shower respectively.

If one compares in Tab. 5.4 the relative efficiencies in the preselection between the different tunes and generators one sees that the jets activity is indeed modelled different in the generators. One observes the largest relative difference in (P7), the central jet veto. The second largest relative difference is affecting the cut on the offline trigger topology. The cut (P4) on the product of the tag jets candidates shows the third largest relative difference between the samples.

It is characteristic for the signal that in the rapidity region between the tagging jet candidates very few hadronic activity is expected due to the lack of colour flow. In case of the signal process only relatively rarely occurring hadronic radiation under large angle to the tagging jets is possibly populating this region. Therefore, most of the hadronic activity between the is accounted for due to the UE. We conclude that the relative large difference in central jet veto efficiency (P7) is depending mostly on the UE model and tuning details. As seen in (P7), the predicted relative efficiency of the veto is varying largely between the generators and their underlying event model used. While Herwig and Pythia tend to occupy the extremes, the Sherpa tune used in this analysis has an efficiency for the jet veto roughly in

the middle of the two former generators.

We studied the difference in more detail in Appendix A, where we also tried several central jet veto strategies with these different signal samples and pursued to identify a central jet veto that minimises the efficiency differences for the signal. But it has to be mentioned, that the selection in Appendix A did not include the offline trigger cut, which has non negligible influence on the selection as seen in Tab. 5.4. But at the time we made the study, no decision on the offline trigger cut had been made. The result of the study was that there are for all tested veto strategies differences in the veto efficiencies between the samples. But a veto condition like the one in (P7) is the best choice among the tested strategies to reduce the differences in efficiency between the samples as much as possible.

A possible explanation for the generator differences in efficiency of finding the offline trigger topology and the differences in the pseudorapidity of the tagging jets candidates, can give the differences in the parton shower models. Most of the hadronic radiation is along or close to the tagging jets candidates. This radiation pattern is described by the parton shower modelling in the generator. Differences in the phenomenological approach would lead to different resulting pseudorapidity and p_{T} distributions between the generators. The influence of the parton shower model is reflected in slightly varying efficiencies for cuts on jets p_{T}, e.g. (P3) for Pythia old and new shower model. We conclude that the differences in the shower model can explain observed relative differences in (P1) and (P4), which seem to be very sensitive to the parton shower model (cmp. Pythia old and new shower for these cuts). Even if the parton shower model is the same changes in the UE tune can influence the tagging jets p_{T} and their η-distributions and the overall hadronic activity in the event. Hence we find differences in the selection efficiencies for e.g. Sherpa with and without UE.

We show at the end of Appendix B that the difference in generator models for various generated signals is not very strong in the selection with a multivariate discriminator. But one has to keep in mind that only the signal was compared in various generator model and tunes. The background against which the signal had to be discriminated was fixed to a single model. As said before the correct modelling of the MC will rapidly improve with the ATLAS data taking going on. Generally we perform our study in a consistent way in one model, restricting ourselves on the model of Sherpa as an example of a possible model. A search performed in data can of course rely on MC generators well tuned to the data.

5.3 A multivariate events selection

In this section we motivate and describe the multivariate selection, applied on the preselected event samples. The preselection was meant to reject to a large extent the dijet background and most of the $t\bar{t}$ background. But the factorisation estimate predicts the QCD dijets to be the dominant background after preselection. As we will motivate later the dijet events are reduced to a level, which can be dealt with finally in the multivariate analysis step. But the W and Z boson events comprise backgrounds which represent more signal like event topologies and are thus expected to be very hard to be reduced further. The relatively loose preselection, as the cuts used were not tuned to be the hardest possible cuts, offered the chance to use some of the preselection variables again in this selection step specifically targeting the W and Z boson backgrounds. The final cut on the output of the multivariate selection is expected to be more efficient than an iteratively tuned series of cuts.

5.3.1 Multivariate classifiers

In a cut analysis each selection variable defined for the event is only considered once and the event is rejected if it fails a specific cut criterion, though it may well be very signal-like in all other criteria. For sensitivity studies for a larger model parameter range, e.g. M_{H} and ω, in which properties of signal and background may vary it is desirable to find more flexible and adaptive criteria that exploit simultaneously many event properties. One possibility to come closer to this goal is to study the given classification

problem in more dimensions simultaneously with a multivariate classifier. The one-dimensional classifier output combines the multi-dimensional information. In this way it is also possible to use only one multivariate analysis design, which is adaptive to the varying signal properties of the studied parameter range using the more-dimensional distributions.

In general a typical multivariate analysis follows three steps, which are listed below.

Discriminant and training

A multivariate classifier can be used to develop the optimal criteria to discriminate between background and signal in a higher dimensional parameter space on basis of variable distributions from large event samples of both classes. Abstractly speaking the separation between signal and background is optimal if a boundary surface in the parameter space can be found such that the majority of signal accumulates on one side and the maximal number of background events on the other side. This step is called learning or training phase, since in this phase events remain in the sample and are exploited several times according their properties. Correlations between the variables can be utilised to optimise the classification of an event as background or signal. For this distinction the classifier builds a discriminant as function of the input variables. The information about how the inspected variables' distributions contribute to this discriminant can be stored in weights. In the application these weight information is used to classify events of new, independent samples (to predict the sensitivity) or in real data (to search for a signal).

Overtraining tests

There is however the danger that the discrimination predicted by the classifier is far too optimistic. This phenomenon is called "overtraining" and shall be explained shortly. The analysis is confronted with such a problem if for example the training is biased by a subclass of events that are very often probed and have a huge impact on the discrimination criteria, to find such subclass events. Especially this can occur due to statistical fluctuations if the sample is not large enough to provide a statistical valid representation of the variables. The cure for this problem is straightforward namely to use large enough samples or robust methods. Therefore, as second step after an analysis is designed, one has to test with an independent sample whether the discrimination power predicted by the training, e.g. in terms of significance or the distribution of the discriminant, agrees with the one found in the independent test sample.

Optimised cut on discriminant for final selection

In a subsequent final step the event selection is performed on a sample independent of the training and overtraining test samples. Stored weights coding the result of the training phase are used to assign to the events a value of the discriminant. Finally an optimised cut on this discriminant provides the classification of events.

5.3.2 General considerations

The task was to find a stable classifier that is adaptive to changes in the signal properties given by signal mass and its decay width. The possible inputs to the multivariate classifier should exhibit some discrimination power to provide a good performance. As the training of classifiers allows for discrimination of signal and background on basis of statistical properties, the classifier should exploit correlations between the input variables during the learning phase. By this ability it is expected to be superior to a simple cut analysis. Lastly the classifier should reproduce the results stable, i. e.that there are enough training events to reach a reliable classification performance and the outcome should be the same if the training samples are randomised, and shall consume only few CPU time. Details how these demands lead to the

choice of a classifier are shifted into Appendix B. We present in the following the chosen classifier and its input and demonstrate its performance in the event selection.

Training samples for the multivariate analysis

Since the size of the available samples in detailed detector simulation was limited, it was decided not to use them in training. The high weights and the too small number of events would have prevented the multivariate training and subsequent selection to yield significant results.

Instead it was made use of the much larger ATLFAST-1 samples in training and the subsequent selection was performed on the fully detector simulated samples.

The assumption legitimating this approach is, that the weights distribution determined during training with the input variables distributions of the fast detector simulation would not differ significantly from weights which would have been determined with equally large fully simulated samples. This assumption can be justified if the input variables distributions are statistically in agreement between both kinds of simulation methods, because the shape of the variables and correlations are exploited for discrimination.

A training was performed for each of the studied signal samples. It showed that to develop a discrimination strategy against the W and Z boson backgrounds it is advisable to feed only these samples into the training phase, not the remaining other backgrounds, which are very limited in MC statistics after the preselection.

5.3.3 Multilayer perceptron as classifier

The multivariate part of the analysis used a specialised toolkit for multivariate analyses, called TMVA [101]. The systematic comparison of possible classifier and input variables, detailed in Appendix B, resulted in the choice of an artificial neural network, called multilayer perceptron (MLP). We will only shortly explain this architecture of computational modelled neurons. The detailed descriptions and references can be found in [101].

Network architecture

Like their biologic counterpart, MLP artificial neurons build directional interconnected structures in layers (see Fig. 5.2). Especially there is one input layer into which the information of the system (variable distributions) is feed, and usually this layer contains as much neurons as input variables. The first layer is followed by one or several hidden layers in which the information from the preceding layers is processed and weighted. All information is combined in one output neuron[2)], which has a continuous output weight between zero and one representing the target values of background and signal.

A single neuron number j in layer l is receiving information from all neurons ($k = 1...n$) of the proceeding layer, $l-1$, by directional connections y_k^{l-1} which like synapses in nature are not passing their information with equal strength but are weighted in their importance with weights $w_{kj}^{l_i}$. Inside the neuron j the neuron response function ρ maps the n-dimensional input to a single output value. The input information received by the synapses is summed according to a so-called synaptic function κ and the threshold behaviour to the summed information is modelled according to a sigmoidial activation function α. In this way the processed information mapped in the response function $\rho = \kappa \circ \alpha$ determines the weight of the single output node of the neuron y_i^l which is connected to input of neurons in the following layer. This way processes the information in a single direction from input to output and is called therefore, the feed-forward mode.

[2)] Alternatively the last layer can comprise of several neurons for classification in more events classes.

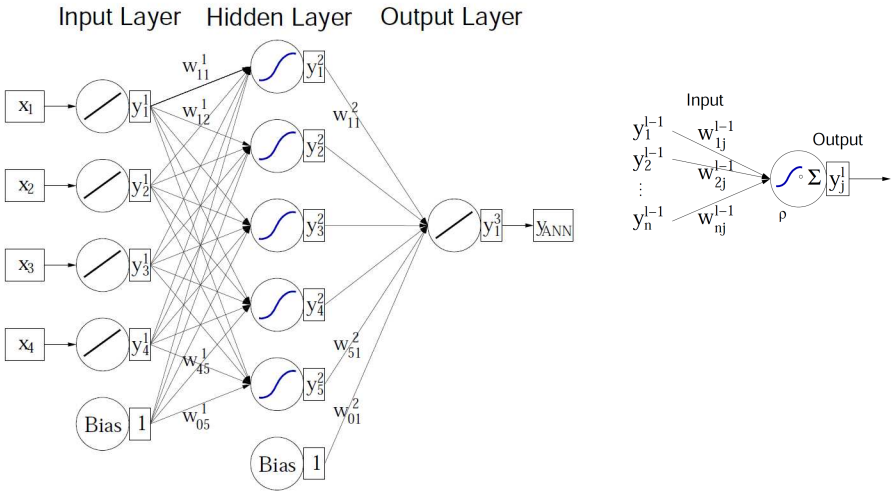

Fig. 5.2: *General design of a feed-forward multilayer perceptron (left side). If only one output neuron is used, the target values are given by the extreme weights 0 and 1. On the right side a detailed view on the information processing in a single hidden layer neuron is shown. The incoming information of interconnections is weighted, determining the synaptic function* κ*. The response function* ρ *is constructed by folding of* κ *with a sigmoidal activation function* α *and maps all inputs on a single output value* y_i^l*, which can be transferred to the next layer.*

Error backward propagation

An important concept to improve a neuronal network's classification performance is to introduce backward propagation algorithms. Such algorithms belong to supervised learning algorithms. The backward propagation uses the fact that during the training phase the true class of a regarded event is known. So the backward algorithm compares the output of the final node with the true target value (0 for background and 1 for signal) for each event, and the difference is interpreted as error. After a training cycle (epoch) is finished the algorithm builds the error function from all events. It can then update the weights of the inputs in a way that the deviation between output an true value is minimised. This can be done once in a training cycle (bulk learning) for the complete neuronal network or in a more efficient way on event by event base (online learning). In online learning the weight changes at the neurons due to the individual regarded events update the error function of the whole network, which is then minimised immediately. The MLP in this analysis used online learning.

Rule of thumb for good performance

In [101] a theorem is quoted that the optimal nonlinear boundary in the parameter space between signal and background (i.e. describing a continuous correlation function between the variables to any precision) can be approximated with arbitrary precision when using a single hidden layer MLP with a large enough number of hidden neurons. In praxi, but this depends on the problem, a much smaller number of neurons in one or two layers may yield equivalent separation power. A very large number of neurons should be avoided since the MLP tends to be unstable and needs more trainings events. By trial and error, we found as an useful rule of thumb if n inputs variables are in the first layer then one obtains best performance by introducing only one hidden layer with the next integer number of $1.5 \times n$ neurons and for the last layer one neuron models the discriminant distributions.

Importance ranking of input variables

There is also an useful definition of importance I_i of the ith input variable. An importance ranking uses the final sum of weights squared assigned to the connections of the n_{var} input layer variable nodes to n_h neurons of the first hidden layer after the training has finished.

$$\mathrm{I}_i = \bar{x}_i^2 \sum_{j=1}^{n_h} \left(w_{ij}^1\right)^2, \quad i = 1, ..., n_{\mathrm{var}} \tag{5.1}$$

In this, $\bar{x}_i$ is the sample mean of variable i [101].

Input variables of the MLP

The multivariate sequence of the analysis became strikingly simple. It occurred that finally five input variables to the MLP were sufficient for describing the correlations and reach a good performance. The input variables to the MLP are formed by the following quantities.

1) M_{j1j2},
   the invariant mass calculated of the tagging jet candidates.

2) $\Delta\Phi_{\mathrm{j1j2}}$,
   the azimuthal angle between the tagging jet candidates.

3) $\Delta\eta_{\mathrm{j1j2}}$,
   the pseudorapidity gap between the tagging jet candidates.

4) $p_{\mathrm{j1}}^{\mathrm{T}}$,
   the transverse momentum of the leading tagging jet candidate.

5) $p_{\mathrm{j2}}^{\mathrm{T}}$,
   the transverse momentum of the subleading tagging jet candidate.

Since the variables do not depend on other than leading and subleading jet measurements and their directions, it is expected that the multivariate method does not depend strongly on different MC generator models (see Appendix B.1.5).

Though variables including third jet properties would have promised a small positive contribution for performance, they were not used at all (see Appendix B). As detailed in Chapter 4 for additional QCD radiation one becomes dependent on generator models[3)]. But as soon as well tuned MC generators to LHC data are available, it may be worth for an hypothetical analysis with 30 fb^{-1} to reaccess the performance with inclusion of third jet properties.

Also it was found that variables describing the $E_{\mathrm{T}}^{\mathrm{miss}}$ direction with respect to tagging jet candidates do not contribute much to the separation. This may be due to the fact that the signal and the dominant background contain real $E_{\mathrm{T}}^{\mathrm{miss}}$ in the samples which is correlated to the selected variables in a way that it is not adding information.

Additionally it was checked that the chosen MLP configuration is still the favourite at two values for the $E_{\mathrm{T}}^{\mathrm{miss}}$ preselection cut, namely 70 GeV to 100 GeV.

The importance of the variables can be calculated according to Eq. 5.1 and is tabulated for the typical example hypothesis, $M_{\mathrm{H}} = 200$ GeV and $\omega = 5$, in Tab. 5.5, indicating that the difference in shape of $\Delta\eta_{\mathrm{j1j2}}$ played a major role. But such information should be taken cum grano salis since the power of the multivariate method comes from the simultaneous evaluation of the correlations in the distributions. As described in Appendix B, in the selection process of discriminating variables we relied vastly on

[3)] For an impression of the possible differences see Appendix B, especially Fig. B.12 to Fig. B.15

inspection of the variable distributions' shapes. Also these numbers in Tab. 5.5, for technical reasons, were inferred from a sub-sample and not from the full statistic available for training. But it was observed that the order is preserved for other sub-samples, while the numbers may change a little bit.

rank	variable	importance I
1	$\Delta\eta_{\mathrm{j1j2}}$	5.009
2	M_{j1j2}	0.352
3	$p^{\mathrm{T}}_{\mathrm{j2}}$	0.341
4	$\Delta\Phi_{\mathrm{j1j2}}$	0.026
5	$p^{\mathrm{T}}_{\mathrm{j1}}$	0.016

Tab. 5.5: Typical example how the MLP used the information in the input distribution, given by the "importance". The signal samples used is a Higgs boson with $M_{\mathrm{H}} = 200$ GeV and $\omega = 5$.

Input distributions in fast detector simulation

In Fig. 5.3 we display the normalised input variable distributions in the ATLFAST-1 samples after preselection, used for the training. As an example again the signal hypothesis $M_{\mathrm{H}} = 200$ GeV and $\omega = 5$ is chosen and the background consists of the W/Z boson plus jets backgrounds.

In order to characterise the ATLFAST-1 distributions a little further we display in Fig. 5.4 the linear correlations determined between the variables. The linear correlations are displayed for the signal, $M_{\mathrm{H}} =$ 200 GeV and $\omega = 5$, in the left panel of Fig. 5.4 and for the W/Z boson plus jets backgrounds in the right panel. Differences in the sizes of linear correlations between variables for background and those for signal can reach up to roughly 14 % , e.g. for $\Delta\Phi_{\mathrm{j1j2}}$ and $p^{\mathrm{T}}_{\mathrm{j2}}$. But for most of the linear correllations the differences stay between some percent to 10 percent if these are compared between background and signal.

Comment on the influence of mass and width properties of the various signal hypotheses

At this place it may be interesting to gain some insight how much the signal properties mass and width influence the shape of the ATLFAST-1 input distributions. More detailed information can be found also in Appendix B.

As shown in the previous section, the preselection served to accumulate events in the weak boson fusion topology plus large missing transverse energy. Therefore, the applied cuts where not specifically designed to be efficient for any particular signal mass or decay-width. During the training phase the MLP should discriminate the signal from the background, using shape differences and information about correlations in the input distributions. Theoretically the training and the subsequent performance of the MLP selection is also depending not only on global differences of the signal compared to the background, but to some extend on more subtle differences in the signal distributions that stem from mass and decay-width differences in the signal hypothesis If especially these width differences are pronounced the analysis can become very width sensitive. But if these width differences are less prominent, we expect that the sensitivity of the analysis is depending on the signal's mass.

In order to get a feeling how the input distribution shape is varying with the choice of the signal hypothesis we display in Fig. 5.5 several signal hypothesis examples. The displayed distributions are normalised to unit area for this shape comparison. We display signals with the mass of 130 GeV, 200 GeV and 300 GeV. For each signal mass we vary the invisible decay-width from small to large by assuming $\omega = 0.1,\ \omega = 1,\ \omega = 5$, and $\omega = 10$.

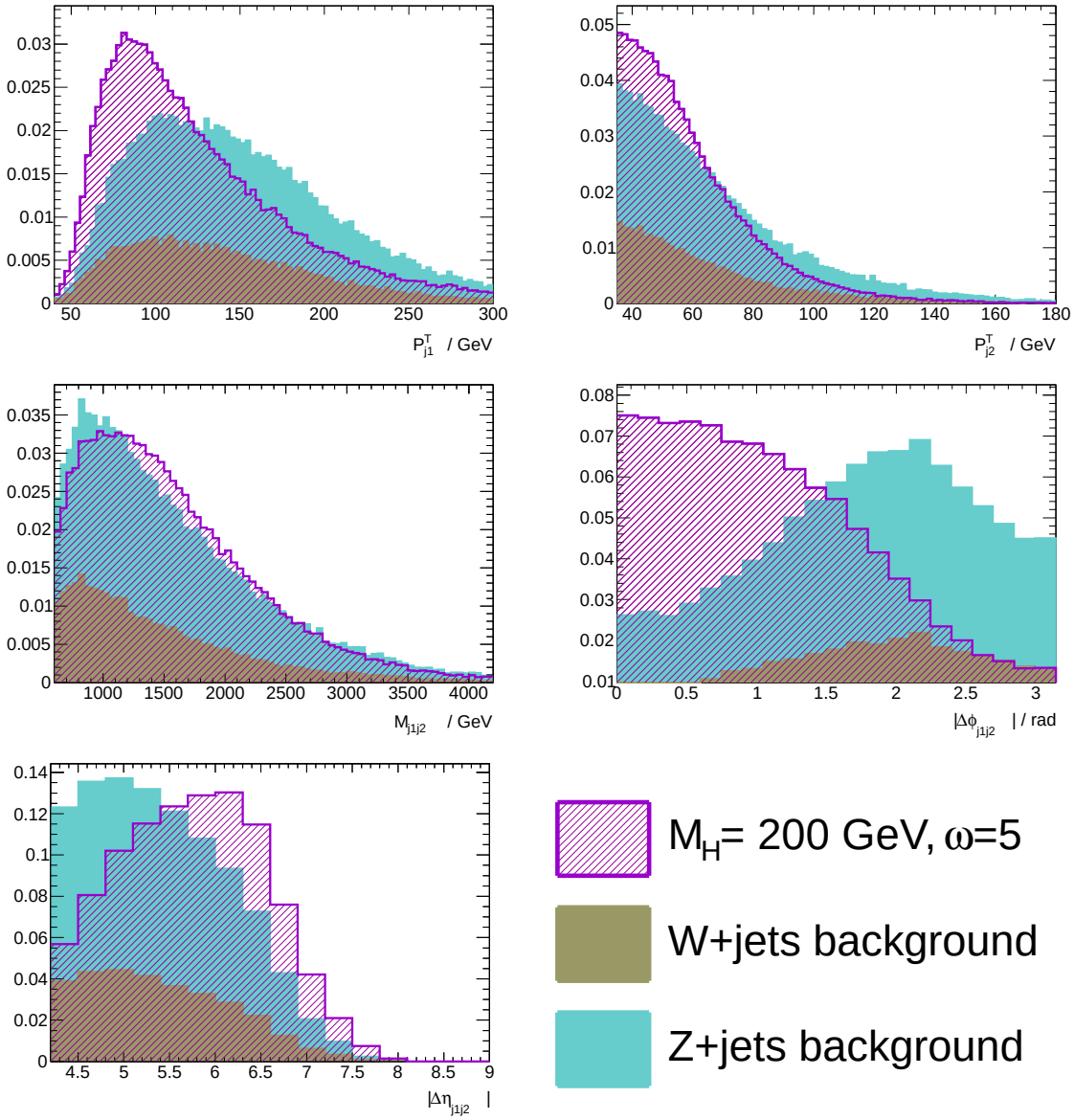

Fig. 5.3: *Distributions of the input variables after the preselection in the ATLFAST-1 samples used for training. Plotted is a signal, $M_{\mathrm{H}} = 200$ GeV and $\omega = 5$, and W boson Z boson background after preselection, against which the multivariate analysis is intended to discriminate. We show the distribution normalised, as they will be normalised in the MLP in order to perform the training according to shape differences and correlations between variables.*

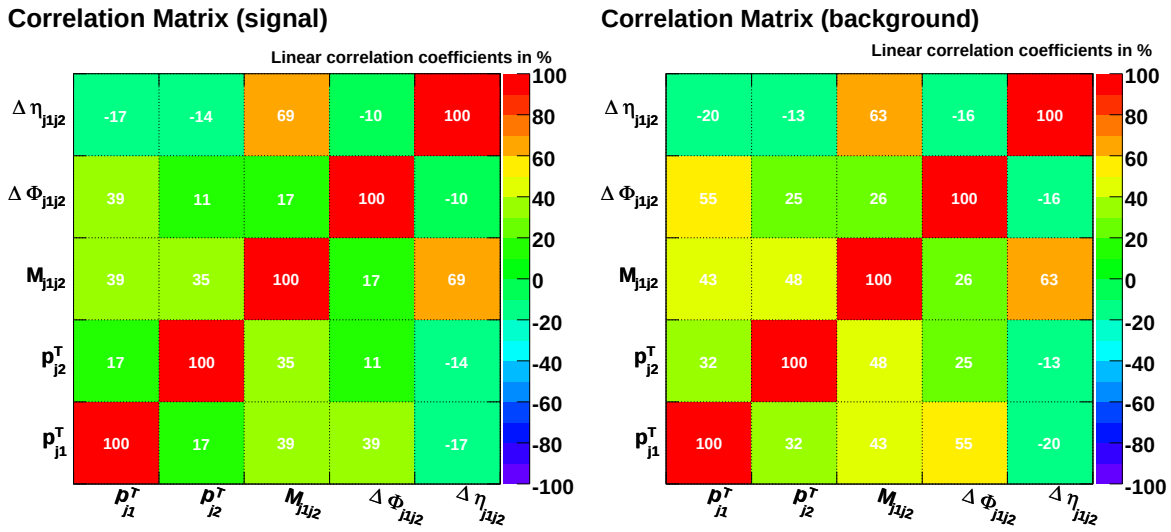

Fig. 5.4: *Linear correlations as determined in the training for the signal, $M_{\mathrm{H}} = 200$ GeV and $\omega = 5$, and the W and Z boson backgrounds. left panel linear correlation in percent between the input variables for the signal, right panel the same for the summed background.*

The impression one gets from this comparison is that the dependence on the signal mass is more important than the shape differences in one mass point with varying width. Some small differences stemming from mass and width in the input variables are visible, especially for the variables M_{j1j2} and $\Delta\eta_{\mathrm{j1j2}}$. In principle, after having trained a MLP with a specific mass and width hypothesis, one can try to introduce also a mass or even width-dependent MLP output cut to optimise the signal efficiencies further. But in the next chapter, we will argue that for the sake of simplicity we determined just one cut on the MLP independent of the signal hypothesis, in order to control and quantify the dominant systematic effects of the expected background.

.

5.3.4 Comparison of input variables distributions in fast to detailed detector simulation

As explained the fast detector simulation determines the weights of the neurons after training, which are stored and used for selection on the fully simulated samples. In this paragraph we therefore present a shape comparison of the input variables used in both steps, i.e. training and selection. This comparison serves as a proof of principle since sufficient statistical agreement opens the possibility to use fast detector simulation in the training phase and in the application of the classifier exclusively the sparse fully detector simulated samples can be used. This is important since we will see in Section 5.3.4, that the MLP training needs at least a certain amount of MC events to perform stable. The more events are used in training the better the learning algorithm will perform.

In Fig.5.6 we show the comparison between fast (blue histogram) and detailed (red histogram) detector simulation in the Z boson plus jets background process for all five input variables after preselection. For the W boson plus jets process, which is the most important background, that should be tackled in the MLP selection we present the input distributions comparison in the Appendix B.2. There we are displaying also the comparison for a typical example of a signal, $M_{\mathrm{H}} = 200$ GeV and $\omega = 5$. In the Z plus jets sample we have a better MC statistics than the W boson plus jets or a typical signal sample. The latter two show larger relative error and fluctuations.

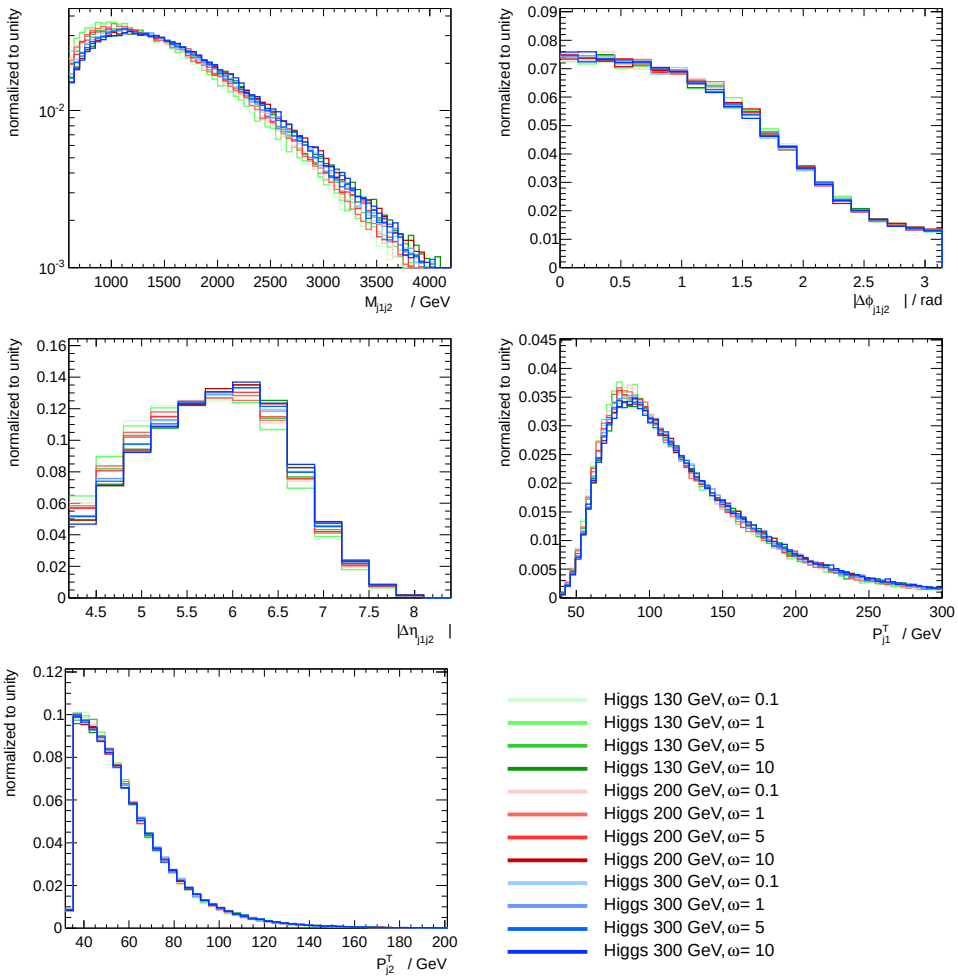

Fig. 5.5: *The five input variable distributions for various signal hypothesis. The distributions are displayed for comparison of possible shape differences due to mass and decay width of the signal. All distributions are normalised to unity to make the shape comparison possible. The distributions are made using the fast detector simulation, like the one entering the training of the MLP.*

Of course there are much less MC events in the detailed detector simulation surviving the preselection cuts compared to the abundant fast simulated events. We think that it is justified to conclude that the description of these five variables build with properties of the tagging jets candidates are in statistical agreement for the various samples. These comparisons support the statement that the shape of the variables coincide in detailed and fast simulation. One reason may be that tagging jet candidates are well isolated objects which often have a relative large p_T and and difference jet building algorithms between fast and detailed simulations are not important. As we will see in the comment presented in the next paragraph, that will not be necessarily the case for additional jets.

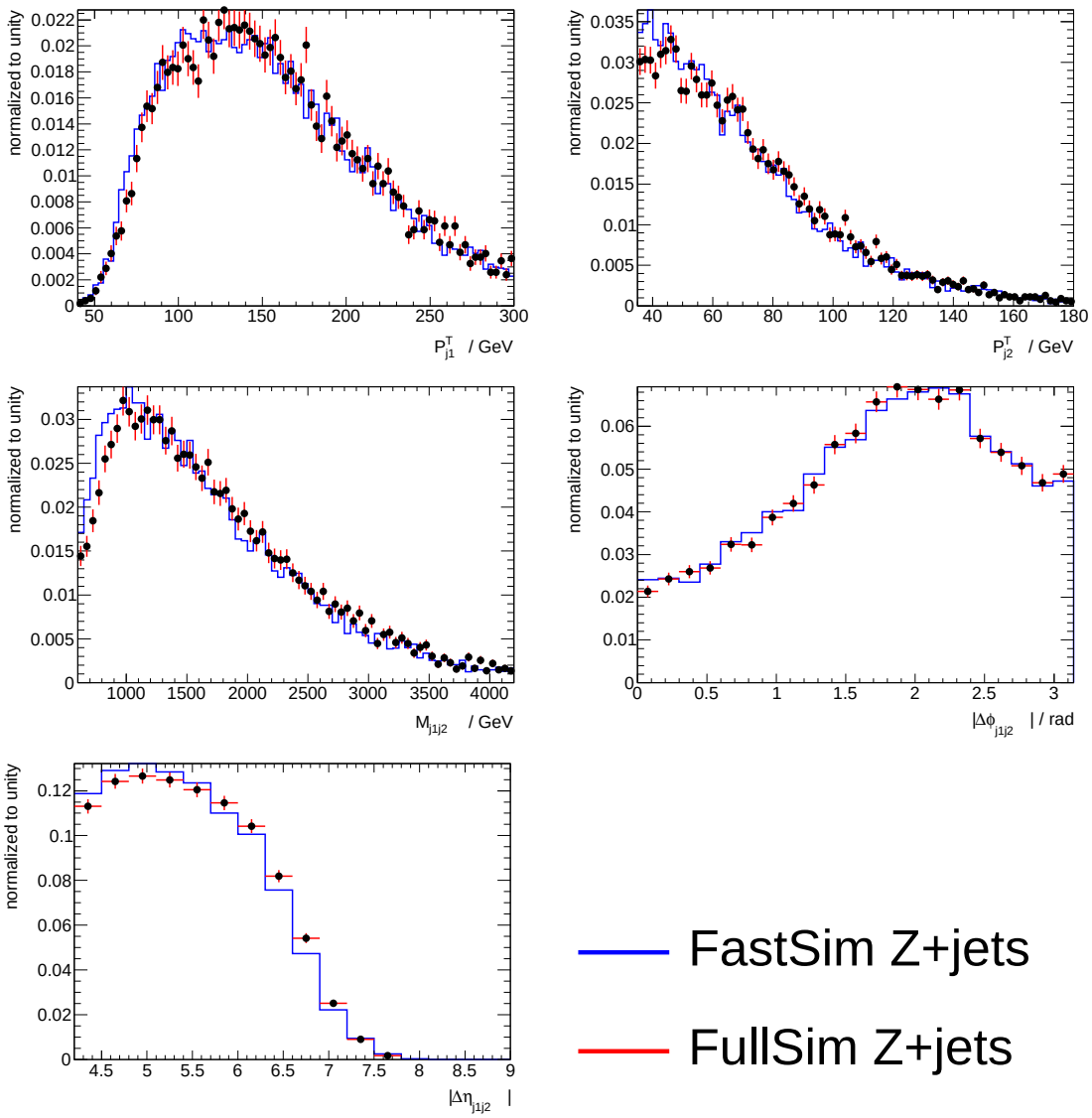

Fig. 5.6: *The five input variable distributions in comparison between fast and detailed simulated events. The distribution are displayed for comparison of possible shape differences in ATLFAST-1 and detailed Geant4 detector simulation. Shown is the Z plus jets background. All distributions are normalised to unity to make the shape comparison possible.*

Comment on the comparison between variables including a third jet in detailed and fast detector simulation

As we have argued abundances of third jets are quite different in fast detector simulation from and fully simulated event. In the later the third jets are relatively sparse since the reconstruction cut and merge and split methods for the used cone-jet algorithm differ from the fast simulation. For that reason we omitted variables with the third jet from our MLP input variables set (see Appendix B). Further the comparison between fast and full detector simulation provided an additional argument against the use of that variables. We found that the shape of variable distributions with the third jet differ considerably. As an example we show in Fig. 5.7 the Zeppenfeld distribution for the third hardest jet $\eta^{\star}_{jet3} = \eta_{j3} - \frac{1}{2} \times (\eta_{j1} + \eta_{j2})$ and the related minimal distance in R of a third jet to the tagging jet $\Delta R^{min}_{tagjets,jet3}$ are shown. Though we were able to map the third jet's distribution of the fast simulation to the detailed simulated iteratively via a weight from a 4^{th} order polynomial function, without distorting the other distributions, we did not introduce these more complicated additional weighting in our analysis. Because we found that the performance of a MLP with these variables is only marginal better than of a MLP without these variables. The only advantage of such large effort with shape reweighting in the shown third jets variables would have been that the fast simulated events efficiency for the mini jet veto in the preselection would have been more similar to the efficiency in the fully simulated sample. To reach a better agreement in efficiencies it would have been additionally required to map the third jet p_{T} spectrum and to adjust the third jet abundances between fast and detailed detector simulation by a random jet killing in the fast simulation events. The correction of the shortcomings in the description of the mini jet veto and third jet variables of the fast detector simulation would introduce much technical complications, but would not improve the analysis very much. One can assume that the shape of the used MLP input variables after preselection is rather independent from the mini jet veto efficiency in the fast simulation. For the final evaluation of the sensitivity the detailed simulated events are used anyway.

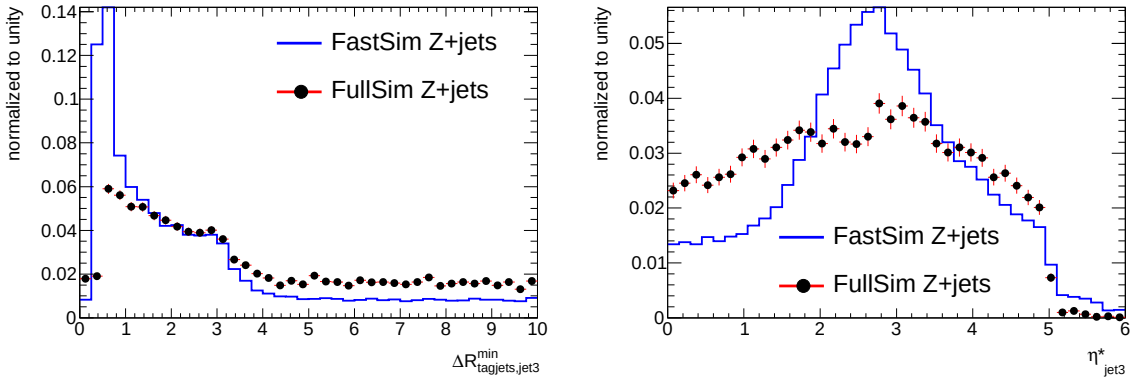

Fig. 5.7: *Distributions of two related* 3^{rd} *leading jet* ($p_{\mathrm{T}} > 15$ GeV) *variables, namely* $\eta*_{jet3}$*,the Zeppenfeld distribution for the third hardest jet, and the minimal distance in R of a third jet to any tagging jet* $\Delta R^{min}_{tagjets,jet3}$*, in the ATLFAST-1 samples used for training in comparison with the detailed detector samples. This shape difference occur due to specific differences in jet reconstruction algorithms. The distributions display the Z+jets background, as example.*

Typical output distributions of the MLP

After describing several properties of the input distributions, it may be also instructive to look at a typical example for the resulting output distribution. The weight of the output neuron which finally classifies the processed input information is usually normalised to an interval [0;1]. Ideally, if the variables have

strong discrimination power, the background peaks strongly at values close to zero and and the signal has a narrow peak at 1. In that way one finds easily a very hard cut on the output and an excellent separation between signal and background.

Fig. 5.8 displays the output distribution found after training in the case of a Higgs with $M_{\mathrm{H}} = 200$ GeV and $\omega = 5$, which is again very representative for all other signals. Unfortunately the ideal separation is not given for the stealthy Higgs sensitivity. The barycentre of background distribution is localised in the middle and has larger tails into the relatively smeared out area where the signal accumulates..

It is not immediately clear where to cut to have a high remaining Higgs signal efficiency and a high expected sensitivity in a selection. If one keeps in mind that the systematics of the background have to be taken into account, it was decided to postpone the choice of an optimal cut until the systematic uncertainties are studied in the next chapter. There we will try to find a cut maximising the sensitivity under the influence of background systematics. At this place we continue to describe general features and cross checks performed with the designed multivariate analysis.

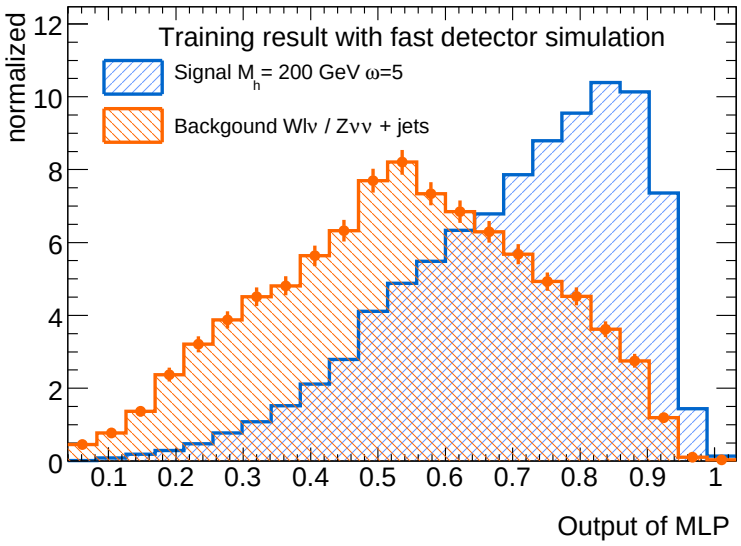

Fig. 5.8: *Typical MLP output distribution of training events. One notes a non optimal discrimination, since the signal example,* $M_{\mathrm{H}} = 200$ GeV *and* $\omega = 5$*, has much overlap with the W and Z boson background, peaking in the middle and not close to zero.*

Stability condition

A series of tests provided the details for the design of the MLP. The number of inputs is $N = 5$, corresponding to an input layer of five neurons. By default the output layer maps the input to one neuron. As for the choice of hidden layers, the layout with best stability was to use only one hidden layer with $N+3$ neurons in it. This corresponds to the rule of thumb given above.

Another important issue for stable training results is to supply the MLP with enough training events. The background and signal are given as weighted events to the MLP, so that the relative importance of the backgrounds is taken into account. In case of a large expected background, a small expected signal may be underrepresented during training. Therefore, the MLP was trained with setting the number of MC events of the signal sample equal to the sum of weights from the background in training. In this way for training a $s/b = 1$ is artificially achieved. Hence, the MLP can adapt to the signal properties with sufficient training events.

$$N_{\mathrm{S\ train}}^{\mathrm{MC}} = \sum_{N_{\mathrm{B\ train}}} w_i \tag{5.2}$$

It was observed that even the large fast detector simulation samples have to be used completely in training to reach the region were training becomes stable. During the training phase the network must have the possibility to see enough events to model the underlying correlations reliably. Only then the training gives a predictions about the form of the background and signal MLP output distribution and thus the achievable discrimination power. This information about the output shape is coded in the the determined weights. Hence if the shape of the output in several randomised trainings differs or changes in the shape occur depending on the used number of training events, this would also be visible in the final selection where the weights are evaluated. This was studied again for the $M_{\mathrm{H}} = 200$ GeV $\omega = 5$ signal hypothesis in training against the background. It was always enough signal left in the samples to fulfil the Eq. 5.2 condition. The critical aspect was whether the left-over background after preselection is sufficient for stable training.

In Fig. 5.9 the shapes of MLP outputs for signal and background are compared for varying numbers of training events. First in the upper row the shapes the training output made with 50% , 80% and all available fast detector simulation background events are shown. One sees that the shapes of the output distributions deviate if the output is produced with only 50% or all events used in background training. If 80% are used, clearly, the output is more similar to the one produced with all events. Equally, in a signal output the MLP needs more events to describe the slope close to 1 of the output distribution stable.

In the lower row the corresponding output distributions of the detailed simulated samples using the weights from a training with 50%, 80% and 100% of the available training events are displayed. The shape varies slightly with the statistics of background used in training but the effect is not to large. As long as a shape difference occurs in the region that would be cut away anyway in the final step, it would have no influence on the result.

A MLP usually gets randomised events, and therefore we tested our MLP setup in three more runs with randomised training samples. This of course was only possible for 50% of the available background events. The result is displayed in Fig. 5.10. For 80% of training events the result of three randomised trainings is shown in Fig. 5.11. Again in the upper row of both figures the training outputs appear and the corresponding selection outputs determined from the weights are shown in the lower row. In comparison of both figures, one sees a clear tendency that for training samples reduced to 50% of size (Fig. 5.10 lower row), the influence of randomly chosen events is stronger and yields more shape differences from run to run. This translates to visible shape changes in the selection output. Even in the output distributions (Fig. 5.11 lower row) using weights produced with 80% of available training events one sees some remaining influence of randomisation. We interpret that fact in a way that we may have reached a sufficiently stable MLP if we use all available events. Of course since no larger samples are available we cannot say to which amount the remaining shape variations would reduce, if one for examples uses twice the available statistics. It would be advisable for an actual search to be performed at 30 fb^{-1} to carry out such test as sketched here, and make sure to use enough MC trainings that a constant shape for the output is reached.

Overtraining checks

The absence of overtraining was checked for the signal hypotheses. A very representative example is given in Fig 5.12. To yield this distribution 50% of the ATLFAST-1 background samples were used in training and the rest in the testing of the trained network. For signal enough MC events were available to maintain $s/b = 1$. The Kolgomorov test indicates that as well for the signal as for the background the output distribution from training is in agreement with the output of the independent training samples, hence there is no indication for overtraining. The same applied to the other signal hypotheses.

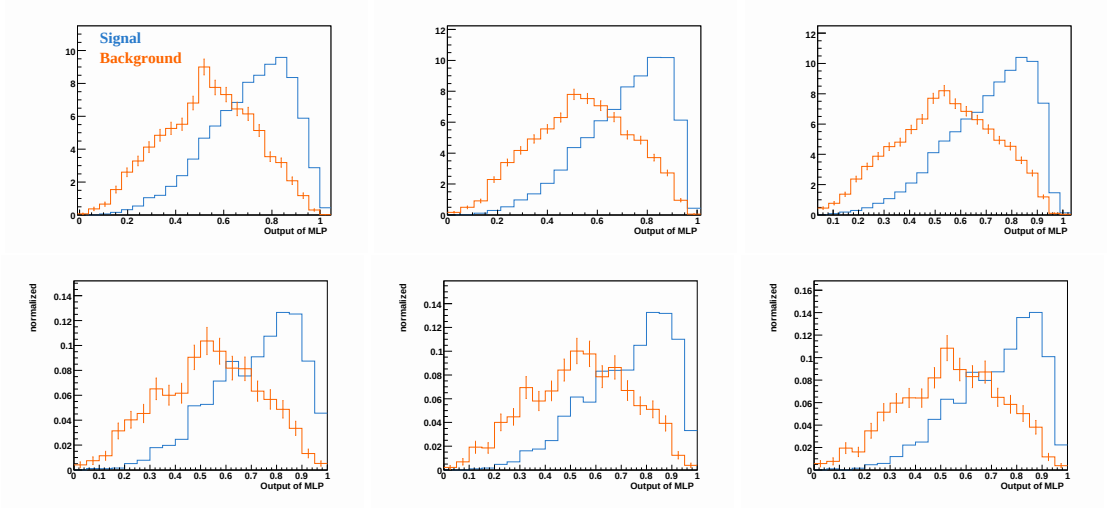

Fig. 5.9: *Influence of number of training events on the MLP output distribution. The output for a signal are the dark blue histograms for the background are the orange histograms. The training MLP output in the ATLFAST-1 samples is shown in the upper row for 50%, 80% and 100% of available W and Z boson background events. The lower row shows MLP output distributions, in the same colour coding, of detailed detector simulated samples that are evaluated with the training weight files corresponding to the plot in the upper row.*

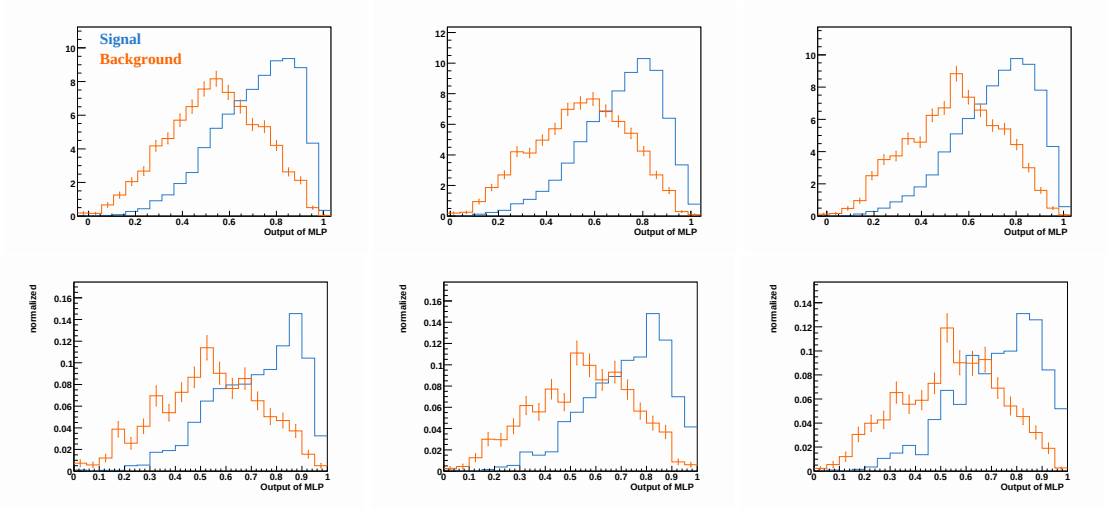

Fig. 5.10: Stability of the MLP selection seen in repeatedly randomised runs with 50% of all available fast detector simulation used in training. For training the samples sample sizes were chosen according to the condition $\sum w_{lum}(B) = N^{MC}(Sig)$, i.e. to artificially force $\frac{S}{B} \sim 1$. The training distributions for signal (dark blue) and background (orange) are displayed in the upper row for a randomised run on the same training sample. The appliciation phase on basis of the training weights consequently used independent events of the detailed dectector simulation. To visualise the effect of ramdom training event choise, the signal and backgrounds output distribution of the application, using the corresponding to the upper row training weights, are shown in the lower row. Compare also Fig. 5.11

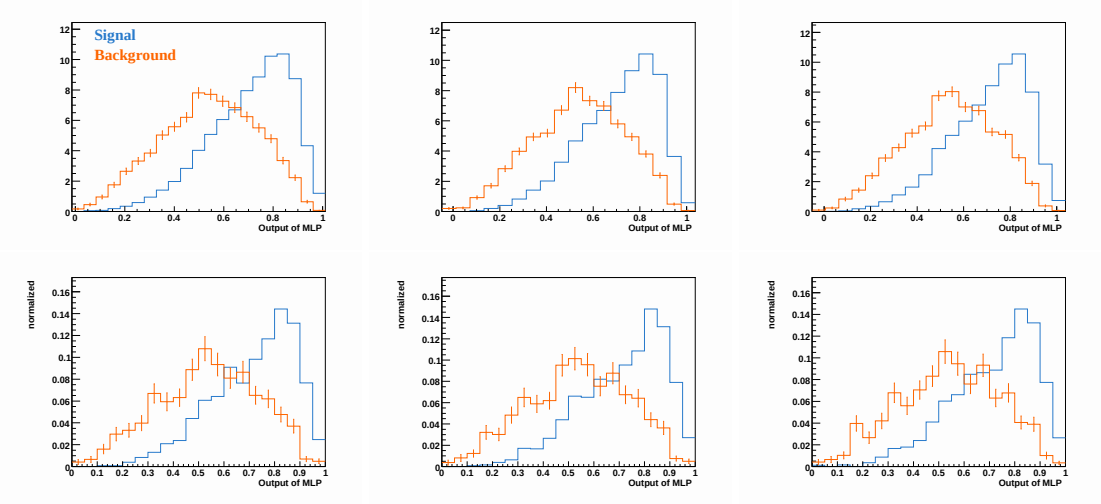

Fig. 5.11: Stability of the MLP selection seen in repeatedly randomised runs with 80% of all available fast detector simulation used in training. For training the samples sample sizes were chosen according to the condition $\sum w_{lum}(B) = N^{MC}(Sig)$, i.e. to artificially force $\frac{S}{B} \sim 1$. The training distributions for signal (dark blue) and background (orange) are displayed in the upper row for a randomised run on the same training sample. The appliciation phase on basis of the training weights consequently used independent events of the detailed dectector simulation. To visualise the effect of ramdom training event choise, the signal and backgrounds output distribution of the application, using the corresponding to the upper row training weights, are shown in the lower row. Compared to Fig. 5.10 the application phase shows more similar results due to the stabalising effect of more training events used.

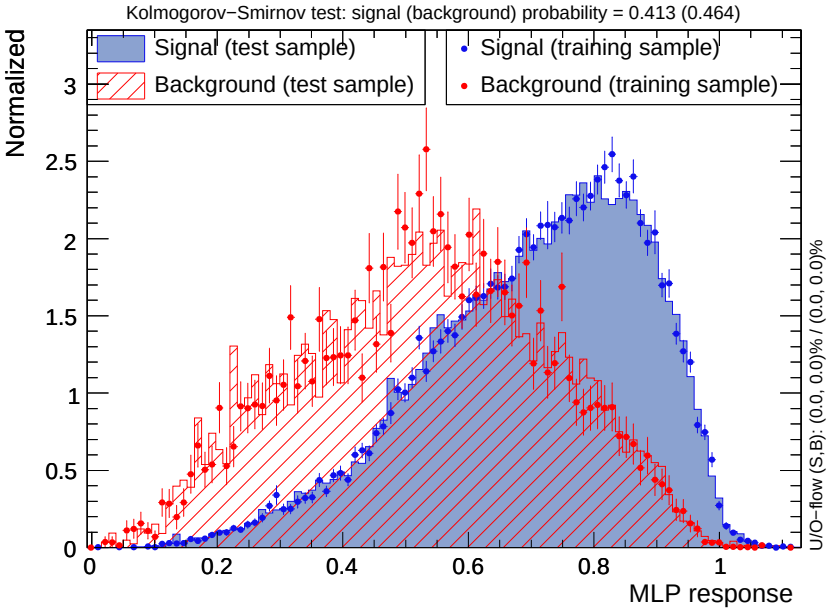

Fig. 5.12: *Distribution of the output value of the MLP in the ATLFAST-1 samples used for training and subsequent testing. Plotted is a signal with* $M_{\mathrm{H}} = 200$ GeV *and* $\omega = 5$ *and the added W and Z boson background. As one sees, the test sample is within the statistical error in agreement with the training distribution, hence overtraining is not present in this case. The same applies to the other signal hypotheses not shown here.*

5.3.5 Estimate of the MLP response for the dijet background

As already explained in Sec. 5.2.1, the dijets background is estimated by factorisation. The calculation yielded a large expectation of roughly 126000 dijet events in 30 fb^{-1}after preselection (Tab. 5.3). Apparently the preselection reduces this background by orders of magnitude, but it remains the largest background. To estimate the response of the used MLP towards the dijets background is difficult, because there are almost no MC events left after preselection that could be passed to the MLP. Therefore, an attempt was made to find conditions under which one can loosen or leave out some preselection cuts to gain more dijet MC events for the MLP selection.

Since the M_{j1j2} is a variable of the MLP too, this cut has clearly to be made in the preselection. Otherwise the phase space of the dijets events processed in the MLP will differ largely from the normally preselected events, and the reduction will be too optimistic. Likewise the trigger topology (one central and one forward jet candidate) and the weak boson fusion topology cuts for the selection of the tagging jets can not be removed from the preselection, for the same reason.

variables		correlation coefficient					
		dijets	$t\bar{t}$	$Z\rightarrow ll$	$Z\rightarrow \nu\nu$	$W\rightarrow l\nu$	signal
p_{T}^{j1}	E_{T}^{miss}	0.19	0.14	0.18	0.52	0.32	0.67
p_{T}^{j2}	E_{T}^{miss}	0.11	0.05	0.09	0.19	0.15	0.31
M_{j1j2}	E_{T}^{miss}	0.06	0.07	0.12	0.11	0.09	0.19
$\Delta\Phi_{j1j2}$	E_{T}^{miss}	−0.23	−0.23	−0.11	−0.34	−0.22	−0.53
$\Delta\eta_{j1j2}$	E_{T}^{miss}	0.03	0.02	0.03	−0.13	−0.07	0.08
I	E_{T}^{miss}	0.12	0.29	0.20	0.28	0.25	0.47
I	$\Delta\Phi_{j1j2}$	−1.0	−0.68	-0.94	−0.96	−0.94	−0.96

Tab. 5.6: The correlation in the MLP inputs with E_{T}^{miss} considered in finding the right grouping of cuts. The numbers were determined in the fully detector simulated samples. The signal is the $M_H = 200$ GeV and $\omega = 5$ hypothesis. The last two lines display information on the missing energy isolation variable, that is defined in Sec. 5.4.2 and used in Sec. 5.4.3.

The cuts on E_{T}^{miss} on the one hand remove many of the dijets and may be made looser. But on the other hand the E_{T}^{miss} is also correlated to the MLP variables to some amount. In Tab. 5.6 we have determined the correlation of the individual variables from the MLP with the E_{T}^{miss} for the various processes which are the QCD dijets (second column), top pairs (third column), Z boson decays into charged leptons (fourth column), Z bosons into neutrinos (fifth column), leptonic W boson decays (sixth column) and a typical signal with $M_H = 200$ GeV $\omega = 5$ (last column). One notes that the E_{T}^{miss} variable is relatively highly correlated with the tagging jet's p_T and even more highly anti-correlated with $\Delta\Phi_{j1j2}$ for all shown processes. Especially the correlation of $\Delta\Phi_{j1j2}$ to E_{T}^{miss} can possibly lead to too large rejection of dijets determined for the MLP. Thus is it advisable to make at least a loose E_{T}^{miss} cut before passing the dijets to the MLP. But it is hard to find a good compromise since even a little harder cut on E_{T}^{miss} will reject many of the sparse dijet MC events. Thus with a too hard cut the determined rejection of the MLP will contain a large statistical uncertainty. We therefore looked for a tendency how large dijets rejections can be achieved, applying the different preselection conditions: $E_{T}^{miss} > 0$ GeV , $E_{T}^{miss} > 20$ GeV and $E_{T}^{miss} > 50$ GeV .

The dijet rejection by a MLP was determined with an output cut of 0.85. As the training with different hypotheses influences the weights of the MLP and thus the rejection of dijets events we made this test for each of our 67 signal hypotheses, at hand. Afterwards we collected the dijet rejection in all of the 67 MLPs trained with an individual hypothesis and determined from these numbers an average rejection.

The Tab. 5.7 gives the results of rejection of dijet as a function of the $E_{\mathrm{T}}^{\mathrm{miss}}$ cut that were found. To give a feeling that the MC statistics is really sparse the second column gives the number of MC events that enter the MLP. In case of $E_{\mathrm{T}}^{\mathrm{miss}} > 0$ GeV and $E_{\mathrm{T}}^{\mathrm{miss}} > 20$ GeV two or three outliers with very low efficiencies occurred. These were excluded in the averaging. And in the case $E_{\mathrm{T}}^{\mathrm{miss}} > 50$ GeV the statistic became very poor. To be conservative also roughly the 30 points found with highest rejections of the order of 10^{-4} were excluded from the quoted average. One observes that without the $E_{\mathrm{T}}^{\mathrm{miss}}$ cut the rejection of dijets is almost complete, but as argued above the correlations between the MLP inputs and $E_{\mathrm{T}}^{\mathrm{miss}}$ can not be neglected. With a rather mild $E_{\mathrm{T}}^{\mathrm{miss}} > 20$ GeV precut we expect a dijet efficiency after MLP cut of the order of 10^{-4}. A harder $E_{\mathrm{T}}^{\mathrm{miss}} > 50$ GeV precut which rejects much of our MC events, yields a dijet efficiency after MLP cut of the order of 10^{-3}.

cut $E_{\mathrm{T}}^{\mathrm{miss}}$ (GeV)	MC events	average $\varepsilon_{\mathrm{MLP}}^{\mathrm{dijets}}$	expected dijets after MLP
0	9750	$2.15\ 10^{-4}$	27
20	2250	$6.0\ 10^{-4}$	98
50	250	$1.6\ 10^{-3}$	199

Tab. 5.7: Expected events in 30 fb^{-1}. The second column gives the number of MC events that enter the MLP. The efficiency $\varepsilon_{\mathrm{MLP}}^{\mathrm{dijets}}$ is the average of the all hypotheses. The cut on the MLP was set to 0.85.

The numbers for dijet efficiency with the $E_{\mathrm{T}}^{\mathrm{miss}} > 50$ GeV are only an estimate on basis of very limited MC statistics. The dijet rejection with the real analysis cut $E_{\mathrm{T}}^{\mathrm{miss}} > 110$ GeV will be smaller and we should expect more dijets events surviving the MLP. But the general conclusion that we draw from Tab. 5.7 is, that a relative hard cut on the MLP, though it was especially trained to tackle the W and Z boson backgrounds, removes very effectively the QCD dijets remaining after preselection. Hence we are optimistic that the QCD dijet level in the analysis can be controlled by the MLP selection strategy. Additional cuts could be introduced, if necessary, suppressing fake $E_{\mathrm{T}}^{\mathrm{miss}}$ in the dijets or a harder MLP output cut be used to suppress the dijets further if an analysis with 30 fb^{-1} data is performed. As we will see later after we have found an optimal cut on the MLP (Chapter 6) the surviving W and Z boson backgrounds, which comprise typically of several thousands events, are much larger than the estimated expected dijet after MLP.

5.4 A simple cut-based events selection

Though it was tried in several stages to stabilise, optimise and judge the performance of the multivariate analysis, an important part of the event selection is done inside of the MLP "black box", using its determined weights.

As a sanity cross check a simple cut-based analysis was deployed, being more transparent. Because of time constraints this cross check was not optimised by iteratively tuning the cuts. It follows mostly the cut-based analysis for the sensitivity of ATLAS towards an invisible Higgs, published in [7]. Though it was found to be a good baseline in this publication also more refined methods of signal extraction were studied like shape analysis in the distribution of $\Delta\Phi_{j1j2}$.

Basically we added to the cuts published in [7] only one ingredient, namely the cleaning for possible fake $E_{\mathrm{T}}^{\mathrm{miss}}$ contributions which is explained in detail in the next paragraph, and we made the cut on the missing $E_{\mathrm{T}}^{\mathrm{miss}}$ isolation tighter.

5.4.1 Cleaning cuts against possible detector related $E_{\mathrm{T}}^{\mathrm{miss}}$ sources

Fake $E_{\mathrm{T}}^{\mathrm{miss}}$ in the calorimeter is produced by mismeasurements of hadronic jets, taus, electrons and photons. Even with no dead read out channels present, the mismeasurements occur in poorly instrumented regions. Specifically in the ATLAS detector these are the transition region, so-called crack region, between barrel and end cap calorimeters ($1.3 < |\eta| < 1.6$) and the gap between central and forward calorimeters around ($3.1 < |\eta| < 3.3$). The detailed detector simulation models effects that can lead to detector induced $E_{\mathrm{T}}^{\mathrm{miss}}$, e.g. if jets are directed into these poorly instrumented regions or partly hitting calorimeter cracks. Though in principle present, the impact of such fake $E_{\mathrm{T}}^{\mathrm{miss}}$ on the selection is usually small in events which contain real $E_{\mathrm{T}}^{\mathrm{miss}}$ from neutrinos. But the $E_{\mathrm{T}}^{\mathrm{miss}}$ spectrum of dijet events is mostly coming from $E_{\mathrm{T}}^{\mathrm{miss}}$caused by detector imperfections.

In the fast detector simulation using only Gaussian parametrisation of the $E_{\mathrm{T}}^{\mathrm{miss}}$ resolution, such fake $E_{\mathrm{T}}^{\mathrm{miss}}$ effects are not described. A former ATLAS study [52], investigated cleaning cuts for the fully simulated dijet samples that remove possible large non Gaussian tails of fake $E_{\mathrm{T}}^{\mathrm{miss}}$ and bring the ratio between $E_{\mathrm{T}}^{\mathrm{miss}}$ in fast and detailed detector simulation closer to one.

Since we are not using fast detector simulation of dijet events but only W and Z boson events with large physical $E_{\mathrm{T}}^{\mathrm{miss}}$ in the multivariate training phase, we are not really affected by such discrepancies. On the other hand, it could prove useful to reject events that contain very probably larger amounts of fake $E_{\mathrm{T}}^{\mathrm{miss}}$ to improve the $E_{\mathrm{T}}^{\mathrm{miss}}$ resolution. For this reason we checked whether the suggested cuts in [52] could be useful for the analysis in terms of enhanced background rejection.

Firstly, events that include at least one jet with a $p_{\mathrm{T}} > 20$ GeV hitting the region ($1.3 < |\eta| < 1.7$) are rejected. Due to the cone size of the jet a partially hit of this region will result into an underestimation of jet energy. Therefore, though the crack with the worst mismeasurement is closely to $|\eta| = 1.5$ a relative large region is vetoed.

Secondly events are rejected that include at least one jet with a $p_{\mathrm{T}} > 20$ GeV and with a ϕ coordinate projection closer than 0.5 of to the $E_{\mathrm{T}}^{\mathrm{miss}}$direction, $\Delta\Phi_{\mathrm{jet},\tilde{\mathrm{E}}_{\mathrm{miss}}^{\mathrm{T}}} < 0.5$. This is motivated by the observation that in case of jet mismeasurements for other reasons than due to the crack region the fake $E_{\mathrm{T}}^{\mathrm{miss}}$ remains often close to the mismeasured jet. This is e.g. the case for leptonic decays within the jet.

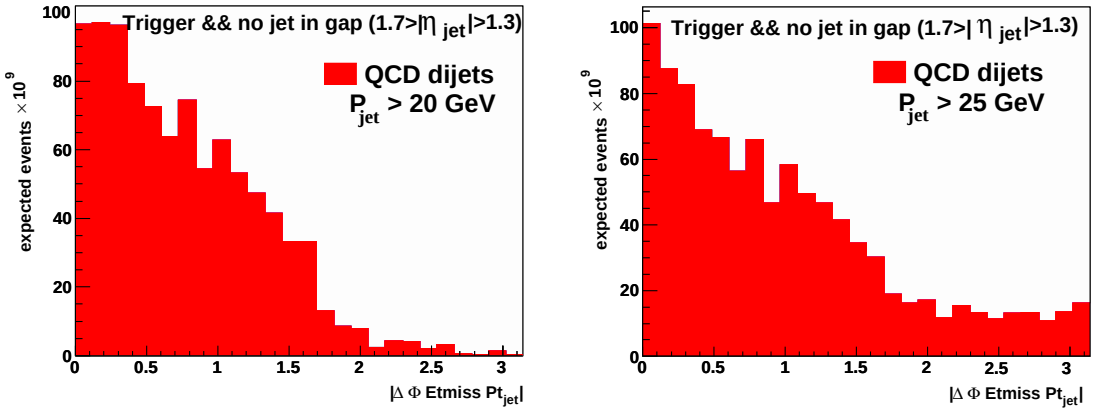

Fig. 5.13: *Distribution of the $\Delta\Phi_{\mathrm{jet},\tilde{\mathrm{E}}_{\mathrm{miss}}^{\mathrm{T}}}$ for jets in dijet events that pass the offline trigger and have no jets pointing to the gap region, left: with a cut on jet p_{T} of 20 GeV the distribution accumulates to values below 1.5 rad. right: with a cut on jet p_{T} of 25 GeV the distribution starts to have tails to larger values.*

Indeed combining both criteria above one looses only about 16.6 % of signal events but 27.5 % less W and Z boson events are selected. From theses results one can conclude that these cleaning can be an useful addition to the preselection of the multivariate analysis. But as demonstrated in Sec. 5.3.4 the number of MC training events is not so plenty that one can afford to apply these cuts on fully and fast

detector simulated samples. In a hypothetical search with 30 fb^{-1} the situation may change. Even if the $E_{\mathrm{T}}^{\mathrm{miss}}$ resolution at that time may be the result of very refined algorithms it seems to be reasonable to cut out at least the crack region if enough data and MC is available.

If one performs a simple cut-based analysis these additional cuts to suppress background can become useful. Therefore, we added this fake-$E_{\mathrm{T}}^{\mathrm{miss}}$ cleaning to the cut-based cross check analysis. As Fig. 5.13 indicates a cut on $p_{\mathrm{T}} > 20$ GeV seems to be advantageous in terms of rejection of dijets by this cleaning criterion. In this context we also checked whether a ΔR criterion is superior to the simple $\Delta\Phi$ projection since the spatial η distance enters in this quantity. A ΔR criterion could be important for recovering events which have a small distance to the $E_{\mathrm{T}}^{\mathrm{miss}}$ direction in the $\Delta\Phi$ projection but the η values are different. Of course one expects not only signal events but also a part of the W and Z boson background to be recovered by such a criterion. Indeed it turned out that the condition $\Delta R_{\mathrm{jet},\tilde{\mathrm{E}}_{\mathrm{miss}}^{\mathrm{T}}} < 1.5$ can be a good alternative to the $\Delta\Phi_{\mathrm{jet},\tilde{\mathrm{E}}_{\mathrm{miss}}^{\mathrm{T}}} < 0.5$ condition. The expected signal stays virtually the same and only a 2% additional gain in W and Z boson background rejection was observed, which indicates that within statistical uncertainties both methodes are comparable. However, the comparison of the distribution of $\Delta R_{\mathrm{jet},\tilde{\mathrm{E}}_{\mathrm{miss}}^{\mathrm{T}}}$ with $\Delta\Phi_{\mathrm{jet},\tilde{\mathrm{E}}_{\mathrm{miss}}^{\mathrm{T}}}$ in case of dijets gave the impression that a simple cut on the projection onto the ϕ coordinate will separate background slightly better. Therefore, we kept the $\Delta\Phi_{\mathrm{jet},\tilde{\mathrm{E}}_{\mathrm{miss}}^{\mathrm{T}}}$ condition.

Choice of the cut on isolation of direction of missing energy

The minimal distance in the ϕ-coordinate projection between one of the tagging jet candidates and the $E_{\mathrm{T}}^{\mathrm{miss}}$ direction, is called missing energy isolation I.

$$I = min|\Delta\Phi_{\mathrm{tagjet},E_{miss}^{\mathrm{T}}}|. \tag{5.3}$$

This variable is very discriminating, since the signal tends to have missing transverse momentum well separated from the tagging jets stemming from Higgs decays between the tagging jets. To visualise the power of the missing energy isolation variable, especially against the QCD dijets, we present in Fig. 5.14 the 2-dimension distribution of the variables I versus $\Delta\Phi_{\mathrm{j1j2}}$ for the W and Z boson backgrounds, the signal with $M_{\mathrm{H}} = 200$ GeV and $\omega = 5$ and the QCD dijets samples. All cuts (C10 to (C10) listed in 5.4.2 are applied to the distributions except for the QCD dijet sample for which we left out the $E_{\mathrm{T}}^{\mathrm{miss}}$cut. The W and Z boson backgrounds tend to populate more homogeneously a lager range in I versus $\Delta\Phi_{\mathrm{j1j2}}$ with out preferring extreme values. One recognises that the signal is slightly tending to occupy a corner of the phase space with a small $\Delta\Phi_{\mathrm{j1j2}}$ and a larger missing energy isolation I. In this region however are the QCD dijets very sparsely present and hardly visible. A combination of I and $\Delta\Phi_{\mathrm{j1j2}}$ cuts is a way to get rid of the dijets effectively in searches for the invisible Higgs boson. This was already observed and exploited in [7]. Therefore, we scanned this cut after applying all other cut for an optimal cut value, in terms of a figure of merit [127]. The result is shown in Fig. 5.15 for the signal hypothesis with $M_{\mathrm{H}} = 200$ GeV and $\omega = 5$, but it was checked that it applies equally well for other hypotheses. As result of this scan we chose a cut on $I > 2.42$, which reduces the W and Z boson background at that stage about 10% while the loss in signal is only 1%. With the information of these preparing studies we finally decided on a sequence of cuts as follows.

5.4.2 Selection cuts

The selection starts with the trigger cuts simulated offline (C1) followed by the conditions (C2-C6) preparing the weak boson fusion topology. The subsequent cuts (C7-C12) accumulate the signal-like invisible decay final state with prominent $E_{\mathrm{T}}^{\mathrm{miss}}$.

(C1) one reconstructed jet (p_{T}>23GeV) within $|\eta| < 3.2$ and one reconstructed jet (p_{T}>23GeV) within $4.9 > |\eta| > 3.2$ and $E_{\mathrm{T}}^{\mathrm{miss}} > 80$ GeV in the event.

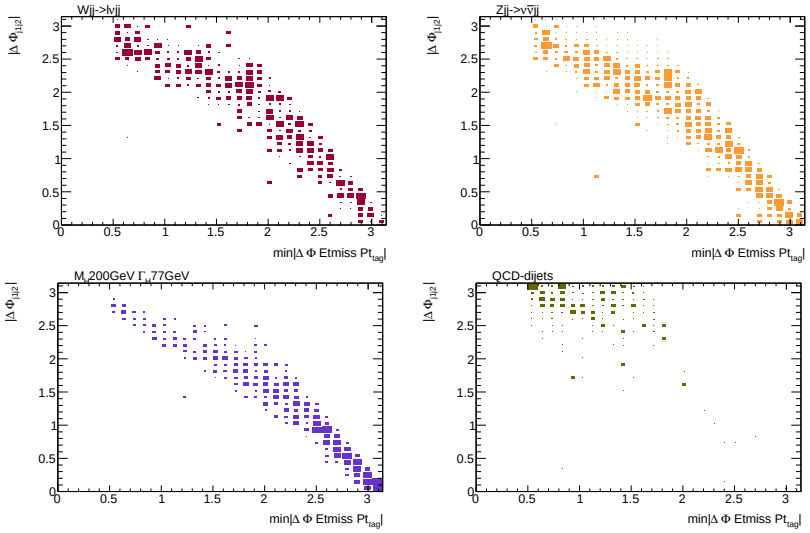

Fig. 5.14: *The distribution of the missing energy separation* $I = min|\Delta\Phi EtmissPt_{tag}|$ *versus* $\Delta\Phi_{\mathrm{j1j2}}$ *after cuts for the W boson background (red histogram), the Z boson background (yellow histogram), the signal (violet histogram) with* $M_{\mathrm{H}} = 200$ GeV *and* $\omega = 5$ *and the QCD dijets samples (green histogram). All cuts (C10 to (C10) listed in 5.4.2 are applied to the distributions except for the QCD dijets, for which we left out the* $E_{\mathrm{T}}^{\mathrm{miss}}$ *cut.*

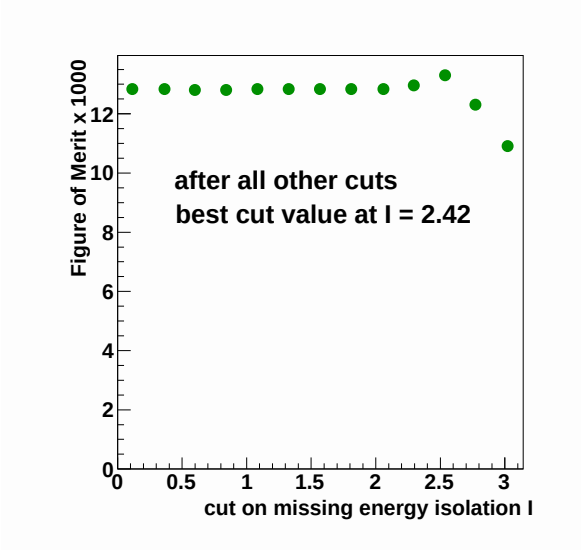

Fig. 5.15: *Optimised cut on the missing energy isolation I. The Signal in this case is a Higgs with* $M_{\mathrm{H}} = 200$ GeV *and* $\omega = 5$. *All cuts of the cut-based selection, detailed in the next section, are applied before, hence the final gain after cuts in the most important at this stage W/Z plus jets boson background rejection is only 10% at this stage but only 1% signal efficiency loss.*

(C2) $p_{\mathrm{j1}}^{\mathrm{T}} > 40$ GeV for the first tagging jet candidate.

(C3) $p_{\mathrm{j2}}^{\mathrm{T}} > 40$ GeV for the second tagging jet candidate.

(C4) $\eta_{\mathrm{j1}} \times \eta_{\mathrm{j2}} < 0$ demanding the two tagging jet candidates to be in opposite hemispheres of the ATLAS detector.

(C5) $\Delta\eta_{\mathrm{j1j2}} > 4.4$.

(C6) $M_{\mathrm{j1j2}} > 1200$ GeV requiring a very high invariant dijet mass in the event.

(C7) events are cleaned for possible source of fake $E_{\mathrm{T}}^{\mathrm{miss}}$. First of all the so-called "crack region" $1.7 > |\eta| > 1.3$ is cut out since it has considerable lower jet reconstruction efficiency. Also there should be no jets with $p_{jet}^{\mathrm{T}} > 20$ GeV closer in the ϕ coordinate projection than $\Delta\Phi_{\mathrm{jet},\tilde{\mathrm{E}}_{\mathrm{miss}}^{\mathrm{T}}} < 0.5$.

(C8) $E_{\mathrm{T}}^{\mathrm{miss}} > 100$ GeV.

(C9) vetoing identified isolated leptons. Events are rejected if an electron or muon with $p_{\mathrm{T}} > 20$ GeV or a tau lepton with $p_{\mathrm{T}} > 30$ GeV is identified in the event. The lepton is checked to have at least a $\Delta R_{\mathrm{nextjet}} > 0.2$ to be called isolated.

(C10) vetoing of central mini jets. Events are rejected if an additional jet with $p_{jet}^{\mathrm{T}} > 30$ GeV if found in a range of $|\eta| < 3.2$.

(C11) the missing energy isolation (defined in Eq. 5.3) is required to be large, i.e. $I > 2.42$.

(C12) the azimuthal difference of the tagging jets is restricted to $\Delta\Phi_{\mathrm{j1j2}} < 1$.

Since the cut-based analysis usues a similar cut in the $E_{\mathrm{T}}^{\mathrm{miss}}$ distribution and generally harder cuts in the same jets kinematic distributions like the preselection of the multivariate analysis, we relinquish to show the cuts sequence here again. The new ingredients, namely the cuts in the missing energy isolation I. and $\Delta\Phi_{\mathrm{j1j2}}$ are motivated already by Fig. 5.14, which contains the cuts(C1) to (C10).

5.4.3 Factorisation approach in the cut-based analysis

The cut-based analysis was performed on the sparse detailed detector simulated background samples. Since very hard cuts are used for background suppression, it was desired to find a factorisation of the cuts to estimate the background contributions. After cuts, only the signal sample has a sufficient statistics left. This offered us the possibility to cross-check the factorisation in the backgrounds by comparing the factorisation result of the signal with the actually not factorised selection on the signal. It could be verified that the numbers were very similar between expected signal after cuts and expected signal in the factorisation approach.

An overview about the grouping of cuts for the factorisation of the cut-based selection is given in Tab. 5.8. Again like in Sec. 5.2.1, the factorisation of the mini jet veto and the isolated lepton veto was made (in block 5 and block 6 in Tab.5.8), and the cuts on the tagging jets were grouped as in the preselection factorisation (block 2). As before loosening the $E_{\mathrm{T}}^{\mathrm{miss}}$ cut provided more dijets and $t\bar{t}$ events for the determination of the individual efficiencies for the blocks of cuts. But as Tab. 5.6 shows, the missing energy isolation I and $\Delta\Phi_{\mathrm{j1j2}}$ are more than 20 % correlated to $E_{\mathrm{T}}^{\mathrm{miss}}$. Also I and $\Delta\Phi_{\mathrm{j1j2}}$ are highly correlated between each other. This forced the cuts on I and $\Delta\Phi_{\mathrm{j1j2}}$ in one block (see block 7 in Tab. 5.8) and after the $E_{\mathrm{T}}^{\mathrm{miss}}$ cut (block 4). For the QCD dijets and $t\bar{t}$ pairs the $E_{\mathrm{T}}^{\mathrm{miss}}$ cut was lowered to 30 GeV. This can be motivated for the QCD dijets by Fig. 5.16, in which the correlation between $E_{\mathrm{T}}^{\mathrm{miss}}$ and I and $\Delta\Phi_{\mathrm{j1j2}}$ for the dijet sample are displayed. Most of the dijets accumulated below $E_{\mathrm{T}}^{\mathrm{miss}} = 30$ GeV.

	combined cuts
block 1	CJ$\oplus$FJ$\oplus E_{\mathrm{T}}^{\mathrm{miss}} > 80$ GeV (C1)
block 2	CJ$\oplus$FJ$\oplus E_{\mathrm{T}}^{\mathrm{miss}} > 0$ GeV weak boson fusion topology (C2-5) $M_{\mathrm{j1j2}} > 1200$ GeV (C6)
block 3	block 2 Anti fake $E_{\mathrm{T}}^{\mathrm{miss}}$ clean (C7)
block 4	dijets,$t\bar{t}$: CJ$\oplus$FJ$\oplus E_{\mathrm{T}}^{\mathrm{miss}} > 0$ GeV W/Z+jets:block 3 $E_{\mathrm{T}}^{\mathrm{miss}} > 100$ GeV (C8)
block 5	CJ$\oplus$FJ$\oplus E_{\mathrm{T}}^{\mathrm{miss}} > 0$ GeV isolated lepton veto (C9)
block 6	CJ$\oplus$FJ$\oplus E_{\mathrm{T}}^{\mathrm{miss}} > 0$ GeV mini jet veto (C10)
block 7	block 3 dijets,$t\bar{t}$: $E_{\mathrm{T}}^{\mathrm{miss}} > 30$ GeV W/Z+jets:$E_{\mathrm{T}}^{\mathrm{miss}} > 100$ GeV I (C11) $\Delta\Phi_{\mathrm{j1j2}}$ (C12)

Tab. 5.8: Combination of cuts used in the factorisation of the background samples in the cut-based selection.

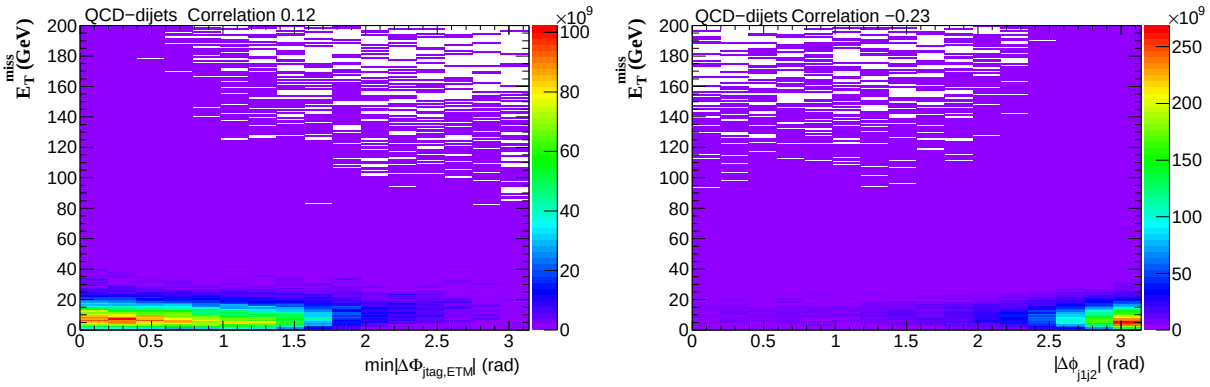

Fig. 5.16: *Correlations found in the QCD dijet samples between $E_{\mathrm{T}}^{\mathrm{miss}}$ and the missing energy isolation $I = \min|\Delta\Phi_{\mathrm{jtag,ETM}}|$ (left) and $E_{\mathrm{T}}^{\mathrm{miss}}$ with $|\Delta\Phi_{\mathrm{j1j2}}|$ (right). As consequence of the observed correlation between these we introduced a $E_{\mathrm{T}}^{\mathrm{miss}} > 30$ GeV cut before factorising the cuts on these two quantities (see Tab. 5.8 block 7).*

Cutflow table for example signal hypothesis $M_{\mathrm{H}} = 200$ GeV and $\omega = 5$ and factorised backgrounds

In 5.9 the results for the estimate of example signal $M_{\mathrm{H}} = 200$ GeV and $\omega = 5$ hypothesis the various background selected are summarised. As one can expect the background processes with large real $E_{\mathrm{T}}^{\mathrm{miss}}$, like the W and Z boson background remain as the dominant backgrounds afters. The top pair background is predicted by the factorisation approach to be well separable. Even with the factorisation we predict that the QCD dijet background will be marginalised below one event. The combination of the requirement $I > 2.42$ with $\Delta\Phi_{\mathrm{j1j2}} < 1$ describes a region of phase space that is hardly populated by the QCD dijets and were the number of MC events became extremely sparse.

cut	Signal	W$\to l\nu$	Z$\to \nu\bar{\nu}$	Z$\to \ell^+\ell^-$	$t\bar{t}$	QCD dijets
(C0) before preselection	81505	116729251	12699690	11465215	13844454	$5.72385{\cdot}10^{14}$
(C1) trigger	11508	3280106	720660	75800	656559	10574750
(C2) jet 1 $p_{\mathrm{T}} > 40$ GeV						
(C3) jet 2 $p_{\mathrm{T}} > 40$ GeV						
(C4) $\eta_{\mathrm{j1}} \times \eta_{\mathrm{j2}} < 0$						
(C5) $\Delta\eta_{\mathrm{j1j2}} > 4.4$						
(C6) $M_{\mathrm{j1j2}} > 1.2$ TeV	3064	188743	33698	4147	16661	320761
(C7) clean for fake $E_{\mathrm{T}}^{\mathrm{miss}}$	2555	101536	19644	1951	4711	95591
(C8) $E_{\mathrm{T}}^{\mathrm{miss}} > 110$ GeV	2170	59198	14140	1196	2872	31905
(C9) isolated leptons veto	2168	45091	13904	798	1263	31336
(C10) central jet veto	1859	25897	9396	592	235	18919
(C11) $I > 2.42$						
(C12) $\Delta\Phi_{\mathrm{j1j2}} < 1$	819	4670	2090	67	46	0

Tab. 5.9: Cutflow for the cut-based selection in number of expected events in 30 fb^{-1}. The signal sample shown is a Higgs boson with $M_{\mathrm{H}} = 200$ GeV and $\omega = 5$.

As mentioned above a comparison between the number of events selected if the high statistics signal sample is passing the not factorised cut flow with the number of estimated selected signal events following from the factorisation ansatz, can provide a feeling for the accuracy of the factorised estimate. In the presented case of the signal hypothesis of $M_{\mathrm{H}} = 200$ GeV and $\omega = 5$ the deviation between the two methods is only 0.8 % (819 expected from factorisation compared to not factorised 826 expected events). This shows that at least for the signal the factorisation works well enough and seems to take correctly into account the correlation between the cut variables suffiently. Of course this conclusion is not necessarily the true for the backgrounds but it is a hint that the factorised numbers for the backgrounds may present a reasonable estimate of the number of events that would be selected in a high statistics background sample.

Again as in the case of the preselection the efficiency for the signal hypothesis is determined as ratio of selected to all event weights. Since this time harder cuts were needed separate the signal from the huge background the efficiencies are much lower than for the relatively lose preselection. The cut-based analysis selected the signal with efficiencies of roughly 1 % up to 2.3 %. The highest efficiencies usually occur for signals that are heavier or very broad, since these contain a larger amount of $E_{\mathrm{T}}^{\mathrm{miss}}$. It should be emphasised that the cut-based selection was intended as a cross check. The cuts were chosen very hard to reduce the background level sufficiently to test for an exclusion in the stealthy Higgs scenario. No particular efforts to optimise the cuts or consider alternative cuts were pursued.

6. Estimate of systematical uncertainties

When running a high energy experiment and selecting data in a physics channel these data is subject to statistical fluctuations. But the relative impact of this statistical fluctuation can become in principle arbitrarily small if one collects data long enough. The same is true for prediction in the physics channel on basis of simulated events. By raising the amount of simulated events the statistical uncertainty on the prediction can be minimised. But the latter is only true if the systematic uncertainties of a measurement are small compared to the statistical uncertainty of the selected event sample. If the systematical uncertainties prove to be larger, they have to be included into the inferring of results since they pose a principal limit on the accuracy.

In this chapter possible contributing sources of systematic uncertainties are named and a rough estimate of the impact on the result of the major sources is given. This is done for the cut-based analysis and the multivariate analysis separately. As announced in this chapter we will optimise the final selection cut on the multivariate output with respect to the expected sensitivity under influence of systematic sources. For this reason the sensitivity and its dependency on the background uncertainty and the limit setting is briefly defined at the beginning of this chapter before the systematics are determined.

6.1 Determination of the upper limit on cross sections and possible exclusion of hypotheses

In general the result of a search can be reported in terms of the model dependent parameter ξ^2, which is the scaling factor of the SM cross section σ_{SM} to the beyond Standard Model cross section σ_{BSM} under consideration. With σ_{BSM} being the stealthy Higgs cross section for invisible decays, it already includes the branching[1)] into invisible particles. By this scaling to a known quantity as the SM cross section, model comparisons become easier.

$$\xi^2 = \frac{\sigma_{\mathrm{BSM}}}{\sigma_{\mathrm{SM}}}. \tag{6.1}$$

In case a search finds no hint for a signal excess above background, e.g. the number of observed candidates is compatible with the number of expected background events, one can report an upper limit on ξ^2. The search will be more sensitive the lower the upper limit on ξ^2 can be pushed.

The result of a search which is only performed once in a given data set is the outcome of a single experiment. If one claims to have excluded a signal on basis of the data, one can ask for the degree of belief in that exclusion. Because clearly there is always the (unwanted but inevitable) possibility due to downward fluctuations of the signal and for the background to wrongly exclude a signal in data. A repetition of the experiment in a newly acquired data set may yield a different result which, correctly, may not exclude the signal if it exists in nature.

Conventionally one tries to reach an exclusion of the “signal plus background” hypothesis at the confidence level (CL) of 95 %. This means in other words that the outcome of repeated searches in independent data sets will only in 5 % or less of all cases come to the wrong conclusion on the basis of the analysed data set that an in nature existing signal is excluded.

[1)] In the literature about invisible Higgs searches one often finds the definition $\xi^2 = \frac{B(\mathrm{H}\to\mathrm{invisible})\sigma_{\mathrm{BSM}}}{\sigma_{\mathrm{SM}}}$

An individual model or "signal plus background" hypothesis is given when the expected signal strength S is fixed by a choice of a point in the stealthy Higgs parameter plane ($M_H - \omega$) corresponding to a ξ^2. One always expects to select B background events from the SM. So the mean number of expected events μ if the signal is present is then $\mu = S + B$. Making an observation of N_{obs} events one can interpret the result in the language of a simple Poisson counting experiment. The probability to observe N_{obs} events when one expect $\mu = S + B$ events according to the "signal plus background" hypothesis is given by

$$P(N_{obs}|signal(\xi^2) + background) = \frac{(S+B)^{N_{obs}} e^{-(S+B)}}{N_{obs}!}. \tag{6.2}$$

In order to test the consistency of a "signal plus background" hypothesis for a given model with the data set one can ask for the probability $P(n \leq n_{obs}|signal(\xi^2) + background)$ that the outcome of the experiment yields $n \leq N_{obs}$ candidates when a specific "signal plus background" hypothesis is realised in nature. The value of the probability $P(n \leq N_{obs}|signal(\xi^2) + background)$ for that is found by integration of the probability distribution from 0 to N_{obs}. Requiring that the value of the probability of finding less than N_{obs} events in data does not exceed 0.05 is therefore equivalent with excluding "signal plus background" hypothesis at 95 % confidence level, since only in 5 % of identical experiments such rates would be observed if the signal is present in nature.

$$P(n \leq N_{obs}|signal(\xi^2) + background) \leq 0.05 \tag{6.3}$$

If no experiment is performed so far and real data is absent, one can characterise the expected sensitivity of the search. For the exclusion of the "signal background" hypothesis one assumes to have observed only the average expected background rate $N_{obs} = B$. But in nature B as well as the measured $\mu_{\text{U.L.}} = S + B$, from which we are going to derive the upper limit of our experiment, can statistically fluctuate. Again one can ask the question under which condition the true "signal plus background" hypothesis can be excluded wrongly. E.g. this could be the case if $N_{obs} = B = \mu_{\text{U.L.}} - q \times \Delta\mu$ is the result of the downward fluctuation of $\mu_{\text{U.L.}}$ of about q times its statistical error $\Delta\mu = \sqrt{S+B}$. In connection with setting upper limits on ξ^2 it is useful for larger numbers to translate the 95 % CL condition Eq. 6.3 into the quantiles of the normal distribution. Since the upper limit is a single sided boundary the quantile of 95 % corresponds to $q = 1.64$ standard deviations.

$$N_{obs} = \mu_{\text{U.L.}} - 1.64 \times \Delta\mu \tag{6.4}$$

Again in other words that means an exclusion of "signal plus background" hypothesis on basis of N_{obs} events happens to be wrong in 5 % or less of the experiments if the signal exist and μ fluctuates down about more than 1.64 standard deviations.

Additionally to the statistical uncertainties one has to deal with systematical uncertainties that influence the expected limit, as explained in the next section.

Inclusion of systematic uncertainty on background

A selection of events has also to include the systematical uncertainties coming along with the selection. If one expects to select the mean number of $\mu = S^{BSM} + B^{MC}$ events the systematic error of the signal ΔS^{BSM}_{sys} and the background ΔB_{sys}, assumed to be uncorrelated, has to be added in quadrature to the statistical error.

With inclusion of systematical uncertainties the exclusion condition Eq. 6.4 becomes

$$N^{obs} = \mu_{\text{U.L.}} - 1.64\sqrt{S^{BSM} + B^{MC} + \Delta B^2_{sys} + \Delta S^{BSM\,2}_{sys}} \tag{6.5}$$

And since we assume in lack of any data to have observed $N^{obs} = B^{MC}$ events we simplify this equation to

$$S^{BSM}_{\text{U.L.}} = 1.64\sqrt{S^{BSM} + B^{MC} + \Delta B^2_{sys} + \Delta S^{BSM2}_{sys}}, \tag{6.6}$$

using $\mu_{\text{U.L.}} = S^{BSM}_{\text{U.L.}} + B^{MC}$ for the mean number of selected events. Replacing $S^{BSM}_{\text{U.L.}} = \varepsilon^{BSM}\sigma^{BSM}_{\text{U.L.}}\mathscr{L} = \varepsilon^{BSM}\xi^2_{\text{U.L.}}\sigma^{SM}\mathscr{L}$ yields an expression for the upper limit quadratically in $\xi^2_{\text{U.L.}}$.

$$\xi^2_{\text{U.L.}} \quad = \quad \frac{1.64\sqrt{\varepsilon^{BSM}\xi^2_{\text{U.L.}}\sigma^{SM}\mathscr{L} + B^{MC} + \Delta B^2_{sys} + \Delta S^{BSM2}_{sys}}}{\varepsilon^{BSM}\sigma^{SM}\mathscr{L}}. \tag{6.7}$$

Solving for $\xi^2_{\text{U.L.}}$ yields and simplify the result algebraically leads to

$$(\xi^2_{\text{U.L.}})_{1,2} = \frac{1.64^2}{2\varepsilon^{BSM}\sigma^{SM}\mathscr{L}}\left(1 \pm \sqrt{1 + \frac{4(B^{MC} + \Delta B^2_{sys} + \Delta S^{BSM2}_{sys})}{1.64^2}}\right) \tag{6.8}$$

In good approximation with deviations within a percent one can neglect the signals statistical error. Additionally in this study is the contribution of the signal's systematic uncertainty is very small compared to the background and its uncertainty. Therefore, we calculate the upper limit on ξ^2 with Eq. 6.9.

$$\xi^2 \approx \frac{1.64\sqrt{(B^{MC} + \Delta B^2_{sys} + \Delta S^{BSM2}_{sys})}}{\varepsilon^{BSM}\sigma^{SM}\mathscr{L}} \approx \frac{1.64\sqrt{(B^{MC} + \Delta B^2_{sys})}}{\varepsilon^{BSM}\sigma^{SM}\mathscr{L}} \tag{6.9}$$

The danger of a false exclusion of a "signal plus background" hypothesis is extremely severe if the number of candidates fluctuates downwards in combination with a systematic overestimation of the expected background. If in the expected mean too few background are assumed, this yields an artificially high extracted signal and therefore a weak upper limit.

When estimating the size of the systematics effects in the next section we apply variations to the input variables, simulating the detector-related systematic effects. Depending on the direction of variation the resulting background expectation after the MLP cut can rise of fall. But for the limit setting we have to take not the largest relative change due to such a variation but that direction of this variation which leads to a systematically smaller background expectation, i.e. an overestimation of the background rate by the nominal prediction.

6.2 Estimate of systematic uncertainties

First we discuss two uncertainties that directly influence the expected event yield via normalisation uncertainties. After that we continue with more intrigued effects of detector-related uncertainties that affect the actual event selection.

Theoretical uncertainties of SM cross sections

The sensitivity study presented is scaled to 30 fb^{-1}. Cross section uncertainties would result in uncertainty of the predicted rates for events from simulated events. The error on the normalisation affects samples differently.

At the time of having collected sufficient integrated luminosity one can assume that the early physics program at the LHC has successfully determined the SM cross section of background processes or at

least devised reliable methods to estimate the background from data. Therefore currently large cross section theoretical uncertainties, e.g. 10 % remaining uncertainty (including PDF sets and QCD scale uncertainities) on the NNLO results for W and Z bosons plus jets or of the NLO $t\bar{t}$ cross section at 14 TeV, quoted to be $\sigma_{t\bar{t}} = (833 \pm 100)$ pb in [129], are not included in the systematic error.

Uncertainties related to limited MC statistics

At various stages the analyses encountered limited MC event statistics. Attempts of estimates by factorisation in the cut-flow selections were made. To supply sufficient statistics for the training of multivariate methods larger ATLFAST-1 samples were used. Still the selection of the fully simulated events has uncertainties of 5 % to 10 % due to the large weights for some backgrounds. In the hope that an analysis in a 30 fb^{-1} scenario would not suffer a lack of fully simulated MC events in training, we quote the sensitivity of such search without a systematic contribution of limited MC samples statistics.

Luminosity uncertainty

In a series of studies published in [7] the estimated uncertainty in the luminosity determination was quoted to be 3 % for 30 fb^{-1} which we will adopt. The uncertainty of the luminosity will result in a normalisation error of measured cross sections or for simulated samples in a global normalisation error, which affects all samples in the same way. This error can be simply added in quadrature to the background uncertainty.

6.2.1 Determination of detector-related systematic uncertainties

The study of detector-related systematic effects follows the recommendation used through out the studies of [7]. These recommendations for the size of systematic variations are based on preliminary studies on simulated events and test beam data before ATLAS started data taking. The recommended numbers are expected to be valid for an assumed collected luminosity of 10 fb^{-1}. Detailed studies of systematic effects are an ongoing task during commissioning and early data taking. A study carried out on a collected data set of 30 fb^{-1} will make use of a detailed description of many detector-related systematic effects. It is not unreasonable to hope that the numbers of [7] will prove to be conservative for the three times larger data set.

Energy scale of jets

The experience at the TeVatron already proved that a good understanding of the jet energy scale (JES) is crucial for many physics analyses at hadron colliders. And the studies of [7] indicated this to be true for the LHC, too. The peculiarity of the presented invisible Higgs study is that it essentially uses jet properties and the amount of $E_{\mathrm{T}}^{\mathrm{miss}}$ in event selection. Therefore, it is expected that the jet energy scale uncertainty will pose the limiting factor for the sensitivity of the search.

Since finally one wants to deduce properties of primary scattered partons from energy deposits in the calorimeter which are clustered by the applied jet algorithm to jets, it will be necessary to unfold the detector effects as accurately as possible. In the following some effects that have to be corrected are listed.

1) correction of the hadronic scale
   Maybe the most important effect is the correction of non-compensation in the ATLAS calorimeters. This means the calorimeter response to hadrons is lower than to electrons and photons. The latter two can be exactly measured in the electromagnetic calorimeters. This defines the EM scale of the calorimeters, which had to be established before by test beams data. Hadrons that reach the

calorimeter develop a shower. The ratio of the electromagnetic to hadronic component in the shower is subject to fluctuations. From the hadronic component due to non compensation only a fraction is measured. This defines the hadronic scale of the calorimeters. Some energy is for example lost in nuclear break up reactions.

2) dead material effects
Likewise one has to correct for energy losses in inactive regions, so-called dead material.

3) shower leakage effects
Further corrections of leakage of particles that are not contained by the calorimeter are applied.

4) pile up effects
Subtraction of the average uncorrelated pile up energy is necessary, at least for higher instantaneous luminosities.

5) effects of jet reconstruction
Inefficiencies specific to jet algorithms like "out of cone" leakage, which refers to hit cells that are not clustered, or from splitting and merging of clusters between jets have to be taken into account. For the precise definition of jet energy scale in relation to the parton level also theoretical shortcomings of the used jet algorithms have to be considered e.g. infrared safety.

For the calibration of the jet energy there exist in principle two methods, namely MC-based calibration studies and in-situ calibration with well understood physics processes. A calibration on basis of simulated events is described in [54]. So called truth jets that include on generator level all stable particles except neutrinos and muons were build with a jet algorithm. These truth jets are then compared to the simulated jets reconstructed by the detailed simulation. Here the jet p_{T} response $R = p_T^{reco\,jet} / p_T^{truth\,jet}$ of the transverse momenta, which is related to the jet energy scale, is defined. As reference the kinematics of the corresponding truth jets is used. The η and p_{T} (on EM scale) dependent average corrections are applied jet for jet to bring R close to one.

In the process to determine these calibration factors from MC one is confronted with some problems. If one uses this MC method it has to be taken into account as uncertainty that particles may fall out of the reconstructed jet but are collected by the truth jet. The used samples and generators have to be validated against data. Only if the agreement between data and MC is sufficient, these samples can be used. It has to be taken into account that shower and underlying event models influence the corrections. Also it is expected that the choice of topology as well as the flavour composition of the simulated jets may be of influence. Therefore, a variety of generators is tested and the effects estimated. Aside from the theoretical model of the MC generation, the correction may also be affected by residual uncertainties stemming from material budget of the calorimeter (dead material) or description of electronic noise and other experimental condition as alignment and beam spot deviations. All those factors have to be quantified by MC variations and use of test beam data. Therefore, the calibration factors will not perfectly calibrate the JES and will contribute to the JES uncertainty.

In [54] these method has been studied and performed on basis of 7 nb^{-1} data collected at $\sqrt{s} = 7$ TeV. The result quotes a total uncertainty below 10 % for jets with a p_{T} of more than 20 GeV and 6.5 % for jets of more than 100 GeV in the barrel. Additionally pile up at that very low luminosity (in average 1.09 pileup events) influences the JES accuracy by about 2 %. These results are already better than the uncertainties assumed in [7].

The MC method sketched above contains many complications. Thus the preferred methods are the so-called "in-situ" calibrations, which will start to be pursued in early data taking. Their advantage is that one can become independent of all modelling shortcomings of simulation since data is used for calibration. As an example one can select a clean sample of a so-called tag photon recoiling against one so-called probe jet. Since the transverse energy of the photon E_T^{EM} can be exact determined in

the electromagnetic calorimeter, the measurement on the probe side gives E_T^{HAD}. Since the transverse momentum is conserved E_T^{HAD}/E_T^{EM} should be one. From these samples one can deduce $\eta-$ and p_{T}-dependent correction factors for the measured hadronic jet energy scale directly in one step. Of course even this method applied on average will deal with residual uncertainties, but it will be the preferred way to determine the the jet energy during data taking. Also the accuracy can improve with longer data taking.

Jet energy scale variations

We gave the short overview about the recent status of the jet energy scale in 6.2.1 to explain that it is difficult to determine. The jet energy scale can also deteriorate even if only very few pile up events are present. Therefore, counter measures like subtraction of the average pile up event contributions have to be applied. Further it shows that early estimates from data (or "in-situ") are quite promising and that uncertainties may have to be considered p_{T}- and $\eta-$dependent.

The recommendation of the published studies [7] available so far were much more crude estimates of the JES.

The hermicity of the calorimeter system allows the efficient reconstruction of jets over a large range of η, though the detector components and properties like granularity and material differ especially between barrel and forward calorimetry. The latter one is expected to measure forward jets not as well at the barrel part. This was taken into account by assigning different JES uncertainties in two pseudorapidity bins. The systematics variations for either up or down scaling is done jet by jet by an amount according to the scaling factor of its respective η-value.

The following scaling factors are given in [7] and are expected to be valid for 10 fb^{-1}.

$$\begin{aligned} E'_{jet} &= (1\pm\ 7\%)\times E_{jet} \text{ for } |\eta| \leq 3.2 \\ E'_{jet} &= (1\pm 15\%)\times E_{jet} \text{ for } |\eta| > 3.2 \end{aligned}$$

When applying such large variations in the systematics the overall uncertainties for the multivariate analysis becomes more than 20 %. We ran our complete analysis and determined with Eq. 6.9 the expected upper linit on ξ^2 , using the expected mean of events and this estimate of systematic background uncertainty. Even with a hard cut on the MLP output larger than 0.9, no exclusion for any stealthy Higgs hypothesis in the scanned parameter range was possible.

Seeing this we decided to turn the question around and to quantify on which level the JES uncertainty is needed for the multivariate analysis to have sensitivity left. We therefore tried first roughly a half of the recommended uncertainties, keeping the two η ranges.

$$\begin{aligned} E'_{jet} &= (1\pm\ 3.5\%)\times E_{jet} \text{ for } |\eta| \leq 3.2 \\ E'_{jet} &= (1\pm\ 7.0\%)\times E_{jet} \text{ for } |\eta| > 3.2 \end{aligned} \tag{6.10}$$

Even that proved to be too large for the multivariate analysis retaining its sensitivity. Eventually we performed the JES variation only within a quarter of the original recommendation, again in two η ranges.

$$\begin{aligned} E'_{jet} &= (1\pm\ 1.75\%)\times E_{jet} \text{ for } |\eta| \leq 3.2 \\ E'_{jet} &= (1\pm\ 3.75\%)\times E_{jet} \text{ for } |\eta| > 3.2 \end{aligned} \tag{6.11}$$

For comparison, in summer 2011 the ATLAS experiment, running at $\sqrt{s} = 7$ TeV and still one order of magnitude below design luminosity, reported to have reached already a JES uncertainty of 2 % to 4 % for a jet's transverse momentum of $p_{\mathrm{T}} = 20$ GeV to $p_{\mathrm{T}} = 2$ TeV over a pseudorapidity region up to $|\eta| = 4.5$ [63], using in-situ techniques with more than 1 fb^{-1} of collected data. The ATLAS technical

design report [53], published 1999, expects even one percent accuracy after many years of data taking at design luminosity, which justifies the above choice. But reaching that level of accuracy is certainly challenging.

Jet energy resolution

The hadronic energy resolution in a non compensating calorimeter is independent of the energy limited by the constant term added, which accounts for the degree of non compensation. But the fluctuation of the electromagnetic fraction in the hadronic shower may be energy dependent. Thus the effects of residual non-compensation[2)] may be also energy dependent and therefore are better be included into the hadronic energy resolution in the stochastic term. To simulate the uncertainty in the jet energy resolution reference [7] suggested to smear the jet energy within the following resolutions,

$$\sigma(E) = 0.45 * \sqrt{E[GeV]} \text{ for } |\eta| \leq 3.2 \quad (6.12)$$

$$\sigma(E) = 0.63 * \sqrt{E[GeV]} \text{ for } |\eta| > 3.2 \quad (6.13)$$

Propagation of changes in jet energy scale to $E_{\mathrm{T}}^{\mathrm{miss}}$

There are no detailed recipes to access a systematic uncertainty on $E_{\mathrm{T}}^{\mathrm{miss}}$. We followed the following approach (recommended by [7]), when applying the variations for the systematic study: After smearing the jet energy resolution according to Eq. 6.12, $E_{\mathrm{T}}^{\mathrm{miss}}$ is recalculated adding the change in the jet energies. But a global uncertainty on the JES due to detector effects may also be reflected in an uncertainty on the $E_{\mathrm{T}}^{\mathrm{miss}}$ which is formed from the calorimeter cells. The effect is thought to be small, as [7] devises to propagate only 5 % of the energy scale changes of the jets to the value of $E_{\mathrm{T}}^{\mathrm{miss}}$. Other influences on $E_{\mathrm{T}}^{\mathrm{miss}}$ are not specifically considered.

Misidentification probability for isolated leptons

The identification of isolated leptons can be missed due to misindentification or non-acceptance. This is expressed in the identification and fake rates for leptons. Also additional jets from pile up may spoil the isolation criteria.

In terms of background yield the uncertainties of fake rates are more important since a systematically too high estimate of the fake rate would lead to an underestimate of the background. On the other hand systematically too low identification efficiencies would lead to an overestimated background.

Without detailed knowledge about the uncertainty of the lepton identification efficiencies and fake rates, we tried to quantify their effect on the selection by randomly rejecting a certain percentage of identified leptons in the isolated lepton veto. If the isolated lepton veto finds an electron it is ignored in 0.2 % of the cases and an isolated muon in 1 % and finaly an identified tau in 5 % of all cases. These estimated numbers (referring to the recipies in [7]) try to reflect the fact that electrons may be found more efficiently as hadrons, hence the errors on such efficiencies may be different.

6.2.2 Determination of the relative systematic change of the number of selected events

The natural way to study the relative changes in the event selection due to detector-related systematic effects is of course to apply the variations, described in Chapter 6.2.1, separately to the fully simulated

[2)] The response of an ideal calorimeter to the injected jet energy should be linear. A source for non-linear response is the so-called non-compensation. It is the different response of the calorimeters to the statistically fluctuating fraction of electromagnetic and hadronic energy in the particle shower that is evolving if a jets hits the calorimeter systems. Calibration methods, as sketched above, aim to restore the linearity as good as possible, but the remaining non-linearity in the energy response after calibration is called “residual non-compensation”.

events and repeat the selection for each systematic variation. Unfortunately, the limited amount of fully simulated events would lead to a large influence of statistical fluctuations in the results. Therefore, once again the larger events samples of ATLFAST-1 events were utilised for statistically more trustworthy results.

The important assumption for this approach is – even if individual cut efficiencies in the parametrised ATLFAST-1 samples differ from the fully simulated samples –, that the relative change in the selection is more or less equal. An estimate of detector-related systematic effects on this assumption may be disputable but for the time being may be sufficient to give an impression on the impact of such effects and identifies possibly limiting systematical effects.

The regarded sources of systematic uncertainties are considered as uncorrelated and hence the variation and determination of their effects are done separately. The relative change in selection for a systematic source α_{sys} is determined in the following way: given that the original number of events that pass the selection is N_{sel}^{orig} and the number of events selected if the systematic variation is made in one direction becomes N_{sel}^{var}

$$\alpha_{sys} = \frac{N_{sel}^{var} - N_{sel}^{orig}}{N_{sel}^{orig}} \tag{6.14}$$

As said the $N_{sel}^{orig/var}$ were determined in the fast detector simulation samples instead of the fully simulated samples, assuming to yield an equivalent α_{sys} with smaller influence of statistical fluctuations.

6.3 Optimisation of MLP output cut under consideration of the main systematic sources

The multivariate classifier is intended to be adaptive in the training phase for the varying signal properties, therefore it has to be studied in principle for all signal hypotheses individually. This can be simplified a little, if one defines a smaller number of hypotheses, claimed to be representative for all possible signal characteristics. These characteristics are determined by the Higgs boson mass and its decay-width. In the header of Tab. 6.1 we define what we understand under a heavy or medium Higgs mass and e.g. a large decay width.

To make sure to include possible effects of the variation in mass and decay width it was tried to choose representative combinations of mass and decay width for the signal and study the systematics at these points. In the lower part of Tab. 6.1 the characteristics of the studied points in terms of mass and decay width as well as the invisible cross section, as measure for the importance of that point in a search, are summarised.

If the influence of mass and width on the observed systematic variation is not strong and the variations do not differ significantly, it would be an option to combine these variations determined in each points, of Tab. 6.1, to a single number for each source of systematics, e.g. by taking the r.m.s or other averages.

Since the MLP is trained with a combined background there is no need to derive the systematic changes per individual background class. Hence for each studied systematic source, described in Section 6.2.1, all background samples are varied during the preselection in the same way and added in the MLP training. The relative change of the systematic source with respect to the unvaried samples in the MLP (Eq. 6.14) are determined simultaneously for many possible selection cuts on the MLP output variable. After the relative change per systematic source is known as function of the MLP output selection cut, the dominant source of systematics can be identified. With this information the optimal cut for a MLP selection that is minimising the ξ^2 can be searched for in the fully simulated samples including the effect of the systematic effect of the dominant source on ξ^2.

definition of characteristics			
narrow	$\lesssim 10$ GeV	light	$130-150$ GeV
medium width	$\lesssim 80$ GeV	medium heavy	$200-400$GeV
broad	$> 100-300$ GeV	heavy	> 400 GeV
characteristic		**chosen signal**	σ_{inv}**(fb)**
narrow$\oplus$light		$M_h = 130$ GeV $\Gamma_h = 5$ MeV	5475
narrow$\oplus$medium heavy		$M_h = 200$ GeV $\Gamma_h = 4.5 GeV$	1996
narrow$\oplus$heavy		$M_h = 300$ GeV $\Gamma_h = 9$ GeV	83
medium width$\oplus$light		$M_h = 130$ GeV $\Gamma_h = 19$ GeV	5943
medium width$\oplus$medium heavy		$M_h = 200$ GeV $\Gamma_h = 77$ GeV	2717
medium width$\oplus$heavy		$M_h = 400$ GeV $\Gamma_h = 66$ GeV	482
broad$\oplus$light		$M_h = 130$ GeV $\Gamma_h = 130$ GeV	5367
broad$\oplus$medium heavy		$M_h = 200$ GeV $\Gamma_h = 200$ GeV	2531
broad$\oplus$medium heavy		$M_h = 250$ GeV $\Gamma_h = 250$ GeV	1701
broad$\oplus$heavy		$M_h = 400$ GeV $\Gamma_h = 370$ GeV	688

Tab. 6.1: Representative points in the $M_{\text{H}} - \Gamma_{\text{H}}$ plane for the study of the systematics. The definitions of the characteristics of signal in the search planes are given in the upper first row. Examples for hypotheses that can represent interesting combinations of these characteristics are presented in the lower rows. At these representative point the systematic studies had been carried out. Not all points are suitable for a promising search though. Unfortunately one observes rather large drop in the signal invisible cross section σ_{inv} e.g. for a narrow but heavy characteristics.

Change of input distributions with systematics variations applied

In Fig. 6.1 to Fig. 6.4 the effects of systematic variations like the smaller of the two studied JES variation (see Eq. 6.10 and Eg. 6.11), which was finally used in the sensitivity study, and the jet energy resolution smearing on the leading jet transverse momentum p_{j1}^{T} and the invariant dijet mass M_{j1j2} are shown. We have chosen to show an example signal hypothesis $M_H = 200$ GeV and $\omega = 5$, (always in the left panel) and important W and Z boson backgrounds added (always in the right panel). The effect of all detector-related systematical variations applied for all the five input variables of the MLP are displayed in the Appendix B.3, for reference. Here we report only the general features visible in the following plots.

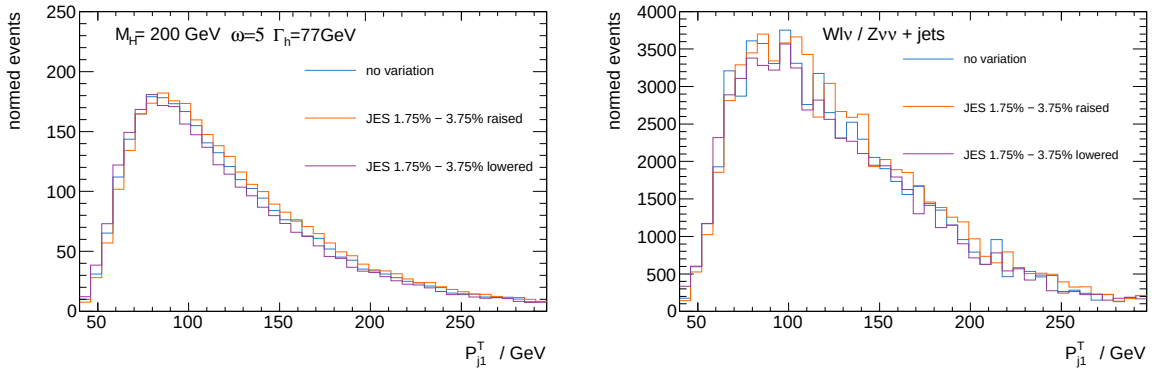

Fig. 6.1: *Systematic variation of the input variable p_{j1}^{T} under the change of the JES about* $1.75\% - 3.75\%$. *Shown are distributions in ATLFAST-1 samples that enter the training of the MLP classifier. Plotted is signal, $M_H = 200$ GeV and $\omega = 5$ (left panel), and the added important W boson and Z boson background (right panel).*

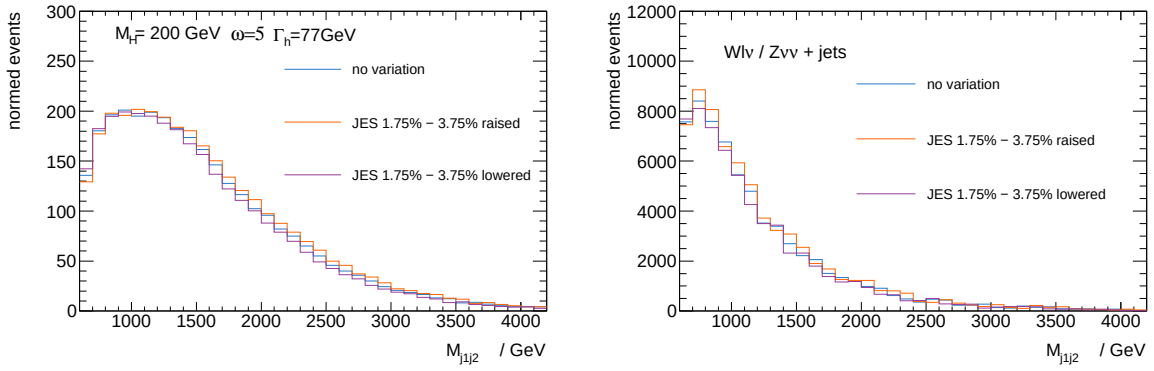

Fig. 6.2: *Systematic variation of the input variable M_{j1j2} under the change of the JES about* $1.75\% - 3.75\%$. *Shown are distributions in ATLFAST-1 samples that enter the training of the MLP classifier. Plotted is signal, $M_H = 200$ GeV and $\omega = 5$ (left panel), and the added important W boson and Z boson background (right panel).*

In the preselection, the tagging jets are most important for discriminating background events from signal like event topologies. Hence cuts on the p_T and invariant mass of the tagging jets candidates are made. The efficiencies for such cuts is raised or lowered with the rescaling of the jet energy scale, which becomes in this way the most important source of detector-related systematical uncertainties. Variables that exploit information about the tagging jet candidates direction are little affected by the variation of the jet energy scale. The general tendency is that the overall number of selected events changes but

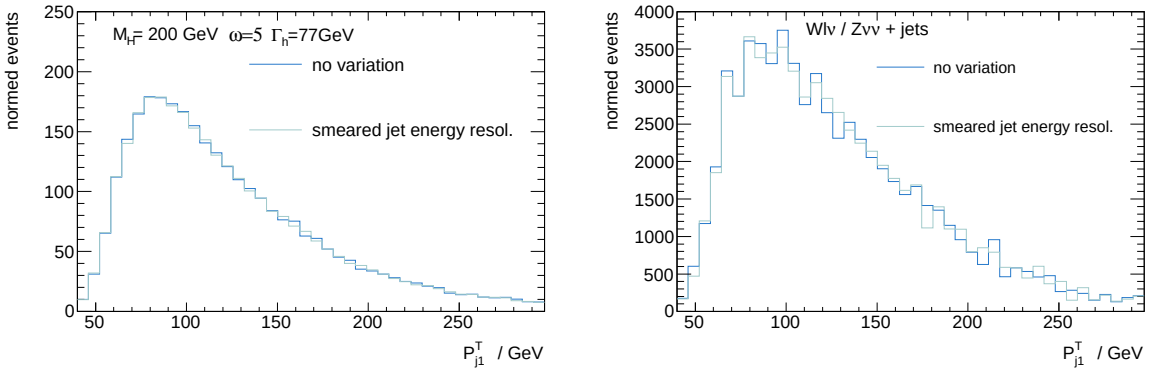

Fig. 6.3: *Systematic variation of the input variable $p_{\mathrm{j1}}^{\mathrm{T}}$ under the random smearing of the jet energy resolution. Shown are distributions in ATLFAST-1 samples that enter the training of the MLP classifier. Plotted is signal, $M_{\mathrm{H}} = 200$ GeV and $\omega = 5$ (left panel), and the added important W boson and Z boson background (right panel).*

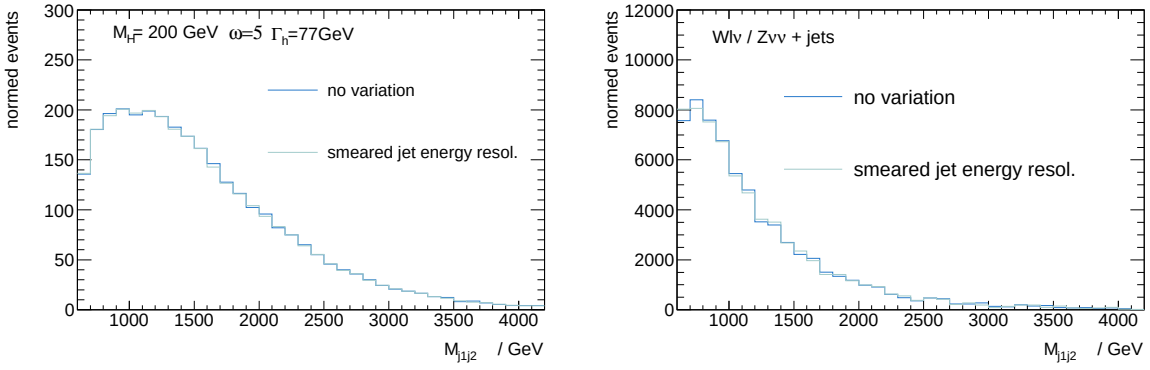

Fig. 6.4: *Systematic variation of the input variable M_{j1j2} under the random smearing of the jet energy resolution. Shown are distributions in ATLFAST-1 samples that enter the training of the MLP classifier. Plotted is signal, $M_{\mathrm{H}} = 200$ GeV and $\omega = 5$ (left panel), and the added important W boson and Z boson background (right panel).*

within the given binning the shape of the input variables distribution varies not significantly, i.e. that the systematic variations do not dramatically alter phase space compared to the unchanged reference distributions. The change in the number of selected events scales roughly with the size of the applied jet energy rescaling.

The random Gaussian smearing of the jet energy resolution can increase or decrease the jet energy resolution, hence in many cases the effect is compensated in a larger sample and the net effect for the selection is expected to remain small. And also, as can be seen in Appendix B.3, the randomly changed veto probability against isolated leptons selects only a slightly different number of events but no special phase space region with respect to the unchanged probability.

Effect of the systematical variations on the MLP output for a typical signal hypothesis, $M_{\mathrm{H}} = 200$ GeV and $\omega = 5$

In Fig. 6.5 the effect of systematic variations like the JES on the input variables variables of the MLP is displayed. In the upper left panel a large and in the upper right panel a smaller variation of the JES are displayed for the important W/Z boson background. In the lower left panel the effect of random smearing of the jet energy resolution and in the lower right panel of the varied veto probability of the isolated lepton veto on the MLP output for W/Z boson background events is shown.

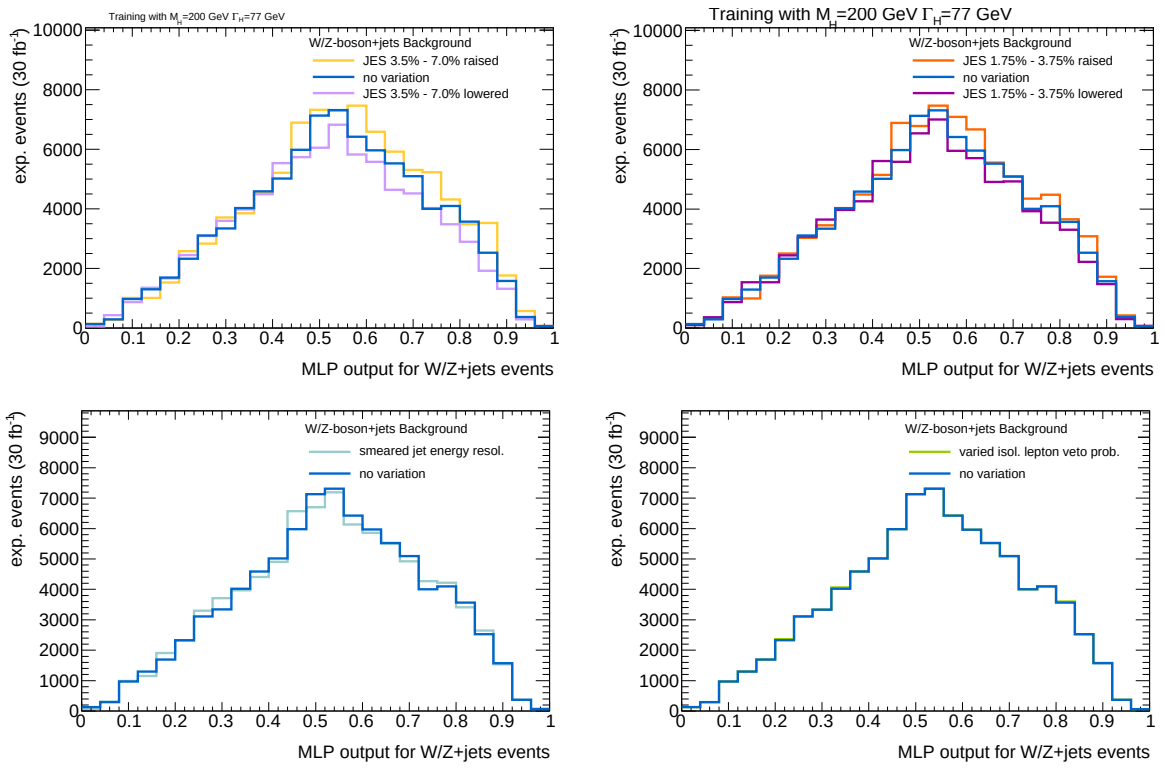

Fig. 6.5: *Distribution of the MLP output for the W/Z boson background, after training with the signal,* $M_{\mathrm{H}} = 200$ GeV *and* $\omega = 5$*. In the upper row the jet energy scale is raised and lowered. For the left upper panel, the JES is varied by 3.75 % to 7.0 % for illustrative purposes. The right upper panel contains the JES variation of 1.75 % to 3.75 %, which is actually used in the sensitivity study. In the lower left panel the effect of the smearing of the jet energy resolution on the MLP output is shown. In the right lower panel the probability of the isolated lepton veto rejecting identified leptons is varied. The latter two sources give only rise to smaller changes in the output distributions.*

In Fig. 6.6 we show the relative change (Eq. 6.14) on the MLP selection for background events due

to the systematic uncertainty broken down by sources in dependence of the applied MLP cut. For these plots we used again the typical example of the MLP training with the the signal, $M_{\mathrm{H}} = 200$ GeV and $\omega = 5$. It is a general feature in all studied hypotheses, that the JES variation make a noticeable effect while the jet energy resolution has only a small effect and the varied veto probability in the isolated lepton veto almost no effect on the resulting MLP output.

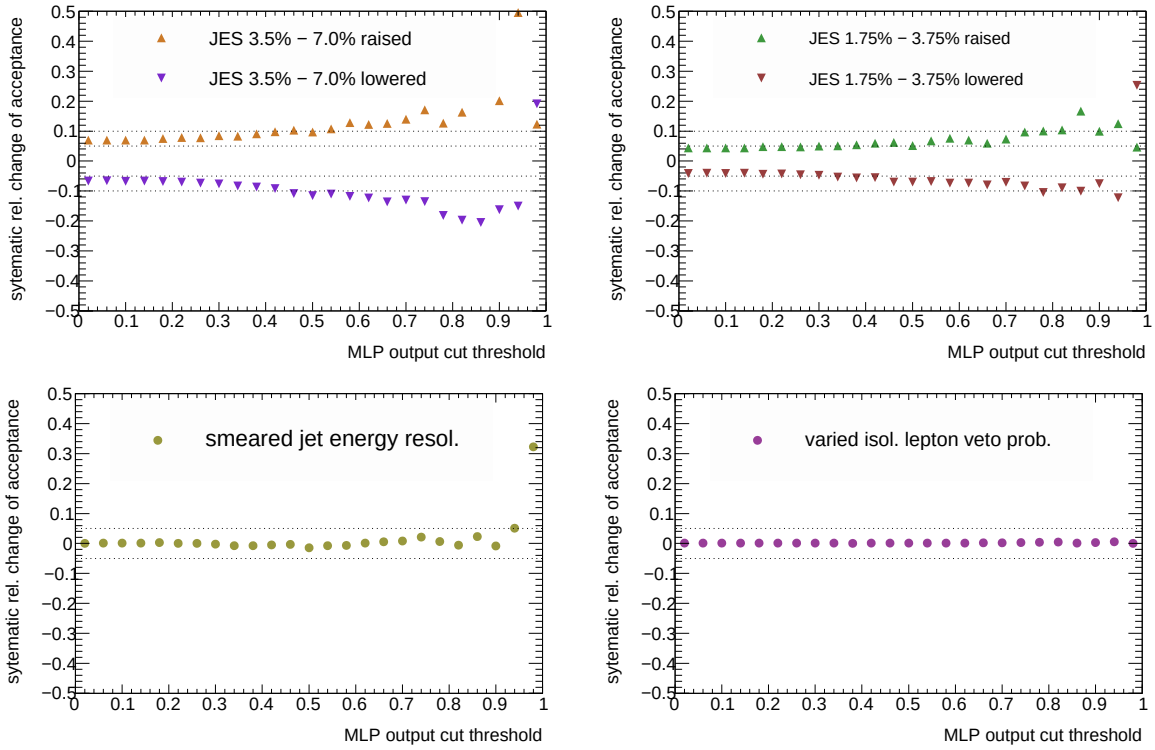

Fig. 6.6: *Relative change of the acceptance of the applied cut on the MLP output distribution due to the regarded experimental systematic uncertainty sources for the W/Z boson background, after training with the signal, $M_{\mathrm{H}} = 200$ GeV and $\omega = 5$. In the upper row the jet energy scale is raised and lowered. For the left upper panel, the JES is varied by 3.75 % to 7.0 % for illustrative purposes. The right upper panel contains the JES variation of 1.75 % to 3.75 %, which is actually used in the sensitivity study. In the lower left panel the effect of the smearing of the jet energy resolution on the MLP output is shown. In the right lower panel the probability of the isolated lepton veto rejecting identified leptons is varied. The latter two sources give only rise to very small changes in the acceptance.*

The difficulties to decide on an optimal cut on the MLP output are demonstrated in Fig. 6.7 for a typical example of a signal hypothesis, $M_{\mathrm{H}} = 200$ GeV and $\omega = 5$. As said before we found that the jet energy scale is the detector uncertainty with the largest influence on the results. In order to give an estimate for the size of this uncertainty that allows for for the exclusion of at least some of the stealthy Higgs hypotheses, we tried out several uncertainties for the jet energy scale as listed in Section 6.2.1. In Fig. 6.7, we show the upper limit on ξ^2 at 95 % CL which can be exluded corresponding to the choice of the cut on the MLP output, called MLP threshold. In calculating ξ^2 we include the systematic uncertainty of the relative change in selected events due to the jet energy variation is determind at such a MLP output treshold cut. Two magnitudes of variations of the jet energy scale are shown, namely the η-dependent variation about $\pm 3.5\%$ to $\pm 7.0\%$ in the left panel and about $\pm 1.75\%$ to $\pm 3.75\%$ right panel.

To guide the eye we introduced a horizontal line below which the exclusion of the stealthy hypothesis can be reached. Ideally ones now wants to seek for a clearly localised minimum of ξ^2 in dependence

of the MLP output cut. Also the determined optimal cut at which ξ^2 becomes minimal should ideally likewise be optimal or proficient for a larger variety of hypotheses. But it is obvious that large fluctuation for harder cuts on the MLP output make it difficult to choose a real minimum, not an accidental one. The second observation is that the larger variations of the jet energy scale in the left panel spoil completely the sensitivity for this stealthy Higgs hypothesis. In the case of the lower jet energy scale variation shown in the plot in the right panel, we see a hint, even if fluctuations are present, that a quite hard cut on the MLP has to be made somewhere above 0.86 to gain sensitivity for the stealthy Higgs hypothesis.

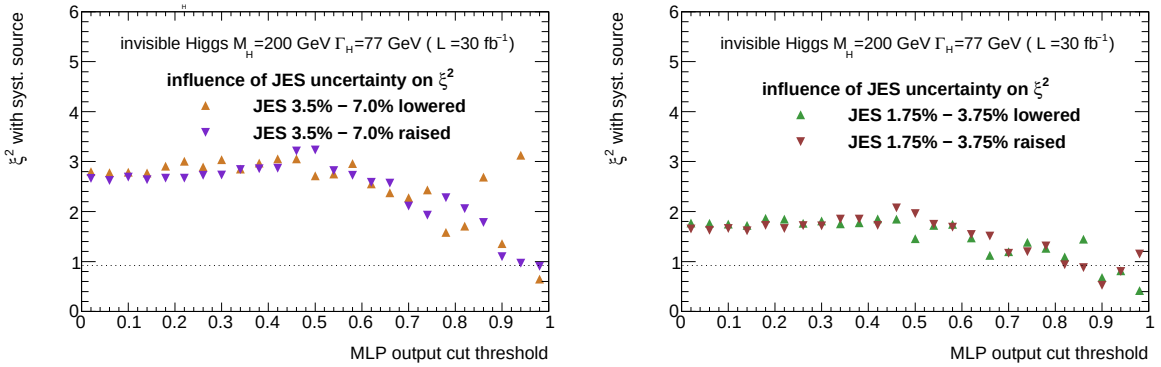

Fig. 6.7: *Attempt to identify an optimal cut on the MLP output with simultaneously considering the dominant detector-related systematic uncertainty of the jet energy scale. For a typical example of a signal hypothesis, $M_{\mathrm{H}} = 200$ GeV and $\omega = 5$, the resulting upper limit on ξ^2 is shown when the MLP output is required to be larger as the MLP threshold cut. The relative change in selected events due to the uncertainty of the jet energy scale determined for the MLP threshold cut is incorporated in the calculation of the upper limit on ξ^2 at this MLP cut threshold. In the left panel the η-dependent variation ranges from $\pm$3.5% to $\pm$7.0% In the right panel the variation is only the half of the left panel, ranging η-dependent from $\pm$1.75% to $\pm$3.75%. The horizontal line in the plots corresponds to the value of ξ^2 below which the hypothesis can be excluded at 95 % CL.*

In the next paragraph we describe how we tried to smooth out the fluctuations for hard cuts on the MLP output and motivate our choice for the final cut from the general tendency we observed.

Observation that the resulting MLP output for the background is quite similar for the studied hypotheses

Though fluctuation of relative changes in the selection acceptances may occur for hard cuts on the MLP output (see e.g. Fig. 6.6), in general the resulting shape of the MLP output from the varied samples is found to be quite similar. As illustration in Fig 6.8 for all the hypotheses that are considered in the systematic study (listed in Tab. 6.1), the corresponding background MLP outputs under variation of the jet energy scale are displayed.

Especially the background shape is not varying much if different hypotheses were used in the training of the MLP as signal. All background distributions peak in the neighbourhood of an output variable value of 0.5 where the position of the peak is not shifted largely for the individual training hypotheses. The slope to lower output variable values looks quite similar. Only the slope towards higher MLP output values (the region where more signal like backgrounds events are intended to accumulate) differs a little for hypotheses with a higher Higgs boson mass used in training, which reflects the varying signal properties mildly, as can be seen in the lowest row in Fig 6.8. This is understandable from the fact that the background after the preselection is always the same for all hypotheses and the input variables of the signal exhibit no strong shape differences for the varying signal hypotheses, which results in quite similar

separation power for the regarded MLP output distributions. While this means that the event selection has no large sensitivity for the stealthy Higgs kinematic properties, this observation is encouraging to try to characterise the impact of a systematic source independently from the signal hypothesis in one number. If all regarded signal hypotheses distributions are added and evaluated graphically, the hope is that an optimal selection cut, which is robust under systematics and applicable for all hypotheses, becomes clearly visible.

Adding all ten MLP output distributions for the background

With the example of the hypotheses displayed in Fig. 6.7 we argued that it is hard to read off an optimal cut on the MLP output due to statistical fluctuations. In general for all ten hypotheses we looked at, there is no clear and stable minimum of the figure of merit ξ^2 visible that would indicate an advantageous selection cut on the MLP. The region of hard cuts on the MLP is naturally a region where statistical fluctuation are prominent. As a solution we decided to combine all the background distributions displayed in Fig 6.8, since they are sufficiently similar. Of course it should be emphasised that the same background events enter into the output distributions in all points, which make them statistically dependent. But combining the background samples before determining the relative change in acceptance due to the systematic source can be interpreted as an alternative to averaging afterwards over all relative changes due to that source.

Dependency of systematic uncertainty on the MLP selection cut for the background distribution of all regarded hypotheses added

In case of adding all the MLP output distributions the fluctuations become less severe and we can recognise the general tendency how large the influence of the systematic uncertainty of source may be. It should be kept in mind, that for quoting the systematic uncertainty of our final result, the upper limit on ξ^2, only relative changes in the direction that lower the background acceptance are relevant. By repeating the evaluation with the ten added background MLP output distributions we yield the following results for the relative change displayed in Fig. 6.9.

1) **larger JES variation**
   In Fig. 6.9 the upper left panel shows the relative deviation in the selection if the η-dependent variation of the jet energy scale is varied in the large range from $\pm$ 3.5% to $\pm$ 7.0 %. With such a large variation of the JES the relative deviation is of the order of 5 % if the MLP cut would be below 0.3 and consistent with values below 10 % for a MLP cut between 0.3 and 0.75. If the MLP output cut is harder than 0.75 the relative downward deviation can be estimated by 20 %. These values we quote simply as reference.

2) **smaller JES variation**
   As we concluded from Fig. 6.7, we better demand the η-dependent variation of the jet energy scale to be smaller, ranging from $\pm$ 1.75 % to $\pm$ 3.75 %. The relative change in the selection due to this finally used variation is displayed in the upper right panel of Fig. 6.9, and is the most important plot since the JES is the dominant detector-related systematic effect. In both cases we see by eye that the adding of the background MLP distribution damped the fluctuations and the relative change for raising and lowering the JES becomes in both cases more symmetric as compared to the corresponding plots in Fig. 6.6 for only a single hypothesis point. Up to a cut of about 0.45 the JES variation leads to a relative changes in the selections of a roughly 5 % but for higher cuts an increase of the change is observed. The influence of statistical fluctuation becomes visible, if the cut on the MLP output is larger as 0.75. For the lowered JES, that we want to use in the analysis, we therefore introduced error bars that stem from the MC statistical uncertainty which is in that

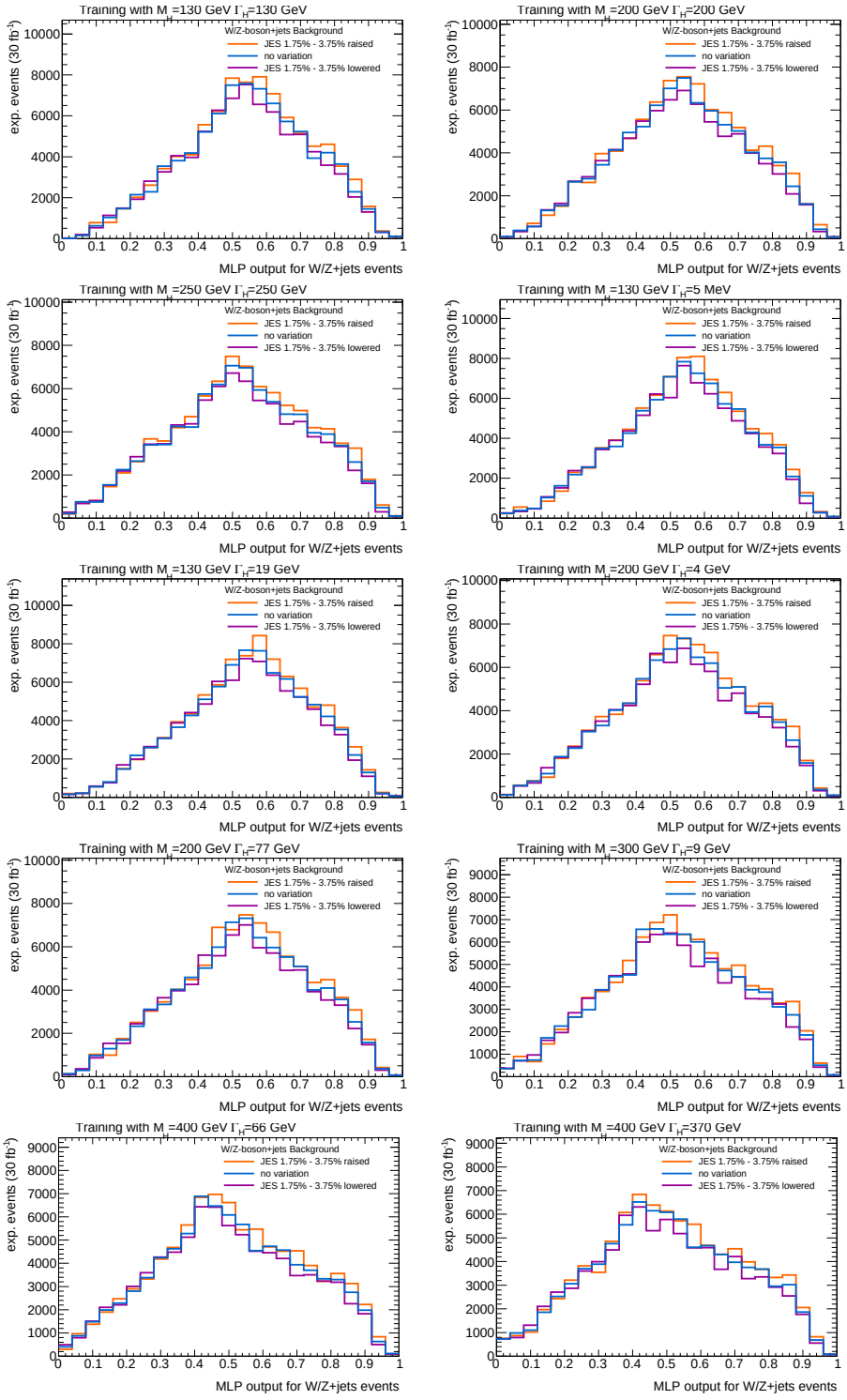

Fig. 6.8: *Normalised distributions of the MLP output used for the systematic uncertainty study for the combined W/Z boson plus jets background after training for the signal hypotheses listed in Tab. 6.1. Plotted is the MLP output for a variation of the jet energy scale by $\pm$ 1.75 % to $\pm$ 3.75 %, depending on the jets' η, which is expected to be the dominant contribution to the systematics. Due to the shape of the distribution a hard cut on the MLP output near one would exhibit large statistical fluctuation, hence the binning chosen is very coarse. Given this coarse binning, one also observes that the shape of the background is not varying very much with the signal hypothesis used in training. This observation justified adding all background MLP output distributions to smooth out statistical fluctuation when looking for an optimised MLP cut under consideration of the main systematical uncertainies.*

range of the order of 10 % to 12 % for the W boson background. We will have a closer look at the fluctuation of relative change for some possible cut values. In the upper right panel of Fig. 6.9, we read off that if the JES is lowered, a cut on the MLP output larger 0.8 would yield a decrease of selected background by -10%, a cut larger 0.84 of -12.7 %, a cut larger 0.88 of -12.7 %, a cut larger 0.88 -11.1 % and finally a cut larger 0.92 a decrease by -16.5 %. We see these numbers become the more unreliable the harder the cut is choosen. If one looks at the general tendency and the given error bars, we conclude that it is justified to assume a general -10 % decrease for MLP output cuts between 0.8 and 0.9.

3) **smeared jet energy resolution**
In the lower left panel of Fig. 6.9 the relative change in selected events after the MLP due to the smearing of the jet energy resolution is plotted. Again the error bars indicate the influence of MC statistical uncertainties. If one evaluates the general tendency by eye it may be justified to say that the effect is always below one or two percent and consistent with zero for the larger MLP cuts above 0.8.

4) **changed isolated lepton veto probability**
The lower right panel of Fig. 6.9 indicates that the relative change in isolated veto probability has generally only a marginal effect of much less than a percent and can be safely neglected.

Dependency of upper limit on ξ^2 including the lowered JES on the MLP selection cut for the background distribution of all regarded hypotheses added

In the last paragraph we found with the use of the added background distributions the important result that we can estimate the systematic influence of a lowered JES by a decrease of -10 % selected background for the range of possible MLP output cuts between 0.8 and 0.9. Next we want to check whether adding the ten MLP output distributions for the background smoothed out the fluctuation sufficiently to identify a clear minimum in the dependency of the upper limit on ξ^2 from the MLP output cut.

In Fig. 6.10 we exemplary show for two signal hypotheses, $M_{\mathrm{H}} = 130$ GeV and $\Gamma_{\mathrm{H}} = 5$ MeV ($\omega = 0.1$), (left panel) and $M_{\mathrm{H}} = 200$ GeV and $\Gamma_{\mathrm{H}} = 77$ GeV ($\omega = 5$) (right panel), the expected upper limit on ξ^2 calculated with the smaller JES variation. Again to guide the eye we introduced a horizontal line below which the sensitivity, i.e. the upper limit on ξ^2 with systematics, would yield an exclusion of the corresponding stealthy Higgs hypothesis.

One sees that the minimum fluctuates for hard cuts above 0.8. This is the direct consequence of the fluctuations seen in that region in the upper right panel of Fig. 6.9. It is interesting to note that for a lighter Higgs mass of about 130 GeV, the expected signal rate is high enough that even a very low MLP cut in the region without fluctuation provides enough sensitivity for model point exclusion. But for assumed Higgs masses of 200 GeV and more one needs to cut harder on the MLP output to suppress the background more effectively. By comparison of plots like Fig. 6.10 for all hypotheses we could not clearly find one optimal cut. But as a general tendency for the need of a hard cut was visible, we decide that a cut at 0.88 would be hardest cut that we would dare to make. Any harder cut would introduce to much fluctuations in the result. But of course if one would had a lot more MC statistics for the background, this estimate for the optimal cut could be made more refined.

6.3.1 Results of the estimate of the size of systematic uncertainties for the multivariate analysis

We collect again the key points concerning our treatment of systematic uncertainties, found in the last paragraphs:

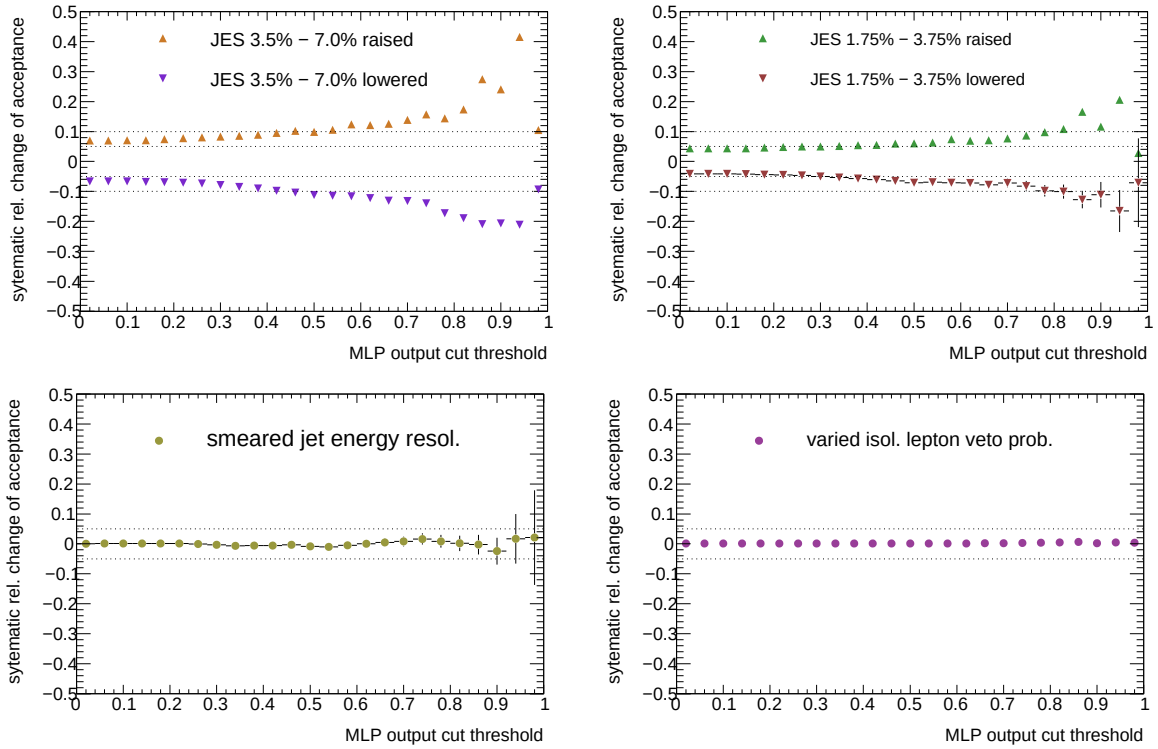

Fig. 6.9: *Dependency of the relative change of the selection acceptances due to various sources of systematic uncertainties as function of the output selection cut for the background distributions of all trainings with the regarded signal hypotheses added. The relative systematic error for a variation is calculated by Eq. 6.14. In the upper row the jet energy scale is raised and lowered. For the left upper panel, the JES is varied by 3.75 % to 7.0 % for illustrative purposes. The right upper panel contains the JES variation of 1.75 % to 3.75 %, which is actually used in the sensitivity study. In the lower left panel the effect of the smearing of the jet energy resolution on the MLP output is shown. In the right lower panel the probability of the isolated lepton veto rejecting identified leptons is varied. The latter two sources give only rise to very small changes in the acceptance.*

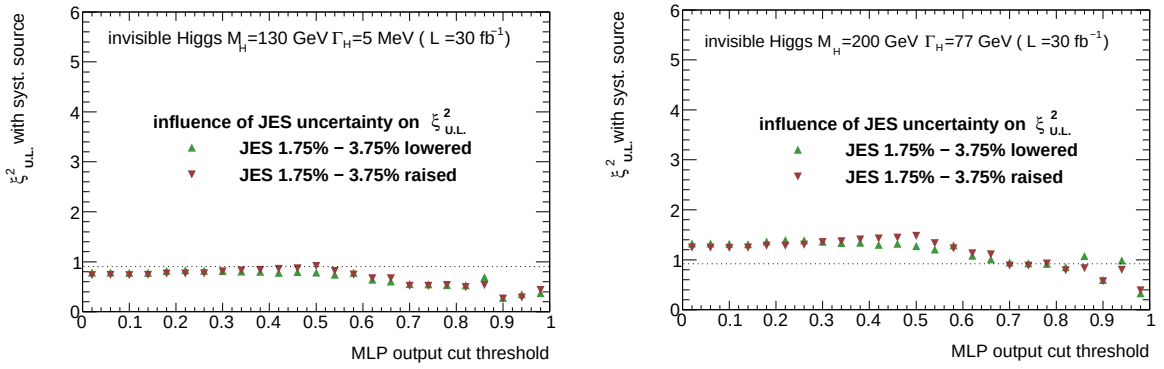

Fig. 6.10: *Dependency of the upper limit on ξ^2 including systematic jet energy scale uncertainty for a η-dependent variation from $\pm 1.75\%$ to $\pm 3.75\%$, on the MLP output selection cut. The relative systematic error for a variation is calculated from the added background MLP outputs of ten signal hypotheses. We display in the left panel the result for a signal hypothesis, $M_{\mathrm{H}} = 130$ GeV and $\Gamma_{\mathrm{H}} = 5$ MeV $(\omega = 0.1)$, and in the right panel for a signal hypothesis, $M_{\mathrm{H}} = 200$ GeV and $\Gamma_{\mathrm{H}} = 77$ GeV $(\omega = 5)$.*

1) **MLP output cut**
   We decided to apply independent of the mass of the Higgs hypothesis a MLP output cut of 0.88, where the results are not subject to too large fluctuations.

2) **Jet energy scale impact**
   Further we determined the size of the expected background systematic uncertainties for a cut of 0.88, from the general tendency in Fig. 6.9, assuming this to be valid for all hypotheses studied and list the numbers in Table 6.2. We use the estimated -10 % in selected background for the downward scaling of the jet energy. For reference we give also the relative changes for the selected signal in the third column of Table 6.2 .

3) **Negligible sources**
   The jet energy resolution and isolated lepton veto probability have been found to be negligible after the MLP selection.

4) **Luminosity uncertainty** The contribution for the expected luminosity uncertainty of 3 % is added in quadrature.

Hence the modulus of the total systematic error for the multivariate selection of the background is estimated after rounding up as 10.5%. With this number we calculated all the upper limits on ξ^2 and present the results in the next chapter. We also give in the third column the resulting relative deviation for the signal corresponding to the various sources of detector-related systematic effects under study. As an estimate of the size of the variation for the signal we took the mean of the relative variation of the signal after a cut of 0.88 on the MLP output distribution. The results for the signal are very similar to those for the background, which indicates that the estimate of the background uncertainty are in the right order of magnitude and are not too much influenced by statistical uncertainties. Not surprisingly the signal identification via tagging jets related variables is depending in a similar way on the JES uncertainty as the background.

Systematical uncertainties (%)			
source		background	signal
JES	$+3.75\%$ (7.0%)	20	18.4
	-3.75% (7.0%)	-20	-17.5
	$+1.75\%$ (3.75%)	10	9.6
	-1.75% (3.75%)	-10	-9.4
Jet energy resolution		< 1	< 1
Isol. lepton veto prob.		≈ 0	≈ 0
Luminosity		3%	
Total		10.5%	9.9%

Tab. 6.2: Considered systematical uncertainties in the multivariate selection, if the MLP cut at 0.88 is applied. For the background uncertainty (column 2) the estimate of the systematic distribution from 10 added background MLP output distributions, described in the text is used. For the signal uncertainty (column 3) the mean of the relative deviations of all the 10 studied signals, at a cut value of 0.88, has been evaluated. The smeared jet energy resolution and the changed isolated lepton veto probability have only a negligible impact on the selection compared to the jet energy uncertainty. The JES variation by the large value given in brackets is not used and only displayed for reference.

6.3.2 Results of the estimate of the size of systematical uncertainties for the cut-based analysis

The variations described in Section 6.2.1 can be straightforwardly applied in the cut-based analysis. It is not necessary to determine the influence of the systematic variations for each single background contribution, since the selected background as a whole enters the limit formula. All background samples are varied the same way giving immediately the relative change in the total expected background that passes all cuts.

As explained we consider only the smaller of the two variations of the JES downwards in the total detector systematical error. A breakdown of the contributions to the total systematical uncertainty is given in the Tab. 6.3, where we compared the effect of systematical uncertainties for the selected background and a signal hypothesis, $M_{\mathrm{H}} = 200$ GeV and $\omega = 5$. Looking at Tab. 6.3, one notes the following:

Systematical uncertainties (%)			
source		background	signal
JES	$+3.75\%$ (7.0%)	16.2	11.6
	-3.75% (-7.0%)	-12.3	-12.3
	$+1.75\%$ (3.75%)	8.5	6.1
	-1.75% (-3.75%)	-6.4	-6.5
Jet energy resolution		2.8	< 1
Isol. lepton veto prob.		< 1	< 1
Luminosity		3%	
Total		7.6%	7.1%

Tab. 6.3: Considered systematical uncertainties in the cut-based selection. We compare the background with the signal hypothesis, $M_{\mathrm{H}} = 200$ GeV and $\omega = 5$. The JES variation by the large value given in brackets is not used and only displayed for reference.

1) **JES is the dominant source of uncertainty**
The jet energy uncertainty is the dominant detector systematic uncertainty. The raising and lowering of the JES energy do not lead to symmetric contributions to the systematic uncertainty. The asymmetry is lower for the signal which also has a higher statistic in MC events.

2) **Influence of fluctuations**
The applied selection cuts in the cut-based analysis are very hard in order to reduce the background. Unfortunately the MC statistical uncertainty is not negligible for the background. Compared to the MLP estimate in Tab. 6.2 the background uncertainty for scaling the JES up and down behaves a little asymmetric, exhibiting a larger relative change for raising the JES. If one compares resulting change in the selection due to the JES for the signal with the background, one observes less asymmetry in case for the signal.

3) **Negligible sources**
The jet energy resolution smearing is not so important as the JES variation. It has a smaller effect for the signal as for the background. The difference in numbers may be due to the lower MC statistics in the background sample. The changed veto probability has a marginal effect below a percent for signal and background and will be neglected further on.

In order to be able to compare to the multivariate analyses we use as relative change due to jet energy variation the numbers corresponding to the η-dependent variation of -1.75% (-3.75%), together with the change due to jet energy resolution. The contribution for the expected luminosity uncertainty of 3 % is added in quadrature.

The numbers for the background in Tab. 6.3 add up to 7.6 % in total. We round up this result and estimate conservatively the impact of the considered systematics on the background to be 8.0 % in total. With this number we calculated the upper limits on ξ^2 and present the results in the next chapter.

7. Sensitivity of ATLAS in the stealthy Higgs scenario

In this chapter the results of the two event selections presented in Chapter 5 are given for the various studied model points of the stealthy Higgs scenario. We compare the expected sensitivity without systematic uncertainties with the reduced sensitivity expected for the detector-related systematic effects, discussed in Chapter 6. First we give the sensitivity in terms of ξ^2, already defined in Chapter 6.1, for various values of couplings ω to the invisible scalars. In the next chapter we will compare the ξ^2 sensitivity for selected values of ω with comparable invisible Higgs searches in the weak boson fusion from ATLAS and CMS. As we have particular interest in the impact of the stealthy Higgs model for the ATLAS Higgs search strategy, we interpret the expected sensitivity as expected exclusion in the $M_H - \omega$-plane of the stealthy Higgs model. A general discussion of the stealthy Higgs scenario at colliders follows in the next chapter.

7.1 Sensitivity in terms of upper limits on ξ^2

The procedure how the upper limit at 95 % CL is calculated from the result of the event selection is described already in Chapter 6.1. The definition of sensitivity at that place was necessary since the sensitivity including the effects of systematic uncertainties served as figure of merit in the determination of a final cut in the output of the multivariate event selection.

7.1.1 Upper limits on ξ^2 with the multivariate search

In Fig. 7.1, we display the expected upper limits at 95% CL on $\xi^2 = \frac{\sigma_{invisible}}{\sigma_{SM}}$ as a function of the Higgs boson mass and as parameter for an assumed fixed coupling ω of the Higgs to the invisible scalars. In each plot two countours are visible: first the expected exclusion on basis of the statical fluctuations of the selected events alone, i.e. without systematic uncertainties, is given by the blue contour. The second countour in red shows how the impact of the systematic background uncertainty of about 10.5 % deteriorates the sensitivity compared to the purely statistical limit.

The decision of applying the cut at a MLP output value of 0.88, implies cut efficiencies for the signal between 13 % to 38 % (as determined for the signal by the fraction of selected shape weights). Typically the efficiencies are above 25 %. One can observe the slight tendency that the efficiencies are lower for the very light signal masses while for larger masses and larger widths the efficiency rises. This may be partly due to an average enhanced amount of E_T^{miss} in the events. Already the optimisation of the MLP described in Appendix B showed a preference for a slightly higher MLP cut at larger masses.

As we have emphasised during the choice of the final cut value on the MLP output, the hard cut introduces a high MC statistical uncertainty. In the case of the cut on the MLP output at 0.88, the typical background MC statistical uncertainty is about 15 %. In order to get a feeling for the size of the effect, we present in Fig. 7.2 for a typical example of the model parameter $\omega = 5$ the quoted limit on ξ^2, and an error band that indicates the size of the uncertainty stemming from the limited size of MC background samples. A conclusion we can draw from the exemplary plot is that a statement on the sensitivity can be made but larger amount of MC events would be desired to make the statement more reliable and precise.

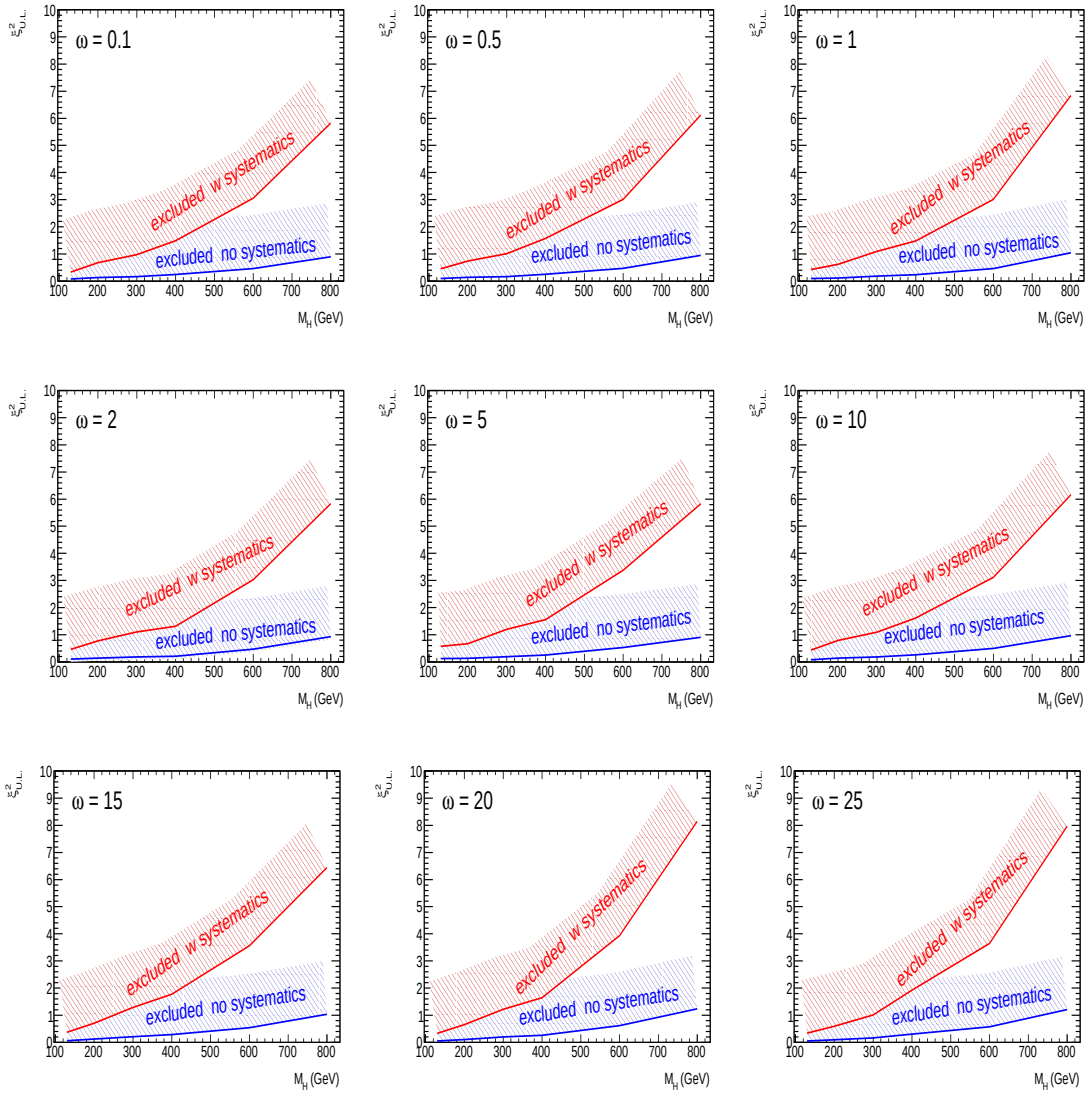

Fig. 7.1: *Expected upper limits at 95 % CL on* $\xi^2 = \frac{\sigma_{invisible}}{\sigma_{SM}}$ *depending on* $\mathrm{M_H}$ *for examples of* $\omega = 0.1$ *up to* $\omega = 25$ *of the stealthy Higgs scenario using the MLP based selection on 30* fb^{-1} *of ATLAS data. The expected exclusion without systematic uncertainties is given by the blue contour. Applying a realistic estimate of detector uncertainties, the expected exclusion will be largely reduced, and only possible above the red contour.*

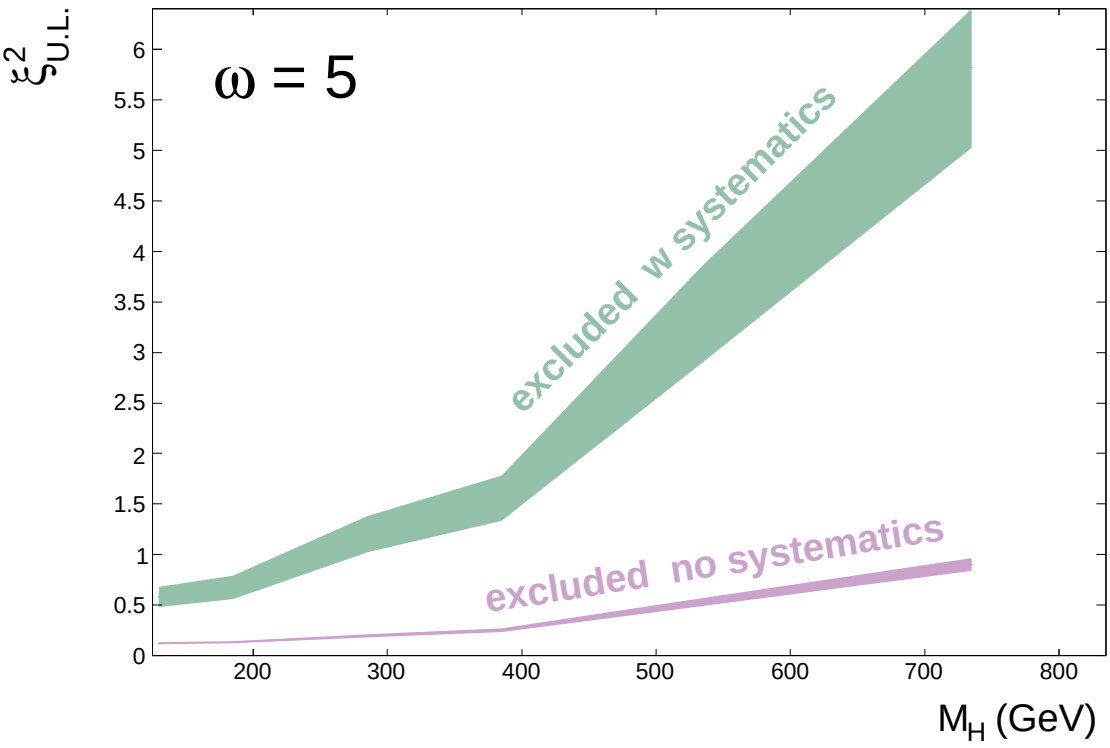

Fig. 7.2: *Influence of the limited MC statistics propagated to the expected upper limits at 95% CL on* $\xi^2 = \frac{\sigma_{invisible}}{\sigma_{SM}}$ *depending on* M_H *for the example of* $\omega = 5$*. The lower contour corresponds to the upper limit on* ξ^2 *without systematic uncertainities and the upper contour includes these into the limit. In both cases the width of the band is indicating the influence of the limited MC statistics of the background samples.*

7.1.2 Upper limits on ξ^2 with the cut-based search

We will give at this place in Fig. 7.3 three examples for the sensitivity towards a 95 % CL upper limit on ξ^2 from the cross check we performed on basis of cuts instead of the multivariate selection. Here specifically the background is the same for the tested signal hypotheses and determined by a factorisation approach since the detailed detector simulated MC was very sparse. After cuts the efficiency for the signal is typically between roughly 1 % and 2.3 %, but the background is sufficiently reduced by the hard cuts. Overall the limits without systematics from the cut-based analysis are quite competitive with those from the multivariate method. The rough estimate on the total detector-related systematic yielded about 8 % uncertainty on the background as derived in the end of the last chapter. With that the sensitivity including systematics compared to the purely statistical exclusion reduces by a factor of almost 7.

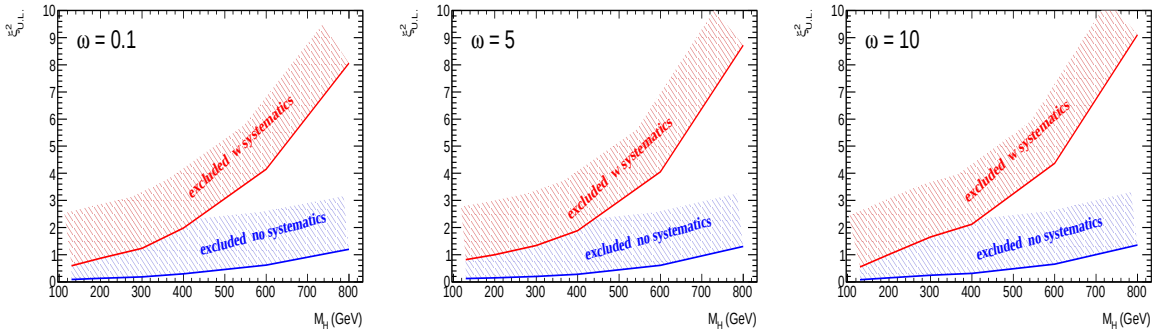

Fig. 7.3: *Expected upper limits at 95 % CL on* $\xi^2 = \frac{\sigma_{invisible}}{\sigma_{SM}}$ *depending on* M_H *for typical examples of* $\omega = 0.1,\ \omega = 5,\ \omega = 10$ *of the stealthy Higgs scenario using the cut-based selection on 30* fb^{-1} *of ATLAS data. The expected exclusion without systematic uncertainties is given by the blue contour. Applying a realistic estimate of detector uncertainties (here 8 % in total) the expected exclusion will be largely reduced, and only possible above the red contour.*

7.2 Exclusion of the stealthy Higgs scenario

In this section the results are presented in terms of the parameter plane of the stealthy Higgs scenario described in Chapter 2.2.4. But we first define the simplifications we made by neglecting some of the model parameters.

7.2.1 Assumptions on the model parameters

We restrict the non vanishing model parameters concerning the SM model extension with scalars to only the most characteristic one, that is the coupling ω between Higgs and Phions. From a scan of this couplings all important implications of the stealthy Higgs scenario can be studied. In particular the Phion's mass and self-coupling are neglected. A non trivial Phion mass m_{Phion} would enter a phase space rescaling of the width, actually reducing the invisible width according to Eq. 2.39. Hence the expected effects of the stealthy Higgs scenario should be weakened in such a case. The Phion self-coupling κ is assumed to be zero. Otherwise non diagonal mass matrices and Higgs-Phion mixing would occur. These would result in additional contributions to the width due to the Higgs-Phions mixing in the propagator, and also modified couplings would alter the production cross sections. This would make an interpretation of the results more complicated. Therefore, the parameter plane of the study is given by $M_H - \omega$, which directly defines an additional invisible decay width Γ_{inv} for the Higgs.

Since we use the normalisation of the signal (Eq. 2.40), which includes the branching into invisible final states, we can define a value expected from theory $\xi^2_{theory} = \frac{\sigma_{stealthy}}{\sigma_{\mathrm{SM}}}$. This ξ^2_{theory} has to be compared to the upper limit at 95% CL of ξ^2, which results from the event selection. In case that $\xi^2 < \xi^2_{theory}$, this particular hypothesis in the stealthy Higgs scenario is expected to be excludable.

7.2.2 Exclusion $\mathrm{M_H} - \omega$-plane with the multivariate search

In Fig. 7.4, we give the expected exclusion at 95% CL with 30 fb^{-1} ATLAS data at $\sqrt{s} = 14$ TeV, found by the multivariate selection, developed for the stealthy Higgs scenario. We decided not to study higher values as $\omega = 25$, because there are no statements by the authors in the literature about the stealthy Higgs scenario about much higher values of ω. The yellow area in the $\mathrm{M_H} - \omega$ parameter plane (for orientation we also include iso-lines of constant invisible widths as verdigris coloured dashed lines), indicates the possible statistical exclusion, if the systematics are absent. The reach of the search would be in this case for masses from 130 GeV to 600 GeV for values larger than $\omega \approx 15$. Regarding lower values of ω, the statistical exclusions is possible down to $\omega \approx 5$ at masses up to 400 GeV. One should keep in mind that for higher Higgs masses the couplings to the Phions have to be large in order to be able to compete with the open channels for visible decays. For light masses, the invisible channel can dominate at lower values of ω and the statistical sensitivity is given to about $\omega \approx 0.1$ for a mass of 130 GeV to $\omega \approx 1$ at a mass of 300 GeV. Including the 10.5 % estimate of total systematics, reduces largely the sensitivity to the stealthy Higgs hypotheses. The remaining sensitivity, enclosed by the red hatched area, is given for the mass of 130 GeV from $\omega \approx 0.1$ to $\omega \approx 20$ and a mass of 200 GeV from $\omega \approx 1$ to $\omega \approx 10$. In order to get an impression how much gain in sensitivity a reduced total systematic uncertainty can provide, we introduced the pink dashed contour, corresponding to a hypothetical exclusion with an uncertainty of 5 % in total. In that case an exclusion would extend to values above $\omega \approx 5$ for masses up to 300 GeV. The assumed 5 % uncertainty are optimistic and experimentally maybe hard to achieve since this uncertainty would correspond to a jet energy uncertainty about a percent and accurate luminosity determination. But even under this very optimistic assumption the reach within the $\mathrm{M_H} - \omega$ parameter plane covers not all possible cases of SM Higgs masses the ATLAS collaboration is prepared to discover.

7.2.3 Exclusion $\mathrm{M_H} - \omega$-plane with the cut-based search

As explained in Chapter 5 as cross check a not particularly optimised cut-based selection was studied. In Fig. 7.5, we give the expected exclusion at 95% CL with 30 fb^{-1} ATLAS data at $\sqrt{s} = 14$ TeV, found by the cut-based selection, where the colour coding is the same as in Fig. 7.4. The statistical exclusion covers for masses up to 400 GeV and ω values larger than $\omega \approx 5$. For a mass of 200 GeV values larger than $\omega \approx 0.5$ can be excluded. At a mass of 300 GeV values larger than $\omega \approx 2$ are statistically excludable. The impact of applying the systematic uncertainty of about 8.0 % reduces the expected exclusion very drastically to an excludable interval of $0.1 \lesssim \omega \lesssim 20$ at a mass of 130 GeV and for 150 GeV the exclusion is expected for $\omega \approx 7$.

7.2.4 Comparison of the sensitivity for the stealthy Higgs from the cut-based and the multivariate analysis

The comparison of Fig. 7.4 with Fig. 7.5 shows that a larger sensitivity is reached with the multivariate method. In the cut-based analysis as well as in the preselection and for the choice of the MLP output cut no mass- or width-dependent cut was applied. However to a certain degree the MLP analysis has the possibility to adapt to mass and width properties in the discrimination between signal and background due to the training. This method can avoid hard cuts and preserves a higher signal efficiency even for signal masses larger than 150 GeV. This may explain the larger reach in sensitivity of the multivariate analysis.

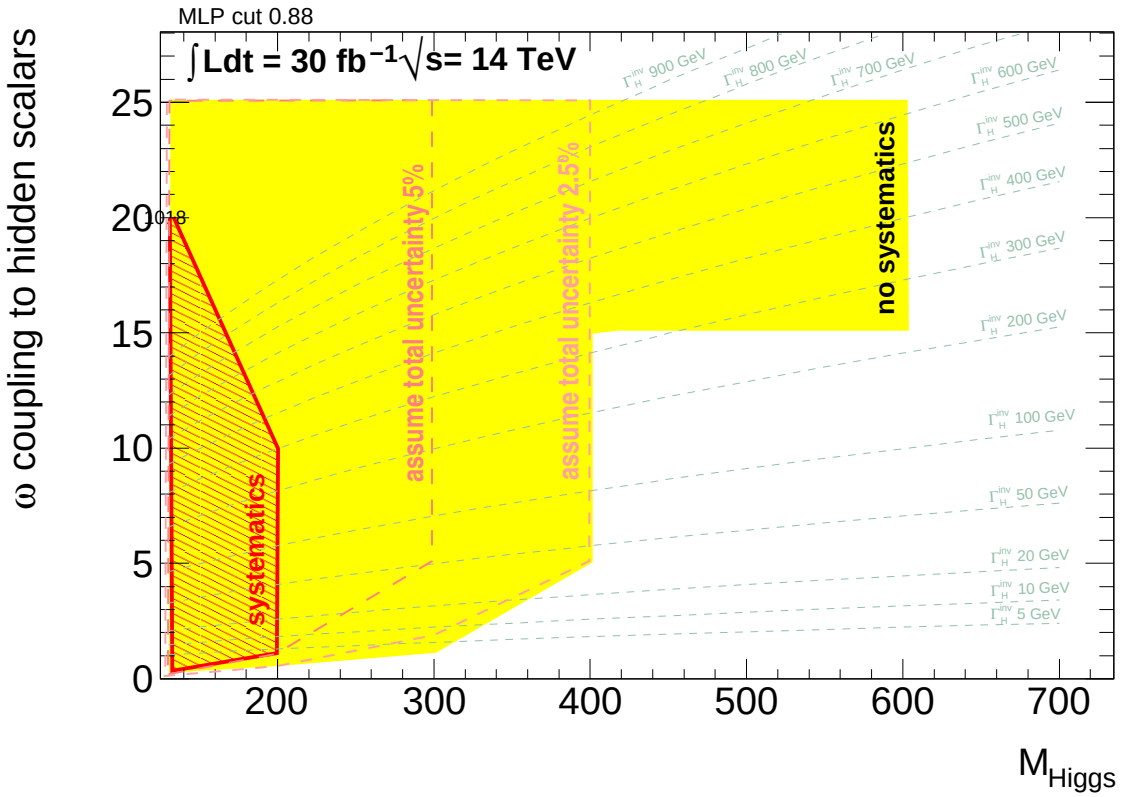

Fig. 7.4: *Expected exclusion in the* $M_H - \omega$*-plane of the stealthy Higgs scenario using the selection of the multilayer perceptron with an output cut of 0.88 with assumed 30* fb^{-1} *of ATLAS data. Higher values as* $\omega = 25$ *were not studied, as there are no statements about possibly much higher values of* ω *in the literature about the stealthy Higgs scenario. The expected exclusion without systematic uncertainties is given by the yellow contour. Applying a realistic estimate of detector uncertainties of the order of 10 %, the expected exclusion will be largely reduced, and only possible within the red hatched contour. To give a feeling of how large the gain of a reduced systematic of 5 % would be, the pink dashed contour is added to the graph. Also isolines of equal invisible widths are drawn as light green dashed curves to guide the eye. No signal MC was generated below Higgs masses of 130 GeV.*

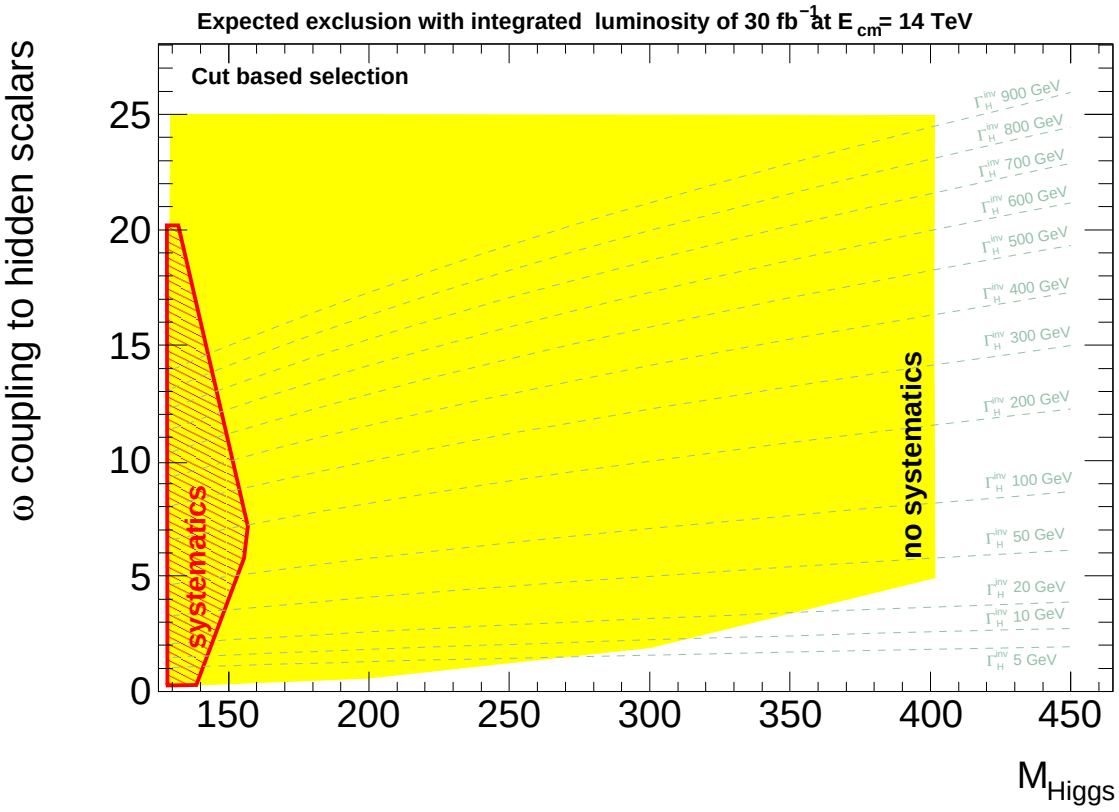

Fig. 7.5: *Expected exclusion in the* $M_H - \omega$*-plane of the stealthy Higgs scenario using the cut-based selection on 30 fb*$^{-1}$ *of ATLAS data. Higher values as* $\omega = 25$ *were not studied. The expected exclusion without systematic uncertainties is given by the yellow contour. Applying an estimate of detector uncertainties for the background of 8.0%, the expected exclusion will be largely reduced, and only possible within the red hatched contour.*

The cut-based analysis was not optimised and also applies relative hard cuts to control the high background level. The background level itself had to be determined by the factorisation and is the same for all tested signal hypotheses. The exclusion using the cut-based approach becomes therefore dependent on the signal efficiency and in case the efficiency is not changing largely between hypotheses the exclusion power still depends on the mass-dependent stealthy cross section. The lower the stealthy Higgs cross section becomes the higher the signal efficiency has to be to reach an exclusion. Hence, the exclusion is to a larger extent subject to the statistical fluctuations within the limited signal MC samples, than the multivariate method with its higher efficiency. Common to both ways of signal selection is the large impact of systematics. In case of the cut-based analysis the hard cuts are vulnerable to systematics and in case of the multivariate analysis the remaining background is relatively large and the upper limits on ξ^2 deteriorate quickly with the included background uncertainty. Even for the mass of 130 GeV where both approaches seem to yield comparable results and are able to be sensitive up to $\omega = 20$, the cut-based analysis seems to be more vulnerable to the impact of systematics. As mentioned the assumed 8.0 % are an estimate that may be affected by the limited MC statistics. For example a value of 8.5 % as total unceratinty may be thinkable and in that case the sensitivity of the cut-based approach is reduced significantly down to $\omega = 10$. From this example one can conclude that the presented cut-based analysis serves only as a crude cross check to the multivariate selection on which we focused. A competitive cut-based analyses would need a dedicated tune of the cuts and study of size of systematics with sufficiently large MC samples. Also in the next chapter when comparing our results to various other studies presented in the field of invisible Higgs searches, we can find examples how further search strategies can refine a cut-based search.

Disentangle width effects in analysis and deterioration by falling cross section

From the input and output shapes in the MLP training we see no significant sensitivity of the chosen variables to the generated Higgs decay width. This was also true for the other variables inspected during optimisation of the MLP. The tagging jet configuration is largely decoupled from the properties of the decaying Higgs boson. Only a small influence Higgs mass on the amount of real $E_{\mathrm{T}}^{\mathrm{miss}}$ in the event is noticeable. As consequence the overall sensitivity is governed by the influence of the mass of the Higgs boson on the cross section, from which the rate of possible invisible decays can be inferred. These invisible rates is typical for the stealthy Higgs scenario. Given the fact that we observed no sensitivity to the Higgs width in weak boson fusion channel for ATLAS, there is no need to perform a special width-dependent search. Instead width-independent searches, as usually performed in other invisible Higgs models, may be interpreted in the stealthy Higgs scenario as well. For the interpretation the results of these searches, have to be rescaled to the invisible decay cross-sections in the stealthy Higgs model.

7.2.5 Possible improvements to the presented study in future

In the following we want to address several aspects that need to be studied further to yield a more realistic estimate of the sensitivity and may give room for improvement in the sensitivity of a search performed in data.

Amount of available MC events

First of all in several stages the limitation of the study by the available number of MC events for the background was noticed. If there would be many more MC events available that are simulated in detailed detector simulation, this could improve the search. Additionally the training would be performed with events simulated with the same algorithms used in data reconstruction. If this number of events is large enough the stability of the MLP should be guaranteed.

Improved coverage with profile likelihood

In future ATLAS will use a profile likelihood (see Higgs combination chapter in [7] and references within) for limit setting. The advantage of this approach is that the systematic uncertainties can be incorporated in a consistent way for the construction of the Neyman interval. Also the scaling factor needed to scale the available MC samples to the quoted luminosity can be introduced as one of the nuisance parameters. Overall it is expected to reach a more realistic and robust coverage as the more conservative approach using Poissonian statistics, pursued here. The result of the profile likelihood is expected to reproduce the Poissonian result in the limit where the expected signal is much smaller than the expected background, which is the case in this search.

Detailed trigger simulation

Also the detailed trigger object simulation available from Athena release 14 on could be used in the preselection. In that way a suitable trigger menu can be determined and it's efficiency would be close to that for data.

Improved suppression of backgrounds with fake $E_{\mathrm{T}}^{\mathrm{miss}}$

At the time of a study with 30 fb^{-1} the learning process about the actual dijet rates in the detector can be assumed to be completed and MC tuned for such processes. Hence the need of harder cut on $E_{\mathrm{T}}^{\mathrm{miss}}$ to suppress such backgrounds or refined strategies like the sketched cleaning cuts against fake $E_{\mathrm{T}}^{\mathrm{miss}}$ in the preselection for multivariate analysis can be discussed.

Easy MLP variables have been identified, performing quite powerful against W and Z boson backgrounds. In case that simple cuts in the preselection will not separate sufficiently dijets and $t\bar{t}$ backgrounds, one can seek with enough MC samples, to design and train a dedicated MLP with simple variables to separated dijets and $t\bar{t}$ background before using a MLP like the one presented here against the remaining W and Z boson backgrounds.

Better understanding of jet energy scales

It will probably hold true that the jet energy scale poses the main source of systematics and will therefore limit the sensitivity even if a large amount of data is collected. The size of the uncertainty will have to be reaccessed in detailed studies, e.g. it may depend on jet algorithm used in ATLAS. The study presented uses the seedless cone algorithm. But in the meantime ATLAS changed to the Anti-k$_{\perp}$ jet algorithm based on topological clusters. The challenging original design goal of ATLAS claims to be able to determine the jet energy scale in the order of 1% [2] eventually. A jet energy scale uncertainty in this order would result in a valuable gain for the search sensitivity.

Better understanding of $E_{\mathrm{T}}^{\mathrm{miss}}$ scales

In order to improve the sensitivity and precision of a future search, the resolution of the $E_{\mathrm{T}}^{\mathrm{miss}}$ and the size of detector-related systematic uncertainties should be studied in detail in data. The precise knowledge of the $E_{\mathrm{T}}^{\mathrm{miss}}$and possible fake contributions can help to further refine the selection strategy. This study propagated changes in the jet energy scale to the $E_{\mathrm{T}}^{\mathrm{miss}}$ calculation. Since for example the cells that are included into the jets and the shape of the η-ϕ region in the calorimeter associated to the jet, depend on the used jet algorithm, this procedure will have to be changed. More likely systematic uncertainties on the $E_{\mathrm{T}}^{\mathrm{miss}}$ scale and resolution are devised by detailed studies at the time 30 fb^{-1} of data are collected. So these numbers will give a more detailed knowledge on the uncertainty of the expected sensitivity.

Correction for pile up influences

The effects of the inevitable pile up events in 30 fb^{-1} of data could unfortunately not be studied since no adequate MC samples were available. From the days of early data taking on it can be observed that the pile up events will influence the $E_{\mathrm{T}}^{\mathrm{miss}}$ resolution. Therefore, refined methods to subtract pile up contributions form the $E_{\mathrm{T}}^{\mathrm{miss}}$ in the event have to be developed. In the moment there is no estimate how big the residual systematic uncertainty on the $E_{\mathrm{T}}^{\mathrm{miss}}$ resolution from pile up will be in a 30 fb^{-1} data sample.

From this follows that the presented study has to be reoptimised with realistic pile up samples before used in data samples. To learn about and gain control over pile up of high luminosity will be crucial for the presented study to be feasible. All algorithms, currently under development, that determine e.g. what fraction of tracks in a jet do not come from the primary vertex and algorithms that flag jets from pile up should be included the search.

Optimised mini jet veto in pile up events

One focus can be whether the mini jet veto can still be applied in high luminosity conditions. The standard veto strategy used in the presented study was checked to yield smallest efficiency differences against varying underlying event models. This of course will be no issue anymore once the MC events are successfully tuned to data. Due to the lack of realistic pile up MC it could not be studied how the standard veto has to be adapted to pile up events. But it is noted that algorithms currently being developed can effectively distinguish between jets from the primary event and pile up jets. Hence, the development of a central central jet veto strategy that is robust under pile up conditions may be possible, but it can be different from the one used in this study.

From the mentioned aspects it becomes clear that it might be very challenging to reach the expected sensitivity in a real search.

8. Interpretation of the results

In the preceding chapter, we presented the expected ATLAS sensitivity in a scenario that allows for large invisible Higgs decay widths in terms of the probed value of ξ^2 and as exclusion of M_{H}-Γ_{H} or M_{H}-ω hypotheses, respectively. Also we gave some comments on possible improvements that could enter a future ATLAS search in real data. We continue with the interpretation in the context of comparable searches and sensitivity studies. We also intend to address the the question in which parameter space loop holes for the Higgs boson remain and how a future linear collider (LC) possibly could assist to exclude or confirm invisible Higgs scenarios in a wider part of the parameter space. An interpretation of the results in the scenario with Higgs-graviscalar mixing described in Chapter 2.2.3 proved that the width dependent search strategy brings no advantage over the standard search strategies for invisible Higgs bosons summarised in Section 8.1. This interpretation is therefore transferred to Appendix D.

8.1 Comparison with published sensitivity to narrow invisible Higgs signals

Motivated by the various models implying invisible Higgs decays, as summarised in Chapter 2, the ATLAS and CMS collaborations started the exploration of invisible Higgs decays simultaneously with the study of the potential in the visible channels. Before comparing with our results, we shortly describe the published ATLAS and CMS results.

8.1.1 Expected sensitivity in ATLAS

As long as the invisible decays have only a very small branching fraction, the Higgs discovery in the visible channels is not endangered.If the precisely measured rate in the visible channels is smaller than expected this may be interpreted as a hint for invisible decays of a Higgs boson with the discovered mass.

Sensitivity to invisible decays for a Higgs produced in the weak boson fusion and ZH and ttH channel

In the case when the invisible branching leads to a considerable reduction of the signal yield in the visible channels, the invisible searches will play an important role. But not all production modes are equally proficient in mass range and sensitivity, which is illustrated by Fig. 8.1 taken from [118], which summarises the sensitivity estimated in 2005 for all modes for invisible Higgs searches. The 95% CL upper limit on the value of $\xi^2 = BR(H \rightarrow \mathit{invisible}) \times \frac{\sigma_{\mathrm{BSM}}}{\sigma_{\mathrm{SM}}}$ is displayed, assuming ATLAS has collected 30 fb^{-1} of data at $\sqrt{s} = 14$ TeV. The main advantage of searches in the weak boson fusion is the relative high production cross section for higher Higgs masses up to 400 GeV. While the weak boson fusion is expected to be sensitive down to $\xi^2 \approx 0.25$ between $M_{\mathrm{H}} = 110$ GeV to $M_{\mathrm{H}} = 250$ GeV, both the top quark associated production and the ZH production, can probe ξ^2 in the mass range between $M_{\mathrm{H}} = 110$ GeV to $M_{\mathrm{H}} = 200$ GeV at a level $\xi^2 \approx 0.5$ to $\xi^2 \approx 1.5$ % and are clearly not competitive with the weak boson fusion searches for the mass range $M_{\mathrm{H}} = 200$ GeV to $M_{\mathrm{H}} = 400$ GeV.

Nevertheless, if in the weak boson fusion channel a Higgs signal is seen, the signal has to be confirmed in at least one of the other channels at the same Higgs boson mass. The knowledge of the mass

may help to optimise the searches in the less sensitive channels further. If further optimisation is not possible, the less sensitive channels can confirm a discovery only with much more collected luminosity.

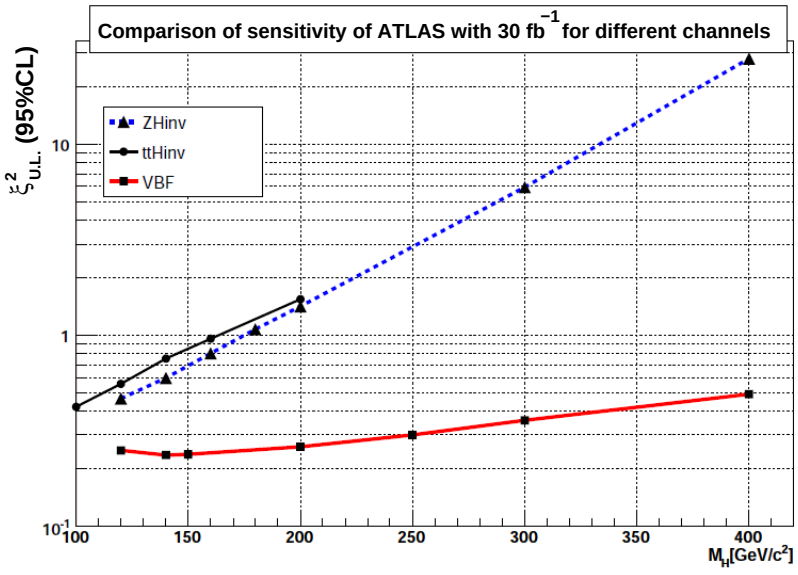

Fig. 8.1: *Estimated sensitivity of ATLAS in Higgs searches for narrow invisible Higgs decays on basis of 30 fb^{-1} of collected data at $\sqrt{s} = 14$ TeV (taken from [118] published 2006). The 95% CL upper limit on ξ^2 is compared for searches using ZH (blue dashed line and triangles), top quark associated (black full line and dots) and weak boson fusion (red full line squares) production modes. The comparison makes the advantage of searches in weak boson fusion mode evident, due to the high cross section over a larger Higgs mass range.*

Updated sensitivity predictions in weak boson fusion and ZH channel

We displayed the older result of [118] in Fig. 8.1 to show the comparison of all three search modes and because ATLAS had not updated the results of the sensitivity to the invisible Higgs boson decays with the top pair associated production since then. For the more important weak boson fusion production channel and the Z bosons associated channel updates are available. These are published in [7] and displayed in Fig. 8.2 for a collected luminosity of 30 fb^{-1} at $\sqrt{s} = 14$ TeV.

The search using weak boson fusion uses mass independent optimised selection cuts and as final step an analysis of the shape of the distribution of the azimuthal angle between the tagging jets. This study used for the first time detailed detector simulation and a motivated assumption about the size of detector-related systematic effects. The shape of the azimuthal tagging jet distribution is very characteristic for the weak boson fusion. One expects the W/Z boson background to be accumulated at values above 1 rad while the signal tends to have smaller values. The knowledge of the azimuthal difference of the tagging jet distribution has a 10 % theory error for the background at LO (5 % at NLO) [7]. In [7] the shape ratio R is definded and related to the value of ξ^2 over the number of background or signal events found a smaller than 1 rad range N^1 or the whole range N^π:

$$R = \frac{\int_0^1 \frac{d\sigma}{d\Phi_{jj}}}{\int_0^\pi \frac{d\sigma}{d\Phi_{jj}}} = \frac{N_B^1}{N_B^\pi}\left[1 + \xi^2\left(\frac{N_S^1}{N_B^1} - \frac{N_S^\pi}{N_B^\pi}\right)\right]$$

By using the shape-ratio the systematic uncertainties can be reduced largely, since some systematic uncertainties e.g. on the theoretical cross sections or the luminosity are expected to cancel out. For comparison a simple cut-based analysis would suffer from large uncertainties from the jet measurements and end up with a total systematic error on the background of 20%. The shape analysis assumes a conservative detector-related systematic uncertainty of only 5.3 % for the background. As conservative estimate 10 % theoretical uncertainty for the background shape are added in quadrature yielding a total systematic uncertainty for the background of 11.3 % in the shape analysis. The impact of systematic uncertainties is not negligible, as can be seen in the left panel by the differences between lower bullets, which give the limit on ξ^2 without and the upper triangles which give the limit of ξ^2 including systematic uncertainties.

In the right panel of Fig. 8.2, the sensitivity of weak boson fusion search is compared to the search in the ZH production channel. In this study the decays Z$\rightarrow e^+e^-$ and Z$\rightarrow \mu^+\mu^-$ are reconstructed, missing energy is coming from H$\rightarrow$invisible. The peculiarity of the ZH study is that it uses a boosted decision tree operating on a large number of variables. In the mass range below 130 GeV the ZH productions cross section is exceeding the weak boson fusion cross section, but this advantage is partially lost by the multiplication with the branching of the Z boson into the two lepton species. As one can see below 150 GeV, the ZH channel is competitive to the weak boson fusion. Especially dealing with leptons, the large uncertainties from the jet measurements in central and forward region are absent and the total systematic uncertainty for the search is estimated to be 7.2%.

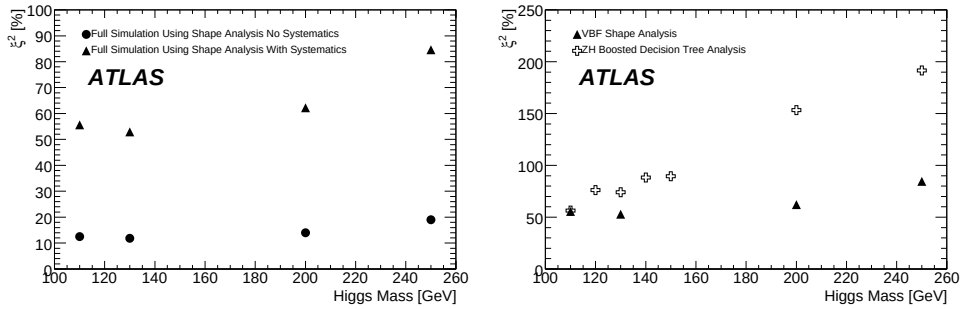

Fig. 8.2: *The ATLAS sensitivity on narrow invisible Higgs decays in terms of an upper limits on ξ^2 at 95% CL. Left panel: Sensitivity for 30 fb^{-1} of data at $\sqrt{s} = 14$ TeV in searches using weak boson fusion production and an analysis of the shape of the distribution of the azimuthal angle between the tagging jets. The impact of systematic uncertainties can be seen in the differences between lower bullets, which give the limit on ξ^2 without and the upper triangles which give the limit of ξ^2 including systematic uncertainities. Right panel: The sensitivity including systematic uncertainties of the shape analysis in the weak boson fusion production (triangles) is compared with the sensitivity of a multivariate analysis, using boosted decision trees, in the ZH production channel (cross markers).*

One can see in comparison of Fig. 8.1 with Fig. 8.2, that the conservative systematic uncertainties in the update of the weak boson fusion channel reduce its sensitivity by a factor 2 to 2.5. One effect is that the new studies applied NLO cross sections to the expected background, which are larger. Additionally it should be mentioned that the results for the weak boson fusion from Fig. 8.1 were made with fast detector simulation. Thus, one will conclude that the fast detector simulation gives too optimistic results that cannot be confirmed by the detailed detector simulation. In the ZH channel, for which both figures contain results from detailed detector simulation, the new search strategy and new systematics have different impact. For masses below 150 GeV the updated sensitivity deteriorates about a factor of two to 1.1, but for higher masses as 200 GeV the sensitivity in the update becomes better up to a factor of two thirds. This may be attributed to the enhanced sensitivity of the multivariate search strategy compared

to a simple cut analysis. In [7] no combination of the weak boson fusion and associated production to improve the sensitivity had been tried. The gain of the combination is certainly not much since the weak boson fusion dominates over the whole mass range.

8.1.2 Expected sensitivity in CMS

In 2009 the CMS Collaboration published a sensitivity study for the invisible Higgs [29]. The CMS study used likewise the weak boson fusion channel at a centre of mass energy of $\sqrt{s} = 14$ TeV to design a search for genuine narrow invisible Higgs decays in a Higgs mass range between 120 GeV to 160 GeV. The CMS detector calorimeter system is completely inside the solenoid and its cryostat, which therefore is not interfering with the jets measurement. But again this purely cut based study found that jet energy scale at the order of 14.8 % and the missing energy resolution at the order of 9.5 % dominantly contribute to the uncertainty of expected signal events. For the background uncertainties no theoretical uncertainty were used since these would be evaluated in a data driven approach. The CMS result is presented in Fig. 8.3. While the upper line with blue triangles corresponds to the expected sensitivity in early data taking with 10 fb^{-1}, the lower line with red triangles is valid for 30 fb^{-1} and can be compared with the right panel of Fig. 8.2. In the studied mass range below 160 GeV the CMS collaboration expects to be double as sensitive as the ATLAS collaboration. In summary the comparison shows that

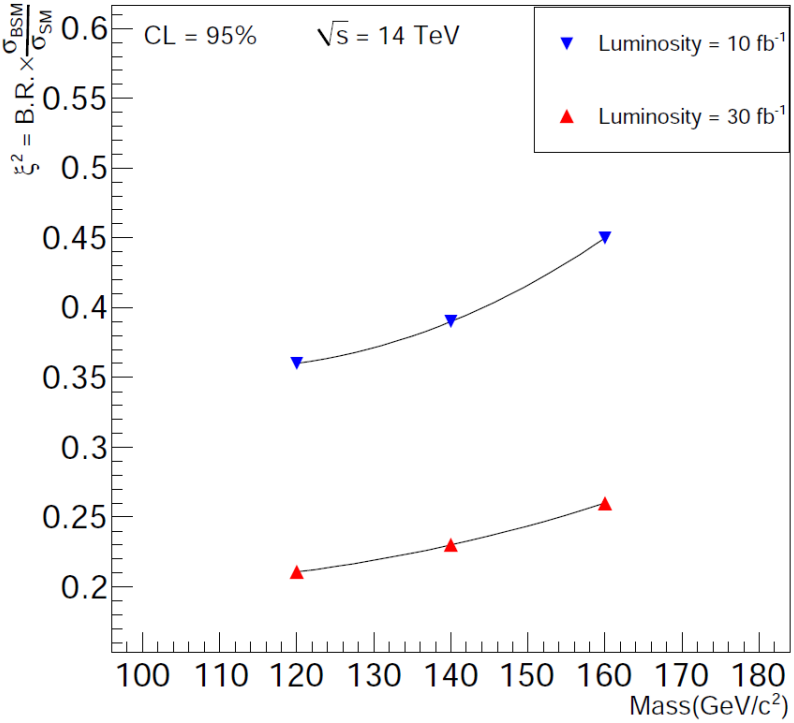

Fig. 8.3: *Expected sensitivity in terms of an upper limits on ξ^2 at 95% CL for narrow invisible Higgs decays in the CMS detector using Higgs production in the weak boson fusion channel. Results are presented for 10 fb^{-1} and 30 fb^{-1}, at $\sqrt{s} = 14$ TeV , from an updated study from 2009 (taken from [29]).*

the expected sensitivities differ between the experiments and channels. Certainly the sensitivity depends on the assumptions of the size of systematics and finally the ATLAS update in the ZH channel confirm, that multivariate methods for sensitivity improvement are worthwhile to study. Concerning the very optimistic prospects for the invisible Higgs published by the CMS collaboration it will be interesting to see if this is realised with real data. If this is the case, the combination of the CMS results with the

ATLAS results is expected to give also a boost in the sensitivity towards the stealthy Higgs scenario.

8.1.3 Comparison to the expected sensitivity of ATLAS towards invisible Higgs decays with large width

In this section we compare the achieved sensitivity of the presented study in terms of limits on ξ^2 with the standard invisible Higgs searches, discussed in Section 8.1.1 and 8.1.2. For this comparison both relevant plots (from Fig. 7.1 and Fig.8.2) are, for convenience, again presented in Fig. 8.4, where the left panel contains the expected ATLAS sensitivity, with 30 fb^{-1} collected at $\sqrt{s} = 14$ TeV, for narrow-width invisible Higgs decays and the right panel the upper limit on invisible Higgs decays with a considerably broader decay-width, where we have chosen the medium large coupling $\omega = 5$ as example.

Comparison of ξ^2 with only statistical uncertainties

The sensitivity for the narrow width invisible Higgs decays in the Higgs mass range between 110 GeV and 260 GeV can be read off to be between $\xi^2 \approx 0.10$ and $\xi^2 \approx 0.20$, if only the statistical uncertainty is considered. The upper limits expected to be set on ξ^2 in case of broad invisible Higgs decays are without systematics uncertainties in the Higgs mass range up to 260 GeV between $\xi^2 \approx 0.15$ and $\xi^2 \approx 0.20$. So the statistical sensitivity is in both scenarios of the same order of magnitude, and small differences can stem from the different search strategies applied and the used MC samples. Generally one observes for both scenarios a lower expected sensitivity for higher Higgs boson masses, which can clearly be seen in the larger mass range presented for the broad invisible Higgs. The sensitivity deterioration is expected due to the lower Higgs production cross section for higher masses.

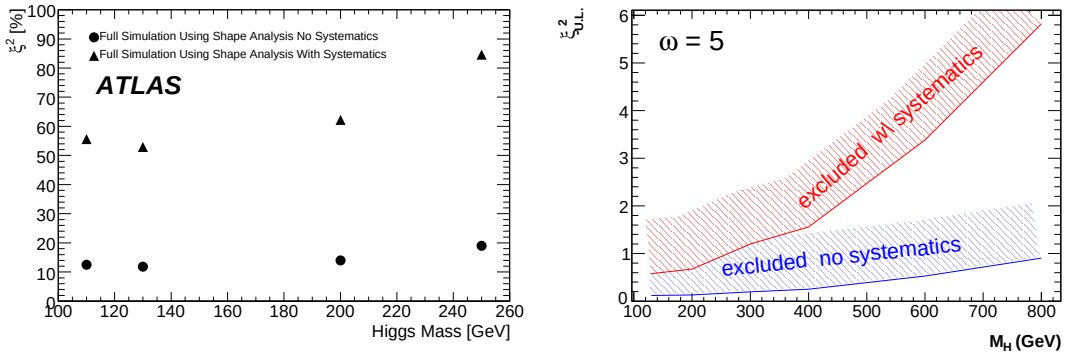

Fig. 8.4: *The ATLAS sensitivity on invisible Higgs decays in terms an upper limit on ξ^2 at 95% CL with 30 fb^{-1} of ATLAS data at $\sqrt{s} = 14$ TeV. Left panel: Sensitivity on ξ^2 in searches using weak boson fusion production and an analysis of the shape of the distribution of the azimuthal angle between the tagging jets. Right panel: Expected upper limits at 95% CL on $\xi^2 = \frac{\sigma_{invisible}}{\sigma_{SM}}$ depending on M_H for a typical example of $\omega = 5$ of the stealthy Higgs scenario using the multivariate method. The expected exclusion without systematic uncertainties is given by the contour.*

Comparison of size and impact of systematic uncertainties

If one compares the impact of the systematic uncertainties the difference between the search strategies becomes more obvious. For a narrow invisible Higgs bosons in the mass range up to 260 GeV the sensitivity is largely reduced by the systematic uncertainties. It is expected to merely reach $\xi^2 \approx 0.50$ and $\xi^2 \approx 0.90$, which corresponds to a reduction about roughly a factor 4 to 5. The value of ξ^2 to which

the study is still sensitive, deteriorates quickly with the rising Higgs mass, surpassing $\xi^2 = 1$ for a Higgs boson of $M_H \approx 300$ GeV. On the first view the dependence of the result from the assumed systematics is very similar for the search for the broad invisible Higgs in the mass range below 260 GeV. For these masses likewise a reduction of exclusion power by the factor 3 to 5 is observed. In the example shown $\xi^2 = 1$ is passed slightly earlier at about a Higgs mass of 260 GeV. For higher Higgs masses with reduced production cross section the deterioration becomes worse and worse, for example for a Higgs mass of about 450 GeV only the value $\xi^2 = 2$ is excludable considering the systematics. It has to be emphasised that for the study of the narrow invisible Higgs a very pessimistic assumption on the knowledge of the jet energy scale was assumed: In dependence of η, an uncertainty between 7 % and 15 % had been applied. But due to the powerful shape analysis, the impact on the result could be controlled. In the study we present here for the broad invisible Higgs decays, we found that such large uncertainties would prevent any exclusion. We therefore assumed uncertainties that are optimistically expected after some years of data taking. Hence we reduced the jet energy scale uncertainty to roughly a quarter of the value used in the narrow Higgs study. This can be seen as indicator that it is more difficult in searches for broad invisible Higgs decays to cope with the impact of the systematic uncertainties. Each time one applies very strict criteria, be it in form of cuts or a highly optimised multivariate selection, the drawback is that the result becomes very vulnerable to the impact of systematic uncertainties. Unfortunately even with the very optimistic assumption on the jet energy scale, the used multivariate strategy ends up with about twice the total systematic uncertainty as the standard invisible Higgs shape analysis, which reduces the sensitivity largely.

Learning that lesson it may be worthwhile in a hypothetical redesign of the stealthy Higgs search to replace the hard cut on the output of the MLP with the following strategy. The azimuthal tagging jet difference is spared out in the MLP, on which only a loose cut with low systematic influence is applied, and the azimuthal tagging jet difference distribution is entering after the MLP into a shape-ratio analysis. This idea is motivated by the following observation: The contribution of the azimuthal difference of the tagging jet candidates to the performance of the MLP may be not such important, since all other variables introduce enough information about the shape differences and variables correlations to guarantee a good performance of the MLP. But as the study [7] proved very impressively, the azimuthal difference of the tagging jet candidates can be an excellent tool in a shape analysis to gain control over systematic uncertainties. Therefore, this could be a very proficient use of this variable to improve the sensitivity of the search.

Mass- and width-dependent invisible stealthy Higgs cross section

If performing the standard invisible search the Higgs is assumed to be produced with SM cross section for the given Higgs mass. Only the invisible branching scales the sensitivity on the expected ξ^2 found in the search. One reason for the difference in sensitivity compared with the stealthy Higgs study, may be that the used formula for the normalisation of the stealthy Higgs cross section is not only depending on the Higgs mass of the pole but also on the invisible width. As expected generically, if allowing for a non trivial decay width, it includes a branching into the invisible states by the Breit-Wigner resonance factor.

We have observed that the stealthy Higgs cross section is confined by the SM cross section. If we fix the mass of the Higgs boson, for some choices of ω the cross section is high but for other choices the cross section is considerable lower than the SM cross section. Also the efficiency is a convolute from the single mass efficiencies that contribute to the Breit-Wigner shaped Higgs mass spectrum around the Higgs pole mass. Varying signal hypotheses contain a varying fraction of light and heavy Higgs masses in this spectrum. The standard analysis for narrow invisible Higgs decays always normalised the signal samples to the full SM model cross section and the efficiency is depending only on the nominal Higgs mass. In comparison the potentially smaller stealthy Higgs cross section explains that not only for many heavy Higgs mass and ω-hypotheses but even for some low Higgs mass and ω-hypotheses, the exclusion

in the stealthy Higgs scenario is more difficult as for the standard analysis for narrow invisible Higgs decays.

The fact that our analysis fails in excluding especially high Higgs masses can be understood by the unfavourable situation of small cross sections. In that case the considerably large systematic uncertainties on the background make it impossible to reach an exclusion. Even if the Higgs mass is lower, some ω-hypotheses cannot be excluded in the presence of systematic uncertainties, in case the cross section of the signal is low for these choices of ω.

8.2 Discussion of implications of occurrence of the stealthy Higgs at the LHC

Whenever one tests experimentally a proposed theoretical model, one seeks to confirm it or rule it out. The regions where the model can neither be discovered nor ruled out should be restricted to a minimum by the design of the search strategy. However, the experimental test of the stealthy Higgs does not only have the aim of scrutinising a model. By devising a mechanism that potentially hides the Higgs at the LHC, the stealthy Higgs has implications on the general strategy for discovering the Higgs. The realisation of the stealthy Higgs in nature alone must not necessarily spoil the prospects of Higgs discovery at the LHC. But if it does, it will happen in a twofold way. Firstly the rate in visible channels is reduced significantly, so that data of the order 100 fb^{-1} is needed for a discovery. Secondly the invisible width being significantly larger than the experimental resolution deteriorates the effectiveness of signal extraction in the visible channels. It is interesting to which extend the coupling to the hidden sector becomes effective in competition with the canonical discovery channels. Only with that knowledge one can evaluate, if the fact that a hypotheses of the stealthy Higgs scenario cannot be excluded at an LHC experiment, has negative consequences for the Higgs discovery.

8.2.1 Identify regions with large invisible branching above the threshold for Higgs decays into two weak bosons

As Fig. 8.2 and Fig. 8.3 show, substantial narrow invisible Higgs decays will be detectable easily below $M_{\mathrm{H}} = 200$ GeV. But the searches for narrow invisible Higgs decays become more and more insensitive for Higgs masses above 250 GeV. Hence in order to hide the Higgs at the LHC in the stealthy Higgs scenario, if we neglect the influence of an invisible width on the signal extraction for a moment, we should seek for hypotheses of $M_{\mathrm{H}} - \omega$ where the invisible decays are large for Higgs masses above 200 GeVto 250 GeV. Then two types of hypotheses can be distinguished:

1) The hypothesis has an ω such that the invisible cross section is small and below the sensitivity of an invisible Higgs search. In this case one has to consider the invisible branching B_{inv}, which scales the reduction of the visible yield by $(1 - B_{\mathrm{inv}})$ (see Chapter 2.2.3 and [66]). The discovery potential in decays of the Higgs into weak bosons will consequently be reduced, but it may well be possible to recover the discovery potential with more collected data.

2) The hypothesis has an ω such that the invisible cross section is large and invisible decays are dominant even for large Higgs masses. In that case the question is whether the standard invisible Higgs searches have a sensitivity down to the value of $\xi^2_{U.L} = \frac{\sigma_{stealthy}}{\sigma_{\mathrm{SM}}}$, which can be difficult for Higgs masses above the threshold for decays into weak bosons. Especially since the stealthy Higgs cross section is bound by the SM cross section, the detection will not be possible in the mass range where the upper limit of the standard invisible Higgs searches is larger than one ($\xi^2_{U.L} > 1$). At the same time the reduction of the visible rate by $(1 - B_{\mathrm{inv}})$ may be so large that even extended data taking could not provide enough luminosity to find the Higgs in the visible channels. In that case a stealthy Higgs would successfully evade its detection at the LHC.

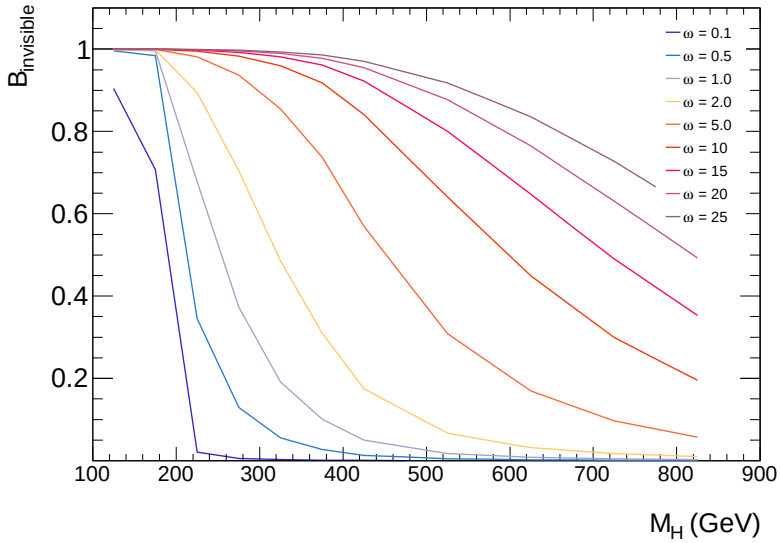

Fig. 8.5: *Invisible branching given in the stealthy Higgs scenario. For $\omega > 5$ even above the threshold for decays into weak bosons the stealthy Higgs can decay considerably into invisible channels leaving for the visible channels only a reduced rate.*

Evolution of invisible branching depending on ω

The question we want to address next, mostly qualitatively, is in which Higgs mass region the suppression of SM search channels by the stealthy Higgs scenario becomes problematic for the ATLAS discovery. Therefore, we show the invisible branching predicted by the stealthy Higgs scenario as function of the Higgs mass for various studied couplings ω in Fig. 8.5. The size of the couplings ω one expects in the model are disputable. Too small couplings, much below unity, will not exhibit a particular stealthy Higgs behaviour and are not representative for the kind of model and too strong couplings, much larger than one, may be also considered as artificial. As invisible Higgs searches below the threshold for Higgs decays into two weak bosons have very good sensitivity we are in the following more interested in the role the stealthy Higgs scenario plays for a Higgs mass above 200 GeV. The following observations can be summarised depending on the value of ω:

1) small $\omega \lesssim 2$
   The invisible branching is dominant for $M_H < 250$ GeV, except for the very small coupling of $\omega = 0.1$, which extents the impact of invisible decays only to $M_H < 200$ GeV. The invisible branching falls very quickly, becoming lower than 20% for 200 GeV $< M_H <$ 450 GeV and plays no role for masses above.

2) medium $\omega \approx 5$
   for this medium coupling the dominant invisible branching is extended up to $M_H < 400$ GeV. Effects in sensitivity due to the width may be experimentally not important.But the fact of high invisible branching is important since in the region 250 GeV $< M_H <$ 300 GeV the narrow width invisible Higgs searches start to lose already much of their sensitivity. It is therefore uncertain if the detection even for the high invisible branching will be possible. The invisible branching falls below 20% at a Higgs mass of 500 GeV. The large invisible branching below 500 GeV will reduce the rate in the visible channels severely.

3) large $\omega \gtrsim 10$
   In the regime of a very strong coupling the invisible branching stays dominant for $M_H \lesssim 500$ GeV.

For even higher Higgs mass the invisible branching ratios are still considerable and stay above 20%, but below the sensitivity of the the narrow width invisible Higgs searches for such high Higgs masses. Also the couplings are so large that the Higgs decay width is considerably smeared out which will cause additional problems in detection at low Higgs masses with searches optimised for narrow invisible Higgs. For couplings of $\omega = 10$ the visible rate of the SM channel will be reduced strongly by factor one half or more in the mass region of at least 250 GeV $< M_H \lesssim$ 600 GeV.

Summarising at this point, we observed that the stealthy Higgs scenario with couplings $\omega \geq 5$ extends a considerable invisible branching in the mass region $M_H > 300$ GeV, where the standard search for invisible Higgs decays has only very limited sensitivity. And at the same time the reduction of visible channels will be not a small effect.

Estimate on expected rate reduction in visible channels

Since in the high Higgs mass range one needs the visible SM channels to find the Higgs we try to get a feeling of how large the expected statistical significance in the visible channels will be degraded by the stealthy Higgs scenario.

The combined discovery potential of all SM channels studied by ATLAS [1)] expressed as statistical significance is shown in Fig. 8.6, taken from [3]. The left panel shows the expectation for 30 fb^{-1} of ATLAS data, the right panel shows how the significance improves for 100 fb^{-1} of ATLAS data.

Clearly with a larger data set, one gains significance in all channels, which should roughly scale with the square root of the luminosity increase. Thus the gain is not very large. As the comparison shows with more than three times the data the discovery potential in the Higgs mass region between 200 GeV and 800 GeV rises only about roughly a factor of 1.5 to 2.

Both plots contain the expected statistical significance, i.e. no systematic uncertainties. This is justified due to the fact that in almost all channels reconstructed mass peaks allow for an accurate data driven determination of the background contribution. By defining a mass window around the peak, one can fit the background contribution from the sidebands in data. The fitted background is subtracted in the signal region and the significance can be determined with good precision, as long as the signal region is not too broad. Only in the H$\rightarrow$WW* channel a mass peak is not reconstructed and only excess events are counted. Hence, an assumed background uncertainty of ± 5 % is included. It is also important to note that no K-factors for the NLO rates are included, since they have also a theoretical error. One should keep in mind that these plots represent a very idealised view on the discovery potential. Included detector-related systematical uncertainties or NLO background rates will reduce the very nice combined discovery potential to some extend. As example for the possible size of such uncertainties, we give an updated discovery potential for 30 fb^{-1} of the most important final state with electron and muons, the ZZ$\rightarrow$ *llll* channel, which includes systematic uncertainties and NLO background in Fig. 8.7. The new evaluated channel contributes to discovery in the Higgs mass range above 200 GeV up to 500 GeV (not anymore up to 600 GeV as in Fig. 8.6). If one compares the significances without systematics (red markers) these are lower in the new study due to more realistic detector simulation and NLO MC. The effect of detector systematics is seen in the difference between the blue and red markers. The systematic uncertainties reduce the significance roughly between 10 % to 30 %. Generally, the expected significance in Fig. 8.7 is about 40 % lower than in Fig. 8.6.

If there are problematic regions due to the presence of the stealthy Higgs in this optimistic scenario, displayed in Fig. 8.6, they will be even more severe in the updated discovery potential with systematics. Also the importance of channels and the relative contribution to the significance in the specific mass

[1)] The expected discovery potential combining all SM search channels for the Higgs with 30 fb^{-1} or 100 fb^{-1} of data at $\sqrt{s} = 14$ TeV, respectively, was published 1999 in [3]. Most of the newer studies, except the important ZZ$\rightarrow$ *llll*, with detailed detector simulation and systematical uncertainties refer to the early discovery potential with 10 fb^{-1} of data or projections for exclusion and discovery at the reduced centre of mass energy of $\sqrt{s} = 7$ TeV at initial data taking.

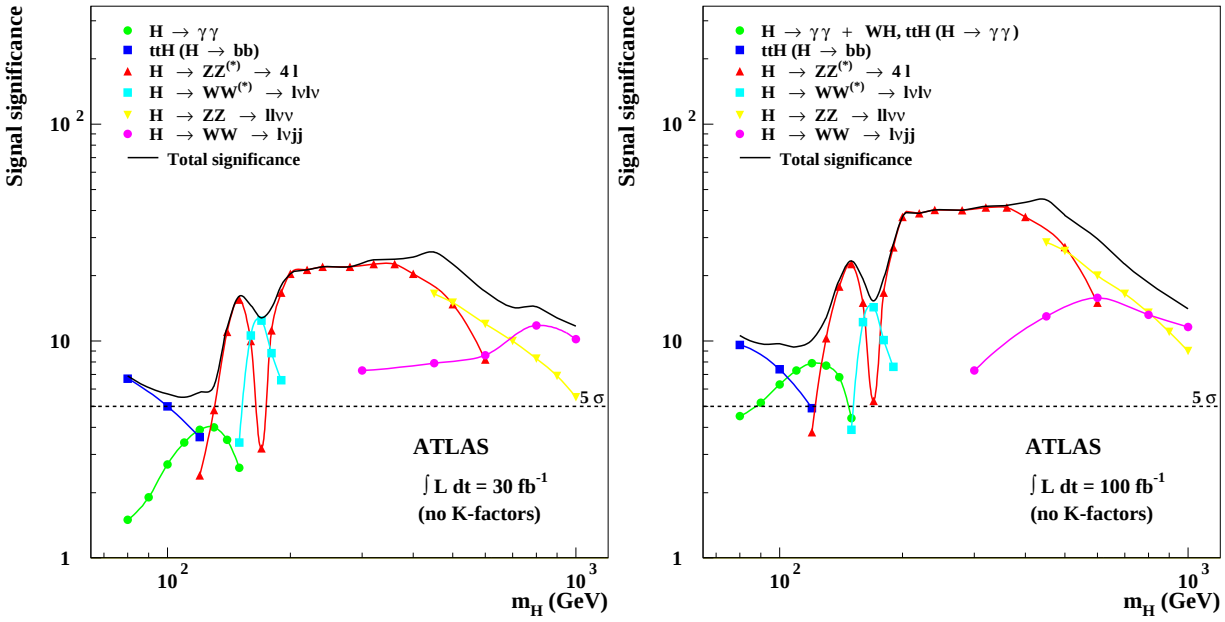

Fig. 8.6: *Left panel: Expected discovery potential with 30 fb^{-1} of ATLAS data at $\sqrt{s} = 14$ TeV. Right panel: Expected discovery potential with 100 fb^{-1} of ATLAS data (taken from [3] published 1999). The plots contain the expected statical significance, i.e. no systematic uncertainties. This is justified due to the fact that in almost all channels reconstructed mass peaks allow for an accurate determination of the significance. Only in the H→WW* channel a mass peak is not reconstructed and only excess events are counted. Hence, a background uncertainty of ±5% is included. It is also important to note that no K-factors for the NLO rates are included, since they have also a theoretical error.*

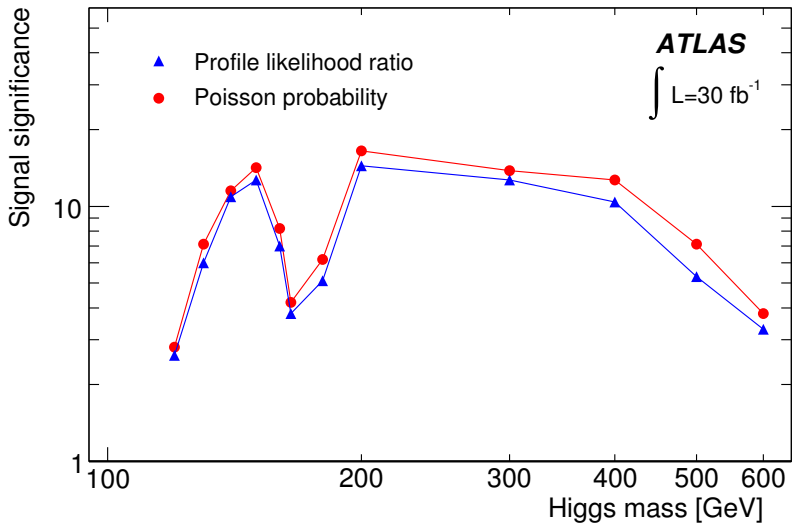

Fig. 8.7: *ATLAS Higgs discovery potential in ZZ→ llll with 30 fb^{-1} of data at $\sqrt{s} = 14$ TeV. The red line with dots does not include systematics and uses Poissonian statistics in determination of the significance. The blue line with triangles includes the systematic uncertainties by a profile likelihood. The reduction of the significance due to systematical uncertainties is not large, which proves that the four lepton channel has a very clean experimental signature. (Taken from [7])*

range will not change with any update. In the interesting mass range 250 GeV $< M_H <$ 600 GeV where the Higgs discovery in presence of the stealthy Higgs scenario has to be made in the visible channels, we find that the significance is lager than 20 up to $M_H \approx 550$ GeV for 30 fb^{-1} of data. The significance is dominated by the experimentally very clean to reconstruct four lepton channel. Then the significance degrades for higher Higgs masses and the WW$\rightarrow jjl\nu$ channel contributes more. We assume for the estimate a statistical significance of 20 (40) for $M_H <$ 550 GeV in the range and of 15 (30) in the range 550 GeV $< M_H <$ 600 GeV, and 10 (20) for higher masses for 30 fb^{-1} (100 fb^{-1}) of data.

To get an impression how large the impact of the competition between visible decays in the canonical discovery channels and additional invisible decays due to the stealthy Higgs scenario can reduce the discovery potential with 30 fb^{-1} of ATLAS data, we calculated the predicted invisible branching fraction for a Higgs mass as function of ω and rescaled the significances (read off from Fig. 8.7 and Fig. 8.6) accordingly. In Table 8.1 we list the estimated Higgs mass regions where the reduction factor for the given ω due to the competition with the invisible channels presses the significance below 5σ. In the second column in Tab. 8.1 we show the problematic Higgs mass regions as function of ω (first column in Tab. 8.1) for the recently studied ZZ$\rightarrow llll$ channel. As one can see in Fig. 8.7 the discovery potential is above 5σ for a Higgs mass from 200 GeV to 500 GeV, but falls quickly for higher Higgs masses so that the channel was studied only up to 600 GeV with 30 fb^{-1}. As said it is a competitions between visible and invisible decays. For a lower Higgs mass the invisible branching can be considerable if the ω has small or medium values. E.g. in case of the single channel ZZ$\rightarrow llll$ a value of $\omega \approx 1$ would spoil the Higgs discovery in this channel with 30 fb^{-1} for a Higgs mass below 230 GeV. In that case the invisible Higgs searches would find the Higgs. Above that mass value the ZZ$\rightarrow llll$ channel would retain its discovery potential. But according to our estimate already for a coupling of $\omega \geq 5$ the whole range up to 500 GeV in which the ZZ$\rightarrow llll$ channel is expected to contribute to a discovery with 30 fb^{-1} of data is endangered to drop below 5 σ. This is problematic since one is not only losing an very important discovery channel but the sensitivity for invisible Higgs decays is hardly given for a Higgs mass much heavier than 200 GeV (see e.g. Fig. 8.2).

In the third column in Tab. 8.1 we present the Higgs mass regions that could drop below 5σ if the promising TDR results of the discovery potential combining all visible channels with 30 fb^{-1} are rescaled. First of all the combination of channels improves the significance. Secondly the mass range in which a 5σ discovery is possible is enhanced by the combination of channels. As a look at Fig. 8.6 proves, the ATLAS TDR claimed to be able to discover the Higgs up to masses above 900 GeV. Again at the lower end of the Higgs mass range, a relatively small value of $\omega \approx 1$ would press the significance below 5σ up to the Higgs mass of 220 GeV. But the combined discovery potential is more robust against the coexistence of visible and invisible Higgs decays. E.g. for $\omega \approx 5$ the discovery of Higgs masses above 355 GeV should be possible with 30 fb^{-1}. For very heavy Higgs bosons above 600 GeV the coupling $\omega \approx 15$ is not spoiling the discovery. But the discovery with 30 fb^{-1} is expected to be lost in the Higgs mass range of 260 GeV to 900 GeV for the extreme value of the coupling $\omega \geq 20$. The conclusion that can be drawn from Tab. 8.1 is, that the existence of a stealthy Higgs can possibly delay a Higgs discovery, because data of the order of 100 fb^{-1} has to be collected to claim a discovery in the visible channels.

8.2.2 Impact of broad invisible Higgs width on signal extraction in visible channels

The second negative effect of the stealthy Higgs scenario on the discovery potential of the Higgs is more difficult to access. In Fig. 8.6, one identifies the ZZ$\rightarrow llll$ or ZZ$\rightarrow ll\nu\nu$ final states to be most important for discovery over the whole heavy Higgs mass range from 200 GeV up to approximately 600 GeV. In this mass range it is possible to define the signal region around the peak location in the reconstructed invariant mass (ZZ$\rightarrow llll$) or a transverse mass (ZZ$\rightarrow ll\nu\nu$). One can use data-driven background determination

significance < 5 in SM channels with 30 fb^{-1} of ATLAS data		
ω	ZZ$\rightarrow llll$	all visible
1	$M_H \lesssim 230$ GeV	$M_H < 220$ GeV
2	$M_H < 310$ GeV	$M_H < 260$ GeV
5	$M_H < 500$ GeV	$M_H < 355$ GeV
10	$M_H < 500$ GeV	$M_H < 400$ GeV
15	$M_H < 500$ GeV	$M_H < 625$ GeV
20	$M_H < 500$ GeV	$M_H < 900$ GeV

Tab. 8.1: *Regions for Higgs masses where a coupling ω (first column) of the stealthy Higgs can spoil a potential Higgs discovery at ATLAS in the visible SM search channels. The invisible branching as function of mass and ω, plotted in Fig. 8.5, was used to scale the significance quoted for 30 fb^{-1} of ATLAS data in Fig. 8.7 and Fig. 8.6. In the second column we give the Higgs mass range, for which the significance in the ZZ$\rightarrow llll$ channel drops below 5σ with 30 fb^{-1}, because of the opening of stealthy Higgs decays into invisible final states. In the third column we give the Higgs mass range for which the combined significance of all visible channels with 30 fb^{-1}, quoted in the ATLAS TDR, drops below 5σ.*

like sideband fits for estimates of the background. Also important is the channel WW$\rightarrow jjl\nu$ for very high masses up to approximately 900 GeV. But in this final state only excess events are counted over the expected background.

The presence of a stealthy Higgs can possibly hamper these signal extraction strategies. As we e.g. described in Section 2.2.3, the total Higgs width in the propagator is important for the s-channel contribution in weak boson scattering. If the Higgs propagator contains a large invisible width, a broad Higgs will occur in the s-channel of the weak boson scattering. Consequently a channel using any mass window technique like ZZ$\rightarrow llll$ will lose sensitivity as the Higgs mass spectrum becomes very broad and smeared out. The effect depending on ω can be potentially large. We think that most probable the background discrimination in the WW$\rightarrow jjl\nu$ would become also experimentally more difficult if the Higgs mass is smeared out.

In the stealthy Higgs scenario the direct decay width becomes arbitrary and by studying a large variation of these widths we already check all possible effects from experimental point of view. In principle a mixing between Phions and Higgs is possible if $\kappa \neq 0$. But for simplicity we restrict ourselves to $\kappa = 0$, i.e. do not allow for Higgs-Phion mixing. With this restriction we avoid the complication that the mixing would lead to altered cross sections (see Section 2.2.4) as well as to an additional contributions to width. Therefore, it is evident that $\kappa \neq 0$ reduces the chances for a Higgs discovery even more.

Thus we note that a large width of the Higgs in the s-channel would spoil the mass window technique, as the mass is smeared out very much. This can potentially harm the significances quoted in Fig. 8.6 and Fig. 8.7, to which extent however is hard to estimate at this place. As we have seen, the invisible Higgs search with weak boson fusion is mostly insensitive to width effects in the final state. However an exclusion of the stealthy Higgs scenario is expected to be only in a very limited parameter region possible with ATLAS. If the Higgs is not found, the reason therefore might remain unresolved. This experimental outcome could occur due to the absence of the SM Higgs or due to the presence of a stealthy Higgs. As consequence of this study, we therefore strongly advise that ATLAS should study the main search channels like ZZ$\rightarrow 4l$ or ZZ$\rightarrow ll\nu\nu$ in the stealthy Higgs scenario specifically to acquire knowledge about the impact of the broad Higgs width using this reconstruction techniques.

8.3 Exclusion of the stealthy Higgs scenario at LEP 2

Of the four LEP experiments only the OPAL collaboration performed a dedicated search for the stealthy Higgs [10], the cited source is appended for fast reference in Appendix C.

It is specifically the technique of recoil mass spectra with the beam energy constraint which allows searches at electron-positron colliders to be sensitive to the width of the Higgs boson. In the experimentally very clean environment of such colliders the broadening of the recoil mass spectrum is visible as soon as it is larger than the mass resolution of typically 3-5 GeV since the systematic uncertainties are usually low. Also due to the lower background, the LEP 2 experiments were typically sensitive to signal cross sections in the order of 0.1 pb. Only near to the kinematic limit of the order of 110 GeV the sensitivity was gradually lost. Unfortunately, the other three LEP experiment made no search in this scenario, the approximately four times higher luminosity would had helped to push the ω exclusion a little bit further.

OPAL data, taken at centre of mass energies between $\sqrt{s} = 183$ GeV and $\sqrt{s} = 206$ GeV, summing to about 630 pb^{-1} was analysed in an optimised Higgs decay-width dependent search. The result is the exclusion of a large part of the parameter space in the stealthy Higgs scenario and summarised in the stealthy Higgs exclusion plot of Fig. 8.8. Problematic parameter combinations, so to say loop holes, can be identified, in which case the stealthy Higgs would have escaped the LEP searches, though it can be produced at the collider. These parts of the parameter space can be characterised as follows.

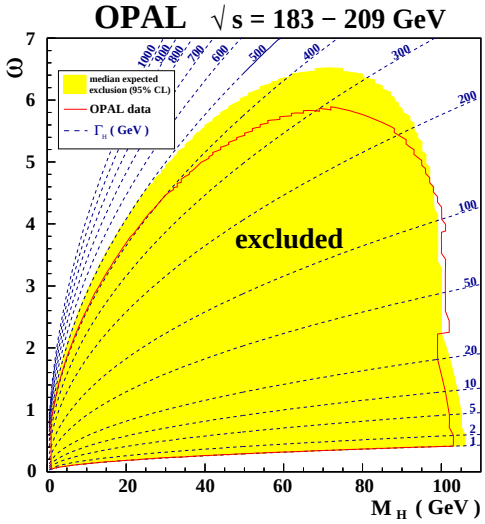

Fig. 8.8: *Result of the OPAL collaboration in a dedicated search for the stealthy Higgs. In yellow the expected exclusion in the M_{H}-ω-plane is marked. The actual exclusion was gained within the red contour, and covers a large part of the accessible parameter space of the model (taken from [10]).*

The effects of the stealthy Higgs scenario are dominant if the values of the coupling to the hidden scalars is non-perturbative. In case that nature contains a very light stealthy Higgs e.g. $M_{\mathrm{H}} \lesssim 20$ GeV with couplings between $\omega \approx 1$ to $\omega \approx 4$ or for a slightly heavier Higgs with mass $M_{\mathrm{H}} \lesssim 40$ GeV and non-perturbative couplings of $\omega > 5$, the OPAL experiment would have missed the exclusion of such stealthy Higgs bosons. Generally for a Higgs with mass $M_{\mathrm{H}} \lesssim 110$ GeV the search failed to exclude couplings of $\omega \gtrsim 6$. On the other hand the effects of a stealthy Higgs scenario will only compete with the visible channels if the coupling remain small. Firstly, if ω is too small to make the Higgs width experimentally resolvable, the invisible branching in the accessible mass range can be considerable. In this case the exclusion has to be made with the LEP combined results [89] for invisible Higgs decays which are sensitive to between a few percent up to ≈ 20 % invisible branching over the accesible mass

range (see Fig. 2.16 in Chapter 2.3). Secondly, the exclusion of even smaller ω, which would only reduce the visible rate moderately is covered at LEP 2 by an interpretation of the negative result of the searches in visible channels.

8.4 Use of ATLAS sensitivity for continuation of the LEP 2 searches

Clearly the advantage of the LHC for searches within a stealthy Higgs scenario is given by the higher accessible mass range. But the signal of an invisible Higgs boson produced in weak boson fusion, which is identified by tagging jet candidates and $E_{\mathrm{T}}^{\mathrm{miss}}$ has to be detected in a hadronically active environment. The backgrounds are very large. Hence, the potentially large systematics uncertainties in the jet and $E_{\mathrm{T}}^{\mathrm{miss}}$ measurements have an immediate impact on the result. It is observed that the detection potential of these events is governed by the cross section. Effects of the larger decay-width for the detection remain mild, since the jet observables hardly change with the width. In other words if using the weak boson fusion channel, there is no particular sensitivity towards the decay-width in the detector. It was observed that the jet energy uncertainty is the main cause that the systematic is spoiling the potential gain in the Higgs mass reach, which will be restricted to relatively low Higgs masses about 200 GeV for 30 fb^{-1} of data. The whole mass range above 200 GeV remains in the stealthy Higgs scenario non-excludable with 30 fb^{-1} of data. The advantage of a high centre of mass energy and high instantaneous luminosity of the LHC compared to LEP 2 is partially neutralised by the complications of finding the stealthy Higgs in the hadronic environment.

Recovery of potential with smaller systematics

In the case that the detector systematic uncertainties especially on the jet energy scale, which according to the ATLAS technical design report is expected to be 1%, can be reduced further, the exclusion of larger values of ω in case of $M_{\mathrm{H}} = 200$ GeV and some hypotheses for $M_{\mathrm{H}} > 200$ GeV may be feasible. E.g. with an assumed total uncertainty of 5 %, this study would have been able to exclude masses up to 300 GeV in the stealthy Higgs scenario (see Fig. 7.4). For this aim also the suggested improvements and changes described in the end of Chapter 7 should be considered. But still not the whole mass range in which the Higgs could be produced at the LHC is covered.

Investigation of Higgs masses below 130 GeV

Though the large masses are barred, the limit of exclusion for lower masses about 110 GeV may provide the link to the LEP 2 search. Looking at the results of this study it can clearly be stated that it was a misconception that the $E_{\mathrm{T}}^{\mathrm{miss}}$ cut would largely spoil the sensitivity for Higgs masses below 130 GeV. It seems to be possible to reach highest sensitivity with a search, even for larger ω, where the signal cross section is highest. With this knowledge it would have been highly desirable to test also masses in the mass range between 110 GeV and 130 GeV. It is very likely that an exclusion can be reached for many ω values since the cross sections are considerable. We suspect that a continuation of the LEP exclusion can most likely be reached in this region, but of course this is one thing that a search at the LHC at 30 fb^{-1} of data has to prove.

8.5 Outlook at ATLAS searches in context of the stealthy Higgs scenario

In this section we summarise possible ways to extend the contribution of the ATLAS experiment in the exploration of the stealthy Higgs scenario. We have found that the weak boson fusion provides no handle on the invisible decay width of the Higgs as observable and is insensitive to width effects. We

therefore shortly comment on the possibility to gain some information about the actual decay width in other channels.

Investigation of width sensitivity in the ZH channel

The shape of variables used in the analysis of the weak boson fusion channel does not exhibit a pronounced dependence on the Higgs decay-width . This can be understood from the fact that they are related to the tagging jets, which receive their p_{T} by the recoil of the emitted weak boson, and are in this way connected quite indirectly to the properties of the Higgs boson which is produced subsequently in the boson fusion. While on the one hand only this indirect connection to Higgs properties is exploitable, the jet-related variables on the other hand are subject to the full uncertainty of the tagging jets measurement, which is reflected by the vulnerability of the study concerning the size of systematics, especially from the jet energy scale. Both addressed issues may be different in the ZH production. Therefore, it would be of high interest to study how sensitive the ZH channel is to the width of the invisible Higgs decays. Firstly the invisible Higgs search strategy in the ZH channels is widely unaffected of uncertainties of the jet energy scale[2)] since it mainly uses observables stemming from the $Z \to ll$ decay products together with $E_{\mathrm{T}}^{\mathrm{miss}}$ to identify the Higgs decays. Though the leptonic decays have only a low branching of about 11 %, they immediately provide an effective trigger. Secondly as the Higgs boson is radiated off by the virtual Z boson which decays subsequently into a lepton pair, the connection to the Higgs boson properties may be more direct. During the so far published analyses a very narrow invariant mass cut of ± 10 GeV around the nominal Z mass has been applied on the dilepton invariant mass. The mass window in case of the stealthy Higgs may have to be retuned. But as pointed out the use of multivariate methods using input variables from the leptonic Z boson decay can improve the sensitivity. It has to be studied if some of these variables are distinctly sensitive to the Higgs width. Maybe the transverse mass of the dilepton and $E_{\mathrm{T}}^{\mathrm{miss}}$ system $m_T = \sqrt{2P_T^{ll} \cdot \not{P}_T (1 - \cos\Delta\Phi_{ll})}$, used in [7, 118] can be such a variable.

The mass range of the ZH or WH associated production remains limited by the quickly falling production cross section for Higgs masses above 200 GeV. But for $M_{\mathrm{H}} \lesssim 130$ at $\sqrt{s} = 14$ TeV, the ZH or WH associated production cross section exceeds the weak boson fusion production cross section. In that regime the invisible Higgs searches in the ZH channel are quite competitive (see Fig. 8.2), and this should also apply in the stealthy Higgs scenario. As said so far no sensitivity study for the dedicated large decay width of the invisible Higgs scenario has been performed in the ZH channel. Thus it is unclear to which degree such a search would be sensitive to the decay width. Theoretically both production channels could be combined in exclusion of model points at lower mass.

Investigation of complex final states for smaller invisible widths

Very recently a new strategy [38] had been suggested, which may be utilised by ATLAS to search for an invisible Higgs with mass below 180 GeV in complex final states and simultaneously gain width sensitivity. Since the Higgs regularises the weak boson scattering amplitudes, a broadened but invisible Higgs can be seen in such processes in a reconstructed diboson mass spectrum. This observation was the motivation for recently undertaken studies of the sensitivity to Higgs width and mass in more complex final states. In [38] complex final states like $pp \to \mathrm{ZZ}t\bar{t}(\bar{b})$ or $pp \to W^+W^-t\bar{t}(\bar{b})$ were regarded. The cross sections for the production of weak boson pairs in association with heavy quarks (beside from top quarks, beauty quarks can become of interest in models that enhance the coupling to those) were calculated. It was argued that for example in a Higgs mass range below 180 GeV the reconstruction of the complex final state will reveal not only the Higgs but is also sensitive to the actual Higgs width in the order of two to eight times of that of the SM Higgs width. These theoretical investigations are only at the

[2)] In the studies done so far jet properties enter only via overlap removal or when jets with high p_{T} in forward direction or b-tagged jets are vetoed to reduce top pair backgrounds

beginning and still to be proved experimentally to be feasible. But these strategies can prove valuable to cover at least for a light Higgs the very small couplings ω, that lead only to a small additional invisible width and hence to a small invisible branching.

Reassessment of the discovery channels like ZZ$\rightarrow llll$, ZZ$\rightarrow llvv$ or WW$\rightarrow jjlv$ in the stealthy Higgs scenario

As indicated before in Section 8.2.2, the failure of large exclusion in the stealthy Higgs scenario implies that the impact on the discovery channels for a heavy Higgs like ZZ$\rightarrow llll$, ZZ$\rightarrow llvv$ or WW$\rightarrow jjlv$ (see Fig. 8.6) has to be reevaluated in the stealthy Higgs scenario. This would give information from what value of ω the discovery of a Higgs with a given mass is potentially lost with the assumed luminosity, due to the smearing of the reconstructed Higgs mass over background, and, maybe more important, if there is the possibility to discover the SM like Higgs with a larger amount of data for a given ω, or not.

8.6 Remaining stealthy Higgs loopholes

Combining the picture from the LEP search and the so far undertaken ATLAS study, one can identify two main regions where the invisible Higgs could escape its detection. Firstly these are very light Higgs bosons, i.e. Higgs masses between of 20 GeV to say 60GeV for which the LEP 2 search left some loopholes, and secondly Higgs bosons much heavier than twice the Z boson mass, which could become possible loopholes for the stealthy Higgs boson at the LHC.

Concerning the loop holes for a light Higgs (see Sec. 8.3), one has to keep in mind that the very light Higgs masses below 60 GeV are practical not accessible in the hadronical background at the LHC. We pointed out before, when discussing the continuation of the LEP 2 search with the LHC, that at the LHC the search strategy relies on possibility to select the signal by a relatively hard cut on $E_{\mathrm{T}}^{\mathrm{miss}}$. Only a hypothetical reexamination of the complete recorded LEP data by the other LEP experiments would had the potential to improve the exclusion by the statistical combination of the results. For the continuation of exclusion near the kinematic limit of LEP 2 at about 110 GeV, we already argued that this has good prospects, especially because the ZH and the weak boson channel are sensitive to such a light invisible Higgs, and should be simply completed. For the light Higgs masses between 100 GeV to 130 GeV it occurs unlikely that the stealthy Higgs scenario will spoil the LHC Higgs discovery, since in this region the sensitivity for invisible Higgs searches are best.

For higher Higgs masses the conditions of detection are more involved. Though we have discussed in Chapter 2 that the combined fit to electroweak precision data prefers a light SM-like Higgs, the existence of a Higgs with a moderate mass in the range of 200 GeV to say 400GeV or even a heavier Higgs boson is not forbidden by a fit with a certain probability. For many of the invisible scenarios listed in Chapter 2, a large branching into visible channels is restored if the Higgs is heavier than two weak bosons. Therefore the sensitivity loss of the standard invisible Higgs searches for Higgs masses larger 200 GeV (Fig. 8.1) poses not a dramatic problem, as long as sufficient data can be collected with the LHC experiments. So far these scenarios are equally probable as scenarios without an invisible Higgs or the stealthy Higgs scenario. It is up to the experiment to clarify which model is realised in nature.

The performed sensitivity study for invisible Higgs bosons succeeded only in excluding very few low Higgs mass hypotheses and proved that the sensitivity is very much deteriorated if the detector-related systematic effects are not under precise control.

This should cause some concern, because the cross sections for Higgs production fall and the search for heavier Higgs is in any scenario more challenging. Hence for the highest Higgs mass hypotheses of about 800 GeV the detection will be extremely difficult, independently of the assumed scenario. Especially for the stealthy scenario one can easily think of a worst case in which the detection of a Higgs boson much heavier than 200 GeV becomes completely spoiled. For example if the Higgs mass is 400

GeV, there can be an ω that contributes to the invisible width exactly in such a way that the invisible branching stays right below the sensitivity of a standard invisible Higgs search and the anyway small rates in the visible channels at the same time are reduced by the invisible rate so, that their detection is becoming very hard or even impossible. If one believes in the possibility of very large ω, one can continue to draw a gloomy picture, in which even for very high Higgs masses almost the complete SM production rate is shifted into the invisible channel. Such decays would not be detectable for masses with sensitivities $\xi^2 > 1$. Assuming such a worst case scenario, the attempt to gain assurance on the nature of the Higgs sector may demand the use of an alternative search technique at a new collider machine, which we will sketch as outlook in the next section.

8.7 Prospects to reconnoitre the stealthy Higgs at a future linear collider

The possible future linear collider (LC) is a project where specifications are not finally determined yet. However, it is clear that the LC shall be an electron positron collider, that delivers high instantaneous luminosities. The question at which centre of mass energy this will happen is still undecided. One can assume that it will be certainly significantly higher than that of LEP 2. Values in discussion range from several hundred GeV to a TeV. Also it would be a very desirable feature to measure at tunable centre of mass energies. Maybe because the specification are still subject to discussion, many theorists are tempted to give guesstimates about the potential of the LC, with appropriate chosen specifications, in their favourite model. In this section we try to argue how the LC can clarify the nature of the stealthy Higgs sector.

At the LC the ZH channel, often referred to as Higgsstrahlung, will provide the major production mode. As already proved by the OPAL search the relative clean non-hadronic environment and especially the constraint beam energy of the colliding point-like particles allow precision measurements of many observables. It is e.g. expected to be able to measure the Higgs invisible branching within a percent range. Such a measurement will heavily rely on the recoil mass spectra method, used already at LEP. With this method the sensitivity of the experiments was in praxi only limited by the kinematic limit. In principle it is thinkable to transfer, modify, and retune the OPAL search strategy for the stealthy Higgs to a LC, which can provide the corresponding observables. With such a strategy it may be likely to investigate a large phenomenology of invisible decays (a selection is given in Chapter 2) and a large parameter range in the stealthy Higgs scenario.

In [37] the authors estimate the cross sections, at a LC operated with $\sqrt{s} = 500$ GeV, for the stealthy Higgs and the $e^+e^- \to Z\nu\nu$ background, which is irreducible. Imposing only a crude acceptance cut and a mass window of $\Delta m = 30$ GeV around the reconstructed Z bosons mass the expected exclusion with 500 fb^{-1} of data, collected in a long term search, is depicted in Fig. 8.9. Practically the sensitivity is again only limited by the kinematic limit of about 400 GeV at the assumed machine. The large mass window around the Z boson mass is reflected in the drop for Higgs masses about 100 GeV, but still the sensitivity in that region is higher than in the LEP 2 search since much more luminosity is assumed and the mass is much below the kinematic limit of the machine. The sensitivity for low mass Higgs boson, with a mass smaller than 200 GeV, reaches values of $\omega = 20$ to $\omega = 26$, which are comparable to the expected ATLAS exclusion with only 30 fb^{-1} of data. For practical purposes this should correspond to the upper end of the parameter space. Values of $\omega \approx 20$ would correspond to very degenerated invisible Higgs bosons with a width of several times its mass. In that sense the notion of a particle is replaced by the notion of a continuum Higgs. The reach in ω will be reduced the closer the Higgs mass is to the kinematic limit. The gain of the LC, aside from its precision would lie in the extended mass reach, which basically scales as $\sqrt{s} - \mathrm{M_Z}$. The LC operated at $\sqrt{s} = 1$ TeV then could even try to access $\mathrm{M_H} \approx 800$ GeV, which is a value of saturation for a heavy Higgs pole in this scenario [77, 79]. But again a word of warning is in order: the dedicated LEP search and the detailed study of expected systematics at the ATLAS detector have shown that there can be large differences between theory expectations and

the experimental accessible parameter range.

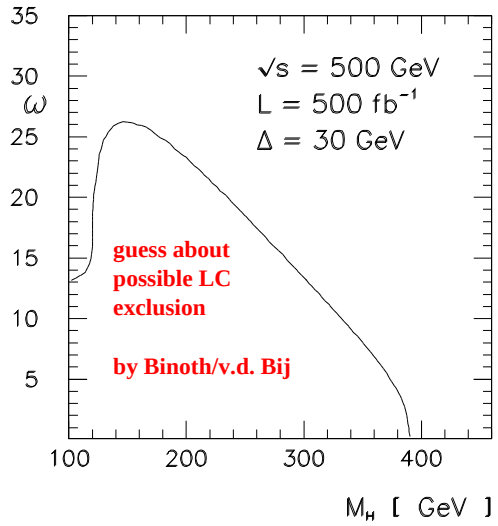

Fig. 8.9: *Projection of theoretical accessible Higgs masses and coupling parameters ω in the stealthy Higgs scenario at a linear collider (LC), that is operated at $\sqrt{s} = 500$ GeV and has collected 500 fb^{-1} of data. The stealthy Higgs is searched in ZH production with large invisible decay-width. The exclusion of parameters is deduced from the number of signal events after imposing a mass window $\Delta = 30$ GeV around the reconstructed Z boson recoil mass spectrum, over the number of expected irreducible $e^+e^- \rightarrow Z\nu\nu$ background events (taken from [37]).*

9. Conclusion and outlook

9.1 Summary

Motivation for the stealthy Higgs model

Since there has been no Higgs discovery in the LEP experiments and at the TeVatron so far, theoretical reasoning was encouraged to find models that could devise a mechanism, which would effectively hide a Higgs boson, that is produced with the SM cross section, from detection with the standard search strategies. This is possible in a model predicting invisible Higgs decays into a hidden scalar sector with a very large decay-width, thus called stealthy Higgs scenario.

The stealthy Higgs model at LEP 2

While waiting for the collected luminosity at the TeVatron to become large enough for stringent exclusion or discovery and the advent of data taking at the LHC at higher centre of mass energies and luminosities, approximately 630 pb^{-1} data from the LEP 2 run ($\sqrt{s} = 183$ GeV to 206 GeV) of the OPAL collaboration were reexamined under the hypothesis of invisible Higgs decays with free decay width. The search excluded a large part of the accessible parameter space of the stealthy Higgs model, which is given by the Higgs mass and the coupling to the hidden scalars ω. The exclusion reached for Higgs masses between 20 GeV and 103 GeV for couplings from $\omega \approx 3.5$ to $\omega \approx 5.5$ leaving values $\omega \gtrsim 1$ to $\omega \approx 2.5$ not excluded for very light Higgs masses below 20 GeV. We chart the OPAL exclusion as magenta line in the summary plot for the circumstances of the stealthy Higgs at colliders (Fig. 9.1). In summary if $\omega \gtrsim 6$ a Higgs boson within the range of LEP 2 could have escaped detection. The sensitivity at LEP 2 was limited to Higgs masses below about 110 GeV to 115 GeV, approaching already the kinematic limit.

Continuation of Higgs searches with ATLAS

In the assumption that the Higgs boson is most probably too heavy to be discovered at LEP 2, the ATLAS experiment at the LHC is designed to discover a Higgs boson in a much larger mass range up to the order of a TeV or to verify alternatively new physics from Higgs-less extensions of the SM. The prospects for a discovery of the Higgs in various visible channels over a large Higgs mass range have been studied the last years and are very promising. Also the discovery of invisible Higgs decays predicted from a variety of models is foreseen possible by invisible Higgs searches in the weak boson fusion channel for Higgs masses up to 400 GeV. But despite of all the promising expectations, one has to be prepared if in the worst case the stealthy Higgs scenario is realised in nature. It is therefore advisable trying to access the impact of the stealthy Higgs scenario for the discovery of a Higgs boson at the LHC.

Search strategy for the stealthy Higgs in the weak boson fusion channel with ATLAS

We attempted to study the sensitivity in the stealthy Higgs scenario with the ATLAS detector. For the first time dedicated MC samples with varying very large invisible Higgs widths were simulated, covering a large parameter space in the stealthy Higgs model, in which the Higgs boson was produced in weak boson fusion. These signal hypotheses together with the main expected background classes were used

in a dedicated event selection. The event selection had to take into account the specific conditions at the LHC and intended to be optimised as much as possible to the Higgs decay width. Hence the event selection proceeded in two steps. A preselection prepared the weak boson fusion topology and separated large reducible backgrounds. For the very hard to separate and partially irreducible W and Z boson plus jets backgrounds, a multivariate event selection was developed. For the optimisation of the multivariate analyses many multivariate classifiers were compared concerning their discrimination power between a signal with various simulated widths and W and Z boson backgrounds. A large number of distributions of variables was inspected with respect to their separation power and whether they exhibit sensitivity on the Higgs decay-width. The optimised classifier turned out to be a multilayer perceptron using only five tagging jet related variables. The performance of the multivariate analysis was cross-checked against a cut analysis, and showed to be advantageous.

Dependency of results from the size of the JES systematic uncertainties

Without considering systematic uncertainties both analyses could exclude a large part of the stealthy Higgs scenario. With systematics a much smaller part of the parameter space remained, in which the stealthy Higgs scenario could be excluded. The exclusion including the estimated systematics is shown as dark blue line in in the summary plot Fig. 9.1. The reach for couplings of $\omega \geq 5$ extends to Higgs masses about 200 GeV. The following observations could be made. The dominant systematic uncertainty proved to be the jet energy scale uncertainty. Applying the assumed jet energy scale uncertainties from [7], which are 7.5 % for $|\eta| < 3.2$ and 15.0 % for $|\eta| > 3.2$ and likewise with these values reduced to the half, no exclusion is posssible. The reached exclusion is possible if the jet energy uncertainty is 1.75 % for $|\eta| < 3.2$ and 3.5 % for $|\eta| > 3.2$ or better. The search assumed the collected luminosity of 30 fb^{-1} of data at $\sqrt{s} = 14$ TeV. Due to the large impact of the systematic uncertainties the sensitivity of the search will not gain much with more collected luminosity. The main aim has to be to reach a very small jet energy uncertainty, to be able to perform such searches. The ATLAS Collaboration expects that the final jet energy uncertainty will be only 1 %. To demonstrate how the sensitivity of the presented study would benefit from such strongly reduced detector-related systematics, we assumed a total uncertainty of 5 %. The exclusion that would have been possible with 5 % total systematic background uncertainty are marked by the dark blue dashed line in Fig. 9.1. In this case the sensitivity would reach to higher couplings. But the mass reach would be extended only slightly to about 300 GeV.

Sensitivity to the width and dependence on the total cross section in the stealthy model

The tagging jet variables show no connection to the Higgs decay-width, i.e. a larger decay-width does not lead to a reduced sensitivity for the weak boson fusion final state in the detector. The generic total cross section in the stealthy Higgs scenario models the decay-width as a Breit-Wigner shape and integrates all the masses contributing to the broad Higgs boson by their SM production cross sections. Thus the invisible cross section depends explicitly on the width and is only bound from above by the mass dependent cross section of the SM at the pole mass. Therefore it is not only difficult to detect the stealthy Higgs because the analysis is vulnerable to jet systematics, but also because the invisible cross section can be considerably lower for some parameters than a comparable SM cross section at the same pole mass.

Expected sensitivity in the stealthy Higgs model and consequences at ATLAS

The performed sensitivity study found only a limited sensitivity for the stealthy Higgs model within the weak boson fusion channel. Hence we tried to identify problematic mass regions where the Higgs boson would neither show up in visible channels nor deliver a large enough invisible rate above the ATLAS sensitivity for the invisible Higgs.

From the two obstructive effects, namely the reduced visible rate due to competition with the invisible decays and the reduced effectiveness of visible signal extraction due to an invisible width of the Higgs considerable larger than the experimental resolution, only the first can be evaluated without further studies.

In Fig. 9.1 we introduced dotted contours in red and dark-red, representing our estimate of the impact of the stealthy Higgs on the visible channels, given in Chapter 8.2.1. In the regions above and left of these contours the visible SM searches with 30 fb^{-1} of data are endangered to drop below 5 σ significance due to the coupling ω. The red-dotted contour comes from a recent study of the $ZZ \rightarrow llll$ channel alone (Fig. 8.7), which includes systematic uncertainties. This channel loses rapidly its discovery potential above a Higgs mass of 500 GeV. Hence the $ZZ \rightarrow llll$ is not studied above a Higgs mass of 600 GeV, where only the $WW \rightarrow lvjj$ channel contributes. One sees that only if the coupling is between $\omega \approx 1$ to $\omega \approx 5$ this channel can retain its discovery potential. For higher couplings the least consequence one expects in this region is that the data taking has to be extended to collect about 100 fb^{-1} for discovery. The dark-red dotted contour interprets the old TDR results of a combination of all visible channels for the Higgs discovery potential (Fig. 8.6). Since many channels are combined the mass range in which a discovery of the Higgs is claimed to be possible reaches up to 800 GeV. Additionally a combination of channel yields a higher discovery potential than only one channel alone. Today one could argue that the TDR represents optimistically high statistical significances. In the old TDR combined result the $ZZ \rightarrow llll$ contributes very much in the mass range between 200 GeVand 600 GeV. In the mass range, below 500 GeV the region in which the combined channels discovery is spoiled by the stealthy Higgs, is smaller as for the $ZZ \rightarrow llll$ channel. And for high Higgs masses above 600 GeV the discovery with 30 fb^{-1} will be possible for couplings up to $\omega \approx 15$.

The second obstruction by the stealthy Higgs is more complex and not easily compensated by collecting more data, since it compromises the selection technique of the most promising detection channels for the Higgs of a mass above 200 GeV. In these channels like $ZZ \rightarrow llll$ or $ZZ \rightarrow llvv$ the invariant mass with high precision, in case of the $ZZ \rightarrow llll$, or a transverse mass in case of $ZZ \rightarrow llvv$ in signal region is reconstructed. The background can be fitted in the sidebands and is subtracted. If the Higgs propagator contains a large invisible width, a broad Higgs will occur in the s-channel of the weak boson scattering. Consequently a channel like $ZZ \rightarrow llll$ will lose sensitivity as the Higgs mass spectrum becomes very broad and smeared out. The effect depending on ω can be potentially large. Also the channels that count the excess over selected background, like $WW \rightarrow lvjj$, may be affected. Therefore, as a consequence of the limited sensitivity to the stealthy Higgs found in this study, we strongly advise that ATLAS reassesses the potential of the mentioned channels in a dedicated stealthy Higgs study.

Higgs graviscalar mixture

Models with large extra dimensions allow an invisible Higgs decay-width due to decays in graviscalars or mixing between the Higgs boson and graviscalars. The characteristic parameters in such models are the number of extra-dimensions δ, the mixing strength ξ and the dimensional reduced Planck mass M_D. The latter is the interesting parameter since it sets the scale on which gravity enters the particle physics. Since we produced signal MC with an invisible width Γ_H, corresponding to a coupling ω and used for our signal normalisation a generic cross-section into which the Higgs width enters directly, we can try to interpret the result for the sensitivity not only in the stealthy Higgs scenario but in a Higgs graviscalar scenario (see Appendix D). We fixed the number of extra dimensions δ and interpreted the OPAL stealthy Higgs search and ATLAS stealthy Higgs sensitivity study as exclusion in the mixing strength ξ and gravity scale M_D parameter plane. The predicted invisible width in the graviscalar mixing scenario remains very small and below the experimental resolution for the accessible parameters. Therefore, the exclusion showed to be less sensitive than the one by the interpretation of the Higgs searches for narrow invisible Higgs decays, which are sensitive to higher Higgs masses. Furthermore, the OPAL search and

ATLAS sensitivity study are not competitive with direct graviton production searches at colliders which succeed in setting much higher exclusions on the dimensional reduced Planck mass as function of δ.

9.2 Conclusion and outlook

We can learn from the discussion presented in this work, if the stealthy Higgs scenario is realised in nature, it will probably complicate or delay the Higgs discovery in certain ranges of Higgs masses above the threshold for decays into weak bosons, if the coupling to the scalars is strong enough, i.e. approximately 5. The main obstructive effect of the stealthy Higgs for discovery is due to the reduction of expected visible Higgs decays in the competition with the new invisible decay channel. We expect that extended data taking, corresponding to an integrated luminosity of the order of 100 fb^{-1} can compensate the reduced visible rate predicted over a large part of the parameter space. Since the width sensitivity of the variables available in weak boson fusion topology is marginal there is experimentally no handle on the invisible width in such a process. The exclusion of the stealthy Higgs via precise determination of the rate of selected candidate events is limited by the small cross section for small couplings and the large impact of the jet energy uncertainties. Therefore, it is difficult to gain insight into the stealthy Higgs sector. However the signal extraction in important discovery channels like ZZ$\rightarrow llll$ or ZZ$\rightarrow llνν$ for Higgs bosons much heavier than 200 GeV becomes maybe impossible in the case of a very broad invisible decay-width of the stealthy Higgs. Moreover, if ATLAS does not see the Higgs in visible channels above $M_H = 200$ GeV after collecting 30 fb^{-1}of data, it will not be able to rule out the stealthy Higgs scenario as reason. Taking the stealthy Higgs scenario literally it only disguises the Higgs sector adding no additional new physics to the SM. Without the possibility to discover or exclude the stealthy Higgs at the LHC the physics results at the LHC could be very limited. We argue that in this very unfavourable situation the study of the stealthy Higgs scenario at a possible future linear collider could decide if the model is realised in nature. A hypothetical exclusion contour of a linear collider experiment with 500 fb^{-1} of data at $\sqrt{s} = 500$ GeV is also sketched in light blue in Fig. 9.1, showing that such a huge experimental effort could cover some important part of the parameter space complementing the LHC experiments. The mesh to catch the Higgs at the LHC may contain loop holes. These loop holes may even remain open for the stealthy Higgs if the centre of mass energy at the LC cannot reach high enough to exclude large Higgs masses above the order of 400 GeV and large ω.

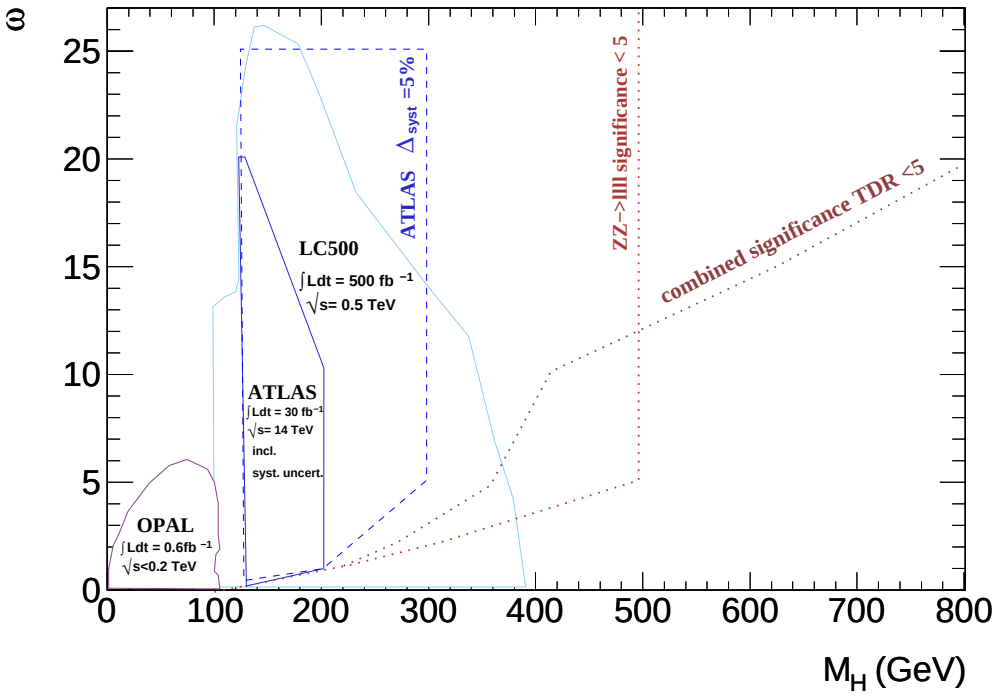

Fig. 9.1: *Summary of the stealthy Higgs model at colliders. Displayed are exclusion contours in the dependence of the parameters Higgs mass, M_H, and coupling ω to a hidden scalar sector. The excluded region by OPAL, given as magenta contour, has specifically high sensitivity to low Higgs masses. The dark blue contour signifies the expected exclusion using weak boson fusion Higgs production by the ATLAS detector. If the total uncertainty can be reduced to 5 % the mass reach can be extended to about 300 GeV and to highest values of ω, as indicated in the dashed dark blue contour. The light blue contour is included to give a feeling for the probable exclusion based on theory calculations at a linear collider operated at $\sqrt{s} = 500$ GeV . A possible mass region in which visible channels lose their 5σ discovery potential due to competition with invisible decays is marked left of the red dotted line for any given ω. The red dotted line stems from the $ZZ \rightarrow llll$ channel, which is for masses between 130 GeV and 500 GeV very important. The result in the $ZZ \rightarrow llll$ channel includes systematics. In the region above the dark red dotted contour one expects the very promising combination of all visible channels for 30 fb^{-1} of data to lose its discovery potential in the stealthy Higgs scenario.*

A. A Study of Generator and Underlying Event Tune Influence on the Central Jet Veto

A.1 Motivation

It was noted [30] in the early nineties, that the weak boson fusion topology due to the lack of colour flow in the leading diagrams exhibits a central gap in the pseudorapidity distribution of accompanying subleading jets. They are more often close to one of the leading jets in forward or backwards direction. This can be seen e.g. in the so-called Zeppenfeld distribution (Fig.A.1) which plots the distance in η-space of the third leading jets towards the averaged η of the leading jets. Since it was proposed from theory side the so called mini jet veto or central jet veto (CJV) became a powerful tool to improve discrimination between the overwhelming QCD background processes and the Higgs boson signal in the weak boson fusion production mode at the LHC, and hence the sensitivity of such searches.

In context of this study we will restrict us to the signal process of a Higgs boson with a mass of 130 GeV produced in weak boson fusion that decays subsequently into an invisible final state. Recent results of ATLAS studies in this channel are published in [7]. To this signal process we regard the mostly irreducible Z boson plus jets production with decay of the Z boson into neutrinos. Though the overwhelming background are the QCD dijets, the available fully simulated samples are far to few to prevent single events from acquiring huge weights. Fortunately the preselection and a cut on the missing transverse energy, which in case of QCD dijets should be only fake missing transverse energy and be rather small, remove most of the dijets. On the other hand the Z boson plus jets background with real missing transverse energy exhibits higher sensitivity to underlying event activity and can be generated with much better statistics.

As up today data a the centre of mass energy as high as 14 TeV had never been taken there are still concerns about the feasibility and efficiency of such a veto in real data analysis. These concerns stem from the following considerations.

The theoretical uncertainties of the exact nature of QCD processes at the LHC are large. The rates of QCD background processes may be higher than predicted and hence the rejection by the veto may not be sufficient. Also these uncertainties affect several aspects of the mini jet veto.

Multiple parton-parton scattering accompanying the hard process in a proton-proton collision is usually referred to as underlying event activity. An intuitive sketch is displayed in Fig.A.2. In particular the modelling of the underlying event activity in such events uses phenomenological models, that are extrapolated from lower centre of mass energies measurements and so far untested. Since this associated jet activity is present for a signal event it may even lead to its rejection by the central jet veto criteria (see A.4).

Even at start up and low luminosity there will be pile-up events and cavern background activity recorded in the ATLAS detector [6]. These will lead to many additional jets from in average 2.3 minimum bias events at instantaneous luminosity of $\mathscr{L} = 10^{33} cm^{-2} s^{-1}$ being present in the detector additional to the hard event. The jets from such uncorrelated events will have a non-negligible probability to trigger the jet veto. Such pile up events are believed to have a much more severe impact on the central jet veto than the underlying event solely.

To account for these concerns and to define the questions we want to investigate, we take the follow-

ing viewpoint in this note. The first task with early data at the LHC will be to measure known Standard Model processes and in this way determine which is the exact trigger rate of the QCD processes. At that point theoretical uncertainties on the cross section of QCD processes will become small. With such data it will also be possible to recognise a correct or favoured underlying event model in the Monte Carlo and to calibrate it to the data. Therefore we try to answer the question whether possible residual deviations or detuning within such a tuning procedure of a generator model may be expected to have a large impact on the central jet veto. As a measure or test case for this residual deviations we use the detuning of the underlying event produced by the Sherpa generator. To assure that this study done before first measurements are available are not to far off the reality, we ask the question how one can devise a central veto condition that is mostly robust against varying generator predictions and the largest expected sources of systematic uncertainties.

With this study we attempted to complement an earlier study [134]. This earlier study compared Pythia, Herwig and Sherpa in WBF H$\rightarrow \tau\tau \rightarrow ll\nu\nu$ analyses and aimed for an optimisation of the standard central jet veto in terms of robustness against generator differences. In that study high statistics samples of the ATLAS fast detector simulation were used and a main observation was that narrowing the η region with vetoed mini jets inside reduces significantly the large differences in the efficiency predictions of the different generators.

This appendix is organised as follows. In section A.2 all investigated Monte Carlo samples are described. In sections A.3 and A.4 we introduce the event selection and veto strategies. The rough estimate of detector systematic effects along with the figure of merit to find the best veto approach are motivated in section A.5. In section A.6 some distributions that can be used to characterise the central jet activity are compared before applying a jet veto for different generators. This is complemented in section A.7 with comparisons of these variables for the tuning variations of the Sherpa generator. The results of the comparison are given section A.8. In section A.9 we shortly discuss pile up effects and conclude in section A.10 with a summary and a comparison of our findings with [134].

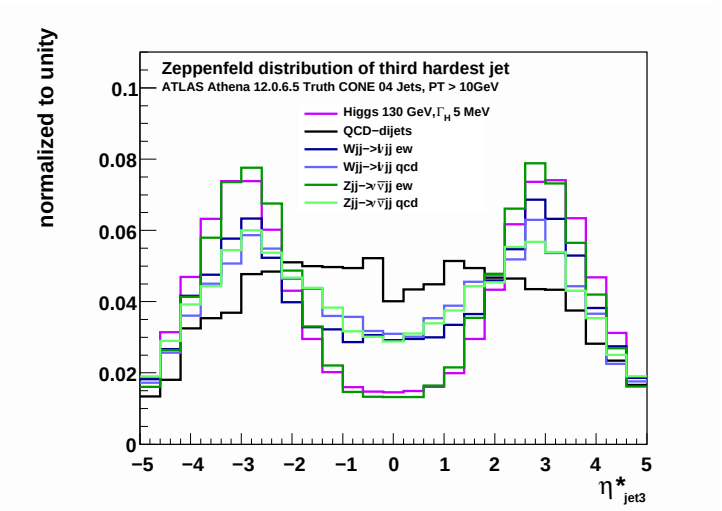

Fig. A.1: *Distribution of the Zeppenfeld variable, η^*_{jet3}, as predicted by the Sherpa 1.0.11 generator at truth level, for an invisible Higgs signal and the most important backgrounds. Only the QCD dijets are done with Pythia 6.4. The plot shows Cone 04 Truth jets, and a minimum $P^T_{jet3} > 10$ GeV is required. The distributions are normalised to unit area after cuts (c 1)-(c 3), described in Section A.3.*

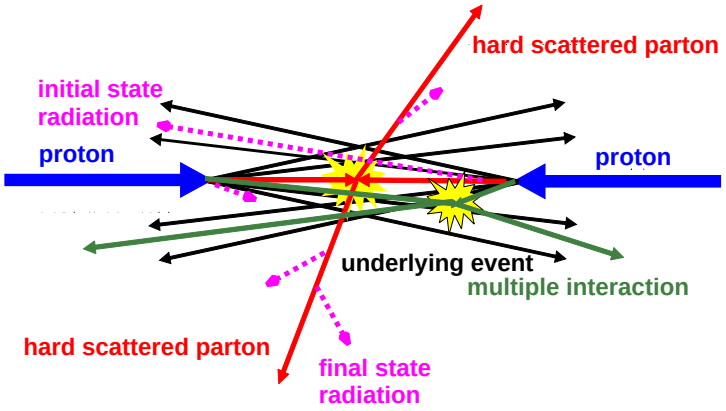

Fig. A.2: *Sketch of a proton proton collision in the ATLAS detector at LHC. Any further scattering of partons additionally to the hard process is usually accounted for as underlying event or sometimes referred to as multiple interactions.*

A.2 Monte Carlo Samples

In this study we compare samples of the signal process $qqH(130\ \text{GeV}) \rightarrow qq + \not{E}_T$ of three leading order matrix element generators namely Herwig, Pythia and Sherpa. To generate an invisible Higgs boson produced in weak boson fusion its decays into a virtual Z boson pair which subsequently decays into neutrinos is forced. The Sherpa generator is also used to generate the irreducible Z plus jets background.

A.2.1 Underlying Event Modelling

These three generators amongst other differences e.g. in scales for QCD radiation provide different models of the underlying event. In principle all three Monte Carlo generators have parameters that allow for a tuning of the underlying event activities. Certainly the probability of multiple interactions in a proton−proton collision depends on the modelling of the matter distribution within the hadrons. All generators supply various matter distributions and some parameters and form factors to tune these to data. The underlying event is tuned to experimental data of hadron collider experiments like UA5 or the TeVatron experiments. It is obvious that an underlying event tune at higher energies can not change matter distribution parameters without losing the valid low energy description of the underlying event. After the matter distribution parameters are fixed at the low energies data a model specific extrapolation to LHC energies is performed (see the example in Fig.A.3). Since the extrapolation to LHC energies depends on the specific model it can lead to significantly differing predictions.

Since the underlying event comprises of $2 \rightarrow 2$ processes that can in principle start right below the scale of the hard process, Q_{hard}, an important parameter is the scale Q_{cut} down to which these processes are allowed (see Fig.A.4). The value of Q_{cut} can be as well fixed by e.g the TeVatron data. In the simplest ansatz the value of Q_{cut} at the LHC can be exponentiated from this reference scale according to

$$Q_{cut}^{LHC} = Q_{cut}^{TeV} \times \left(\frac{E_{cm}^{LHC}}{E_{cm}^{TeV}}\right)^{\alpha_r}.$$

Since the ratio of centre of mass energies and the cut value of the reference scale are given, the exponentiation parameter α_r becomes the only free parameter to adjust the underlying event activity at the LHC centre of mass energy. Independently of the choice of α_r the evolution always starts at the right value at the reference scale connection evolutionary the TeVatron and LHC energies.

A second possibility is to recall that the QCD $2 \rightarrow 2$ processes account for the underlying event. The probability for partons in the hadron to take part in a scattering processes of a transferred momentum

scale of t is therefore strongly depending on the parton distribution function (PDF) probed at the corresponding scale. Since the PDF sets the result of fitting procedures to a variety of experimental data sets, the predictions of the PDF sets at the probed scale can largely differ (see example in Fig.A.5). It is clear that the cross section of the underlying event scattering is a function not only of the energy scale but also of the probability for finding the partons hence the PDF set used, which is summarised symbolically in the following formula

$$d\sigma^{UE}(2 \to 2) \approx f(t, PDF)\frac{\alpha_s^2(t)}{t^2}dt.$$

Though the underlying event settings in Herwig and Pythia can be varied we decide to use the Sherpa generator for this exercise. The argument is that there is a physically valid default setting at TeVatron centre of mass energy and the evolution can be controlled in an easy way via the exponentiation parameter. Also the exchange of PDF sets is possible.

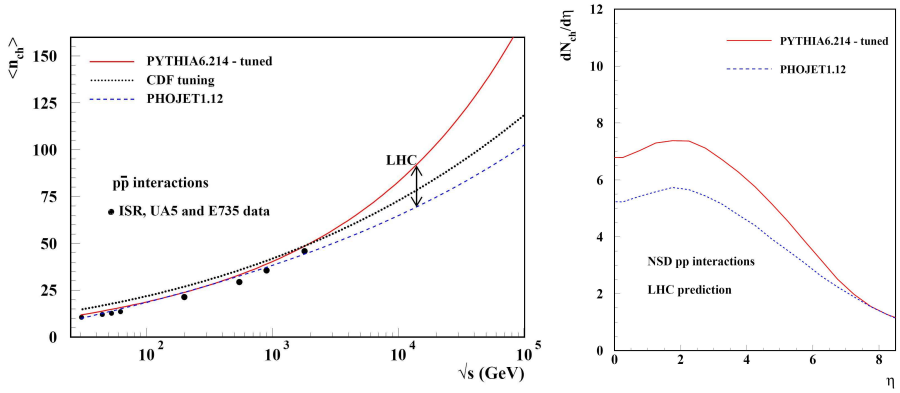

Fig. A.3: *Predicted centre of mass energy dependence of charged particle pseudorapidity distribution and density for non-single diffractive inelastic collisions. The underlying event description of the different MC generators (here an example of Phojet 1.2 and the old Pythia 6.214) is tuned to match the existing hadron collider data up to energies of 1.96 TeV. Above that centre of mass energy the extrapolation to LHC energies depends on the specific model an can lead to significantly differing predictions.*

A.2.2 Sherpa Event Samples

A signal hypothesis with Higgs boson mass of 130 GeV (see Tab.A.1) and the important Z boson plus jets background (see Tab.A.2) is simulated with the leading order Monte Carlo generator Sherpa 1.0.11 [84, 113].

For a defined initial state, in case of the LHC proton-proton collisions, and specified final state, the Sherpa module AMEGIC++ [111] automatically constructs the exact Born level matrix elements for given number of electroweak and strong couplings and performs the phase-space integration. The APACIC++ 2.0 module [112] matches the outgoing partons to a virtuality and angular ordered parton shower. This matching uses the CKKW matching algorithm [45] in order to avoid double counting of additional gluon radiation emerging from the hard matrix element. E.g. for the signal sample with up to three matched jets, in average one forth of the Sherpa events have a third jet originating directly from the matrix element and not from a parton shower.

In the Sherpa signal samples (DS9011) a Higgs boson with a mass of 130 GeV is produced in vector boson fusion and Higgsstrahlung ($\approx 20\%$). Up to three jets were generated by the exact matrix element. A matching scale with the parton shower of $(5\,\text{GeV}/14\,\text{TeV})^2$ for $2 \to 4$ processes and of $(20\,\text{GeV}/14\,\text{TeV})^2$ for the $2 \to 5$ processes, respectively is chosen. No ATLAS standard filtering (see

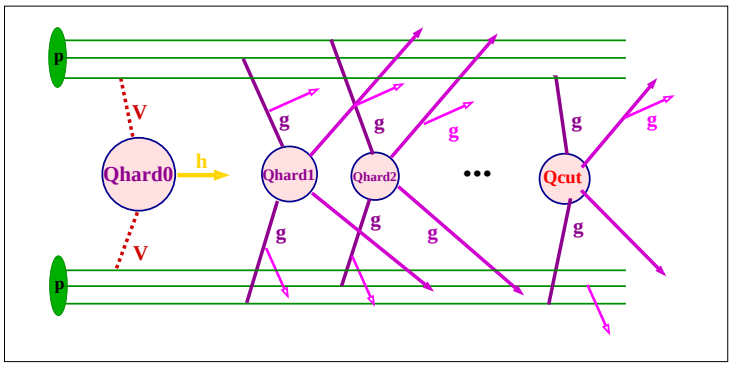

Fig. A.4: *Sketch of the scales involved in the underlying event modelling. The hard process is symbolised by the blob labelled with the transverse momentum scale Q_{hard0} at which fusion of two weak bosons (V) to the Higgs boson (h) takes place. Any further $2 \rightarrow 2$ scattering of partons (symbolised as blobs Q_{hardi}) additionally to the hard process happens at energy ordered scales down to a lowest scale $Q_{hardn} \equiv Q_{cut}$. At all stages initial state (ISR) or final state (FSR) radiation can occur, indicated as gluon arrows (labelled with g). The probability to have a very active underlying event raises when Q_{cut} is lowered.*

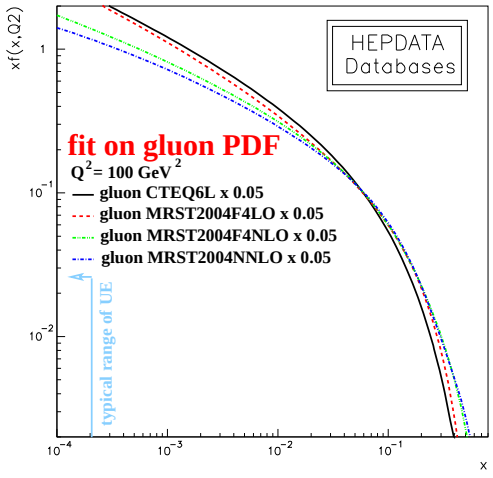

Fig. A.5: *Example of the differences in the parton distribution function at a transferred momentum scale of* $Q^2 = 100$ GeV . *Indicated also is the low x-range in which the underlying event contributions are significant.*

Section 4.3.3) for a preselection of tagging jet candidates in weak boson fusion topology in the events is applied.

The Z boson plus jets background sample was generated separately as a sample containing only the electroweak contributions (DS9010) and a sample containing only the strong interaction Feynman diagrams (DS9089).

In sample DS9010 up to three partons can stem from the matrix elements, yielding a leading order cross section of 9.6 pb with a statistical error of 0.15 %. Additionally the ATLAS VBF filtering was applied with an efficiency of (29.7 ± 0.4) %. For DS 9089 up to four partons were generated from the exact matrix element leading to a cross section of 9596 pb at Born level with a statistical error of 0.8 %. ATLAS VBF filtering was applied leading to a very low efficiency of (3.6 ± 0.1) %.

A.2.3 Underlying Event Settings in Sherpa

Sherpa also allows to apply an underlying event model in proton-proton collisions. The corresponding Sherpa module for generating the underlying event is called AMISIC. It is activated by setting MI_HANDLER = Amisic in MI.dat. While the additional jets originating from matched parton shower radiation of the leading jets tend to be radiated off under small angles to these jets the gluon radiation from the underlying event populates also the central η region between the tagging jets. In Sherpa the reference scale Q_{cut}^{TeV} is called SCALE_MIN and the evolution parameter for c.m.s energy dependence α_r is called RESCALE_EXPONENT.

Tune-1- **ATLAS CSC default**

The ATLAS default tune for the AMISIC module handling the underlying event aims to tune the underlying event of Pythia 6.323 in ATLAS tune [150]. Comparing the distributions of Z$\rightarrow \nu\bar{\nu}$ samples like $\frac{dN_{tracks}}{d\eta}$, $\frac{1}{N}\frac{dN}{dP^T_{tracks}}$, $\frac{1}{N}\frac{dN}{dP^T_{Z^0}}$ this choice raises the average $< \frac{dN_{tracks}}{d\eta} >$ from 4.7 to 6.3 which is in good agreement with the value for Pythia ($< \frac{dN_{tracks}}{d\eta} >= 6.2$). It should be emphasised once more that this tune has no other aim than to map the Sherpa underlying event to that from the Pythia LHC tune by means of a good agreement in the P^T of the Z boson and the average number of charged particles per η-interval. It should not be expected in any case that this tune would yield a realistic description of physics processes at the TeVatron.

For the background samples the underlying event is simulated according to the ATLAS CSC recommendations, i.e. setting steering parameters in MI.dat to SCALE_MIN=2.57 for the minimal perpendicular momentum of the $2 \rightarrow 2$ underlying events. The evolution to LHC energies is governed by the RESCALE_EXPONENT = 0.16. In case of the signal some variations of this ATLAS default are introduced additionally.

Tune-2- **Extrapolated from tune to TeVatron data**

Avoiding the obvious flaw of the ATLAS default tune is to use a Sherpa tune that is fixed at TeVatron data and to rely on the Sherpa exponentiation of the cut scale. The Sherpa authors manage to tune the underlying event of Sherpa 1.0.11 in excellent agreement with Run II Tevatron data. The choice of parameters are SCALE_MIN=2.25 and RESCALE_EXPONENT = 0.25. In that way one can be sure that the tune has some connection to existing measurements.

Tune-3- **Raising Q_{cut} by 30 %**

Since the underlying event is most sensitive to the variation of the IR cut-off scale and at the same time there may be large model dependencies on the evolution of this scale, we prepare a sample with the value of Q_{cut} raised about 30 % with respect to the default value. In that way the underlying event activity is stopped already at a higher scale and should be expected to be suppressed. This specific value of Q_{cut} is chosen since it is the highest possible scale in Sherpa

1.0.11 before the non-diffractive cross section becomes smaller than the hard cross section and no events are generated.

Tune-4- **Lowering Q_{cut} by 30 %**
Complementary we also simulated a sample where the cut-off scale is lowered about 30 % with respect to the default value. This sample is expected to exhibit the largest underlying event activity.

Tune-5- **Use MRST2004NLO as PDF**
All the Sherpa samples above use the CTEQ6L parton distribution function sets [126]. As discussed above the PDF sets may influence the underlying event probability. An exchange of the PDF sets means that one has to retune to the data for lower centre of mass energies. Such a retune is far beyond the scope of this study. But we want to do a simple cross check of possible PDF set and PDF uncertainty dependence of the central jet veto by replacing (without retuning) the CTEQ6L with a PDF set that is available in leading and next to leading order. We intended therefor to produce a sample with MRST2004 LO to compare it directly with a MRST2004 NLO sample [115]. Unfortunately a technical problem prevented us from making the MRST2004 LO sample. Nevertheless it can be used to check the influence of a large variation in the PDF sets and may be cum grano salis compared against the CTEQ6L which is modelled at LO with NLO α_s.

Tune-6- **Turn off underlying event completely**
As a reference to get a feeling for the size of underlying event effect we also prepare a sample without underlying event (Set in the MI.dat card by MI_HANDLER = None).

All choices of the parameters are summarised in Tab.A.1.

A.2.4 Herwig event samples

The events are generated in the Athena 12.0.6.5 framework using the CSC standard job option of the data set DS5335. The weak boson fusion Higgs production and decay is calculated at leading order of the matrix element with the HERWIG 6.5 generator. The multiple parton-parton interactions that contribute to the underlying event are produced by the interfaced JIMMY v4.1 generator [55], which uses angular ordered showering. For the Herwig generator there is also a larger sample corresponding to the instantaneous luminosity of $\mathscr{L} = 10^{31}\, cm^{-2}\, s^{-1}$ (see Tab.A.3).

A.2.5 Pythia event samples

Similarly the CSC job option of DS5337 is used to generate the same signal process with Pythia 6.4 [143].

Since Pythia 6.3 the old mass ordered parton shower [144] based on simple string fragmentation was replaced by a new shower model [141]. This uses the evolution of interleaved transverse-momentum-ordered showers and sums over all ISR occurring in previous multiple interactions in the showering. As can be seen below the new parton shower model leads to a considerably harder P^T spectrum of the jets. The new so-called power shower is believed by the author to give a much more accurate modelling of the underlying physics.

Nevertheless we also produced a sample with the old parton shower model of Pythia 6.2, that is still available in Pythia 6.4, to contrast it with the new one. This was even more desirable since a former study [134] has shown that the standard implementation of a central jet veto is not advisable in the case that nature has chosen a model like the new parton shower of Pythia. The details on the Pythia samples are listed in Tab. A.3.

A.2.6 Full detector simulation

All generated events are passed to the detailed Geant4 simulation of the response of the ATLAS detector. The simulation framework uses Athena Release 12.0.6.5 with the detector geometry database coded as ATLAS-CSC-01-02-00 and the trigger configuration coded as CSC-06. After simulating the digital detector output from this physics objects, the events are reconstructed using Athena 12.0.6.5. A cone jet algorithm with cone size of $\Delta R = 0.40$ is used to find truth jets and reconstructed jets from calorimeter towers. The EventView algorithms, i.e. the default high pt-view package as it is contained in the 12.0.7 group area, is used to remove a potentially overlap between different reconstruction physics objects.The high pt-view algorithms require a minimum P_T of 10 GeV in case of truth jets and a P_T of 15 GeV in case of reconstructed jets within a pseudorapidity range of $|\eta| < 5$. Finally a root ntuple containing all variables of the non overlapping reconstructed objects is analysed within the ROOT 5.18 framework.

Underlying event	$Q_{cut}^{LHC}(GeV)$	SCALE_MIN	RESCALE_EXPONENT	# Events
ATLAS default	3.56	2.57	0.16	48k
TeVatron tune	3.75	2.25	0.25	48k
$Q_{cut} + 30\%$	5.43	2.25	0.43	48k
$Q_{cut} - 30\%$	2.59	2.25	0.075	47k
No UE	-	-	-	54k
MRST2004NLO	3.56	2.57	0.16	49k
MRST2004LO		not available		

Tab. A.1: *Analysed Sherpa 1.0.11 H→invisible samples. The Higgs mass in all samples is 130 GeV and the invisible width is 5 MeV assuming a leading order VBF production cross section of σ_{NLO} =4.13 pb. The PDF set used except for the last two samples is CTEQ6L. These samples differ only in the way the underlying event is generated or tuned from the CSC DS9011. For completeness the choice of the generator parameters SCALE_MIN and RESCALE_EXPONENT resulting in a defined Q_{cut}^{LHC} are given.*

CSC Dataset	Parton number	σ_{LO} (pb)	VBF Filter Eff.	# Events
9010	3	9.6	0.297	300k
9089	4	9596	0.036	296k

Tab. A.2: *Analysed Sherpa $Z\rightarrow \nu\bar{\nu}$ samples. Parton number refers to the maximal number of outgoing partons of the matrix elements. The LO cross section includes the CKKW matching efficiency. Both samples are generated with the ATLAS default underlying event.*

CSC Dataset	Generator	Comment	σ_{NLO} (pb)	VBF Filter Eff.	# Events
5335	Herwig 6.5	Angular ordered Shower	4.13	1	48k
5335	Herwig 6.5	$\mathscr{L} = 10^{31}\, cm^{-2}\, s^{-1}$	4.13	1	24.5k
5337	Pythia 6.4	Old mass ordered Shower	4.13	1	49k
5337	Pythia 6.4	New interleaved Power Shower	4.13	1	47.5k

Tab. A.3: *Analysed samples contributing to the generator comparison and the estimate of pile-up influences.*

A.3 Event Preselection

It should be stated explicitly that no attempt is made to simulate offline trigger cuts that will be unavoidable in real data analysis. This is due wish not to reduce the small amount of simulated Monte Carlo events and the expectation that the veto characteristic is not strongly depending on the trigger selection.

Therefore, a series of loose preselection cuts aimed to select good tagging jet candidates characterising a weak boson fusion event. This is necessary since the Sherpa signal sample contains about 20 % of events where the Higgs is produced in associated production instead of VBF, while the the other generator's samples (Herwig and Pythia) consist of pure VBF events. After the following cuts (C 1 - C 3) the associated production fraction virtually vanished and the sample are comparable to each other.

(C 1) There should be two tagged jets candidates, labelled j_1 and j_2, in the event with the a transverse momentum for both jets to be $p^T_{j1/j2} > 20$ GeV.

(C 2) A spacing between both tagging jets heading to opposite hemispheres ($\eta_{j1} \times \eta_{j1} < 0$) of the detector resulting in a gap of $|\eta_{j1} - \eta_{j1}| > 4.2$ and a separation $\Delta R_{j1j2} > 1$ is required.

(C 3) The invariant mass M_{j1j2} of the two tagging jet candidates should exceed 600 GeV.

(C 4) A cut on the missing energy $\not{E}_T > 70$ GeV is introduced.

(C 5) Any additional jet to the tagging jets in the event should have an minimal p^T_{jet} of 15 GeV to be studied as potential veto jet in the CJV.

The strong cut on the missing transverse energy (C 4) is very specific for invisible Higgs boson searches. The canonical value is at usually at about 100 GeV. But the value chosen here is still loose enough to be not to far away from cuts that are used in analyses with e.g. τ final states. This is done in the hope to characterise central jet vetos more general than only for invisible finals states.

A.4 Considered Veto Strategies

Veto-1- This veto is derived from the veto used in some of ATLAS VBF Higgs searches by defining and vetoing central jets as jets in a fixed $|\eta|$<3.2 range and with $p^T >$20 GeV. For an optimisation the following ranges of p^T_{cut} and η_{cut} are both scanned simultaneously in ten steps: $p^T_{cut} \in \{15\text{ GeV}; 60\text{ GeV}\}$ and $|\eta_{cut}| \in \{0.5; 3.2\}$.

Veto-2- This veto is not using fixed η ranges. The strategy is looking instead on the relative η distance to the tagging jet, defining case-by-case a veto region in between the tagging jets. This is introduced, since it may occur the case that one or two boosted tagging jets aim more to the central region. One defines $\eta^{min,max}_{cut} = (1-\alpha) \times \eta^{min,max}_{tag}$. Jets found within the interval $[\eta^{min}_{cut}, \eta^{max}_{cut}]$ are vetoed. The approach is to define a topological region around the tagging jets in which the additional jets are accounted to be FSR of the tagging jets and not counted as central. For an optimisation the following ranges of p^T_{cut} and of the parameter α are both scanned simultaneously in ten steps: $p^T_{cut} \in \{15\text{ GeV}; 60\text{ GeV}\}$ and $\eta^{min,max}_{cut} = (1-\alpha) \times \eta^{min,max}_{tag}$ with $\alpha \in \{0.0; 0.45\}$.

Veto-3- This is a refined version of veto-2 by using ΔR= $\sqrt{\Delta\eta^2 + \Delta\phi^2}$ isolation cone of variable size. In this way not only $\Delta\eta$ but $\Delta\phi$ information contributes. Additional jets are vetoed if their ΔR with respect to the jets exceeds ΔR_{cut}. For an optimisation the following ranges of p^T_{cut} and of the parameter ΔR_{cut} are both scanned simultaneously in ten steps: $p^T_{cut} \in \{15\text{ GeV}; 60\text{ GeV}\}$ and $\Delta R_{cut} \in \{0.0; 4.0\}$.

Veto-4- To apply this veto one determines the rest frame of the dijet system consisting of the two tagging jet candidates. Any possible other vetoed jet is boosted in this rest frame and the minimal angle $\Delta\phi^{rest}$ to the back-to-back dijets is determined. Additional jets are vetoed if their ϕ to the dijets direction exceeds $\Delta\phi_{cut}$. For an optimisation p_{cut}^{Trest} in the rest frame and $\Delta\phi_{cut}^{rest}$ are both scanned simultaneously in ten steps: $p_{cut}^{T} \in \{15\text{ GeV}; 60\text{ GeV}\}$ and $\Delta\phi_{cut}^{rest} \in \{0^\circ; 90^\circ\}$.

Veto-5- This veto applies a cut in the distribution of the Zeppenfeld variable $\eta^\star = \eta_{central\,jet} - \frac{1}{2} \times (\eta_{tag1} + \eta_{tag2})$. Additional jets are vetoed if their $\eta^\star$ is smaller than $|\eta_{cut}^\star|$. For an optimisation p_{cut}^{T} and $\eta_{cut}^\star$ are both scanned simultaneously in ten steps: $p_{cut}^{T} \in \{15\text{ GeV}; 60\text{ GeV}\}$ and $\eta_{cut}^\star \in \{0.5; 3.2\}$.

Veto-6- This veto uses the transverse momentum imbalance $p^{Timbal.}$ as a criteria to measure the amount of central FSR. The following quantity is defined.as modulus of the vectorial sum of the transverse momenta of the tagging jet candidates along with the missing E^T vector; $p^{Timbal.} = |\vec{p}_{tag1}^{\,T} + \vec{p}_{tag2}^{\,T} + \vec{E}_{miss}^{T}|$. The accuracy of the calculation of the imbalance depends explicitly on the accuracy of the missing energy measurement. In an event with a small amount or no additional QCD radiation this imbalance should be small. Since all additional radiation is neglected the imbalance grows with the occurrence of additional jets. Events are vetoed if their $p^{Timbal.}$ exceeds the cut value. For an optimisation a maximal allowed imbalance $p_{cut}^{Timbal.max}$ is scanned in ten steps: $p_{cut}^{Timbal.max} \in \{5\text{ GeV}; 50\text{ GeV}\}$.

Veto-7- The last veto applies a cut on the centrality of the potential veto jet as criteria. The centrality $\eta^{centr.}$ defined as $\eta^{centr.} = Min\{(\eta_{veto\,jet} - Min\{\eta_{tag1}; \eta_{tag2}\}); (Max\{\eta_{tag1}; \eta_{tag2}\} - \eta_{veto\,jet})\}$. It turns out to be the more positive the more centrally between the tagging jets. For an additional jet 'outside' namely between tagging jet and beam pipe the variable chances sign. Additional jets are vetoed if their $\eta^{centr.}$ to the jets exceeds $\eta_{cut}^{centr.}$. For an optimisation p_{cut}^{T} and $\eta_{cut}^{centr.}$ are both scanned simultaneously in ten steps: $p_{cut}^{T} \in \{15\text{ GeV}; 60\text{ GeV}\}$ and $\eta_{cut}^{centr.} \in \{0.0; 4.0\}$.

Therefore, with exception of the 1-dim. veto-6, for each veto 100 working points are studied. This scan needs to be rather coarse since the statistic of the fully simulated samples is very limited. It is desired to collect enough entries in a scanned bin to avoid setting the optimal criteria according to an incidental fluctuation.

A.5 Estimated Detector Systematics on Averaged Significance as Figure of Merit

A.5.1 Considered Systematics

As argued already in Section A.1, with the availability of the first measurements the theoretical uncertainties on the background rates that are today very large will become negligible and are therefor not considered here as a contribution to the systematic uncertainties of the central jet veto.

The jet energy scale (JES) variations are considered as dominant systematics. The effects of the small systematic uncertainties of the reconstructed jet axis in η and ϕ are neglected (P. Loch private communication 2008). Also an additional fudging of the JES resolution as proposed in the CSC studies is not applied because this parametrises detector-non-compensation effects in the early phase of data taking.

Assuming a collected luminosity of 10 fb^{-1}, the CSC studies devise the following treatment of the JES systematics. Within a η-range of $|\eta| \leq 3.2$ an energy scaling of $\pm 7\%$ and outside the barrel range, for $|\eta| > 3.2$, an energy scaling of $\pm 15\%$ is applied. After changing the energy scale in the jets, a correction of the missing energy measurement is introduced by recalculating the missing energy in the

following way (where the index $jets fromAOD$ refers to the unscaled original energies present in the analysis object data, AOD):

$$\Delta E^T(x) = \pm 0.05 * (|\sum_{all\,jets} E_{jets\,fromAOD}(x) - \sum_{all\,jets} E_{jetsvariedJES}(x)|)$$
$$\Delta E^T(y) = \pm 0.05 * (|\sum_{all\,jets} E_{jets\,fromAOD}(y) - \sum_{all\,jets} E_{jetsvariedJES}(y)|)$$
$$E^T_{missnew}(x) = E^T_{fromAOD}(x) - \Delta E^T(x) \;\; ; \;\; E^T_{missnew}(y) = E^T_{fromAOD}(y) - \Delta E^T(y).$$

We also check the effect of the half of the systematics variations to account for a better understanding of the JES in later years of ATLAS running, when Higgs scenarios like the stealthy Higgs [36] may be considered.

The relative systematic error from the jet energy scale uncertainty on the jet veto is defined by

$$(N_{surv}(varied) - N_{surv}(orig))/N_{surv}(orig)$$

and evaluated for each considered working point. Here $N_{surv}(orig)$ stands for the original number of events passing the VBF preselection and subsequently the central jet veto and N_{surv}(varied) for the number of events that pass VBF selection and the veto after the JES is varied and the missing energy is newly calculated.

A.5.2 Definition of a Figure of Merit

The ATLAS Higgs boson searches express their sensitivity towards the presence of the Higgs boson signal in the so called significance. This variable normalises a possible observed excess in signal like events by the expected fluctuations or error of the background rate. The significance is usually calculated after a full and refined analysis of the data, with the aim of optimal discrimination between signal and background, including for example the full set of cuts.

In our search for a suitable figure of merit we decide to use the significance for expressing the sensitivity of specifically the central jet veto, too. But here we analyse only a not very restrictive subset of the canonical analyses cuts with the idea to keep as much of the sparse fully simulated events as possible and to become not to specific on an invisible final state. Therefore, even when we are quoting significance it should be kept in mind that the actual value recited after the fully-fledged analysis including systematic studies will be different.

As a figure of merit a significance is used given by

$$< \mathscr{S} >= \frac{1}{3} \sum_{i \in \{Sherpa, HerwigPythiaOld\}} \frac{S_i + \Delta_{sys} S_i}{\sqrt{B + (\Delta_{sys} B)^2}}.$$

In the formula above S_i is the expected number of signal events predicted from one of the compared generator and B the expected number of background events, scaled to a luminosity of 30 fb^{-1}. The idea behind this is to get from averaging over the varying selected signal predictions between a measure for the common generator prediction. The background sample is always the Z plus jets sample generated with Sherpa 1.0.11. Choose the direction of variation in which B gets enhanced due to the JES systematics.

As can be seen in Section A.6.3 the new Pythia power shower exhibits a qualitatively different behaviour in the QCD radiation pattern from all other considered generators. Therefore, we decide to exclude the Pythia power shower in the optimisation. This can be justified with the argument that in this way one finds an optimal veto and working point for relatively mild deviating generators. If the first measurements hint that the Pythia power shower is a valid model for nature it will be possible to find an appropriate veto and working point especially for a significance optimisation in that model as demonstrated in Sec.A.8.3.

A.6 Comparison of Signal Distributions with Different Monte Carlo Generators

For the generation of an invisibly decaying Higgs boson produced in VBF three Born-level generators are regarded, namely Pythia, Herwig and Sherpa. Even if the VBF production process is treated at Born-level the matrix elements calculated by Sherpa contain Higgsstrahlung graphs (see Sec.A.2.2). Furthermore as the different Monte Carlo generators apply different models of parton showers and underlying event description, the distributions of tagging and central jets are expected to differ. In order to give an estimate of such effects signal samples of Higgs mass $M_{\mathrm{H}} = 130$ GeV generated with Herwig-Jimmy 6.5, Sherpa 1.0.11 and Pythia 6.4 with old parton shower and the new interleaved shower model are compared in this section.

A.6.1 Normalisation

All distributions (Fig. A.6 to A.19) in this section are displayed after a series of loose tagging jet cuts, selecting a typical VBF jet topology. For comparison all these distributions are normalised to an arbitrary cross section after cut (C 1) to (C 3) as given in section A.3. After these cuts less than 1 % of all Higgs boson events stemming from associated production in the Sherpa samples and the sample size can be corrected for the number of weak boson fusion events [134]. The differences in jet multiplicities in the differents samples is in this way directly comparable.

Especially the distribution of the third and the fourth hardest jet suffer from larger statistical fluctuations regarding the fully simulated events. We therefore, provide the truth distributions with a very large statistics that the errors become of the size of the marker. So one can see what behaviour is expected in the distributions according to the truth information.

A.6.2 Kinematic Properties of the Leading and Subleading Jet

First the kinematic properties of the leading and subleading jet are compared in Fig. A.6 to A.13, to verify that all generators reproduce the typical weak boson topology satisfactorily. As can be seen in Fig. A.6 and A.7, the new parton shower model of Pythia tends to yield harder jets, whereas Pythia's old partons shower is in agreement with the Herwig prediction for the leading jets. Sherpa produces a leading jet spectrum peaking a little bit lower than Herwig and old and new Pythia shower. Generally the reconstructed jets seem to be biased towards slightly harder P^T spectra. Nevertheless, the predictions for the pseudorapidity distributions of the leading (Fig. A.8) and subleading jet (Fig. A.9) have only little variation in the shape for the different generators. Herwig and Pythia with old shower agree best, while the new shower of Pythia peaks at a little bit smaller absolute values of η. In contrast the Sherpa pseudorapidity distributions peak at the largest η values of all regarded generators. As a well known fact the jet reconstruction becomes inefficient in the region around $|\eta| \approx 3.2$, where the junction between barrel and end cap is located. Similarly the small deviations between generators in the pseudorapidity related distributions of the hardest jets (Fig. A.10 and A.11) reflect the differences in the P^T and η spectra. We observed that the distribution of the invariant jet masses of the leading jets (Fig.A.12) are in good agreement. One may notice the slightly higher jet masses for Pythia's new shower according to the higher jet transverse momentum. Again the predicted azimuthal angular differences between the leading jets (Fig. A.13) is in good agreement for all compared generators.

A.6.3 Kinematic Properties of the Third and Fourth Hardest Jets

Secondly Fig. A.14 to Fig. A.19 show distributions for the next hardest jets to the leading and subleading jet. Of some interest are possible differences in the third and fourth hardest jets, since the presence of a central jet with sizable transverse momentum is of importance for the signal acceptance of an applied central mini-jet veto. Such additional jets are described in all generators by their the parton shower

models. In the case of Sherpa the third jet is allowed to stem from the exact matrix element down to a CKKW matching scale of 20 GeV. Indeed this is true in average for every fourth event. Jets below that scale are from the parton shower only.

As stated before the minimal P^T to which jets are build differs for truth and reconstructed jets. To yield comparable distributions for the third and the fourth hardest jets in the following a common cut of $P^T > 15\,\text{GeV}$ is made (C 5). Unfortunately this reduces the statistical significance of especially the distributions involving the fourth jet strongly. In Fig.A.14 and A.15 the P^T spectra of the third and the fourth jets are displayed. The Herwig spectrum is comparable to the old Pythia shower but the new Pythia shower is producing significantly more and slightly harder jets. In the case of Sherpa the production rate of third jets that may stem from both matrix elements or parton shower is somewhere in between Herwig and the new Pythia. This picture remains valid even for the fourth jet. The fourth hardest jets is generated via parton shower in all compared generators, but it can consist of gluon radiation dominantly emitted under small angles along the tagging jets and centrally emitted gluon radiation for the underlying event, depending also on the setting for the underlying event activity.

If one compares the η distributions for the third and fourth jet (Fig. A.16 and A.17), large differences in the generator predictions become obvious. First of all one notes that the radiation of the third and even the fourth jet tends to peek more in forward or backward direction for Sherpa exhibiting the most prominent dip in the pseudorapidity distributions. This is a clear indication that the major fraction of additional jets in Sherpa are generated by final state radiation and not by the underlying event. In contrary the new shower model of Pythia produces a very busy and flat distribution of third and forth jets in the central eta region between $|\eta| \approx 3$. The old shower model of Pythia predicts a smaller abundance for the third jet that are peaking more around $|\eta| \approx 3$ leaving a central rapidity gap recognisable, while this gap vanishes for the the fourth jet that may stem from the very active underlying event most of the time. The Herwig prediction for the pseudorapidity distribution of the third jet is almost flat but third jets are less abundant than in the new Pythia shower model. For the η of the fourth jet Herwig predicts the most prominent accumulation of jets at small pseudorapidity values around $|\eta| \lesssim 2.5$.

A variable that serves as a measure of hadronic activity in the η regions between the tagging jets of VBF events is the so-called Zeppenfeld variable. The variable is defined as $\eta^\star = \eta_{jet3} - \frac{1}{2} \times (\eta_{jet1} + \eta_{jet2})$. While for most of the backgrounds the Zeppenfeld variable peaks around zero, a large dip in this region is expected for VBF events due to the lack of colour exchange between the tagging jets. Generally speaking a large dip in the Zeppenfeld variable for the signal is desirable offering the possibility to apply an effective central jet veto.

The distributions of the Zeppenfeld variable, $\eta^\star_{jet3}$, is shown in Fig. A.18. Sherpa shows the most distinctive and widest gap in the pseudorapidity distribution peaking at values around 3. Though the old shower Pythia's dip is comparable pronounced peaking at lower pseudorapidity distribution about 2 it is not as wide as for Sherpa. The new shower model of Pythia generates so many jets over the central region between $|\eta| \lesssim 2$ that no rapidity gap in the Zeppenfeld variable is present. An analogue variable, $\eta^\star_{jet4}$, constructed with the use of the fourth jet instead of the third jet is plotted in Fig. A.19. Again as seen before in the η_{jet4} distribution Sherpa is the only MC generator that shows a clear dip in the pseudorapidity distribution, while the other generators fill this region with jets and Pythia with its new shower model produces the highest jet rate.

It is remarkable that though for Herwig the truth jets distribution of the Zeppenfeld variable constructed with use of the third jet (Fig. A.18) is flat in the full simulation a clear dip in the Zeppenfeld variable in the central region occurs. Similarly the visible accumulation around zero in the Zeppenfeld variable constructed with use of the fourth jet (Fig. A.19) for truth jets is flattened for fully reconstructed jets. The observation that the full reconstruction flattens central peaks and amplifies existing dips holds true also for the other generators, but less pronounced. This may be an effect of differences in the jet algorithms between truth and full detector simulation like splitting and merging of jets and calibration of calorimeter cells and noise cuts. Also one has to keep in mind that the reconstruction efficiency for

jets has an turn on around the threshold of the reconstruction cut biasing the spectra towards harder jets. Moreover in particular the reconstruction efficiency varies with η. For example the more expressed dip in full simulation may be due to a reduced jet efficiency in the crack region around $\eta| \approx 1.7$. Similarly a reduced jet efficiency in the end caps in forward regions may forge the slopes in the $|\eta|$ range between 3 and 4 further compared to truth jets.

The abundance of jets with sizable $P^T \approx 20\,\text{GeV} - 65\,\text{GeV}$ and the absence of suppression of hadronic radiation in central region of the η spectrum observed for the new Pythia shower model lead to the assumption that if this is truly realised in nature the central jet veto is not very useful for the analyses. On the other hand the situation looks more optimistic if the Sherpa prediction is realised in nature. Because Sherpa exhibits a radiation pattern of the additional jets with an emphasised activity along tagging jets even well visible for the forth jet. This gives rise to the assumption that a jet veto in Sherpa can be restricted to a larger pseudorapidity range.

Nevertheless a jet veto that should work robust for different Monte Carlo generators is expected to operate in pseudorapidity ranges, referring to Fig.A.16 to A.19, where the difference between the generators are smallest.

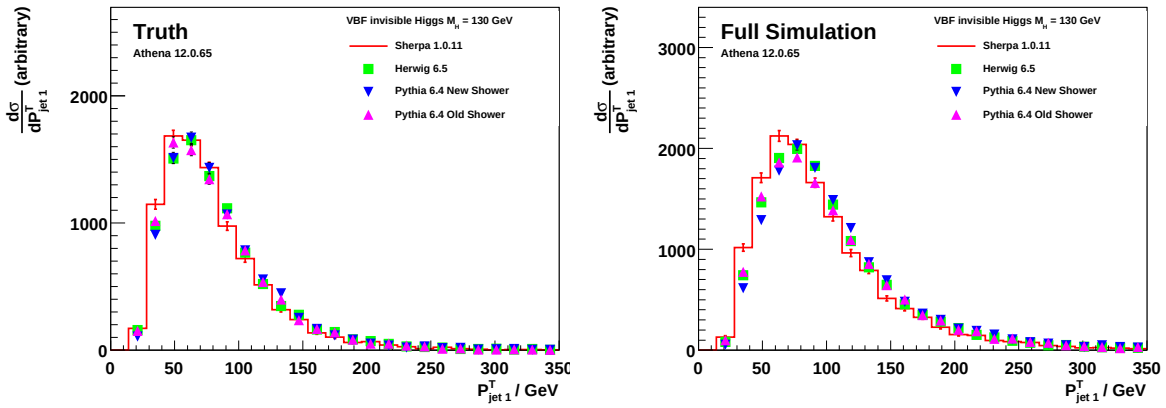

Fig. A.6: *Distribution of the leading jet's transverse momentum, P^T_{jet1}, as predicted by the different MC generators for an invisibly decaying Higgs boson with a mass of 130 GeV produced in VBF. The distributions are normalised to an arbitrary cross-section after (c 1)-(c 3). The left plot shows the distribution of cone 04 Truth jets, the plot on the right side depicts the results of full detector simulation and reconstruction of cone 04 calorimeter tower jets.*

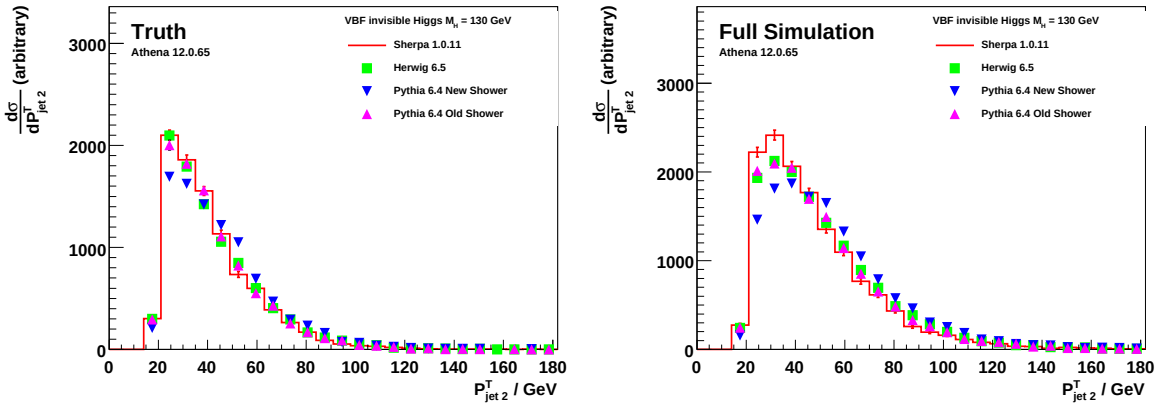

Fig. A.7: *Distribution of the subleading jet's transverse momentum, P^T_{jet2}, as predicted by the different MC generators for an invisibly decaying Higgs boson with a mass of 130 GeV produced in VBF.*

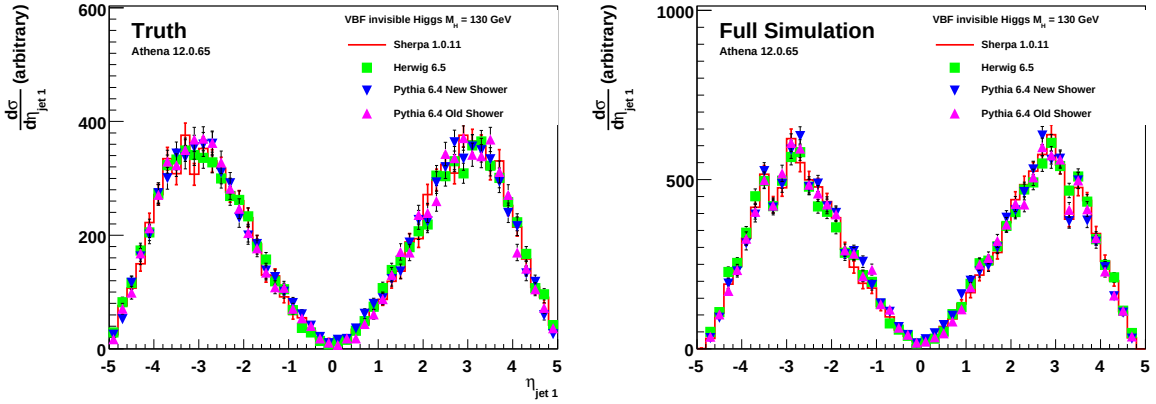

Fig. A.8: *Pseudorapidity distribution of the leading jet, η_{jet1}, as predicted by the different MC generators for an invisibly decaying Higgs boson with a mass of 130 GeV produced in VBF.*

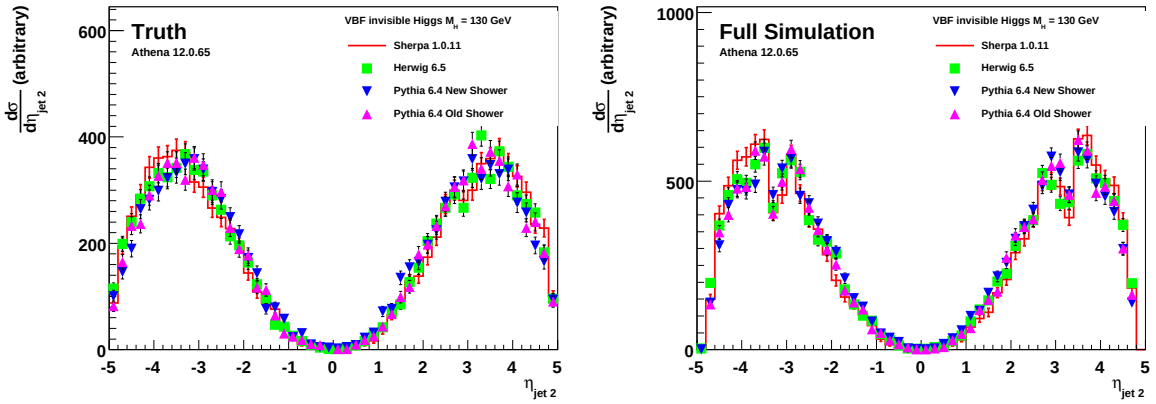

Fig. A.9: *Pseudorapidity distribution of the subleading jet, η_{jet2}, as predicted by the different MC generators for an invisibly decaying Higgs boson with a mass of 130 GeV produced in VBF.*

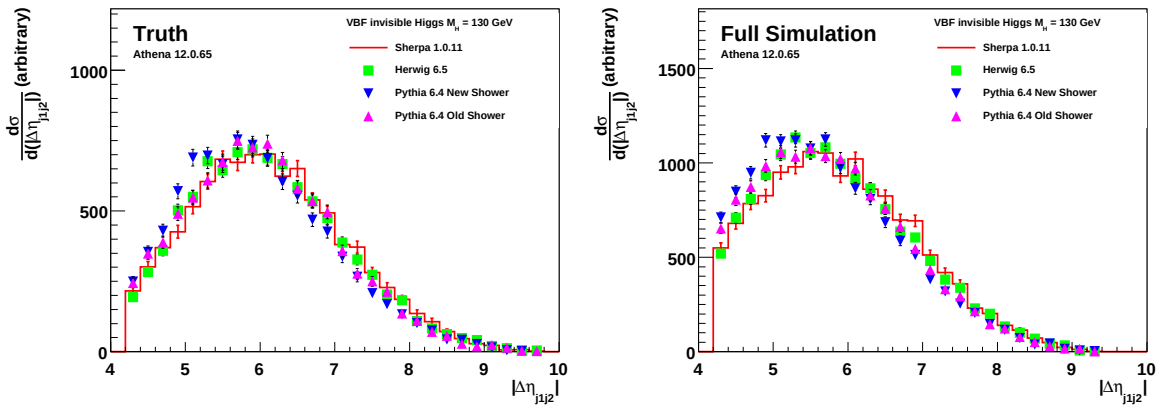

Fig. A.10: *Distribution of the pseudorapidity gap $\Delta\eta_{j1j2}$ between the leading and subleading jet as predicted by the different MC generators for an invisibly decaying Higgs boson with a mass of 130 GeV produced in VBF.*

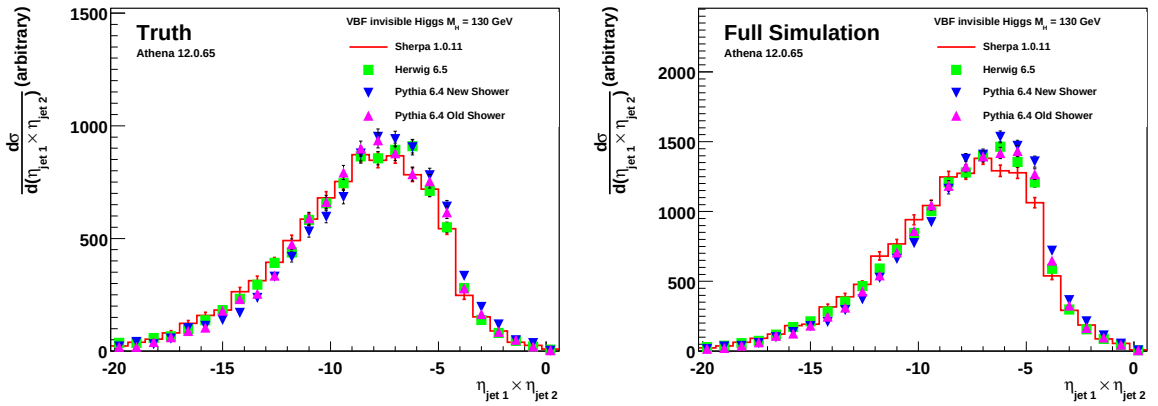

Fig. A.11: *Distribution of the product pseudorapidity $\eta_{j1} \times \eta_{j2}$ between the leading and subleading jet as predicted by the different MC generators for an invisibly decaying Higgs boson with a mass of 130 GeV produced in VBF. The leading jets are selected to lie in opposite hemispheres in order to be tagging jet candidates.*

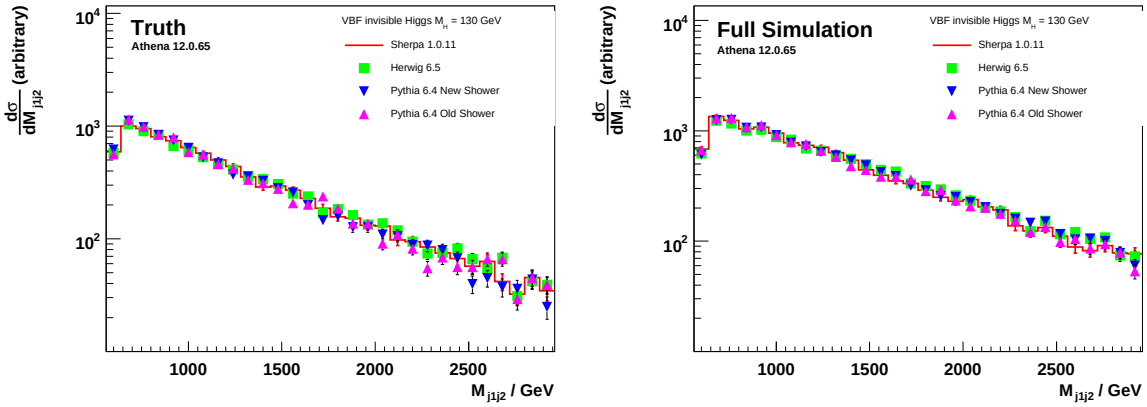

Fig. A.12: *Distribution of the invariant mass* M_{j1j2} *between the leading and subleading jet as predicted by the different MC generators for an invisibly decaying Higgs boson of mass 130 GeV produced in VBF.*

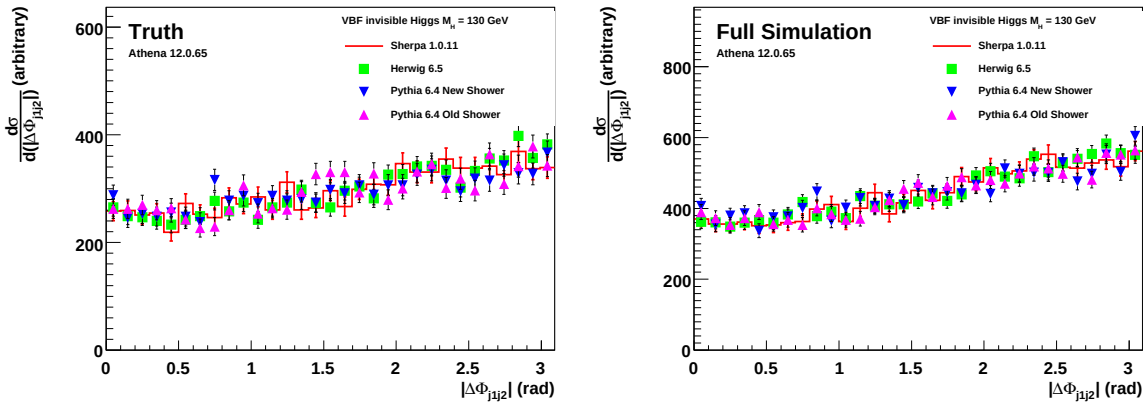

Fig. A.13: *Distribution of the absolute azimuthal angular difference,* $|\Delta\Phi_{j1j2}|$*, between the leading and subleading jet as predicted by the different MC generators for an invisibly decaying Higgs boson with a mass of 130 GeV produced in VBF. The leading jets are typically accumulating at* π *but depending on the boost of the Higgs boson the recoiling jets become acoplanar for a large fraction of events.*

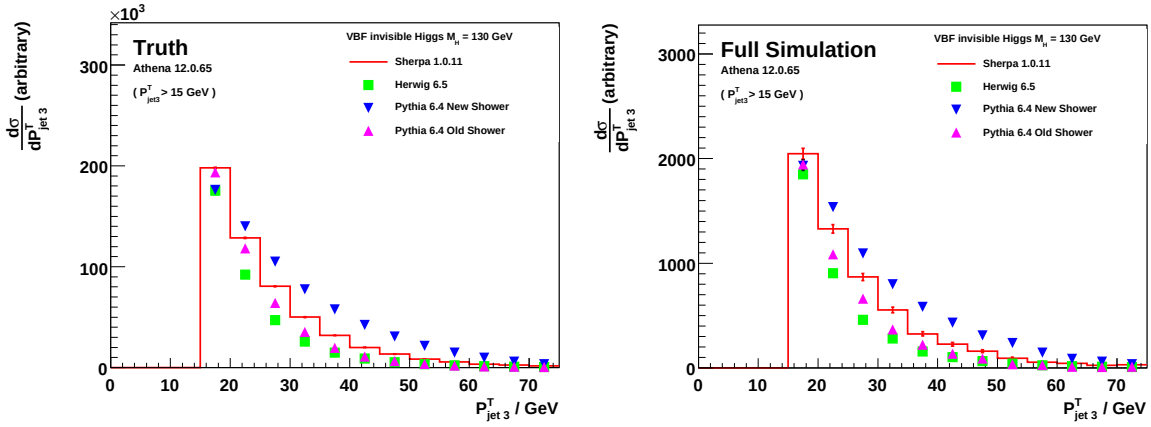

Fig. A.14: *Distribution of the transverse momentum, P^T_{jet3}, of the third hardest jet as predicted by the different MC generators for an invisibly decaying Higgs boson with a mass of 130 GeV produced in VBF. A transverse momentum cut of $P^T > 15$ GeV is applied.*

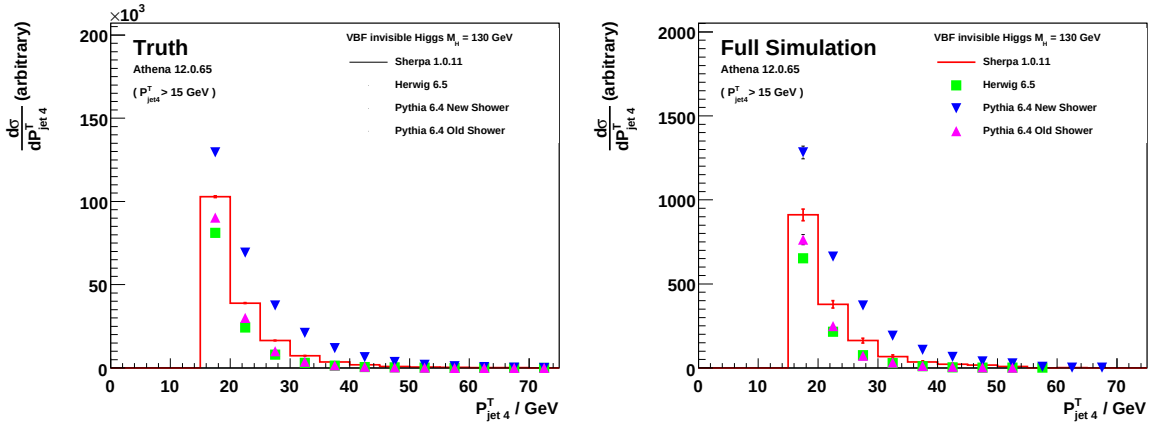

Fig. A.15: *Distribution of the transverse momentum, P^T_{jet4}, of the fourth hardest jet as predicted by the different MC generators for an invisibly decaying Higgs boson with a mass of 130 GeV produced in VBF. A transverse momentum cut of $P^T > 15$ GeV is applied.*

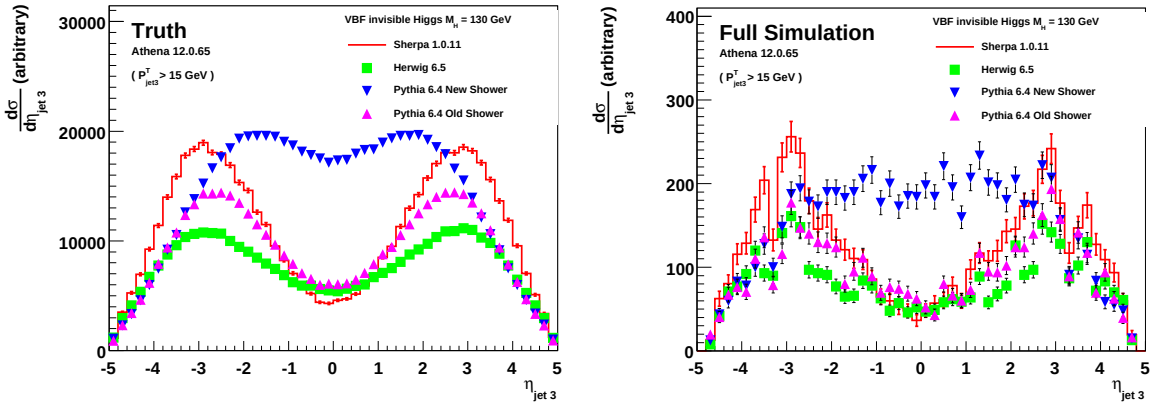

Fig. A.16: *Pseudorapidity distribution, η_{jet3}, of the third hardest jet as predicted by the different MC generators for an invisibly decaying Higgs boson with a mass of 130 GeV produced in VBF. A transverse momentum cut of $P^T > 15$ GeV is applied.*

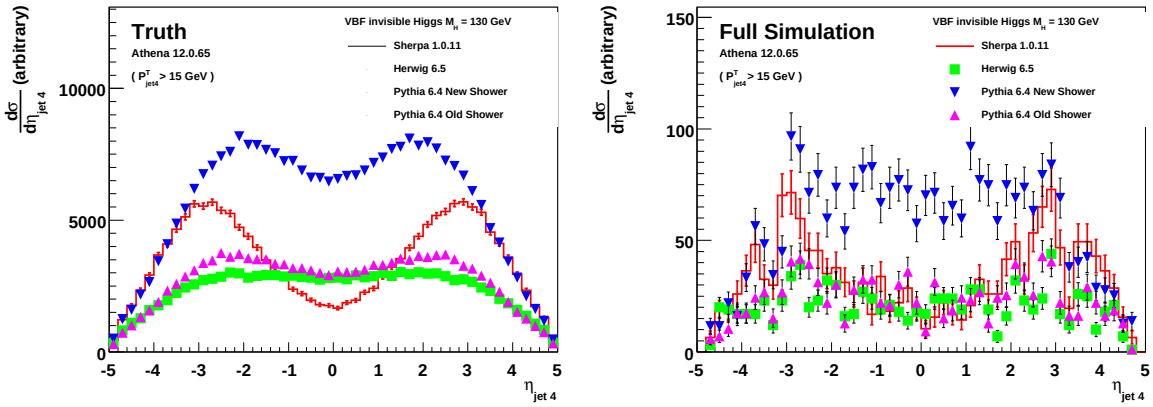

Fig. A.17: *Pseudorapidity distribution, η_{jet4}, of the fourth hardest jet as predicted by the different MC generators for an invisibly decaying Higgs boson with a mass of 130 GeV produced in VBF. A transverse momentum cut of $P^T > 15$ GeV is applied.*

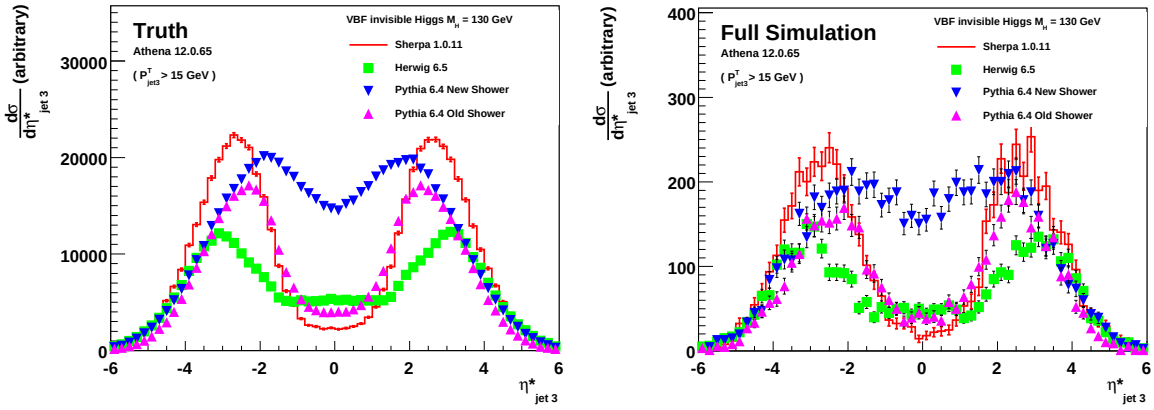

Fig. A.18: *Distribution of* $\eta^{\star}_{jet3} = \eta_{jet3} - \frac{1}{2} \times (\eta_{jet1} + \eta_{jet2})$*, the so-called Zeppenfeld variable, as predicted by the different MC generators for an invisibly decaying Higgs boson with a mass of 130 GeV produced in VBF. A transverse momentum cut of* $P^T > 15$ GeV *is applied.*

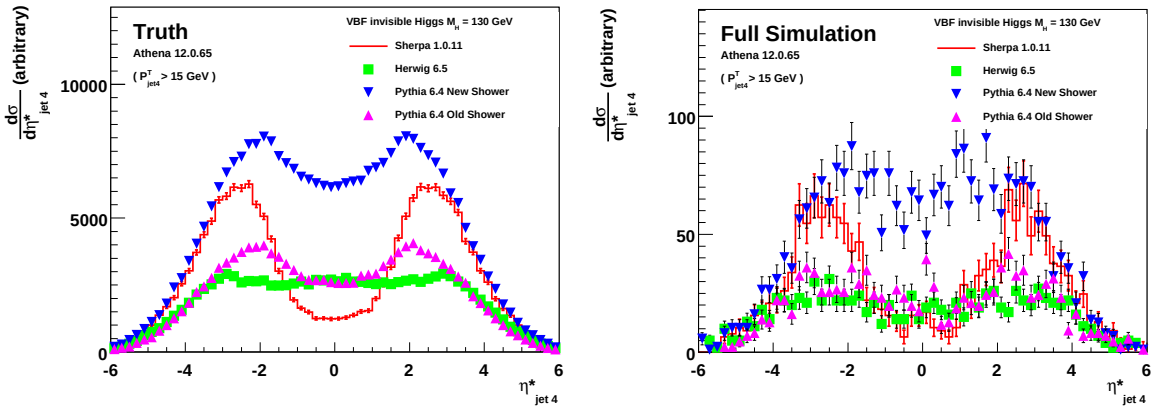

Fig. A.19: *Distribution of* $\eta^{\star}_{jet4} = \eta_{jet4} - \frac{1}{2} \times (\eta_{jet1} + \eta_{jet2})$ *as predicted by the different MC generators for an invisibly decaying Higgs boson with a mass of 130 GeV produced in VBF. A transverse momentum cut of* $P^T > 15$ GeV *is applied.*

A.7 Comparison of Signal Distributions with Different Underlying Event Tunes in Sherpa 1.0.11

In this section we want to investigate how the distributions of variables shown in the last sections change under the detuning of the underlying event in a specific generator, namely Sherpa 1.0.11. This information about underlying event tune parameter dependencies can be useful if one wants to tackle the question whether residual detuning may affect predictions on central jet veto efficiencies. A comparison to other generators of the last section can be made by eye because of the red histogram of the TeVatron-fixed underlying event tune which appears in both sections.

We focus on the properties of third and forth hardest jets in the events since the variation of the Q_{cut} scale has no visible influence on the distributions of the leading and subleading jets from the hard matrix element, which are displayed in Sec.A.6.2. Though in principle the exchange of the parton distribution function should influence all jets, the differences for the distributions of the leading and subleading jets are found to be very small and well contained within the statistical errors of the samples.

A.7.1 Scale Variations in the Underlying Event

As described shortly in Sec.A.2.3 the tune determines the average number of (charged) particles produced per pseudorapidity interval. The energy of these particles is only measured in the calorimeter system. These energies are collected by jet building algorithms. The resulting jet depends on the jet algorithms applied. It can deviate e.g. in how well jet boundaries are defined and in that way in the amount of lateral energy leakage. Therefore, in principle it may be of interest to study the underlying event with different jet algorithm too. But this would be beyond the scope of this study and we decide to restrict ourselves to the simple cone jet algorithm with an opening cone size of $\Delta R = 0.4$.

Keeping in mind our ignorance about how large we have to vary Q_{cut} to account for residual uncertainties in underlying event tunes after first data we tried to find a symmetrical Q_{cut} scale variation in which different underlying event activity becomes visible if collected by calorimeter-based algorithms. Naively, one would expect that first of all one has to raise the number of additionally produced particles in a spatial interval over a certain threshold before a cone jet is built up in this region.

The Fig.A.20 to A.23 show the transverse momentum of the third and forth jet along with the Zeppenfeld distribution and the pseudorapidity distribution of the fourth jet in comparison to the ATLAS default tune sample the TeVatron tuned sample and the symmetrical variations around its cut scale of about 30 %. Differences between the samples are now in the abundance of jets more than in general pseudorapidity QCD radiation patterns.

It is notable that though the TeVatron fixed tuned and CSC ATLAS default tune Q_{cut} differs about 5 %, but the differences in the distributions are almost neglectible. For the extremely raised Q_{cut} of 30 % above the value suggested from the TeVatron data the underlying event activity ceases since the non diffractive cross section is lowered (see e.g. Fig.A.21). Although this scenario is not expected to be realistic. On the other hand a lowering of Q_{cut} about 30 % yields a large enhancement of the lowest additional jets with $p^T \lesssim 30$ GeV (see Fig.A.20 and A.22). This value predicts an overall enhancement of small angle FSR from jets (see e.g. peak region in Fig.A.23) as well as central jet activity from the underlying event parton shower at central pseudorapidity.

We can conclude from these plots that only a relatively large overestimation of much more than 5 % of Q_{cut} in data tuned models can have a possible negative effect on the applied central jet veto.

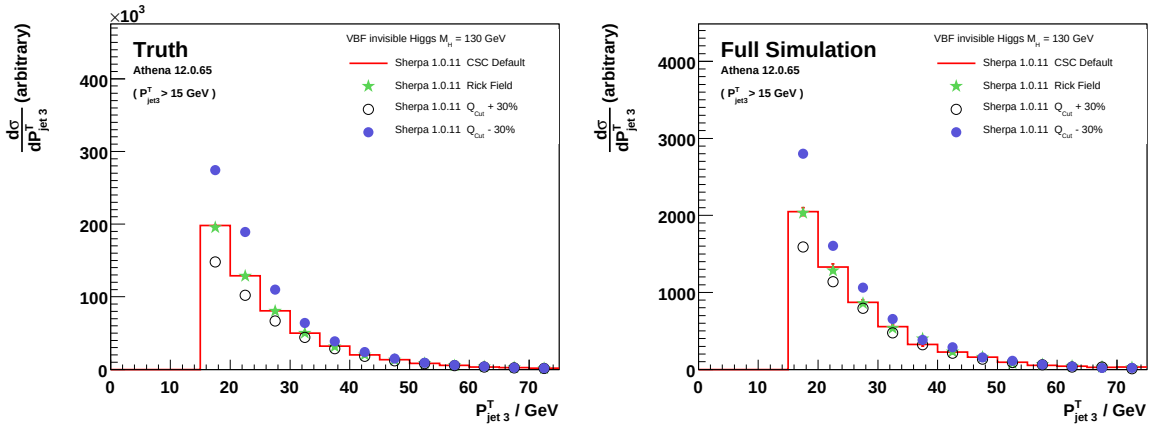

Fig. A.20: *Distribution of the third hardest transverse momentum P^T_{jet3} as predicted by the different Sherpa1.0.11 underlying event Q_{cut} scale settings for an invisibly decaying Higgs boson with a mass of 130 GeV produced in VBF. A transverse momentum cut of $P^T > 15$ GeV is applied.*

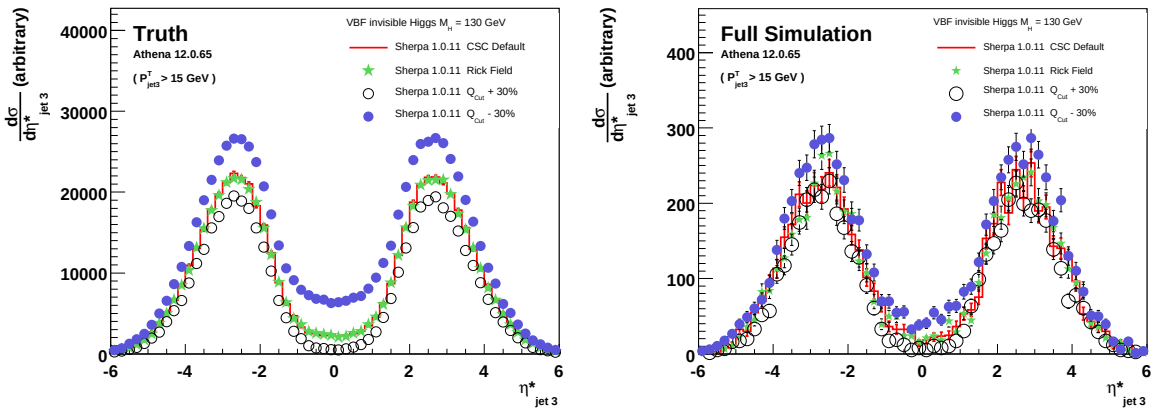

Fig. A.21: *Distribution of $\eta^{\star}_{jet4} = \eta_{jet4} - \frac{1}{2} \times (\eta_{jet1} + \eta_{jet2})$ as predicted by the different Sherpa1.0.11 underlying event Q_{cut} scale settings for an invisibly decaying Higgs boson with a mass of 130 GeV produced in VBF. A transverse momentum cut of $P^T > 15$ GeV is applied.*

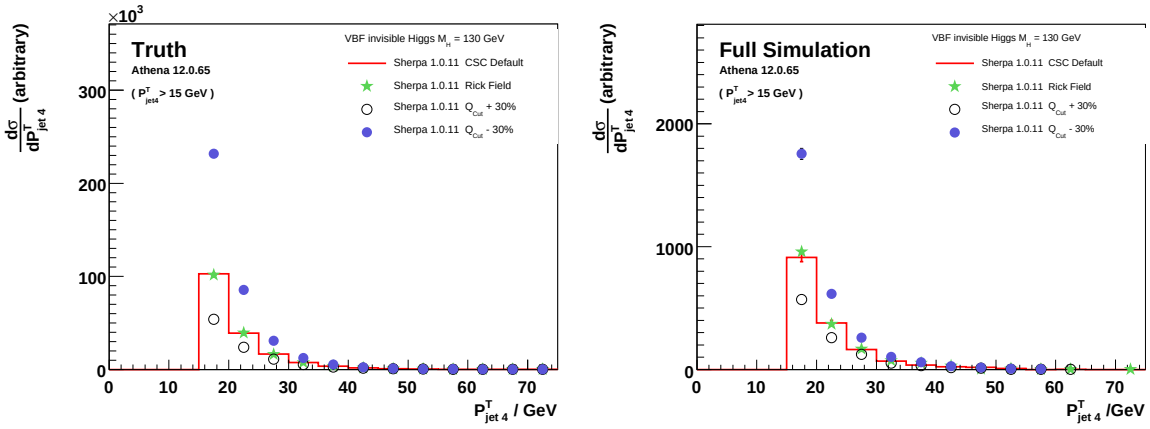

Fig. A.22: *Distribution of the forth hardest transverse momentum P^T_{jet3} as predicted by the different Sherpa1.0.11 underlying event Q_{cut} scale settings for an invisibly decaying Higgs boson with a mass of 130 GeV produced in VBF. A transverse momentum cut of $P^T > 15$ GeV is applied.*

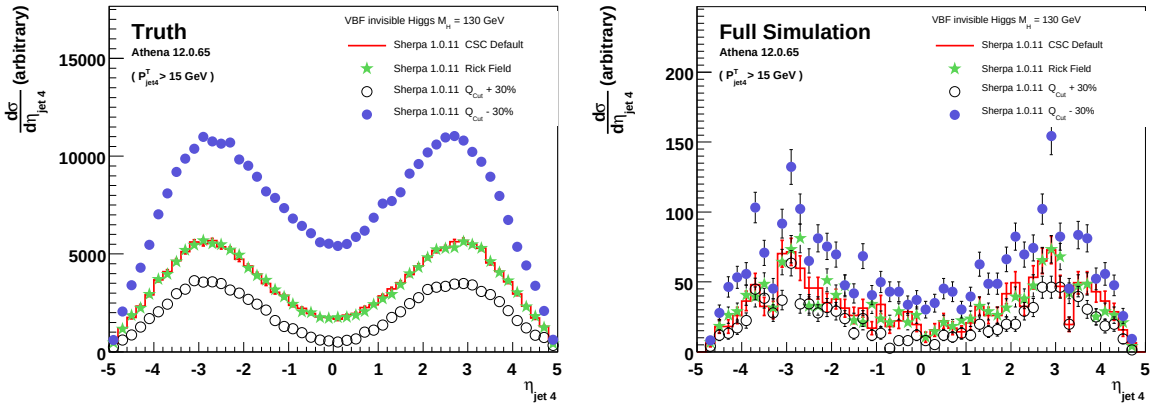

Fig. A.23: *Distribution of the pseudorapidity of the forth hardest jet in the event, η_{jet4}, as predicted by the different Sherpa1.0.11 underlying event Q_{cut} scale settings for an invisibly decaying Higgs boson with a mass of 130 GeV produced in VBF. A transverse momentum cut of $P^T > 15$ GeV is applied.*

A.7.2 PDF Exchange and the Underlying Event

For this check of a parton distribution function dependence we compared in Fig.A.24 to Fig.A.27 the third and forth jet properties of a sample with MRST2004 with the TeVatron tuned sample, which contains CTEQ6L. The MRST2004 sample will not be expected to coincide with the correct exponentiation of the TeVatron tune to LHC centre of mass energies because if PDF's are exchanged, one has to do a retune of parameters to the TeVatron data.

There exist many PDF set to various data and subsets of data. Also fitting methods and treatment of parameters like the scales and couplings vary. A complete study is beyond the scope of this work. So we arbitrarily choose a set that is available in LO and NLO and checked that it deviates from the default CTEQ6l (see. Fig.A.5). From the plot of the PDF's it is not clear how large the effects on the reconstructed jets will be in terms of jet momentum spectra and abundance. Our approach is just a quick check for the magnitude of effects and the main interest in this study is therefore whether effects in such entities are visible.

Obviously the chosen MRST2004 NLO works against the parton shower activity in the underlying event, because the NLO sample distributions become almost indistinguishable to distributions without UE. Though we have choosen only an arbitrary part of the available PDF sets we conclude from these plots that residual uncertainties of parton distribution functions will most probably have no effect on the efficiency of an applied central jet veto.

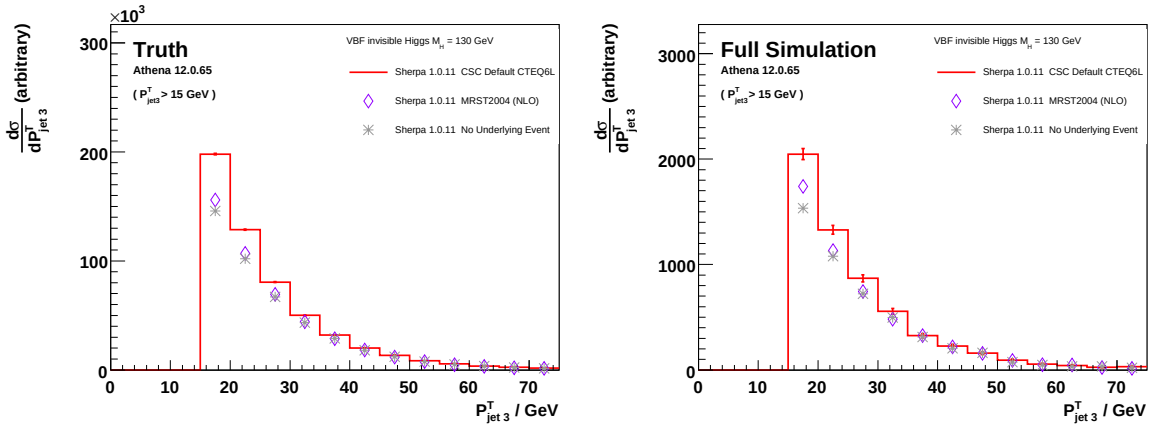

Fig. A.24: *Distribution of the third hardest transverse momentum P^T_{jet3} as predicted by the different PDF choices in Sherpa1.0.11 for an invisibly decaying Higgs boson with a mass of 130 GeV produced in VBF. A transverse momentum cut of $P^T > 15$ GeV is applied.*

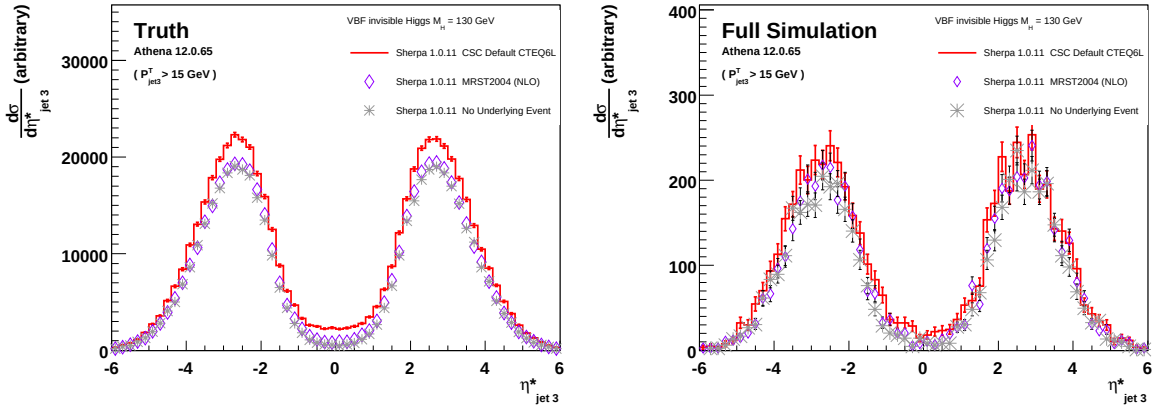

Fig. A.25: *Distribution of* $\eta^{\star}_{jet4} = \eta_{jet4} - \frac{1}{2} \times (\eta_{jet1} + \eta_{jet2})$ *as predicted by the different PDF choices in Sherpa1.0.11 for an invisibly decaying Higgs boson with a mass of 130 GeV produced in VBF. A transverse momentum cut of* $P^T > 15$ GeV *is applied.*

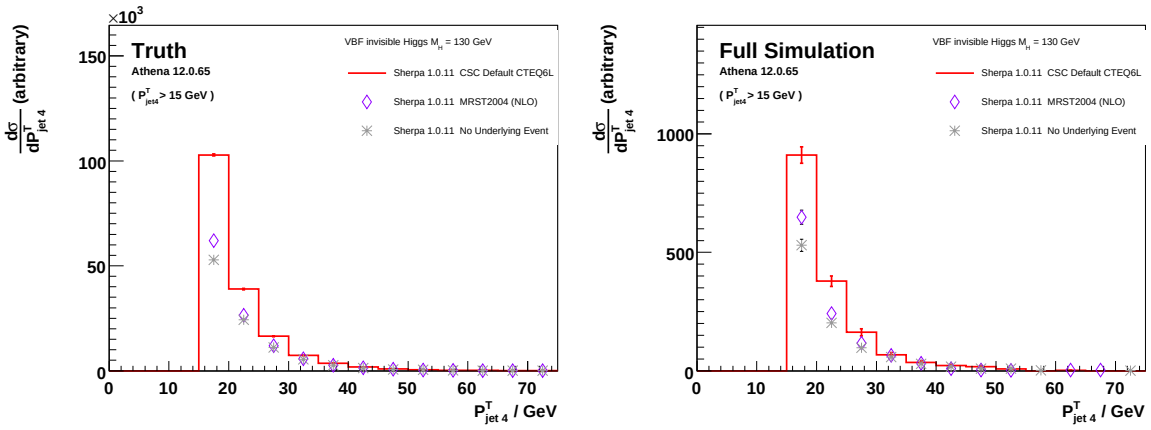

Fig. A.26: *Distribution of the forth hardest transverse momentum* P^T_{jet3} *as predicted by the different PDF choices in Sherpa1.0.11 underlying event for an invisibly decaying Higgs boson with a mass of 130 GeV produced in VBF. A transverse momentum cut of* $P^T > 15$ GeV *is applied.*

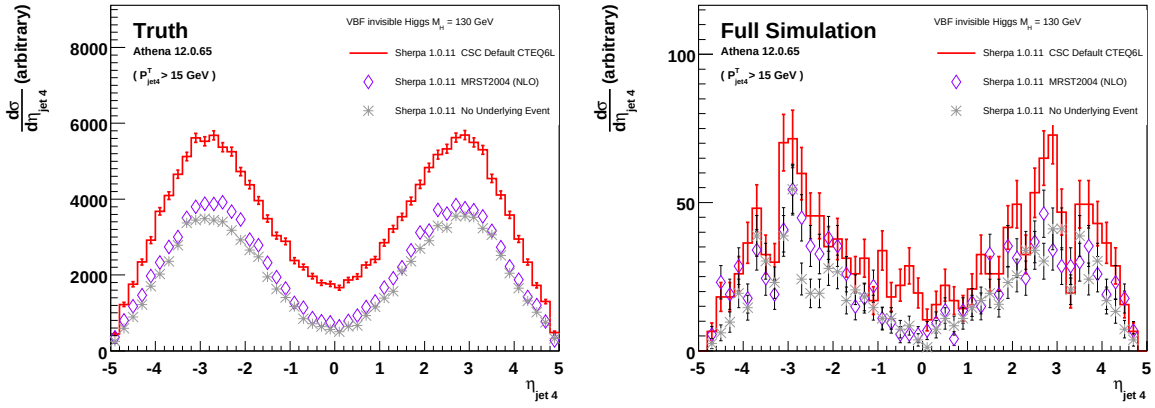

Fig. A.27: *Distribution of the pseudorapidity of the forth hardest jet in the event, η_{jet4}, as predicted by the different PDF choices in Sherpa1.0.11 for an invisibly decaying Higgs boson with a mass of 130 GeV produced in VBF. A transverse momentum cut of $P^T > 15$ GeV is applied.*

A.8 Search for an Effective Jet Veto Strategy Using Various Monte Carlo Generators

In the following we collect the tabulated results of the study to find an optimised jet veto condition. For comparison we start in A.8.1 with a compilation of the significances including systematic uncertainties at the stage where only cut (C 1) to (C 4) are applied. This can be compared in the following with the results for varying generator predictions using the figure of merit with the Sherpa TeVatron fixed tune and Herwig and the old shower model in Pythia (see Sec.A.8.2). Below (see Sec.A.8.3) we also investigate how the central jet veto behaves with the new power shower model in Pythia. Also we compare various underlying event tunes in Sherpa against each other (see Sec.A.8.4).

A.8.1 Significances for the Signal Samples without Central Jet Veto

The results in Tab.A.4 display the significances including the estimated systematic contributions for each individual signal sample when only applying cut (C 1) to (C 4) for discriminating signal against background. Keeping in mind that these cuts only rely on the tagging jets characteristics and the missing energy in the event that is predicted similar for all generators considered one suspects the variation of significance between 0.58 and 0.67 being predominantly due to statistical fluctuations in the varied JES. This is visible in the spread of the errors of the signal, while the background sample remains the same. Naturally effects of the different underlying events of radiation pattern only play a marginal role at this stage of selection. We will refer to Tab.A.4 later when deciding what the improvement by a central jet veto studied in the next paragraphs is gained for problematic samples like Pythia with power shower or Herwig at $\mathscr{L} = 1 \times 10^{33}\, cm^{-2}\, s^{-1}$.

Signal sample	$\mathscr{S}_{syst}$	ΔS_{syst}	ΔB_{syst}
full size JES systematics			
ATLAS default	0.64	6.3%	14.7%
TeVatron tune	0.64	6.4%	14.7%
$Q_{cut} + 30\%$	0.64	6.5%	14.7%
$Q_{cut} - 30\%$	0.67	6.2%	14.7%
MRST2004 NLO	0.61	6.9%	14.7%
no UE	0.63	6.8%	14.7%
Herwig	0.67	5.3%	14.7%
Pythia Old PS	0.58	6.5%	14.7%
Pythia New PS	0.62	5.5%	14.7%
Herwig $\mathscr{L} = 1 \times 10^{33}\, cm^{-2}\, s^{-1}$	0.62	6.3%	14.7%
half size JES systematics			
ATLAS default	1.30	3.2%	7%
TeVatron tune	1.29	3.0%	7%
$Q_{cut} + 30\%$	1.28	2.8%	7%
$Q_{cut} - 30\%$	1.36	2.8%	7%
MRST2004	1.23	3.3%	7%
no UE	1.27	3.2%	7%
Herwig	1.37	2.7%	7%
Pythia Old PS	1.18	3.2%	7%
Pythia New PS	1.26	2.8%	7%
Herwig $\mathscr{L} = 1 \times 10^{33}\, cm^{-2}\, s^{-1}$	1.26	3.0%	7%

Tab. A.4: Significance and contributing systematic uncertainty for the considered signal samples after cuts (C 1) to (C 4) but before any central jet veto. In the upper part the full systematic variation of the JES is used as devised by studies of 10 pb^{-1}. In the lower part only half of this variation is applied, assuming better knowledge after long time data taking.

A.8.2 Optimised Veto Strategy for Sherpa, Herwig and Pythia with Old Shower

In Tab.A.5 the optimal choices of a veto condition for each of the considered vetos after cuts (C 1) to (C 4) are compared. The significance $\mathscr{S}$, serving as our F.o.M., is arithmetically averaged from Pythia old parton shower model, Herwig, Sherpa in a TeVatron physics tune signal samples at $M_H = 130$ GeV. The qualitatively deviating predictions of Pythia's new power shower model are treated separately in A.8.3. Analysed backgrounds are the Sherpa $Z \rightarrow \nu\bar{\nu}$ samples. The average significance $\mathscr{S}_{syst}$ includes uncertainties of JES on signal and background. For the detector systematic uncertainties effects on the result the jet energy scale variations and missing transverse energy corrections are considered, both to the full and to half extend. This corresponds to the expectation that the uncertainties predicted for 10 pb^{-1} of data in the early phase can be reduced further by dedicated studies in later longtime running of the ATLAS detector.

In Tab.A.6 for the three best performing vetos a breakdown of the size of systematic uncertainties associated with JES rescaling and the missing energy correction is given. In case of signal the errors associated to the Herwig sample have been quoted as typical. Since the error of an upward scaling in the JES always leads to an increase of the expected number of background events B the errors inferred by the upward scaling are used. The reason for the increase may be that more events pass the transverse momentum cut in the VBF pre-selection. We observe roughly that a doubled JES systematics leads to a significance reduced by the factor two.

One identifies the three best performing vetos to be veto-4, veto-1, veto-3 in optimistic scenario for the systematic uncertainties and veto-1, veto-3, veto-4 for the more pessimistic 10 pb^{-1} scenario (see Tab.A.6). It is notable that though the ranking with these three best performing vetos is changing the second best veto reaches almost the performance of the best veto. For that reason, one can not give a clear recommendation but has at hand three more or less equally well performing vetos.

A slight tendency can be seen for recommending veto-1. Given that veto-1 represents the simplest approach to a central jet veto it performs surprisingly well. The veto-1 has the best performance in the optimistic scenario and is almost as good as the leading veto-4 in the pessimistic scenario but with the need to readjust the transverse momentum cut a little. It seems that the larger uncertainty in the JES prefers a hardening of the transverse momentum cut down to a value between 15 GeV and 20 GeV. A possibility to become independent of the size of expected uncertainties considered here is to chose a $p^T > 20$ GeV cut in both scenarios. Then the performance is deteriorated about 3 % with respect to the optimal choice, which is still agreable.

The working point of the best performing veto 4 in the pessimistic scenario is valid in the optimistic scenario too, which is clearly desirable, albeit it looses about 3 % to the best possible result in that case.

Though veto-3 uses a bit more of spatial information of the ΔR of the veto jets this yields compatible results within 3.5 % to the best but too needs a choice of the working point according to the size of the uncertainties. It may be that a gain by the use of such distinct spatial information in the veto is compensated by the averaging of deviating generator predictions in calculating the significance for the veto-4. In that sense the veto-4 can be an option as soon the generator models can be fixed to data at the LHC.

From what is said above we can confirm and recommend the use of veto-1 with the working point $p^T_{cut} > 20$ GeV and $|\eta_{cut}| < 3.2$, which is a good compromise between an effective discrimination of the difficult Z boson background and independence from the size of expected systematic influences.

A.8.3 The New Power Shower in Pythia and the Central Jet Veto

In Tab.A.7 we collect the best veto conditions of the various approaches for the case that the new power shower description in Pythia is physically valid. The discrimination between Pythia new power shower and background after (C 1) to (C 4) only, expressed as significance, is 0.62 for full size jet energy scale

Averaged Significance from Sherpa Herwig Pythia Old Parton Shower				
	VBF+$\not\!\!E_T > 70$ GeV cuts half JES uncert.		VBF+$\not\!\!E_T > 70$ GeV cuts full JES uncert.	
	$\mathscr{S}_{syst}$	veto cond.	$\mathscr{S}_{syst}$	veto cond.
veto-1	2.39	$p^T_{cut} > 20\,\text{GeV}\ \|\eta_{cut}\| < 3.2$	1.15	$p^T_{cut} > 15\,\text{GeV}\ \|\eta_{cut}\| < 3.2$
veto-2	2.04	$p^T_{cut} > 20\,\text{GeV}\ \|\eta\|^{min,max}_{cut} < \|\eta\|^{min,max}_{tag}$	1.01	$p^T_{cut} > 15\,\text{GeV}\|\eta\|^{min,max}_{cut} < \|\eta\|^{min,max}_{tag}$
veto-3	2.38	$p^T_{cut} > 20\,\text{GeV}\ \|\Delta R^{tag}_{cut}\| > 0.6$	1.12	$p^T_{cut} > 15\,\text{GeV}\ \|\Delta R^{tag}_{cut}\| > 0.1$
veto-4	2.32	$p^{\star T}_{cut} > 20\,\text{GeV}\ \|\Delta\Phi^{trans.}_{cut}\| > 0^\circ$	1.16	$p^{\star T}_{cut} > 20\,\text{GeV}\ \|\Delta\Phi^{trans.}_{cut}\| > 0$
veto-5	1.79	$p^T_{cut} > 15\,\text{GeV}\ \|\eta^\star_{cut}\| < 2.9$	0.87	$p^T_{cut} > 15\,\text{GeV}\ \|\eta^\star_{cut}\| < 2.9$
veto-6	1.92	p^T-Imbalance $> 5\,\text{GeV}$	0.96	p^T-Imbalance $> 20\,\text{GeV}$
veto-7	2.04	$p^T_{cut} > 20\,\text{GeV}$ Centrality> 0	1.01	$p^T_{cut} > 15\,\text{GeV}$ Centrality> 0

Tab. A.5: *Suggested best veto conditions for the various central jet vetos using the averaged prediction of the significance $\mathscr{S}$ from the different MC eventgenerators compared. The significance $\mathscr{S}$ is arithmetically averaged from Sherpa, Herwig and old Pythia parton shower signal samples at* $\text{M}_\text{H} = 130$ GeV. *We are considering the impact of two values for the JES on our F.O.M, the significance $\mathscr{S}_{syst}$ and give a list of the recommended veto conditions in terms of maximal significance, for both JES variations.*

Best Three Significances in the MC-generator Comparison							
		full size JES systematics					
$\mathscr{S}_{syst}$ in workpoint		ΔS_{syst}	DOWN	UP	ΔB_{syst}	DOWN	UP
veto-4	1.161		-6.1 %	3.3 %		-15.2 %	12.6 %
veto-1	1.154		-4.6 %	2.0 %		-14.6 %	13.1 %
veto-3	1.119		-4.5 %	1.9 %		-15.0 %	13.9 %
		half size JES systematics					
$\mathscr{S}_{syst}$ in workpoint		ΔS_{syst}	DOWN	UP	ΔB_{syst}	DOWN	UP
veto-1	2.392		-2.1 %	2.1 %		-6.5 %	5.8 %
veto-3	2.384		-2.0 %	2.0 %		-6.6 %	5.9 %
veto-4	2.318		-2.1 %	1.8 %		-7.1 %	6.2 %

Tab. A.6: The three best performing veto approaches found after cuts (C 1) to (C 4) in the MC generator comparison by looking for the maximal significance $\mathscr{S}_{syst}$, serving as F.O.M. $\mathscr{S}_{syst}$ is determined applying two values of an estimate of JES uncertainty. A breakdown of the size of systematic uncertainties on $\mathscr{S}_{syst}$ associated with up and down scaling of the JES and the appropriate missing energy corrections is given for the signal (ΔS_{syst}) in column 3 and 4 and for the background (ΔB_{syst}) in column 5 and 6. In case of signal the errors associated to the Herwig sample have been quoted as typical.

variation and 1.26 if the half size is taken (see Tab.A.4). We find that the discrimination can be approved with all veto approaches. The range of improvement is 8 % to 46 % in case of half-size systematics and 6 % to 37 % in case of full extent.

The work point of some vetos change significantly e.g. in the transverse momentum cut with respect to the combined generators optimisation which may justify the separate treatment. If not changing the work points of the vetos defined in Sec.A.8.2, the significance for the Pythia power shower sample is up to 6 % worse than in the case of re-adjusted work points. Therefore, it may be worthwhile to adjust a central jet veto to the new shower conditions.

As in the combined generators optimisation the three best performing vetos are veto-1, veto-3, veto-4 in the optimistic scenario and veto-1, veto-4, veto-3 in the pessimistic scenario, where the difference between veto-3 and veto-4 is marginal.

The most important veto-1 becomes favoured in both scenarios and again a littler lower transverse momentum cut in the pessimistic scenario with a larger JES variation is found. And as before it is possible to use in the pessimistic scenario a $p_{cut}^{T} > 20$ GeV cut which this time reduces the significance of only 1 %. For veto-4 we observe the stability of the work point under both JES variations and the work point of veto-3 is depending much on the JES variation size with respect to p_{cut}^{T} and not dramatically on ΔR_{cut}.

All in all these findings too encourage the general choices of the working point $p_{cut}^{T} > 20$ GeV and $|\eta_{cut}| < 3.2$, in veto-1.

Maximal Significance from Pythia with the New Power Shower				
	VBF+$\not{E}_T > 70$ GeV cuts half JES uncert.		VBF+$\not{E}_T > 70$ GeV cuts full JES uncert.	
	$\mathscr{S}_{syst}$	veto cond.	$\mathscr{S}_{syst}$	veto cond.
veto-1	1.84	$p_{cut}^{T} > 20\,\text{GeV}\ \|\eta_{cut}\| < 3.2$	0.86	$p_{cut}^{T} > 15\,\text{GeV}\ \|\eta_{cut}\| < 3.2$
veto-2	1.63	$p_{cut}^{T} > 30\,\text{GeV} \|\eta\|_{cut}^{min,max} < \|\eta\|_{tag}^{min,max}$	0.81	$p_{cut}^{T} > 30\,\text{GeV} \|\eta\|_{cut}^{min,max} < \|\eta\|_{tag}^{min,max}$
veto-3	1.79	$p_{cut}^{T} > 20\,\text{GeV}\ \|\Delta R_{cut}^{tag}\| > 0.6$	0.85	$p_{cut}^{T} > 30\,\text{GeV}\ \|\Delta R_{cut}^{tag}\| > 0.1$
veto-4	1.72	$p_{cut}^{\star T} > 20\,\text{GeV}\ \|\Delta\Phi_{cut}^{trans.}\| > 0^{\circ}$	0.85	$p_{cut}^{\star T} > 20\,\text{GeV}\ \|\Delta\Phi_{cut}^{trans.}\| > 0$
veto-5	1.36	$p_{cut}^{T} > 15\,\text{GeV}\ \|\eta_{cut}^{\star}\| < 2.9$	0.66	$p_{cut}^{T} > 15\,\text{GeV}\ \|\eta_{cut}^{\star}\| < 3.2$
veto-6	1.42	p^{T}-Imbalance $> 35\,\text{GeV}$	0.70	p^{T}-Imbalance $> 20\,\text{GeV}$
veto-7	1.63	$p_{cut}^{T} > 30\,\text{GeV}$ Centrality> 0	0.81	$p_{cut}^{T} > 30\,\text{GeV}$ Centrality> 0

Tab. A.7: *The recommended veto conditions in terms of maximal significance $\mathscr{S}_{syst}$ including systematic uncertainties for the various jet veto approaches applied to the Pythia with new Power Shower sample alone, after cuts (C 1) to (C 4). We are considering the impact of two values for the JES on our F.O.M, the significance $\mathscr{S}_{syst}$.*

A.8.4 Effects on a Jet Veto Strategy from Residual Uncertainties in the Underlying Event Tune of Monte Carlo Generators

In Sec. A.7.1 and A.7.2 one can notice that the different underlying event tunes can be grouped in three classes. Firstly the samples of low underlying event activity like $Q_{cut}+30\%$ and MRST2004NLO, secondly of moderate activity like ATLAS default and TeVatron fixed tune and thirdly enhanced activity with the $Q_{cut}-30\%$ sample. In a rough estimate one can think of the spread in the predictions amongst these samples as a residual uncertainty or mistuning after tuning a model to first data. We are interested in the size of effects and whether the choice of the veto conditions would be dramatically different. Therefor, we repeat the search for an optimal choice in the veto approaches (see Tab.A.8).

The significances are now averaged using all Sherpa signal samples so their values and the optimal work points found are expected to be different from the combined generator study. Interestingly, while the work points of the half JES variation change only a little, the full JES variation yields larger deviating work points. A closer look shows that the yielded optimal averaged significances are missed at most of 1-2 % and even only in a few cases, if the optimal working points are replaced by the ones found in the combined generator study. This hints to a more or less incidential choice of the deviating workpoint driven by small statistical fluctuations in the underlying events comparison.

The ranking of the three best performing vetos is veto-1, veto-3, veto-4 in the optimistic scenario and veto-1, veto-4, veto-3 in the pessimistic scenario. This is consistent with the earlier result in the combined generator study. The work point in veto-4 again is unchanged despite of the change in the JES variation, while for veto-3 a larger variation of the JES leads to an earlier rejection of jets with $p^T_{cut} > 15$ GeV. In both scenarios the veto-1 is favoured. While in the optimistic scenario of a half extend JES variation yields the same work point as in A.8.2 we see a very different pseudorapidity cut in the full JES variation case. This may be due to the influence of the $Q_{cut}-30\%$ sample. This is the only sample in the collection whose overall jet activity is enhanced in the central region too. It seems that low energy jets in this region can trigger the veto if the JES uncertainty is taken into account. As it is desirable to choose the work point independently from the size of the JES variation, we check that a cut condition $p^T_{cut} > 20$ GeV and $|\eta_{cut}| < 3.2$ in the pessimistic scenario would result in a loss of 5 %.

Since the differences in work point choice and averaged significances are not significant we conclude that optimal choice for a central jet veto covers as given in A.8.2, will cover safely all effects of a residual mistune of the underlying event.

A.9 Estimate of Pile-up Influences

The cross-section for inelastic, non-diffractive pp interactions at the LHC is expected to be around 67 mb [88]. At design luminosity ($\mathscr{L} = 10^{34} cm^{-2} s^{-1}$), the average number of minimum-bias events is 23 per bunch crossing, varying according to a Poissonian distribution. Any collision recorded in the ATLAS detector therefore contains a superposition of particles coming from several events. In general the particles from a single "interesting physics" event will have triggered the readout, and additional particles will come from other uninteresting pp collisions. It is believed that the pile up may become the main obstacle in applying an effective central jet veto since if not recognised jets from pile up events may trigger an applied central jet veto even in case of a signal event. Therefore, the performance of a central jet veto gets worse in case of pile up. It has to be considered whether it remains useful to apply the veto under high luminosity pile up conditions.

To get a rough estimate about the size of deterioration we apply the different jet veto approaches to a signal sample with pile up. Only the Herwig sample DS5335 is available with sufficient statistics for this cross check. It has to be emphasised that the simulated pile up is corresponding to the very low instantaneous luminosity of $\mathscr{L} = 1 \times 10^{33} cm^{-2} s^{-1}$ where $\lesssim 3$ minimal bias events are expected.

This extra events are immediately seen in an increase of the lower transverse momentum jet activity

Averaged Significance from Sherpa Underlying Event Tunes				
	VBF+$\not\!\!E_T > 70$ GeV cuts half JES uncert.		VBF+$\not\!\!E_T > 70$ GeV cuts full JES uncert.	
	$\mathscr{S}_{syst}$	veto cond.	$\mathscr{S}_{syst}$	veto cond.
veto-1	2.25	$p_{cut}^T > 20\,\text{GeV}\ \|\eta_{cut}\| < 3.2$	1.12	$p_{cut}^T > 15\,\text{GeV}\ \|\eta_{cut}\| < 2.6$
veto-2	1.95	$p_{cut}^T > 20\,\text{GeV} \|\eta\|_{cut}^{min,max} < 0.85 \|\eta\|_{tag}^{min,max}$	0.98	$p_{cut}^T > 15\,\text{GeV} \|\eta\|_{cut}^{min,max} < 0.75 \|\eta\|_{tag}^{min,max}$
veto-3	2.23	$p_{cut}^T > 20\,\text{GeV}\ \|\Delta R_{cut}^{tag}\| > 0.6$	1.05	$p_{cut}^T > 15\,\text{GeV}\ \|\Delta R_{cut}^{tag}\| > 0.6$
veto-4	2.19	$p_{cut}^{\star T} > 20\,\text{GeV}\ \|\Delta\Phi_{cut}^{trans.}\| > 0^\circ$	1.10	$p_{cut}^{\star T} > 20\,\text{GeV}\ \|\Delta\Phi_{cut}^{trans.}\| > 0$
veto-5	1.73	$p_{cut}^T > 15\,\text{GeV}\ \|\eta_{cut}^\star\| < 2.3$	0.85	$p_{cut}^T > 15\,\text{GeV}\ \|\eta_{cut}^\star\| < 2.3$
veto-6	1.87	p^T-Imbalance $> 5\,\text{GeV}$	0.91	p^T-Imbalance $> 5\,\text{GeV}$
veto-7	1.95	$p_{cut}^T > 20\,\text{GeV}$ Centrality> 0	0.97	$p_{cut}^T > 15\,\text{GeV}$ Centrality> 0

Tab. A.8: *Suggested best veto conditions for the various central jet vetos using the averaged prediction of the significance $\mathscr{S}$ from the Sherpa underlying event tune. The significance $\mathscr{S}$ is arithmetically averaged from all Sherpa signal samples at* $M_H = 130$ GeV. *We are considering the impact of two values for the JES on our F.O.M, the significance $\mathscr{S}_{syst}$ and give a list of the recommended veto conditions in terms of maximal significance, for both JES variations. The results of the optimal working point vary only slightly.*

Best Three Significances from Sherpa Underlying Event Tunes							
		full size JES systematics					
$\mathscr{S}_{syst}$	in workpoint	ΔS_{syst}	DOWN	UP	ΔB_{syst}	DOWN	UP
veto-1	1.12		-6.4 %	4.1 %		-14.4 %	12.6 %
veto-4	1.10		-6.8 %	4.2 %		-15.2 %	12.6 %
veto-3	1.05		-6.6 %	4.3 %		-15.0 %	13.9 %
		half size JES systematics					
$\mathscr{S}_{syst}$	in workpoint	ΔS_{syst}	DOWN	UP	ΔB_{syst}	DOWN	UP
veto-1	2.25		-2.7 %	1.6 %		-6.5 %	5.8 %
veto-3	2.23		-2.7 %	1.7 %		-6.6 %	5.9 %
veto-4	2.19		-3.1 %	2.0 %		-7.1 %	6.2 %

Tab. A.9: The three best performing veto approaches found after cuts (C 1) to (C 4) in the Sherpa UE tuning comparison by looking for the maximal significance $\mathscr{S}_{syst}$, serving as F.O.M. $\mathscr{S}_{syst}$ is determined applying two values of an estimate of JES uncertainty. A breakdown of the size of systematic uncertainties on $\mathscr{S}_{syst}$ associated with up and down scaling of the JES and the appropriate missing energy corrections is given for the signal (ΔS_{syst}) in column 3 and 4 and for the background (ΔB_{syst}) in column 5 and 6. In case of signal the errors associated to the TeVatron tune of Sherpa sample have been quoted as typical.

with a $p^T \lesssim 35$ GeV (see Fig.A.28). These jets often are the third and fourth hardest jets after the leading jets and are observed to fill the central pseudorapidity gap completely in a way that the Herwig sample with very low luminosity pile up mimics the Pythia 6.4 sample with no pile up but the new power shower. Though it should be mentioned that the significances for the "Power Shower" scenario yielded with the vetos are even about 17 % worse compared to significances found with the Herwig pile up sample. This is another prove how large the additional jet activity in the power phower scenario becomes in contrast to the other models.

In Tab.A.10 the search for a good veto working point using the Herwig $\mathscr{L} = 1 \times 10^{33}\, cm^{-2}\, s^{-1}$ sample is summarised. Again it proves that the veto-1, veto-3, veto-4 remain the best performing. In case of pile-up activity the veto 1 can be operated at the same working point as before, $p^T_{cut} > 20$ GeV and $|\eta_{cut}| < 3.2$, in both scenarios and will yield good results. The result for a Herwig sample without pile up would be 24 % better than for the pile-up sample. Again with the same veto condition as in all other checks before veto-4 can operated with a compatible result. For veto-6 we note that it becomes most sensitive to the extra jets in pile-up and needs to be operated at significantly higher jet momentum imbalance in the event cut as without pile up.

One should keep in mind that because the extra jets are also subject to the detector uncertainties the situation becomes worse if the uncertainties are enlarged. The direct comparison of the Herwig sample with and without pile up is resulting in a loss in sensitivity in case of pile-up of typically 22 % to 35 % for half and 26 % to 41 % for full size of uncertainties respectively using the same working points as defined in A.8.2.

As a result one observes a general deterioration in the figure of merit of best veto conditions (see Tab.A.10) compared to samples without pile-up. But more important the central jet veto still improves the significance with respect to the preselection. The situation should be even worse for the nominal low luminosity $\mathscr{L} = 2 \times 10^{33}\, cm^{-2}\, s^{-1}$ where $\lesssim 5$ minimal bias events are expected.

A counter measure that immediately comes to ones mind may be to harden the transverse momentum cut on central veto jet candidates. But within the Atlas Collaboration many more refined efforts have been started to use information about the displaced vertices of tracks from jets reconstructed with respect to those from the hard physics event. Those tracks can be treated special or be rejected in jet reconstruction or other characteristics may be applied to identify the pile up contribution [108, 135, 137]. The preliminary results look very promising so that it can be possible to recover a large fraction of the deterioration in the central jet veto efficiency through pile up. It can therefor be assumed that the best veto found without pile up will remain compatible even under severe pile up conditions.

Maximal significance $\mathscr{S}$ from Herwig at $\mathscr{L} = 1 \times 10^{33}\, cm^{-2}\, s^{-1}$				
	VBF+$\not{E}_T > 70$ GeV cuts half JES uncert.		VBF+$\not{E}_T > 70$ GeV cuts full JES uncert.	
	$\mathscr{S}_{syst}$	veto cond.	$\mathscr{S}_{syst}$	veto cond.
veto-1	2.18	$p^T_{cut} > 20\,\text{GeV}\ \|\eta_{cut}\| < 3.2$	1.02	$p^T_{cut} > 20\,\text{GeV}\ \|\eta_{cut}\| < 3.2$
veto-2	1.88	$p^T_{cut} > 20\,\text{GeV}\ \|\eta\|^{min,max}_{cut} < \|\eta\|^{min,max}_{tag}$	0.93	$p^T_{cut} > 30\,\text{GeV}\|\eta\|^{min,max}_{cut} < \|\eta\|^{min,max}_{tag}$
veto-3	2.17	$p^T_{cut} > 20\,\text{GeV}\ \|\Delta R^{tag}_{cut}\| > 0.6$	1.02	$p^T_{cut} > 25\,\text{GeV}\ \|\Delta R^{tag}_{cut}\| > 0.1$
veto-4	2.09	$p^{\star T}_{cut} > 20\,\text{GeV}\ \|\Delta\Phi^{trans.}_{cut}\| > 0^\circ$	1.03	$p^{\star T}_{cut} > 20\,\text{GeV}\ \|\Delta\Phi^{trans.}_{cut}\| > 0$
veto-5	1.55	$p^T_{cut} > 20\,\text{GeV}\ \|\eta^\star_{cut}\| < 2.3$	0.74	$p^T_{cut} > 20\,\text{GeV}\ \|\eta^\star_{cut}\| < 2.9$
veto-6	1.57	p^T-Imbalance $> 35\,\text{GeV}$	0.81	p^T-Imbalance $> 20\,\text{GeV}$
veto-7	1.88	$p^T_{cut} > 20\,\text{GeV}$ Centrality> 0	0.93	$p^T_{cut} > 30\,\text{GeV}$ Centrality> 0

Tab. A.10: *We apply all central jet veto approaches to the Herwig pile-up sample alone. We are considering the impact of two values for the JES on our F.O.M, the significance $\mathscr{S}_{syst}$ and give a list of the recommended veto conditions in terms of maximal significance, for both JES variations.*

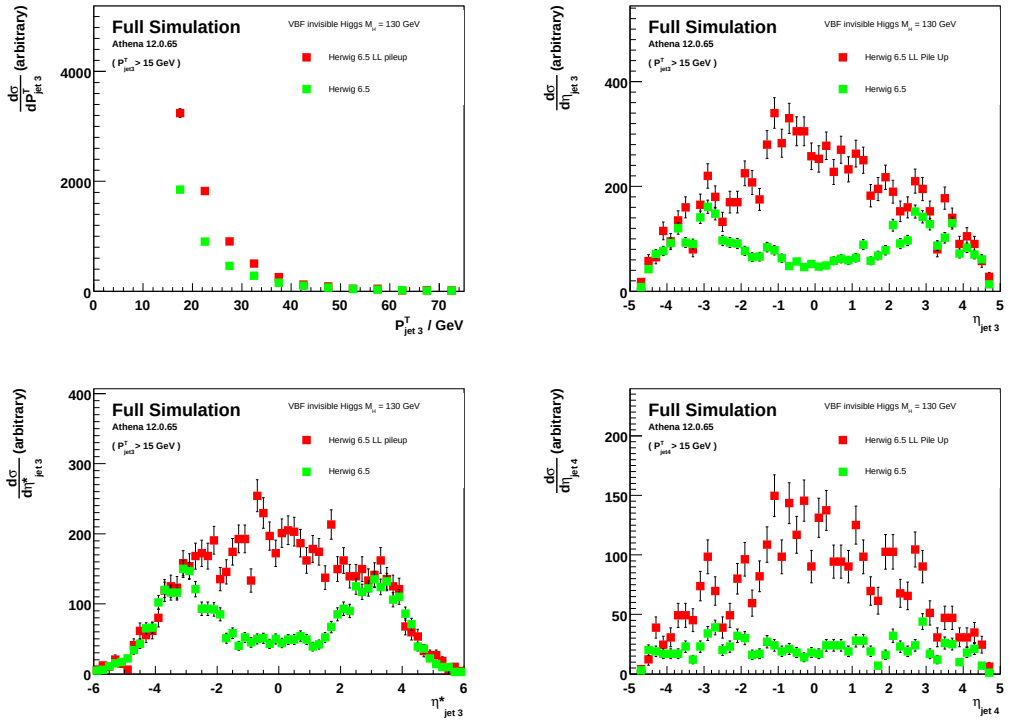

Fig. A.28: *Comparison of the* 3^{rd} *and* 4^{th} *hardest jet in the Herwig sample with* $\mathscr{L} = 0$ *(no pile-up green) and* $\mathscr{L} = 1 \times 10^{33}\, cm^{-2}\, s^{-1}$ *(with pile-upred).*

A.10 Conclusion

In this study we investigated the predictions of various Monte Carlo generator models for the next hardest jets to the tagging jets in the channel of weak boson fusion Higgs boson production with invisible Higgs decay. The observed differences depend strongly on the generator's shower model.

Using ATLAS full detector simulation we devised optimal working points for seven central jet veto approaches in a combined generator comparison. We regarded as main source of detector systematic uncertainties jet energy scale variations and missing energy resolution. Since the size of the JES variation has to be determined we considered a pessimistic scenario where the expected uncertainties are given for 10 pb^{-1} and a more optimistic scenario expecting that the size of the uncertainty can be reduced to half of the initial expectation. We observed a dependence of the work point from the size of the JES variation. This may be explained that above a certain uncertainty in the JES, low energy jets are more and more relevant to the central jet veto conditions.

Three vetos labelled as veto-1, veto-3, veto-4 in SecA.4 perform best in all scenarios. We devise the simplest veto-1 to be operated at $p^T_{cut} > 20$ GeV and $|\eta_{cut}| < 3.2$ with only slight losses to the best possible results. Its advantage is that it is also working with the more active power shower in the newest Pythia versions sufficiently well. In this way we confirm the commonly used veto strategy in ATLAS. It is notable that the veto-4 has only one work point, $p^{\star T}_{cut} > 20$ GeV and $|\Delta\Phi^{trans.}_{cut}| > 0^\circ$, that is valid in all cross checks so seen to exhibit some robustness if one is willing to tolerate a slightly suboptimal performance in some scenarios compared to veto-1.

Only a large mistune of the Q_{cut} scale in Sherpa 1.0.11 of much more than 5 % leads to a notable change in the jet's radiation and the effects of a residual mistune in the underlying event are very small concerning a central jet veto.

At last we compare the vetos under pile up corresponding to a very low instantaneous luminosity of $\mathscr{L} = 1 \times 10^{33} cm^{-2} s^{-1}$. The result is that at the best working point the performance can be reduced in the worst case to 46 % under pile-up influence. The recommended work point veto-1 is proved to be less affected by the pile-up with a deterioration of significance about 24 %. Nevertheless it must be emphasized that the veto still improves the signal-background discrimination. So it was concluded that ongoing and future efforts to identify jets from pile-up events will crucially improve the effectiveness of applying central jet vetos.

A.10.1 Comparison to Former Studies

At this point we shortly want to compare our findings to the result of the complementary study described in [134]. This study focused on a very different final state, namely weak boson fusion $H \rightarrow \tau^+\tau^- \rightarrow l^+l^- + 4\nu$. It uses huge fast simulation samples of the signal done in Herwig, Pythia Old/New and Sherpa and regards as backgrounds only the QCD contributions from $Z \rightarrow \tau^+\tau^- \rightarrow l^+l^- + 4\nu$ and a $t\bar{t}$ dilepton sample. It seeks for an optimisation in the standard veto of type 1 and the "in-between-tagging-jet" veto like type 2 in Sec.A.4. The study observes large differences in the veto efficiencies stemming from the uses of different generators and consequently uses a figure of merit that tries to minimise this spread in the efficiencies and simultaneously yields good background discrimination measured, with the expected number of signal (S) and background (B), by $S/\sqrt{B}$ after the complete analysis cutflow.

One main conclusion in [134] is that an analysis of a Pythia with new power shower sample leaving out the central jet veto yields a better significance than one derived with a veto. In disregarding the Pythia New sample for optimisation this study recommends an optimal working point for a type 1 veto p^T_{cut} (the lowest studied value) and a very narrow pseudorapidity region around the centre with $|\eta_{cut}| < 1.6$.

In a direct comparison with the veto type recommended, we see that our result $p^T_{cut} > 20$ GeV and $|\eta_{cut}| < 3.2$ differs from the former result. Possible explanations are: We aim for a realistic study in fully detailed detector simulation including expected systematic uncertainties in the jet energy reconstruction. Also we want to disentangle as most as possible the generator description effects at the stage of the jet veto. Therefore, we apply the jet veto as last criteria after a loose preselection. This is also necessary because we are very limited in the statistics of our fully simulated events compared with [134]. We choose our background according to the fact that it may be very difficult to reject by a central jet veto when parton shower and underlying event are badly understood and do not regard the same backgrounds as in [134].

All this may contribute to different findings but most of all we use a very different definition of the figure of merit. In contrast to [134] we do not seek for a minimisation of veto efficiency differences. Since efficiency differences can be subject to fluctuations in statistical limited samples and may lead to instabilities in the optimisation. Also the efficiencies are indirectly contained in the number of signal events entering the figure of merit. The included expected detector uncertainties contribute directly to our figure of merit. Our figure of merit prefers work points where the difference in selected background events becomes small, since the uncertainty on the background rate enters quadratically, not work point where the differences in the selected signal rate becomes small. In this we suspect the main reason for the differences in the recommendation of this study and in [134].

B. Details on the choice of a suitable multivariate classifier

As the principle decision had been made to use a multivariate analysis instead of a cut based analysis, the question arose what could be the classifier of choice. In the following we want to sketch the ample study undergone to find a suitable classifier.

This study was complicated by the fact that simultaneously the following questions had to be answered:

1) Which classifier is best when the signal is depending on mass and width? To access that point, four masses from light to heavy Higgs and widths, from very small, over medium to a large width of 300 GeV were compared simultaneously. In fact this was the main complication since every partial result had to be verified to be true for all of these signal hypotheses.

2) Which minimal set of inputs has best sensitivity towards a signal depending on mass and width? Each classifier regarded was trained several times with subsets of variables according to their importance. Less important variables had to be identified and excluded from the sets. The results were compared not only between classifiers but also for hypotheses as stated in cypher 1.

3) Which classifier is best if the preselection cut on $E_{\mathrm{T}}^{\mathrm{miss}}$ of 70 GeV and 100 GeV are compared ? This meant the results of cypher 1 and cypher 2 were compared on samples with two different $E_{\mathrm{T}}^{\mathrm{miss}}$ precuts additionally.

4) Which classifier is best if, for a Higgs mass of 130 GeV and only a small width, Sherpa and Herwig and Pythia MC generators are compared ? This was relatively straight-forward to answer since it included only one Higgs mass and was compared only for one type of chosen classifier.

B.1 TMVA toolkit

An easy to use and extremely versatile tool to perform a multivariate analysis is the toolkit for multivariate analysis TMVA [101]. This program is permanently expanded and provides a large variety of multivariate methods. These methods differ in the degree of complexity and the kinds of problems they can deal best with. Another aspect is that some classifiers need very much CPU time or need many events to model the correlation function between the variables correctly and find an optimal discrimination boundary in the higher dimension parameter space of the problem.

Several classifiers were tested, we focused on those that were formally known to be used in particle physics as Fisher's discriminant, likelihoods, neural networks and boosted decision trees. Besides of those we also regarded some more exotic classifiers and probability density estimators like k-nearest neighbours and the selection according to an ensemble of rules provided by the RuleFit algorithm. A short description of all classifiers and references are given in the TMVA manual [101]. Classifiers that took very long in preliminary tests or applied specific decorrelation algorithms to the data were not considered for practical purposes, like the wish for fast and as much as possible simple algorithms.

B.1.1 Evaluation of classifier performance

In the comparison of classifiers and in reducing the number of input variables one needs a measure of performance, in order to quantify the gain or trade off. There are several ways to judge the performance of a classifier.

Figure of merit

First one can perform a cut on the output distribution of the classifier optimising a figure of merit (F.O.M.). We chose a F.O.M that gives a frequentist definition of sensitivity of a search for new phenomena introduced in [127]. It is particularly suitable for optimisation, being independent of a-priori expectations about the presence of a signal. Thus maximising the F.O.M. allows for the determination of an output cut that is optimal both for setting limits and for making a discovery. The simple approximate formula used is given by

$$\text{F.O.M.}^{\text{Punzi}} = \frac{\varepsilon_S(t)}{\frac{a}{2} + \sqrt{B(t)}}. \tag{B.1}$$

In the formula above $B(t)$ is the expected background at the 'working point' t. In searches for unknown signals one uses the signal efficiency $\varepsilon_S(t)$ at the workpoint rather than an expectation of specific signal rate. One has to chose for a the (double or single sided) quantile of sigma corresponding to the aimed discovery or exclusion confidence level. In our case we choose the single-sided quantile corresponding to a 95 % CL.

With the F.O.M one compares the classifier at a single optimal working point, i.e. the cut on the output distribution. This cut is found by scanning the background and signal efficiencies. If the cut becomes too hard the statistical fluctuation will lead to unreliable comparisons. Therefore we introduced the condition that the background should not be reduced to less than 10% in the working point.

An alternative way to evaluate the performance, described in the next paragraph, is not restricted to one cut or working point t, but compares the whole range of possible cuts on the output of a classifier, and is therefore more robust in case of low statistics.

Receiver operation characteristics

The receiver operation characteristics (ROC) is used as a measure of sensitivity in signal detection theory. For a binary classifier system the ROC curve gives the true positive rate, vs. false positive rate as its discrimination threshold is varied. If a ROC curve is plotted in terms used by particle physicist it translates into the purity vs. efficiency or rejection vs. efficiency curves. All definitions have in common that the area under the ROC curve should ideally be maximal for the best classifier.

In order to find the better classifiers we used both criteria, F.O.M and ROC.

Training samples for the choice of the classifier

In order to have large enough samples for training, testing and evaluation of the classifiers, ATLFAST-1 samples are used. The signal samples are summarised in Tab. B.1. The choices of the inspected mass and decay width combinations account for light (130 GeV), intermediate (200 GeV and 500 GeV) and heavy (800 GeV) Higgs boson masses. The width of the light Higgs is varied from MeV to 300 GeV. The signal is normalised to the SM cross section of the Higgs pole mass even when the width changes largely. By using the same normalisation for the several widths, it is hoped to compare and identify directly possible effects of the width changes in the training phase.

For example the 130 GeV samples are normalised with the LO weak boson fusion cross section at $\sqrt{s} = 14$ TeV to $\sigma_{LO} = 3.93pb$. If the performance in the classifiers changes for the various Sherpa 130 GeV samples, this might be attributed to the width differences.

The other decision made before designing the multivariate analysis was to optimise the separation against W and Z bosons backgrounds. For this reason the corresponding ATLFAST-1 samples listed in Tab. 4.1 were used as background samples in the training.

Generator	M_H (GeV)	Γ_H(GeV)	nom. σ(pb)	ATLFAST-1 events
Sherpa	130	0.005	3.93	2×10^6
Sherpa	130	10	3.93	2×10^6
Sherpa	130	50	3.93	2×10^6
Sherpa	130	100	3.93	2×10^6
Sherpa	130	200	3.93	2×10^6
Sherpa	130	300	3.93	2×10^6
Sherpa	200	1.4	2.41	2×10^6
Sherpa	500	67	0.545	2×10^6
Sherpa	800	307	0.188	2×10^6
Herwig	130	0.005	3.93	2×10^6
Pythia	130	0.005	3.93	2×10^6

Tab. B.1: Signal samples used in the comparison of classifiers. These large samples used only fast detector simulation.

Remark on shape differences in the E_T^{miss} spectra of various signals

The very initial plan for this study was to consider differences in the shape between the E_T^{miss} spectra of the various hypotheses. Since the amount of missing energy from the invisible Higgs decay and therefore, also of its transverse component E_T^{miss} in the event could be correlated to the width properties and yield characteristic shape differences in the spectrum. But two facts rendered this plan unfeasible.

First the shape differences in E_T^{miss} predicted by the MC generator were not very large and characteristic. We therefore, present in Fig. B.1 for various hypotheses with Higgs masses between 130 GeV and 800 GeV and largely varying widths up to about 300 GeV the E_T^{miss} distribution before cut, just to get an impression of the size of the shape differences. The signals are generated with Sherpa and the ATLFAST-1 detector simulation is used. We emphasise that ATLFAST-1 samples contain no fake E_T^{miss} by construction and the E_T^{miss} calculation in ATLFAST-1 is based on the smeared truth particle energy entries in the calorimeter cells (see Section 3.3.6).

The shape differences exhibited in Fig. B.1 for the various samples are very small. Yet, heavier and broader invisible Higgs decays tend to have higher tails to larger E_T^{miss} values. Also if the Higgs becomes very heavy it is more likely to be produced almost a rest and the transverse momentum is limited in such cases.

In fact during the optimisation of the multivariate analysis we tried amongst many others variables as the missing transverse momentum or its direction in $\Delta\Phi$ to the tagging jets. But the E_T^{miss} was soon disregarded from the pool of promising variables and also the direction variables constructed with E_T^{miss} were not exhibiting any particular advantage in discrimination power compared to the variables finally

chosen (see B.1.4). This may contradicts the naïve expectations, but presumably the correlations between the finally regarded inputs variables already carried most of the exploitable information of the invisible Higgs final state for the use in the MLP within their correlations.

Secondly the reconstruction of the $E_{\mathrm{T}}^{\mathrm{miss}}$ and the refinement of its resolution is improving rapidly with beginning of the ATLAS data taking. Further it is expected that pile up and backgrounds with fake $E_{\mathrm{T}}^{\mathrm{miss}}$ distort the $E_{\mathrm{T}}^{\mathrm{miss}}$ spectrum. The sources of fake $E_{\mathrm{T}}^{\mathrm{miss}}$ in the detector which are spoiling the $E_{\mathrm{T}}^{\mathrm{miss}}$ resolution are currently under study.

Also a precise treatment of pile up and the estimate of systematic uncertainties for the $E_{\mathrm{T}}^{\mathrm{miss}}$ measurements are developed for the first time with beginning data taking by the ATLAS collaboration. Without these efforts finished, a realistic estimate of the sensitivity of ATLAS towards the stealthy Higgs scenario using $E_{\mathrm{T}}^{\mathrm{miss}}$ and related variables shape information is very hard to perform. Therefore, we restricted the use of $E_{\mathrm{T}}^{\mathrm{miss}}$ to the necessary cut in the preselection for identifying invisible Higgs decays. As described in the following we tested our optimisation for two different cuts on $E_{\mathrm{T}}^{\mathrm{miss}}$ whether the optimal classifier and variable sets change or not.

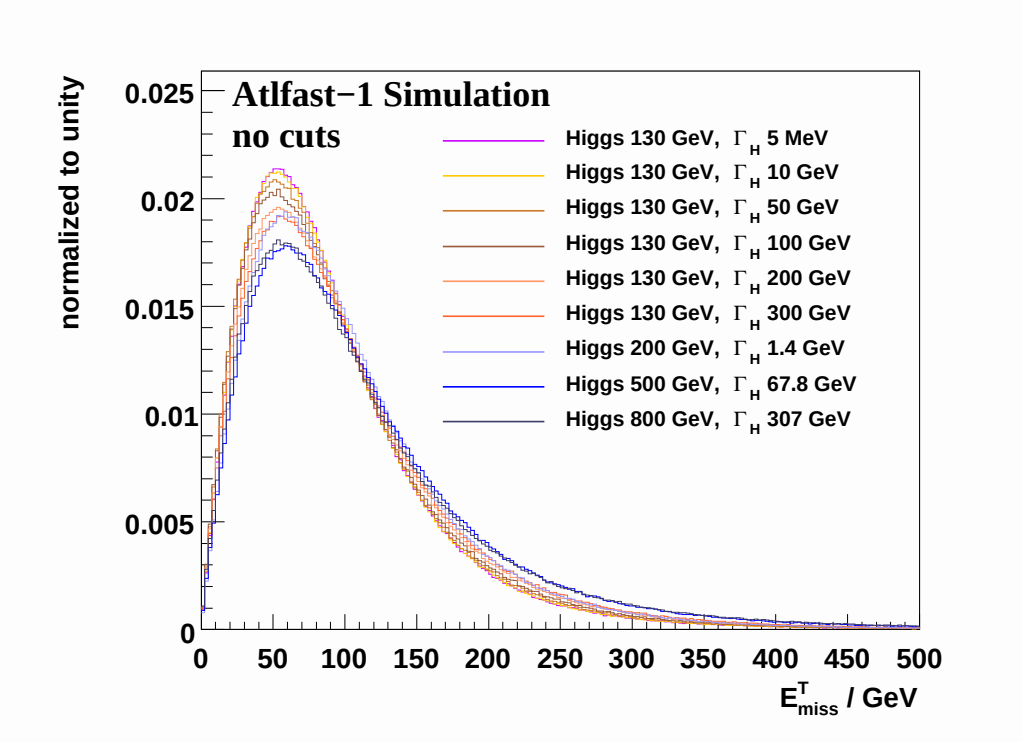

Fig. B.1: *Distribution of the transverse missing energy without cuts in the Sherpa ATLFAST-1 samples used for the classifier choice. These signal samples represent hypotheses with Higgs masses between 130 GeV and 800 GeV and largely varying widths up to about 300 GeV.*

B.1.2 List of promising input variables

After a preselection, very similar to the one used finally in the analysis, several variable distributions were judged by eye, whether difference in shape between several typical signal distributions and the W and Z boson plus jets background are exhibited.

In total 67 variables were constructed and judged. In the building of the variables we not only used combinations of $E_{\mathrm{T}}^{\mathrm{miss}}$ and tagging jets kinematic variables, but also included third and fourth hardest

jet variables and looked a topological information as all kinds of differences between variables in phase space e.g. $\Delta\eta$, $\Delta\Phi$ or ΔR. Some variables were evaluated in lab or rest frame.

For a signal hypothesis two parameters may have influence on the variable distributions, i.e. mass and decay width. But there was no strong dependence seen on the width of the signal.

Also only a few variables showed really strong shape differences between signal and background, most variables displayed more subtle differences. We will not give a complete list of all constructed variables here, but focus in the following on the few more promising variables that were identified in the shape comparison between signal and background distributions.

In total 14 variables have been identified as possibly valuable input variables, and are listed below. The majority of variables (1-7) are build by quantities of the tagging candidates. Two variables (8-9) include direction information of the $E_{\mathrm{T}}^{\mathrm{miss}}$ to the tagging jets. And a last group of variables (10-14) are calculated from the properties of a third leading jet with a $p_{\mathrm{T}} > 15$ GeV, if found in an event, and its direction to the tagging jets.

Some are of course highly correlated and the lesser performing are likely to be expelled in the next steps.

1) M_{j1j2}
   is the invariant mass calculated of the tagging jet candidates.

2) $\Delta\Phi_{\mathrm{j1j2}}$
   is the azimuthal angle between the tagging jet candidates.

3) $\Delta\eta_{\mathrm{j1j2}}$
   is the pseudorapidity gap between the tagging jet candidates.

4) $\eta_{\mathrm{j1}} \times \eta_{\mathrm{j2}}$
   is the product of the tagging jet candidates pseudorapidities.

5) $p_{\mathrm{j1}}^{\mathrm{T}}$
   is the transverse momentum of the leading tagging jet candidate.

6) $p_{\mathrm{j2}}^{\mathrm{T}}$
   is the transverse momentum of the subleading tagging jet candidate.

7) η_{j1}
   is the pseudorapidity of the leading tagging jet candidate.

8) $\Delta\Phi(p_{\mathrm{j1}}^{\mathrm{T}}, \vec{E}_{\mathrm{miss}}^{\mathrm{T}})$
   is azimuthal difference between the transverse momentum of the leading tagging jet candidate and the direction of $E_{\mathrm{T}}^{\mathrm{miss}}$.

9) $\Delta\Phi(p_{\mathrm{j2}}^{\mathrm{T}}, \vec{E}_{\mathrm{miss}}^{\mathrm{T}})$
   is azimuthal difference between the transverse momentum of the subleading tagging jet candidate and the direction of $E_{\mathrm{T}}^{\mathrm{miss}}$.

10) $min(\Delta R_{\mathrm{tag,j3}})$
    is the minimal distance $\Delta R = \sqrt{(\eta_{\mathrm{tag}} - \eta_{\mathrm{tag,j3}})^2 - (\phi_{\mathrm{tag}} - \phi_{\mathrm{tag,j3}})^2}$ to one of the tagging jet candidates. For the third jets is required $p_{\mathrm{T}} > 15$ GeV.

11) $\Delta\Phi_{\mathrm{j1j3}}$
    is azimuthal difference between a third jet the leading tagging jet. For the third jets is required $p_{\mathrm{T}} > 15$ GeV.

12) $\Delta\Phi_{\mathrm{j2j3}}$
is azimuthal difference between a third jet the subleading tagging jet. For the third jets is required $p_{\mathrm{T}} > 15$ GeV.

13) $\eta^{\star}_{\mathrm{j3}}$
is the Zeppenfeld variable [30] for a third jet $\eta^{\star}_3 = \eta_3 - \frac{1}{2}(\eta_1 + \eta_2)$. The emission pattern of a potential third jet differs for the signal with a lack of colour exchange in the weak boson fusion for the background processes with colour exchange.

14) $\Delta\Phi(j_3, (j_1 j_2)_{\mathrm{restframe}})$
The two tagging jets $(j_1 j_2)$ are boosted back into their rest frame. The azimuthal angle of a third jet j_3 to this axis of the dijet system is evaluated in that frame. For the third jets is required $p_{\mathrm{T}} > 15$ GeV.

In Fig. B.3-B.16 the distributions of these 14 variables in the ATLFAST-1 samples used in the classifier study are presented. The distributions shown are after an early version of preselection cuts similar to the final preselection. Main difference is a low tagging jet cut $p_{\mathrm{T}} > 20$ GeV and a reduced $E_{\mathrm{T}}^{\mathrm{miss}} > 100$ GeV cut. Additionally it was checked that a lowered cut on $E_{\mathrm{T}}^{\mathrm{miss}} > 70$ GeV in the event would not change the evaluation of the usefulness of the variable.

All variables are presented in the following way. In the left panel the comparison of the signal hypotheses tabulated in Tab. B.1 is presented. To improve the visibility of the legend we first present in Fig. B.2 only the legends that are always the same in all distributions in Fig. B.3-B.16.

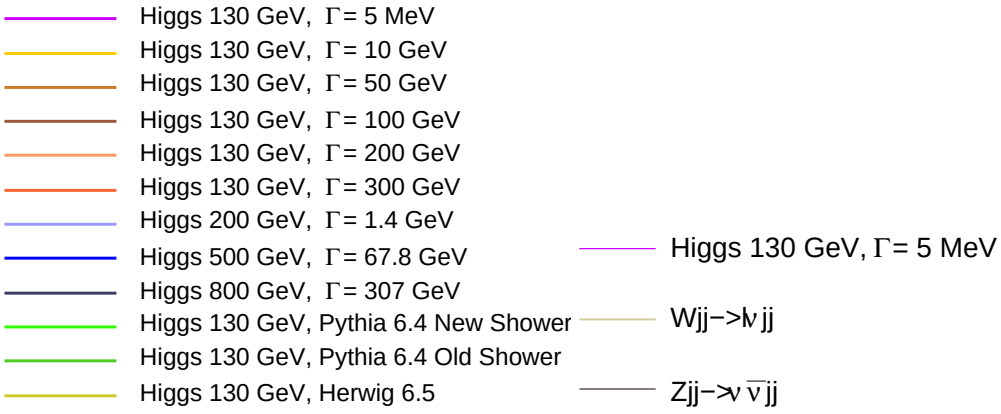

Fig. B.2: *Left panel: Legend applicable for a comparison of several signal hypotheses distributions after preselection. Right panel: Legend applicable for a comparison between shape of signal and W and Z bosons backgrounds after preselection.*

In case of the signal distributions, three features can be compared. The first feature is the width influence at the examples of a $\mathrm{M_H} = 130$ GeV signal and varied invisible width from no extra width to very large. These correspond to the magenta (no extra width) and orange to red shaded histograms. The second feature is the influence of the Higgs mass comparing $\mathrm{M_H} = 130$ GeV with $\mathrm{M_H} = 200$ GeV up to $\mathrm{M_H} = 800$ GeV . These histograms are denoted with shades of the colour blue, the heavier the darker. Lastly the third feature is the comparison between Sherpa, Herwig and Pythia's old and new shower model for $\mathrm{M_H} = 130$ GeV , corresponding to green shaded histograms. In the right panel the W and Z boson background are given as green/brown histograms. As reference and guideline for the eye to compare shape of background and the signal, the signal of the first row in Tab. B.1 appears also as violet histogram in the right penal.

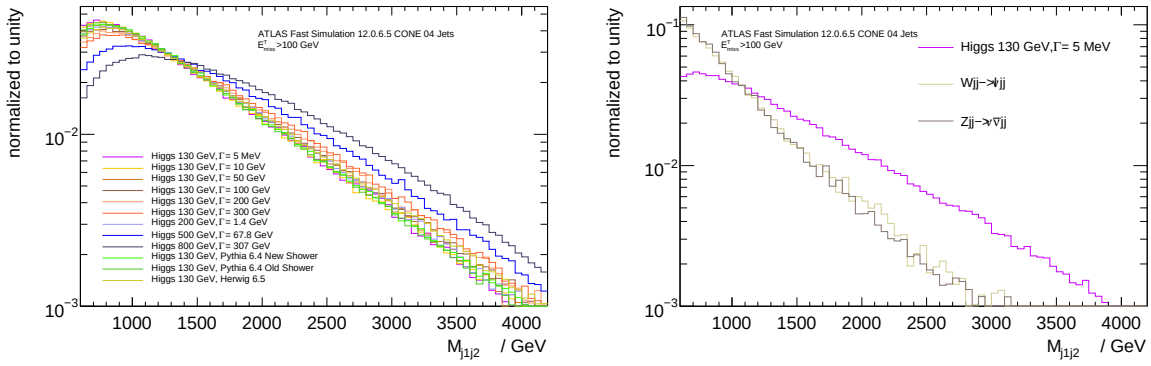

Fig. B.3: *Distributions of the variable no. 1 in the ATLFAST-1 samples used for the classifier choice. Plotted are in the left panel a comparison of several signal hypotheses. A comparison between shape of signal and W and Z bosons background after preselection is shown in the right panel.*

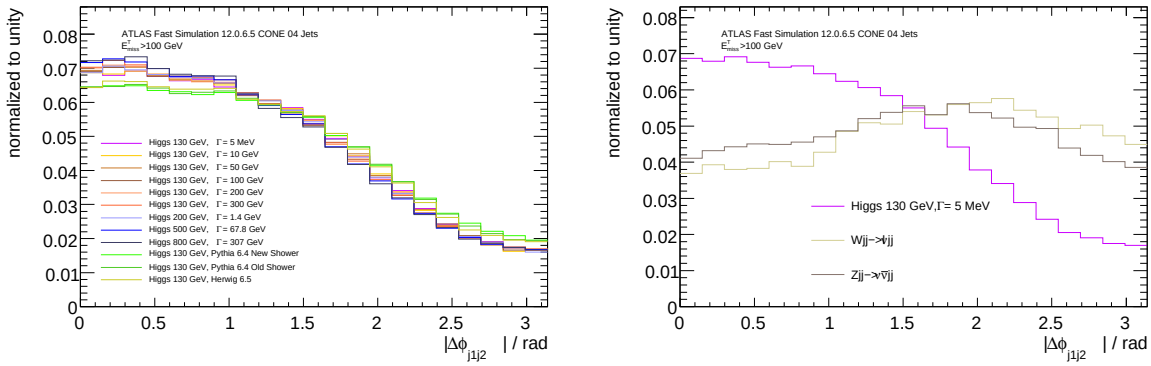

Fig. B.4: *Distributions of the variable no. 2 in the ATLFAST-1 samples used for the classifier choice. Plotted are in the left panel a comparison of several signal hypotheses. A comparison between shape of signal and W and Z bosons background after preselection is shown in the right panel.*

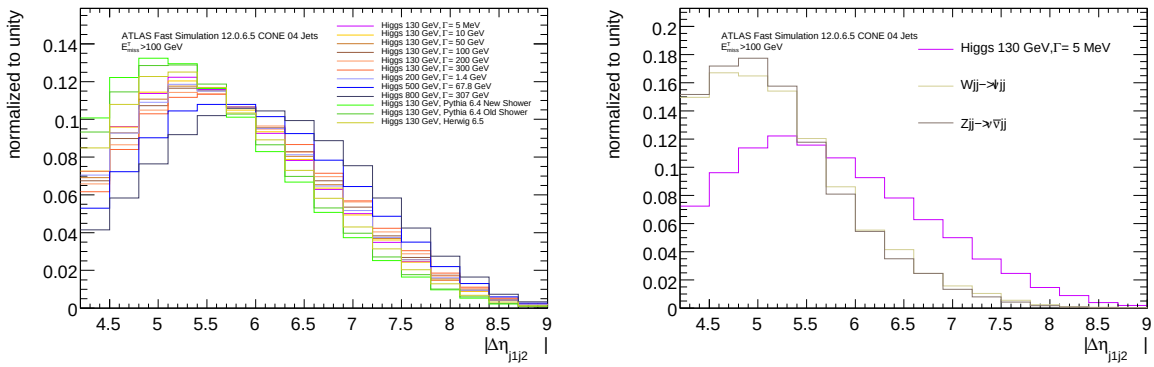

Fig. B.5: *Distributions of the variable no. 3 in the ATLFAST-1 samples used for the classifier choice. Plotted are in the left panel a comparison of several signal hypotheses. A comparison between shape of signal and W and Z bosons background after preselection is shown in the right panel.*

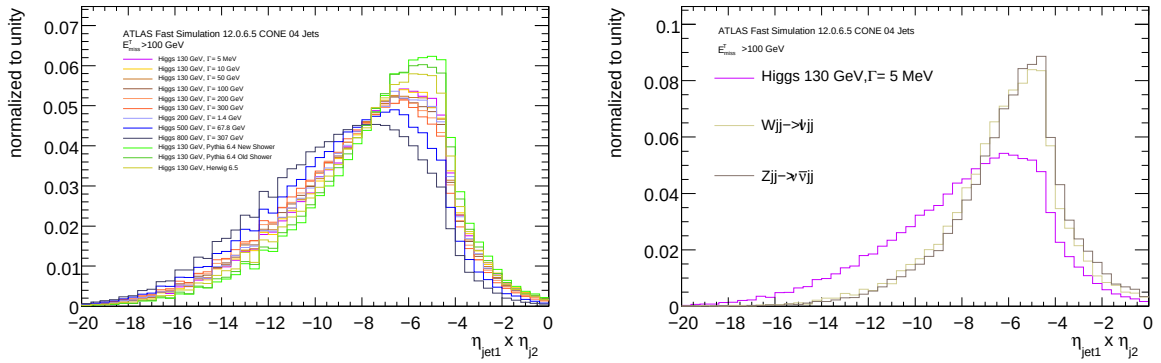

Fig. B.6: *Distributions of the variable no. 4 in the ATLFAST-1 samples used for the classifier choice. Plotted are in the left panel a comparison of several signal hypotheses. A comparison between shape of signal and W and Z bosons backgrounds after preselection is shown in the right panel.*

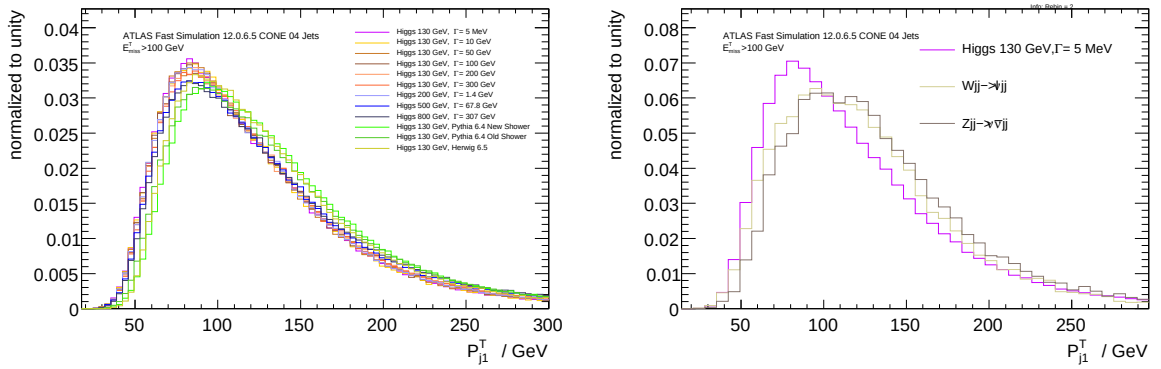

Fig. B.7: *Distributions of the variable no. 5 in the ATLFAST-1 samples used for the classifier choice. Plotted are in the left panel a comparison of several signal hypotheses. A comparison between shape of signal and W and Z bosons backgrounds after preselection is shown in the right panel.*

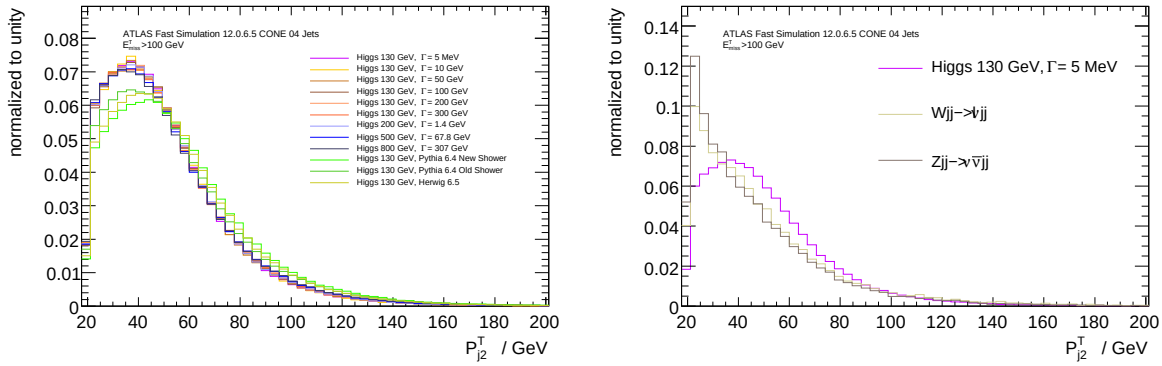

Fig. B.8: *Distributions of the variable no. 6 in the ATLFAST-1 samples used for the classifier choice. Plotted are in the left panel a comparison of several signal hypotheses. A comparison between shape of signal and W and Z bosons backgrounds after preselection is shown in the right panel.*

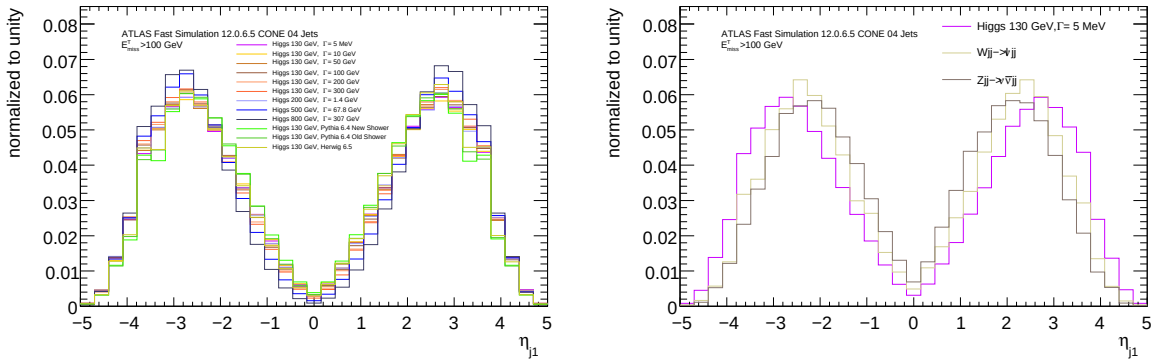

Fig. B.9: *Distributions of the variable no. 7 in the ATLFAST-1 samples used for the classifier choice. Plotted are in the left panel a comparison of several signal hypotheses. A comparison between shape of signal and W and Z bosons backgrounds after preselection is shown in the right panel.*

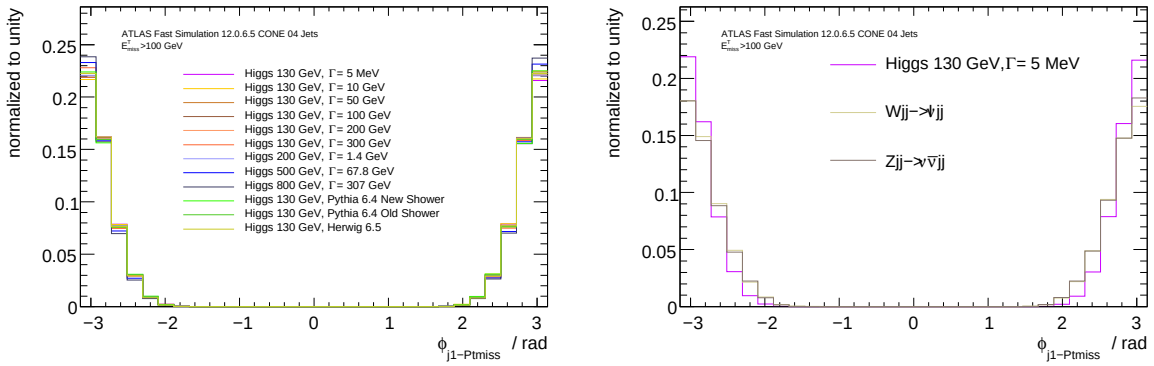

Fig. B.10: *Distributions of the variable no. 8 in the ATLFAST-1 samples used for the classifier choice. Plotted are in the left panel a comparison of several signal hypotheses. A comparison between shape of signal and W and Z bosons backgrounds after preselection is shown in the right panel.*

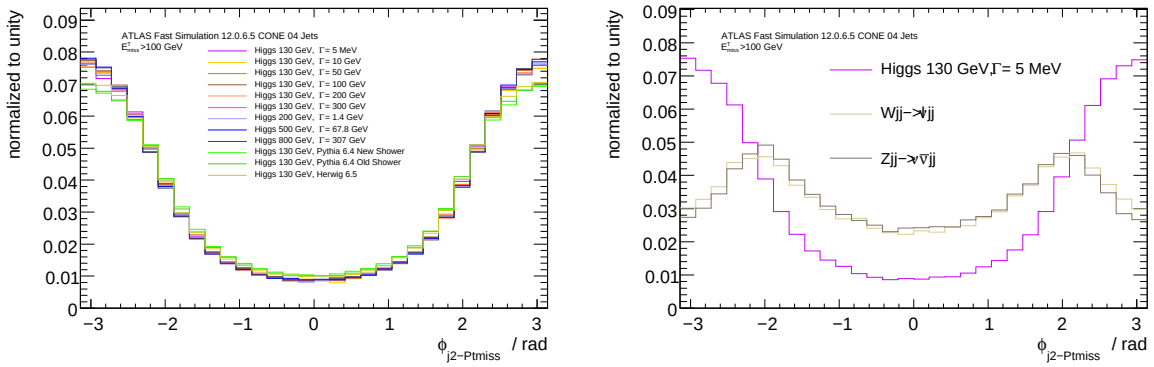

Fig. B.11: *Distributions of the variable no. 9 in the ATLFAST-1 samples used for the classifier choice. Plotted are in the left panel a comparison of several signal hypotheses. A comparison between shape of signal and W and Z bosons backgrounds after preselection is shown in the right panel.*

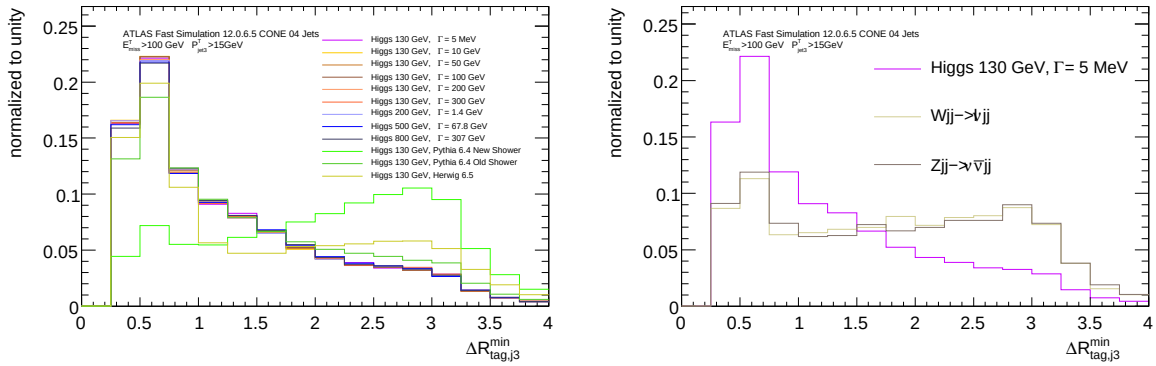

Fig. B.12: *Distributions of the variable no. 10 in the ATLFAST-1 samples used for the classifier choice. Plotted are in the left panel a comparison of several signal hypotheses. A comparison between shape of signal and W and Z bosons backgrounds after preselection is shown in the right panel.*

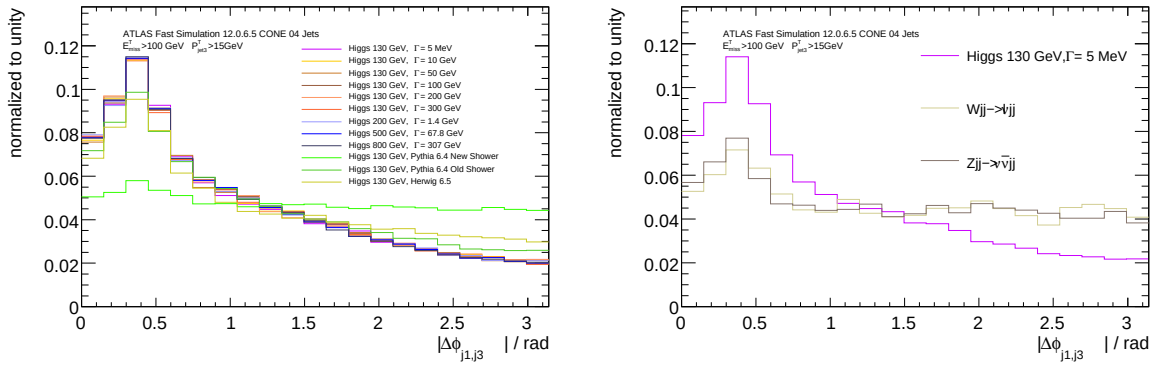

Fig. B.13: *Distributions of the variable no. 11 in the ATLFAST-1 samples used for the classifier choice. Plotted are in the left panel a comparison of several signal hypotheses. A comparison between shape of signal and W and Z bosons backgrounds after preselection is shown in the right panel.*

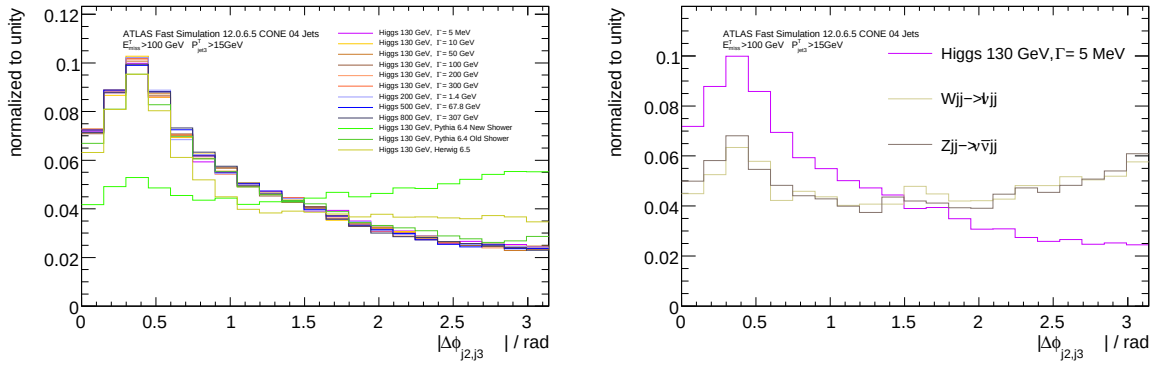

Fig. B.14: *Distributions of the variable no. 12 in the ATLFAST-1 samples used for the classifier choice. Plotted are in the left panel a comparison of several signal hypotheses. A comparison between shape of signal and W and Z bosons backgrounds after preselection is shown in the right panel.*

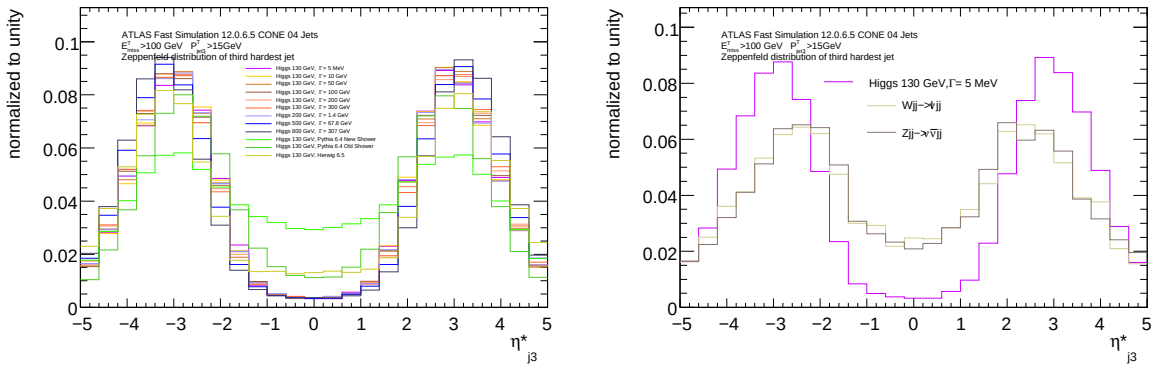

Fig. B.15: *Distributions of the variable no. 13 in the ATLFAST-1 samples used for the classifier choice. Plotted are in the left panel a comparison of several signal hypotheses. A comparison between shape of signal and W and Z bosons backgrounds after preselection is shown in the right panel.*

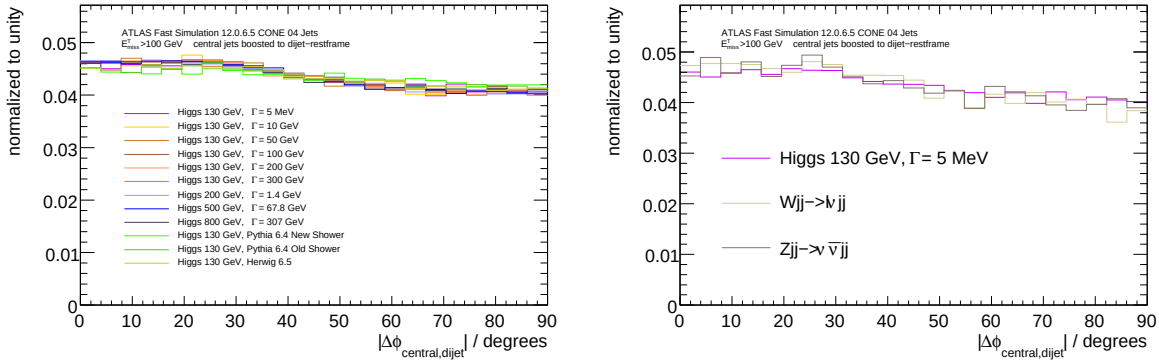

Fig. B.16: *Distributions of the variable no. 14 in the ATLFAST-1 samples used for the classifier choice. Plotted are in the left panel a comparison of several signal hypotheses. A comparison between shape of signal and W and Z bosons backgrounds after preselection is shown in the right panel.*

Observations

We note in the distributions displayed in Fig. B.3-B.16 the following general features:

1) in the signal distributions describing the tagging jet kinematics (Fig. B.3-B.16), the differences in the distributions that are visible for Sherpa samples appear for different Higgs masses. In other words the tagging jets distributions depend a little bit on the Higgs mass.

2) in the signal distributions describing the tagging jets kinematics (Fig. B.3-B.16), the 130 GeV Higgs mass point is shown with a variation of the decay width. But the differences in the distributions of the tagging jets are only mild, even if the width becomes large. In other words the tagging jets distributions exhibit no significant dependence on the Higgs decay width.

3) There are striking generator model differences between Herwig, Pythia in old and new parton shower model and Sherpa, if one regards variables that include additional jets (Fig. B.3-B.16). In Sherpa these jets can stem from the matrix element and in the other generators these jets stem from showering only. In that aspect we choose an practical approach. For the moment we deliberately assume the Sherpa model as one possible model and conduct our study to be consistent with the Sherpa MC for signal and main background. The results of the study are then a proof of principle, how sensitive ATLAS can be in the stealthy Higgs model. In early data taking, studies of the QCD physics underlying the models in generators will be able to decide which model is realised in nature and also the tuning of the models to the data in the generators will be perfected. At that stage the sensitivity may be reaccessed with the improved models. Though the exploitation of third jet variables may improve the signal background discrimination, it would be desirable to perform the sensitivity study as much as independent from variables with third jets to avoid the influence of generator models on the results.

4) We have not explicitly analysed the potentially high correlation between these many variables. Since we will try out of various classifiers for this set of variables, this aspect can be dealt with in that step. Because it is known, while high correlations between variables do not improve performance of some classifiers like the classical likelihood, correlations can add information and improve discrimination for other classifiers like the neural networks.

Considered classifiers

To get acquainted with the variety of classifiers at hand, we made preparing tests with a reduced set of only 6 variables (see first row in Tab. B.2). We tried out classifiers that were used in previous high energy physics analyses. We aimed to identify a robust method, which should be as simple as possible and for which people have already an experience, e.g. the Fisher's discriminant as a linear discriminant analyser (LDA) or the artificial neural networks (MLP), boosted decision trees (BDT) and likelihood discriminator. Also we added two more unknown probability density estimators like the k-nearest neighbours algorithm (kNN) or the ensemble rules learning algorithm, called RuleFit.

The tested likelihood showed no good performances and were in average very slow, especially when decorrelation was applied. Hence, they were not regarded any further. The Fisher discriminant, which is a classifier without need of training, served as a transparent baseline discriminator. Though it is a well known fact that correlation among variables can deteriorate the Fisher's discriminant performance.

B.1.3 Performance optimisation of classifiers

Step 1 boiling down the 14 variables to only the most useful variables

The 14 variables were the starting point and tested in the classifiers given in the second row of Tab. B.2. Though a classifier like the boosted decision tree can be fed with even not useful variables which are simply ignored during training, clearly it is advisable to keep an analysis as simple as possible. All the classifiers therefore were run with all 14 variables simultaneously. The classifiers summarise after training the importance of the individual variables. The measure of importance is specifically defined for each classifier [101]. It had been carefully inspected which variables were used best in the individual classifier. This made it possible to exclude for each classifier the worst performing variables. In this step the likelihood classifier exhibited very bad performance that it was depreciated in the next step. At this early stage it showed that the MLP was always very good performing, e.g. if one compared the area below the ROC curve to other classifiers.

.

Classifier	**1**	**2**	**3**	**4**	**5**	**6**	**7**	**8**	**9**	**10**	**11**	**12**	**13**	**14**	**comment**
various tested Fig.	X	X	$\oplus P_{\text{miss}}^{\text{T}}$			X	X	$\oplus min(\lvert\Delta\Phi(p_{\text{tag}}^{\text{T}}, \vec{E}_{\text{miss}}^{\text{T}}\rvert)$							Likelihood not useful
Fisher,MLP RuleFit,kNN BDT	X	X	X	X	X	X	X	X	X	X	X	X	X	X	variables ranking
Fisher	X	X	X	X			|X|		|X|			X			low perf.
(vs. MLP)	X	X	X	X			|X|		|X|						baseline
MLP	X		X	X		X	X	X	X	X			X		good
	X		X	X			X	X	X	X			X		indep. inputs
RuleFit	X	X	X		X	X				X					good perf.
(vs. MLP)	X	X	X		X	X		X		X					instable rank.
BDT	X	X	X	X	X	X					X	X	X		robust but
(vs. MLP)	X	X	X	X	X	X				X	X	X	X		many inputs
kNN	X	X	X	X					X	X					robust
(vs. MLP)	X	X	X	X			X		X	X					but slow

Tab. B.2: *Summary of studied classifiers and their variables combinations. IN row 1 the result of the preparing classifier test is summarised. From row 2 on the classifier comparison and optimisation is summarised. We compared the Fisher's discriminant (Fisher), multilayer perceptron (MLP), boosted decision trees (BDT), rule based selection (RuleFit) and the k-nearest neighbour (kNN) classifiers. A variable entering the input variables set is marked by X. In the first column the used classifiers are listed. If more than one classifier is listed in the cell, these were compared in one TMVA training simultaneously. Especially from row 3 on, the listed classifier has been simultaneously compared with a MLP with the same input variable set. For the Fisher's discriminant inputs had to be antisymmetrised by taking the modulus.*

Step 2 finding best classifier in runs on most useful variables

The remaining relative important variables of a classifier were further inspected by grouping them in maximal two newly combined variable sets per classifier. Thereby we neglected one or two of the least important variables to check whether the performance can be reached with a minimal set. In row 3 to 7 of Tab. B.2 the variables and classifier combinations are summarised.

Again the performances of the classifiers were compared over the range of hypotheses given in Tab. B.1 with respect to some classifier specific performance information like variables importance and the F.O.M and mostly the ROC criteria. The later was very useful in a direct comparison with the MLP, hence the MLP was spotted of being well performing in step 1. This comparison with a subset of variables was done in the following way that the same set of variables in a MLP was compared with the classifier under study (e.g. Fisher's discriminant, BDT, RuleFit, kNN) to see whether a MLP would beat the classifier.

In Tab. B.3 we give examples for some equally well performing MLP input sets.

MLP0	MLP1	MLP2	MLP3	MLP4
M_{j1j2}	$\Delta\Phi(p_{\mathrm{j1}}^{\mathrm{T}}, \vec{E}_{\mathrm{miss}}^{\mathrm{T}})$	$\eta_{\mathrm{j3}}^{\star}$	$p_{\mathrm{j1}}^{\mathrm{T}}$	$\Delta\eta_{\mathrm{j1j2}}$
$\Delta\Phi_{\mathrm{j1j2}}$	$p_{\mathrm{j1}}^{\mathrm{T}}$	$\eta_{\mathrm{j1}} \times \eta_{\mathrm{j2}}$	$\Delta\Phi_{\mathrm{j1j3}}$	M_{j1j2}
$p_{\mathrm{j2}}^{\mathrm{T}}$	M_{j1j2}	$\Delta\Phi(p_{\mathrm{j1}}^{\mathrm{T}}, \vec{E}_{\mathrm{miss}}^{\mathrm{T}})$	$\Delta\Phi_{\mathrm{j2j3}}$	$\eta_{\mathrm{j1}} \times \eta_{\mathrm{j2}}$
$min(\Delta R_{\mathrm{tag,j3}})$	$\Delta\Phi_{\mathrm{j1j2}}$	$\Delta\Phi(p_{\mathrm{j2}}^{\mathrm{T}}, \vec{E}_{\mathrm{miss}}^{\mathrm{T}})$	$\eta_{\mathrm{j3}}^{\star}$	$\Delta\Phi_{\mathrm{j1j2}}$
$\Delta\eta_{\mathrm{j1j2}}$	$p_{\mathrm{j2}}^{\mathrm{T}}$	η_{j1}	$\eta_{\mathrm{j1}} \times \eta_{\mathrm{j2}}$	$\Delta\Phi(p_{\mathrm{j2}}^{\mathrm{T}}, \vec{E}_{\mathrm{miss}}^{\mathrm{T}})$
$p_{\mathrm{j1}}^{\mathrm{T}}$	$min(\Delta R_{\mathrm{tag,j3}})$	M_{j1j2}	M_{j1j2}	$min(\Delta R_{\mathrm{tag,j3}})$
	$\Delta\eta_{\mathrm{j1j2}}$	$p_{\mathrm{j2}}^{\mathrm{T}}$	$\Delta\Phi_{\mathrm{j1j2}}$	η_{j1}
		$min(\Delta R_{\mathrm{tag,j3}})$	$p_{\mathrm{j2}}^{\mathrm{T}}$	
		$\Delta\eta_{\mathrm{j1j2}}$	$min(\Delta R_{\mathrm{tag,j3}})$	
			$\Delta\eta_{\mathrm{j1j2}}$	

Tab. B.3: The input variables combinations for the MLP's that performed as well as the other tested classifiers. But also this good performance seemed to be stable over the tested hypothesis, while classifiers like RuleFit and kNN showed unstable training results and the BDT used many variables without exceeding the MLP performance.

The corresponding ROC curves are displayed in Fig. B.17 for three signal hypotheses. One sees the variables set in the column named MLP2 performs best for low masses and widths but falls back behind MLP0 or MLP1 variable combinations for higher mass. But generally the differences are marginal. Only the many variables set in column MLP3 is clearly disfavoured in all cases. Generally the small set of input variables of MLP0 performs at least as second best. This was interpreted as a hint that number of the possible useful variables can be very small.

Comparison of multivariate classifiers for signal and background discrimination

It was observed that though the performance seemed to be well, looking at all signal hypotheses the RuleFit[1)] and the kNN, which was also slow, seemed to yield very unstable results, hence they were depreciated. Boosted decision trees performed quite good when comparing the F.O.M, but needed between 9 to 10 variables. It was interesting to see that the MLP with less variables performed in terms of the

[1)] RuleFit reached in some cases the best F.O.M values with few variables. RuleFit determines sets of selection rules which model the variables phase space in training. It was observed that the number of rules needed for classification spread over a large variety from 9 rules to 79 rules comparing rather similar signals. This effect was not understood and hence RuleFit was depreciated.

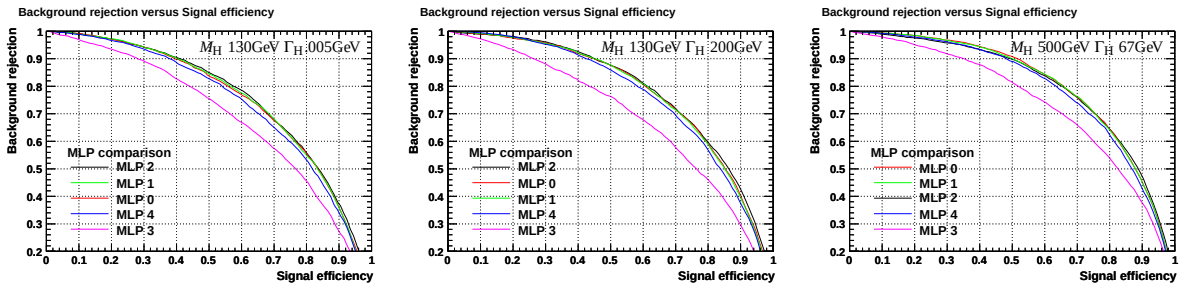

Fig. B.17: *Examples of ROC curves for various MLP showing the performance's on three M_H and Γ_H signal hypotheses. The same W and Z bosons backgrounds were used for training.*

F.O.M only slightly worse. This was seen as a hint that one can tune the MLP to a lesser number of variables without much trade off in performances.

Depreciation of third jet related variables

Though some of the third jet variables, namely $min(\Delta R_{\text{tag,j3}})$ and the highly correlated Zeppenfeld variable $\eta^{\star}_{\text{j3}}$, are contained in the best performing MLP combinations, the decision was made to depreciate them. The reason was that the description of these variables differs visibly in fast and detailed detector description. While this is possible to correct by reweighting it was noted also that the abundance of low p_{T} reconstructed third jets is overestimated by the fast detector simulation. The fewer cases of events with a third jet reconstructed by the more refined algorithms in full detector simulation would lead to a strong reduction of discrimination power.

Last but not least it was mentioned several times that the description of third jets depends on generator modelling so far untested at the LHC. In some years from now on, one can expect that ATLAS has sufficient background and signal MC at hand, which is very accurately tuned to the data. Then the generator model dependencies will be not involved anymore. Under such conditions, it may be worthwhile to reaccess the presented third jet variables and check whether they provide discrimination power.

We describe in the next paragraph that we were able to identify variables using only the two tagging jet candidates properties that perform almost as good and provide a more robust and simple analysis.

Step 3 tuning the MLP

From the beginning of the classifier test, the MLP proved to be always among the better or best performing classifiers. Therefore, in step 2 we always tested the classifier under consideration i.e. Fisher, RuleFit, BDT and kNN vs. a MLP with the same inputs. The result showed that the MLP is very competitive. If it was not exceeding the classifier the MLP performance was only slightly worse than the considered classifier. Therefore, step 2 provided a very detailed test of the MLP with several input variables. In Tab. B.3 we summarised the five best performing MLP's run in step 2. Quite independent from the mix of input variables the MLP show good performance. On the basis of this test the MLP became the classifier of choice.

We chose to optimise the MLP classifier in a third steps further. Because the best MLP found in step 2 contained the variable depending on the third jet $min(\Delta R_{\text{tag,j3}})$, we sought to replace that variable. For that we took the best ranked variables of the two tagging jet candidates and combined them in four additional MLP's that are summarised in Tab. B.4.

Note, that we also wanted to quantify a possible performance loss by depreciating the third jet variables. Therefore, as reference MLP0 of Tab. B.3, which was second best performing but most simple MLP is step 2 appears again. MLP1 is even simpler as it is MLP0 without $min(\Delta R_{\text{tag,j3}})$. The other

MLP's grouped the strongest tagging jet variables and especially tried to make use of the direction of $E_{\mathrm{T}}^{\mathrm{miss}}$ towards the tagging jets, since $\Delta\Phi(p_{\mathrm{j2}}^{\mathrm{T}}, \vec{E}_{\mathrm{miss}}^{\mathrm{T}})$ showed shape difference.

MLP0	MLP1	MLP2	MLP3	MLP4
M_{j1j2}	M_{j1j2}	$\Delta\Phi(p_{\mathrm{j1}}^{\mathrm{T}}, \vec{E}_{\mathrm{miss}}^{\mathrm{T}})$	$p_{\mathrm{j1}}^{\mathrm{T}}$	$\Delta\Phi(p_{\mathrm{j2}}^{\mathrm{T}}, \vec{E}_{\mathrm{miss}}^{\mathrm{T}})$
$\Delta\Phi_{\mathrm{j1j2}}$	$\Delta\Phi_{\mathrm{j1j2}}$	$p_{\mathrm{j1}}^{\mathrm{T}}$	$p_{\mathrm{j2}}^{\mathrm{T}}$	$p_{\mathrm{j1}}^{\mathrm{T}}$
$p_{\mathrm{j2}}^{\mathrm{T}}$	$p_{\mathrm{j2}}^{\mathrm{T}}$	M_{j1j2}	M_{j1j2}	M_{j1j2}
$\Delta\eta_{\mathrm{j1j2}}$	$\Delta\eta_{\mathrm{j1j2}}$	$\Delta\Phi_{\mathrm{j1j2}}$	$\Delta\Phi_{\mathrm{j1j2}}$	$\Delta\Phi_{\mathrm{j1j2}}$
$p_{\mathrm{j1}}^{\mathrm{T}}$	$p_{\mathrm{j1}}^{\mathrm{T}}$	$p_{\mathrm{j2}}^{\mathrm{T}}$	$\Delta\Phi(p_{\mathrm{j1}}^{\mathrm{T}}, \vec{E}_{\mathrm{miss}}^{\mathrm{T}})$	$p_{\mathrm{j2}}^{\mathrm{T}}$
$min(\Delta R_{\mathrm{tag,j3}})$		$\Delta\eta_{\mathrm{j1j2}}$	$\Delta\Phi(p_{\mathrm{j2}}^{\mathrm{T}}, \vec{E}_{\mathrm{miss}}^{\mathrm{T}})$	$\Delta\eta_{\mathrm{j1j2}}$
			η_{j1}	
			$\eta_{\mathrm{j1}} \times \eta_{\mathrm{j2}}$	
			$\Delta\eta_{\mathrm{j1j2}}$	

Tab. B.4: *Summary of studied MLP inputs in order to find a minimal set of good performing variables without third jet variables. Therefor MLP1 to MLP4 were tested against the best MLP with a third jet variable, i.e. MLP0. Additionally the contribution of $E_{\mathrm{T}}^{\mathrm{miss}}$ direction information was studied in MLP2 to MLP4, finding no significant contribution by this information.*

In Fig. B.18 the ROC curves of the MLP0 to MLP4 are compared over a range of hypotheses. The plots are done with a preselection cut $E_{\mathrm{T}}^{\mathrm{miss}} > 100\,\mathrm{GeV}$ close to the final cut value. One sees that the reference MLP with the third jet variable $min(\Delta R_{\mathrm{tag,j3}})$, that we decided to replace, really showed the best performance. But most important the difference in the area under the ROC curves is small for all other tested MLP. As a second evaluation criterion, in Fig. B.19 the F.O.M values gained by the compared MLP of step 3 (Tab. B.4) are shown. In fact the F.O.M became only approximately 5 % worse compared to the best MLP with the third jet variable by depreciating $min(\Delta R_{\mathrm{tag,j3}})$, as can be seen in Fig. B.19. Clearly the MLP0 reaches the highest values. The other MLP's perform quite similar. Since the F.O.M.'s are determined at a working point that may not be the actual working point in the analysis, the ROC curves are taken more into account for a decision. Generally, as Fig. B.18 indicates the area below the ROC curves differs only very little for most for all tested signal hypotheses. Considering all these information, this comparison enabled us to chose the simplest MLP without expecting a loss in performance more than a few percent.

Observations

The dependence on the decay width seems rather mild. The rise in the F.O.M. visible in the Fig B.19 is very shallow for Higgs bosons with mass of 130 GeV and varying width. If differences in performance are observed the may also stem from the preselection. Signal samples with a larger decay width tend to pass the preselection cut on $E_{\mathrm{T}}^{\mathrm{miss}}$ more often. Since such signal show a slightly better performance in the F.O.M., which depends on the efficiency. A similar argument applies for the heavier Higgs masses. We observed that the optimal cut on the MLP output tends to be slightly harder if the Higgs is heavier. This reduces the number of expected background events. The reduced background expectation leads to higher values of the F.O.M.

It was very surprising that the very strong shape difference in the variable $\Delta\Phi(p_{\mathrm{j2}}^{\mathrm{T}}, \vec{E}_{\mathrm{miss}}^{\mathrm{T}})$ was not improving the MLP analyses. This can be seen e.g. in the comparison of the F.O.M of MLP1 with MLP2 to MLP4 in Fig B.19. It may be caused by the fact that the dominant discrimination comes from the description of the correlations between the variables. Therefore, the other variables may have approximated these correlations well enough and no improvement was added by $\Delta\Phi(p_{\mathrm{j2}}^{\mathrm{T}}, \vec{E}_{\mathrm{miss}}^{\mathrm{T}})$.

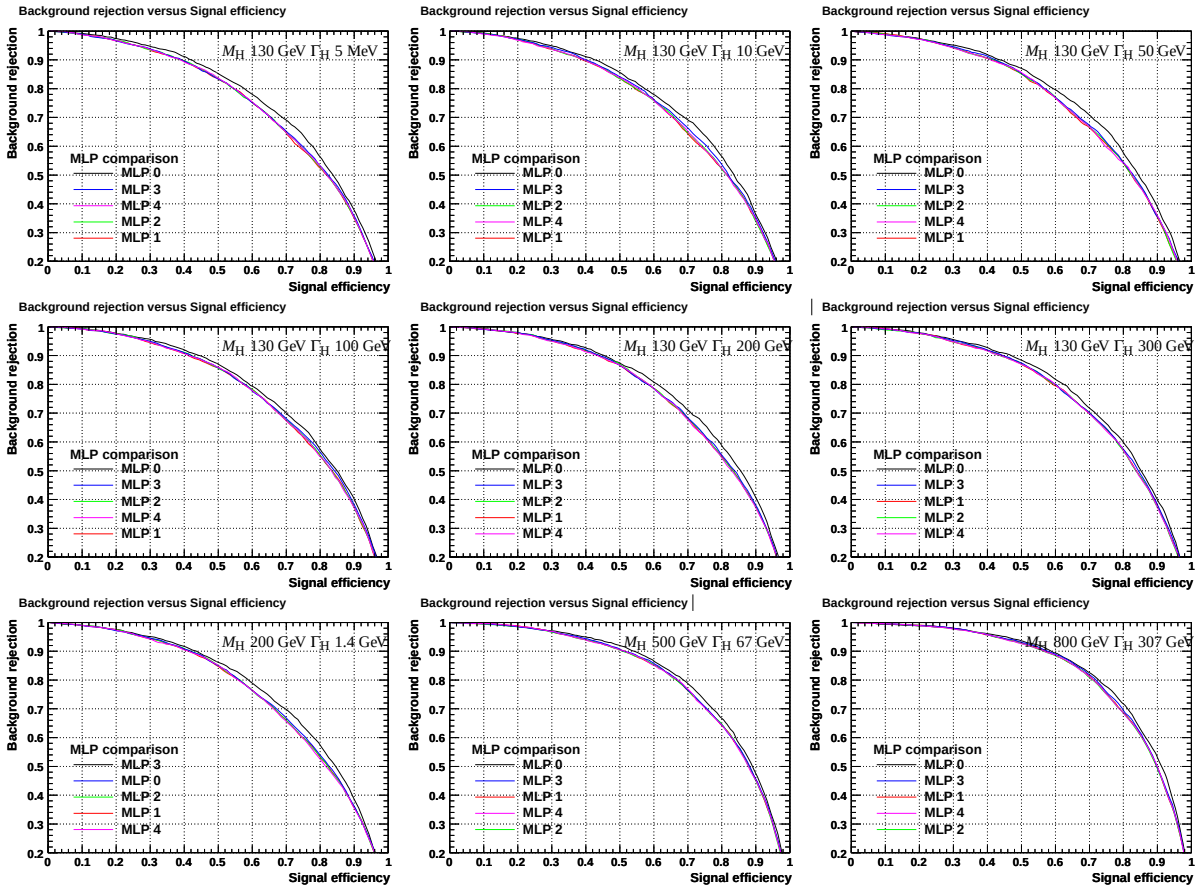

Fig. B.18: *Examples of ROC curves for various MLP showing the performances on all regarded* M_H *and* Γ_H *signal hypotheses. The legend entries are ordered according to their area under the ROC curve, largest area mentioned first.*

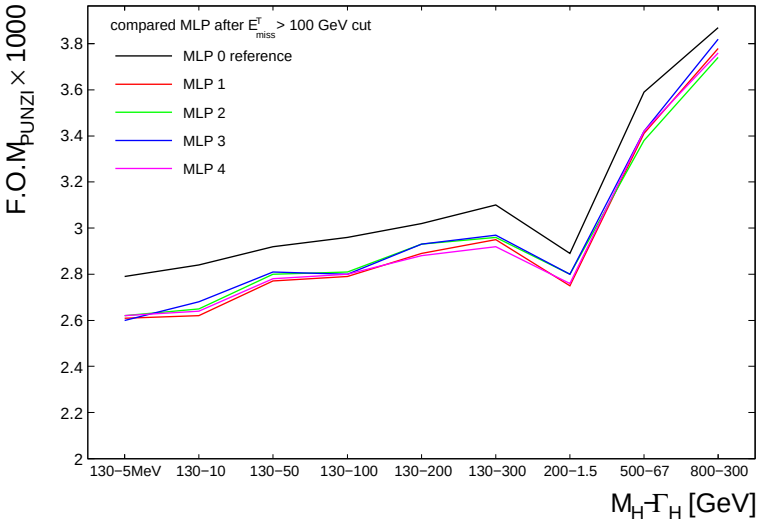

Fig. B.19: *Comparison of the F.O.M as a function of the tested M_H and Γ_H signal hypotheses, reached for the reference MLP0 and the MLP1 to MLP4. The highest F.O.M is indeed reached by the reference MLP0, but the MLP1 to MLP4 reach all very similar values of the F.O.M., which is only a few percent worse. For higher Higgs mass the cut on the MLP output can be made harder and more background is suppressed, which yields higher values of the F.O.M.*

B.1.4 Choice of MLP design for the multivariate analysis

The final choice, MLP1 from Tab. B.4, is a very good compromise between performance and complexity. Its good performance seemed to be stable over the tested hypothesis. Also only five variables, using exclusively tagging jet candidates quantities, are sufficient to yield that good performance. From analysis point of view a simple analysis is always preferable, with respect to stability and influence of systematic uncertainties. Especially the use of $E_{\mathrm{T}}^{\mathrm{miss}}$ not only in the preselection, could have propagated a new systematical impact of this quantity into the multivariate part of the analysis.

B.1.5 Additional tests on the MLP performance

Overtraining test

During all phases is was assured that there was no overtraining of the classifiers present biasing the performance. This was done by evaluating the control plots TMVA produces automatically. Two kind of plots can be used to look for possible overtraining. As one measure for overtraining can serve an error function of the MLP, which measures the deviation between the response and the desired target value (background= 0, signal= 1) for each event during the training. The summed error function plotted as function of the training cycles should decrease monotonically. A rising in the error function may indicate overtraining. More directly overtraining can be checked during the test phase after training. In this phase plot like the one in Fig. 5.12 compare the MLP output from the training phase with the output gained with the training weights evaluated in statistically independent samples. Both output distributions should be in statistical agreement if no overtraining is present.

Influence of a $E_{\mathrm{T}}^{\mathrm{miss}}$ precut set to 70 GeV or to 100 GeV

The missing energy in the event is one most important selection criteria in the preselection, which is not entering the variables of the multivariate analysis, since a hard cut was made to separate the dijet backgrounds beforehand. In contrast, jet related variables of the preselection enter the multivariate analysis studied here, because the precut values were chosen to be not very hard. But since the scale of $E_{\mathrm{T}}^{\mathrm{miss}}$ may be affected by uncertainties it would be desirable to chose a multivariate analysis design that is optimal even at different scales of $E_{\mathrm{T}}^{\mathrm{miss}}$. Since the final $E_{\mathrm{T}}^{\mathrm{miss}}$ cut is close to 100 GeV the results on this samples were regarded as more important for the choice. Nevertheless all rankings in performance were checked to be valid on the samples with preselection cut of 70 GeV.

Influence of generator difference

After the choice of a multilayer perceptron as multivariate classifier, it was compared for the Higgs boson mass 130 GeV and a few MeV width whether the performance of the five best MLP's is very sensitive on the different MC event generators. We had corresponding samples of Sherpa, Herwig and Pythia6.4, run with old and new parton shower model available. Judging from the ROC curve comparison diplayed in Fig. B.20, strong generator model dependence was not observed in any of the best MLP's (this is true for MLP4 not shown here). We show in Fig. B.20 the results of a comparison after a preselection cut $E_{\mathrm{T}}^{\mathrm{miss}} > 100$ GeV as example, but it was checked that a lower cut of 70 GeV does not change the picture.

One observes that the signal MC generator used is not affecting the ROC curves of all tested MLP's very much. This may be due to the fact that the background MC was the same in all MLP trainings. In fact the difference in the ROC curve is very small for the MLP0 with $min(\Delta R_{\mathrm{tag,j3}})$, which is very sensitive to differences in the underlying model of additional jet radiation. But as seen before this variable is not contributing very much to the discrimination power of the MLP0. We conclude, that a possible difference in third jet distributions of the signal may not be visible in this comparison and that the small differences observed in the ROC curves may be solely due to statistical fluctuations rather due to model differences. In other words the test of the MLP's with signal MC from different generators and same background samples give a hint that the method is rather robust against generator modelling differences.

B.2 Additional comparison of the input variables distributions in detailed and fast detector simulations

As shown in Fig. 5.6 in Chapter 5.3.4 there is a sufficient agreement in the shape of tagging jet distributions between detailed and fast detector simulation for the Z boson plus jets background. Since we presented the shape comparison after the complete standard preselection, the MC events of the detailed detector simulation became sparse compared to the ATLFAST-1 samples. The fluctuations may make the judgement of the degree of agreement difficult. In Fig. B.21 to Fig. B.22 we present for reference the comparison plots of the input variables after preselection for fast (blue histogram) and full (red histogram) detector simulation for the W boson plus jets samples and for a signal, $M_{\mathrm{H}} = 200$ GeV and $\omega = 5$. Though the fluctuations and the MC statistical errors are larger, we conclude that these comparison plots confirm the statistical agreement between the samples and the claim that the shape of the input variables is described in the same way in both kinds of simulations, hence ATLFAST-1 samples can be used as the training samples of the MLP.

B.3 Influence of systematical variations on the input variable distributions

In Section 6.3 we optimised the cut on the MLP output distributions under consideration of the influence of the detector related systematical uncertainties. There we gave only some examples for the effect of

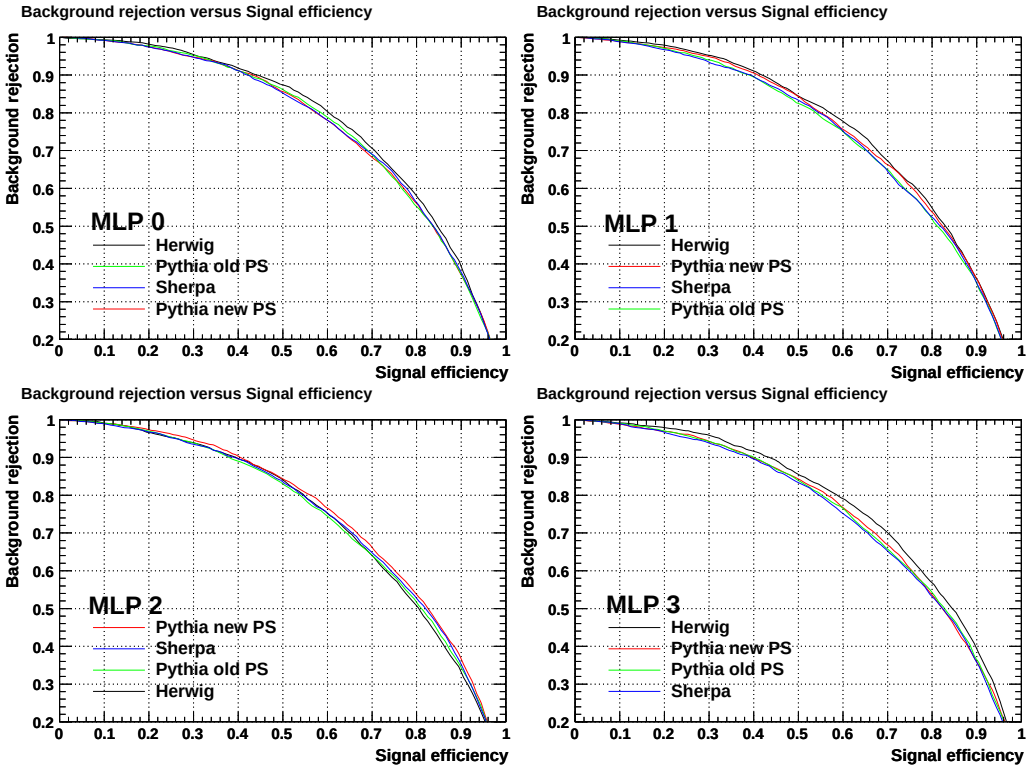

Fig. B.20: *Examples of ROC curves for various MLP's showing the performances on a signal,* $M_{\mathrm{H}} = 130$ GeV *and* $\Gamma_{\mathrm{H}} = 5$ MeV*. This signal is generated with Herwig, Sherpa or Pythia in two kind of parton shower models. The preselection cut* $E_{\mathrm{T}}^{\mathrm{miss}} > 100$ GeV *was applied for training. No specific generator dependencies of the MLP's performance is visible. This is also true, if a preselection cut* $E_{\mathrm{T}}^{\mathrm{miss}} > 70$ GeV *is used.*

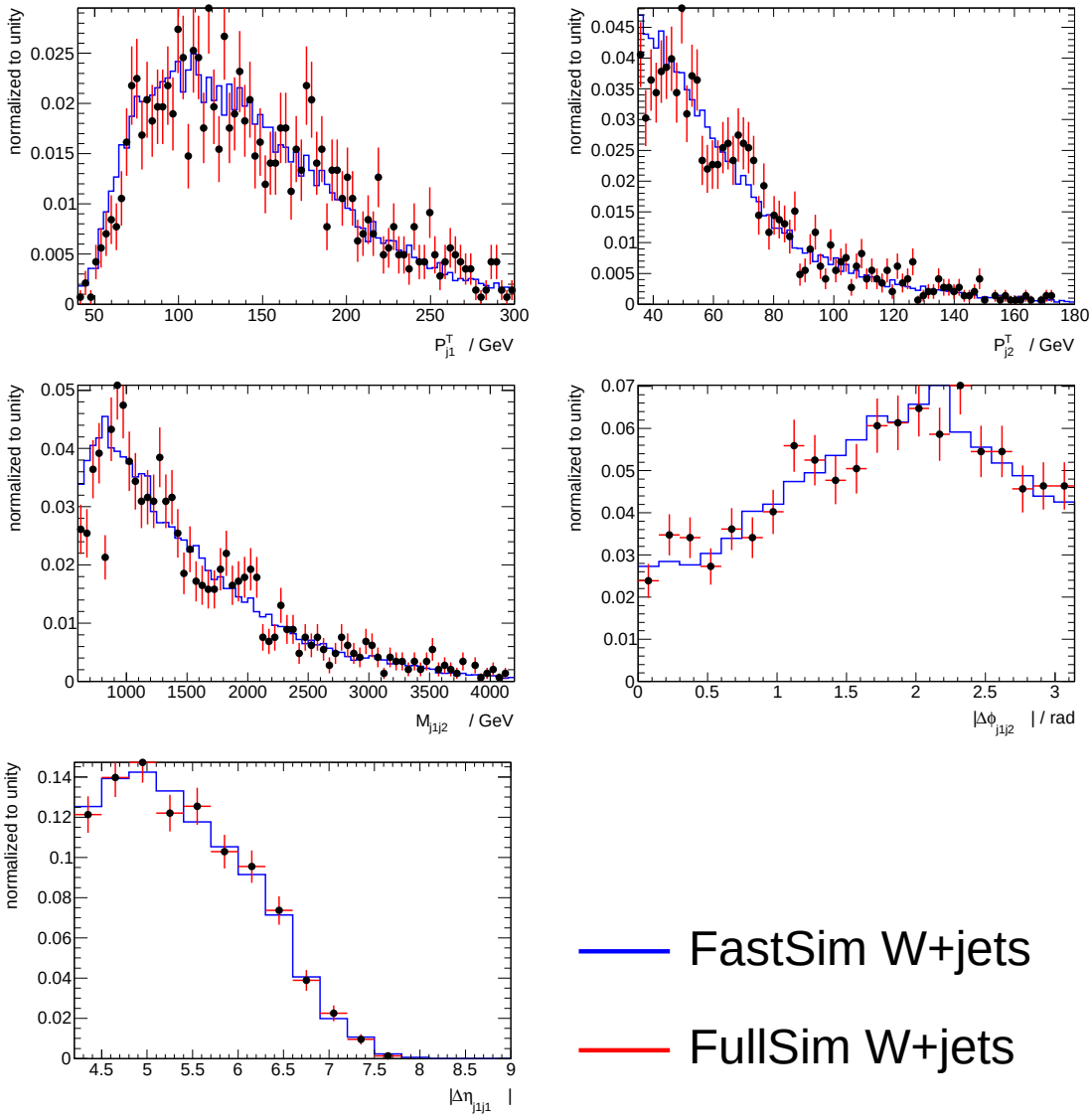

Fig. B.21: *The five input variable distributions in comparison between fast and detailed simulated events. The distribution are displayed for comparison of possible shape differences in ATLFAST-1 and detailed Geant4 detector simulation. Shown is the W plus jets background. All distributions are normalised to unity to make the shape comparison possible.*

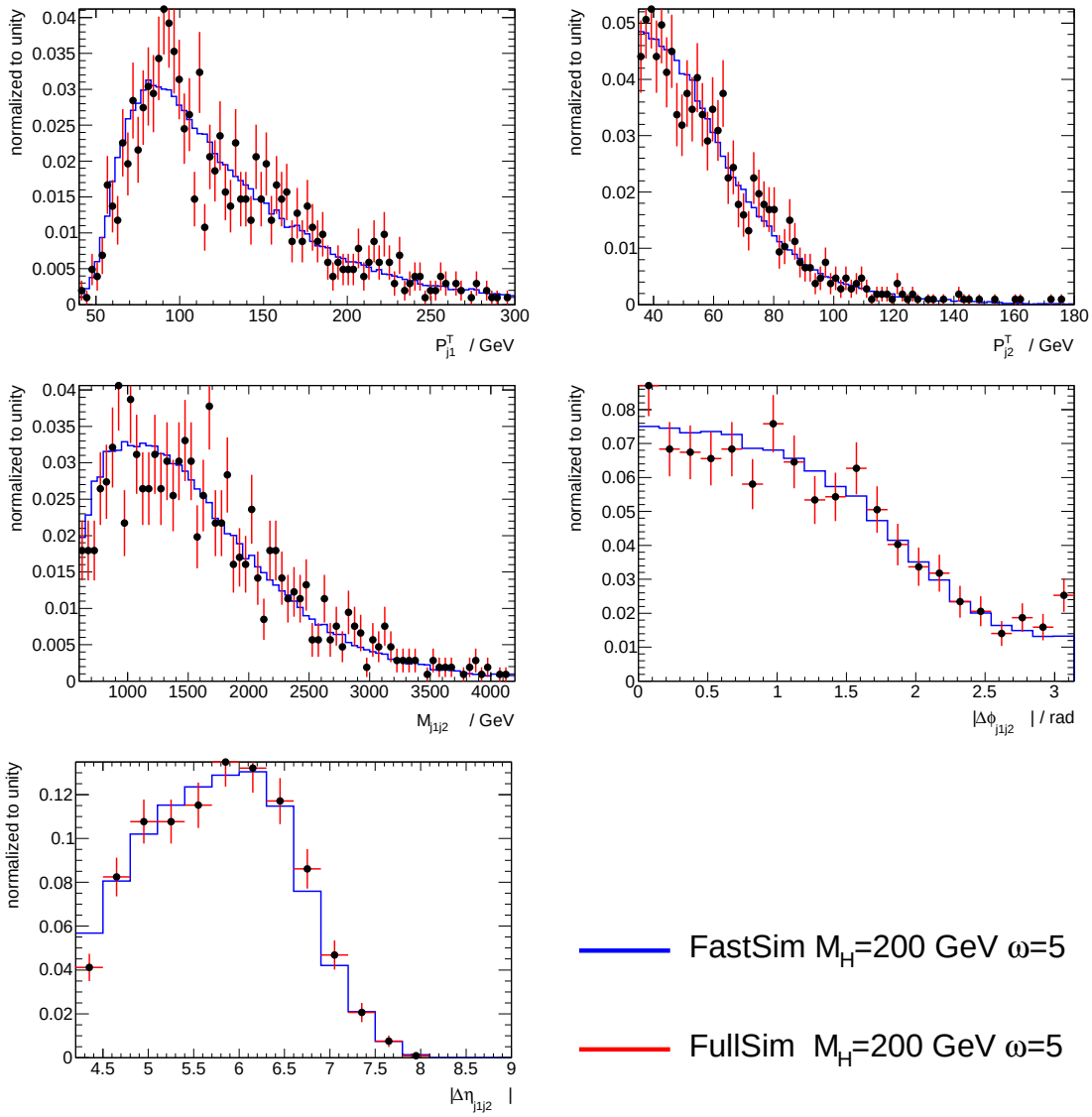

Fig. B.22: *The five input variable distributions in comparison between fast and detailed simulated events. The distribution are displayed for comparison of possible shape differences in ATLFAST-1 and detailed Geant4 detector simulation. Shown is a signal with* $M_{\mathrm{H}} = 200$ GeV *and* $\omega = 5$. *All distributions are normalised to unity to make the shape comparison possible.*

the JES rescaling and the jet energy resolution smearing on the input variables distributions of the MLP and reported the general tendency and relative importance of the various systematical variations. Here we want to display all input variables ATLFAST-1 distributions with the variations applied during the systematical studies for reference.

In Fig. B.23 to Fig. B.42 the effects of all studied systematic variations on the five input variables of the MLP are displayed. We have chosen to show an example signal hypothesis $M_{\mathrm{H}} = 200$ GeV and $\omega = 5$, (always in the left panel) and important W and Z bosons backgrounds added (always in the right panel). The following variables are presented,

1) $p_{\mathrm{j1}}^{\mathrm{T}}$
   is the transverse momentum of the leading tagging jet candidate.

2) $p_{\mathrm{j2}}^{\mathrm{T}}$
   is the transverse momentum of the subleading tagging jet candidate.

3) M_{j1j2}
   is the invariant mass calculated of the tagging jet candidates.

4) $\Delta\Phi_{\mathrm{j1j2}}$
   is the azimuthal angle between the tagging jet candidates.

5) $\Delta\eta_{\mathrm{j1j2}}$
   is the pseudorapidity gap between the tagging jet candidates.

beginning with the larger of the two JES rescaling followed by the smaller one that was finally used in the MLP analysis and the jet energy resolution smearing and the varied isolated lepton veto probability. The later one are shown to prove that their effect is very small compared to the JES rescaling effects.

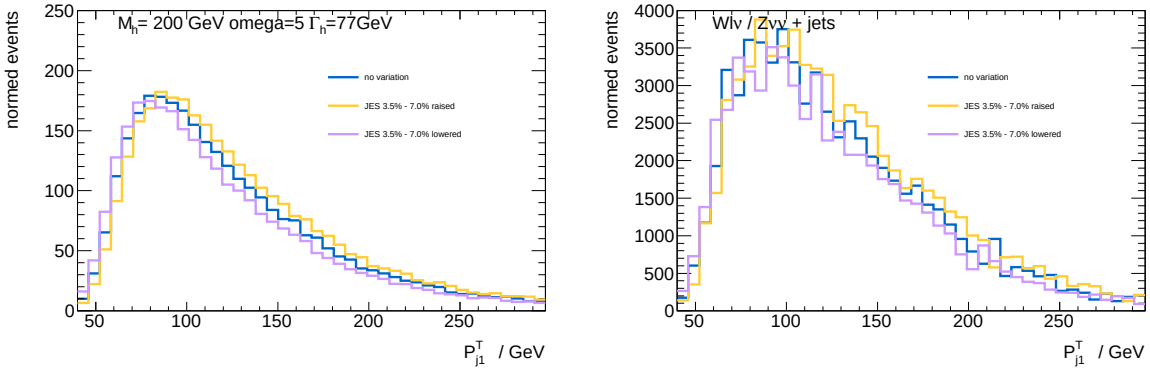

Fig. B.23: *Systematic variation of the input variable* $p_{\mathrm{j1}}^{\mathrm{T}}$ *under the change of the JES about* $3.75\% - 7.5\%$*. Shown are distribution in ATLFAST-1 samples that enter the training of the MLP classifier. Plotted is signal,* $M_{\mathrm{H}} = 200$ GeV *and* $\omega = 5$ *(left panel) and the added important W and Z bosons backgrounds (right panel).*

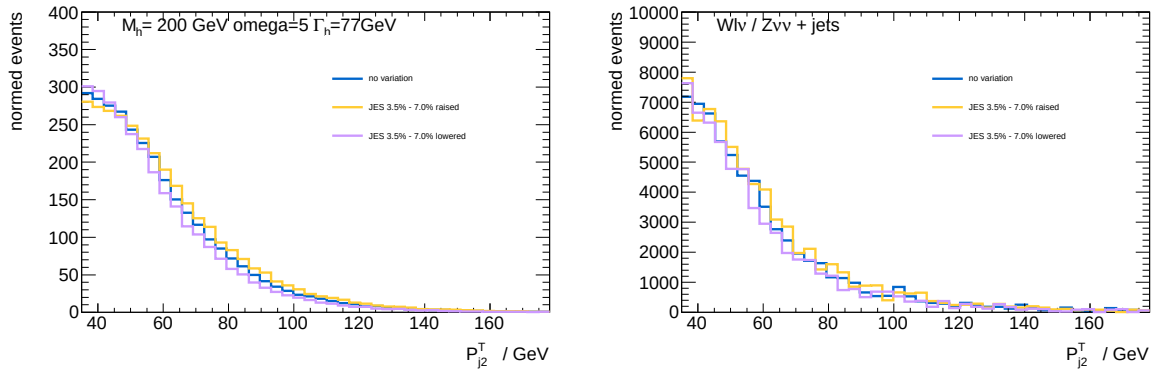

Fig. B.24: *Systematic variation of the input variable* $p_{\mathrm{j2}}^{\mathrm{T}}$ *under the change of the JES about* $3.75\% - 7.5\%$. *Shown are distribution in ATLFAST-1 samples that enter the training of the MLP classifier. Plotted is signal,* $M_{\mathrm{H}} = 200$ GeV *and* $\omega = 5$ *(left panel) and the added important W and Z bosons backgrounds (right panel).*

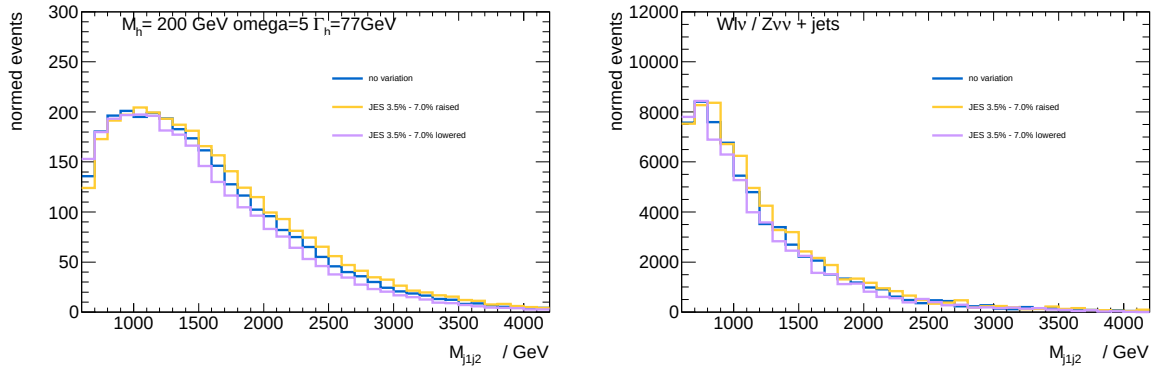

Fig. B.25: *Systematic variation of the input variable* M_{j1j2} *under the change of the JES about* $3.75\% - 7.5\%$. *Shown are distribution in ATLFAST-1 samples that enter the training of the MLP classifier. Plotted is signal,* $M_{\mathrm{H}} = 200$ GeV *and* $\omega = 5$ *(left panel) and the added important W and Z bosons backgrounds (right panel).*

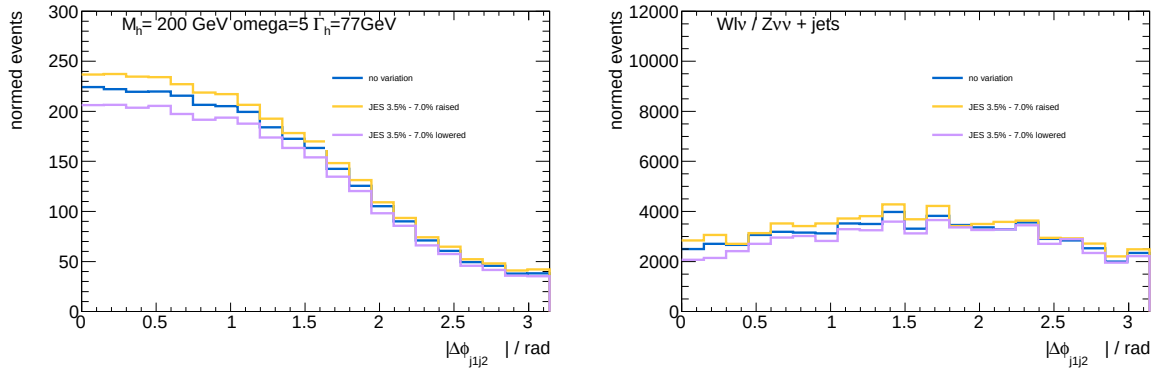

Fig. B.26: *Systematic variation of the input variable* $\Delta\Phi_{\mathrm{j1j2}}$ *under the change of the JES about* $3.75\% - 7.5\%$. *Shown are distribution in ATLFAST-1 samples that enter the training of the MLP classifier. Plotted is signal,* $M_{\mathrm{H}} = 200$ GeV *and* $\omega = 5$ *(left panel) and the added important W and Z bosons backgrounds (right panel).*

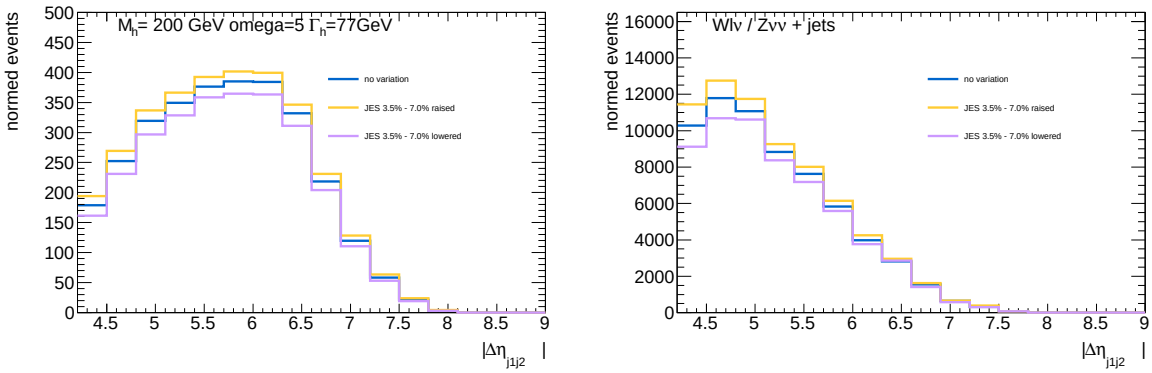

Fig. B.27: *Systematic variation of the input variable* $\Delta\eta_{j1j2}$ *under the change of the JES about* 3.75% – 7.5%. *Shown are distribution in ATLFAST-1 samples that enter the training of the MLP classifier. Plotted is signal,* $M_H = 200$ GeV *and* $\omega = 5$ *(left panel) and the added important W and Z bosons backgrounds (right panel).*

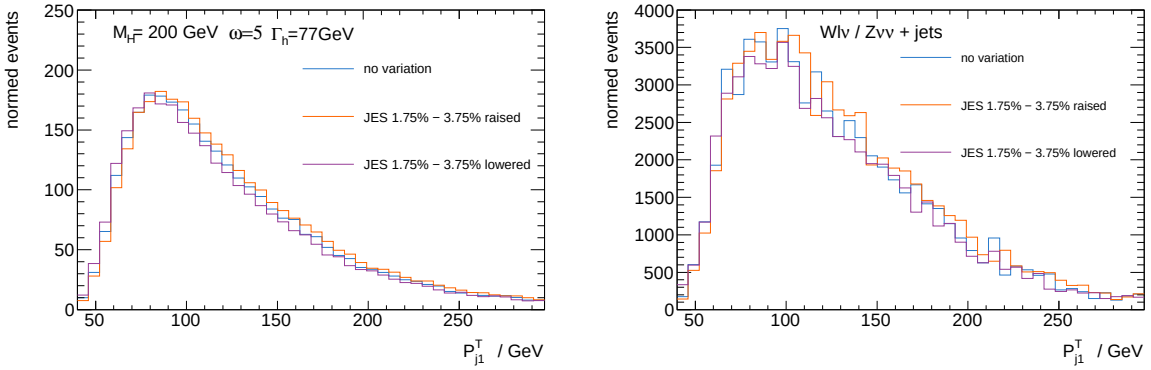

Fig. B.28: *Systematic variation of the input variable* p_{j1}^T *under the change of the JES about* 1.75% – 3.75%. *Shown are distribution in ATLFAST-1 samples that enter the training of the MLP classifier. Plotted is signal,* $M_H = 200$ GeV *and* $\omega = 5$ *(left panel) and the added important W and Z bosons backgrounds (right panel).*

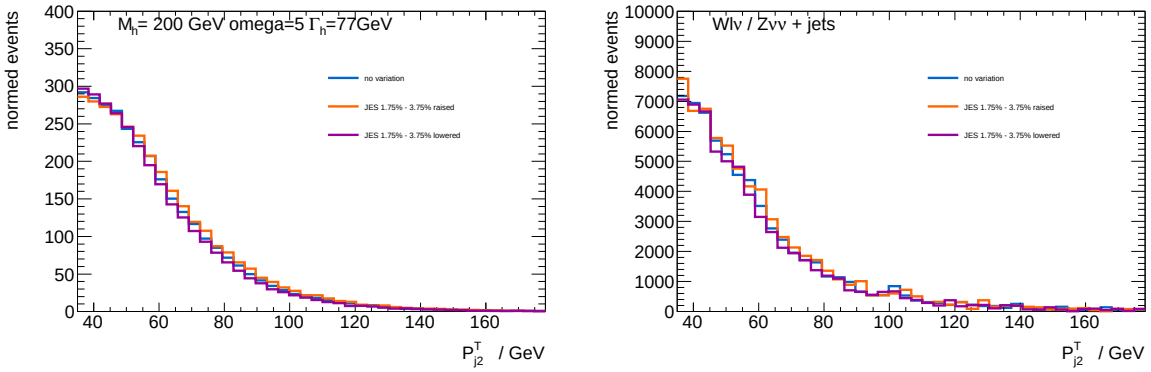

Fig. B.29: *Systematic variation of the input variable* p_{j2}^T *under the change of the JES about* 1.75% – 3.75%. *Shown are distribution in ATLFAST-1 samples that enter the training of the MLP classifier. Plotted is signal,* $M_H = 200$ GeV *and* $\omega = 5$ *(left panel) and the added important W and Z bosons backgrounds (right panel).*

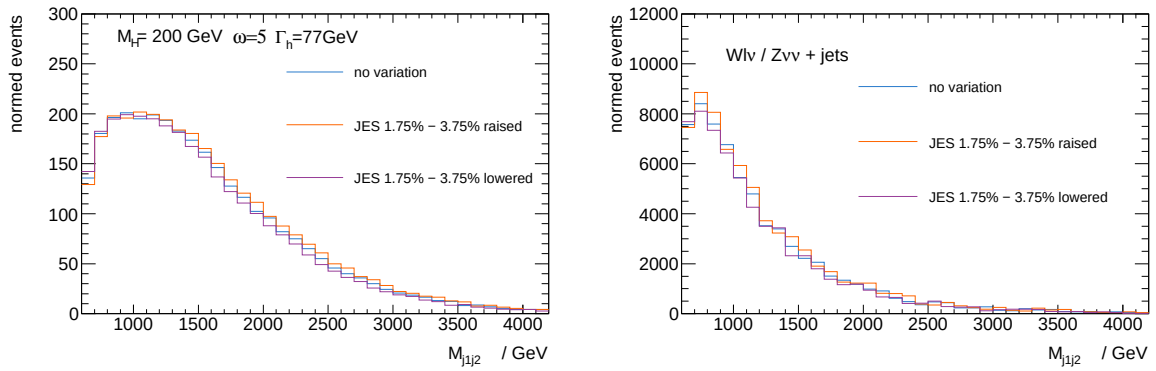

Fig. B.30: *Systematic variation of the input variable* M_{j1j2} *under the change of the JES about* 1.75% – 3.75%. *Shown are distribution in ATLFAST-1 samples that enter the training of the MLP classifier. Plotted is signal,* $M_{\mathrm{H}} = 200$ GeV *and* $\omega = 5$ *(left panel) and the added important W and Z bosons backgrounds (right panel).*

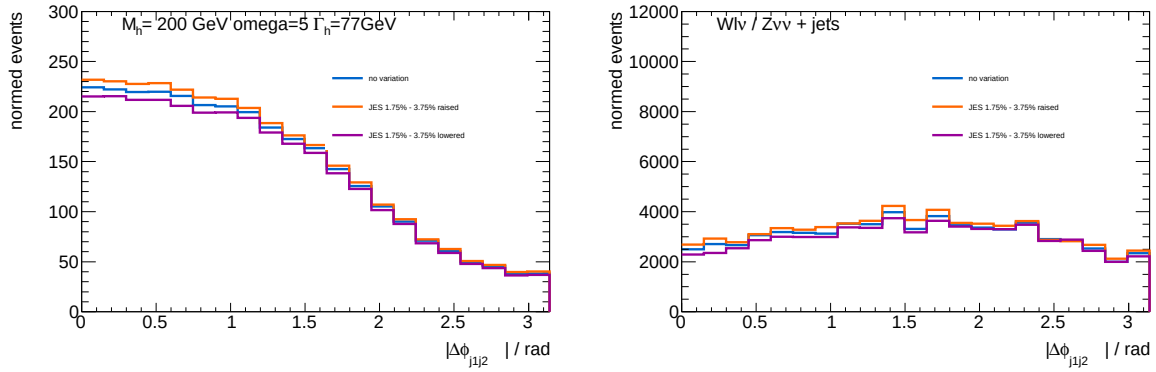

Fig. B.31: *Systematic variation of the input variable* $\Delta\Phi_{\mathrm{j1j2}}$ *under the change of the JES about* 1.75% – 3.75%. *Shown are distribution in ATLFAST-1 samples that enter the training of the MLP classifier. Plotted is signal,* $M_{\mathrm{H}} = 200$ GeV *and* $\omega = 5$*,(left panel), and the added important W boson Z boson background (right panel).*

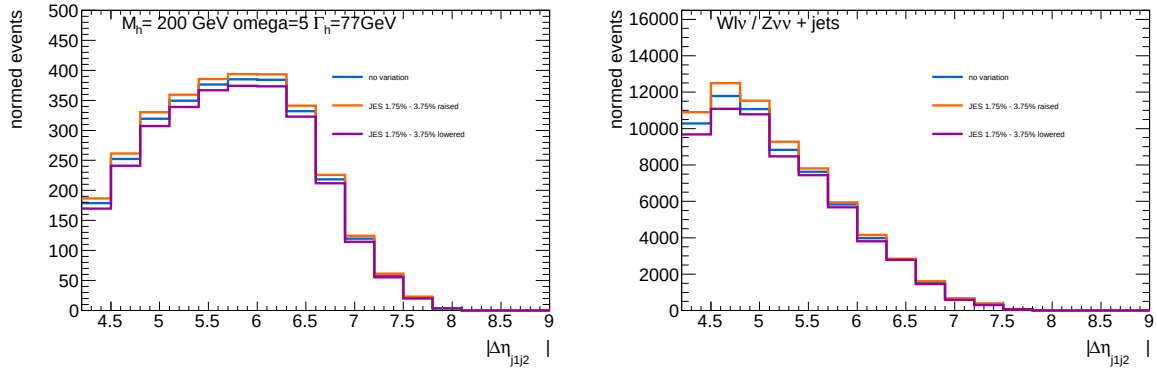

Fig. B.32: *Systematic variation of the input variable* $\Delta\eta_{\mathrm{j1j2}}$ *under the change of the JES about* 1.75% – 3.75%. *Shown are distribution in ATLFAST-1 samples that enter the training of the MLP classifier. Plotted is signal,* $M_{\mathrm{H}} = 200$ GeV *and* $\omega = 5$ *(left panel) and the added important W and Z bosons backgrounds (right panel).*

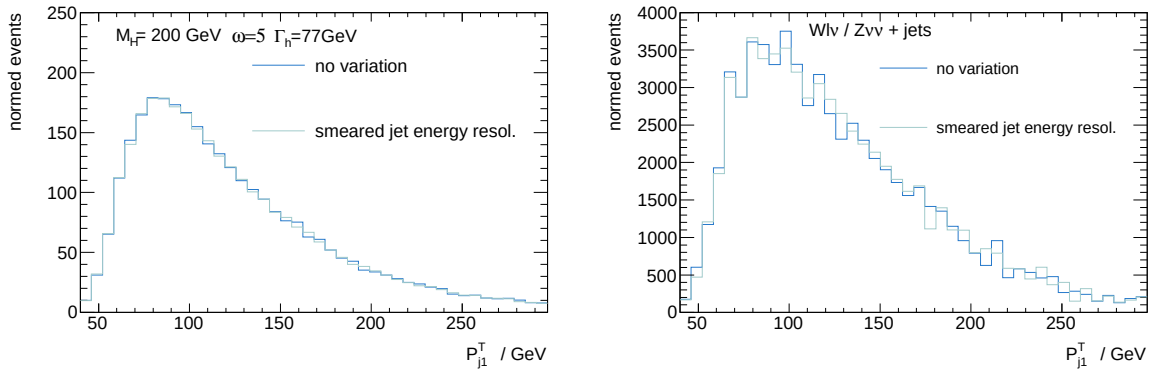

Fig. B.33: *Systematic variation of the input variable p_{j1}^{T} under the random smearing of the jet energy resolution. Shown are distribution in ATLFAST-1 samples that enter the training of the MLP classifier. Plotted is signal, $M_H = 200$ GeV and $\omega = 5$ (left panel) and the added important W and Z bosons backgrounds (right panel).*

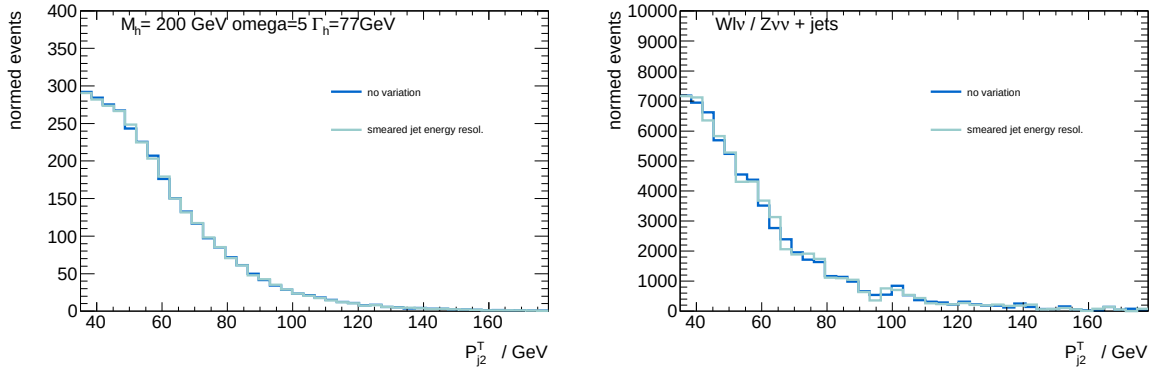

Fig. B.34: *Systematic variation of the input variable p_{j2}^{T} under the random smearing of the jet energy resolution. Shown are distribution in ATLFAST-1 samples that enter the training of the MLP classifier. Plotted is signal, $M_H = 200$ GeV and $\omega = 5$ (left panel) and the added important W and Z bosons backgrounds (right panel).*

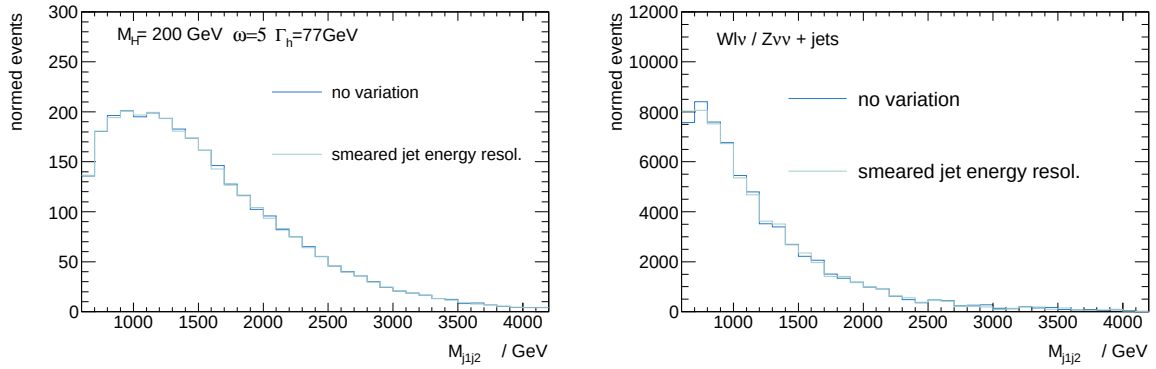

Fig. B.35: *Systematic variation of the input variable M_{j1j2} under the random smearing of the jet energy resolution. Shown are distribution in ATLFAST-1 samples that enter the training of the MLP classifier. Plotted is signal, $M_H = 200$ GeV and $\omega = 5$ (left panel) and the added important W and Z bosons backgrounds (right panel).*

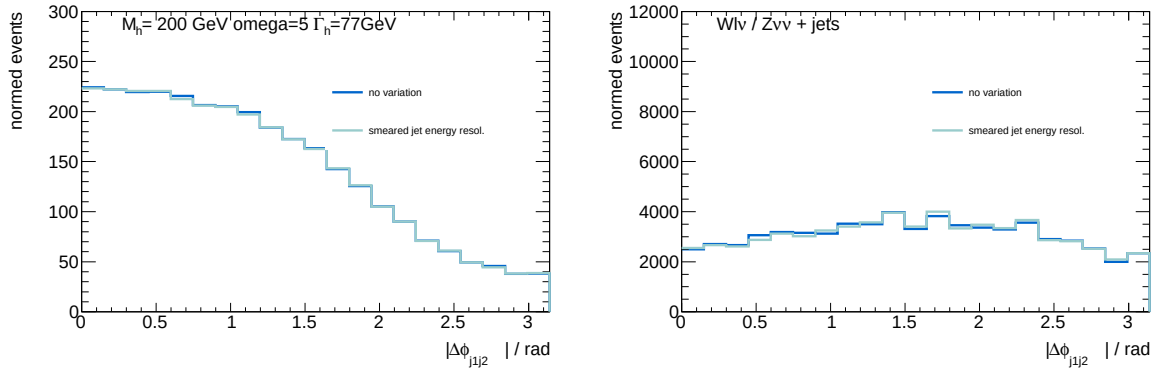

Fig. B.36: *Systematic variation of the input variable $\Delta\Phi_{j1j2}$ under the random smearing of the jet energy resolution. Shown are distribution in ATLFAST-1 samples that enter the training of the MLP classifier. Plotted is signal, $M_H = 200$ GeV and $\omega = 5$ (left panel) and the added important W and Z bosons backgrounds (right panel).*

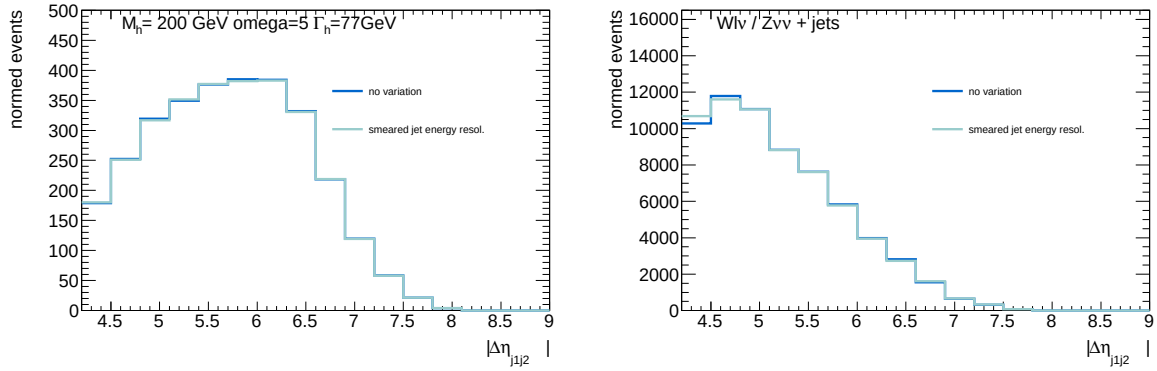

Fig. B.37: *Systematic variation of the input variable $\Delta\eta_{j1j2}$ under the random smearing of the jet energy resolution. Shown are distribution in ATLFAST-1 samples that enter the training of the MLP classifier. Plotted is signal, $M_H = 200$ GeV and $\omega = 5$ (left panel) and the added important W and Z bosons backgrounds (right panel).*

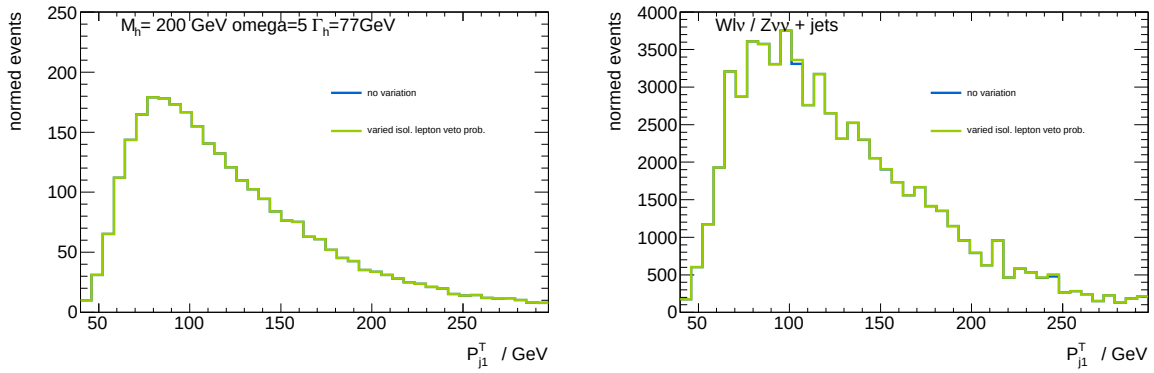

Fig. B.38: *Systematic variation of the input variable $p_{\mathrm{j1}}^{\mathrm{T}}$ under a changed veto probability for isolated leptons. Shown are distribution in ATLFAST-1 samples that enter the training of the MLP classifier. Plotted is signal, $M_{\mathrm{H}} = 200\,\mathrm{GeV}$ and $\omega = 5$ (left panel) and the added important W and Z bosons backgrounds (right panel).*

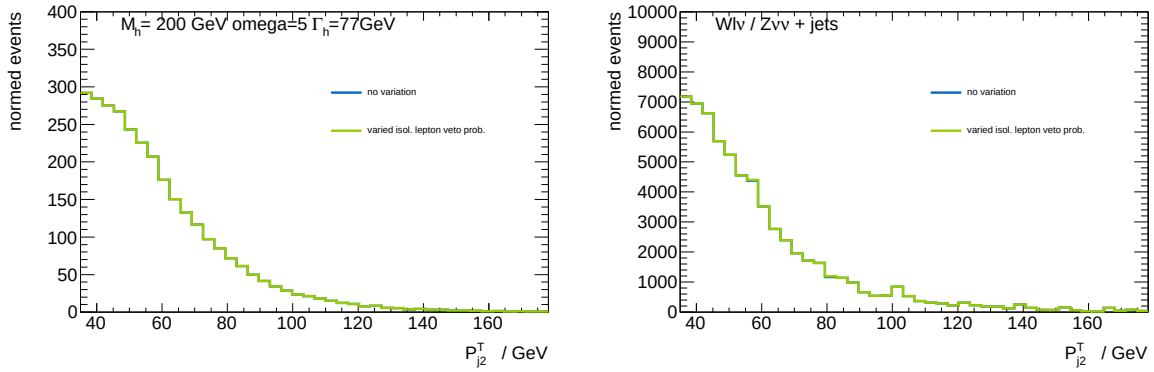

Fig. B.39: *Systematic variation of the input variable $p_{\mathrm{j2}}^{\mathrm{T}}$ under a changed veto probability for isolated leptons. Shown are distribution in ATLFAST-1 samples that enter the training of the MLP classifier. Plotted is signal, $M_{\mathrm{H}} = 200\,\mathrm{GeV}$ and $\omega = 5$ (left panel) and the added important W and Z bosons backgrounds (right panel).*

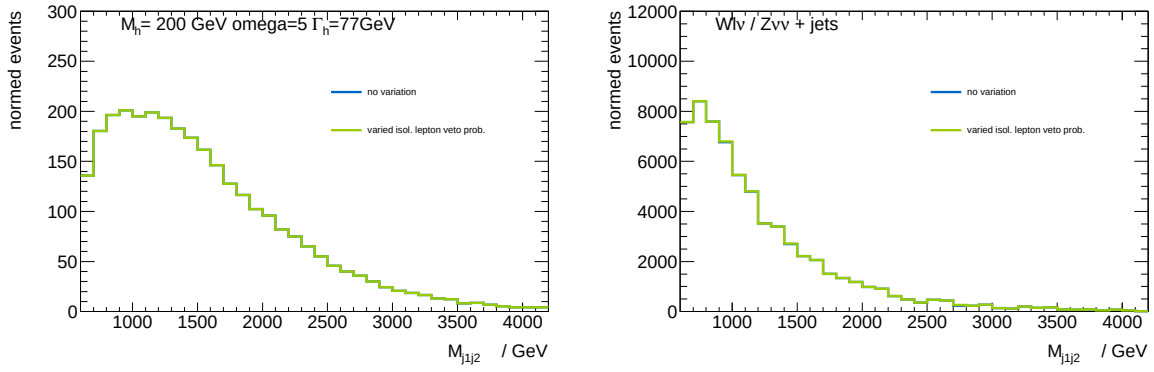

Fig. B.40: *Systematic variation of the input variable M_{j1j2} under a changed veto probability for isolated leptons. Shown are distribution in ATLFAST-1 samples that enter the training of the MLP classifier. Plotted is signal, $M_{\mathrm{H}} = 200\,\mathrm{GeV}$ and $\omega = 5$ (left panel) and the added important W and Z bosons backgrounds (right panel).*

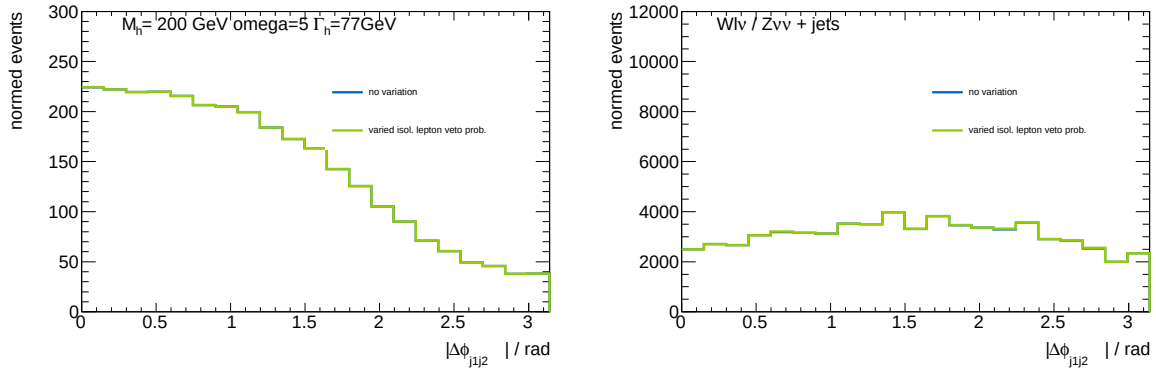

Fig. B.41: *Systematic variation of the input variable $\Delta\Phi_{j1j2}$ under a changed veto probability for isolated leptons. Shown are distribution in ATLFAST-1 samples that enter the training of the MLP classifier. Plotted is signal, $M_H = 200$ GeV and $\omega = 5$ (left panel) and the added important W and Z bosons backgrounds (right panel).*

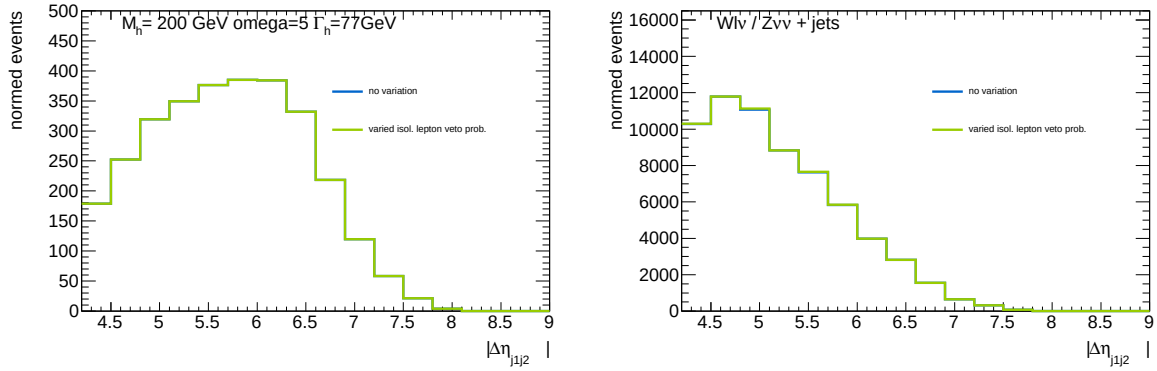

Fig. B.42: *Systematic variation of the input variable $\Delta\eta_{j1j2}$ under a changed veto probability for isolated leptons. Shown are distribution in ATLFAST-1 samples that enter the training of the MLP classifier. Plotted is signal, $M_H = 200$ GeV and $\omega = 5$ (left panel) and the added important W and Z bosons backgrounds (right panel).*

C. Search for Invisibly Decaying Higgs Bosons with Large Decay Width Using the OPAL Detector at LEP

This specifically mass and width dependent invisible Higgs search in the OPAL data [10] was basically designed during a diploma thesis as an proof of principle and there utilised for a search only in the highest centre of mass energy data above 206 GeV. During the beginning of this thesis some major extension and modifications have been undertaken. In particular the decay-width range of the search was extended and made in finer steps. This implied to extend the optimised coverage with specifically chosen mass and width dependent searches. It was also checked that this searches can be used at lower centre of mass energies hence the complete OPAL data set from $\sqrt{s} = 183$ GeVto206 GeV was analysed during this time. Furthermore the complete systematic uncertainties were determined in several representative search points (since the kinematic properties of the signal varied) by the use of data surrogates, that rendered signal free.

For the reason that most of the work was done during this thesis and for reference the published version of this search is appended here.

EUROPEAN ORGANIZATION FOR NUCLEAR RESEARCH

OPAL PR417
CERN-EP-2006-026
August 3, 2006

Search for Invisibly Decaying Higgs Bosons with Large Decay Width Using the OPAL Detector at LEP

The OPAL Collaboration

Abstract

This paper describes a topological search for an invisibly decaying Higgs boson, H, produced via the Bjorken process ($e^+e^- \to \mathrm{HZ}$). The analysis is based on data recorded using the OPAL detector at LEP at centre-of-mass energies from 183 to 209 GeV corresponding to a total integrated luminosity of 629 pb^{-1}. In the analysis only hadronic decays of the Z boson are considered. A scan over Higgs boson masses from 1 to 120 GeV and decay widths from 1 to 3000 GeV revealed no indication for a signal in the data. From a likelihood ratio of expected signal and Standard Model background we determine upper limits on cross-section times branching ratio to an invisible final state. For moderate Higgs boson decay widths, these range from about 0.07 pb (M_{H} = 60 GeV) to 0.57 pb (M_{H} = 114 GeV). For decay widths above 200 GeV the upper limits are of the order of 0.15 pb. The results can be interpreted in general scenarios predicting a large invisible decay width of the Higgs boson. As an example we interpret the results in the so-called stealthy Higgs scenario. The limits from this analysis exclude a large part of the parameter range of this scenario experimentally accessible at LEP 2.

(Submitted to Eur. Phys. J.)

The OPAL Collaboration

G. Abbiendi[2], C. Ainsley[5], P.F. Åkesson[7], G. Alexander[21], G. Anagnostou[1], K.J. Anderson[8], S. Asai[22], D. Axen[26], I. Bailey[25], E. Barberio[7,p], T. Barillari[31], R.J. Barlow[15], R.J. Batley[5], P. Bechtle[24], T. Behnke[24], K.W. Bell[19], P.J. Bell[1], G. Bella[21], A. Bellerive[6], G. Benelli[4], S. Bethke[31], O. Biebel[30], O. Boeriu[9], P. Bock[10], M. Boutemeur[30], S. Braibant[2], R.M. Brown[19], H.J. Burckhart[7], S. Campana[4], P. Capiluppi[2], R.K. Carnegie[6], A.A. Carter[12], J.R. Carter[5], C.Y. Chang[16], D.G. Charlton[1], C. Ciocca[2], A. Csilling[28], M. Cuffiani[2], S. Dado[20], A. De Roeck[7], E.A. De Wolf[7,s], K. Desch[24], B. Dienes[29], J. Dubbert[30], E. Duchovni[23], G. Duckeck[30], I.P. Duerdoth[15], E. Etzion[21], F. Fabbri[2], P. Ferrari[7], F. Fiedler[30], I. Fleck[9], M. Ford[15], A. Frey[7], P. Gagnon[11], J.W. Gary[4], C. Geich-Gimbel[3], G. Giacomelli[2], P. Giacomelli[2], M. Giunta[4], J. Goldberg[20], E. Gross[23], J. Grunhaus[21], M. Gruwé[7], A. Gupta[8], C. Hajdu[28], M. Hamann[24], G.G. Hanson[4], A. Harel[20], M. Hauschild[7], C.M. Hawkes[1], R. Hawkings[7], G. Herten[9], R.D. Heuer[24], J.C. Hill[5], D. Horváth[28,c], P. Igo-Kemenes[10], K. Ishii[22], H. Jeremie[17], P. Jovanovic[1], T.R. Junk[6,i], J. Kanzaki[22,u], D. Karlen[25], K. Kawagoe[22], T. Kawamoto[22], R.K. Keeler[25], R.G. Kellogg[16], B.W. Kennedy[19], S. Kluth[31], T. Kobayashi[22], M. Kobel[3,t], S. Komamiya[22], T. Krämer[24], A. Krasznahorkay Jr.[29,e], P. Krieger[6,l], J. von Krogh[10], T. Kuhl[24], M. Kupper[23], G.D. Lafferty[15], H. Landsman[20], D. Lanske[13], D. Lellouch[23], J. Letts[o], L. Levinson[23], J. Lillich[9], S.L. Lloyd[12], F.K. Loebinger[15], J. Lu[26,b], A. Ludwig[3,t], J. Ludwig[9], W. Mader[3,t], S. Marcellini[2], A.J. Martin[12], T. Mashimo[22], P. Mättig[m], J. McKenna[26], R.A. McPherson[25], F. Meijers[7], W. Menges[24], F.S. Merritt[8], H. Mes[6,a], N. Meyer[24], A. Michelini[2], S. Mihara[22], G. Mikenberg[23], D.J. Miller[14], W. Mohr[9], T. Mori[22], A. Mutter[9], K. Nagai[12], I. Nakamura[22,v], H. Nanjo[22], H.A. Neal[32], R. Nisius[31], S.W. O'Neale[1,*], A. Oh[7], M.J. Oreglia[8], S. Orito[22,*], C. Pahl[31], G. Pásztor[4,g], J.R. Pater[15], J.E. Pilcher[8], J. Pinfold[27], D.E. Plane[7], O. Pooth[13], M. Przybycień[7,n], A. Quadt[31], K. Rabbertz[7,r], C. Rembser[7], P. Renkel[23], J.M. Roney[25], A.M. Rossi[2], Y. Rozen[20], K. Runge[9], K. Sachs[6], T. Saeki[22], E.K.G. Sarkisyan[7,j], A.D. Schaile[30], O. Schaile[30], P. Scharff-Hansen[7], J. Schieck[31], T. Schörner-Sadenius[7,z], M. Schröder[7], M. Schumacher[3], R. Seuster[13,f], T.G. Shears[7,h], B.C. Shen[4], P. Sherwood[14], A. Skuja[16], A.M. Smith[7], R. Sobie[25], S. Söldner-Rembold[15], F. Spano[8,y], A. Stahl[13], D. Strom[18], R. Ströhmer[30], S. Tarem[20], M. Tasevsky[7,d], R. Teuscher[8], M.A. Thomson[5], E. Torrence[18], D. Toya[22], P. Tran[4], I. Trigger[7,w], Z. Trócsányi[29,e], E. Tsur[21], M.F. Turner-Watson[1], I. Ueda[22], B. Ujvári[29,e], C.F. Vollmer[30], P. Vannerem[9], R. Vértesi[29,e], M. Verzocchi[16], H. Voss[7,q], J. Vossebeld[7,h], C.P. Ward[5], D.R. Ward[5], P.M. Watkins[1], A.T. Watson[1], N.K. Watson[1], P.S. Wells[7], T. Wengler[7], N. Wermes[3], G.W. Wilson[15,k], J.A. Wilson[1], G. Wolf[23], T.R. Wyatt[15], S. Yamashita[22], D. Zer-Zion[4], L. Zivkovic[20]

[1]School of Physics and Astronomy, University of Birmingham, Birmingham B15 2TT, UK
[2]Dipartimento di Fisica dell' Università di Bologna and INFN, I-40126 Bologna, Italy
[3]Physikalisches Institut, Universität Bonn, D-53115 Bonn, Germany
[4]Department of Physics, University of California, Riverside CA 92521, USA
[5]Cavendish Laboratory, Cambridge CB3 0HE, UK
[6]Ottawa-Carleton Institute for Physics, Department of Physics, Carleton University, Ottawa, Ontario K1S 5B6, Canada
[7]CERN, European Organisation for Nuclear Research, CH-1211 Geneva 23, Switzerland
[8]Enrico Fermi Institute and Department of Physics, University of Chicago, Chicago IL 60637, USA
[9]Fakultät für Physik, Albert-Ludwigs-Universität Freiburg, D-79104 Freiburg, Germany
[10]Physikalisches Institut, Universität Heidelberg, D-69120 Heidelberg, Germany
[11]Indiana University, Department of Physics, Bloomington IN 47405, USA
[12]Queen Mary and Westfield College, University of London, London E1 4NS, UK
[13]Technische Hochschule Aachen, III Physikalisches Institut, Sommerfeldstrasse 26-28, D-52056 Aachen, Germany

[14]University College London, London WC1E 6BT, UK
[15]Department of Physics, Schuster Laboratory, The University, Manchester M13 9PL, UK
[16]Department of Physics, University of Maryland, College Park, MD 20742, USA
[17]Laboratoire de Physique Nucléaire, Université de Montréal, Montréal, Québec H3C 3J7, Canada
[18]University of Oregon, Department of Physics, Eugene OR 97403, USA
[19]CCLRC Rutherford Appleton Laboratory, Chilton, Didcot, Oxfordshire OX11 0QX, UK
[20]Department of Physics, Technion-Israel Institute of Technology, Haifa 32000, Israel
[21]Department of Physics and Astronomy, Tel Aviv University, Tel Aviv 69978, Israel
[22]International Centre for Elementary Particle Physics and Department of Physics, University of Tokyo, Tokyo 113-0033, and Kobe University, Kobe 657-8501, Japan
[23]Particle Physics Department, Weizmann Institute of Science, Rehovot 76100, Israel
[24]Universität Hamburg/DESY, Institut für Experimentalphysik, Notkestrasse 85, D-22607 Hamburg, Germany
[25]University of Victoria, Department of Physics, P O Box 3055, Victoria BC V8W 3P6, Canada
[26]University of British Columbia, Department of Physics, Vancouver BC V6T 1Z1, Canada
[27]University of Alberta, Department of Physics, Edmonton AB T6G 2J1, Canada
[28]Research Institute for Particle and Nuclear Physics, H-1525 Budapest, P O Box 49, Hungary
[29]Institute of Nuclear Research, H-4001 Debrecen, P O Box 51, Hungary
[30]Ludwig-Maximilians-Universität München, Sektion Physik, Am Coulombwall 1, D-85748 Garching, Germany
[31]Max-Planck-Institute für Physik, Föhringer Ring 6, D-80805 München, Germany
[32]Yale University, Department of Physics, New Haven, CT 06520, USA

[a] and at TRIUMF, Vancouver, Canada V6T 2A3
[b] now at University of Alberta
[c] and Institute of Nuclear Research, Debrecen, Hungary
[d] now at Institute of Physics, Academy of Sciences of the Czech Republic 18221 Prague, Czech Republic
[e] and Department of Experimental Physics, University of Debrecen, Hungary
[f] and MPI München
[g] and Research Institute for Particle and Nuclear Physics, Budapest, Hungary
[h] now at University of Liverpool, Dept of Physics, Liverpool L69 3BX, U.K.
[i] now at Dept. Physics, University of Illinois at Urbana-Champaign, U.S.A.
[j] and Manchester University Manchester, M13 9PL, United Kingdom
[k] now at University of Kansas, Dept of Physics and Astronomy, Lawrence, KS 66045, U.S.A.
[l] now at University of Toronto, Dept of Physics, Toronto, Canada
[m] current address Bergische Universität, Wuppertal, Germany
[n] now at University of Mining and Metallurgy, Cracow, Poland
[o] now at University of California, San Diego, U.S.A.
[p] now at The University of Melbourne, Victoria, Australia
[q] now at IPHE Université de Lausanne, CH-1015 Lausanne, Switzerland
[r] now at IEKP Universität Karlsruhe, Germany
[s] now at University of Antwerpen, Physics Department,B-2610 Antwerpen, Belgium; supported by Interuniversity Attraction Poles Programme – Belgian Science Policy
[t] now at Technische Universität, Dresden, Germany
[u] and High Energy Accelerator Research Organisation (KEK), Tsukuba, Ibaraki, Japan
[v] now at University of Pennsylvania, Philadelphia, Pennsylvania, USA
[w] now at TRIUMF, Vancouver, Canada
[x] now at DESY Zeuthen

[y] now at CERN
[z] now at DESY
[*] Deceased

C.1 Introduction

An intense search for the Higgs boson was undertaken by all of the four LEP experiments in various Standard Model and non–Standard Model search channels. Searches for the Standard Model Higgs boson, exploiting the prediction for its decay modes and also searches for invisible Higgs boson decays as predicted by various extensions of the Standard Model, excluded Higgs masses up to 114.4 GeV [1,2]. These latter searches assumed a rather small invisible decay width comparable to the predicted Standard Model decay width for a light Higgs boson and well below the experimentally achievable mass resolution of about 3 to 5 GeV.

Recent theories that postulate the existence of additional spatial dimensions offer a new possibility for invisible Higgs decays [3]. In such theories the Planck mass is lowered to the TeVrange and a rich spectrum of new particles appears, like graviscalars in the case of flat extra dimensions. Hence the Higgs boson can mix with the graviscalars, which leads to a missing energy signature in the detector [3]. This mixing can result in a large invisible decay width of the Higgs boson, depending on the model parameters, and would therefore alter the Standard Model branching ratios. As a consequence of the broadening of the Higgs resonance in the recoil mass spectrum, the signal-to-background ratio can deteriorate significantly. In a worst case scenario, searches optimised under the assumption of a narrow Higgs resonance might have missed the detection of a kinematically accessible Higgs boson at LEP.

This paper describes a search for the Higgs boson, H, which imposes no constraints on the total decay width. The Higgs boson is assumed to be produced in association with a Z boson via the Bjorken process, $e^+e^- \to \mathrm{HZ}$, where the Z is required to decay hadronically and the invisible Higgs boson is detected as missing energy E_{MIS} in the event. The results are presented in a model-independent way in terms of limits on the Bjorken production cross-section times branching ratio, $\sigma(M_{\mathrm{H}},\Gamma_{\mathrm{H}}) \times \mathrm{BR}(\mathrm{H} \to E_{\mathrm{MIS}})$, at a centre-of-mass energy of 206 GeV, where Γ_{H} is the Breit–Wigner width of the Higgs boson. A simple model extending the Standard Model with additional $\mathrm{SU(3)_C \times SU(2)_L \times U(1)_Y}$ singlet fields which interact strongly with the Higgs boson ("stealthy Higgs scenario" [4]) is chosen as an example for the interpretation of the result. This interaction gives rise to a large invisible decay width of the Higgs boson. This dedicated search expands on the previous decay-mode-independent search [5] carried out by the OPAL Collaboration which reported for the first time limits on the HZ production cross-section, interpreted in the stealthy Higgs model.

The paper is organised as follows. Section 2 introduces the stealthy Higgs scenario. Section 3 gives details about the modelling of signal and background. Section 4 describes the search and the results are interpreted in Section 5. We summarise the results in Section 6.

C.2 The stealthy Higgs scenario

In general renormalisable theories there might be other fundamental scalars, in addition to the Standard Model Higgs boson, that do not interact with normal matter. To investigate the influence of a hidden scalar sector on the Higgs observables the stealthy Higgs scenario conjectures the existence of additional $\mathrm{SU(3)_C \times SU(2)_L \times U(1)_Y}$ singlet fields called phions. Radiative corrections to weak processes are not sensitive to the presence of singlets in the theory because no Feynman graphs containing singlets appear at the one-loop level. Since effects at the two-loop level are below the experimental precision, the presence of a singlet sector is not ruled out by any LEP 1 precision data [4]. These phions would not interact via the strong or electro-weak forces, but couple only to the Higgs boson [4], thus offering invisible decay modes to the Higgs. The width of the Higgs resonance can become large if either the number of such singlets, N, or the coupling, ω, is large, thus leading to a broad mass spectrum recoiling against the reconstructed Z boson.

The Lagrangian of the scalar sector in this model contains only four additional parameters compared to the Standard Model. Not listing the unchanged couplings of the Higgs boson to the fermions, the

scalar part of the Lagrangian is given by

$$\mathscr{L}_{\text{scalar}} = \mathscr{L}_{\text{Higgs}} + \mathscr{L}_{\text{phion}} + \mathscr{L}_{\text{interaction}} \tag{C.1}$$

$$\mathscr{L}_{\text{Higgs}} = -\partial_\mu \phi^\dagger \partial^\mu \phi - \lambda\,(\phi^\dagger\phi - \frac{v^2}{2})^2 \tag{C.2}$$

$$\mathscr{L}_{\text{phion}} = -\frac{1}{2}\,\partial_\mu \vec{\varphi}\,\partial^\mu \vec{\varphi} - \frac{1}{2} m^2_{\text{phion}}\,\vec{\varphi}^2 - \frac{\kappa}{8N}\,(\vec{\varphi}^2)^2 \tag{C.3}$$

$$\mathscr{L}_{\text{interaction}} = -\frac{\omega}{2\sqrt{N}}\,\vec{\varphi}^2\,\phi^\dagger\phi. \tag{C.4}$$

The term $\mathscr{L}_{\text{Higgs}}$ describes the usual Standard Model Higgs doublet ϕ acquiring the Standard Model vacuum expectation value, v, and having its self-coupling λ. In the free Lagrangian of scalar singlets, $\mathscr{L}_{\text{phion}}$, the singlets with mass m_{phion} are denoted as the O(N)-symmetric multiplet $\vec{\varphi}$. The phions also have a self-coupling κ, which is fixed at $\kappa(2M_Z) = 0$, to allow for the widest parameter range of the model. The self coupling term entering loop calculations is suppressed like $1/N$. The interaction term between the Higgs and the additional phions, $\mathscr{L}_{\text{interaction}}$, leads to the phenomenological consequence of invisible Higgs decays because the Higgs boson couples to the phions independently of their mass. The strength of the coupling is instead proportional to the coupling constant ω, which is a free parameter of the model. Even though the vacuum-induced mass term of the phions after the symmetry-breaking is suppressed like $1/\sqrt{N}$ [4], the phions occur in loop corrections to the Higgs boson propagator and therefore affect the resonance width of the Higgs boson. An analytic expression [6] for the change in the Higgs width compared to the Standard Model decay width, Γ_{SM}, can be found in the limit $N \to \infty$, when neglecting the self-coupling of the phions as a small effect:

$$\Gamma_{\text{H}}(M_{\text{H}}) = \Gamma_{\text{SM}}(M_{\text{H}}) + \frac{\omega^2 v^2}{32\,\pi\,M_{\text{H}}} \times \sqrt{1 - 4m^2_{\text{phion}}/M^2_{\text{H}}}. \tag{C.5}$$

The cross-section for the Bjorken process can be calculated from Equations 9 and 10 of reference [4]. Using the parametrisation for the invisible decay width (Equation 1 and 2 in [7]) one can express the total cross-section for the production and invisible decay by

$$\sigma_{(\text{e}^+\text{e}^-\to\text{Z}+E_{\text{MIS}})} = \int ds_I\,\sigma_{(\text{e}^+\text{e}^-\to\text{ZH})}(s_I)\,\frac{\sqrt{s_I}\quad\Gamma^{\text{inv}}_{\text{H}}}{\pi((M^2_{\text{H}} - s_I)^2 + s_I\,\Gamma^2_{\text{H}})}. \tag{C.6}$$

Here s_I denotes the invariant mass squared of the invisible decay products of the Higgs boson. The production rate of these invisible masses is given by the Standard Model cross-section[1)] $\sigma_{(\text{e}^+\text{e}^-\to\text{ZH})}(s_I)$ for a Higgs boson of mass $\sqrt{s_I}$. Hence the Standard Model cross-section completely determines the dependence of the total cross-section on the centre-of-mass energy (see e.g. in [8]). Therefore the total cross-section goes rapidly to zero for Higgs boson masses above the kinematic limit. The effect of the convolution with the Breit-Wigner-like function is a broadening of the resonance in the recoil mass spectrum and hence a dilution of the signal-to-background ratio. In extreme cases of large invisible decay width one could expect the Higgs recoil mass spectrum to mimic the background. In such extreme cases even a light and kinematically accessible Higgs boson might have escaped detection at LEP.

In Section C.5.2 we derive limits on the stealthy Higgs model under the assumption of $m_{\text{phion}} = 0$. By simulating signal spectra for different Higgs boson masses M_{H} and widths Γ_{H}, we set limits in the ω-M_{H} plane in the large N limit.

[1)] By choosing $\omega > 0$ one can prevent the phions from acquiring a non-zero vacuum expectation value and avoid a Higgs-phion mixing due to a non-diagonal mass matrix. In case of non-zero mixing, the couplings of the lightest scalar to the gauge boson would decrease proportional to the cosine of the mixing angle. As a consequence the cross-section of the Bjorken process would be lowered.

C.3 Data sets and Monte Carlo samples

C.3.1 The OPAL detector and event reconstruction

The OPAL detector [9], operated between 1989 and 2000 at LEP, had nearly complete solid angle[3)] coverage and excellent hermeticity. The innermost detector of the central tracking was a high-resolution silicon microstrip vertex detector [10] which lay immediately outside the beam pipe. The silicon microvertex detector was surrounded by a high precision vertex drift chamber, a large volume jet chamber, and *z*–chambers which measured the *z* coordinates of tracks, all in an uniform 0.435 T axial magnetic field. A lead-glass electromagnetic calorimeter with presampler was located outside the magnet coil. In combination with the forward calorimeters, a forward ring of lead-scintillator modules (the "gamma catcher"), a forward scintillating tile counter [9, 11], and the silicon-tungsten luminometer [12], the calorimeters provided a geometrical acceptance down to 25 mrad from the beam direction. The silicon-tungsten luminometer served to measure the integrated luminosity using small angle Bhabha scattering events [13]. The magnet return yoke was instrumented with streamer tubes and thin gap chambers for hadron calorimetry and is surrounded by several layers of muon chambers.

The analysis is based on data collected with the OPAL detector at LEP 2 from 1997 to 2000 at centre-of-mass energies between 183 and 209 GeV. The integrated luminosity analysed is 629.1 pb^{-1}. To compare with the Standard Model Monte Carlo the data are binned in five nominal centre-of-mass-energy points, corresponding to the energies at which the Monte Carlo is produced, as detailed in Table C.1.

A fast online filtering algorithm classifies the events as multi-hadronic. Events are reconstructed from tracks and energy deposits ("clusters") in the electromagnetic and hadronic calorimeters. All tracks and energy clusters satisfying quality requests similar to those described in [14] are associated to form "energy flow objects". The measured energies are corrected for double counting of energy in the tracking chambers and calorimeters by the algorithm described in [14]. Global event variables, such as transverse momentum and visible mass, are then reconstructed from these objects and all events are forced into a two-jet topology using the Durham algorithm [15].

C.3.2 Signal and background modelling

To determine the detection efficiency for a signal from an invisibly decaying Higgs boson and the amount of expected background from Standard Model processes, several Monte Carlo samples are used. Signal events for a hypothetical Higgs boson mass M_{H} decaying with arbitrary broad width Γ_{H} are simulated by reweighting invisibly decaying events of type $\mathrm{H} \to \chi_1^0\chi_1^0$. The mass of neutralinos χ_1^0 is chosen such that the Higgs boson with mass m_i can decay into a pair of neutralinos, which leave the detector without being detected. These Higgs bosons with decays into 'invisible' particles are generated with masses m_i from 1 GeV to 120 GeV with the HZHA [16] generator. The HZHA events are generated assuming the Standard Model production cross-section $\sigma_{(\mathrm{e^+e^-}\to\mathrm{ZH})}$ for the Higgs boson. The test masses m_i are spaced in steps of 1 GeV. The spacing of the test masses is chosen such that they are not resolved by the detector in the signal yielded after a reweighting procedure described in the following. From Equation C.6 one extracts the event weights $w_i(m_i; M_{\mathrm{H}}, \Gamma_{\mathrm{H}})$ for a mass point m_i contributing to the search for a Higgs boson of mass M_{H} and total decay width Γ_{H}. The total decay width Γ_{H} is defined as the sum of Standard Model width and invisible width $\Gamma_{\mathrm{H}}^{\mathrm{inv}}$.

$$w_i(m_i; M_{\mathrm{H}}, \Gamma_{\mathrm{H}}) \;=\; \frac{\frac{d\sigma}{dm_i}(m_i)}{\sum_{m_j=1\,\mathrm{GeV}}^{120\,\mathrm{GeV}} \frac{d\sigma}{dm_j}(m_j)} \tag{C.7}$$

[3)] OPAL used a right-handed coordinate system. The *z* axis pointed along the direction of the electron beam and the *x* axis was horizontal pointing towards the centre of the LEP ring. The polar angle θ was measured with respect to the *z* axis, the azimuthal angle ϕ with respect to the *x* axis.

$$\frac{d\sigma}{dm_i}(m_i) = \frac{\sigma_{(e^+e^- \to ZH)}(m_i)\ 2m_i^2\Gamma_H^{inv}}{\pi((M_H^2 - m_i^2)^2 + m_i^2\Gamma_H^2)}. \quad \text{(C.8)}$$

The Standard Model cross-section $\sigma_{(e^+e^- \to ZH)}$ for the Bjorken production process in Equation C.8 propagates the centre-of-mass energy dependence of the total cross-section into the weights. The unweighted signal Monte Carlo samples contain 2000 events per mass point m_i. In the reweighted signal Monte Carlo sample all test masses contribute according to their weight. The reweighted masses M_H range from 1 to 120 GeVspaced in steps of 1 GeV. The smallest width simulated by this procedure is a Γ_H of 1 GeVand the largest a Γ_H of 3 TeV. The detection efficiency for a Higgs boson with M_H and Γ_H is estimated by the sum of selected event weights assuming binomial errors.

The classes of Standard Model background processes considered are two-photon[2)], two- and four-fermion processes. For simulation of background processes the following generators are used: KK2F [17] and PYTHIA [18] ($q\bar{q}(\gamma)$), GRC4F [19] (four-fermion processes), PHOJET [20], HERWIG [21], Vermaseren [22] (hadronic and leptonic two-photon processes). For Monte Carlo generators other than HERWIG, the hadronisation is done using JETSET 7.4 [18]. The integrated luminosity of the main background Monte Carlo samples is at least 15 times the statistics of the data for the two-fermion background, 24 times for the four-fermion background and 30 times for the two-photon background. The Monte Carlo events are passed through a detailed simulation of the OPAL detector [23] and are reconstructed using the same algorithms as for the real data.

C.4 Search for $e^+e^- \to HZ$ with $Z \to q\bar{q}$ and $H \to E_{MIS}$ final state

The event selection is intended to be efficient for the complete range of possible Higgs masses M_H and corresponding decay widths Γ_H studied in this search. The preselection cuts remain relatively loose and are intended to accumulate signal like event topologies in the data. The final discrimination between signal and background is done by a likelihood-based selection. The optimised likelihood selection has to account for the fact that the kinematical properties of the signal change considerably over the range of masses and width hypotheses considered.

C.4.1 Event topologies

The signal signature is generally characterised by an acoplanar two-jet system from the Z boson decay. We use the term 'acoplanar' for jet pairs if the two jet axes and the beam axis are not consistent with lying in a single plane. The decay products of the Z boson are preferentially emitted into the central part of the detector, recoiling against the invisibly decaying Higgs boson. This is because, in contrast to the irreducible background of $ZZ \to q\bar{q}\,\nu\bar{\nu}$ which is produced with an angular dependence of the differential cross-section proportional to $\cos^2\theta$, the Bjorken process is proportional to $\sin^2\theta$. The Higgs boson decay leads to a large missing momentum and a significant amount of missing energy. In two-photon processes, where the incoming electron and positron are scattered at low angles, usually one or both of the electrons remain undetected. Events of this type have large missing momentum with the missing momentum vector, $\vec{p}_{MIS}$, pointing at low angles to the beam axis. The two-photon events have a small visible invariant mass M_{VIS} and a tiny transverse momentum p_{MIS}^T but a considerable longitudinal momentum along the z-axis in the common case that the two photons do not have equal energy. Due to these special characteristics this background can be easily reduced to a negligible level.

The two-fermion background important for this search consists of $Z/\gamma^* \to q\bar{q}(\gamma)$ events. These events tend to have a big cross-section if one or more initial state radiation photons (abbreviated as ISR photons) are emitted so that the effective centre-of-mass energy $\sqrt{s'}$ is reduced to a value near the Z-resonance

[2)] Two-photon interactions occur when an electron and a positron at high energies and in close proximity emit a pair of photons which interact via the electromagnetic force to generate a fermion pair.

(so-called radiative return events). The emission of ISR photons happens predominantly at small polar angles. In case of a mismeasurement or escape of the ISR photons through the beam pipe these events have a sizeable missing momentum preferentially oriented at small polar angles, close to the beam pipe. In such events the two jets are almost coplanar.

The most difficult background to separate is four-fermion processes with neutrinos in the final state, such as $\mathrm{W^+W^-} \to \ell^{\pm}\nu\ \mathrm{q\bar{q}}$ and $W^{\pm}e^{\mp}\nu \to \mathrm{q\bar{q}}e^{\mp}\nu$ with the charged lepton escaping detection. The irreducible background to this search stems from $\mathrm{ZZ} \to \nu\bar{\nu}\mathrm{q\bar{q}}$ (about 28 % of all ZZ decays) leading to a signature indistinguishable from a signal event with a Higgs mass close to the Z boson mass. The vector bosons are usually not produced at rest, leading to a transverse momentum of the two-jet system and therefore to a large acoplanarity of the jets, as in the signal case. Furthermore, the missing momentum vector points into the central detector more often than for the two-fermion case. To discriminate between this background and the signal one can exploit the difference in the angular distribution of the differential production cross-section.

C.4.2 Preselection

In order to reduce the amount of background data only events fulfilling the following quality criteria are analysed. From cut No.(5) onwards, the cut values were defined using as a guide a simple figure of merit based on the efficiency and expected background. The following cuts remove almost all the two-photon background:

(1) To reduce two-photon and accelerator induced background, track criteria are applied demanding that more than 20 % of all tracks be qualified as good measured tracks [24] and that at least 6 of them be found.

(2) A forward energy veto rejects events with more than 5 GeV in either the left or right compartment of the gamma catcher calorimeters or the silicon tungsten luminometers. Events with more than 2 GeV in the forward calorimeters are also removed.

(3) The missing transverse momentum p^T_{MIS} should exceed 1 GeV and M_{VIS} has to be larger than 4 GeV.

(4) Less than 20 % of the measured visible energy E_{VIS} should be located close to the beam pipe in the region $|\cos\theta| > 0.9$.

(5) The visible energy E_{VIS} must be less than 90 % of $\sqrt{s}$.

(6) It is required that the visible mass of the event should be of order M_{Z}, i.e. $55\ \mathrm{GeV} < M_{\mathrm{VIS}} < 105\ \mathrm{GeV}$. An asymmetric cut around the Z mass is chosen, since with increasing Higgs mass M_{H} the Z bosons will be more and more off-shell.

The remaining backgrounds at this stage, which are more difficult to remove, are mismeasured $\mathrm{Z}/\gamma^* \to \mathrm{q\bar{q}}$ events, four-fermion processes with neutrinos in the final state, such as $\mathrm{W^+W^-} \to \ell^{\pm}\nu\mathrm{q\bar{q}}$ and $W^{\pm}e^{\mp}\nu \to \mathrm{q\bar{q}}e^{\mp}\nu$ with the charged lepton escaping detection (see Table C.2).

(7) To select events that are well measured in the detector with a visible mass M_{VIS} close to M_{Z} and a sizeable transverse momentum p^T_{VIS} the following criterion is applied: $M_{\mathrm{VIS}} + 5 \times p^T_{\mathrm{VIS}} > \sqrt{s}/2$

(8) A large part of the $\mathrm{q\bar{q}}$ events and the remaining two-photon background is eliminated by requiring the visible transverse momentum $p^T_{\mathrm{VIS}} > 6\,\mathrm{GeV}$.

(9) To remove backgrounds in which particles go undetected down the beam pipe, the projection of the visible momentum along the beam axis, p^z_{VIS}, is required to be less than $0.294\sqrt{s}$.

(10) To reduce the radiative $q\bar{q}(\gamma)$ background, the polar angle of the missing momentum vector must lie within the region $|\cos\theta_{MIS}| < 0.9$.

(11) The axes of both jets, reconstructed with the Durham algorithm, are required to have a polar angle satisfying $|\cos\theta| < 0.9$ to ensure good containment. Furthermore this cut exploits the fact that events of the WW and ZZ background are produced according to an angular distribution proportional to $\cos^2\theta$.

(12) The remaining background from $Z/\gamma^* \to q\bar{q}$ is characterised by two jets that tend to be back-to-back with small acoplanarity angles, in contrast to signal events in which the jets are expected to have some acoplanarity angle due to the recoiling Higgs boson. Here the acoplanarity angle $\phi_{ACOPLAN}$ is defined as $180^\circ - \phi_{jj}$ where ϕ_{jj} is the angle between the two jets in the plane perpendicular to the beam axis. This background is suppressed by requiring that the jet-jet acoplanarity angle be larger than 5°.

(13) W^+W^- events with one of the W bosons decaying leptonically and the other decaying into hadronic jets are rejected by requiring that the events have no isolated leptons. In this context, leptons are low-multiplicity jets with one, two or three tracks, associated to electromagnetic or hadronic energy clusters, having an invariant mass of less than 2.5 GeVand momentum in excess of 5 GeV. In the case of a single-track candidate, the lepton is considered isolated if there are no additional tracks within an isolation cone of 25° half-angle, and if the electromagnetic energy contained between cones of 5° and 25° half-angle around the track does not exceed 5 % of the sum of the track energy and the electromagnetic energy within the 5° half angle cone. In the case of a two- or three-track candidate, consisting of the tracks and electromagnetic or hadronic energy clusters confined to a cone of 7° half-angle, the lepton is considered isolated if the sum of track and electromagnetic energy between the 7° half-angle cone and a 25° half-angle isolation cone does not exceed 15 % of the lepton energy.

For each individual centre-of-mass energy there is good agreement between the numbers of expected background events and observed candidates after the preselection. Table C.2 gives the number of preselected events summed over all centre-of-mass energies. Figure C.1 shows the distributions for background classes summed over all centre-of-mass energies and three arbitrarily scaled signal distributions (at a centre-of-mass energy of 206 GeV). The efficiencies of the preselection vary on average between 39 % and 55 % for small decay widths and between 45 % and 53 % for larger decay widths above Γ_H = 100 GeV.

C.4.3 Likelihood analysis

To consider the changing kinematic properties of the signal hypotheses in an optimal way, five different likelihood-based analyses for the signal and background discrimination were applied after the preselection. By a likelihood analysis we denote the combination of a set of likelihood input variables, a so-called likelihood, and the corresponding reference distributions of these variables. The reference distributions are filled with events of the specific classes for which the likelihood is calculated. The classes considered in this search are the two- and four-fermion backgrounds and the signal events. The two-photon events are negligible after the preselection. The search uses combinations of two likelihoods and three fixed signal mass ranges for unweighted reference histograms.

To compare the kinematic properties of a selected data event to the hypothesis (M_H,Γ_H) when evaluating the likelihood, one in principle has to fill weighted signal reference distributions for each hypothesis (M_H,Γ_H). This will soon lead to an unmanageable technical effort, given the number of hypotheses scanned. Therefore a compromise was sought in which certain kinematic properties of the signal were emphasised and simultaneously the number of reference histograms kept small. This was achieved by

filling unweighted signal reference histograms. For most of the (M_{H},Γ_{H}) hypotheses all signal masses were used for filling the reference histograms. This reflects the fact that for a very large decay width of the Higgs boson the possible values of kinematical variables are also smeared out over a large range. It was, however, found that the sensitivity of the likelihood selection (i.e. the median expected upper limits on $\sigma(M_{\mathrm{H}},\Gamma_{\mathrm{H}}) \times \mathrm{BR}(\mathrm{H} \to E_{\mathrm{MIS}})$) could be increased further for small widths below 50 GeVby filling reference histograms with signal masses from 50-80 GeVand from 80-120 GeVfor intermediate and heavy Higgs boson masses respectively. A first likelihood was designed for a signal consisting of small masses ($M_{\mathrm{H}} < 80$ GeV) or large masses and a very large width ($\Gamma_{\mathrm{H}} \geq 110$ GeV). In this likelihood input variables are used exploiting the characteristics of the dominant fraction of light masses in the signal mass distribution. However for signal masses above $M_{\mathrm{H}} = 80$ GeVand small or moderate (i.e. below 110 GeV) decay widths, the contribution of large masses dominates the signal mass distribution. In this case the kinematics and topology of the signal events are determined by the higher masses close to the kinematic limit. A second likelihood is therefore built with input variables optimised for such signal characteristics. In the following the choice of the inputs for the two optimised likelihoods are presented.

The first three input variables are used in both likelihoods (see Figure C.3) .

(1) $(1+\mathscr{P}(M_{\mathrm{VIS}} \equiv \mathrm{M_Z}))^{-1}$
$\mathscr{P}(M_{\mathrm{VIS}} \equiv \mathrm{M_Z})$ is the probability of a kinematical χ^2 fit of the jet four-vectors under the assumption that the invariant mass of the two jets is compatible with the Z boson mass. The uncertainties on the measured jet energies are of the order of 5-10 GeV, while the jet directions are measured to approximately 1-2° [25]. This variable depends only weakly on the Higgs mass. For events with non-converging fit the probability is set to zero. They therefore accumulate at a value of 1.

(2) $-\log y_{32}$
The Durham algorithm groups two energy flow objects i and j into a jet as long as their separation in phase space $y_{ij} = 2 \times min(E_i^2, E_j^2) \times (1-\cos(\theta_{ij}))/E_{\mathrm{VIS}}^2$ is smaller then the cut value y_{cut}. The number of jets in an event is predefined to be 2, y_{32} is the value of y_{cut} where the two-jet topology of the event changes to a three-jet topology. Hence the negative logarithm of the so-called jet resolution parameter y_{32} is a measure for the jet topology being more two-jet like (large value of $-\log y_{32}$) or three-jet like (small value of $-\log y_{32}$).

(3) $p_{\mathrm{MIS}}^T/\sqrt{s}$
The transverse missing momentum p_{MIS}^T is one of the most prominent characteristics of signal-like events, but depends very much on the Higgs boson mass. For a heavy Higgs boson produced close to the kinematic threshold almost at rest, the Z boson has almost no boost and decays into two more or less back-to-back jets. In this case the discriminating power of the variable is lost.

The next three variables (see Figure C.4) complete the first likelihood, which is used for all Higgs masses in the domain of very large width > 110 GeVor low Higgs masses < 80 GeV.

(4) ϕ_{ACOL}
The acolinearity angle ϕ_{ACOL} of the two-jet system is obtained by subtracting the three-dimensional angle between the reconstructed jet-axes from 180°. Events containing a low-mass Higgs boson exhibit on average a larger acolinearity than the background.

(5) $|\cos\theta^*|$
The Gottfried-Jackson angle θ^*, is defined as the angle between the flight direction of the Z boson in the laboratory frame and the direction of the decay products of the Z boson boosted into the Z boson rest-frame. The variable tends to have smaller values for the signal.

(6) $-\log y_{21}$
The variable $-\log y_{21}$ is analogous to $-\log y_{32}$ and measures the compatibility of the event with a two-jet topology. Two-jet events tend to accumulate at small values of $-\log y_{21}$.

The last three variables (see Figure C.5) tune the second likelihood to become more sensitive for large Higgs boson masses and small to moderate widths.

(7) $E_{JET}^{Max}/\sqrt{s}$
The variable E_{JET}^{Max} measures the energy of the most energetic of the two jets. This is on average higher for the four-fermion background, due to the boost of the W and Z pairs, whereas heavy Higgs bosons and a Z boson are produced at rest.

(8) $R_{P_{ti}}$
This variable is the significance of the acoplanarity between the two jets, taking into account detector resolution and acceptance. The discrimination power is enhanced by weighting the acoplanarity with the average jet polar angle, since transverse jet directions are more precisely measured at large polar angles. Signal events tend to have a more significant acoplanarity and thus larger values of $R_{P_{ti}}$ than background. The precise definition of $R_{P_{ti}}$ can be found in the OPAL analyses of $ZZ \to q\bar{q}\nu\overline{\nu}$ events [26].

(9) $(M_{VIS} + M_{MIS})/(M_{VIS} - M_{MIS})$
This variable, described in [27], uses two strongly correlated quantities, the invariant missing mass M_{MIS} and the visible mass of the event M_{VIS}. Depending on the mass reconstruction accuracy it can have positive or negative values. The signal distribution of this variable is broader and accumulates at higher values than for the two- and four-fermion events, which are distributed more narrowly around the origin.

From the two likelihoods and three ranges of signal masses filled in the reference histograms one has six analyses to search for the different hypotheses in M_H and Γ_H. The study of the median expected $\sigma(M_H, \Gamma_H) \times BR(H \to E_{MIS})$ shows that five of these six are sufficient to have an optimally efficient analysis for each signal hypothesis characterised by M_H and Γ_H (see Figure C.2) in the range studied. Likelihood 1 was not used with the reference distribution filled for the signal mass range of 80 to 120 GeV. Figure C.6 a) to c) and g) to h) display examples for the likelihood distributions of all five analyses used. In the histograms the events selected at all five centre-of-mass energies are added up, although each centre-of-mass energy was evaluated separately in the limit setting as explained in Section C.5.1. The appropriate likelihood was calculated for each background, data and signal event. In case of a signal event it was added to the histogram with the weight defined in Equation C.7. The number of expected signal events is normalised according to Equation C.6. The use of different analyses gives rise to varying shapes of the likelihood distributions of the background. Also the various shapes of the signal likelihood distributions are visible for different M_H and Γ_H. Since the form of the likelihood distributions for signal and background can yield additional information in the limit calculation, only a loose cut is applied in the likelihood selection, requiring a signal likelihood larger than 0.2.

C.4.4 Correction of background and signal efficiencies

A correction is applied to the number of expected background events and the signal efficiencies due to noise in the detectors in the forward region which is not modelled by the Monte Carlo. The forward energy veto used in the preselection can accidentally be triggered by machine backgrounds. The correction factor is derived from the study of random beam crossings, and applied individually for each year of data taking. Random beam crossing events were recorded when no physics trigger was active. The fraction

of events that fail the veto on activity in the forward region is below 3.4 % for all runs analysed. The detailed breakdown of the fraction of accidentally vetoed events is given in the last column of Table C.1.

C.4.5 Systematic uncertainties

A possible signal in the data would reveal itself by altering the shapes of the distributions of the discriminating variables. Thus a systematic deviation in the description of a reconstructed observable between Standard Model Monte Carlo and a data sample in which the signal is absent, could wrongly be attributed to the presence of a signal.

The systematic uncertainties in the Monte Carlo description of the kinematic event variables are studied in two control samples at a centre-of-mass energy of 206 GeV. In the first control sample, called two-fermion control-sample in the following, radiative returns contributing to the $q\bar{q}(\gamma)$ processes with photons detected at large angles are selected and the tagged ISR photon is removed from the event in Monte Carlo and data. This creates a $q\bar{q}$-like topology with missing momentum at large angles. The second control sample, called four-fermion control-sample, is obtained by selecting $W^+W^- \to q\bar{q}l\nu$ events and removing the identified isolated lepton from the events in Monte Carlo and data. After this procedure these two control samples possess a topology very similar to signal events. For all kinematic variables x of the preselection and the likelihood selection the mean $\overline{x}$ and the width of the distribution (*RMS*) are compared between Monte Carlo and data, for the two-fermion and four-fermion control-samples. The observables in the two-fermion and four-fermion Monte Carlo are then modified separately according to $x_{\mathrm{MC}}^{\mathrm{NEW}} = (x_{\mathrm{MC}}^{\mathrm{OLD}} - \overline{x}_{\mathrm{MC}}) \times \frac{RMS_{\mathrm{DATA}}}{RMS_{\mathrm{MC}}} + \overline{x}_{\mathrm{DATA}}$. Then all five likelihood selections are repeated separately and the relative change in the number of selected events compared to the unmodified case is taken as the systematic uncertainty.

Since the analysis labelled A1 in Table C.3 is used over a large range of the search plane (see Figure C.2), the systematic uncertainties on the background determined in this analysis A1 are taken as an estimate for the background for all analyses. To determine the effect of the systematic uncertainty on the signal efficiencies, one has to take into account the fact that the kinematic properties of the signal depend on the assumed Higgs mass and decay width. Twelve representative hypotheses are studied with M_{H} chosen to be 20, 60 or 110 GeVand Γ_{H} taking values of 5, 20, 70 and 200 GeV. For these hypotheses the signal Monte Carlo is modified according to the four-fermion correction factors, representing the dominant remaining background after the cut on the signal likelihood. The relative change in selected event weights compared to the unmodified case is then taken as an estimate of the systematic uncertainty on the signal efficiency for a given hypothesis. The root-mean-square of all twelve hypotheses is applied as an (M_{H},Γ_{H})-independent estimate for the whole search area and for all centre-of-mass energies (see Table C.4).

The W pairs are very effectively reduced in the preselection by the isolated lepton veto. Due to the importance of this veto the uncertainty from the lepton isolation angle and the vetoed cone energy is studied in the following way. The half-cone angle of the outer cone is increased and decreased by two degrees, following the studies in [28], and the relative effect on the selection determined. Furthermore the cone energy is varied by 7.4 % and the analyses are repeated. The value of the cone energy rescaling is determined by the relative deviation of the mean of the measured energy of the lepton candidates in the inner cone between data and Monte Carlo in the $W^+W^- \to q\bar{q}l\nu$ sample. For signal efficiencies an analogous study was performed at the twelve points described above. Both results for the relative change of the selection for the cone opening half-angle and cone energy variation are added in quadrature and the root-mean-square of the 12 (M_{H},Γ_{H}) hypotheses was taken to yield the total uncertainty associated with the isolated lepton veto (see Table C.4).

The theoretical prediction on the cross-section for the two- and four-fermion processes adds an uncertainty of 2 % to the background uncertainty [29]. Finally, the uncertainty due to the limited Monte Carlo statistics is evaluated.

Table C.5 summarises the results of the studies. All uncertainties are assumed to be uncorrelated and the individual contributions are added in quadrature to obtain the total systematic uncertainties on the background expectation and signal efficiency. The dominant systematic uncertainties on the signal efficiency arise from the description of the kinematic variables. The background expectation is more affected by the uncertainty in the isolated lepton veto, as the main contribution of the background stems from four-fermion processes. But the uncertainty associated with the description of the kinematic variables is of similar magnitude. The limits quoted in Section C.5.1 were calculated including the uncertainties of Table C.5. To estimate the extent to which the limits depend on the size of the systematic uncertainties, the limit calculation was repeated doubling the systematic uncertainties. A comparison of the limits with single and double systematic uncertainties, done at similar representative points as used for the systematic studies, showed that the excluded cross-sections typically decrease between a half and one and a half percent. A maximal reduction of 2.1 % was found.

C.5 Results

The results of the search using each of the five different likelihood selections, labelled A1-A5, after a cut on the likelihood larger than 0.2 are summarised in Table C.6, which compares the numbers of observed candidates with the Standard Model background expectations. The data are compatible with the Standard Model background expectations. The remaining four-fermion background consists predominantly of W pairs, representing roughly three quarters of the background at energies above the Z pair threshold. Figure C.7 shows examples for signal efficiencies. For small decay widths the dependence on the centre-of-mass energy is weak up to $M_{\mathrm{H}} \approx 80\,\mathrm{GeV}$, and for large widths it is weak up to the kinematic limit. Because of the centre-of-mass energy dependence of the Bjorken cross-section of a Higgs boson with mass M_{H}, the lower centre-of-mass energies contribute more significantly to the sensitivity for lighter Higgs bosons (see e.g. in [8]). For very light Higgs bosons the efficiency is moderately reduced by the preselection cuts demanding a sizeable amount of missing energy. In the case of broader Higgs resonances with high mass, one observes a generally enhanced efficiency since the chance of selecting events from the low mass tail compensates the suppression due to the falling production cross-section of a heavy Higgs boson.

C.5.1 The upper limits on the production cross-section times branching ratio

Upper limits are calculated on the model-independent cross-section $\sigma(M_{\mathrm{H}},\Gamma_{\mathrm{H}}) \times \mathrm{BR}(\mathrm{H} \to E_{\mathrm{MIS}})$ scaled to $\sqrt{s} = 206\,\mathrm{GeV}$. As the likelihood distributions are only loosely cut, one can use not only the information from the integral number of selected events (Table C.6) but also from the shape in a likelihood ratio [30] to set more sensitive upper limits. For each centre-of-mass energy separately, each bin with a signal likelihood larger than 0.2 in the distributions of expected signal, background and selected data is treated as a search channel. For each centre-of-mass energy the number of expected signal events is scaled to the total cross-section (Equation C.6). As with the analysis described in [31], the likelihood distributions are given as discriminating input to a limit program [32]. A likelihood ratio is used to determine the signal confidence level, $\mathrm{CL_S}$, defined in [30, 32], which excludes the presence of a possible signal according to the modified frequentist approach [32]. Additionally the program calculates the median upper number of signal events that could be excluded at 95 % confidence level (CL). This number is then scaled to the total cross-section at the centre-of-mass energy of 206 GeV for each (M_{H},Γ_{H}) hypothesis. The systematic uncertainties on the background expectations and signal selection efficiencies are included according a generalisation of the method described in [33].

A very fine scan of the (M_{H},Γ_{H})-plane was performed by simulating the spectra of Higgs bosons with a mass M_{H} from 1 to 120 GeV and widths Γ_{H} starting at 1 GeV up to 3 TeV. The Higgs boson mass was simulated in steps of $\delta M_{\mathrm{H}} = 1\,\mathrm{GeV}$. Simulated values of Γ_{H} are spaced in steps of 1 GeV up to

5 GeV. A spacing of $\delta\Gamma_H = 5$ GeVis chosen from Γ_H = 5 GeVto Γ_H = 750 GeV. Above this value steps of $\delta\Gamma_H = 50$ GeVare adopted up to the maximal Γ_H of 3 TeV.

Examples of the projections of the observed upper cross-section limits together with the median expected upper limits and the corresponding one and two standard deviation bands on the expected limits are displayed in Figure C.8 for some choices of Γ_H. Above a width of 300 GeVthe exclusion plots look quite similar to the example displayed in Figure C.8i) because the excluded limits do not change very much. The observed limits for $\Gamma_H \gtrsim 60$ GeVare well contained in the one standard deviation bands on the expectations and generally do not exceed two standard deviations except in Figure C.8 a) at M_H = 114 GeV. The discontinuities in the graphs correspond to changes in the analyses. As one can observe, below $\Gamma_H \lesssim 40$ GeVthe analysis are changed more often. Therefore the chance is higher that in a few bins there are statistical fluctuations in the selected data, that lead to a deviation of more than one standard deviation around the median. Also the data selected are highly correlated, as one can see for example in the upward fluctuation around M_H = 114 GeVvisible in Figure C.8 a)-c). All results for the observed upper limits on $\sigma(M_H, \Gamma_H) \times \mathrm{BR}(H \to E_{MIS})$ are summarised in a contour plot (Figure C.9) in the scanned (M_H,Γ_H)-plane. Above Γ_H = 200 GeVthe observed upper limits are in the range of 0.15 pb to 0.18 pb for all M_H and vary very little. For such large Γ_H the recoil mass distribution of the Higgs tends to be more and more uniformly stretched out over the mass range explored. There is not much difference in the selection of signal events for a Higgs boson with e.g. a width of 400 GeVor 600 GeVin the considered range of Higgs masses. This prevents any specific discriminating kinematical properties from being assigned to the expected signal as signal masses of a broad kinematical range are selected with roughly equal probability. Therefore only one likelihood analysis is used in this part of the search area, selecting the same subset of data and background. Since the upper limit on the model-independent cross-section refers to a production cross-section at a centre-of-mass energy of 206 GeV, it must become independent of (M_H,Γ_H) for an extremely large Γ_H. In this case the shape of the Higgs signal would just be a box, weighted with the production cross-section from 1 GeVto the kinematic limit of about 115 GeV. The data are then compared to an approximately constant signal expectation. Hence the upper limit on the cross-section is approximately independent of the (M_H,Γ_H) hypothesis at a value of roughly 0.16 pb. For resonances with a decay width smaller than 200 GeVthere are regions where the limits are below 0.15 pb or even 0.1 pb for M_H between 60 and 74 GeV. In this mass range the number of data events selected is smaller than expected. Above M_H of 85 GeVthe upper limits become larger than 0.2 pb and rise considerably for small widths below 40 GeV(see Figure C.8 a-e). This is due to the fact that the Higgs mass approaches the kinematic limit and the likelihoods which rely on kinematical variables like p^T_{MIS} lose discrimination power. A maximal value of 0.57 pb is observed for M_H of 114 GeVand Γ_H of 1 GeVcorresponding to a circa two-σ excess in the data.

It should be kept in mind that no optimisation of the search has been performed for Γ_H below 5 GeV. In the region of heavy Higgs boson mass $\gtrsim 105$ GeVand small width a search using recoil mass spectra would be more sensitive. Therefore this region is more sensitively covered by searches that have been performed by the LEP experiments documented in [2].

C.5.2 Interpretation of the result in the stealthy Higgs scenario

Interpreting the width Γ_H of a Higgs boson according to Equation C.5, and setting m_{phion} to zero, it was possible to set limits on ω in the stealthy Higgs scenario. A range from $\omega = 0.04$ to $\omega = 24.45$ was probed. The excluded regions are shown in Figure C.10 at 95 % confidence level (CL) in the ω-M_H parameter space. To illustrate the Higgs boson width according to Equation C.5, contours of fixed Γ_H corresponding to a given mass M_H and coupling ω are added to the plot. The maximum excluded invisible width is about Γ_H = 400 GeVfor Higgs boson masses $\lesssim 35$ GeV, decreasing slowly to Γ_H = 115 GeVfor M_H = 100 GeV. The minimal exclusion of $\omega = 0.04$ is observed at M_H = 1 GeVand the maximal exclusion is $\omega = 5.9$ for M_H = 73 GeV. For ω between 0.04 and 0.59 a Higgs mass from 1 to

103 GeV could be excluded. The maximal excluded Higgs mass was 103 GeV for width between 1 and 3 GeV, compared with the expected exclusion of 106 GeV.

The results presented in this study extend the previous decay-mode independent searches for new scalar bosons with the OPAL detector [5] to regions of larger couplings and higher Higgs boson masses. In [5] an interpretation within the stealthy Higgs model yielded a maximal excluded coupling ω for masses around 30 GeV, where ω was excluded up to $\omega = 2.7$. That study excluded Higgs boson masses up to M_{H} = 81 GeV. It should be pointed out that the decay-mode independent searches also studied Higgs widths between 0.1 and 1 GeV and therefore cover the gap between searches within scenarios assuming a narrow decay width of the invisibly decaying Higgs boson [2] and the search presented in this paper up to M_{H} = 81 GeV.

C.6 Conclusions

A dedicated search was performed in the channel $\mathrm{e^+e^-} \to \mathrm{HZ}$ with $\mathrm{Z} \to \mathrm{q\bar{q}}$ and the non-Standard Model decay $\mathrm{H} \to E_{\mathrm{MIS}}$ final state allowing for invisible decay widths of the Higgs boson from 1 GeV up to 3 TeV. The data taken by the OPAL detector at LEP above the W pair threshold were analysed. No indication for a signal was found and upper limits were set on $\sigma(M_{\mathrm{H}}, \Gamma_{\mathrm{H}}) \times \mathrm{BR}(\mathrm{H} \to E_{\mathrm{MIS}})$. The maximal upper limit is 0.57 pb at M_{H} = 114 GeV and Γ_{H} = 1 GeV. Over the scanned region of the (M_{H},Γ_{H})-plane upper limits are generally of the order of 0.15 pb, especially for large values of $\Gamma_{\mathrm{H}} \gtrsim 400$ GeV or Higgs boson masses $\lesssim 85$ GeV.

The limits were interpreted in the stealthy Higgs scenario assuming the presence of a large number of massless singlet states. Limits were calculated on the coupling ω to a hidden scalar sector of the Higgs boson with a given mass M_{H}. A large part of the parameter plane kinematically accessible with LEP 2 was excluded extending a previous exclusion published in [5]. Values for ω between 0.04 (M_{H} = 1 GeV) and 5.9 (M_{H} = 73 GeV) were excluded, and for certain values of ω Higgs boson masses are excluded up to M_{H} = 103 GeV. The possible non-detection of a light Higgs boson at the LEP searches due to non-Standard Model invisible Higgs boson decays is therefore restricted to the case of extremely large decay widths $\gtrsim 400$ GeV.

Acknowledgements

We particularly wish to thank the SL Division for the efficient operation of the LEP accelerator at all energies and for their close cooperation with our experimental group. In addition to the support staff at our own institutions we are pleased to acknowledge the Department of Energy, USA, National Science Foundation, USA, Particle Physics and Astronomy Research Council, UK, Natural Sciences and Engineering Research Council, Canada, Israel Science Foundation, administered by the Israel Academy of Science and Humanities, Benoziyo Center for High Energy Physics, Japanese Ministry of Education, Culture, Sports, Science and Technology (MEXT) and a grant under the MEXT International Science Research Program, Japanese Society for the Promotion of Science (JSPS), German Israeli Bi-national Science Foundation (GIF), Bundesministerium für Bildung und Forschung, Germany, National Research Council of Canada, Hungarian Foundation for Scientific Research, OTKA T-038240, and T-042864, The NWO/NATO Fund for Scientific Research, the Netherlands.

Bibliography

[1] R. Barate *et al.*, ALEPH Collaboration, Phys. Lett. B **565**, 61 (2003).

[2] LEP Higgs Working Group, "Searches for invisible Higgs bosons: Preliminary combined results using LEP data collected at energies up to 209-GeV," [arXiv:hep-ex/0107032].

[3] G.F. Giudice, R. Rattazzi and J.D. Wells, Nucl. Phys. B **595**, 250 (2001). M. Battaglia, D. Dominici, J.F. Gunion and J.D. Wells, "The invisible Higgs decay width in the ADD model at the LHC," [arXiv:hep-ph/0402062].

[4] T. Binoth and J.J. van der Bij, Z. Phys. C **75**, 17 (1997).

[5] G. Abbiendi *et al.*, OPAL Collaboration, Eur. Phys. J. C **27**, 311 (2003).

[6] J.J. van der Bij, "The minimal non-minimal standard model," [arXiv:hep-ph/0603082].

[7] T. Binoth and J.J. van der Bij, "The stealthy Higgs model at future linear colliders," [arXiv:hep-ph/9908256].

[8] J.F. Gunion, H.E. Haber, G.L. Kane and S. Dawson, "The Higgs Hunter's Guide," (Addison-Wesley, Reading MA, 1990), p.140.

[9] K. Ahmet *et al.*, OPAL Collaboration, Nucl. Instr. and Meth. A **305**, 275 (1991).

[10] S. Anderson *et al.*, Nucl. Instr. and Meth. A **403**, 326 (1998).

[11] G. Aguillon *et. al.*, Nucl. Instr. and Meth. A **417**, 266 (1998).

[12] B.E. Anderson *et al.*, IEEE Trans. on Nucl. Science **41**, 845 (1994).

[13] K. Ackerstaff *et al.*, OPAL Collaboration, Phys. Lett. B **391**, 221 (1997).

[14] G. Abbiendi *et al.*, OPAL Collaboration, Eur. Phys. J. C **26**, 479 (2003).

[15] N. Brown and W.J. Stirling, Phys. Lett. B **252**, 657 (1990). G.D. Cowan, J. Phys. G **17**, 1537 (1991).

S. Catani, Y.L. Dokshitzer, M. Olsson, G. Turnock and B.R. Webber, Phys. Lett. B **269**, 432 (1991).

S. Bethke, Z. Kunszt, D.E. Soper and W.J. Stirling, Nucl. Phys. B **370**, 310 (1992). [Erratum-ibid. B **523**, 681 (1998)].

N. Brown and W.J. Stirling, Z. Phys. C **53**, 629 (1992).

[16] P. Janot, CERN 96-01, Vol.2, 309 (1996).

[17] S. Jadach, B.F. Ward and Z.Wąs, Comp. Phys. Comm. **130**, 260 (2000).

[18] T. Sjöstrand, Comp. Phys. Comm. **82**, 74 (1994). T. Sjöstrand, LU TP 95-20.

[19] J. Fujimoto *et al.*, Comp. Phys. Comm. **100**, 128 (1997). J. Fujimoto *et al.*, CERN 96-01, Vol.2, 30 (1996).

[20] E. Budinov *et al.*, CERN 96-01, Vol.2, 216 (1996). R. Engel and J. Ranft, Phys. Rev. D **54**, 4244 (1996).

[21] G. Marchesini *et al.*, Comp. Phys. Comm. **67**, 465 (1992).

[22] J.A.M. Vermaseren, Nucl. Phys. B **229**, 347 (1983).

[23] J. Allison *et al.*, OPAL Collaboration, Nucl. Instr. and Meth. A **317**, 47 (1992).

[24] M.Z. Akrawy *et al.*, OPAL Collaboration, Phys. Lett. B **253**, 511 (1991).

[25] G. Abbiendi *et al.* OPAL Collaboration, Phys. Lett. B **453**, 138 (1999).

[26] G. Abbiendi *et al.*, OPAL Collaboration, Phys. Lett. B **476**, 256 (2000). G. Abbiendi *et al.*, OPAL Collaboration, Eur. Phys. J. C **32**, 303 (2003).

[27] M. Acciarri *et al.*, L3 Collaboration, Phys. Lett. B **485**, 85 (2000).

[28] G. Abbiendi *et al.*, OPAL Collaboration, Eur. Phys. J. C **7**, 407 (1999).

[29] M.W. Grunewald *et al.*, "Four-fermion production in electron positron collisions," [arXiv:hep-ph/0005309].

[30] A.L. Read, J. Phys. G **28** 2693 (2002).

[31] G. Abbiendi *et al.*, OPAL Collaboration, Eur. Phys. J. C **40**, 317 (2005).

[32] T. Junk, Nucl. Instrum. Meth. A **434**, 435 (1999).

[33] R.D. Cousins and V.L. Highland, Nucl. Instrum. Meth. A **320**, 331 (1992).

binned $\sqrt{s}$	**nominal $\sqrt{s}$ (GeV)**	**year**	**int. luminosity (pb^{-1})**	**accid. veto (%)**
$>$ 180–186	183	1997	40.0	3.37
$>$ 186–193	189	1998	199.8	2.24
$>$ 193–198	196	1999	70.4	2.53
$>$ 198–203	200	1999	112.0	2.96
$>$ 203–209	206	2000	206.9	2.22

Tab. C.1: *Breakdown of the analysed integrated data luminosities according to the centre-of-mass energies. The data was binned in five nominal centre-of-mass energies. The last column states the reduction of the signal efficiencies and expected background rates due to accidental triggering of the forward energy veto in the preselection, which is not modelled in the Monte Carlo.*

cut	$\gamma\gamma$	**qq(γ)**	**4-fermion**	**total SM**	**data**
(1)-(5)	48795	15639	4880	69314	74178
(6)	148	10359	1394	11901	11779
(7)	62	9128	1336	10526	10472
(8)	44	4897	1167	6108	6264
(9)	33	1061	964	2058	2116
(10)	18	425	895	1338	1387
(11)	18	423	879	1320	1368
(12)	4	68	820	892	899
(13)	4	60	441	505	498

Tab. C.2: *Expected number of Standard Model background events after the preselection normalised to a data luminosity of 629.1* pb^{-1}*. The total SM background after preselection is expected to be 505* $\pm$ *5(stat)* $\pm$ *21(syst). The contributions of the different subclasses are broken down in column two to four for the two-photon, two-fermion and four-fermion processes respectively.*

analysis			**background uncertainty**	
label	likelihood	reference mass range (GeV)	**kinematic var.**	**isol. lepton veto**
A1	1	1–120	2.4 %	2.4 %
A2	2	1–120	1.6 %	2.3 %
A3	1	50–80	1.0 %	2.5 %
A4	2	50–80	1.6 %	2.6 %
A5	2	80–120	1.1 %	1.5 %
choice for uncertainty			2.4 %	2.4 %

Tab. C.3: *Results of the study of systematic uncertainties of the expected background for the five kinds of analyses, labelled A1-A5, used in the search (see Figure C.2) at a centre-of-mass energy of 206 GeV. Since the analysis labelled A1 covers the largest part of the search area, its uncertainty was chosen as representative uncertainty on the background due to the uncertainty in the kinematic variables and the isolated lepton veto at all centre-of-mass energies.*

signal hypothesis M_H (GeV)	Γ_H (GeV)	efficiency uncertainty kinematic var.	isol. lepton veto
20	**5**	0.6 %	0.6 %
20	**20**	0.4 %	0.7 %
20	**70**	0.3 %	0.7 %
20	**200**	0.1 %	0.7 %
60	**5**	0.7 %	0.8 %
60	**20**	0.7 %	0.8 %
60	**70**	0.2 %	0.8 %
60	**200**	0.3 %	0.7 %
110	**5**	5.5 %	0.7 %
110	**20**	2.9 %	0.8 %
110	**70**	1.3 %	0.8 %
110	**200**	0.1 %	0.8 %
all M_H and Γ_H		1.9 %	0.7 %

Tab. C.4: *Results of the study of systematic uncertainties in twelve representative (M_H,Γ_H)-points at a centre-of-mass energy of 206 GeV. For each source the root-mean-square of the individual uncertainties in the twelve points was taken to get an (M_H,Γ_H) independent estimate of the uncertainty at all centre-of-mass energies.*

source	background uncertainty	efficiency uncertainty
kinematic variables	2.4 %	1.9 %
isolated lepton veto	2.4 %	0.7 %
limited MC statistics	1.0 %	0.2 %
prediction 2- and 4-f cross-sect.	2.0 %	-
total uncertainty	4.1 %	2.0 %

Tab. C.5: *Results of the study of systematic uncertainties of the background for the five analyses (see Table C.3) and of the signal efficiencies in twelve representative (M_H,Γ_H)-points (see Table C.4) at a centre-of-mass energy of 206 GeV. The total uncertainty on background expectation and signal efficiency is applied at all centre-of-mass energies and for all (M_H,Γ_H) hypotheses.*

label	reference masses	likelihood	2-fermion	4-fermion	total SM	data
A1	1–120 GeV	type 1	11	374	$385 \pm 4 \pm 16$	369
A2	1–120 GeV	type 2	3	378	$381 \pm 4 \pm 16$	370
A3	50–80 GeV	type 1	5	315	$320 \pm 3 \pm 13$	305
A4	50–80 GeV	type 2	2	315	$317 \pm 3 \pm 13$	310
A5	80–120 GeV	type 2	8	247	$255 \pm 3 \pm 11$	253

Tab. C.6: *The likelihood selection of events with a signal likelihood exceeding 0.2 according to the different search strategies. The individual contributions to the total Standard Model background of two-fermion and four-fermion background is broken down in the second and third column respectively. For the total Standard Model background the statistical and the systematic uncertainty is also given.*

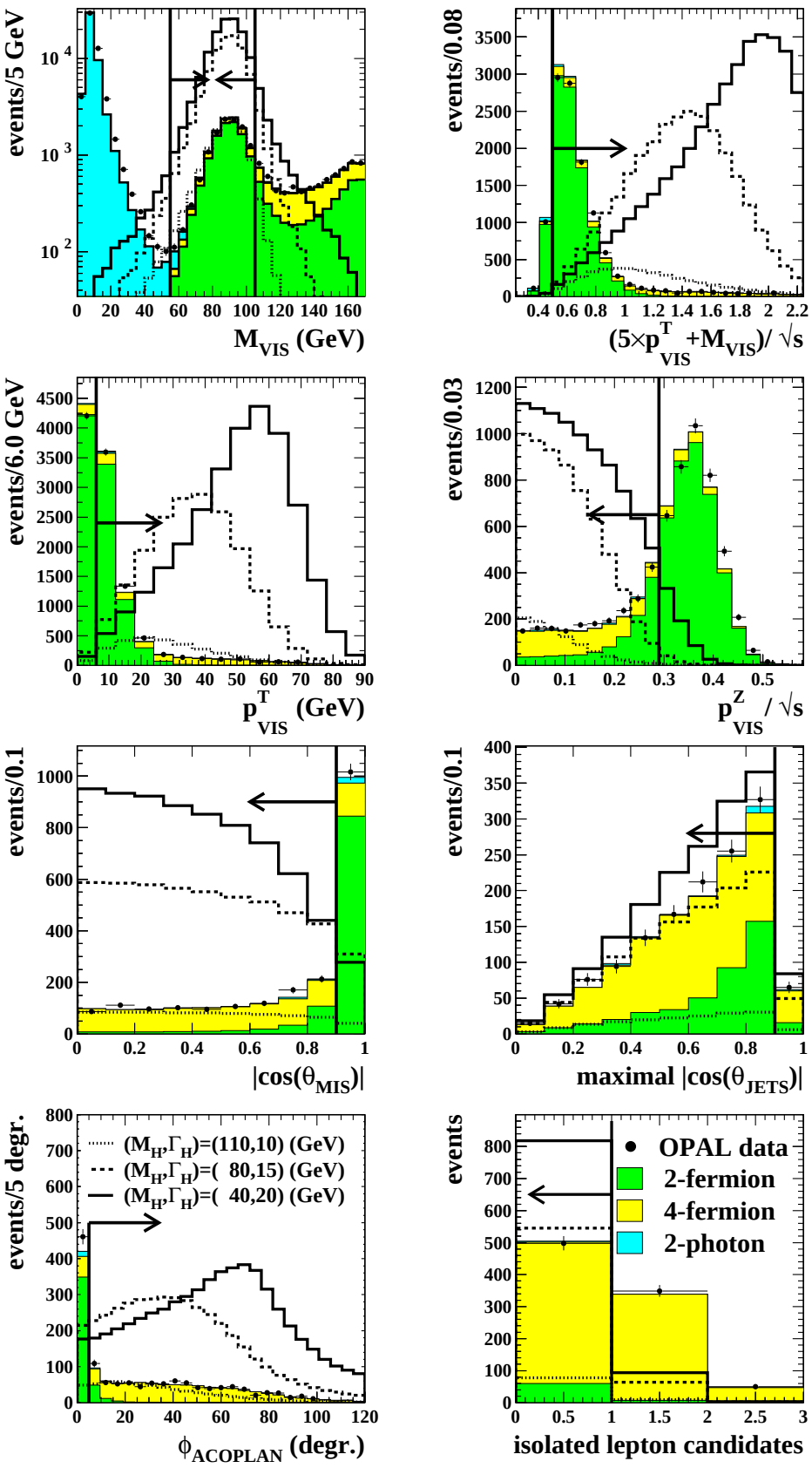

Fig. C.1: *Distribution of the preselection variables after the preselection cuts (1)-(5). All classes of Standard Model background and data are added for all analysed centre-of-mass energies. The distributions of three arbitrarily scaled signal hypotheses at* $\sqrt{s} = 206$ *GeVare displayed as open histograms.*

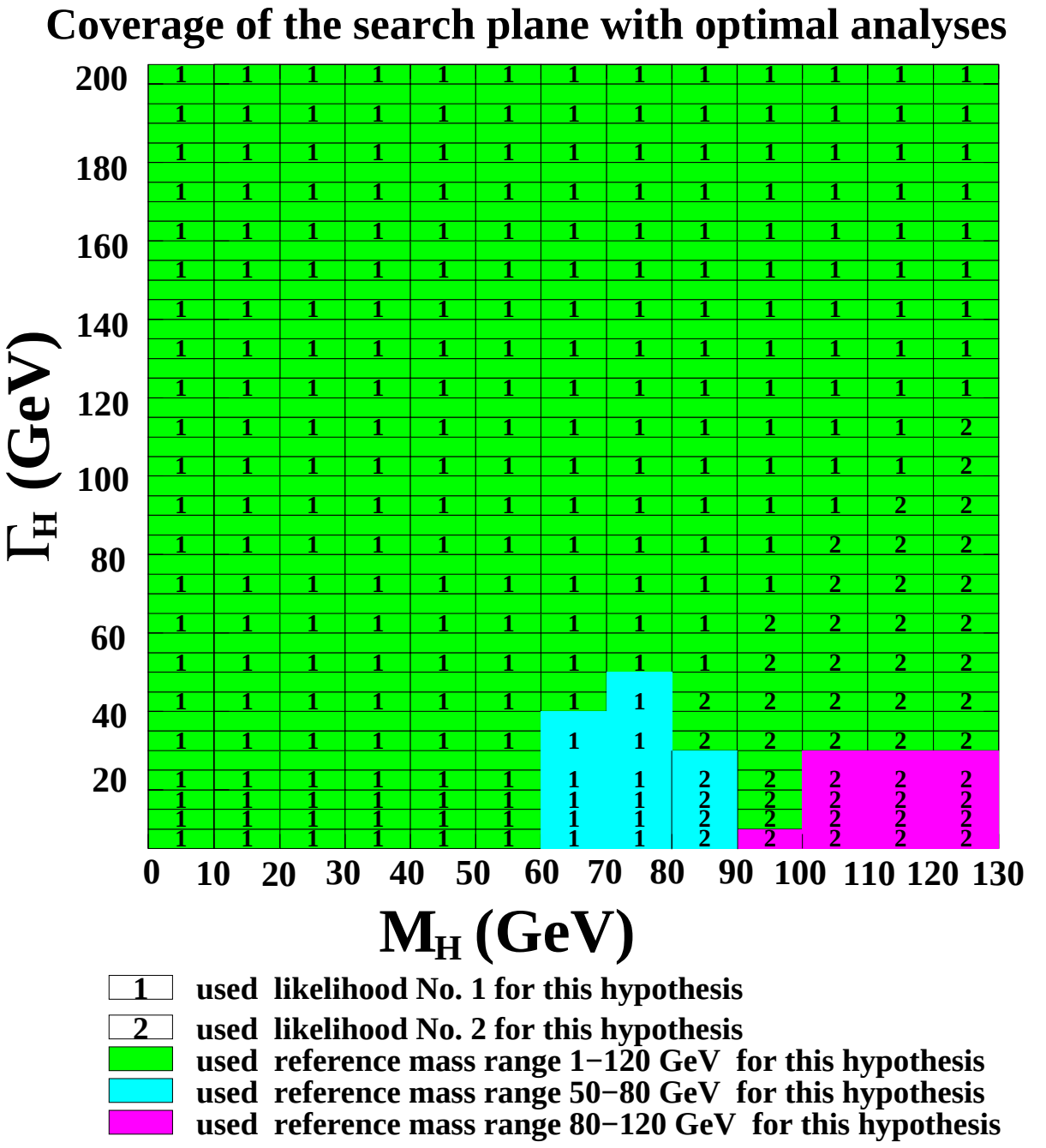

Fig. C.2: *In total five analyses were used to cover the plane of hypothetical Higgs mass and decay width pairings. The analyses differ in whether the first or second likelihood was used (denoted by the number in the cell) and what signal masses where used in filling the reference histograms (depicted by the shading of the cell). The pattern resulted from an optimisation starting with* Γ_H *= 5 GeVup to 50 GeV. Below* Γ_H *= 5 GeVthe pattern was simply continued and not optimised anymore. Above 50 GeVa simple continuation of the pattern was found and proved to be sufficiently sensitive.*

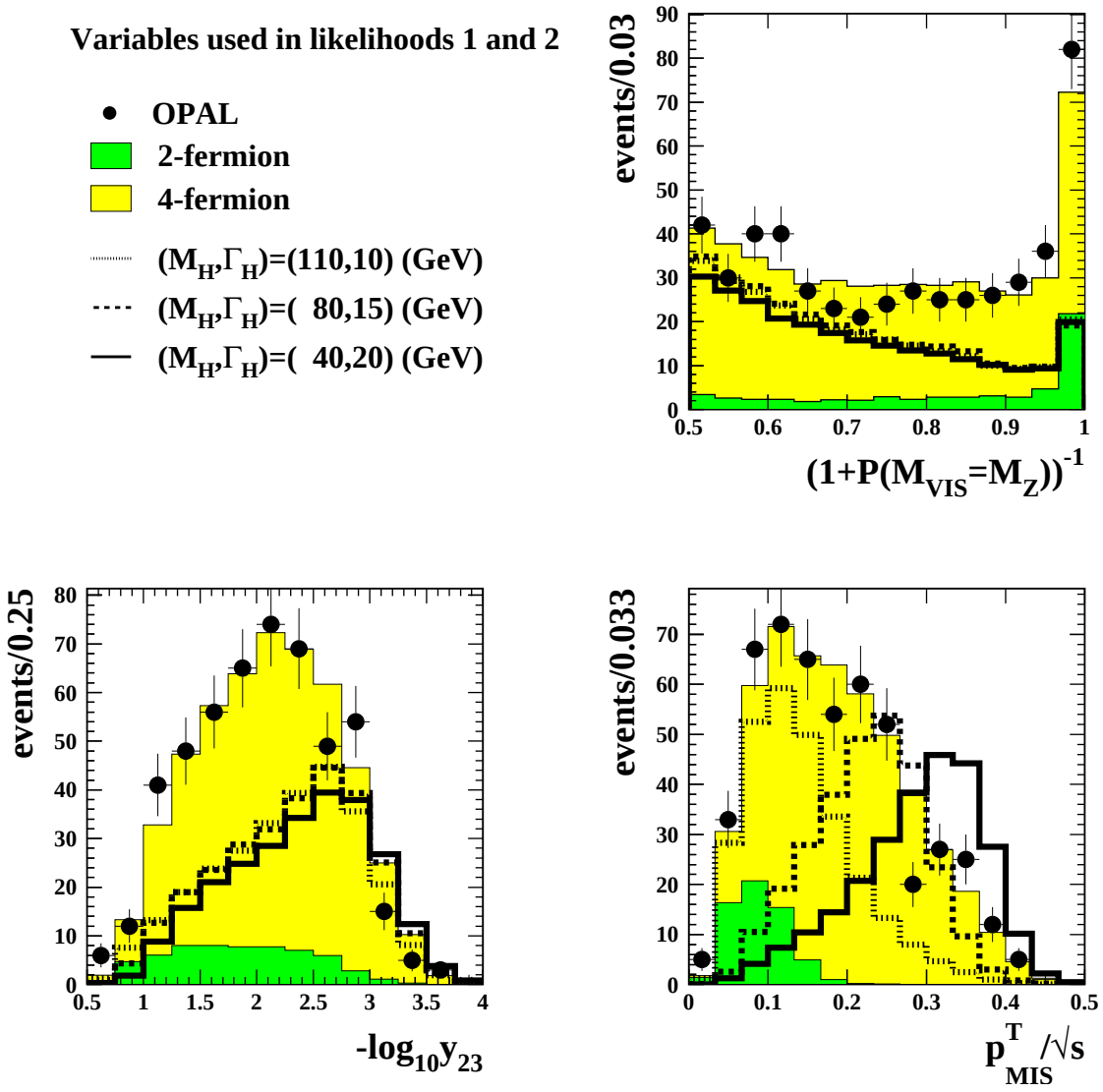

Fig. C.3: *Distributions of the likelihood variables. All classes of Standard Model background and data are added for all centre-of-mass energies analysed. The distributions of three arbitrary scaled signal examples at* $\sqrt{s} = 206$ GeV *are displayed as open histograms. The variables shown contribute to likelihood 1 and 2 as they exploit general properties of the signal signature.*

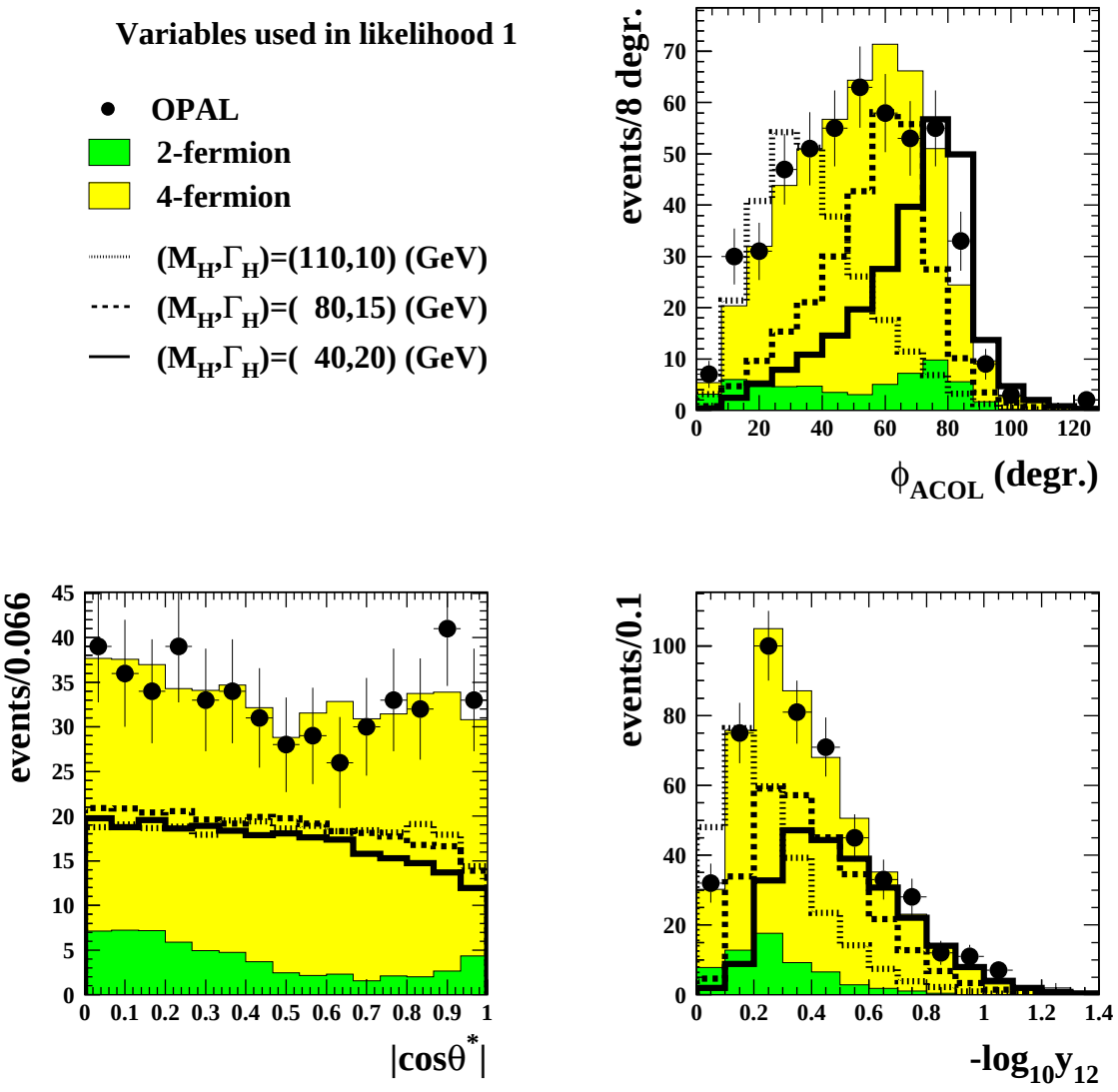

Fig. C.4: *Distributions of the likelihood variables. All classes of Standard Model background and data are added for all centre-of-mass energies analysed. The distributions of three arbitrary scaled signal examples at* $\sqrt{s} = 206$ GeV *are displayed as open histograms. The variables shown are combined with the ones of Figure C.3 to construct the likelihood 1 used in a general search at different* M_{H} *and* Γ_{H}.

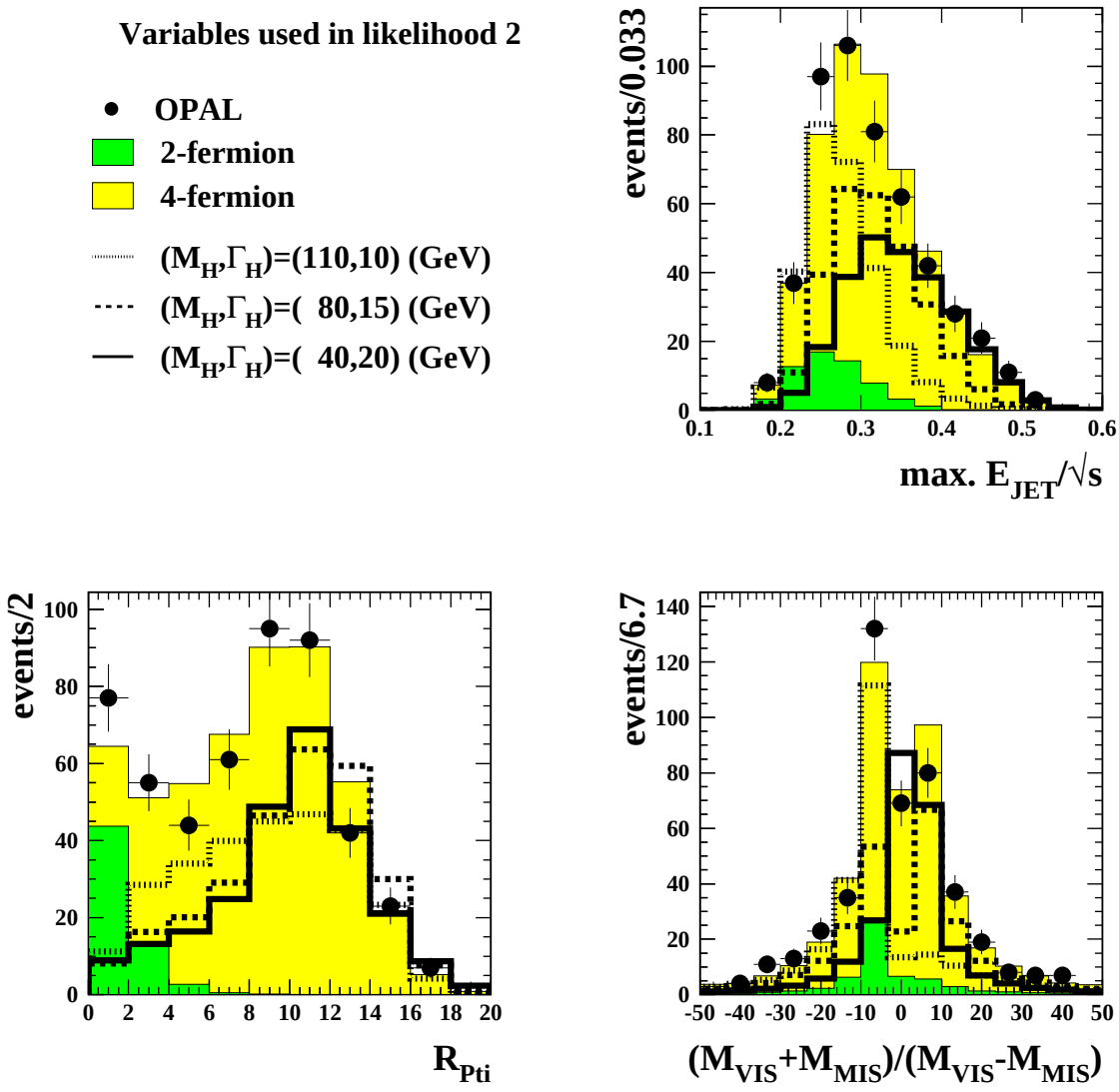

Fig. C.5: *Distributions of the likelihood variables. All classes of Standard Model background and data are added for all centre-of-mass energies analysed. The distributions of three arbitrary scaled signal examples at* $\sqrt{s} = 206$ GeV *are displayed as open histograms. The variables shown have a larger discrimination power for a heavier Higgs boson and contribute with the variables of Figure C.3 to the second likelihood.*

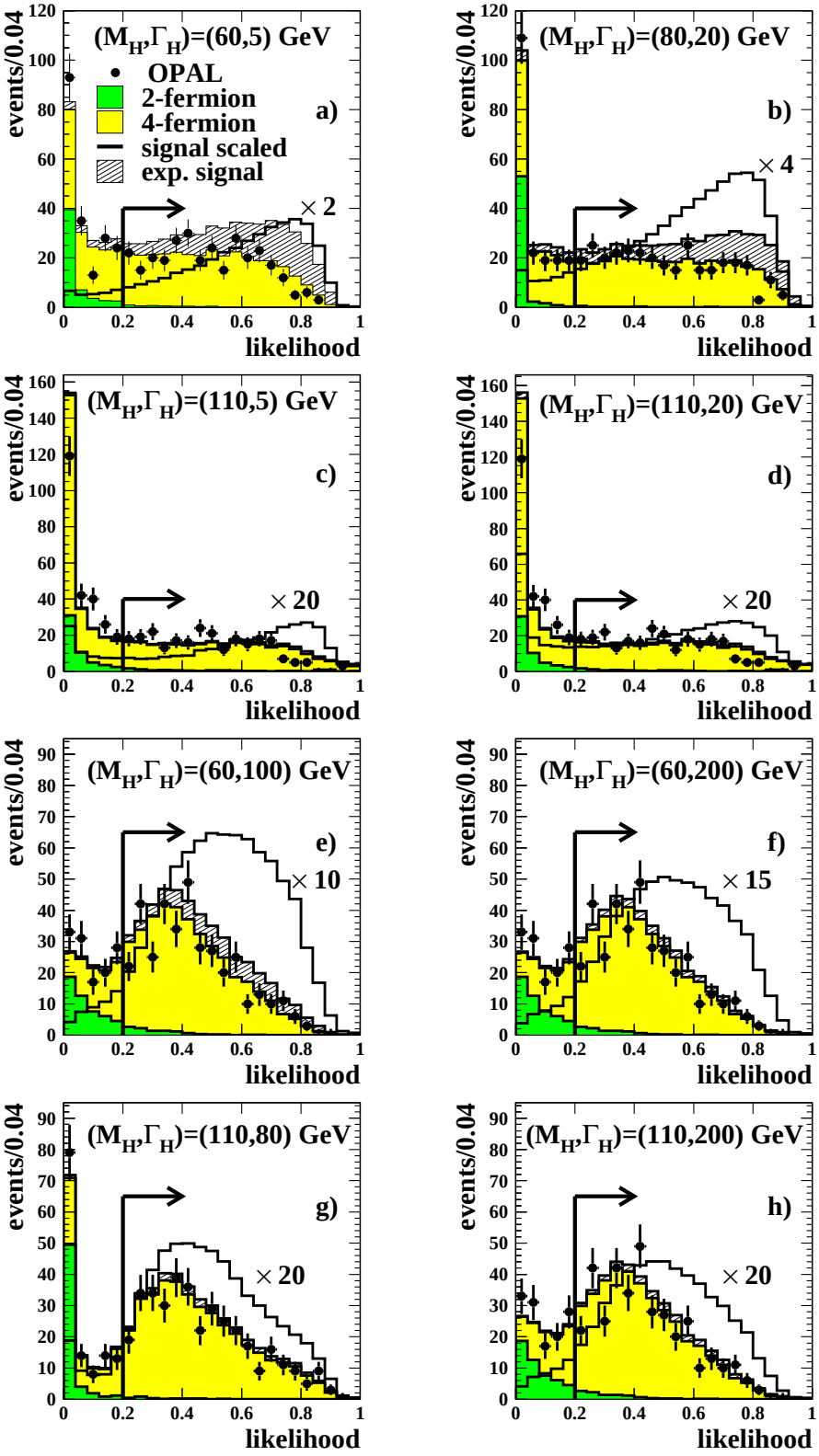

Fig. C.6: *Examples of some of the likelihood selections. Figure C.6 e), f), h) corresponds to analysis A1 (as labelled in Table C.3 and C.6), a) to A3, b) to A4 and c), d) to A5. The OPAL data and the expected 2-fermion and 4-fermion background are added for all analysed centre-of-mass energies. The signal hypothesis in the hatched histograms is normalised to the number of expected signal events and added to the background. The open histograms display the shapes of scaled signal distributions.*

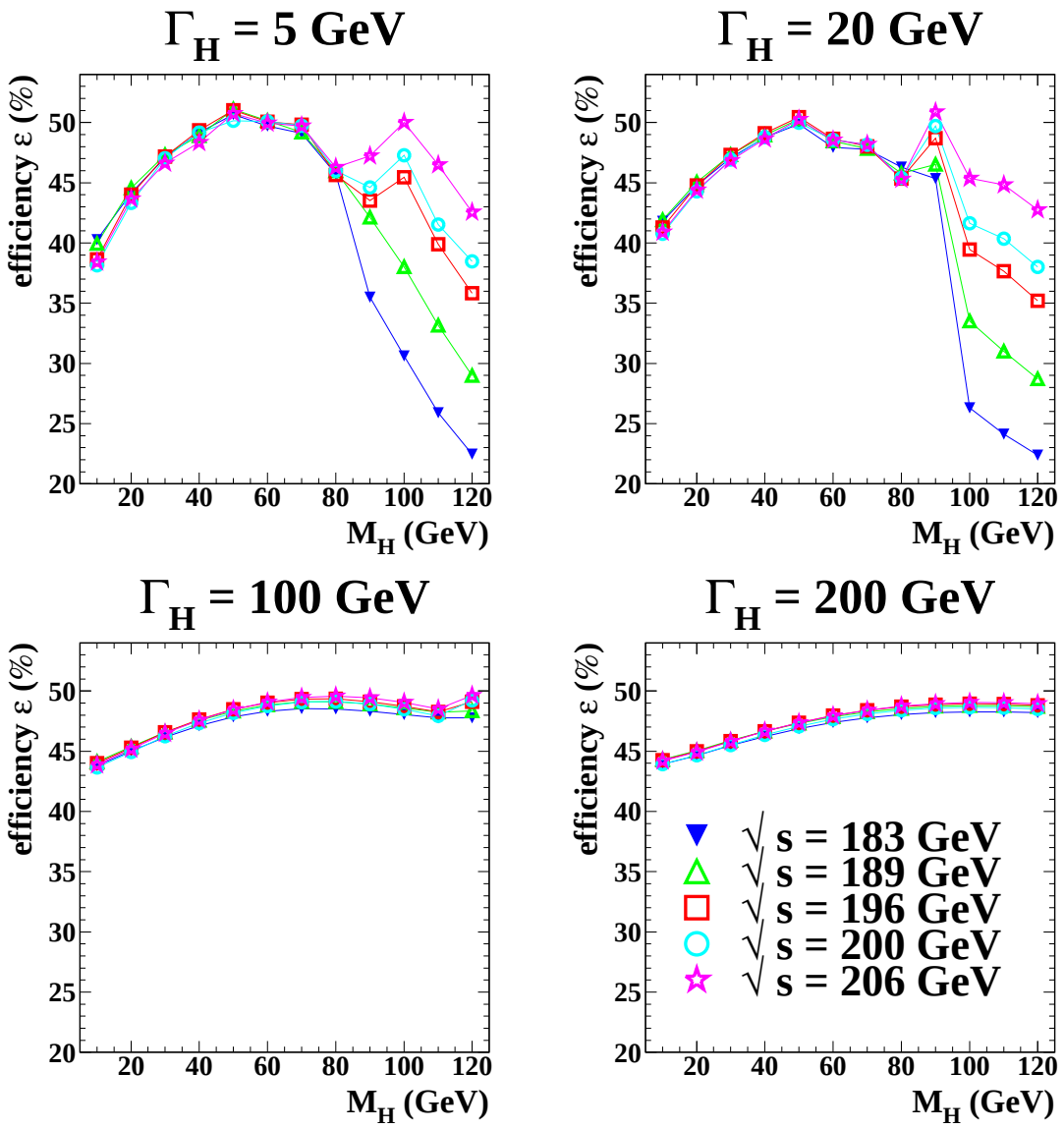

Fig. C.7: *Examples for the selection efficiency after a cut on the signal likelihood greater than 0.2 versus the Higgs mass M_H as function of the assumed decay width Γ_H at the different $\sqrt{s}$. The error is the binomial error on the selected event weights and smaller than the markers. Lines are added to guide the eye. A signal in the range of 80 to 90 GeVsuffers from a drop in the efficiency due to the relatively large remaining W- and Z-pair backgrounds. For a smaller widths Γ_H the efficiency to detect a relatively heavy (above 100 GeV) and more Standard Model like Higgs boson is more restricted by the available $\sqrt{s}$. For a large Γ_H signal hypothesis, the kinematic distributions of events and the distribution of weights assigned to these events are broader. Therefore it is more likely to select a larger fraction of the event weights leading to more uniform efficiency, that does not depend very much on the centre-of-mass energy.*

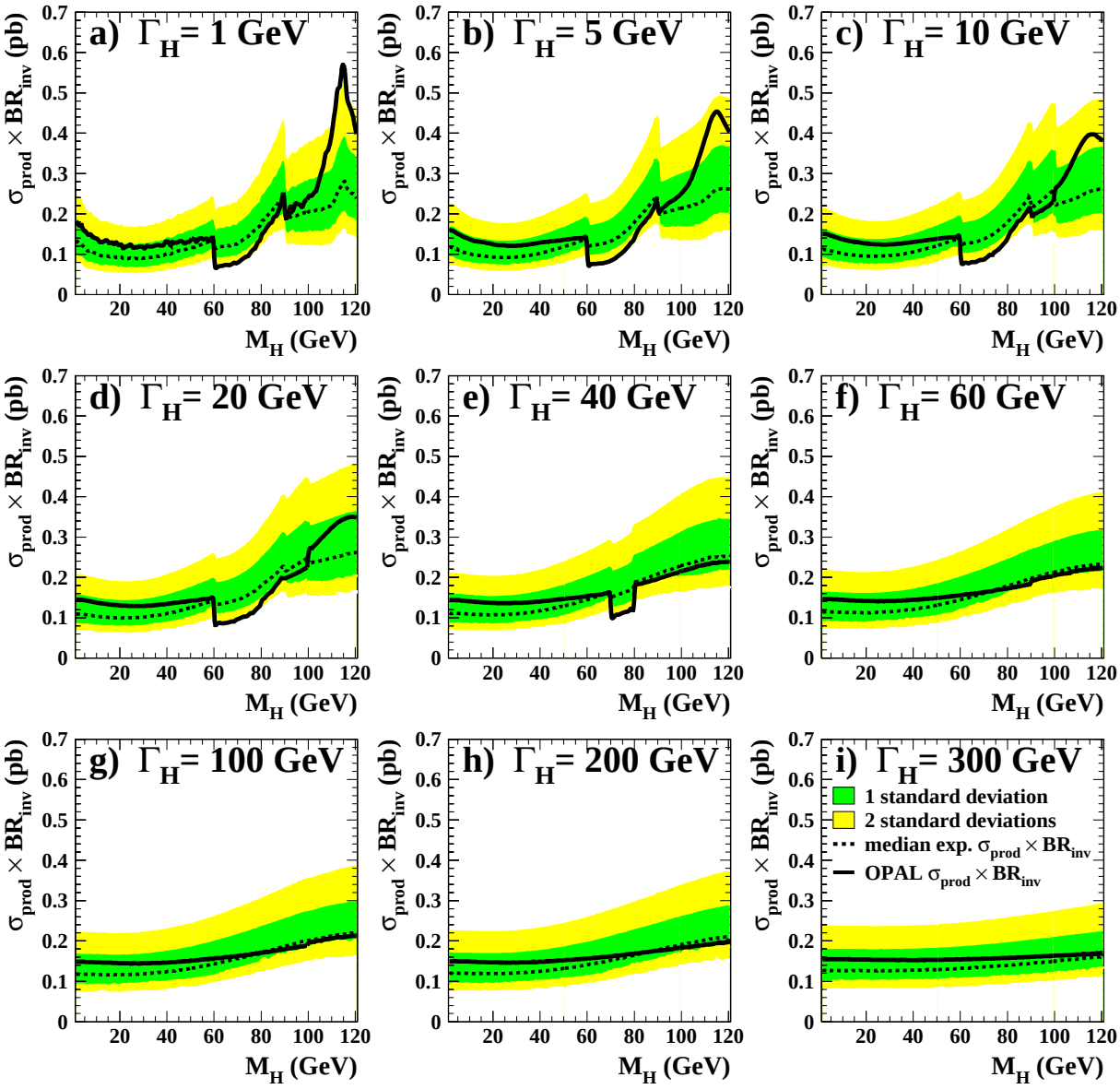

Fig. C.8: *The model independent upper limits at 95 % CL on the production cross-section times branching ratio, $\sigma_{\mathrm{prod}} \times BR_{\mathrm{inv}}$, scaled to a centre-of-mass energy of 206 GeVfor Higgs mass M_{H} and some examples of the Higgs decay width Γ_{H}. The discontinuities in the limits reflect the changes in the analysis used at this mass (see Figure C.2).*

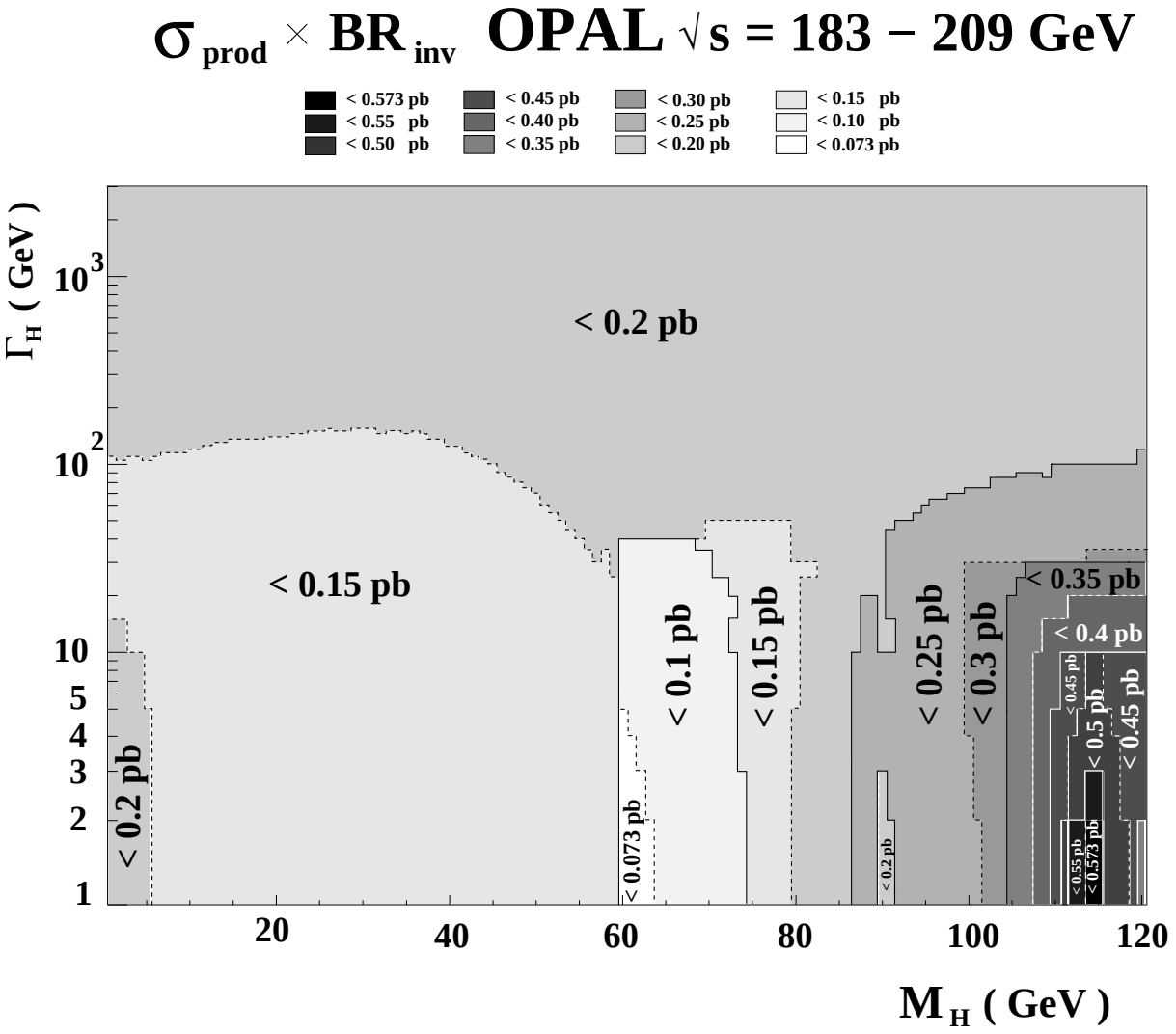

Fig. C.9: *The exclusion contours at 95 % CL on the model independent production cross-section times branching ratio, $\sigma_{\mathrm{prod}} \times BR_{\mathrm{inv}}$, for Higgs boson mass M_{H} and the Higgs boson decay width Γ_{H} up to 3 TeV(note a change in logarithmic scale below Γ_{H} = 5 GeVfor better visibility). Solid and dashed lines delimit areas of excluded upper limits. Cross-sections times branching ratio between 0.07 pb and 0.57 pb are excluded with the OPAL data above $\sqrt{s} = 183$ GeV.*

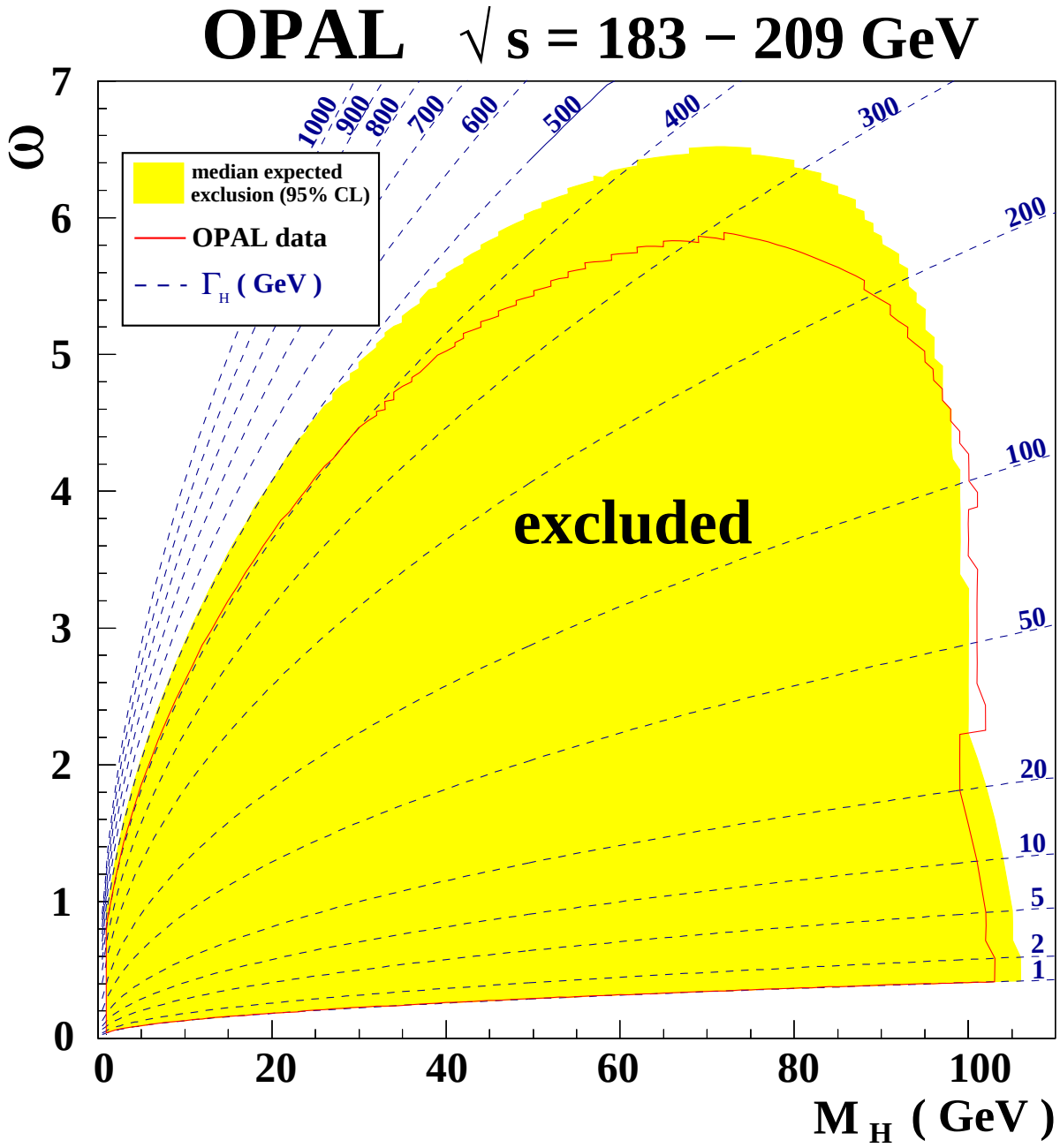

Fig. C.10: *The exclusion contours at 95 % CL on the Higgs mass M_{H} and the Higgs-phion coupling ω of the stealthy Higgs model. The values of ω are related to the decay width Γ_{H} via $\Gamma_{\mathrm{H}}(M_{\mathrm{H}}) = \Gamma_{\mathrm{SM}}(M_{\mathrm{H}}) + \frac{\omega^2 v^2}{32\pi M_{\mathrm{H}}}$, in the case of massless phions (see Equation C.5). Contours of fixed Γ_{H} are also shown in the plot as dashed lines.*

D. Interpretation in an extra-dimensional model with Higgs graviscalar mixing

As described in Chapter 2.2.3, models [66] that describe hypothetical large extra-dimensions obtain scalar Kaluza-Klein excitations. Since their mass spacing is dense for the usual choice of the size of the extra-dimensions two effects of interaction with the Higgs boson occur in such models. The by far dominant effect is the mixing between the Higgs boson and a graviscalar of the Kaluza-Klein tower and a possible the escape of such a mixed state into the bulk of extra-dimension providing effectively a large invisible width of a light Higgs boson. Therefore, the parameter space of the Higgs sector in the ADD models is additionally to the Higgs boson mass, M_{H} extended by the number of extra-dimension δ and the scale on which the gravity influences the SM physics, which is given by the D-dimensional reduced Planck mass M_{D}, and the strength parameter ξ of the mixing term. The second minor effect that would become noticeable only in precision measurements for very high Higgs masses close to the scale where the gravity is the the direct decay into pairs of graviscalars, which gives a small correction to the invisible width of the Higgs. But this width can be surely neglected as long no experiment exist that resolve the width of the Higgs boson precise enough.

It was explained in Chapter 2.2.3 that in all s-channel processes the Higgs will exhibit these additional invisible width by intermediate resonances, hence the SM cross section is reduced by the scaling factor of $\frac{1}{1-r}$ where $r = \frac{\Gamma_{\mathrm{mix}}}{\Gamma_{\mathrm{SM}}}$. Therefore, searches for invisible decays may be utilised in cases the Higgs discovery potential decreases strongly below 5σ. Under the assumption that the production cross section on lower order stay the same as for the SM, the presence of the graviscalars in the Higgs propagator is completely accounted for by generating the invisible width, that broadens the Higgs boson into a Breit-Wigner shaped resonance. Hence, a generic normalisation with the cross section for the stealthy Higgs boson presented as Eq. 2.40 seems reasonable. Therefore, if on can set limits in the M_{H}-Γ_{H} plane, an interpretation in the parameters δ and ξ from the scalar sector of the ADD model is feasible.

D.1 Attempt to interpret the OPAL search in the Higgs-graviscalar mixing scenario

In this section we make the attempt to interpret the results presented in appendix C of the search of the OPAL Collaboration for an invisible Higgs in the Higgs-graviscalar mixing scenario If a hypothesis in the M_{H}-Γ_{H} plane could be excluded at 95 % CL by the search, the formula for effective invisible width is given by Eq. 2.33, which we cite[1)] here once more, is evaluated for a fixed δ, to find the ξ and M_{D}

[1)] Note, in several publications of the authors a typo in the exponent of the factor $20^{(\delta-2)}$ replaced the correct factor $20^{(2-\delta)}$ in the approximations of the invisible width, yielding an extremely large width for $\delta > 2$. But naturally, in the model the width falls with rising number δ of extra-dimensions, which can be envisioned as a reduced graviscalar state density in more extra-dimensions that overlap with the Higgs and are available for mixing. In preparation of the interpretation we cross-checked the formula with the published values, which were unfortunately only for $\delta = 2$ available. There the typo makes no difference. The assumption induced by the faulty formula of considerable larger width as the detector resolution motivated the interpretation of the search in the mixing scenario. We found only later the typo in the publication. And we see now that the correct values are not as large that the width dependent search becomes necessary.

values corresponding to the excluded M_{H}.

$$\begin{aligned}\Gamma_{\mathrm{inv}} &\equiv \Gamma(h \to graviscalar) = 2\pi\xi^2 v^2 \frac{3(\delta-1)}{\delta+2} \frac{m_h^{1+\delta}}{M_D^{2+\delta}} S_{\delta-1} \\ &\sim (16\,MeV) 20^{2-\delta} \xi^2 S_{\delta-1} \frac{3(\delta-1)}{\delta+2} \left(\frac{m_h}{150\,GeV}\right)^{1+\delta} \left(\frac{3\,TeV}{M_D}\right)^{2+\delta}. \end{aligned} \tag{D.1}$$

The formula is evaluated for $\delta = 2$ to $\delta = 6$.

Generally the OPAL search was limited in the Higgs mass range below 110 GeV, due to the kinematic limit. Also the search was designed to look for Higgs decays that are considerable broader than the mass resolution of the detector given by approximately 3 GeV to 5 GeV. The Higgs mixing scenario predicts the largest invisible widths for $\delta = 2$ for low Higgs masses. In the $\delta > 2$ case the width becomes very large for higher Higgs masses. In Tab. D.1 we calculated with Eq. 2.40 some typical invisible width from the strong mixing. The general feature of Eq. D.1 is that the width diminishes with rising number δ. The width rises naturally with the mixing strength parameter ξ, but if the scale M_{D} on which gravity enters is high then this width is strongly suppressed again. And the width will be larger as higher the Higgs mass predicted is. In other words fixing all other parameters as width and ξ the highest sensitivity on M_{D} is reached for high Higgs masses. Given the typical mass resolution in a LEP experiment, one sees in Tab. D.1, that the width stays well below the mass resolution for scales of gravity above 1 TeV. There is no need to perform a width optimised search at LEP in this scenario.

invisible decay width (GeV) by strong Higgs graviscalar mixing $\xi = 1$				
	M_{H}(GeV)	$M_{\mathrm{D}} = 1.5$ TeV	$M_{\mathrm{D}} = 1.0$ TeV	$M_{\mathrm{D}} = 0.5$ TeV
$\delta = 2$	100	0.36	1.81	28.95
	110	0.48	2.41	38.54
$\delta = 3$	100	0.08	0.58	18.53
	110	0.11	0.85	27.13
$\delta = 4$	100	0.01	0.11	7.23
	110	0.02	0.18	11.72
$\delta > 4$	100	not resolved		
	110			

Tab. D.1: Calculated invisible width using Eq. D.1 for various M_{D}, assuming strong mixing ($\xi = 1$), in dependence from the number of extra-dimensions. Here it becomes clear that at LEP for scales of M_{D} not already excluded the width is always of the order or below the mass resolution, i.e. 3 to 5 GeV for the LEP detectors.

The interpretation in the ADD model of the width dependent OPAL search (dark blue contour) as well as the combined result of the invisible Higgs searches by the four LEP experiments (dark green contour) are shown in Fig. D.1 and Fig. D.2. The combined result of the LEP experiments is the exclusion of invisible Higgs decays at lower mass limit of 114.4 GeV (taken from [89]). This LEP combination used optimised searches for the narrow Higgs scenario and much luminosity using data up to $\sqrt{s} = 209$ GeV. The limit is naturally more stringent as from the width dependent OPAL search alone. Since for the regarded mass range below 110 GeV the Higgs is very narrow, even a small mixing parameter $\xi < 1$ will yield almost 100% branching into invisible final states. Therefore the combined result of the LEP experiments on exclusion of invisible Higgs decays will give also a higher sensitivity on M_{D}, which is illustrated by the dark green contour in Fig D.1 and Fig D.2.

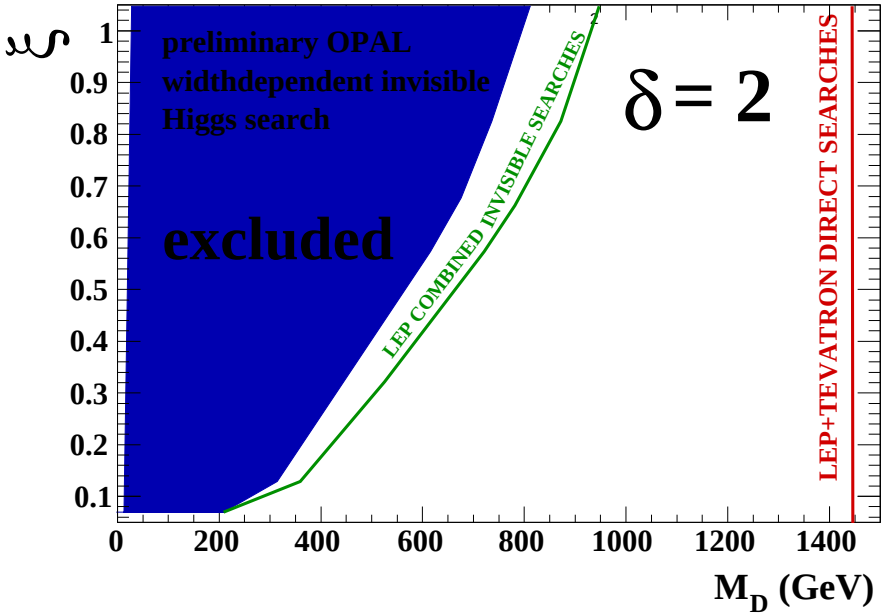

Fig. D.1: *Interpretation of the excluded M_H-Γ_H hypotheses in the OPAL broad invisible Higgs search as excluded part (dark blue) in the M_D-ξ plane in the Higgs graviscalar mixing scenario. In this scenario is $\delta = 2$ chosen. But even for large mixing of $\xi = 1$ the invisible width from mixing stays below the experimental resolution in the probed mass range, being typically 3 to 5 GeV for the LEP detectors. In that case an interpretation of the LEP combined searches for invisible Higgs yields higher sensitivity for M_D. This is indicated by the green contour. The red vertical lines correspond to lower limits on M_D, set by direct graviton searches. These can access a higher mass range since no associated Z boson is produced. The sensitivity of the OPAL search alone and also invisible Higgs searches in Higgs strahlungs process cannot match these direct limits.*

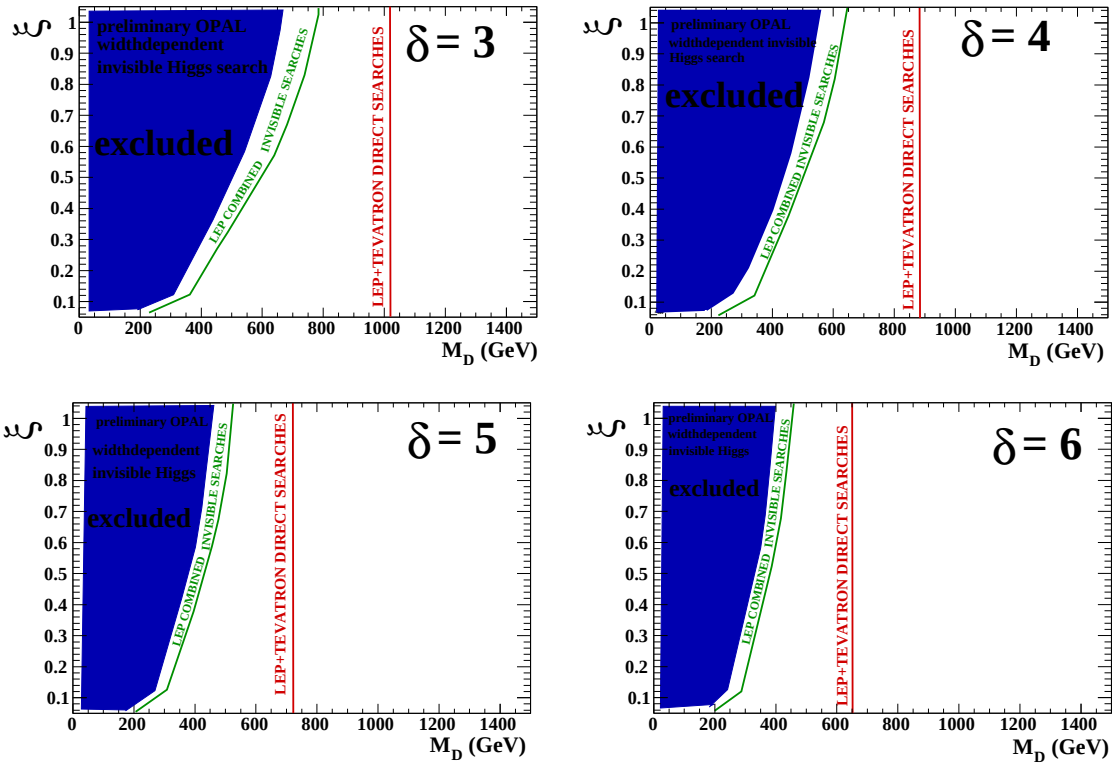

Fig. D.2: *Interpretation of the excluded M_H-Γ_H hypotheses in the OPAL broad invisible Higgs search as excluded part(dark blue) in the M_D-ξ plane in the Higgs graviscalar mixing scenario. The contours correspond to a scenario with scenario $\delta = 3$ (upper left panel), $\delta = 4$ (upper right panel) and $\delta = 5$ (lower left panel), $\delta = 6$ (lower right panel). Also the corresponding exclusion following from the LEP combined limit on the invisible Higgs are given as green contour. The red vertical lines correspond to lower limits on M_D, set by direct graviton searches (Tab. D.2). The sensitivity of the OPAL search alone or searches for invisible Higgs decays in the Higgsstrahlung process cannot match these direct search limits.*

Comparison with direct search for Higgs graviton mixing at LEP

From searches for direct graviton production lower limits on the scale of gravity M_{D} can be deferred. Hence, several collider experiments performed searches for the direct production in various channels. Generally, direct graviton production in colliders would lead to distinct missing energy signature. At LEP 2 direct graviton production can be searched in processes like $e^+e^- \to \gamma \not{E}_T$ or $e^+e^- \to \mathrm{Z}\not{E}_T$. At the TeVatron these searches can use channels like $p\bar{p} \to \gamma \not{E}_T$ or $p\bar{p} \to \mathrm{jets}\not{E}_T$. In Tab. D.2 LEP and TeVatron combined lower limits (depending on the assumed number of extra-dimensions), taken from [82], are listed. Also these direct search limits are included as red vertical line into Fig.D.1 and Fig. D.2, for the corresponding assumed number of δ. For comparison with these direct searches, we collect again

lower bound	$\delta = 2$	$\delta = 3$	$\delta = 4$	$\delta = 5$	$\delta = 6$
M_{D}(TeV)	1.45	1.09	0.87	0.72	0.65

Tab. D.2: Lower bounds on M_{D} from combination of direct TeVatron and LEP 2 searches for graviton productions in extra-dimensions.(Taken from [82])

in Tab. D.3 the lower limits on M_{D} assuming strong Higgs-graviscalar mixing $\xi = 1$, in dependence from the number of extra-dimensions, for the width dependent OPAL and LEP combined invisible Higgs searches. From the comparison one sees that the OPAL search or even the combined LEP result on invisible Higgs searches using the Z boson associated production is not competitive in probing M_{D} with the direct limits from the combined TeVatron and LEP 2 results. This may not only come from the much larger exploited amount of data in the combination of TeVatron and LEP data, but also from the fact that the limits from direct graviton production have a larger mass reach, since no associated Z boson has to be produced. Also it is important to note, that the direct limits do not depend on assumptions about the mixing strength ξ. Nevertheless the OPAL search can confirm the exclusion in a large part of the parameter space of this extra-dimensional scenario. As long as no high Higgs masses can be probed, the direct searches for graviton production will bring more enlightenment on the realised scale of gravity in nature. The invisible Higgs searches are in this context necessary for the clearance of the Higgs sector that will have considerably reduced branching in the canonical visible channels.

lower bound on M_{D}(TeV)					
for $\xi = 1$.	$\delta = 2$	$\delta = 3$	$\delta = 4$	$\delta = 5$	$\delta = 6$
OPAL $M_{\mathrm{H}} > 103$ GeV	0.79	0.67	0.54	0.46	0.39
LEP 2 $M_{\mathrm{H}} > 114$ GeV	0.94	0.78	0.63	0.53	0.45

Tab. D.3: Lower bounds on M_{D}, assuming strong Higgs-graviscalar mixing $\xi = 1$, in dependence from the number of extra-dimensions. Here the the OPAL width dependent search is compared with LEP combined invisible Higgs limit. It is assumed to have a width at the order of the mass resolution, i.e. 3 to 5 GeV. See also Fig. D.1 and Fig. D.2.

D.2 Interpretation of expected ATLAS sensitivity in a Higgs-graviscalar mixing model

The LHC provides centre of mass energies that become of the order of the so far tested gravity scales. It is interesting to see the prospects for invisible Higgs searches in this scenario. In Fig. D.3 from [65] assuming a Higgs mass of 120 GeV, the estimated discovery contours in invisible Higgs searches, on

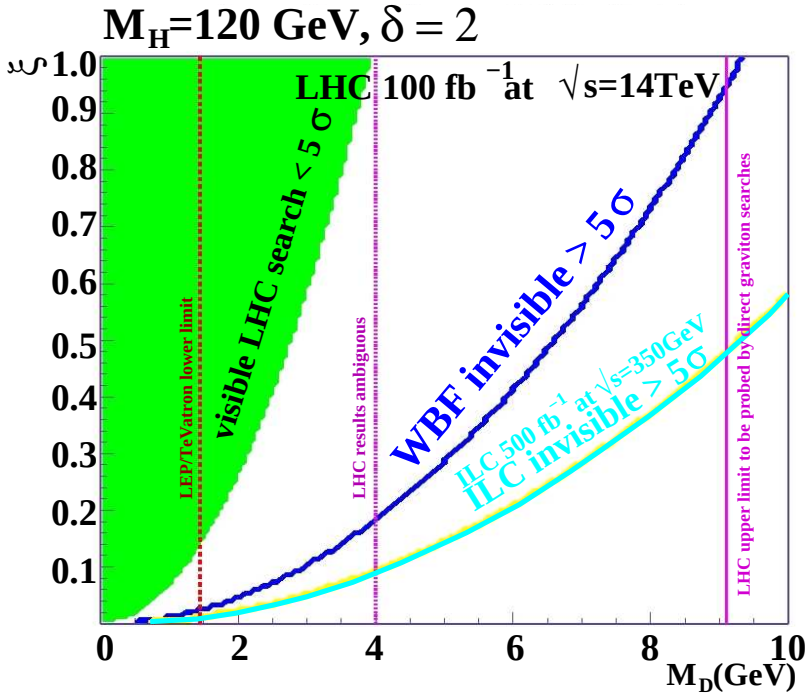

Fig. D.3: *Invisible decay width effects in the ξ - M_D plane for M_H=120 GeV with $\delta = 2$. The green regions indicate where the Higgs signal at the LHC drops below the 5 σ threshold for 100 fb^{-1} of data. The regions above the blue bold line are the parts of the parameter space where the LHC invisible Higgs signal in the WW-fusion channel exceeds 5 σ significance. The solid vertical line at the largest M_D value in each figure shows the upper limit on M_D which can be probed at the 5 σ level by the analysis of jets/γ with missing energy at the LHC. The middle dotted vertical line shows the value of below which the theoretical computation at the LHC is ambiguous – a signal could still be present there, but its magnitude is uncertain. The dashed vertical line at the lowest M_D value is the 95% CL lower limit coming from combining Tevatron and LEP/LEP2 limits. The regions above the cyan line are the parts of the parameter space where the LC invisible Higgs signal will exceed 5 σ assuming $\sqrt{s} = 350$ GeV and $L = 500 fb^{-1}$ (from [65]).*

basis of studies from 2005, are indicated. For the LHC, 100 fb^{-1} of data collected at $\sqrt{s} = 14$ TeV are assumed. As the significance in the visible channels drops below 5σ (green area) due to the invisible graviscalar decays, the discovery in the extra-dimensional scenario still can be made using the invisible channel. In case of Higgs mass set to 120 GeV, in the Higgs graviscalar scenario the invisible branching is high but no dilution due to a very large decay width is expected, if the gravity scale is high enough. E.g for $\delta = 2$ and $\xi = 1$ the invisible Higgs width will be 0.62 GeV in case of $M_D = 1500$, and 50 GeV in case of $M_D = 500$. In conclusion, whenever the sensitivity for a light Higgs boson is lost due to the suppression of the canonical decay modes, the invisible rate is large enough to still ensure detection through the *WW* fusion channel.

But in case the Higgs probed at the LHC becomes heavier, it may be that the Higgs width exceeds the experimental resolution and a width dependent search will become handy. For that reason we wanted to attempt to interpret the expected excluded hypotheses in a scenario with Higgs-graviscalar mixing. As for the LEP search, we first give an overview of the calculated invisible width contribution in the graviscalar scenario for some typical masses in Tab. D.4.

invisible decay width (GeV) by strong Higgs graviscalar mixing $\xi = 1$				
	M_H(GeV)	$M_D = 1.5$ TeV	$M_D = 1.0$ TeV	$M_D = 0.5$ TeV
$\delta = 2$	130	0.8	4.	64.
	200	2.8	15.	232.
	800	183.	926.	$\gg$ TeV
$\delta = 3$	130	0.2	1.7	53.
	200	1.2	9.	296.
	800	312.	2372	$\gg$ TeV
$\delta = 4$	130	0.04	0.4	27.
	200	0.3	3.6	233.
	800	327.	3726	$\gg$ TeV
$\delta > 4$	130	not resolved		
	200			
	800	$\mathcal{O}$(100 GeV)	$\gg$ TeV	

Tab. D.4: Calculated invisible width using Eq. D.1 for various M_D, assuming strong mixing ($\xi = 1$) in dependence from the number of extra-dimensions. The example Higgs masses of 130 GeV and 200 GeV are expected to lie within the sensitivity of ATLAS invisible Higgs searches in 30 fb^{-1}of data at $\sqrt{s} = 14$ TeV, while 800 GeV is outside. As for LEP for scales of M_D not already excluded and Higgs masses accessible within the LHC mass range, the width is always of the order or below the mass resolution.

The parameter space accessible for exclusion with the width dependent search is displayed as light blue area in Fig. D.4 and Fig. D.5. The parameter space is not expected to be probed far beyond the existing lower bounds (red vertical lines). The reach for higher gravity scales above the lower bounds becomes smaller, if the number of extra-dimensions is raised.

For the comparison, we interpreted the published updated invisible Higgs sensitivity study of ATLAS [7] from 2008, assuming Higgs production in weak boson fusion with SM cross sections and 30 fb^{-1} of data at $\sqrt{s} = 14$ TeV . Then the lower limits at 95% CL on the invisible branching for a given Higgs mass can be translated into the $M_D - \xi$-plane. The result is marked in Fig. D.4 and Fig. D.5, by the green contours. In the area above these contours, the narrow width search would be able to detect an invisible Higgs, the potential to exclude the Higgs would be even larger. On the other hand the width dependent search can only exclude a much smaller part of the parameters space compared to the narrow width optimised search. As Tab. D.4 demonstrates higher Higgs masses mark the part of the parameter space in which a width dependent search strategy would be appropriate. Though it is clear, since the sensitivity for very heavy Higgs masses, is lost due to the small cross section and the large systematics impact, a width dependent search in the Higgs-graviscalar mixing scenario is not beneficial. Since for the covered mass range the mixing induced width stays small, the narrow invisible Higgs search are more sensitive on M_D. But again to improve the direct limits on M_D in an unique way (i.e. not depending on ξ), one has to use other channels that produce gravitons with large rate and exploit the full mass range of the LHC. As an example, it is estimated that the corresponding scales of M_D which can be probed in mono jet searches at the LHC for direct graviton production (violet vertical line in Fig. D.3) are about 4 times higher as the existing lower bounds.

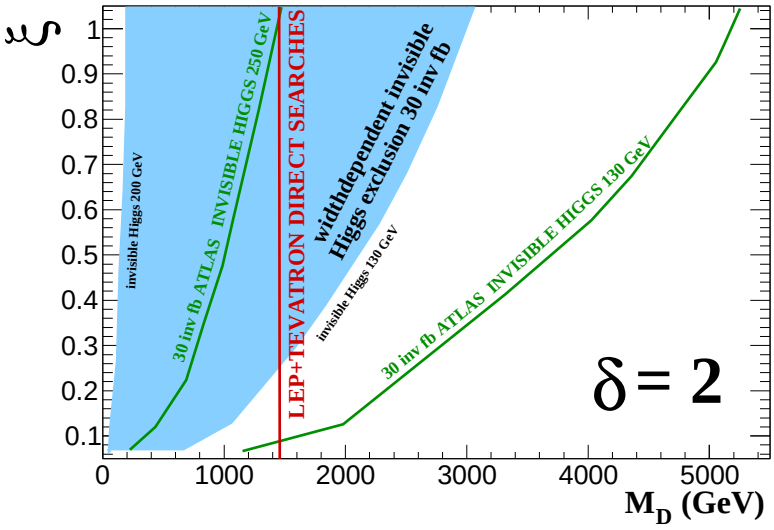

Fig. D.4: *Interpretation of the expected excluded M_H-Γ_H hypotheses in the broad invisible Higgs scenario as excluded part (light blue) in the M_D-ξ plane in the Higgs-graviscalar mixing scenario. In this scenario is $\delta = 2$ chosen. But even for large mixing of $\xi = 1$ the invisible width from mixing stays below the experimental resolution. In that case an interpretation of the ATLAS sensitivity for a narrow invisible Higgs [7] yields higher sensitivity for M_D. This is indicated by the green contours for Higgs masses of 130 GeV and 250 GeV. The red vertical line corresponds to lower limits on M_D, set by direct graviton searches.*

New strategy for Higgs mass and width sensitivity in complex final states at the LHC

As already mentioned in Chapter 2.2.3, the Higgs regularises the weak boson scattering amplitudes. A broadened but invisible Higgs can be seen in such processes. This observation was the motivation for recently undertaken studies for the sensitivity to Higgs width and mass in more complex final states. In [38] complex final states like $pp \rightarrow ZZt\bar{t}(\bar{b})$ or $pp \rightarrow W^+W^-t\bar{t}(\bar{b})$ were regarded. The cross sections for the production of weak boson pairs in association with heavy quarks (beside from top quarks, beauty quarks can become of interest in models that enhance the coupling to those) were calculated. It was argued that for example in a Higgs mass range below 180 GeV the reconstruction of the complex final state will reveal not only the Higgs but is sensitive to the actual Higgs width in the order of two to eight times of the SM Higgs width. These theoretical investigation are only at the beginning and still to be proved experimentally to be feasible, but with reference to Tab. D.4 this width sensitivity provided by these search channels would match very well to requirements of ATLAS studies in the light Higgs-graviscalar mixing scenario.

Interplay of ILC and LHC

We have seen that the situation at the LHC can become problematic if the Higgs is very heavy and the scale of gravity M_D is several TeV. From this, one concludes that it needs more luminosity and a more precise analysis method like the information stemming form recoil mass spectra. The reconstruction of recoil mass spectra is very well possible at electron-positron colliders, if the Higgs is produced in Higgsstrahlung. The sensitivity for the light Higgs at higher values of M_D will be reached due to a possible future linear collider (LC), which is intended to be an electron-positron collider. The LC would be a machine that could deliver large luminosity at high centre of mass energies, providing the sensitivity

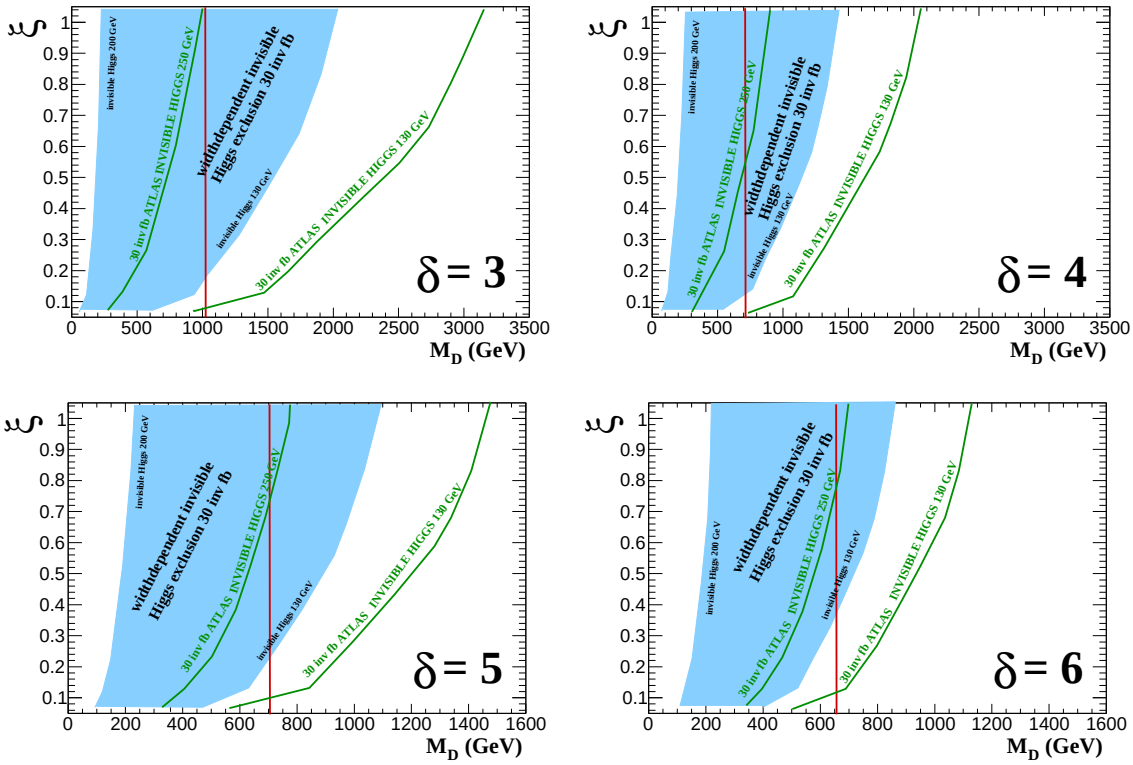

Fig. D.5: *Interpretation of the expected excluded M_H-Γ_H hypotheses in the broad invisible Higgs scenario as excluded part(light blue) in the M_D-ξ plane in the Higgs graviscalar mixing scenario. The contours correspond to a scenario with scenario $\delta = 3$ (upper left panel), $\delta = 4$ (upper right panel) and $\delta = 5$ (lower left panel), $\delta = 6$ (lower right panel). Also the discovery contours for a light invisibly decaying Higgs form the ATLAS studies [7] are given as green contours. The red vertical lines correspond to lower limits on M_D, set by direct graviton searches (Tab. D.2). The sensitivity of the width dependent search cannot match searches for narrow invisible Higgs decays in the low Higgs mass range.*

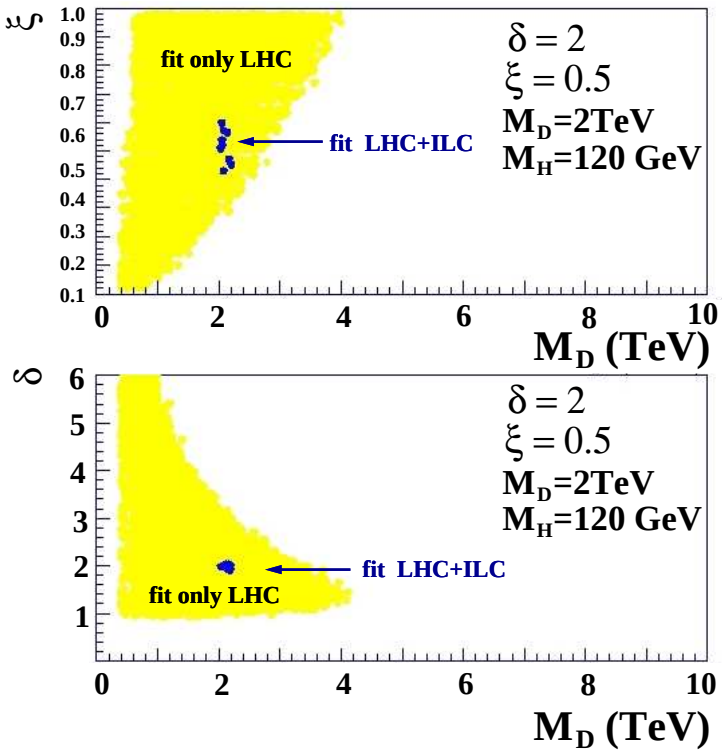

Fig. D.6: *Expected precision of a combined $\Delta\chi^2$-fit from LHC and LC data. Assumed is a scenario of $\delta = 2$ and $\xi = 0.5$, when the scale of gravity is $M_{\rm D} = 2$ TeV, and the Higgs has a mass of $M_{\rm H} = 120$ GeV. The yellow areas give the 95% CL contours of a fit to the model parameters with the LHC data alone (assuming $\sqrt{s} = 14$ TeV and $L = 100 fb^{-1}$) and the smaller blue contour is the estimated improvement of the fit result by adding LC data (assuming $\sqrt{s} = 500$ GeV and $L = 500 fb^{-1}$ plus $\sqrt{s} = 1000$ GeV and $L = 1000 fb^{-1}$).*

for higher values of $M_{\rm D}$. In Fig. D.3 the enhanced potential for discovery compared to the LHC (having collected 100 fb^{-1} of data at $\sqrt{s} = 14$ TeV) is indicated by the cyan contour, assuming for a LC operated at $\sqrt{s} = 350$ GeV and collected data of $L = 500$fb^{-1}. In case that higher scales of $M_{\rm D}$ are realised in nature the weak boson fusion invisible searches lose sensitivity for small ξ, since the invisible rate which is inverse proportional to $M_{\rm D}$ drops. In that case the LC can bring much improvement. The possibility to reconstruct recoil mass spectra in invisible Higgs searches in the LC will provide a very sensitive method for discovery, fully compensating for the reduction of the invisible rate for large $M_{\rm D}$.

Aside from the discovery, the determination of the nature of the extra-dimensions will pose a great challenge even for a LC. In Fig. D.6, from [65], the result of a fit on the model parameters displayed as 95% CL regions. The yellow contour assuming 100 fb^{-1} data from the LHC at design luminosity. One sees that the LHC allone will fail to unravel the nature of extra-dimensions. A tunable LC may be used to measure the cross sections at two centre of mass energies like $\sqrt{s} = 500$ GeV and $\sqrt{s} = 1000$ GeV, which gives very strong constraints. A precision measurement possibly on the percent level of the invisible branching at the LC can in combination with the LHC data narrow the fit region that the accuracy with which ξ is known allows a precise fit and to pinpoint the number of extra-dimension δ, as Fig. D.6 illustrates. But it must be emphasised that that would be the outcome of a long physics program. This extrapolation assumed 500 fb^{-1} at $\sqrt{s} = 500$ GeV plus 1000 fb^{-1} at $\sqrt{s} = 1000$ GeV. But still this is a further example how the LC with its high precision can complement the knowledge about discoveries made at the LHC.

Bibliography

[1] G. Aad et al. Inner detector - technical design report. 1, 1997.

[2] G. Aad et al. *ATLAS detector and physics performance: Technical Design Report, 1*. Technical Design Report ATLAS. CERN, Geneva, 1999. Electronic version not available.

[3] G. Aad et al. *ATLAS detector and physics performance: Technical Design Report, 2*. Technical Design Report ATLAS. CERN, Geneva, 1999. CERN-LHCC-99-15.

[4] G. Aad et al. Atlas pixel detector electronics and sensors. *Journal of Instrumentation*, 3, 2008.

[5] G. Aad et al. The atlas transition radiation tracker (trt) proportional drift tube: Design and performance. *Journal of Instrumentation*, 3, 2008.

[6] G. Aad et al. The ATLAS Experiment at the CERN Large Hadron Collider. *JINST*, 3:S08003, 2008.

[7] The ATLAS Collaboration: G. Aad, E. Abat, and Abbott. Expected performance of the atlas experiment - detector, trigger and physics. pages 1419–1450, 2008.

[8] K. Aamodt et al. The ALICE Experiment at the CERN LHC. *Journal of Instrumentation*, 3, 2008.

[9] V. M. Abazov et al. Search for higgs boson production in dilepton and missing energy final states with 5.4 fb^{-1} of $p\bar{p}$ collisions at $\sqrt{s} = 1.96\,tev$. *Phys. Rev. Lett.*, 104(6):061804, Feb 2010.

[10] G. Abbiendi et al. Search for invisibly decaying Higgs bosons with large decay width using the OPAL detector at LEP. *Eur. Phys. J.*, C49:457–472, 2007.

[11] E. Accomando et al. Workshop on CP Studies and Non-Standard Higgs Physics. 2006.

[12] E. G. Adelberger, Blayne R. Heckel, and A. E. Nelson. Tests of the gravitational inverse-square law. *Ann. Rev. Nucl. Part. Sci.*, 53:77–121, 2003.

[13] O. Adriani et al. The lhcf detector at the cern large hadron collider. *Journal of Instrumentation*, 3, 2008.

[14] S. Agostinelli et al. G4–a simulation toolkit. *Nuclear Instruments and Methods in Physics Research Section A: Accelerators, Spectrometers, Detectors and Associated Equipment*, 506(3):250 – 303, 2003.

[15] S. N. Ahmed et al. Measurement of the total active B-8 solar neutrino flux at the Sudbury Neutrino Observatory with enhanced neutral current sensitivity. *Phys. Rev. Lett.*, 92:181301, 2004.

[16] Z. Ahmed et al. Dark Matter Search Results from the CDMS II Experiment. *Science*, 327:1619–1621, 2010.

[17] R. Akhoury, J. J. van der Bij, and H. Wang. Interplay between perturbative and non-perturbative effects in the stealthy Higgs model. *Eur. Phys. J.*, C20:497–505, 2001.

[18] B. C. Allanach et al. Les Houches 'Physics at TeV Colliders 2003' Beyond the Standard Model Working Group: Summary report. 2004.

[19] J. Allison, K. Amako, et al. Geant4 developments and applications. *Nuclear Science, IEEE Transactions on*, 53(1):270 –278, Februar 2006.

[20] G. Altarelli and G. Parisi. Asymptotic freedom in parton language. *Nuclear Physics B*, 126(2):298 – 318, 1977.

[21] A. Alves et al. The lhcb detector at the lhc. *Journal of Instrumentation*, 3, 2008.

[22] G.and others Anelli. The totem experiment at the cern large hadron collider. *Journal of Instrumentation*, 3, 2008.

[23] P. L. Anthony et al. Observation of parity nonconservation in møller scattering. *Phys. Rev. Lett.*, 92(18):181602, May 2004.

[24] Ignatios Antoniadis, Nima Arkani-Hamed, Savas Dimopoulos, and G. R. Dvali. New dimensions at a millimeter to a Fermi and superstrings at a TeV. *Phys. Lett.*, B436:257–263, 1998.

[25] Nima Arkani-Hamed, Savas Dimopoulos, and G. R. Dvali. The hierarchy problem and new dimensions at a millimeter. *Phys. Lett.*, B429:263–272, 1998.

[26] A. Artamonov et al. The atlas forward calorimeters. *JINST*, 3(02):P02010, 2008.

[27] K. A. Assamagan et al. The Higgs working group: Summary report 2003. 2004.

[28] Omri Bahat-Treidel, Yuval Grossman, and Yoram Rozen. Hiding the Higgs at the LHC. *JHEP*, 05:022, 2007.

[29] Sunil Bansal, K. Mazumdar, and J. B. Singh. Search for invisible Higgs in CMS. *PoS*, HCP2009:063, 2009.

[30] V. Barger, R. J. N. Phillips, and D. Zeppenfeld. Minijet veto: a tool for the heavy higgs search at the lhc. *Physics Letters B*, 346(1-2):106 – 114, 1995.

[31] M. Battaglia, D. Dominici, J. F. Gunion, and J. D. Wells. The invisible Higgs decay width in the ADD model at the LHC. 2004.

[32] K. Belotsky, Daniele Fargion, M. Khlopov, R. Konoplich, and K. Shibaev. Invisible Higgs boson decay into massive neutrinos of 4th generation. *Phys. Rev.*, D68:054027, 2003.

[33] Edmond L. Berger and John M. Campbell. Higgs boson production in weak boson fusion at next-to- leading order. *Phys. Rev.*, D70:073011, 2004.

[34] S. Bertolini and A. Santamaria. Stability of the vev hierarchy and higgs boson invisibility in majoron models. *Physics Letters B*, 213(4):487 – 492, 1988.

[35] T. Binoth, A. Ghinculov, and J. J. van der Bij. NLO correction to Higgs boson parameters in the 1/N expansion. *Phys. Lett.*, B417:343–346, 1998.

[36] T. Binoth and J. J. van der Bij. Influence of strongly coupled, hidden scalars on Higgs signals. *Z. Phys.*, C75:17–25, 1997.

[37] T. Binoth and J. J. van der Bij. The stealthy Higgs model at future linear colliders. *Sitges 1999 Physics and experiments with future linear e+ e- colliders*, pages 591–595, 1999.

[38] E. E. Boos, S. V. Demidov, and D. S. Gorbunov. Invisible Higgs in weak bosons associative production with heavy quarks at LHC: probing mass and width. 2010.

[39] Oliver Brein, Abdelhak Djouadi, and Robert Harlander. NNLO QCD corrections to the Higgs-strahlung processes at hadron colliders. *Phys. Lett.*, B579:149–156, 2004.

[40] C. P. Burgess, Maxim Pospelov, and Tonnis ter Veldhuis. The minimal model of nonbaryonic dark matter: A singlet scalar. *Nucl. Phys.*, B619:709–728, 2001.

[41] Matteo Cacciari, Gavin P. Salam, and Gregory Soyez. The anti-k_t jet clustering algorithm. *JHEP*, 04:063, 2008.

[42] R. N. Cahn and Sally Dawson. Production of very massive higgs bosons. *Physics Letters B*, 136(3):196 – 200, 1984.

[43] John M. Campbell, J. W. Huston, and W. J. Stirling. Hard Interactions of Quarks and Gluons: A Primer for LHC Physics. *Rept. Prog. Phys.*, 70:89, 2007.

[44] S. Catani, Yu. L. Dokshitzer, M. H. Seymour, and B. R. Webber. Longitudinally-invariant k[perpendicular]-clustering algorithms for hadron-hadron collisions. *Nuclear Physics B*, 406(1-2):187 – 224, 1993.

[45] S. Catani, F. Krauss, R. Kuhn, and B. R. Webber. QCD Matrix Elements + Parton Showers. *JHEP*, 11:063, 2001.

[46] Donatella Cavalli et al. Performance of the atlas fast simulation atlfast. Technical Report ATLAS Internal Note ATL-PHYS-INT-2007-005, CERN, Geneva, 2007.

[47] D. G. Cerdeno, A. Dedes, and T. E. J. Underwood. The minimal phantom sector of the standard model: Higgs phenomenology and Dirac leptogenesis. *JHEP*, 09:067, 2006.

[48] M. S. Chanowitz. *Proceedings of the 23rd International Conference on High Energy Physics*. World Scientific, Singapore, 1987.

[49] S. Chatrchyan et al. The cms experiment at the cern lhc. *Journal of Instrumentation*, 3, 2008.

[50] Y. Chikashige, Rabindra N. Mohapatra, and R. D. Peccei. Are There Real Goldstone Bosons Associated with Broken Lepton Number? *Phys. Lett.*, B98:265, 1981.

[51] M. L. Ciccolini, S. Dittmaier, and M. Kramer. Electroweak radiative corrections to associated W H and Z H production at hadron colliders. *Phys. Rev.*, D68:073003, 2003.

[52] Y Coadou, Pa Malecki, and E Richter-Was. Prospects for physics measurements with the w $\rightarrow \tau\nu$ process for 100 pb-1 with the atlas detector. Technical Report ATL-PHYS-INT-2009-011. ATL-COM-PHYS-2008-112, CERN, Geneva, Aug 2008.

[53] The ATLAS Collaboration. *ATLAS detector and physics performance: Technical Design Report*. Technical Design Report ATLAS. CERN, Geneva, 1999. Electronic version not available.

[54] The ATLAS Collaboration. Jet energy scale and its systematic uncertainty for jets produced in proton-proton collisions at sqrt(s) = 7 tev and measured with the atlas detector. Technical Report ATLAS-CONF-2010-056, CERN, Geneva, Jul 2010.

[55] G. Corcella et al. HERWIG 6.5: an event generator for Hadron Emission Reactions With Interfering Gluons (including supersymmetric processes). *JHEP*, 01:010, 2001.

[56] K.S. Cranmer. The atlas analysis architecture. *Nuclear Physics B - Proceedings Supplements*, 177-178:126 – 130, 2008. Proceedings of the Hadron Collider Physics Symposium 2007, Proceedings of the Hadron Collider Physics Symposium 2007.

[57] Hooman Davoudiasl, Ryuichiro Kitano, Tianjun Li, and Hitoshi Murayama. The new minimal standard model. *Phys. Lett.*, B609:117–123, 2005.

[58] Daniel de Florian and Massimiliano Grazzini. Higgs production through gluon fusion: Updated cross sections at the tevatron and the lhc. *Physics Letters B*, 674(4-5):291 – 294, 2009.

[59] Francesco D'Eramo. Dark matter and Higgs boson physics. *Phys. Rev.*, D76:083522, 2007.

[60] Marco A. Diaz, M. A. Garcia-Jareno, Diego A. Restrepo, and J. W. F. Valle. Seesaw Majoron Model of Neutrino Mass and Novel Signals in Higgs Boson Production at LEP. *Nucl. Phys.*, B527:44–60, 1998.

[61] Keith R. Dienes, Emilian Dudas, and Tony Gherghetta. Light neutrinos without heavy mass scales: A higher- dimensional seesaw mechanism. *Nucl. Phys.*, B557:25, 1999.

[62] Abdelhak Djouadi. The anatomy of electroweak symmetry breaking: Tome i: The higgs boson in the standard model. *Physics Reports*, 457(1-4):1 – 216, 2008.

[63] C Doglioni. Jet energy scale uncertainty and resolution in the atlas experiment. Technical Report ATL-COM-PHYS-2011-884, CERN, Geneva, Jul 2011. 21/07/2011.

[64] Yuri L. Dokshitzer. Calculation of the Structure Functions for Deep Inelastic Scattering and e+ e- Annihilation by Perturbation Theory in Quantum Chromodynamics. *Sov. Phys. JETP*, 46:641–653, 1977.

[65] Daniele Dominici. Probing extra dimensions through the invisible Higgs decay. *Czech. J. Phys.*, 55:B627–B634, 2005.

[66] Daniele Dominici and John F. Gunion. Invisible Higgs Decays from Higgs Graviscalar Mixing. *Phys. Rev.*, D80:115006, 2009.

[67] Manuel Drees. An Introduction to supersymmetry. 1996.

[68] G. Duckek et al. *ATLAS computing: Technical Design Report*. Technical Design Report ATLAS. CERN, Geneva, 2005. revised version submitted on 2005-06-20 16:33:46.

[69] Richard Keith Ellis. An update on the next-to-leading order Monte Carlo MCFM. *Nucl. Phys. Proc. Suppl.*, 160:170–174, 2006.

[70] Stephen D. Ellis and Davison E. Soper. Successive combination jet algorithm for hadron collisions. *Phys. Rev. D*, 48(7):3160–3166, Oct 1993.

[71] F. Englert and R. Brout. Broken symmetry and the mass of gauge vector mesons. *Phys. Rev. Lett.*, 13(9):321–323, Aug 1964.

[72] Lyndon Evans and Philip Bryant. Lhc machine. *Journal of Instrumentation*, 3(08):S08001, 2008.

[73] T. Figy, C. Oleari, and D. Zeppenfeld. Next-to-leading order jet distributions for Higgs boson production via weak-boson fusion. *Phys. Rev.*, D68:073005, 2003.

[74] Stefano Frixione, Paolo Nason, and Bryan R. Webber. Matching NLO QCD and parton showers in heavy flavour production. *JHEP*, 08:007, 2003.

[75] Stefano Frixione and Bryan R. Webber. Matching NLO QCD computations and parton shower simulations. *JHEP*, 06:029, 2002.

[76] S. Gabriel and S. Nandi. A new two Higgs doublet model. *Phys. Lett.*, B655:141–147, 2007.

[77] A. Ghinculov, T. Binoth, and J. J. van der Bij. Higgs mass saturation effect and the LHC discovery potential. *Phys. Lett.*, B427:343–347, 1998.

[78] A. Ghinculov, T. Binoth, and J. J. van der Bij. Nonperturbative Higgs propagator: NLO correction in the 1/N expansion. *Phys. Rev.*, D57:1487–1494, 1998.

[79] Adrian Ghinculov and Thomas Binoth. On the position of a heavy Higgs pole. *Phys. Lett.*, B394:139–146, 1997.

[80] F. Gianotti et al. Physics potential and experimental challenges of the LHC luminosity upgrade. *Eur. Phys. J.*, C39:293–333, 2005.

[81] Gian F. Giudice, Riccardo Rattazzi, and James D. Wells. Graviscalars from higher-dimensional metrics and curvature-Higgs mixing. *Nucl. Phys.*, B595:250–276, 2001.

[82] Gian Francesco Giudice and Alessandro Strumia. Constraints on extra dimensional theories from virtual graviton exchange. *Nucl. Phys.*, B663:377–393, 2003.

[83] Sheldon L. Glashow. Partial-symmetries of weak interactions. *Nuclear Physics*, 22(4):579–588, 1961.

[84] Tanju Gleisberg et al. SHERPA 1.alpha, a proof-of-concept version. *JHEP*, 02:056, 2004.

[85] J. Goldstone. Field theories with Âń superconductor Âż solutions. *Il Nuovo Cimento (1955-1965)*, 19:154–164, 1961. 10.1007/BF02812722.

[86] V. N. Gribov and L. N. Lipatov. e+ e- pair annihilation and deep inelastic e p scattering in perturbation theory. *Sov. J. Nucl. Phys.*, 15:675–684, 1972.

[87] David J. Griffiths. *Introduction to Elementary Particles*. Wiley-VCH, Hoboken NJ, 2nd edition edition, October 2008.

[88] Atlas Pile Up Performance Group. Atlas pile-up simulation and perfomance documentation. Technical report, CERN, Geneva, 2008.

[89] LEP Higgs Working Group. Searches for invisible Higgs bosons: Preliminary combined results using LEP data collected at energies up to 209 GeV. 2001.

[90] G. S. Guralnik, C. R. Hagen, and T. W. B. Kibble. Global conservation laws and massless particles. *Phys. Rev. Lett.*, 13(20):585–587, Nov 1964.

[91] Rudolf Haag, Jan T. Lopuszanski, and Martin Sohnius. All possible generators of supersymmetries of the s-matrix. *Nuclear Physics B*, 88(2):257 – 274, 1975.

[92] Naoyuki Haba, Kin-ya Oda, and Ryo Takahashi. Dirichlet Higgs in extra-dimension, consistent with electroweak data. 2009.

[93] Naoyuki Haba, Kin-ya Oda, and Ryo Takahashi. Phenomenological Aspects of Dirichlet Higgs Model from Extra-Dimension. *JHEP*, 07:079, 2010.

[94] J. P. Hall, S. F. King, R. Nevzorov, S. Pakvasa, and M. Sher. Novel Higgs Decays and Dark Matter in the E(6)SSM. 2010.

[95] Tao Han, G. Valencia, and S. Willenbrock. Structure function approach to vector boson scattering in p p collisions. *Phys. Rev. Lett.*, 69:3274–3277, 1992.

[96] S. Heinemeyer, W. Hollik, and G. Weiglein. FeynHiggs: a program for the calculation of the masses of the neutral CP-even Higgs bosons in the MSSM. *Comput. Phys. Commun.*, 124:76–89, 2000.

[97] Peter W. Higgs. Broken symmetries and the masses of gauge bosons. *Phys. Rev. Lett.*, 13(16):508–509, Oct 1964.

[98] Peter W. Higgs. Spontaneous symmetry breakdown without massless bosons. *Phys. Rev.*, 145(4):1156–1163, May 1966.

[99] G. Hinshaw et al. Five-Year Wilkinson Microwave Anisotropy Probe (WMAP[1]) Observations:Data Processing, Sky Maps, & Basic Results. *Astrophys. J. Suppl.*, 180:225–245, 2009.

[100] Stefan Hoeche et al. Matching parton showers and matrix elements. 2006.

[101] Andreas Hoecker et al. TMVA - Toolkit for Multivariate Data Analysis. *arXiv:physics/0703039*, Mar 2007.

[102] Wei-Shu Hou. CP Violation and Baryogenesis from New Heavy Quarks. *Chin. J. Phys.*, 47:134, 2009.

[103] Keiji Igi and Muneyuki Ishida. Predictions of pp, $\bar{p}p$ total cross section and ρ ratio at LHC and cosmic-ray energies. *Phys. Lett.*, B622:286–294, 2005.

[104] R. Jones and D. Barberis. The atlas computing model. *IEEE Transactions on Nuclear Science*, 56(5):2850, 2009.

[105] Anjan S. Joshipura and Saurabh D. Rindani. Fast neutrino decay in the minimal seesaw model. *Phys. Rev. D*, 46(7):3000–3007, Oct 1992.

[106] Anjan S. Joshipura and Saurabh D. Rindani. Majoron models and the Higgs search. *Phys. Rev. Lett.*, 69:3269–3273, 1992.

[107] Anjan S. Joshipura and J. W. F. Valle. Invisible higgs decays and neutrino physics. *Nuclear Physics B*, 397(1-2):105 – 122, 1993.

[108] S. Kaiser. Central-jet veto in vbf h->ww with pile-up. Technical report, CERN, Geneva, Jun 2008.

[109] T. W. B. Kibble. Symmetry breaking in non-abelian gauge theories. *Phys. Rev.*, 155(5):1554–1561, Mar 1967.

[110] F. Krauss. Matrix elements and parton showers in hadronic interactions. *JHEP*, 08:015, 2002.

[111] F. Krauss, R. Kuhn, and G. Soff. AMEGIC++ 1.0: A Matrix element generator in C++. *JHEP*, 02:044, 2002.

[112] F. Krauss, A. Schalicke, and G. Soff. APACIC++ 2.0: A Parton cascade in C++. *Comput. Phys. Commun.*, 174:876–902, 2006.

[113] Frank Krauss, Andreas Schälicke, Steffen Schumann, and Gerhard Soff. Simulating $w/z+jets$ production at the cern lhc. *Phys. Rev. D*, 72(5):054017, Sep 2005.

[114] F Maltoni and S Willenbrock. Higgs cross sections at hadron colliders. Technical report, TeV4LHC Higgs working group, Geneva, Oct 2009.

[115] A. D. Martin, R. G. Roberts, W. J. Stirling, and R. S. Thorne. Physical gluons and high E(T) jets. *Phys. Lett.*, B604:61–68, 2004.

[116] Stephen P. Martin. A Supersymmetry Primer. 1997.

[117] Stephen P. Martin and James D. Wells. Motivation and detectability of an invisibly-decaying Higgs boson at the Fermilab Tevatron. *Phys. Rev.*, D60:035006, 1999.

[118] Frank Meisel, Michael Dührssen, Michael Heldmann, and Karl Jakobs. Study of the discovery potential for an invisibly decaying higgs boson via the associated zh production in the atlas experiment. Technical Report ATL-PHYS-PUB-2006-009. ATL-COM-PHYS-2005-066, CERN, Geneva, 2005.

[119] Kirill Melnikov and Frank Petriello. Electroweak gauge boson production at hadron colliders through $o(\alpha_s^2)$. *Phys. Rev. D*, 74(11):114017, Dec 2006.

[120] K. Nakamura et al. The review of particle physics. *Journal of Physics G*, 37:075021, 2010.

[121] H. P. Nilles. Supersymmetry, supergravity and particle physics. *Physics Reports*, 110(1-2):1 – 162, 1984.

[122] G Nunes Hanninger, M Schumacher, and N Wermes. Level-1 trigger studies for the invisibly decaying higgs boson produced in vector boson fusion. Technical Report ATL-COM-PHYS-2008-151, CERN, Geneva, Sep 2008. This note presents the results of my Master's Thesis work carried out until February 2007.

[123] C. Ohm and T. Pauly. The atlas beam pick-up based timing system. *Nuclear Instruments and Methods in Physics Research Section A: Accelerators, Spectrometers, Detectors and Associated Equipment*, 623(1):558 – 560, 2010. 1st International Conference on Technology and Instrumentation in Particle Physics.

[124] Michael E. Peskin and Tatsu Takeuchi. New constraint on a strongly interacting higgs sector. *Phys. Rev. Lett.*, 65(8):964–967, Aug 1990.

[125] James Pinfold. Technical design report of the moedal experiment. Technical Report CERN-LHC-2009-006. MoEDAL-TDR-001, CERN, Geneva, 2009.

[126] J. Pumplin et al. New generation of parton distributions with uncertainties from global QCD analysis. *JHEP*, 07:012, 2002.

[127] G. Punzi. Sensitivity of searches for new signals and its optimization. 2003.

[128] D. Rainwater and D. Zeppenfeld. Observing $h[over \rightarrow]w^{(*)}w^{(*)} \rightarrow e^{\pm}\mu^{\mp}p_T$ in weak boson fusion with dual forward jet tagging at the cern lhc. *Phys. Rev. D*, 60(11):113004, Nov 1999.

[129] D. D. Rebuzzi et al. Cross-sections for Standard Model processes for the Atlas CSC studies. 2009.

[130] Sabine Riemann. Precision electroweak physics at high energies. *Reports on Progress in Physics*, 73(12):126201, 2010.

[131] Sabine Riemann. Precision electroweak physics at high energies. *Rept. Prog. Phys.*, 73:126201, 2010.

[132] Kurt Riesselmann. Limitations of a standard model Higgs boson. 1997.

[133] Thomas G. Rizzo. Probes of universal extra dimensions at colliders. *Phys. Rev. D*, 64(9):095010, Oct 2001.

[134] M Röder et al. Different monte carlo generators in higgs vbf analyses and cjv optimisation. Technical Report ATLAS-PHYS-COM-2008-025, CERN, Geneva, Mar 2008. This note presents the results of my Master's Thesis work carried out until February 2008.

[135] C. Ruwiedel. Update on the jet veto/tag studies with pileup. Technical report, CERN, Geneva, Mar 2008.

[136] C Ruwiedel, G Gaycken, and J Kroseberg. Study of the use of jet-vertex association for the suppression of pileup jets in the central jet veto in vbf $h \to \tau^+\tau^- \to lh$. Technical Report ATL-PHYS-INT-2009-069, CERN, Geneva, Jul 2009.

[137] C Ruwiedel, G Gaycken, and J Kroseberg. Study of the use of jet-vertex association for the suppression of pileup jets in the central jet veto in vbf $h \to \tau^+\tau^- \to lh$. Technical Report ATL-COM-PHYS-2009-237, CERN, Geneva, 2009.

[138] A. D. Sakharov. Violation of CP Invariance, c Asymmetry, and Baryon Asymmetry of the Universe. *Pisma Zh. Eksp. Teor. Fiz.*, 5:32–35, 1967.

[139] A. Salam. *in Elementary Particle Theory, p. 367.* Almqvist and Wiksell, Stockholm, 1968.

[140] Gavin P. Salam and Gregory Soyez. A practical Seedless Infrared-Safe Cone jet algorithm. *JHEP*, 05:086, 2007.

[141] T. Sjostrand and Peter Z. Skands. Transverse-momentum-ordered showers and interleaved multiple interactions. *Eur. Phys. J.*, C39:129–154, 2005.

[142] Torbjorn Sjostrand. Monte Carlo Generators. 2006.

[143] Torbjorn Sjostrand, Stephen Mrenna, and Peter Z. Skands. PYTHIA 6.4 Physics and Manual. *JHEP*, 05:026, 2006.

[144] Torbjörn Sjöstrand and Maria van Zijl. A multiple-interaction model for the event structure in hadron collisions. *Phys. Rev. D*, 36(7):2019–2041, Oct 1987.

[145] Gregory Soyez. The SISCone and anti-k_t jet algorithms. 2008.

[146] Michael Spira and Peter M. Zerwas. Electroweak symmetry breaking and Higgs physics. *Lect. Notes Phys.*, 512:161–225, 1998.

[147] L Tompkins. Performance of the atlas minimum bias trigger in pp collisions at the lhc. Technical Report ATL-DAQ-PROC-2010-033, CERN, Geneva, Sep 2010.

[148] J. J. van der Bij. Radiative corrections in a minimal extension of the standard model. *Nucl. Phys. Proc. Suppl.*, 116:427–431, 2003.

[149] J. J. van der Bij. SM scalar and extra singlet(s). 2007.

[150] J. Virzi. Status of the sherpa validation. Technical report, CERN, Geneva, Oct 2005.

[151] Steven Weinberg. A model of leptons. *Phys. Rev. Lett.*, 19:1264–1266, 1967.

[152] G. P. Zeller et al. A precise determination of electroweak parameters in neutrino nucleon scattering. *Phys. Rev. Lett.*, 88:091802, 2002.

[153] Shou-hua Zhu. Detecting an invisibly Higgs boson at Fermilab Tevatron and CERN LHC. *Eur. Phys. J.*, C47:833–837, 2006.

Acknowledgements

I want to thank very much Prof. Dr. M. Kobel for patiently supervising this thesis. Also I want to thank Prof. Dr. I. Brock for being so kind to be the second assessor and examiner of this thesis and Prof. Dr. H. Dreiner and Prof. Dr. H. Beck for taking part as examiners in defense of the thesis. I am grateful for the countless advice and help I received from my colleaques. I will gratefully remember the good spirit of cooperation experienced over time with many colleaques, as Dr. N. Möser, Dr. M. Warsinsky, Dr. J. Schumacher and Prof. Dr. M. Schumacher, to name but a few. Especially, I want to thank Dr. W. Mader for his efforts in the practical supervision of the thesis. Also I thank Dr. A. Vest and Dr. X. Prudent, F. Seifert and P. Anger for proof reading parts of this thesis. With no doubt I have to gratefully mention the support from Dr. R. Schwierz and A. Petzold by maintaining stable and reliable working infrastructure at the IKTP all the time. Finally, I want to thank very much Prof. Dr. W. Nagel and his team of the Zentrums für Informationsdienste und Hochleistungsrechnen (ZIH). Without the ZIH facilities for high performance computing and the support of the ZIH team, most notably G. Juckeland and J. Doleschal, this work would not have been possible.